AD-A244 904

196100-25-F

Final Report

STUDY OF THE MICROWAVE RESPONSE OF SEA ICE

R.G. ONSTOTT

DTIC
ELECTE
JAN 14 1992
S B D

DECEMBER 1991

92-01172

⊘ΣERIM   P.O. Box 134001
Ann Arbor, MI 48113-4001

92 1 13 080

REPORT DOCUMENTATION PAGE

Form Approved
OMB No. 0704-0188

1a REPORT SECURITY CLASSIFICATION	1b RESTRICTIVE MARKINGS

2a SECURITY CLASSIFICATION AUTHORITY	3 DISTRIBUTION/AVAILABILITY OF REPORT
2b DECLASSIFICATION/DOWNGRADING SCHEDULE	**UNLIMITED**

4 PERFORMING ORGANIZATION REPORT NUMBERS(S)	5. MONITORING ORGANIZATION REPORT NUMBER(S)
196100-25-F	

6a NAME OF PERFORMING ORGANIZATION	6b OFFICE SYMBOL (if applicable)	7a. NAME OF MONITORING ORGANIZATION
Environmental Research Institute of Michigan		Office of Naval Research

6c ADDRESS (City, State, and ZIP Code)	7b. ADDRESS (City, State, and ZIP Code)
P.O. Box 134001 Ann Arbor, MI 48113-4001	SAR Division, Code 11201 NASA Headquarters 800 N. Quincy St. 600 Independence Ave., So. Arlington, VA 22217-5000 Washington, DC 20546

8a NAME OF FUNDING /SPONSORING ORGANIZATION	8b OFFICE SYMBOL (if applicable)	9. PROCUREMENT INSTRUMENT IDENTIFICATION NUMBER
Office of Naval Research		N00014-86-C-0469

8c ADDRESS (City, State, and ZIP Code)	10. SOURCE OF FUNDING NUMBERS			
SAR Division, Code 11201 NASA Headquarters 800 N. Quincy St. 600 Independence Ave., So. Arlington, VA 22217-5000 Washington, DC 20546	PROGRAM ELEMENT NO.	PROJECT NO.	TASK NO.	WORK UNIT ACCESSION NO.

11 TITLE (Include Security Classification)

Study of the Microwave Response of Sea Ice

12 PERSONAL AUTHOR(S)

Robert G. Onstott

13a TYPE OF REPORT	13b. TIME COVERED	14. DATE OF REPORT (Year, Month, Day)	15. PAGE COUNT
Final	FROM 5/86 TO 2/91	December 1991	311

16 SUPPLEMENTARY NOTATION

17 COSATI CODES			18. SUBJECT TERMS (Continue on reverse if necessary and identify by block number)
FIELD	GROUP	SUB-GROUP	

19 ABSTRACT (Continue on reverse if necessary and identify by block number)

This report documents work which has been performed to develop further the application of microwave science to geophysical property retrieval using satellite synthetic aperture radar (SAR). Efforts have included in-situ observations of the microwave properties of sea ice, the documentation of the physical properties which control backscatter intensity, the conduction of laboratory-based studies, the further development and utilization of electromagnetic models, the development of an empirical scattering responses, and the determinations of the sources of backscatter. Included herein is an executive summary of the research approach. Journal and proceeding papers are included to provide the summary of the results obtained.

20 DISTRIBUTION/AVAILABILITY OF ABSTRACT	21 ABSTRACT SECURITY CLASSIFICATION
☒ UNCLASSIFIED/UNLIMITED ☐ SAME AS RPT ☐ DTIC USERS	UNCLASSIFIED

22a NAME OF RESPONSIBLE INDIVIDUAL	22b TELEPHONE (Include Area Code)	22c OFFICE SYMBOL
Robert G. Onstott	313-994-1200	

DD Form 1473, JUN 86   *Previous editions are obsolete.*
ERIM 116

∑ERIM

CONTENTS

TABLES

iii

ΣERIM

I. EXECUTIVE SUMMARY

Fundamental Purpose of Study

The overall purpose of this work has been to further develop the application of microwave science to geophysical property retrieval using satellite synthetic aperture radar (SAR). Efforts toward this goal have included in-situ observations of the microwave properties of sea ice, the documentation of the physical properties which control backscatter intensity, the conduction of laboratory-based studies, the further development and utilization of electromagnetic models, the development of empirical scattering responses, and the determinations of the sources of backscatter.

Research Approach

One objective has been to advance the ability to extract sea ice geophysical information; in particular, type, thickness, state, and physical properties. Improved ice thickness determination, the discrimination among the thinnest ice types, the detection of open water, the detection of the start of the summer melt season, and the detection of the start of the freeze-up during fall are critical inputs in the study of climate change. This has been pursued by documenting the microwave response for various sea ice conditions and the associated physical properties. Hypotheses have been developed based on scattering theory as to the controlling physical properties from which expected backscatter regimes may be anticipated. In addition, parametric tests have been performed to predict the sensitivity of the backscatter response for the various ice forms to temperature, salinity, density, embedded scatterer distributions, dielectric properties, surface roughness statistics, and the characteristics of a surface snow or slush layer. Through the development of expected trends and sensitivities,

1

and with the intercomparison of the frequency and angular response trends of empirical data, a honing of our theoretical understanding has been achieved.

Laboratory Investigations - CRRELEX

A series of laboratory investigations (CRRELEX ' 88, '89, and '90) were conducted of the microwave and physical properties of sea ice grown in an outdoor tank located at the U.S. Army Cold Regions Research and Engineering Laboratory. Polarimetric radar measurements were made in conjunction with extensive passive microwave and ice physics observations. A fully integrated study was achieved where the properties of the ice were controlled (to an acceptable degree at this time) and well characterized. Emphasis was directed to the characterization of the microwave properties of young sea ice forms. This included the examination of the ability to discriminate between new ice and water, the discrimination of young ice types, and the development of an integrated electromagnetic theory for sea ice and snow. With the improvement in the theoretical formulation of sea ice microwave and millimeter-wave signatures, electromagnetic models may begin to contribute to the retrieval of physical property information using satellite derived data. Bistatic radar measurements were also made for the first time ever to document the anisotropic nature of the complex dielectric properties of the sea ice sheet, knowledge important to the theoretical modeling of random media.

Development of Radar Look Up Tables for ASF/GPS

During this period, the development, refinement, integration and testing of radar look-up tables of sea ice radar scattering coefficients was accomplished for use in the National Aeronautics and Space Administration (NASA) Geophysical

Processing System (GPS), whose purpose is to provide ice type as well as other geophysical data products based on satellite SAR microwave signal information. Efforts focussed on tables applicable to ERS-1 (C/VV/23°), J-ERS-1 (L/HH/35°), EOS (C/POL/20°-50°), and SIR-C (L-C-X/POL/20°-50°).

Investigations Performed

A number of investigations have been undertaken and are summarized in Table 1. The year, name of the investigation, site location, month of the activity, ice types observed, and scattering measurement frequencies are indicated.

3

Table 1.

INVESTIGATIONS PERFORMED

YEAR & INVESTIGATION	LOCATION	MONTH	ICE TYPES	FREQUENCY BANDS
1990 CRRELEX	ICE TANK	JAN	OW-ThFY & UREA ICE	L C X Ka (POL) Ku (BISTATIC)
1989 CEAREX	FRAM STR	JAN-MAR	OW-MY	P L C X Ku Ka W
1989 CRRELEX	ICE TANK	JAN/FEB	OW-ThFY	L C X Ka (POL)
1988 CEAREX	FRAM STR	SEPT-DEC	OW-ThFY	P L C X Ku Ka W
1988 CRRELEX	ICE TANK	JAN-FEB	OW-ThFY	L C X (POL) X Ku Ka W
1988 BEEPERS	BOTHNIA	MAR	BRACKISH	X
1987 MIZEX	FRAM STR	MAR	OW-MY	P L C X Ku Ka
1985 CRRELEX	ICE TANK	JAN-MAR	OW-ThFY	C X Ku

Legend:
OW is open water.
ThFY is thin first year ice.
MY is multiyear ice.
POL indicates fully polarimetric radar operation mode.
BISTATIC indicates that bistatic measurements were made.

4

ERIM

Summary of Results

A large number of in-situ observations have been made during this research period. These data provide documentation of the backscatter response and physical properties for the many sea ice forms in various regions and as a function of season. Based on these data, the sensitivity of radar backscatter to changes in physical properties are being established. Results have also been supportive of the quantitative and qualitative interpretation of aircraft SAR observations. The active microwave measurements chapter in the upcoming ONR/NASA Sea Ice Monograph is devoted to the results obtained from these microwave characterizations studies.

These measurements have been, and are being used, in the theoretical and empirical modeling of the electromagnetic properties of sea ice by this investigator and others. A chapter in the Sea Ice Monograph is devoted to this modeling work. Additional contributions have been made to the Polarimetry and CRRELEX chapters.

In summary,

- A library of scattering coefficients have been assembled for sea ice for various seasons and locations.

- Documentation of sea ice conditions and the physical properties responsible for backscatter has been accomplished.

- The importance of the low density ice layer in the upper portion of an ice sheet composed multiyear sea ice has been documented and studied. It has been shown that the properties of this layer determines the backscatter intensity for multiyear ice. This work has

5

guided the types of in-situ measurements necessary to fully
characterize multiyear ice during in-situ sampling programs.

• A description of the seasonal cycle has been made for first-year and
  multiyear ice.

• A sea ice scattering model has been developed which includes
  surface scatter (small perturbation model, physical optics,
  geometrical optics), an integrated volume-surface scattering
  (radiative transfer model), and volume scattering only (second-order
  Born approximation / Kong). These models have been used in
  conjunction with the study of the acquired empirical data. They
  have been used in parametric studies to determine sensitivities to
  environmental conditions.

• A dielectric model [Kovacs, 1986] has been modified to provide
  predictions of permittivity profile, bulk dielectric constant, and
  penetration depth. This model is based on a two-phase dielectric
  mixing model by Tinga. This model is used in conjunction with the
  EM backscatter models.

• The surface roughness statistics for a large number of ice forms
  during different seasons has been compiled. These data will be
  available in the form of a Technical Report. A table of results has
  been presented in the Sea Ice Monograph. The change in roughness
  during the evolution of young first-year ice has been documented.

6

- The evolution of open water to first-year ice has been studied. The case for the evolution to new ice will appear in the Sea Ice Monograph and in an upcoming paper. The evolution to first-year ice is still under study and has been discussed at IGARSS.

- An approach as to how satellite SAR may be used to improve ice concentration estimates during summer has been made [Cavalieri et al, 1990]. This technique is based on using SAR to estimate the areal coverage of open water melt pools on ice floes.

- Radar look up tables for ERS-1, JERS-1, and Radarsat have been developed for utilization in the Alaskan SAR Facility Geophysical Processing System.

- The importance of the frost flower layer on young sea ice has been documented further. Results show that the development of this layer is related to the age and thickness of the thin ice. Work is continuing to determine how this may be used to improve the determination of ice thickness for sea ice cases below 1 m.

- Millimeter-wave measurements have been added to the microwave characterization of sea ice forms.

- Fully polarimetric radar measurements have been made in the field and in the laboratory.

7

- The first bistatic measurement of simulated sea ice has been made in the study of the anisotropy of sea ice.

- The utilization of both active and passive microwave signature has been studied and reported.

- Radar reflectivity measurements have been made and analyzed to document the change in the dielectric properties of sea ice as it evolves from open water to young sea ice.

- It has been observed that frost flower development on young first-year ice is related directly to its scattering coefficient, that the state of frost flower development and ice thickness (first-year) are related, and that this relationship may provide a means to improve the discrimination of young sea ice types.

- It has been observed that there may be a relationship between the properties of the low density layer on multiyear and the thickness of the ice sheet.

Detailed discussions of results and findings are presented in the publications section which has been included herein.

PUBLICATIONS FROM ONR SPONSORED WORK - FY85/FY91
Robert G. Onstott
September 1991

91-C   Onstott, R.G. and T. Grenfell, "Active and Passive Microwave Observations
of Arctic Sea Ice ᴺuring the Fall Freeze-Up," **Proceedings of IGARSS'91**,
Espoo, Finland, 3-6 June 1991.

91-C   Onstott, R.G., "Active Microwave Observations of Arctic Sea Ice During the
Fall Freeze-Up," **Proceedings of IGARSS'91**, Espoo, Finland, 3-6 June 1991.

91-C   Shuchman, R.A., R.G. Onstott, C.C. Wackerman, C.A. Russel, and L.L.
Sutherland, "Multi-Frequency SAR, SSM/I and AVHRR Derived Geophysical
Information of the Marginal Ice Zone," **Proceedings of IGARSS'91**, Espoo,
Finland, 3-6 June 1991.

91-C   Jentz, R.R., C.C. Wackerman, R.A. Shuchman, and R.G. Onstott, "NASA,
Navy, and AES/York Sea Ice Concentration Comparison of SSM/I Algorithms
with SAR Derived Values," **Proceedings of IGARSS'91**, Espoo, Finland, 3-6
June 1991.

91-C   Onstott, R.G., R.A. Shuchman, and C.C. Wackerman, "Polarimetric Radar
Measurements of Arctic Sea Ice During the Coordinated Eastern Arctic
Experiment," **Proceedings of IGARSS'91**, Espoo, Finland, 3-6 June 1991.

91-P   Tucker, W.B., T.C. Grenfell, R.G. Onstott, D.K. Perovich, A.J. Gow,
R.A. Shuchman, and L.L. Sutherland, "Microwave and Physical
Properties of Sea Ice in the Winter Marginal Ice Zone," **Journal of
Geophysical Research**, Vol. 96, No. C3, pp. 4573-4587, March 15, 1991.

90-B   Shuchman, R.A. and R.G. Onstott, "Remote Sensing of the Polar
Oceans", Chapter 3, pg. 123-167, **Polar Oceanography**, ed. Walker
Smith, Academic Press, New York, New York, 1990.

LEGEND:
B = Book, P = Journal Paper, I = Journal Paper in Progress,
IC = Invited Conference Paper, C = Conference Paper, R = Technical Report

90-P Cavalieri, D.J., B.B. Burns, and R.G. Onstott, "Investigation of the Effects of Summer Melt on the Calculation of Sea Ice Concentration Using Active and Passive Microwave Data," **Journal of Geophysical Research**, Vol. 95, No. C4, pg. 5359-5369, April 1990.

90-P Gogineni, S., R.K. Moore, Q. Wang, A. Gow, and R.G. Onstott, Radar Backscatter Measurements Over Saline Ice," **International Journal of Remote Sensing**, Vol. 11, No. 4, 603-615, 1990.

90-IC Onstott, R.G., "Microwave and Surface Observations in Support of Radar Altimeter Studies," **Proceedings AGU Altimeter Workshop**, New Orleans, Naval Oceanographic and Atmospheric Research Laboratory, Report # SP-059:321:90, September 1990. (paper not included)

90-R Onstott, R.G., "Polarimetric Radar Measurements of Artificial Sea Ice During CRRELEX '88," ERIM Technical Report #196100-23-T, Ann Arbor, Michigan, April 1990.

90-I Onstott, R.G., "Description of the Microwave Response of Sea Ice and Its Incorporation into the Geophysical Sea Ice Processor at the Alaska SAR Facility via Look Up Tables," to be submitted to **Journal of Geophysical Research Oceans**, 1991. (paper not included)

90-I Kwok, R., B. Holt, F. Carsey, J. Curlander, and R. Onstott, "An Overview of the Geophysical Sea Ice Products Generated at the Alaska SAR Facility," to be submitted to **Journal of Geophysical Research**, January 1991. (paper not included)

90-C Onstott, R.G., "Near Surface Microwave Measurements of Arctic Sea Ice During the Fall Freeze Up," **Proceedings of IGARSS '90 Symposium**, College Park, Maryland, May 1990.

90-C Onstott, R.G., "MIZEX '84 Multifrequency Helicopter-Borne Altimeter Observations of Summer Marginal Sea Ice," **Proceedings of IGARSS '90 Symposium**, College Park, Maryland, May 1990.

90-C Onstott, R.G., "Polarimetric Radar Measurements of Arctic Sea Ice During CEAREX," **Proceedings of IGARSS '90 Symposium**, College Park, Maryland, May 1990.

90-C   Onstott, R.G. and R.A. Shuchman, "Comparison of SAR and Scatterometer Data Collected During CEAREX," **Proceedings of IGARSS '90 Symposium,** College Park, Maryland, May 1990.

90-C   Onstott, R.G., "Polarimetric Radar Measurements of Artificial Sea Ice," **Proceedings of URSI '90 Symposium,** Hyannis, Massachusetts, May 1990.

90-C   Onstott, R.G., "Theoretical and Experimental Study of the Radar Backscatter of Arctic Sea Ice," **Proceedings of URSI '90 Symposium,** Hyannis, Massachusetts, May 1990.

90-I   Onstott, R.G., "Multifrequency Helicopter-Borne Altimeter Observations of Summer Marginal Sea Ice," to be submitted to **Journal of Geophysical Research.** (paper not included)

90-C   Sheen, D.R. and R.G. Onstott, "Effects of Channel Imbalance, Coupling, and Noise in Polarimetric Radar Measurements," **Proc. of IGARSS '90 Symposium,** College Park, Maryland, May 1990.

89-C   Shuchman, R.A., C.C. Wackerman, A.L. Maffett, R.G. Onstott, and L.L. Sutherland, "The Discrimination of Sea Ice Types Using SAR Backscatter Statistics," **Proceedings of IGARSS '89 Symposium,** Vancouver, BC, 1989.

89-C   Onstott, R.G. and S.H. Gaboury, "Active Microwave Classification of Sea Ice," **Proceedings of IGARSS '89 Symposium,** Vancouver, BC, 1989.

89-C   Onstott, R.G., "Polarimetric Radar Measurements of Artificial Sea Ice," **Proceedings of IGARSS '89 Symposium,** Vancouver, BC, 1989.

89-C   Onstott, R.G. and R.A. Shuchman, "Scatterometer Measurements of Wind, Waves and Ocean Fronts During NORCSEX," **Proceedings of IGARSS '89 Symposium,** Vancouver, BC, 1989.

89-C   Onstott, R.G., "Active Microwave Classification of Sea Ice," **North American Sea Ice Symposium,** University of Massachusetts, Amherst, MA, 1989.

11

88-C   Onstott, R.G., R.A. Shuchman, "Multifrequency and Multipolarization Scatterometer for Remote Sensing," presented at **Polar Regions Workshop**, Monterey, CA., January, 1988.

88-C   Onstott, R.G. and S.H. Gaboury, "A Polarimetric Microwave Scatterometer," **Proceedings of IGARSS'88**, Edinburgh, UK, 12-16 September 1988.

88-C   Shuchman, R.A., R.G. Onstott, L.L. Sutherland, and C.C. Wackerman, "Intercomparison of Synthetic- and Real-Aperture Radar Observations of Arctic Sea Ice During Winter MIZEX'87," **Proceedings of IGARSS'88**, Edinburg, UK, 12-16 September 1988.

88-C   Onstott, R.G. and R.A. Shuchman, "Radar Backscatter of Sea Ice During Winter," **Proceedings of IGARSS'88**, Edinburgh, UK, 12-15 September 1988.

88-C   Onstott, R.G., S.H. Gaboury, J. Bredow, and P. Gogineni, "Active Microwave Measurements of Artificial Sea Ice," **Proceedings of IGARSS'88**, Edinburg, UK, 12-16 September 1988.

87-P   Livingstone, C.E., R.G. Onstott, L.D. Arsenault, A.L. Gray, and K.P. Singh, "Microwave Sea Ice Signatures Near the Onset of Melt," <u>**IEEE Transactions on Geoscience and Remote Sensing**</u>, Vol. GE-25, No. 2, March 1987.

87-P   Onstott, R.G., T.C. Grenfell, C. Matzler, C.A. Luther, and E.A. Svendsen, "Evolution of Microwave Sea Ice Signatures During Early Summer and Midsummer in the Marginal Ice Zone," <u>**Journal of Geophysical Research**</u>, Vol. 92, No. C7, pp. 6825-6835, June 30, 1987.

86-C   Onstott, R.G. and R. W. Larson, "Microwave Properties of Sea Ice in the Marginal Ice Zone," **Proceedings of IGARSS'86**, Zurich, Switzerland, 8-11 September 1986.

86-C   Onstott, R.G. and R.A. Shuchman, "A SAR/Scat Intercomparison of Microwave Signatures of Arctic Sea Ice," **Proceedings of the International Union of Radio Science Symposium**, Durham, N.H., 28 July - 1 August, 1986.

86-C   Onstott, R.G., "An Inter-Sensor Comparison of the Microwave Signatures of Arctic Sea Ice," **Proceedings of IGARSS'86**, Zurich, Switzerland, 8-11 September 1986.

ACTIVE AND PASSIVE MICROWAVE OBSERVATIONS OF ARCTIC SEA ICE DURING THE FALL FREEZE-UP

Robert G. Onstott
Center for Earth Sciences
Advanced Concepts Division
Environmental Research Institute of Michigan
P.O. Box 8618 Ann Arbor, MI 48107 USA

Thomas Grenfell
Atmospheric Sciences Department
University of Washington
Seattle, Washington

ABSTRACT

Microwave measurements of sea ice were acquired during the September-October 1989 segment of the Coordinated Eastern Arctic Experiment (CEAREX). During this period an intensive series of in-situ observations were made to study several distinct ice types. In particular, the variation in the physical and microwave properties in the uppermost portion of multiyear ice was studied extensively. Active microwave measurements were made at L-, C-, X-, Ku-, Ka-, and W-bands while passive microwave measurements were made at C-, X-, Ku-, Ka-, and W-bands. Characterization measurements were performed to document the physical and electrical properties in the upper tens of centimeters of the ice sheets.

Key words: Microwave, sea ice, radar, radiometer

INTRODUCTION

Surface based active and passive microwave measurements were made in conjunction with ice property measurements during October in the regions located to the North and East of Svalbard. Measurements were made from the ice-strengthened ship R/V *Polarborn* which served as a drifting station by allowing the ship to be frozen within the ice pack next to a vast multiyear ice floe composed of ice of dissimilar origins. In-situ observations of microwave signatures and physical properties were obtained at a large number of stations during this 8-week period when mean air temperatures were in continual decline. Ice forms in the immediate vicinity of the drift station included multiyear-hummock (numerous sites), multiyear-meltponds (numerous sites), very old multiyear ice, typical multiyear ice, second year ice, first year, and a refrozen lead. Variations in the thickness, density, bubble size and roughness associated with the ice located in the uppermost portion of multiyear ice sheets were detected and documented.

MICROWAVE DATA COLLECTION

The objective of this investigation was to determine, under the freezing conditions of fall, the active and passive microwave signatures for a variety of types of ice and to relate these signatures to the physical properties of the ice. Study sites were selected by visual observations from the surface which suggested ice age and formation conditions and, more specifically, by an initial survey performed by transecting about the ice matrix with a radiometer. Specific ice sites were then surveyed and a location nomenclature developed.

Microwave data were then collected utilizing surface-based towers which were positioned at each of the various sites to obtain angular response data. The towers were also transported about the sites so that inter-floe and intra-floe spatial variation in microwave signatures could be addressed further. The microwave sensor matrix is provided in Table 1. In general, measurements were made from 5 to 94 GHz at various polarizations and angles ranging from 0° to 75°. A photograph is provided in Figure 1 and shows a radiometer being operated from a bipod. Also in this photo is the sled and the various radars mounted at a height of 3 meters.

DISCUSSION

Sites surveyed included young, first-year, and multiyear ice. Systematic variation in the properties in the uppermost portion of multiyear ice sheets was observed. Results from the study of the relationship between the microwave signatures and the variation in the physical properties of low density ice was presented. A cross-sectional diagram of the general structure of multiyear ice found during this investigation is illustrated in Figure 2. Observations were made to specifically determine the sensitivity to multiyear ice with a rough surface, to various thicknesses of low density ice in the upper most portion of the ice sheet (called snice in Figure 2), to the secondary or transitional bubble layer, to the variation in the distributions in bubbles in the upper portion of the ice sheet, and to density variations. A summary of the characterization of the upper portion of the ice sheet for the major multiyear ice sites investigated is presented in Table 2. In addition, the active and passive microwave signatures of the major ice types were intercompared, and the ability to discriminate among them and the added information gained through the fusion of active and passive microwave data was discussed.

Figure 1. This photograph shows a radiometer operated
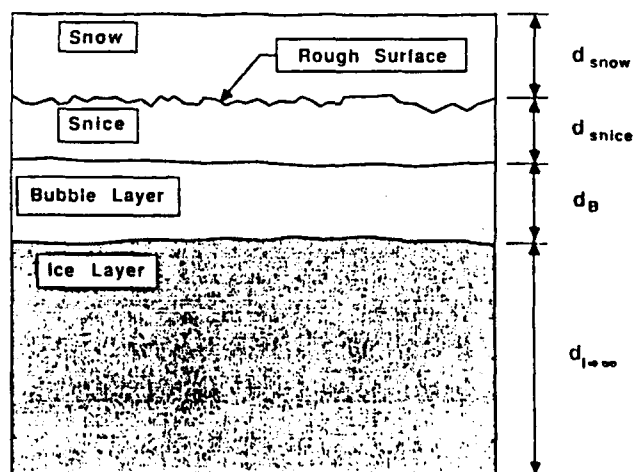from a bipod and the sled and radar assembly.

Figure 2. Cross-sectional view of multiyear sea ice.

Table 1.

Microwave Sensor Measurement Matrix

	C	X	Ku	Ka	W	Angle
Radar	--	VV HH VH HV	VV HH VH HV	VV HH	VV HH	0° to 70°
Radio-meter	V H	V H	V H	V H	V H	25° to 70°

RS-90-015b-R2

Table 2.
UPPER ICE SHEET CHARACTERIZATIONS

Site	Surface Roughness		Low Density Ice Layer									
Drift Station	σ cm rms	l cm	Layer #1					Layer #2				
			Thickness	Salinity	Density	Mean Bubble Diameter	Mean Void Diameter	Thickness	Salinity	Density	Mean Bubble Diameter	Mean Void Diameter
	cm		cm	0/00	gm/cc	mm	cm	cm	0/00	gm/cc	mm	cm
Location 1	0.70±0.12	3.0±1.5	8.5±0.9	2.1	0.673	6.0	0.3	4.9±0.3	0.3	0.874	0.0	0.0
Location 4	0.23±0.05	3.5±0.3	12.4±0.3	0.1	0.651	3.3	0.1					
Location 7	0.14±0.02	2.0±1.3	5.0±0.8	0.0	0.457	2.5	0.8	3.5±0.4	0.0	0.778	4.0	0.2
Location 9	0.77±0.12	4.8±1.2	4.9±1.0	0.0	0.513	2.3	0.7	4 9±0.4	0 0	0.728	4.3	0.0
Location 13	1.01±0.31	3.2±1.2	3.0+1.3	0.0	0.513	3.3	0.5	13.6±0.4	0.0	0.929	1.0	0.0
Alpha												
Location	0.33±0.21	4 7±1.9	14 3±0.3	0.0	0.758	1.6	0.5					
100 Meter												
Location	0.85±0.40	3.9±2.4	13.3±1.4	0 0	0.551	0 8	0 0					
DEL MP												
Location	0 08+0.03	2.8±1.9	5.2±0.3	0 0	0.914	1.3	0.0	4 8±0.3	0.0	0 918	0 0	0 0

ACTIVE MICROWAVE OBSERVATIONS OF ARCTIC SEA ICE DURING THE FALL FREEZE-UP

Robert G. Onstott
Center for Earth Sciences
Advanced Concepts Division
Environmental Research Institute of Michigan
P.O. Box 8618 Ann Arbor, MI 48107 USA

ABSTRACT

Near-surface millimeter and microwave measurements were made during September-October, the fall freeze-up period, in regions located to the North and East of Svalbard. Microwave signatures and physical properties were acquired at a large number of stations and included floes composed of multiyear, first-year, young, and nilas sea ice. Systematic variation in the thickness and density of the ice located in the uppermost portion of multiyear ice sheets was observed. In this paper, the measured and predicted backscatter response was examined at 10 GHz. The impact of fall freeze up on microwave signatures is also presented.

Key Words: Sea ice, microwave, radar, and fall.

INTRODUCTION

The characterization of the microwave properties of sea ice was conducted during the September-October 1989 segment of the Coordinated Eastern Arctic Experiment (CEAREX) in regions located to the North and East of Svalbard. During this investigation the ice-strengthened ship R/V *Polarborn* was allowed to freeze within the ice pack next to a vast multiyear ice floe composed of ice of dissimilar origins. In-situ observations of microwave signatures and physical properties were obtained at a large number of stations during this 8-week period when mean air temperatures were in continual decline. Ice forms in the immediate vicinity of the drift station included multiyear-hummock (numerous sites), multiyear-meltponds (numerous sites), very old multiyear ice, typical multiyear ice, second year ice, first year, and a refrozen lead. Variations in the thickness, density, bubble size and roughness associated with the ice located in the uppermost portion of multiyear ice sheets were detected and documented. Selected examples are provided here to illustrate the impact of these combinations of parameters on their microwave signatures. In addition, the impact of fall freeze up on the microwave signatures of four major sea ice types is presented.

The backscattering data described here were collected utilizing a surface-based tower which was positioned at each of the various sites to obtain angular response data. The tower was also transported using a snowmobile to interconnect these sites so that the inter and intra floe spatial variation in microwave signatures could be addressed further. It is also believed that the physical properties which where sampled discretely may also be extended by their association with their microwave signatures. Polarization diversified data were acquired at 9.38, 18, 35, and 94 GHz over the incidence angle range from 0° to 70°. In this paper, only data at 10 GHz is presented. Sensor specifications are summarized in Table 1.

One of the initiatives of this study is to obtain a better understanding of the mean and variation in the physical properties of sea ice forms and to accompany these observations with their microwave signatures over a wide range of frequencies, polarizations, and angles. Scene variability is important in the context of both geophysical information and physical property retrieval. The data collected are also critical in the validation and development of theoretical sea ice models. For brevity, the discussion presented here is limited to the variation in the properties of the upper-most portion of multiyear ice. In addition, only one of a possible of three major multiyear ice floes will be considered, and only five of a possible ten sites within this floe will be presented.

IMPACT OF FALL FREEZE UP

The impact of fall freeze up has been examined for the time period of about 1 to 15 October when air temperatures ranged from -15°C to-20°C. General results for the four major ice types (multiyear, first year, young, and nilas) are summarized in Table 2. For the cases of multiyear ice, first year ice, and new ice, their signatures are very similar to those obtained during winter conditions. A key factor is that enough cooling has occurred that the cold waves have propagated far enough into the ice sheet so that the above is true. The ice form that is impacted during fall is that of young sea ice. It's physical properties and signature is influenced by slow growing conditions, i.e. the air temperatures are still moderate when compared with winter conditions. The ice in a refrozen lead next to the drift ship did not congeal quickly or thoroughly. The top few centimeters were composed of brine enriched snow (salinity = 26 ppt) and slush. When the sheet became thick enough (35 cm) the upper portion of the lead froze more completely

and a signature enhancement was noted. A discussion of the anatomy of a freezing lead is provided in Gow et al [1].

PHYSICAL AND MICROWAVE PROPERTIES

Five multiyear ice sites have been selected as representative. Four of these sites are from hummocks and one is from a fresh water meltpool. Their physical properties are summarized in Table 3. Important observations will be summarized here. The low density ice (LDI) in the upper portion of the ice sheet is one of the two sources which produce an enhanced backscatter. A pressure ridge which is a topographical feature represents the second. To highlight the importance of the LDI layer, the backscatter response of a hummock and a fresh water meltpool which were separated by fifty meters and were resident on the same multiyear ice floe is provided in Figure 1. The critical difference between these two scenes is the number of discrete scatterers (i.e. gas bubbles) in the top 15 cms of the ice. In addition, the number of scatterers for a given bubble size is related to density. The hummock has a density of 651 kgm^{-3}, while the meltpool has a density of 914 kgm^{-3}, that of pure ice. The lower the density of the LDI layer, the greater is the number of discrete scatterers for the given bubble size. In the incidence angle region from 30° to 60°, the difference (> 15 dB) between these two multiyear ice responses is striking and the mechanism well-defined.

The interface between snow and LDI may be smooth, moderately rough, or very rough. Rms heights ranged from 0.14 to 1.01 cm. Correlation lengths were very similar with a range from 2.0 to 4.6 cm. It is typically necessary to characterize the LDI layer as a layer of ice with a very low density which is then proceeded by a transitional layer, often composed of large globs, which has a density which falls between that of the upper most LDI layer and that of pure ice. The bulk of the remaining ice sheet also has a density similar to that of pure ice. A cartoon is presented in Figure 2 to illustrate the three ice layers and the range of the critical physical properties for the sites under discussion.

The angular responses of the backscatter response of the four multiyear hummock sites are shown in Figure 3 for like (VV and HH) and cross polarization (VH and HV). The width of the mean angular response interval is about 5 dB for like-polarization, cross-polarization is about one dB wider. A preliminary examination of the ability to predict the ranking between these four sites has been made. Basic "rules of thumb" have been generated for the range of physical property parameters measured during the characterization of these sites and using a radiative transfer model with a rough surface and Rayleigh scatterers [2,3]. The results of a parametric study are summarized here:

1) Increasing the bubble diameter from 2 to 3 to 4 mm increases the like-pol return by 5 and 3 dB and the cross-pol return by 8 and 5.5 dB, respectively. Hence, the depolarization ratio decreases from 10 to 7 to 4.5 dB.

2) Increasing the rms roughness from 0.125 to .5 causes a reduction in $\sigma°$ of 2 to 3 dB ($O_{inc} = 0°$ to 55°), with the decrease increasing with incidence angle. Increasing the roughness to 1.0 cm causes an additional decrease of 3 to 6 dB.

3) Increasing the density from 500 to 600 to 700 kgm^{-3} causes a reduction in $\sigma°_{like}$ of 1 and 1.5 dB, respectively. $\sigma°_{cross}$ showed a 2 and 3 dB reduction.

4) If the thickness of the LDI layer is changed from 5 to 10 to 20 cm, then $\sigma°_{like}$ increases by 2.5 dB and then 3 dB. $\sigma°_{cross}$ increased by 5 dB in each case.

5) Varying the correlation length from 2 to 5 cm produced little effect.

The parameters which appear outstanding for each site are now discussed. The slight salinity in the case of Site DS-4 appears important because the LDI layer was well developed, but the overall return was slightly weaker than two other cases. Site DS-7 may be considered to be typical. Site DS-9 is interesting because it represents the weakest like-pol response in this set. Rms roughness was found to be greater for this site. As was noted in the parametric study an increase in roughness will cause a reduction in the like-pol response with little subsequent reduction in the cross-pol response, except at the largest angles. The cross-pol response for this site falls in the middle of the response range for these sites. Site DS-13 is of particular interest in that it fits in the upper portion of both the like and cross polarization response ranges. Its LDI layer is a bit unique in that the upper most portion is relatively thin, but of very low density (513 kgm^{-3}), and is followed by a very high density layer (929 kgm^{-3}) which contains some extremely large globs (diameters of 1 cm). Large bubbles contribute to large cross-sections and to minimizing depolarization ratios.

SUMMARY

Fall freeze up in mid-October was found to have its greatest impact on the microwave signature of young sea ice. This was attributed to warm temperatures and slow growing conditions when compared to those of winter. Ice signatures for multiyear, first year, and nilas were found to be winter-like. The physical properties of the upper 10 to 20 cm of multiyear ice are shown to control the microwave process. A discussion of property and signature variability was based on measurements obtained from five representative sites.

ACKNOWLEDGEMENTS

REFERENCES

[1] A.T. Gow, D.A. Meese, D.K. Perovich, and W.B. Tucker, "The Anatomy of a Freezing Lead," JGR, vol. 95, no. C10, Oct. 15, 1990, pp. 18,221-18,232.

[2] A.K. Fung, and H.J. Eom, "Application of a Combined Rough Surface Volume Scattering Theory to Sea Ice and Snow," IEEE Trans., vol. GE-20, no. 4, October 1982, pp. 528-536.

[3] Y.S. Kim, R.K. Moore, and R.G. Onstott, "Theoretical and Experimental Study of Radar Backscatter from Sea Ice," Univ. of Kansas, Lawrence, Kansas, RSL Tech. Report 331-37, January 1984.
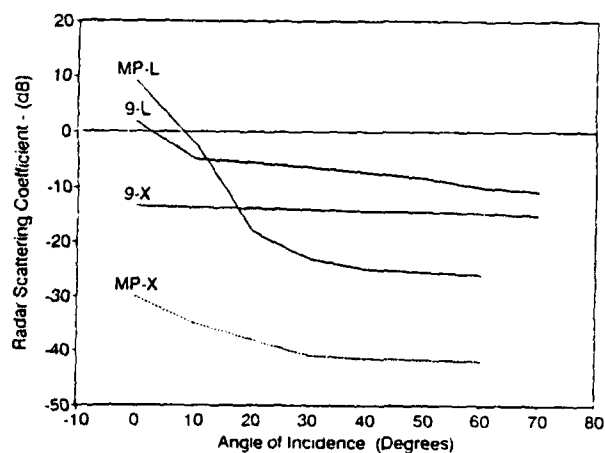
Figure 1. The angular response for the radar scattering coefficient of a multiyear ice hummock and meltpool are shown at 10 GHz. The responses at VV and HH polarizations were nearly identical, as was the case for VH and HV polarizations.
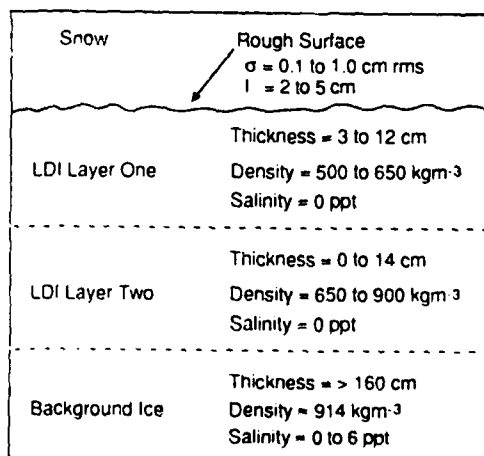

Figure 3. The angular response of the scattering coefficients for four multiyear ice hummocks at 10 GHz and like- and cross- polarizations. The responses at VV and HH polarizations were nearly identical, as were the VH and HV responses.

Figure 2. This is a cross-section view of the upper portion of the ice sheet.

Table 1.

CEAREX Surface-Based Radar System Specifications

Type	FM-CW
Frequency (GHz)	10
FM Sweep (Mhz)	1000
Antenna Beamwidth (°)	9
Polarizations[1]	V H X
Height (m)	3
Footprint[2] (m)	0.7
N Frequency[3]	3.5
N Spatial[4]	4.7
N Total[5]	16
σ Precision[6] (Db)	±1.9

[1]V=VV, H=HH, X=VH or HV
[2]Footprint at 40°
[3]Number of Independent Samples via Excess Bandwidth
[4]Independent Samples per Spatial Footprint
[5]Total Number of Independent Samples per Footprint
[6]Precision Based Upon Translating One Footprint Only (90%confidence)

Table 2.

Preliminary Results for Sea Ice During Fall Freeze-Up

Ice Type	Preliminary Results	Comments
Multiyear	Quickly attains winter signature.	1) Only need to cool top 10 cm. 2) $T_m = -10°C$ adequate, probably 3) Ice sheet (bulk) was still near zero in Nov.
First Year	Quickly attains winter signature.	1) Frost flower development slow compared to winter. 2) Transition of bulk dielectric constant (80 to 20 to 4) for top of ice sheet delayed.
Young	Big Impact! Signature evolution impacted by slow growing conditions. Signature not winter-like.	1) Ice does not congeal quickly or thoroughly 2) Top few cms composed of brine enriched snow and slush. 3) Congealed ice sheet produces signature enhancement
Nilas	Quickly attains winter signature.	1) Only needs to cool top few cms. 2) $T_m = -10°C$ adequate, probably.

Table 3.

Upper Ice Sheet Characterizations

Parameter		DS - 4	DS - 7	DS - 9	DS - 13	DS - MP
σ cm rms		0.23 ± .05	0.14 ± .02	0.77 ± .12	1.01 ± .31	0.8 ± .03
ℓ cm		3.5 ± .3	2.0 ± 1.3	4.6 ± 1.2	3.2 ± 1.2	2.8 ± 1.9
LDI-1	Thickness - cm -	12.4 ± .3	5.0 ± .6	4.9 ± 1.0	3.0 ± 1.3	5.2 ± .3
	Salinity - ppt -	0.1	0.0	0.0	0.0	0.0
	Density - kgm³	651	457	513	513	914
	Bubble Dia - mm	3.3	2.5	2.3	3.3	1.3
	Void Dia - mm	1	8	7	5	0
LDI - 2	Thickness - cm -	--	3.5 ± .4	4.9 ± .4	13.6 ± .4	4.8 ± .3
	Salinity - ppt -	--	0	0	0	0
	Density - kgm³	--	728	728	929	919
	Bubble Dia - mm	--	4	4.3	1	0
	Void Dia - mm	--	2	0	0	0

LDI = Low Density Ice Layer

MULTI-FREQUENCY SAR, SSM/I AND AVHRR DERIVED
GEOPHYSICAL INFORMATION OF THE MARGINAL ICE ZONE

R.A. Shuchman, R.G. Onstott, C.C. Wackerman, C.A. Russel, and L.L. Sutherland
Center for Earth Sciences, Advanced Concepts Division
Environmental Research Institute of Michigan
P.O. Box 8618, Ann Arbor, MI 48107 USA

O.M. Johannessen, J.A. Johannessen, and S. Sandven
Nansen Remote Sensing Center
Bergen, Norway

P. Gloerson
NASA Goddard Space Flight Center
Greenbelt, MD 20771

ABSTRACT

Coincident three frequency aircraft synthetic aperture radar (SAR), NOAA satellite Advanced Very High Resolution Radiometer (AVHRR), and DMSP satellite Special Sensor Microwave Imager (SSM/I) data were collected during the Seasonal Ice Zone Experiment (SIZEX) phase of the Coordinated Eastern Arctic Experiment (CEAREX). The SIZEX/CEAREX experiments discussed in this paper occurred in the March 1989 time frame in the Greenland Sea Marginal Ice Zone (MIZ), centered at approximately 77° N and 0° longitude. The aircraft X-, C-, and L-band SAR data were co-registered on a 5 km grid with the passive optical AVHRR, infrared AVHRR, and passive microwave SSM/I data. The SAR had a resolution of approximately 10 meters while the AVHRR and SSM/I resolutions were 1 km and 25 km, respectively.

Ice information from individual sensors were first compared, then the sensor measurements were used together to provide information on ice edge location, spatial ice type maps, and ice concentration. In addition, information on the locations of eddies, local wind speed, and sea surface temperature over the non-ice covered areas of the MIZ were generated. Data fusion of SAR and SSM/I data proved to be particularly useful in separating open leads from frozen leads.

KEYWORDS: SAR, SSM/I, AVHRR, data fusion, CEAREX, marginal ice zone, sea ice, concentration

1.0 INTRODUCTION

This paper describes the fusion of synthetic aperture radar (SAR), Special Sensor Microwave Imager (SSM/I), and NOAA Advanced Very High Resolution Radiometer (AVHRR) data to study arctic processes. These data were collected during the SIZEX/CEAREX experiments that occurred in the Greenland Sea in March of 1989.

By the turn of the century large amounts of SAR satellite imagery of the polar regions will be available. These data will come from a series of satellites: European ERS-1, Canadian RADARSAT, Japanese ERS-1, SIR-C/X-SAR, and EOS. Thus, the combination of SAR, SSM/I and AVHRR satellite data will become central to the assessment of arctic environments.

2.0 SIZEX/CEAREX DATA SET

The SIZEX/CEAREX data discussed in this paper was collected on 17 and 20 March 1989 in the Greenland Sea Marginal Ice Zone (MIZ) centered at approximately 77°N and 0° longitude. The 17 and 20 March data are representative of nine coincident SAR, SSM/I, and AVHRR data sets collected during the month long expedition.

The ice strengthened research vessel *Polarbjorn* operated within the scene covered by the SAR mosaic and satellite data. Sea truth, meteorology, and physical ice property measurements were made from the ship. Table 1 is an example of the types of sea ice and their physical properties characterized during the remote sensing collections. The wind speed and air temperature as measured by the ship for 17 and 20 march were 5.4 m/s, -23.2°C, 3.5 m/s and -15°C respectively.

The high resolution SAR was also used to detect icebergs and gravity waves as they propagated from the open ocean into the ice pack, although this will not be discussed in this paper.

Figure 1 presents the SSM/I, AVHRR and SAR data for 20 March. The 25 km resolution SSM/I brightness temperatures were converted to total ice concentration and multiyear fraction using the standard NASA algorithms [1] and converted to surface wind speed over open water using a Navy algorithm [2]. The 1 km resolution AVHRR channel 4 (infrared) was transformed directly into sea surface temperature values. This data along with the AVHRR channel 2 (visible) data is presented in Figure 1. The SAR data in Figure 1 has a resolution of approximately 10 m and a wavelength of 5.6 cm (C-band) with vertical transmit and receive polarization. Recall that the new European Space Agency ERS-1 SAR satellite will use the same frequency and polarization combination [3]. The images in Figure 1 were each scaled differently. The SSM/I concentrations were scaled between 0 and 100% where 0 is black and 100% is white. The SSM/I wind speed estimates were scaled between 0 (black) and 40 (white) knots. The AVHRR derived surface temperatures were scaled between -25°C (black) and 0°C (white).

The SSM/I and AVHRR data products described above were resampled on a 5 km grid and coregistered based on their latitude and longitude values. The SAR mosaic for 20 March

was manually interpreted on a 5 km grid as described in [4] to extract total ice concentration, multiyear fraction, floe size, lead, and ridge statistics (see table 3). This data was also registered on the same latitude/longitude grid to facilitate comparisons between the sensors.

3.0 DATA FUSION RESULTS

Each of the three sensors provides a number of geophysical data products for the Polar Ocean region. Table 2 summarizes each of these data products as well as presents parameters that can be enhanced by combining the individual sensors.

A comparison of ice products generated from individual sensors can be generated to test consistency between sensors. Figures 2 and 3 compare the SAR derived total ice concentrations with those obtained from the SSM/I for 17 and 20 March, respectively. In general the agreement is quite good. The same is not true for the multiyear fraction comparisons (see Figures 4 and 5). On both days the SSM/I under-predicted the multiyear fraction when compared to the SAR. The coarse resolution of the SSM/I (25 km) may be the cause of the underestimate. Fusion of the high resolution SAR (10 m) can alleviate this problem.

Figure 6 shows a blending of the SAR, SSM/I, and AVHRR data products and demonstrates how a composite picture of the MIZ can be constructed by data fusion. The ice edges derived from each sensor individually are compared in Figure 6. The three edge lines agree to within 25 km (the resolution of the SSM/I). Note that the combination of the sensors presents a fairly complete environmental picture of the MIZ.

Additional data products can be derived from the sensors by combining the raw data values from multiple sensors first, and then deriving ice information. Figure 7 presents the results of combining the SAR intensity values with the SSM/I 37 GHz horizontal polarized brightness temperatures. Notice that the SAR alone cannot differentiate open water from first year ice, but a combination of the SAR and the SSM/I can easily differentiate the two. While the SSM/I alone does a good job of this, fusing the SAR with the SSM/I a data product of much higher resolution can be obtained. This result may allow one to more accurately classify the various stages of lead evolution. Surface winds over the leads and at the ice margins may also be more differentiable using a combination of active/passive microwave sensors.

4.0 CONCLUDING REMARKS

Using a data set in the MIZ of the Greenland Sea, SAR, SSM/I, and AVHRR data was compared and then blended to provide a more accurate picture of the sea ice and liquid ocean geophysics. Detailed comparisons between the SAR, AVHRR, and SSM/I indicated:
1) The ice edge position was in agreement to within 25 km,
2) The SSM/I SAR total ice concentration compared favorably, however the SSM/I significantly underpredicted the multiyear fraction,
3) Combining high resolution SAR with SSM/I can potentially map open water and new ice features in the MIZ which can not be mapped by the single sensors, and

4) The combination of all three sensors provide accurate ice information as well as sea surface temperature and wind speeds.

REFERENCES

[1] Gloerson, P., et al., "Reduction of Weather Effects in the Calculation of Sea Ice Concentration from Microwave Radiance", J. Geophys. Res., Vol 91, pp 3913-3919, 1986.

[2] Hollinger, J., "DMSP Special Sensor Microwave/Imager Calibration/Validation", DMSP Final Report Vol. 1, Space Sensing Branch of the Naval Research Laboratory, Washington, DC, July 1989.

[3] Shuchman, R.A., The Use of Synthetic Aperture Radar to Map the Polar Oceans, Proc. of OCEANS '90, Washington, DC, September 24-26, 1990 pp 402-409.

[4] Burns, B.A., et al., "Multisensor Comparison of Ice Concentration Estimates in the Marginal Ice Zone," J. Geophys. Res., Vol 92, C7, June 1987, pp. 6843-6856.

Table 1.
Examples of Sea Ice Physical Properties During CEAREX March 1989

Description	Multiyear	Thick First-Year	Young First-Year	Thin First-Year
Ice Thickness - m	2.55 ± .64	1.64	0.215 ± .4	0.42
Snow Thickness - cm	26 ± 19	9.5	8	5
T_{ia} - °C	-18.3 ± 3.6	-19.7	-17.5 ± 3.5	-25
$T_{surface}$ - °C	-16.2 ± 3.6	-13.2	-12.0 ± 2.8	-20
Salinity - PPT	0.17 ± .19	8.4 ± 3.0	9.9	7.9
Depth - cm	12	8	6	3
Density - kgm/m³	0.716 ± .19	.900 ± .03	0.844	0.359
Brine Volume	0.757 ± .83	51 ± 3	35	38

Table 2.
Remote Sensing Derived Polar Ocean Geophysical Parameters vs. Sensor

Geophysical Parameter	SAR	SSM/I	AVHRR	Combination
Total Ice Concentration	Yes	Difficult at the MIZ	Difficult at the MIZ	Needed for MIZ and First-Year vs. Open Water
Multi-Year Fraction	Yes	Yes	No	SAR/SSM/I Improves Accuracy
Floe Size	Yes	No	1 km or Greater	Not Needed
Ridges	Yes	No	No	Not Needed
Leads	Yes	No	1 km or Wider	SAR/SSM/I Will Discriminate Open Water vs. New Ice
Ice Eddies	Yes	No	No	Not Needed
Eddies in Open Water	Maybe	No	Yes	AVHRR/SAR Will Map Open Water
Winds at Ice Edge	Maybe	Yes	No	SAR/SSM/I can Potentially Produce High Resolution Estimates
Ice Kinematics	Yes	No	Gross Movement Only	Not Needed
Icebergs	Yes	No	Lg > 1 km	Not Needed
Gravity Wave Propagation Into the Ice	Yes	No	No	Not Needed

Table 3.
Manual Interpretation of the SAR March 20 Mosaic

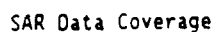|	Min	Max	Mean
Total Ice Concentration (%)	0	100	59.2
Multiyear Fraction (%)	0	95	34.5
Floe Size (m)	0	5000	771.6

31.4% of Image Contained Leads
< 1% of Image Contained Major Ridges

SSM/I Derived Total
Ice Concentration
0 to 100 Percent

SSM/I Derived Multiyear
Fraction 0 to 100 Percent

SSM/I Derived Near Surface
Wind Speed 0 to 40 Knots

AVHRR
Channel 2 (Visible)

SAR Data Coverage

AVHRR Derived Sea Surface
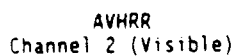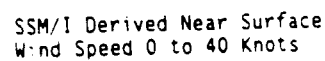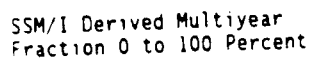Temperature -25 to 0 Degrees C
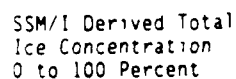
SAR Mosaic

SAR Manual Interpretation
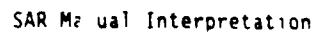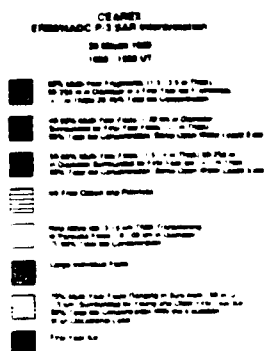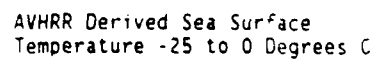
Figure 1. SSM/I, AVHRR, and SAR Data for 20 March CEAREX Test Site

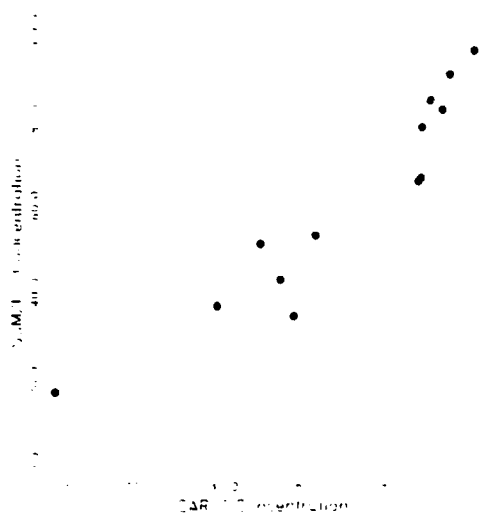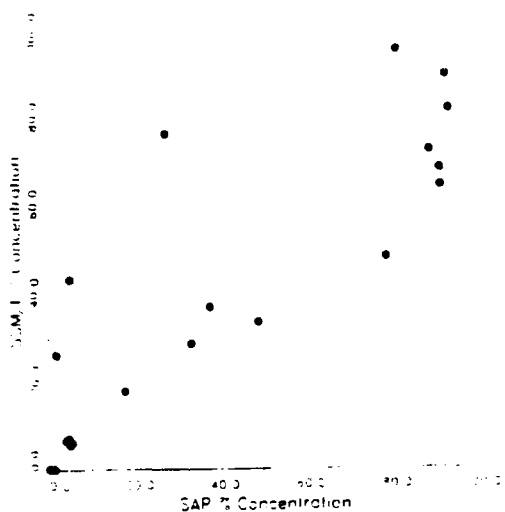Figure 2. Comparison of SAR and SSM/I
Total Ice Concentration for 17 March

Figure 5. Comparison of SAR and SSM/I
Multiyear Fraction for 20 March

Figure 3. Comparison of SAR and SSM/I
Total Ice Concentration for 20 March
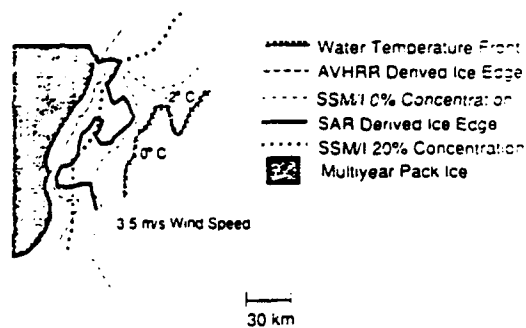
Figure 6. Composite Ice Edge

SAR vs SSM/I 37GHz H
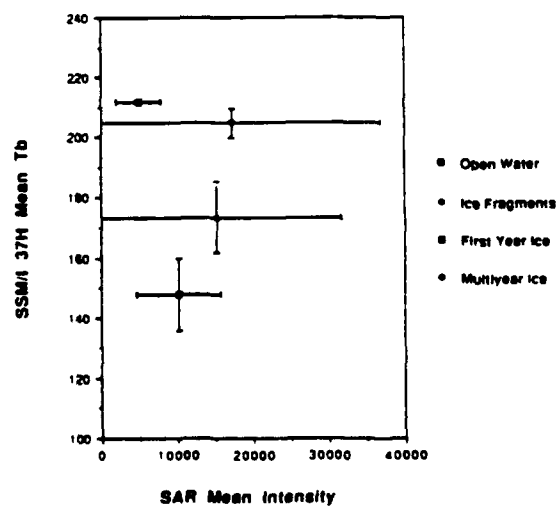

Figure 4. Comparison of SAR and SSM/I
Multiyear Fraction for 17 March

Figure 7. Ice Type Derivation From
Combination of SAR and SSM/I

NASA, NAVY, AND AES/YORK SEA ICE CONCENTRATION COMPARISON OF SSM/I ALGORITHMS WITH SAR DERIVED VALUES

R.R. Jentz, C.C. Wackerman, R.A. Shuchman, and R.G. Onstott
Center for Earth Sciences, Advanced Concept Division
Environmental Research Institute of Michigan
Ann Arbor, Michigan 48107 USA

Per Gloersen and Don Cavalieri
Laboratory for Hydropsheric Processes
NASA Goddard Space Flight Center
Greenbelt, Maryland 20771 USA

Rene Ramseier and Irene Rubinstein
Atmospheric Environment Service
Centre for Research in Experimental Space Science
York University, North York M3J 3K1 Canada

Joey Comiso
Oceans and Ice Branch
NASA Goddard Space Flight Center
Greenbelt, Maryland 20771 USA

James Hollinger
Space Sensing Branch
Naval Research Laboratory
Washington, D. C. 20375-5000 USA

ABSTRACT

Previous research studies have focused on producing algorithms for extracting geophysical information from passive microwave data regarding ice floe size, sea ice concentration, open water lead locations, and sea ice extent. These studies have resulted in four separate algorithms for extracting these geophysical parameters. Sea ice concentration estimates generated from each of these algorithms (i.e., NASA/Team, NASA/Comiso, AES/York, and Navy) are compared to ice concentration estimates produced from coincident high resolution Synthetic Aperture Radar (SAR) data. The SAR concentration estimates are produced from data collected in both the Beaufort and Greenland Sea in March 1988 and March 1989, respectively. The SAR data is coincident to the passive microwave data generated by the Special Sensor Microwave/Imager (SSM/I).

KEYWORDS: Sea Ice Comparison, SAR, SSM/I, Sea Ice Concentration, Sea Ice Algorithm Comparison

1.0 INTRODUCTION

The polar research community has been interested in the determination of sea ice products from the arctic region since the launch of the Nimbus 5 Electrically Scanning Microwave Radiometer (ESMR) in 1972, and continued through 1987 with the Nimbus 7 Scanning Multichannel Microwave Radiometer (SMMR). Presently, the polar research community has focused its attention towards the SSM/I which was launched in June of 1987 aboard the Defense Meteorological Satellite Program (DMSP) Spacecraft F8. The SSM/I is the first of seven planned SSM/Is scheduled for launch over the next two decades which will make available passive microwave imagery of the arctic region well into the twenty first century [1].

Since 1972 the polar research community has been developing sea ice product algorithms designed to extract geophysical information about the arctic. The focus of these algorithms has been the generation of ice floe size distributions, open water lead locations, sea ice concentration maps, and sea ice extent (the location of the boundary between open water and the ice pack) which may assist in the generation of global climate models helping us to further understand our biosphere. During this period several research teams have developed algorithms which produce both the total and fractional sea ice percentages from passive microwave data.

Verification of the results generated from these sea ice concentration algorithms was performed separately by various research teams. Their approach (when ground truth data was not available) has been to compare the results produced from coincident data sets collected by multiple sensors, then try and explain any discrepancies found. High resolution aircraft SAR systems can provide such a verification since the generation of reliable ice concentration estimates can be performed [2]. These studies show that the high spatial resolution associated with SAR imagery provides the ability to delineate individual floes and leads which make the determination of ice concentration easier. The research effort reported here is focused on trying to determine the strengths, weaknesses, and accuracy of several concentration algorithms by adopting the same method. The approach of this analysis is to compare ice concentration estimates generated by four of the most widely used concentration algorithms (i.e. NASA/Team, NASA/Comiso, AES/York, and Navy) to ice concentration estimates produced from coincident high resolution SAR data. Since the potential of imaging radars for discriminating sea ice types has been demonstrated using manual photographic interpretation techniques [3], the SAR concentration estimates are generated manually from a SAR photographic mosaic.

2.0 SYSTEM AND MISSION DESCRIPTION

The current SSM/I is a multichannel passive microwave radiometer built by Hughes Aircraft. It was designed to provide synoptic maps of atmospheric, oceanographic, and selected land parameters on a global scale. The SSM/I contains seven linearly-polarized channels operating at four separate frequencies (i.e., both horizontal and vertical polarization at 19.3, 37.0, and 85.5 GHz and vertical polarization at 22.2 GHz). The SSM/I satellite is in a circular sun-synchronous near-polar orbit at an altitude of approximately 800 km. The orbit period is 102.0 minutes producing 14.1 full orbit revolutions every day. The scanning antenna is tilted at a 45 degree angle to the satellite spin axis and sweeps out a 1400 km wide swath in 1.9 seconds. The resolution, or footprint, of the SSM/I brightness temperatures varies according to the frequency, where the footprint is approximately 55, 49, 32,

and 13 km for the 19.3, 22.2, 37.0, and 85.5 GHz channels respectively [1].

The high resolution SAR data used in this analysis was generated from the Naval Air Development Center (NADC) SAR built by the Environmental Research Institute of Michigan (ERIM), also referred to as the NADC/ERIM P-3 SAR. The NADC/ERIM P-3 SAR is a multifrequency, polarimetric, SAR installed in a U.S. Navy P-3 aircraft. It is a side-looking SAR that operates in both strip-map and spotlight mode. The center frequencies are 9.35 GHz, 5.30 GHz, and 1.25 GHz corresponding to X, L, and C bands respectively. The system is capable of recording polarimetric data corresponding to all of the elements of the polarization matrix (i.e. HH, VV, HV, and VH polarizations) where transmit and receive polarizations can be altered on a pulse-by-pulse basis.

The remote sensing data used in this comparison consists of imagery recorded in the Beaufort Sea on both 18 and 19 March 1988 and in the Greenland Sea on 17 and 20 March 1989. The SAR data was recorded with an azimuth resolution of 2.8 meters (the direction parallel to the flight track) and a range resolution of 3.2 meters (the direction orthogonal to the flight track). This imagery was collected at C-band with VV-polarization and is coincident to the SSM/I overflights.

3.0 ICE CONCENTRATION ALGORITHM DESCRIPTION

The four concentration algorithms included in this study are the NASA/Team, NASA/Comiso, AES/York, and Navy ice concentration algorithms. The NASA/Team algorithm is a multichannel concentration algorithm which generates both the total ice percentage as well as the multiyear ice fraction. It utilizes both the polarization and spectral gradient ratios from the 19.3 and 37.0 GHz channels to determine the percentage of multiyear sea ice [4,5]. The multichannel techniques used by this algorithm were adopted from those developed for the multichannel SMMR sensor which requires a unique emissivity for each of the assumed ice types within the scene. The NASA/Team algorithm uses the "global" set of tie points listed in [4] as the required set of emissivity values. The NASA/Comiso algorithm presented in this analysis is also a multichannel algorithm which produces the total ice percentage only from the 19.3 and 37.0 GHz SSM/I brightness temperatures. However, this algorithm is less rigid than the NASA/Team algorithm. It allows for modification of the tie points representing the emissivity of each ice type taking into account the spatial and temporal variability of the physical characteristics associated with different areas within the arctic [6]. The AES/York algorithm was designed to retrieve not only the basic SSM/I parameter of total sea ice concentration, but also identify first-year, multiyear, thin ice, and open water within the SSM/I footprint. Like the two NASA algorithms it uses both the 19.3 and 37.0 GHz channel data to determine these ice types. It also uses fixed tie points representing the emissivities of each passive microwave ice type signature [7]. The Navy algorithm is a tailored version of the AES/York algorithm. It generates the total ice percentage within an SSM/I footprint along with the predominate ice type where the predominate ice type can be either first-year or multiyear [1]. Like the other algorithms, the Navy

algorithm uses both the 19.3 and 37.0 GHz brightness temperatures to determine the total ice percentage. This algorithm, along with the NASA/Comiso algorithm, is used primarily for determining sea ice extent as well as the first-year/multiyear ice pack boundaries.

4.0 ICE CONCENTRATION ALGORITHM COMPARISON

The SAR ice concentration estimates are derived manually from a photographic mosaic which was produced by optically processing the digital SAR data. The photographic mosaic represents an area of continuous SAR coverage on approximately a 3.0 meter grid. The SAR concentration estimates are produced by dividing the SAR mosaic into a 5.0 km grid and manually interpreting the total ice percentage along with the multiyear, first-year, and open water ice fractions. Sea ice concentration maps are then generated on a 1 km grid for each of the sea ice concentration estimates. These concentration maps are produced using a two dimensional cubic spline interpolation scheme. The SSM/I concentration maps are produced from data collected by multiple orbits of the SSM/I satellite (orbits spanning the same time over which the SAR data was collected). Both the SAR and SSM/I sea ice concentration maps then represent a one-to-one mapping of the fractional ice type over a given latitude and longitude region.

The Beaufort Sea data collected on 18 and 19 March 1988 represent areas of 100% total ice concentrations where the 18 March mosaic crosses the first-year/multiyear ice pack boundary and the 19 March mosaic data was collected in the multiyear ice pack. This is an ideal data set for measuring the strengths of the Navy algorithm which produces a total ice concentration estimate along with the predominate ice type. Figure 1 shows the multiyear sea ice concentration estimates for three of the concentration algorithms (NASA/Team, AES/York, and Navy) along with the SAR estimates plotted as a function of latitude for the 18 March mosaic data (remember the 18 March mosaic crosses the first-year/multiyear ice pack boundary). Notice that the AES/York and Navy algorithm estimates track the SAR estimates close in the first-year ice pack, while the NASA/Team algorithm estimates are closer to the SAR estimates in the multiyear ice pack. Also notice that all three algorithm estimates are higher than the SAR estimates (approximately 40% to 50% higher) and that the NASA/Team estimates are much higher than the SAR within the first-year ice pack (approximately 30% higher). This misclassification of first-year ice by the NASA/Team algorithm is probably due to the pressure ridges associated with first-year ice in the Beaufort Sea. Figure 2 illustrates the corresponding plot of the concentration estimates as a function of latitude for the 19 March mosaic data. The Navy algorithm estimates the entire area as 100% multiyear sea ice, as expected, and the AES/York estimates are all 40% to 50% higher than the SAR estimates. However, the NASA/Team algorithm produced multiyear concentration estimates consistent with the SAR estimates.

The Greenland Sea data collected on 17 and 20 March 1989 represents areas of the Marginal Ice Zone (MIZ) which contains varying amounts of open water, first-year, and multiyear sea ice. This data is good for testing the accuracy of the NASA/Team and AES/York fractional ice type estimates along with the total ice percentage.

Figure 3 is a plot of the total ice concentration estimates versus the Corresponding SAR estimates for the 17 March 1989 data. The key on the plot illustrates a symbol for each of the four algorithms (the NASA Alg. refers to the NASA/Team algorithm and the Comiso Alg. refers to the NASA/Comiso algorithm) along with the slope "a" and y-intercept "b" of the linear regression analysis. Notice that the linear trend corresponding to each of the algorithm estimates is relatively close to the line with slope 1.0 and y-intercept 0.0 (this is the line where y=x representing an exact match between the SAR and SSM/I estimates). The AES/York estimates provide the best match while the NASA/Comiso estimates have a slope very near 1.0 shifted by -9.096. Figure 4 illustrates the corresponding plot for the 20 March 1989 data. Again, this plot shows relatively good results for the NASA/Team, AES/York, and Navy algorithms while the NASA/Comiso algorithm tends to underestimate the total ice concentrations. Figures 5 and 6 show plots of multiyear ice concentrations versus the SAR estimates for the 17 and 20 March 1989 data sets, respectively. These plots show that the Navy algorithm generates ice concentrations that are consistently higher than the SAR. This is expected since this algorithm generates a total ice concentration value. Both the NASA/Team and AES/York algorithms produce multiyear estimates that are consistently lower than the SAR. This is surprising since the multiyear estimates generated for the Beaufort Sea data were consistently higher than the SAR. This might be due to different characteristics in the multiyear ice signatures between the two locations, or possibly the absence of pressure ridges from first-year ice in the MIZ (remember the NASA/Team algorithm misclassified approximately 30% of the first-year ice as multiyear ice on the 18 March 1988 Beaufort Sea data).

5.0 CONCLUSIONS

The NASA/Team algorithm generated multiyear ice concentration estimates similar to the SAR in the multiyear ice pack for the 19 March 1988 Beaufort Sea data (mean difference of approximately 6.5%). It also produced a misclassification error of approximately 30% (due to the pressure ridges) in the first-year ice pack for the 18 March 1988 Beaufort Sea data. The AES/York and Navy algorithms were not affected by the pressure ridges in the first-year sea ice, both produced a 0% multiyear estimate in the first-year ice area. Both the AES/York and Navy algorithms were able to distinguish between the first-year/multiyear ice pack boundaries, but they also overestimate the ice concentrations in the multiyear pack. The total ice concentration estimates derived from the 17 and 20 March 1989 Greenland Sea data are relatively close to the SAR estimates for the NASA/Team, AES/York and Navy algorithms. Each of these algorithms produced a Normalized Standard Error (NSE) less than 0.1, where the NSE is computed as the mean difference between the SSM/I and SAR estimates divided by the mean square of the SAR estimates (NSE equal to zero means no difference between the SAR and SSM/I derived concentration estimates). The NASA/Comiso algorithm underestimated the total ice percentage for the 20 March 1989 data (NSE equals 0.2). However, a much larger discrepancy was found in the multiyear estimates. The Navy algorithm which produces a total ice

estimate containing mostly multiyear sea ice generated NSE values of 0.285 and 0.450 for both the 17 and 20 March Greenland Sea data respectively. The AES/York algorithm generated NSE values of 0.320 and 0.553, and the NASA/Team algorithm NSE values were 0.467 and 0.681 for the 17 and 20 March 1989 Greenland Sea data respectively. This implies that even though the Navy algorithm generates a total ice estimate, the estimates are closer to the SAR estimates than the NASA/Team or AES/York algorithm estimates.

REFERENCES

[1] Hollinger, J., "DMSP Special Sensor Microwave/Imager Calibration/Validation," DMSP Final Report Vol. 1, Space Sensing Branch of the Naval Research Laboratory, Washington, D.C., July 1989.

[2] Burns, B. A., et al., "Computer-Assisted Techniques for Geophysical Analysis of SAR Sea-Ice Imagery", Pro. Nineteenth International Symposium on Remote Sensing of Environment, ERIM, Ann Arbor, MI, pp. 947-959, 1985.

[3] Gray, A. L., et al., "Simultaneous Scatterometer and Radiometer Measurements of Sea-Ice Microwave Signatures," IEEE J. Oceanic Eng., vol. OE-7, 1982, pp. 20-32.

[4] Cavalieri, D. J., et al., "Determination of Sea Ice Parameters with the Nimbus 7 SMMR", J. Geophys. Res., vol. 89, pp. 5355-5369, 1984.

[5] Gloersen, P., et al., "Reduction of Weather Effects in the Calculation of Sea Ice Concentration from Microwave Radiance", J. Geophys. Res., vol. 91, pp. 3913-3919, 1986.

[6] Comiso, J. C., "Characteristics of Arctic Winter Sea Ice From Satellite Multispectral Microwave Observations", J. Geophys. Res., vol. 91 pp. 975-994, Jan. 1986.

[7] Ramseier, R. O., "Canadian Validation of The SSM/I and AES/York Algorithms for Sea-Ice Parameters", DSS File No. 62SS.KM168-7-7059, June 1990.

SSM/I Sea Ice Concentrations
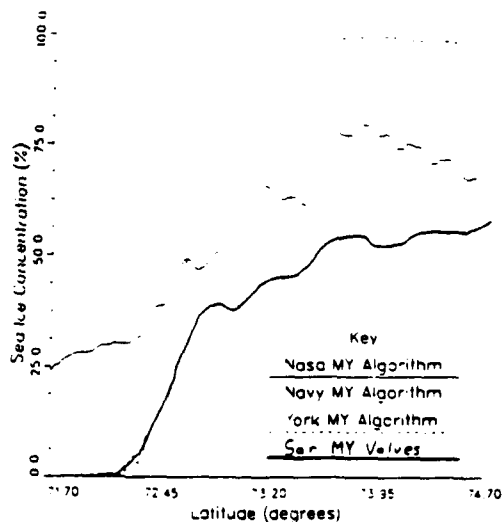## March 18 1988

Figure 1. Multiyear Concentration Estimates for NASA/Team, Navy, AES/York and SAR Algorithms using 18 March 1988 Beaufort Sea Data.

Total Ice Algorithm Comparison
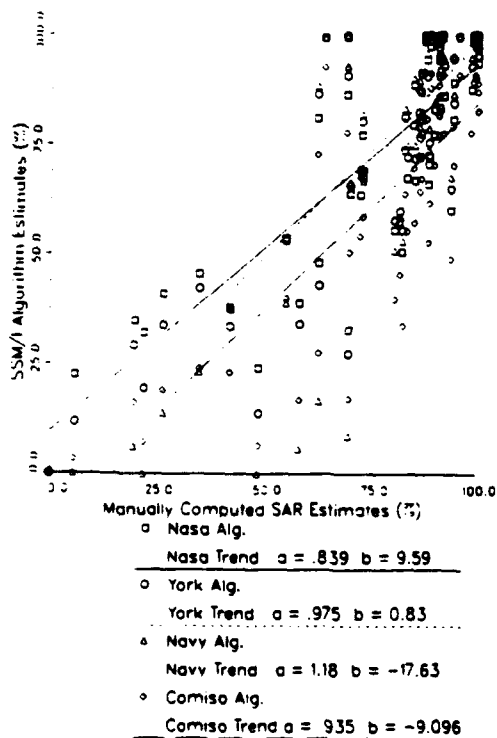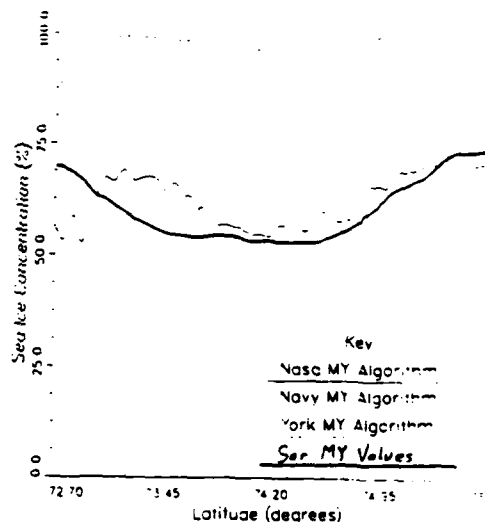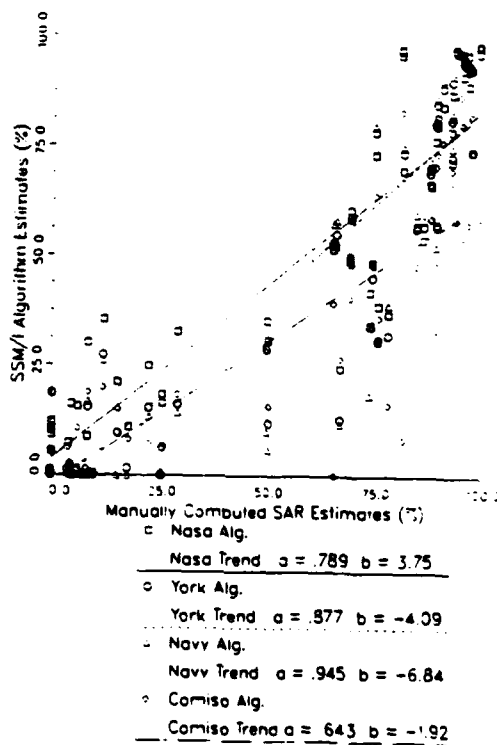## March 17 1989 Cearex Data

Figure 3. Total Ice Concentration Estimates vs SAR for 17 March 1989 Greenland Sea Data.

SSM/I Sea Ice Concentrations
March 19 1988

Figure 2. Multiyear Concentration Estimates for NASA/Team, Navy, AES/York and SAR Algorithms using 19 March 1988 Beaufort Sea Data.

Total Ice Algorithm Comparison
March 20 1989 Cearex Data

Figure 4. Total Ice Concentration Estimates vs SAR for 20 March 1989 Greenland Sea Data.

MultiYear Algorithm Comparison
March 17 1989 Cearex Data

- □ Nasa Alg.
  Nasa Trend a = '93 b = 8.64
- ○ York Alg.
  York Trend a = .436 b = 6.49
- ∴ Navy Alg.
  Navy Trend a = 1.08 b = 8.79
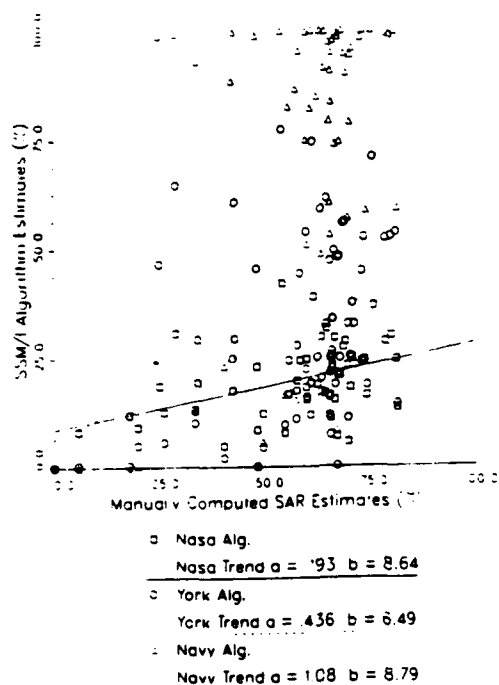
Figure 5. Multiyear Ice Concentration Estimates vs SAR for 17 March 1989 Greenland Sea Data.

MultiYear Algorithm Comparison
March 20 1989 Cearex Data

- □ Nasa Alg.
  Nasa Trend a = .077 b = 4.35
- ○ York Alg.
  York Trend a = .345 b = -2.56
- ∴ Navy Alg.
  Navy Trend a = 1.49 b = -5.14
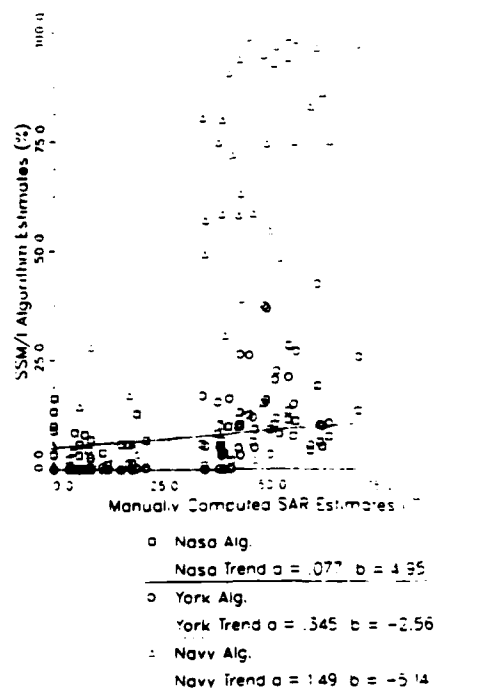
Figure 6. Multiyear Ice Concentration Estimates vs SAR for 20 March 1989 Greenland Sea Data.

POLARIMETRIC RADAR MEASUREMENTS OF ARCTIC SEA ICE DURING THE COORDINATED EASTERN ARCTIC EXPERIMENT

R.G. Onstott, R.A.Shuchman, and C.C. Wackerman
Center for Earth Sciences
Advanced Concepts Division
Environmental Research Institute of Michigan
P.O. Box 8618 Ann Arbor, MI 48107 USA

ABSTRACT

Surface-based scatterometer and airborne synthetic aperture radar (SAR) data of Arctic sea ice in Fram Strait were obtained during March 1989 as part of the Coordinated Eastern Arctic Experiment (CEAREX). Statistics of scattering coefficients, polarization ratios, depolarization ratios, phase differences, and correlation coefficients have been determined at frequencies of 1.25, 2.0, 5.25, 9.38, and 35 GHz to describe the scattering behavior for each of the major ice types. Ice form categories were numerous and included multiyear, first-year, nilas, and the thinnest forms, including very fine spicules of ice in suspension. These statistics have been calculated because they are unique, may be understood theoretically and empirically, and serve as the basis to discriminate image features.

Key Words: sea ice, radar, polarimetry

INTRODUCTION

Polarimetric radar observations were made of sea ice in the Greenland Sea during the March segment of the Coordinated Eastern Arctic Experiment (CEAREX). During this period an intensive series of in-situ observations were made to study several distinct ice types. Aircraft overflights were also conducted. One of the objectives of this investigation is to determine, under winter conditions, the active and passive microwave signatures for a variety of types of ice and to relate these signatures to the physical properties of the ice. A second objective is to determine the utility of a polarimetric synthetic aperture radar (SAR) to improve the accuracy of geophysical properties generated for the Arctic. Also of particular interest is to develop the ability to discriminate open water, new ice, and nilas.

During CEAREX, full complex scattering matrix data were acquired at frequencies in the bands from L to Ka. The purpose in acquiring these data is many fold and includes the improvement in the understanding of the scattering properties of all ice forms by the complete characterization of the scatter field over a very wide range of frequencies. The study of the optimal radar parameter combinations and the determination of the utility of the very robust, polarimetrically capable radars also benefit from these data collections and study. With a polarimetric radar,

information gained is based on the exploitation of the true complex scattering coefficients. This may be obtained from the phase difference between returns at VV and HH polarizations, the differences in the backscatter intensities at the various polarizations (i.e. VV, VH, HH, and VH), and the correlations between these complex scattering coefficients. It is hypothesized that if the full scattering matrix is acquired that physical property information associated with preferred geometric orientations or internal anisotropic physical-dielectric properties will be more accurately obtained. This would then lead to improved ice type discrimination, feature identification, and geophysical property retrievals. This may allow computer algorithms to be simplified because of the ability to select an optimum subset of parameters from the scattering matrix, and possibly the relaxing of SAR resolution requirements while maintaining algorithm performance.

EXPERIMENT DESCRIPTION

Radar backscatter data were acquired at frequencies of 1.8, 5, 10, and 35 GHz from the rail of the ice strengthened ship R/V *Polarbjorn* using a polarimetric scatterometer. The ERIM/NADC P-3 SAR was operated at 1.25, 5.25, and 9.38 GHz to image the regions which were the subject of the intensive in-situ investigations. Sites were located near the open water at the ice edge of the marginal ice zone (MIZ) to the giant floes (diameters greater than 10 km) in the ice pack located a distance of 35 nm from the ice edge. In summary, observations included open water, pancake ice, nilas ice, young ice, first year ice, and multiyear ice. These radar observations were carried out in conjunction with the detailed characterization measurements. A summary of the physical properties for four major ice types is provided in Table 1.

PREDICTED UTILITY

An analysis was performed to determine the ability to exploit the polarization ratio and phase difference for five clutter types including open water, very new ice, new ice, first year ice, and multiyear ice. Response functions derived from the small perturbation scattering model for smooth surfaces were created as a function of incidence angle and

are provided in Figures 1 and 2. Proper dielectric constant values are critical in this study and were derived from previous radar reflectivity measurements. Essential trends are described herein. In the transition from open water to new ice, brine is deposited on the surface of the new ice, hence, its dielectric constant will be higher than that of open water. Within hours, however, the ice thickens and the dielectric constant reduces. By the time grey ice or first year ice has evolved there is an order of magnitude change in dielectric constant. The dielectric constant for multiyear ice (the upper portion of the ice sheet) is about 30% smaller than that for first year ice. Results show that dielectric constant and incidence angle drive these ratios, with the largest differences occurring when there are larger differences in dielectric constant. Ratios among the ice types become larger with increasing incidence angle. Based upon these results and the L, C, X SAR data, it appears that the greatest ability to discriminate new ice and water is obtained at L-band by using the polarization ratio to segment open water and then detecting at VV-polarization the very weak returns produced by the nilas as contrasted to the stronger returns of open water.

DISCUSSION

A set of four SAR images (HH, HV, VH, VV) obtained at 9.38 GHz is provided in Figure 3 to illustrate ice conditions found in the Greenland Sea on 21 March. This scene was selected because it includes open water, nilas, young first year, and multiyear ice which were identified by both helicopter reconnaissance and in-situ sampling. One of the important features in this image set is the extensive lead area, much of which is in open water. Very thin ice was found to form in the shadowed regions of the open water lead which lie close to the vast multiyear ice floe (lower right hand corner). Adjacent to this lead in the lower left hand corner is a band composed of various stages of grey ice. A diagram of sea ice types identified from the SAR imagery is presented in Figure 4.

In general, the information within the four images of different polarizations is very similar, except in the case of the young ice types. Interestingly, the like-pol responses are different enough to have utility, and the comparison between the like- and cross-pol responses are even more dramatic. Hence, polarization diversification for use in separating young ice forms will be examined with interest. The nilas formed in the shadow areas produced a barely detectible enhancement in backscatter return at VV-polarization. The edge between ice and water was delineated. Contrast between these two ice types improved with decreasing frequency (i.e. at C- and L-band). The cluttering between the various young ice forms in the grey ice band suggests a sensitivity to roughness scales at this frequency.

A set of SAR derived products has been generated and is provided in Figure 5. These include σ°_{vv}, σ°_{hh}, σ°_{hv}, span, polarization ratio, depolarization ratio, correlation coefficient, and co-pol phase difference. These results and their interpretation were one of the focusses of the discussion of this presentation. These data were contrasted with preliminary results obtained by the surface-based scatterometer. These results are included in Table 2 for reference.

SUMMARY

A comprehensive collection of data has been obtained to characterize the microwave properties of Arctic sea ice and to allow further refinement of satellite SAR geophysical algorithms. Included is a critical set of data in which areas of open water, new ice, nilas, and young first year have been identified by in-situ observations.
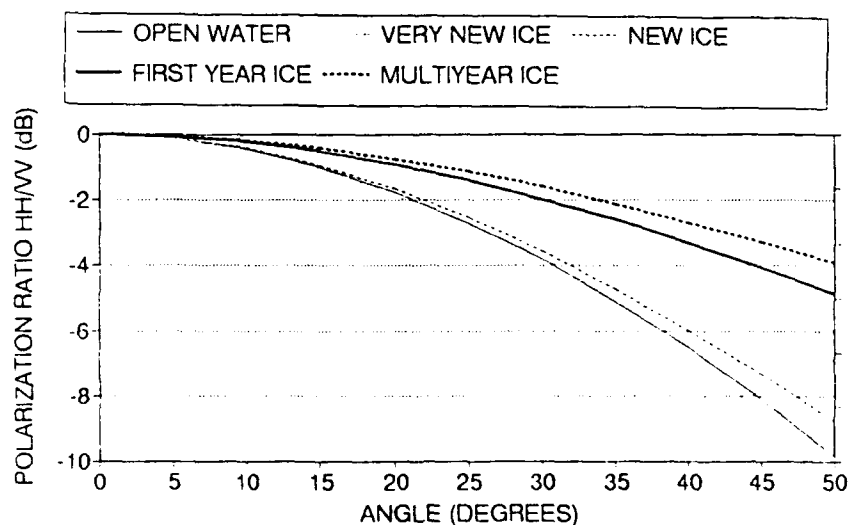
ACKNOWLEDGEMENTS

Figure 1. The Polarization Ratio ($\sigma^\circ_{HH}/\sigma^\circ_{VV}$) for Open Water, Very New Ice, New Ice, First Year Ice, and Multiyear Ice has Been Calculated Based on the Small Perturbation Model and Measured Dielectric Constants.
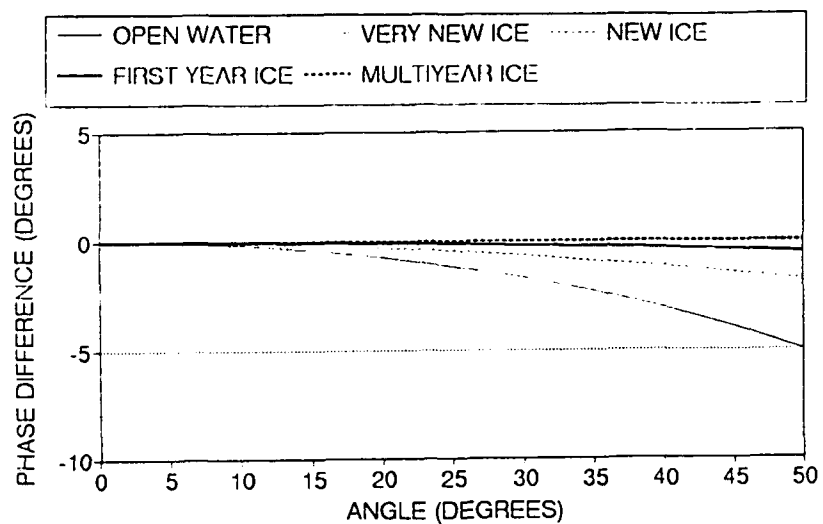
Figure 2. The Phase Difference Ratio ($\phi_{hh\,vv}$) for Open Water, Very New Ice, New Ice, First Year Ice, and Multiyear Ice has Been Calculated Based on the Small Perturbation Model and Measured Dielectric Constatns.
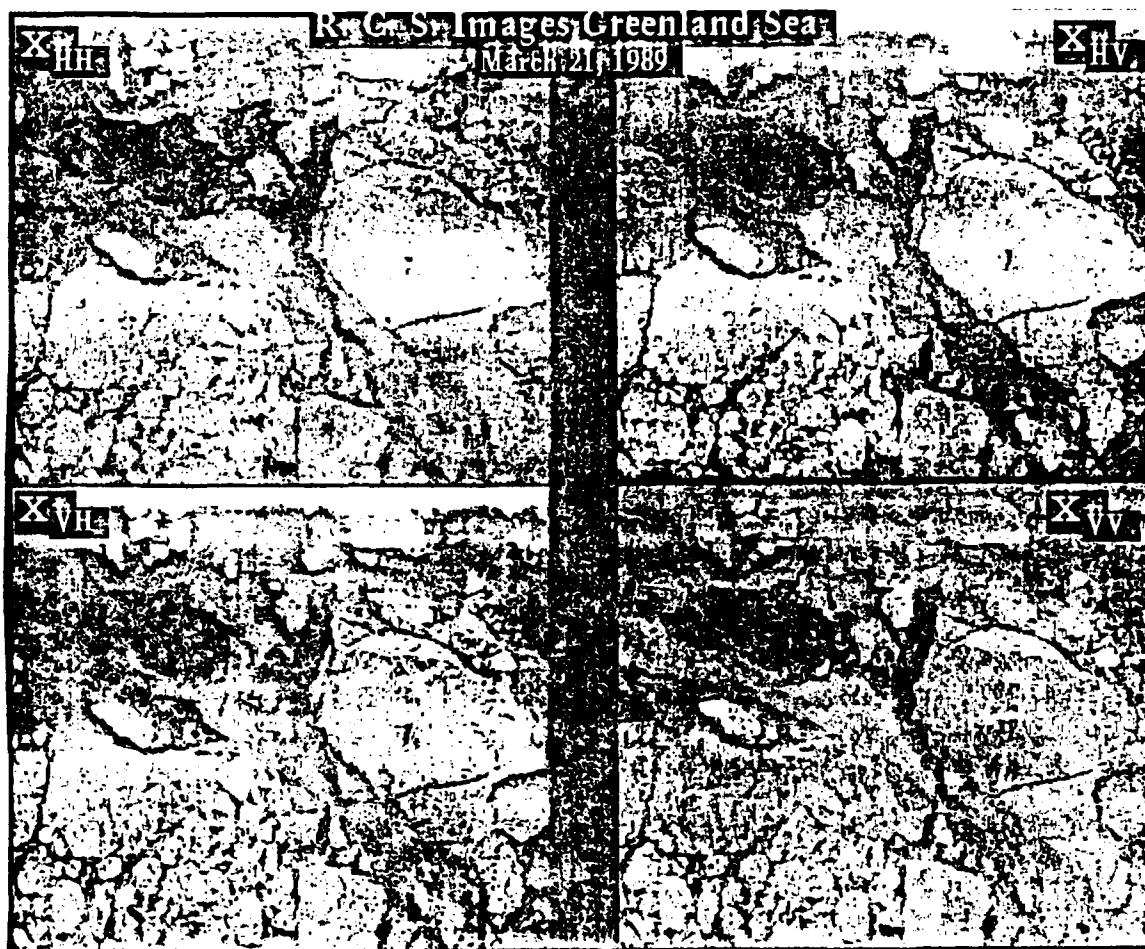

Figure 3. This X-band Quad-Pol SAR image was obtained in March 1989 during the Coordinated Eastern Arctic Experiment in the Greenland Sea.
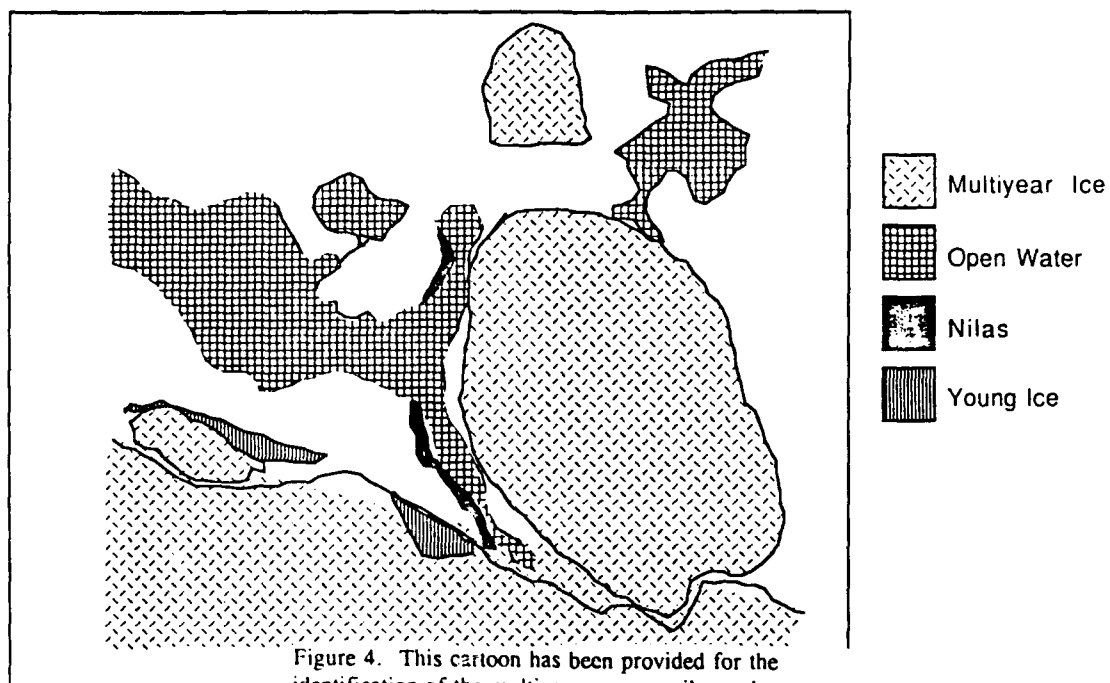
Figure 4. This cartoon has been provided for the identification of the multiyear, young, nilas and open water sites.

Table 1.

Examples of Sea Ice Physical Properties During CEAREX March 1989

Description	Multiyear	Thick First-Year	Young First-Year	Thin First-Year
Ice Thickness - m	2.55 ± .64	1.64	0.215 ± .4	0.42
Snow Thickness - cm	26 ± 19	9.5	8	5
T_{AIR} - °C	-18.3 ± 3.6	-19.7	-17.5 ± 3.5	-25
$T_{Ice/Surface}$ - °C	-16.2 ± 3.6	-13.2	-12.0 ± 2.8	-20
Salinity - PPT	0.17 ± .19	8.4 ± 3.0	9.9	7.9
Depth - cm	12	8	6	3
Density - kgm/m³	0.716 ± .19	.900 ± .03	0.844	0.359
Brine Volume	0.757 ± .83	51 ± 3	35	38

Table 2.

Preliminary Polarimetric Scatterometer Results

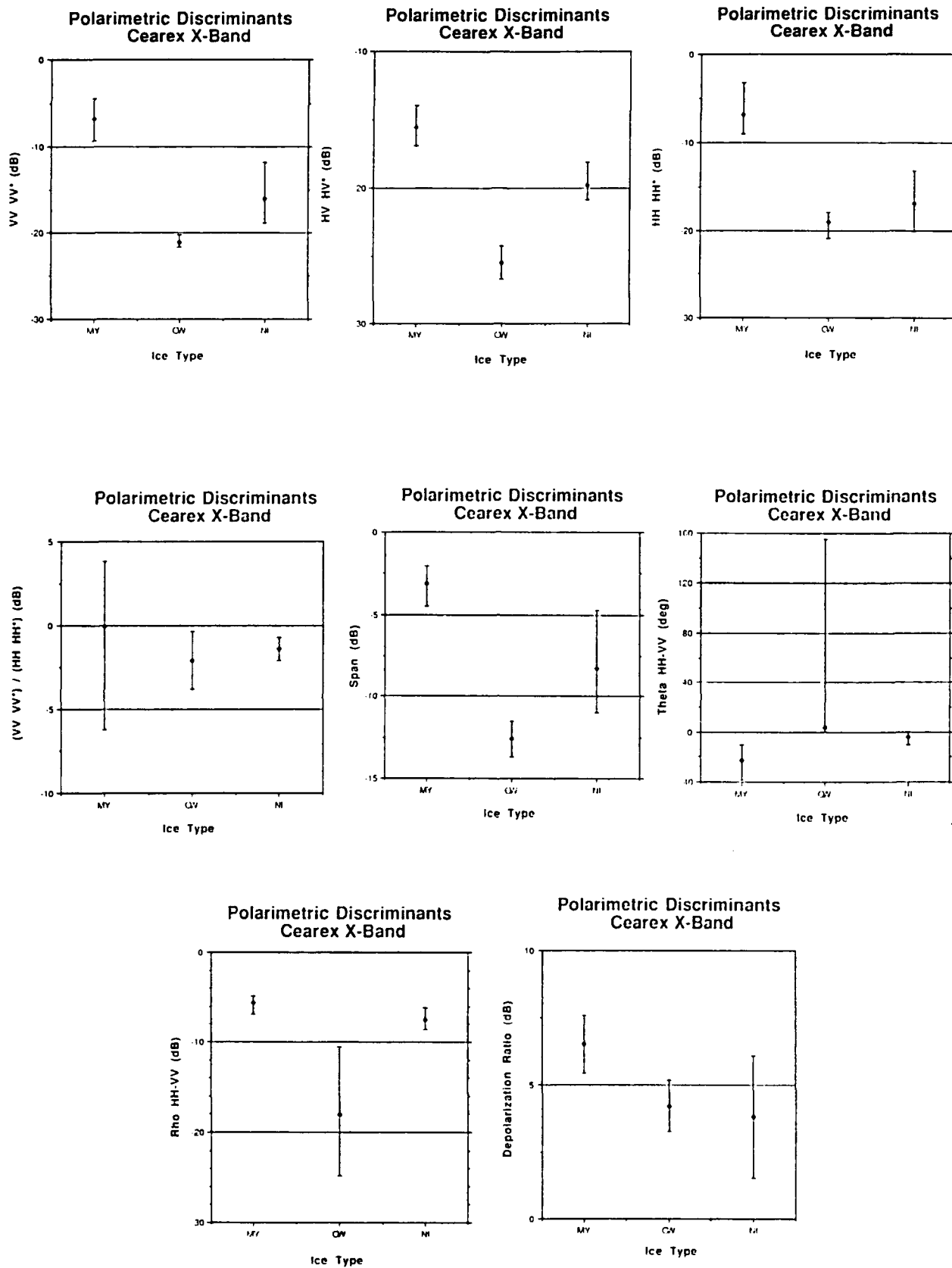| Scene	Dielectric Constant	Surface Roughness	$\sigma^\circ_{VV}/\sigma^\circ_{HH}$	$\frac{(\sigma^\circ_{VV} + \sigma^\circ_{HH})}{(\sigma^\circ_{VH} + \sigma^\circ_{HV})}$	Correlation Coefficient
Open Water	Large (≈ 40)	σ ≈ 0.2 cm l ≈ 7 cm	≈ 4 dB	≈ 20 dB	≈ 0.99
Nilas (2 cm)	Large	σ ≈ 0.05 cm l ≈ 1 cm	≈ 2 dB	≈ 20 dB	≈ 0.98
Grey (20 cm)	Low (≈ 4)	σ ≈ 0.05 cm l ≈ 1 cm	≈ 0 dB	≈ 16 dB	≈ 0.95
First Year (160 cm)	Low (≈ 4)	σ ≈ 0.2 cm l ≈ 7 cm	≈ 1 dB	≈ 12 dB	≈ 0.80
Multiyear (> 300 cm)	Low (≈ 3)	σ ≈ 0.2 cm l ≈ 7 cm	≈ 0 dB	≈ 9 dB	≈ 0.70

Figure 5. Polarimetric discriminant at X-band calculated for multiyear ice, nilas, and open water for 21 March CEAREX site.

Microwave and Physical Properties of Sea Ice in the Winter Marginal Ice Zone

W. B. Tucker III,[1] T. C. Grenfell,[2] R. G. Onstott,[3] D. K. Perovich,[1] A. J. Gow,[1] R. A. Shuchman,[3] and L. L. Sutherland[3]

Surface-based active and passive microwave measurements were made in conjunction with ice property measurements for several distinct ice types in the Fram Strait during March and April 1987. Synthetic aperture radar imagery downlinked from an aircraft was used to select study sites. The surface-based radar scattering cross section and emissivity spectra generally support previously inferred qualitative relationships between ice types, exhibiting expected separation between young, first-year and multiyear ice. Gradient ratios, calculated for both active and passive data, appear to allow clear separation of ice types when used jointly. Surface flooding of multiyear floes, resulting from excessive loading and perhaps wave action, causes both active and passive signatures to resemble those of first-year ice. This effect could possibly cause estimates of ice type percentages in the marginal ice zone to be in error when derived from aircraft- or satellite-borne sensors.

Introduction

The final field program of the Marginal Ice Zone Experiment (MIZEX) took place in March and April 1987. As with previous MIZEX field investigations, this experiment was carried out primarily in the Fram Strait. This particular program consisted of the winter phase of the experiment whose primary objective was to examine ice-ocean-atmosphere MIZ processes during the period of maximum ice extent. A detailed description of MIZEX objectives is presented by *Wadhams et al.* [1981]. Many of the results from the summer MIZEX programs are described in the special Marginal Ice Zone Research issue of the *Journal of Geophysical Research* (volume 92, number C7, 1987).

The objectives of the investigation described here were to determine, under winter conditions in the MIZ, active and passive microwave signatures for a variety of characteristic ice types and to relate these signatures to the physical properties of the ice. These joint measurements were conducted from the ice-strengthened Norwegian vessel *Polar Circle*. At selected sites, a variety of measurements were made, the most basic of which included documentation of the ice physical properties. Snow thickness surveys and pits excavated in the snow were used to furnish snow depths and physical properties. Radar backscatter and passive microwave measurements were made at a variety of frequencies, polarizations, and incidence angles. Both active and passive microwave systems were also routinely operated as the ship moved through the ice, thereby obtaining a large set of data encompassing a variety of ice conditions in the MIZ. Occasionally, the passive microwave system was mounted on a sled which was pulled across the floe in order to assess the small-scale within-floe variations.

[1]U.S. Army Cold Regions Research and Engineering Laboratory, Hanover, New Hampshire.

[2]Department of Atmospheric Sciences, University of Washington, Seattle.

[3]Environmental Research Institute of Michigan, Ann Arbor.

Instruments and Measurements

Synthetic Aperture Radar

Synthetic aperture radar (SAR) data collection missions were flown on a daily basis throughout MIZEX '87 using the Intera STAR systems. The Intera STAR 1 and STAR 2 are X band (0.032-m wavelength) HH polarization radars with resolutions ranging from 4 to 24 m. The high/low resolution swath width is 23/43 km for STAR 1 and 17/63 km for STAR 2. Each mission covered approximately a 200 by 200 km area surrounding the *Polar Circle*. During overflights, SAR data were transmitted via radio link to the *Polar Circle*, where they were used to select sites for the comprehensive microwave and physical properties investigations.

Ice Physical Properties

The physical properties description consisted of a detailed characterization of the snow cover and the underlying sea ice. Snow characterization entailed a snow thickness survey and an examination of the snowpack stratigraphy. The surveys typically consisted of snow depths measured on a grid of 25 or more locations spaced at 3 to 5 m. Snow stratigraphy was investigated by excavating a snow pit and measuring vertical profiles of snow temperature, density, ionic conductivity, and crystal size and type. In addition, solid snow specimens were prepared for later, more detailed structural studies, by filling the pore spaces of a sample with dimethyl phthalate and freezing the sample.

Our description of each site included floe size and qualitative surface topography information. At least one 80-mm-diameter ice core was taken through the entire thickness of each floe to enable analysis of the ice structural and physical properties. These cores were used to determine vertical profiles of ice temperature, salinity, density, and crystalline structure for successive 10-cm increments of core. Brine and air volumes were calculated using the measured parameters and the relationships formulated by *Cox and Weeks* [1983].

Passive Microwave

Passive microwave measurements were obtained at 10, 18, 37, and 90 GHz (X, K, K_a, and W bands) at a nadir angle of 50°, alternating between vertical and horizontal polariza-

tions. While the ship was moving, the four radiometers were mounted approximately 15 m above the ice, and continuous traverses of brightness temperature were recorded. At the ice stations when the ship was stationary against the selected floe, the radiometers were mounted on a sled, and traverses across the ice floe were carried out with the antenna pointed at 50° from nadir.

The effective emissivity at frequency ν for polarization p is determined from the formula [Grenfell and Comiso, 1986]

$$e_\nu(p, \theta) = (T_B - T_{sky})/(T_s - T_{sky}) \qquad (1)$$

where T_B is the brightness temperature of the surface at a nadir angle θ, T_{sky} is the brightness temperature of the sky at zenith angle θ, and T_s is the physical temperature at the snow-ice interface. This formula is appropriate for the determination of emissivity for a surface based measuring system in that it includes the entire atmospheric contribution to the sky radiation.

Present models calculate the microwave emissivity from the physical structure of the medium in terms of the relationship

$$e_\nu(p, \theta) = 1 - R_\nu(p, \theta) - S_\nu(p, \theta) \qquad (2)$$

where R is the effective surface reflectance and S is an angular integration of the surface and volume scattering. Each of these quantities is a function of frequency, polarization, and angle of observation. A distinction is made between reflectance and surface scattering in that the reflectance consists of the relative intensity of the coherent reflected field where surface scattering refers to the incoherently scattered field. R is determined largely by the bulk dielectric properties of the medium, while S (surface and volume scattering) is dependent on the distribution of inhomogeneities in the medium as well as the bulk dielectric constant.

Radar Backscatter

The backscatter measurements were obtained using two radar scatterometer systems operating from the the rail of the upper decks of the Polar Circle, about 15 m above the ice. Backscatter data were acquired at 1.5, 5.25, 9.38, 18, and 35 GHz (L, C, X, K_u, and K_a bands), although logistical considerations sometimes made it necessary to restrict the frequencies to 18 and 35 GHz only. In this paper we present results only from VV polarization, as it was the only polarization for which a complete set of measurements was obtained. Where other polarizations were available, corresponding values for HH polarization were usually found to be about 2–4 dB lower, while cross polarization was typically 20–30 dB lower. Data were collected at fixed angles as the ship transited the ice, while angular response measurements were made at selected stationary sites.

We use the conventional definition of radar scattering coefficient (σ_{vv}^0) as the average scattering cross section per unit area. The subscripts denote the received and transmitted polarizations respectively, and σ_{vv}^0 is given by the following expression [Ulaby et al., 1982, equation 11.2]

$$\sigma_{vv}^0 = \pi R^2 P_{vr}/AP_{vt} \qquad (3)$$

where R is the range to the target, P_{vr} is the total power scattered at V polarization by an equivalent isotropic scat-

terer in the direction of the receiver, P_{vt} is the transmitted power density at V polarization, and A is the illuminated area. Since only VV polarization results are presented here, we adopt the convention that σ^0 implies σ_{vv}^0.

Except for near-nadir viewing, where the backscatter is influenced predominantly by total scattering and surface reflection effects, the radar return is dominated by the combination of surface and volume scattering. Spatial fluctuations in the dielectric properties of the medium determine the magnitude of the scattering.

RESULTS

Combined measurements of ice and microwave properties were made at about 25 floes. Five specific sites representing the distinctive ice types observed during the experiment were selected for this investigation (Figure 1). The selected ice types consisted of pancake (P), multiyear (M), flooded multiyear (MF), first-year (F) and very young (50–100 mm thick) ice or nilas (N). Our observations indicated that the various ice types are fairly well intermixed throughout the Fram Strait MIZ. The major exception is pancake ice, which was generally found close to the ice edge, where the wave action needed to form this kind of ice is prevalent.

Figure 2 is a SAR mosaic of an area of the ice in Fram Strait, approximately 400 × 180 km. This particular image was collected on April 4, 1987, roughly the midpoint of the experiment. The area encompassed by the image is outlined in Figure 1. Typical ice types are identified on the SAR image. In general, bright tones on the image correspond to multiyear ice, while the darker tones are various stages of young ice. The blackest signatures are indicative of open water. We place a high degree of certainty on the identification of the designated ice types because they were identified directly by helicopter reconnaissance. This entailed carrying the downlinked SAR image on helicopter flights shortly after the actual SAR flight and locating recognizable features on the image (i.e., leads, large floes, etc). Ice in the vicinity of recognizable features was also identified as to type, concentration and mixture. This information has been used for the development of SAR interpretation algorithms [Shuchman et al., 1989; Wackerman et al., 1988].

No attempts were made to extract SAR backscatter values for the detailed study sites because sites were often located on floes that could not be distinctly identified on the image. Also, the SAR was not calibrated in an absolute sense, which leads to difficulty in attempting to compare backscatter values for particular ice types between different SAR flights.

Nilas, April 8, 1987

Figure 3 contains composite results of the nilas investigation site. The photograph (Figure 3a) shows the vast expanse (~5–10 km) of 20- to 60-mm-thick nilas ice that was examined. Small ice sheet overthrusts ranging from 15 to 20 mm high occurred every 0.2 to 0.5 m. At this particular site, both thermal growth and the subsequent rafting were responsible for increasing the ice thickness. Indeed, that case is suggested by the vertical thin section photograph of 30-mm-thick nilas shown (Figure 3b), which shows a mixed structure of granular and small columnar crystals, generally a type of structure that precedes purely congelation ice
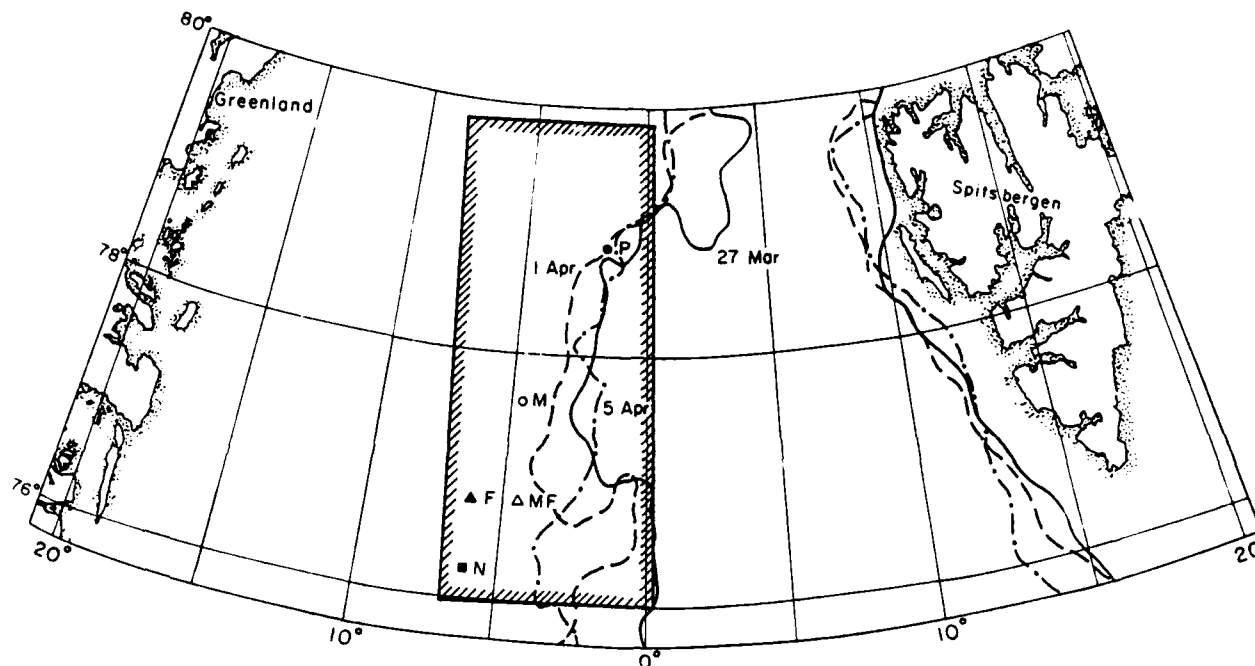
Fig. 1. Sampling sites in the Fram Strait with approximate location of the ice edge on March 27, April 1 and April 5, 1987. Sites are designated by ice type for first-year (F), nilas (N), pancake (P), multiyear (M), and flooded multiyear (MF). Box indicates approximate area covered by SAR image shown in Figure 2.

growth. The structural discontinuity in the middle of the sample is attributed to rafting of one sheet upon another. The high salinities, ranging from 14.3 to 16.2‰, were a result of rapid freezing and hence brine retention within the granular ice structure. Density was also relatively high, about 0.92 Mg m^{-3}, indicating minimal entrapment of air in the ice.

The emissivity spectra for this case (Figure 3c) represent averages over a distance of several hundred meters and show a strong increase from 10 to 90 GHz at both vertical and horizontal polarizations. Also shown for reference are the spectra measured for open water. The error bars represent standard deviations, or uncertainty in the measurements. The spectra are intermediate between that of open water and that of thick first-year ice. This probably results from a combination of two effects. The real part of the dielectric constant of brine decreases with increasing frequency, giving the lowest ice-air surface reflectivity at 90 GHz. According to Table 1, where optical thicknesses have been estimated for first-year ice types, at lower frequencies the ice is not optically thick, so the underlying water significantly increases the net reflectivity at 10 and 18 GHz. The difference in slopes between V and H polarization is most likely due to the presence of small-scale surface roughness elements on a size scale which would scatter weakly at 37 GHz but significantly more at 90 GHz.

Backscatter coefficients for nilas (Figure 3d) are the smallest of all the ice types investigated in this study. The σ^0 values presented here, however, are up to 30 dB higher for K_u band over incidence angles of 30° to 50° than results of Onstott and Shuchman [1988] for undisturbed nilas. The increase shown here is probably due to the backscatter from the numerous exposed edges created by overthrusting, and possibly, the higher surface dielectric due to flooding with seawater. The scattering coefficients for nilas decreased

rapidly with increasing nadir angle from −5 dB at 20° to between −15 and −17 dB at 50° at both K_u and K_a bands.

Pancake Ice, March 29, 1987

Pancakes existed in both loosely aggregated and closely packed forms at this site (Figure 4a). The individual pancakes ranged in size from 0.3 to over 1.5 m in diameter and 50 to 130 mm in thickness. The raised edges or rims, which ranged in height from 10 to 50 mm above the relatively flat surface, resulted from collisions between individual pancakes and from the freezing of seawater and frazil which splashed onto the edges of the pancakes. As the thin section in Figure 4b indicates, the structure of this ice is very similar to that of the previously described nilas. Specifically, the texture appears to consist of closely packed platey-type crystals. This type of structure has been observed in young ice forming in a disturbed water column [Eicken and Lange, 1989]. This is certainly reasonable in this case because pancake formation itself is indicative of growth in a disturbed or wind-whipped sea. Salinity of the pancakes ranged from 9 to 12‰, somewhat less than that of the nilas. However, bulk ice density was the same as the nilas, 0.92 Mg m^{-3}.

The emissivity spectra for pancake ice (Figure 4c) are again spatial averages and represent a composite of the pancakes and the open water surrounding them. In accordance with Table 1, the ice is optically thick at all frequencies except 10 GHz, which results in a higher, flatter spectrum than for nilas. The rather high degree of polarization (defined as $[e_v(V, \theta) − e_v(H, \theta)]/[e_v(V, \theta) + e_v(H, \theta)]$) is probably due to the contribution of the open water but may also be indicative of a smooth ice surface.

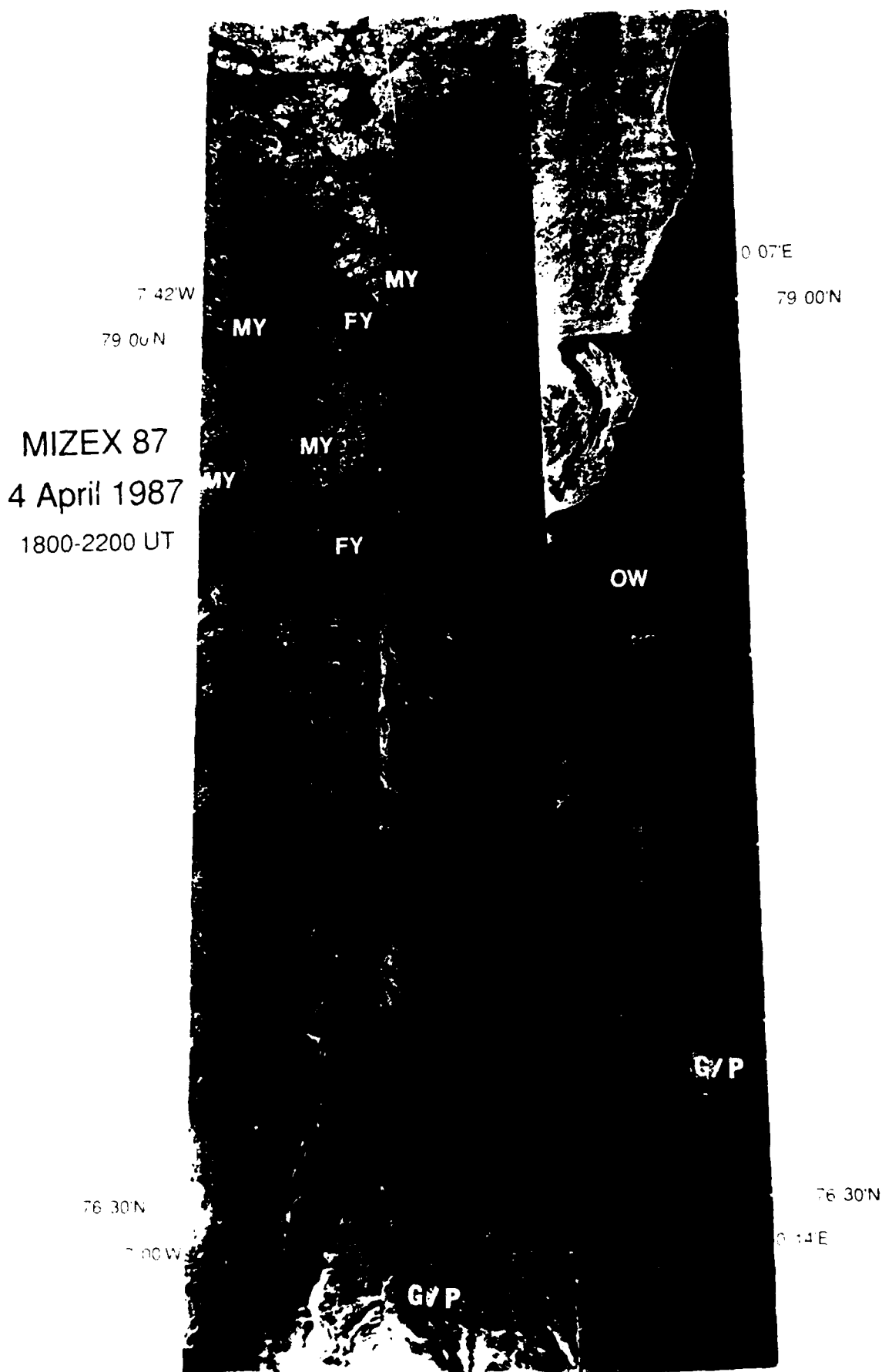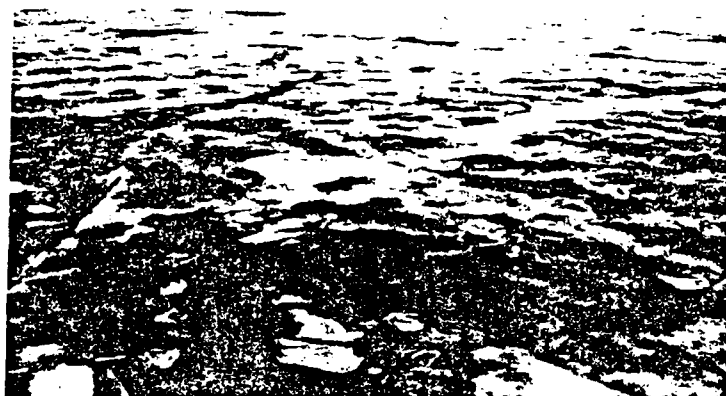Backscatter coefficients for the pancake ice are quite

Fig. 2.　SAR image mosaic of the Fram Strait marginal ice zone on April 4, 1987. Typical ice types identified by helicopter reconnaissance are multiyear (MY), first-year (FY), and grease and pancake (G/P) ice and open water (OW).
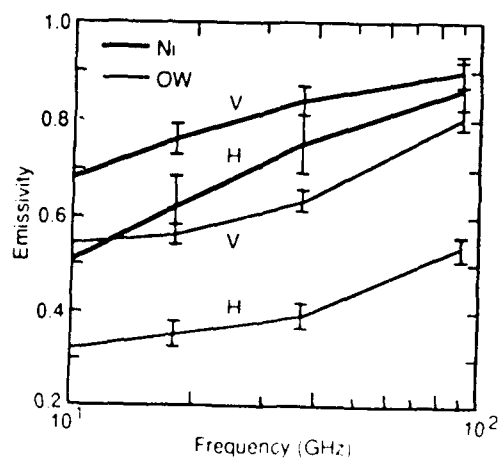
a

Thickness = 0.03 m
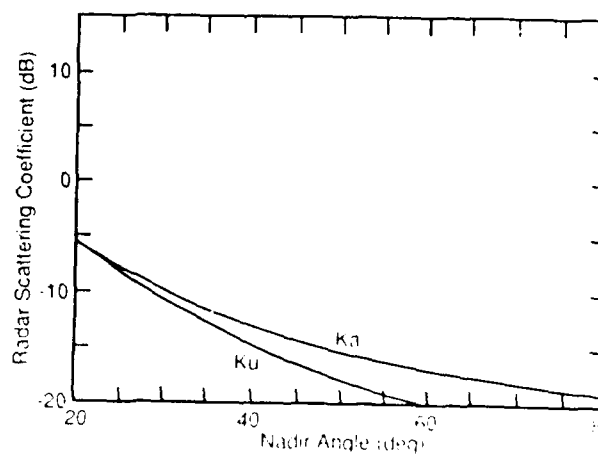Salinity = 15. 3 ‰
Density = 0.92 Mg m^{-3}

b

Top

Bottom

c

d

Fig. 3. Nilas ice, April 8, 1987. (a) photograph of site, (b) vertical thin section of ice, (c) passive microwave emissivity for vertical and horizontal polarizations, and (d) radar backscatter coefficient. Emissivities are also shown for open water.

TABLE 1. Optical Depths as a Function of Frequency for Thin
Ice Types

	Optical Depth τ			
	10 GHz	18.7 GHz	37 GHz	90 GHz
30-mm nilas	1.2	3.4	6	12
50-mm pancakes	2	5.7	10	20
1-m first-year ice	40	114	200	400

Uncertainty in optical thicknesses is estimated to be 50%, depending on fluctuations in brine volume. Optical depths τ are estimated from the results of Grenfell [1986] and Grenfell and Comiso [1986]. Estimates for the 1-m ice assume salinities consistent with thinner ice; thus optical depths may be slightly high. Ice is referred to as being optically thick if τ exceeds 4, for which 98.2% of the incident radiation on the layer would be absorbed.

variable owing to differences in the heights of the rims surrounding the pans. Results for two cases at the pancake ice site are shown in Figure 4d. The solid lines are for the predominant pancake type ice, and the crosses are from an area of thicker and rougher pancake ice. For the case represented by the solid curves, the pan rims were rather small, and σ^0 values at K_u and K_a bands are only slightly above the values for nilas. The angular dependence was also similar, including the crossover at nadir angles of 20° to 25°. Scattering at X band, however, was from 7 to 15 dB greater than that at K_a and K_u bands. For the rougher pancakes, the σ^0 at 40° was enhanced by about 17 dB at K_a band, and the difference between K_a and K_u increased to about 8 dB.

First-Year Ice, April 6, 1987

This site was located on a 100-m-diameter floe contained within a several-kilometer expanse of thin first-year ice (Figure 5a). The ice at the coring site measured 0.36 m thick and was overlain by 100 mm of snow. The snow had a density of 0.09 Mg m^{-3} and consisted of 0.25- to 1.00-mm needle and stellar crystals. This area was free of major ridges, although many small cracks and some rafting were evident once the snow cover was removed. The ice surface consisted of raised edges 10 to 100 mm high, occurring every 5 to 10 m. The crystalline texture (Figure 5b) through the entire ice thickness consisted of fine-grained columnar ice crystals indicating that growth had occurred under relatively calm conditions. The salinity of the ice ranged from 7 to 9.8‰ with a bulk salinity of 8.6‰. Bulk density of the ice was 0.92 Mg m^{-3}. The combination of thin ice and the insulating effect of the thick snow cover resulted in a relatively warm ice surface temperature of −3.5°C.

The emissivities for this case (Figure 5c) are very close to unity, the spectra are quite flat, and the difference between vertical and horizontal polarizations is small, consistent with a variety of observations made to date from the surface, aircraft, and satellites [Grenfell, 1986; Cavalieri et al., 1984a, b]. The ice was optically thick (Table 1), implying that emission was primarily from the surface. The smaller difference between $e_v(V, 50)$ and $e_v(H, 50)$ as compared with younger ice types was probably a result of influences of the snow layer and lower salinity. This may also account for the slight decrease at 90 GHz. The spectra of thick first-year ice seem to be rather insensitive to ice conditions and have been used as a benchmark point for almost all sea ice work to date.

The backscatter coefficients (Figure 5d) are indicative of first-year ice having a surface roughness of the order of a few millimeters [Kim et al., 1985; Onstott et al., 1979]. This small roughness was not detected by our properties measurements, however. The backscatter coefficients at K_u and K_a band are 10 and 18 dB greater, respectively, at 25° than those for pancake ice, and σ^0 decreases almost linearly with frequency. Sigma values at all frequencies decrease more slowly with increasing nadir angle than for either pancakes or nilas.

Multiyear Ice, April 3, 1987

This site was located on a 100 × 200 m floe embedded in a loosely concentrated field of similar sized floes (Figure 6a). The floe had a hummocky surface with general relief of about 0.5 m and also featured a 4-m-high ridge on one side (not shown in the photograph of Figure 6a). It appeared that the floe contained a substantial amount of deformed ice. This was verified by three thickness measurements which ranged from 3.01 m at the coring location near the center of the floe to 4.46 m on the flank of the ridge. A thorough snow survey revealed a rather thick layer with depths ranging from 0.14 to 1.20 m, about a mean of 0.40 m. The snowpack consisted of a 60-mm surface layer of 1- to 2-mm-long delicate needles with a density of 0.09 Mg m^{-3}. The surface layer was underlain by a layer varying in thickness containing 0.3- to 0.5-mm-diameter rounded grains with density of 0.31 Mg m^{-3}. The crystal structure of the underlying ice (Figure 6b) was primarily columnar, with only a 0.20-m-thick layer of granular ice at the surface and a mixed congelation and granular ice layer from 1.0 to 1.2 m below the surface. There was, however, a significant amount of inclined columnar ice in this core, indicating previous deformation or ridging. During normal undisturbed ice growth, columnar crystals are oriented vertically; thus the occurrence of inclined crystals in a vertically drilled core usually implies the presence of tilted ice blocks. The salinity of this floe was quite low, being typical or multiyear ice, with a bulk salinity of 2.9‰. Discontinuities in the salinity profile may correspond either to structural breaks or to annual transitions. It is logical for salinity discontinuities to appear in deformed (ridged) ice because normal vertical drainage patterns are likely to be interrupted by the existence of an inclined block-granular ice structure. Also typical of multiyear ice is the low-density ice constituting the upper layers. Such structure results from the desalination and thermal modification of the upper layers during summer, leading to increased porosities and, consequently, lowered densities in near surface ice.

The present measurements represent our first surface-based radiometric observations over winter multiyear ice. For this case, several spectra were obtained (Figure 6c). They show a pronounced negative spectral gradient (de$_v$(p, θ)/dv) considered characteristic on the basis of previous aircraft and satellite observations [Cavalieri et al., 1984b; Troy et al., 1981]. This might be due to strong volume scattering in the low-loss, desalinated, near-surface layers. The light solid and dashed spectra were obtained from different locations on this floe. The increase in emissivity between 37 and 90 GHz is unexpected and results from the very thick snow layer which is not transparent at 90 GHz. Variations at 90 GHz over snow covered ice will, in general,
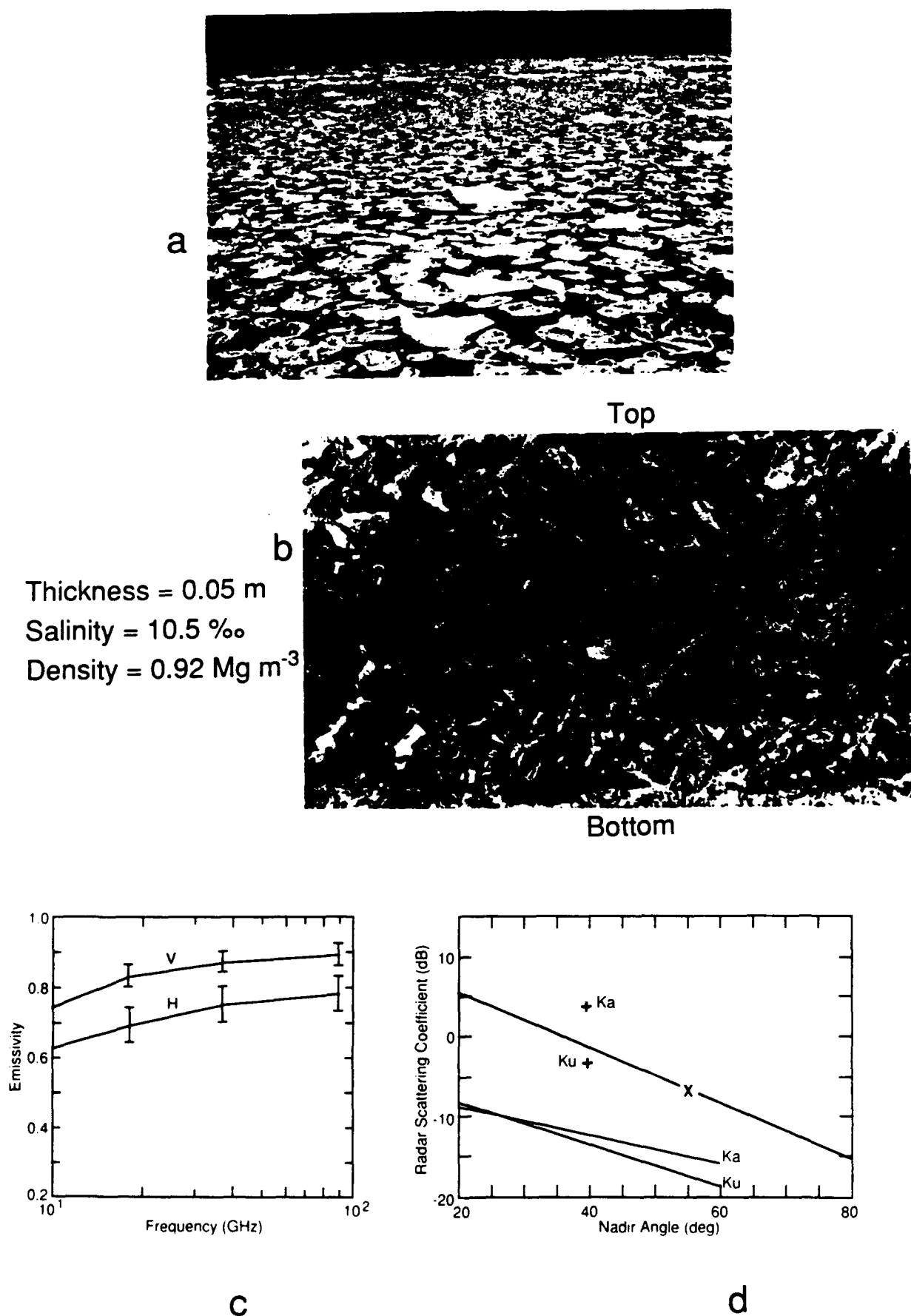
a

Top

b

Thickness = 0.05 m
Salinity = 10.5 ‰
Density = 0.92 Mg m⁻³

Bottom

Fig. 4. Pancake ice. March 29. 1987: (a) photograph of typical pancake conditions. (b) vertical thin section. (c) emissivity. and (d) backscatter coefficient. Data indicated by crosses on the backscatter plot are from an area of thicker and rougher pancakes.
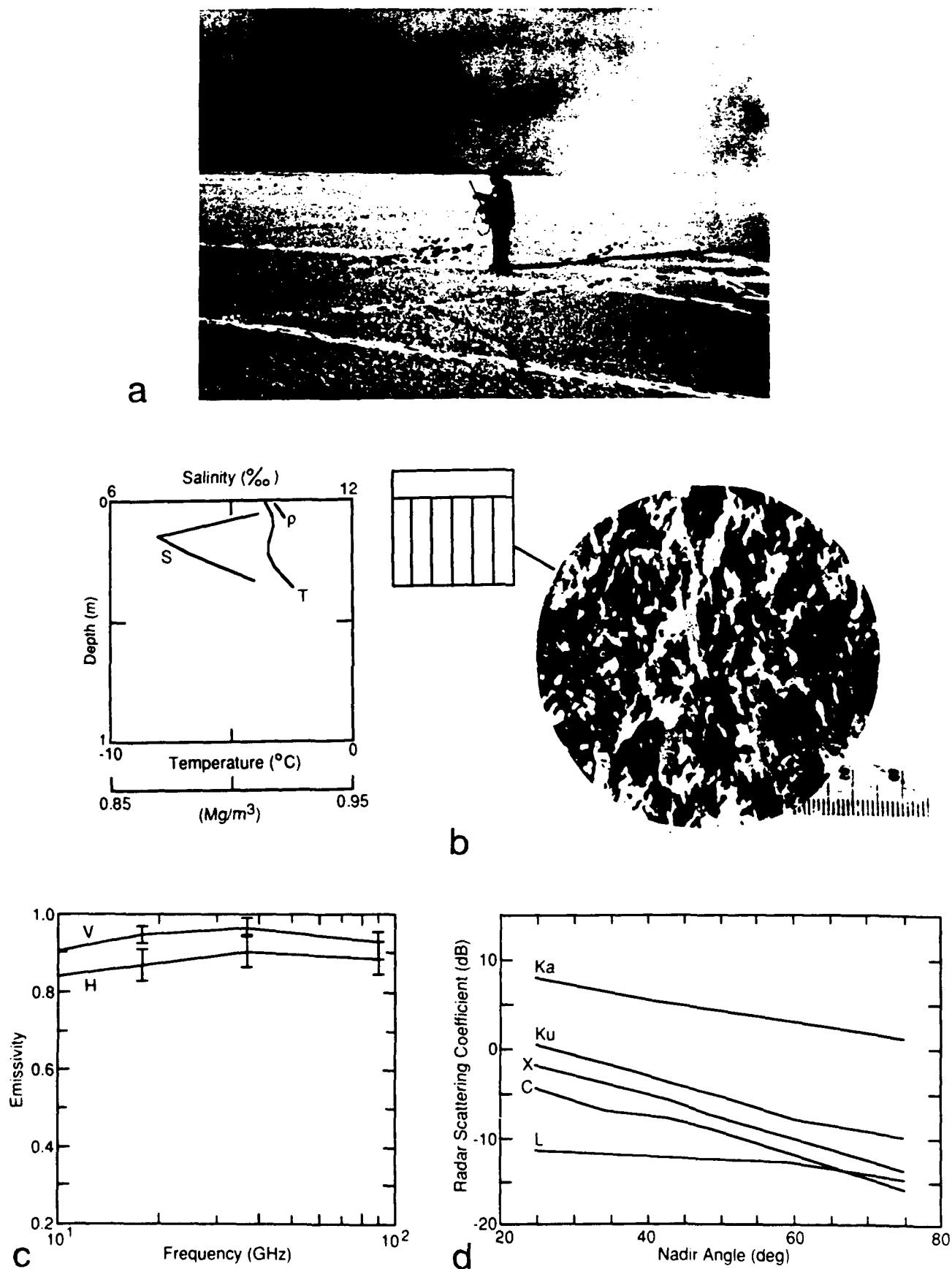
Fig. 5. First-year ice. April 6, 1987: (a) photograph of site. (b) properties and structural profile. (c) emissivity. and (d) backscatter coefficient. Curves labeled S, T, and ρ on the properties profile are salinity, temperature, and density.
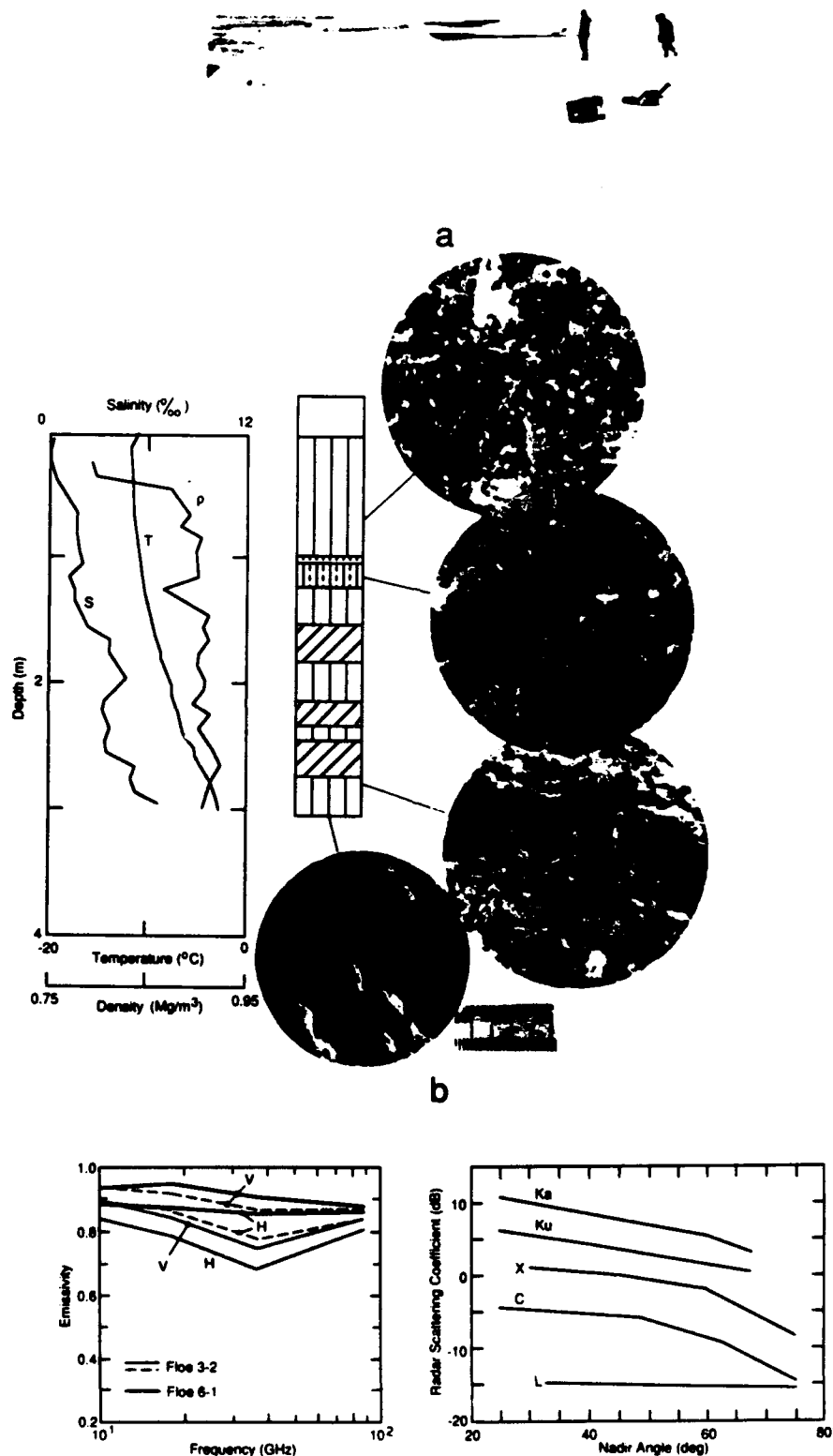
Fig. 6. Multiyear ice, April 3, 1987: (a) photograph of site (b) properties and structural profile, (c) emissivity, and (d) backscatter coefficient. Two emissivity spectra are presented for this site (3-2) in addition to that from another multiyear site (6-1).

be sensitive to snow grain size and density. The dark solid curve, obtained from a hummock on a different floe, shows a weak negative spectral gradient.

Multiyear ice produced the strongest backscatter (Figure 6d) of the ice types considered in this investigation. This is consistent with observations made under cold conditions in other geographic areas [Onstott et al., 1982]. The angular response of the radar scattering coefficients at frequencies from 1.5 to 35 GHz is smooth, the scattering increases uniformly with frequency, and the curves are evenly spaced with respect to each other. In fact, the backscatter intensity (calculated as $10^{[\sigma(dB)/10]}$) is proportional to the square of the frequency. Such a uniform increase suggests that the backscatter originates from the same roughness elements and internal inhomogeneities (e.g., air bubbles).

Flooded Multiyear Ice, April 7, 1987

The photograph in Figure 7a shows the 50 × 70 m multiyear floe on which flooding of the surface by seawater significantly altered the physical and microwave properties. This floe was covered by snow averaging 0.84 m thick, one of the thickest snow covers observed on the experiment. The snowpack consisted of three distinct layers. The top layer was 0.08 m of new snow composed of 1.0- to 1.5-mm stellar dendrites of density 0.07 Mg m^{-3}. At the bottom was a 0.14-m layer of 0.31 Mg m^{-3} density depth hoar consisting of 3- to 4-mm scrolls. The remainder of the snowpack was 0.40 Mg m^{-3} density, 0.2- to 0.5-mm rounded grains. Ice thickness at the coring location was 4.10 m. Surface topography was consistently low, with generally less than 0.3 m relief. Ice structure, as shown in Figure 7b, was a mixture of columnar, inclined columnar and granular. Granular ice made up 32% of the entire core. The presence of inclined columnar ice in conjunction with granular ice in the structural profile implies that this ice had undergone deformation at some point during evolution [Tucker et al., 1987].

The most unusual feature of this multiyear floe was the very high salinity values in the upper 0.4 m. Salinities of 6 to 10‰ are normally associated with first-year ice. We attribute high salinities in this instance to flooding of the surface by seawater which seeped into and became trapped in the porous upper layers. The flooding likely resulted from depression of the floe by the excessive snow load and associated wave action. This situation was supported by the observation that at the time of coring there was less than 10 mm of freeboard in the core hole. Once again the low density of the ice near the surface, so typical of multiyear floes, was evident here. The depressed freeboard and possibly the intrusion of seawater appear to have warmed the ice. The lowest temperature was slightly below −5°C, whereas for the dry multiyear floe, described earlier, the minimum ice temperature was about −12°C.

Representative emissivity spectra for two flooded multiyear ice sites are shown in Figure 7c. These are essentially indistinguishable from that of first-year ice. This results from the modified high salinity layer at the base of the snow and in the upper 0.4 m of the ice. The two pairs of curves show results from sites with differing snow characteristics: the curves from the April 7 floe (Figure 7c, floe 7-1) described here had thicker snow. The values at 90 GHz are controlled by the characteristics of the overlying snow layer. Consequently, for the thicker snow, they are the same as for the case of dry multiyear ice.

The flooding of snow-covered multiyear ice by seawater has a dramatic effect on the backscattering properties. The flooded multiyear ice has a signature similar to that of typical first-year ice. As can be seen by comparing Figure 7d with Figure 6d, the dry multiyear ice, the σ^0 values are reduced by 4 and 10 dB at 35 and 18 GHz, respectively, for the flooded floe. The difference in reduction suggests that the snow layer contributes significantly to the backscattering at 35 GHz.

DISCUSSION

The greatest difference between first-year and multiyear ice backscatter levels is produced at a frequency of 18 GHz; however, the differences in emissivity are greatest at 37 GHz. Although this difference may be attributed to the possibility that the active and passive sensors were focused on slightly different areas of the same floe, it may also be due to cracks or other surface inhomogeneities in the first-year ice, which produce enhanced backscattering at 37 GHz but which have little effect on the integrated scattering. The smooth increase in scattering with frequency for multiyear ice appears to be consistent with the emissivity spectra.

The radar contrast between multiyear and rough first-year ice is least in the angular region near 25°. For frequencies between 5 and 35 GHz, the contrast ranges between 2.5 and 7.5 dB. At 1.5 GHz, these ice types show similar backscatter levels, with the first-year ice returns higher by 1 to 2 dB. This may have been the result of greater surface roughness on the 0.10- to 0.30-m scale for the first-year ice.

The changes between multiyear and flooded multiyear in the emissivity spectra and the backscattering appear consistent. At K_a band the backscatter at large nadir angles was reduced significantly on the flooded multiyear, while the emissivity increased measurably. At 18 GHz, however, the reduction in backscatter was larger than that at 35 GHz, yet no effect was measurable in $e_v(V, 50)$. This seems consistent with the notion that the snow-ice interface was very strongly absorbing and that the snow cover was almost transparent at 18 GHz but much less so at 37 GHz.

Within the present levels of accuracy, the emissivity spectra found in the Greenland Sea MIZ for the younger ice types are at least qualitatively consistent with corresponding observations in other locations at similar times of year. We do not know if this is true for winter multiyear ice, however, because we have no previous data for comparison. Both the present observations and aircraft data [Troy et al., 1981] show that the multiyear spectra are quite variable, even on a single floe (Figure 6c). Although the multiyear ice in the MIZ is structurally similar to multiyear ice in the eastern Arctic, the increase in snow cover modifies the microwave signatures directly because it represents a significant extra scattering layer whose structural properties can evolve rapidly during warming events. A thick snow cover also has an indirect effect in that it provides enough additional mass to make surface flooding relatively common in the presence of ocean swell.
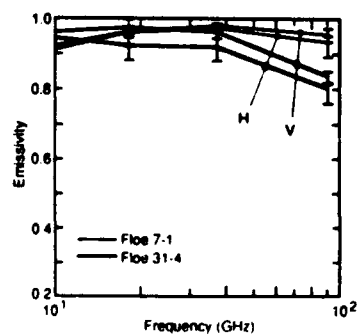
We are interested in assessing which of the physical properties besides snow cover that were measured significantly affect the microwave properties. There are, of course, extremely important properties that were beyond the scope of our measurement program. As was previously inferred, surface roughness is very important. Also, the distribution of
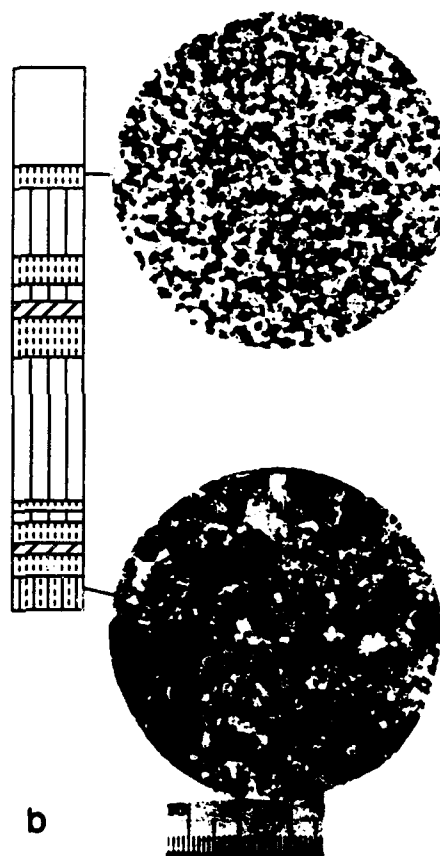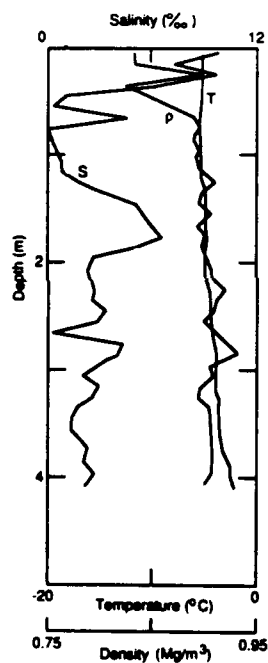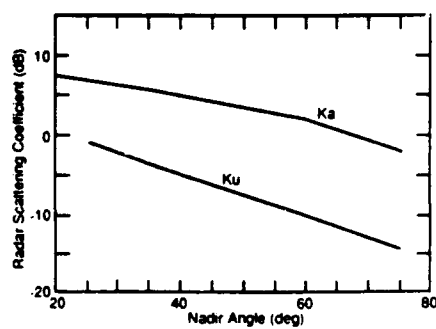
Fig. 7.   Flooded multiyear ice. April 7, 1987: (a) photograph of floe, (b) properties and structural profile, (c) emissivity, and (d) backscatter coefficient. Emissivity spectra are shown for this site plus an additional flooded multiyear floe.

TABLE 2. Summary of Basic Ice Properties for Each Ice Type With Passive Microwave Polarization and Gradient Ratios and Active Microwave Gradient Ratios

	Nilas	Pancake	First-Year	Multiyear	Flooded Multiyear
Date	April 8	March 29	April 6	April 3	April 7
Latitude (North)	76°15.0'	78°50.3'	76°44.8'	77°36.9'	76°49.5'
Longitude (West)	6°03.0'	1°39.8'	6°16.8'	4°54.8'	4°44.2'
Physical properties					
Snow depth, m	0.00	0.00	0.10	0.40	0.84
Ice thickness, m	0.03	0.05	0.36	3.01	4.10
Density (top 0.1 m), Mg m^{-3}	0.92	0.92	0.92	0.79	0.84
Bulk salinity, ‰	15.30	10.50	8.60	2.76	3.21
Percent granular	100	100	0	2	32
Percent columnar	0	0	100	62	62
Percent inclined	0	0	0	30	6
Passive microwave					
PR (18 GHz)	0.220	0.092	0.044	0.041	0.032
GR (37, 18 GHz)	0.074	0.024	0.010	−0.055	0.008
Active microwave					
GR (K_u, K_a)	−0.280	−0.115	−0.753	−0.383	−0.798

liquid and vapor within the ice determines the degree of volume scattering [*Tsang and Kong*, 1981; *Stogryn*, 1985, 1987]. Clearly, the dielectric properties of sea ice play a large role in determining the microwave signatures. Since the bulk dielectric constants of sea ice and snow are strongly modulated by the amount and distribution of liquid (both brine and fresh water), the salinity and temperature of the ice are of primary importance. Therefore it is meaningful to compare the microwave signatures with the first-order properties of the ice that were measured.

In Table 2 we present a synopsis of the important physical data that were documented in this investigation. The table also contains ratios which are useful in summarizing important results of the microwave signatures. For the microwave radiometry we show the gradient ratio GR and the polarization ratio PR used in the scanning multichannel microwave radiometer (SMMR) "team algorithm" for the determination of concentration and the identification of first-year/multiyear ice type distribution [*Cavalieri et al.*, 1984b]. These ratios are given by

$$PR(18) = \frac{e_{18}(V, 50) - e_{18}(H, 50)}{e_{18}(V, 50) + e_{18}(H, 50)} \quad (4)$$

$$GR(37, 18) = \frac{e_{37}(V, 50) - e_{18}(V, 50)}{e_{37}(V, 50) + e_{18}(V, 50)} \quad (5)$$

Similarly, a gradient ratio has been calculated for the radar backscatter for K_u and K_a bands (18 and 35 GHz) at a nadir angle of 40° from the following definition:

$$GR\ (K_u, K_a) = \frac{I(\sigma^0 K_u) - I(\sigma^0 K_a)}{I(\sigma^0 K_u) + I(\sigma^0 K_a)} \quad (6)$$

where $I(\sigma^0)$ are the backscattered intensities determined from the transformation $I = 10^{[\sigma(dB)/10]}$. The order of the frequencies has also been reversed from those in the passive gradient ratio (equation (5)). In this manner, the radar gradient ratio varies in the same sense as the passive; that is, greater scattering at higher frequency gives a more negative value of GR. While this parameter may not be useful for the first generation of single-frequency radar satellites, it is introduced here because it very likely provides a measure of

the size distribution of scattering inhomogeneities either in the ice or on the surface. Thus we feel that GR(K_u, K_a) should be useful for improving the capability of distinguishing ice types when appropriate instrumentation becomes available.

In Table 2, PR(18) shows a steady decrease with ice age from initial formation through thick first-year ice, while the differences between first-year, dry multiyear, and flooded multiyear are small. GR(37, 18) decreases consistently with the age of the ice with exception of the flooded multiyear ice, whose value is very nearly that of first-year ice.

The large negative values of the radar gradient ratio, GR(K_u, K_a), are anticipated because radar scattering cross sections typically increase with increasing frequency; both theory and observations support this trend. The differences between nilas and pancake cases are nearly indistinguishable. The raised edges of the pancakes and overthrust edges of nilas were large relative to the K_u and K_a band wavelengths (about 17 and 8.7 mm, respectively), and they appear to have produced similar backscatter intensities. With its very large negative value, first-year ice is quite distinct from dry multiyear or the new ice types. It is important to note that the gradient ratios for first-year and flooded multiyear are similar, which implies that even this active microwave ratio is masked by flooding.

Table 2 also indicates that the passive microwave gradient ratios can be related to the age of the ice. The passive ratios also appear to correlate well with the salinity, generally decreasing when the salinity decreases, thus reinforcing the relationship to the age of the ice. While a relationship between ice age or salinity and the radar gradient ratio is not apparent, there are distinct differences between thick first-year, multiyear, and young ice types. In the case of the flooded multiyear, the increased brine volume in upper layers resets the salinity to be practically the same as that of first-year ice, and the observed microwave signatures are consistent with this "effective" age.

Contrasts between emissivity and backscatter cross sections at Ka band are shown in Figure 8. Similar behavior was observed at 18 GHz. The points are ordered by increasing σ^0 and range from open water through dry multiyear ice. The points for open water were taken from *Grenfell and Comiso*
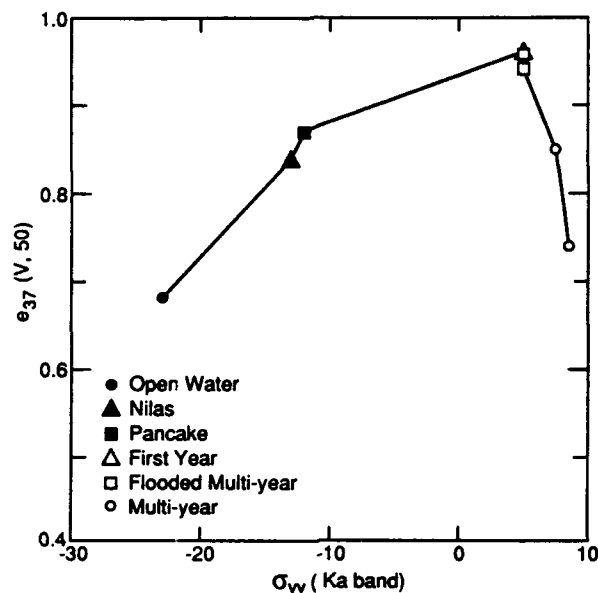
Fig. 8. Emissivity at 37 GHz versus radar backscatter at K_a band for open water, nilas, pancake, first-year, two flooded multiyear, and two multiyear sites.

[1986] and from *Onstott and Shuchman* [1988]. There appear to be two correlation regimes. The first covers the thin ice types through first-year ice where both e_ν and σ^0 increase together, and the second includes the first-year and multi-year cases for which e_ν decreases with further increase in σ^0. In the first regime we believe that the emissivity is increasing because of decreasing reflectivity as the ice thickens while scattering increases owing to the development of surface roughness. In the second regime it is our opinion that scattering becomes dominant and emissivity decreases as scattering increases. First-year and flooded multiyear ice are located at the apex where scattering begins to contribute significantly to the emissivity.

Although using the combination of emissivity and back-

scatter at a single frequency (Figure 8) to distinguish between ice types is superior to using either separately, results are less than satisfactory. The ice type separation shown in Figure 8 is apparently similar to radiometric cluster plots [e.g., *Cavalieri et al.*, 1984b]. More information appears to be provided if we include the polarization and gradient ratio values from Table 2. Two likely representations are shown in Figures 9 and 10, where we have plotted the passive gradient and polarization ratios, respectively, against the active gradient ratio.

In Figure 9, the active gradient ratio separates open water from nilas and pancakes from first-year ice, showing that these pairs which are unresolved by GR(37, 18), have very different scattering characteristics. The passive gradient
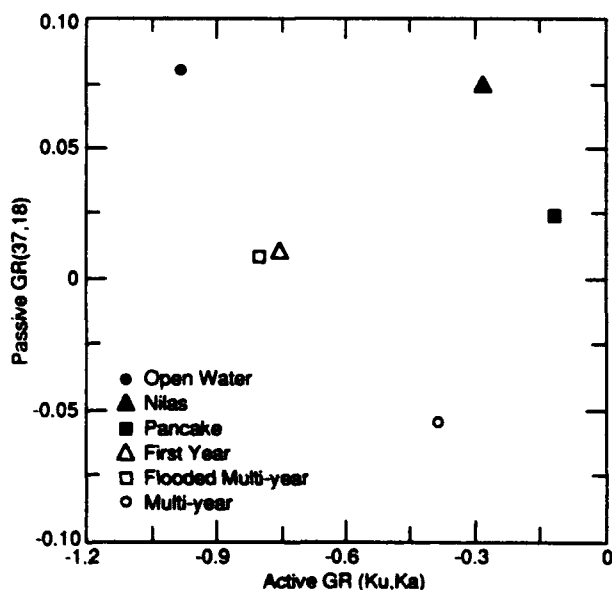
Fig. 9. Passive gradient ratio, GR(37, 18), versus active gradient ratio, GR(K_u, K_a), for the different ice types.
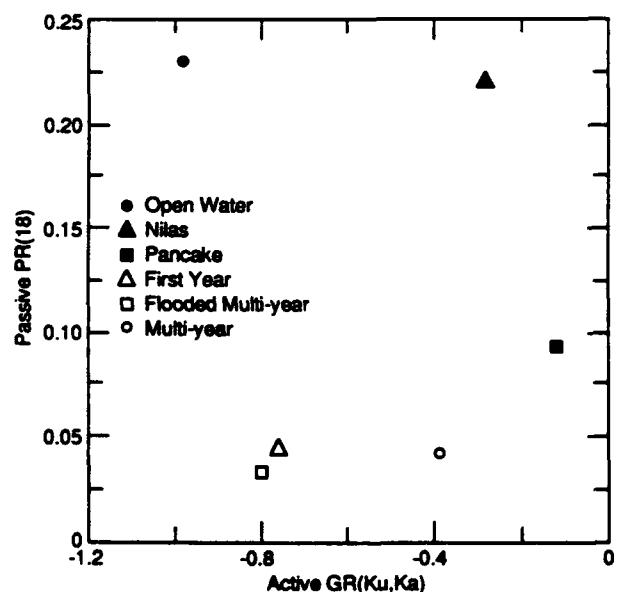

Fig. 10. Passive polarization ratio, PR(18), versus active gradient ratio, GR(K_u, K_a), for the different ice types.

ratio clearly separates the dry multiyear ice from the other categories and the pancakes from the nilas. Neither measure is adequate for distinguishing the first-year from the flooded multiyear ice, however. The polarization ratio, shown in Figure 10, provides three resolved groups: (1) open water and nilas, (2) pancakes, and (3) the first-year and multiyear ice types. Combined with GR(K_u, K_a), all ice types except the first-year and flooded multiyear are separable.

It appears that similar information can be obtained from either of the two representations (Figures 9 and 10). In both cases the ability to distinguish between ice types is improved over the combination of emissivity and backscatter at a single frequency (Figure 8). The information contained in Figures 9 and 10 appears to have at least one additional degree of freedom.

CONCLUSIONS

The major thrust of this paper has been to examine microwave properties for a variety of ice types whose signatures were recorded in conjunction with a first-order characterization of ice properties. The ultimate goal is, of course, to use airborne or satellite-derived remote sensing data to differentiate between distinct ice types. Microwave signatures are affected by the properties of the ice including surface roughness, brine and liquid content, void distribution, as well as properties of the snow cover. Although the properties within single ice types can have large spatial and temporal variability, we found that certain ice types have characteristic microwave signatures.

For young and first-year ice types, emissivities are consistent with other observations that have been made. The emissivity spectra for pancake ice is slightly higher and flatter than that for nilas. The radar backscattering cross sections for pancake and nilas are very similar, however. The distinction between thicker first-year ice and the thinner ice types is quite clear for both the passive and active microwave signatures. The emissivity of thicker first-year ice at all frequencies is close to unity, while the backscatter coefficients for this ice type are larger at K_u and K_a bands than for new ice.

The emissivities over snow covered multiyear ice were found to have a negative spectral gradient, consistent with results from aircraft measurements in the central Arctic although with somewhat less gradient. Radar backscatter was the strongest of any ice type examined, and the scattering increased uniformly with frequency. For flooded multiyear ice, however, both emissivities and backscatter were nearly indistinguishable from first-year ice.

Snow covers were thicker in the eastern Arctic than have been found in other parts of the Arctic. A thicker snow cover will certainly affect the microwave signatures directly, but more importantly, they are sometimes thick enough to depress the floe and cause flooding. If flooded multiyear ice makes up a significant percentage of the multiyear ice fraction within the marginal ice zone, this may have a profound impact on the concentration of first-year/multiyear ice percentages derived from airborne and satellite-borne radars and radiometers. This may explain a significant part of the apparent discrepancy between SMMR and surface and submarine observations [*Cavalieri et al.*, 1984b] of multiyear/first-year ice percentages.

Ice type separation is clearly improved using a combina-

tion of active and passive microwave signatures. The separation becomes even more distinct if gradient and polarization ratios for emissivity are contrasted to a gradient ratio calculated for the active microwave backscatter. Using this method, all ice types examined in this study were separable except first-year and flooded multiyear.

Although we have presented only a few cases, they are generally representative of the ice types found in the Greenland Sea marginal ice zone. Further study will be necessary to determine uncertainties in the signatures and to fully understand the relationships between the microwave signatures and more detailed ice properties.

REFERENCES

Cavalieri, D. J., P. Gloersen, T. T. Wilheit, and C. Calhoun, Passive microwave characteristics of the Bering Sea ice cover during MIZEX-West, *IEEE Trans. Geosci. Remote Sens.*, *GE-24*, 3–37, 1984a.

Cavalieri, D. J., P. Gloersen, and W. J. Campbell, Determination of sea ice parameters with Nimbus 7 SMMR, *J. Geophys. Res.*, *89*, 5355–5369, 1984b.

Cox, G. F. N., and W. F. Weeks, Equations for determining the gas and brine volumes in sea ice samples, *J. Glaciol.*, *29*, 306–316, 1983.

Eicken, H., and M. A. Lange, Development and properties of sea ice in the coastal regime of the southeastern Weddell Sea, *J. Geophys. Res.*, *94*, 8193–8206, 1989.

Grenfell, T. C., Surface based passive microwave observations of sea ice in the Bering and Greenland Seas, *IEEE Trans. Geosci. Remote Sens.*, *GE-24*, 378–382, 1986.

Grenfell, T. C., and J. C. Comiso, Multifrequency passive microwave observations of first-year sea ice grown in a tank, *IEEE Trans. Geosci. Remote Sens.*, *GE-24*, 826–831, 1986.

Kim, Y. S., R. K. Moore, R. G. Onstott, and S. Gogineni, Towards identification of optimum radar parameters for sea ice monitoring, *J. Glaciol.*, *31*, 214–219, 1985.

Onstott, R. G., and R. A. Shuchman, Radar backscatter of sea ice during winter, in *Proceedings of International Geoscience and Remote Sensing Symposium (IGARSS '88)*, vol. 11, pp. 1115–1118, European Space Agency Publications Division, Noordwijk, Netherlands, 1988.

Onstott, R. G., R. K. Moore, and W. F. Weeks, Surface based scatterometer results of Arctic sea ice, *IEEE Trans. Geosci. Remote Sens.*, *GE-17*, 74–85, 1979.

Onstott, R. G., R. K. Moore, S. Gogineni, and C. V. Delker, Four years of low altitude sea ice broadband backscatter measurements, *IEEE J. Oceanic Eng.*, *OE-7*(1), 44–50, 1982.

Shuchman, R. A., C. C. Wackerman, A. L. Maffett, R. G. Onstott, and L. L. Sutherland, The discrimination of sea ice types using SAR backscatter statistics, paper presented at International Geoscience and Remote Sensing Symposium (IGARSS '89), IEEE, Vancouver, Canada, 1989.

Stogryn, A., Strong fluctuation theory for moist granular media, *IEEE Trans. Geosci. Remote Sens.*, *GE-23*, 78–83, 1985.

Stogryn, A., An analysis of the tensor dielectric constant of sea ice at microwave frequencies, *IEEE Trans. Geosci. Remote Sens.*, *GE-25*, 147–158, 1987.

Troy, B. E., J. Q. Hollinger, R. M. Lerner, and M. M. Wisler, Measurements of microwave properties of sea ice at 90 GHz and lower frequencies, *J. Geophys. Res.*, *86*, 4283–4289, 1981.

Tsang, L., and J. A. Kong, Application of strong fluctuation random medium theory to scattering from vegetation-like half space, *IEEE Trans. Geosci. Remote Sens.*, *GE-19*, 62–69, 1981.

Tucker, W. B., III, A. J. Gow, and W. F. Weeks, Physical properties of summer sea ice in the Fram Strait, *J. Geophys. Res.*, *92*, 6787–6803, 1987.

Ulaby, F. T., R. K. Moore, and A. K. Fong, *Microwave Remote*

Sensing: Active and Passive, vol. 2, *Radar Remote Sensing and Surface Scattering and Emission Theory*, pp. 457–1064, Addison Wesley, Reading, Mass., 1982.

Wackerman, C. C., R. R. Jentz, and R. A. Shuchman, Sea ice type classification of SAR imagery, in *Proceedings of International Geoscience and Remote Sensing Symposium (IGARSS '88)*, vol. 1, pp. 425–428, European Space Agency Publications Division, Noordwijk, Netherlands, 1988.

Wadhams, P., S. Martin, O. M. Johannessen, W. D. Hibler III, and W. J. Campbell, MIZEX: A program for mesoscale air-ice-ocean interaction experiments, in Arctic Marginal Ice Zones, I, Research Strategy, *CRREL Spec. Rep. 81-19*, pp. 1–20, U.S. Army Cold Reg. Res. and Eng. Lab., Hanover, N. H., 1981.

A. J. Gow, D. K. Perovich, and W. B. Tucker III, U.S. Army Cold Regions Research and Engineering Laboratory, Lyme Road, Hanover, NH 03755.

T. C. Grenfell, Department of Atmospheric Sciences, AK-40, University of Washington, Seattle, WA 98195.

R. G. Onstott, R. A. Shuchman, and L. L. Sutherland, Environmental Research Institute of Michigan, Ann Arbor, MI 48107.

3 Remote Sensing of the Polar Oceans

Robert A. Shuchman and Robert G. Onstott
Radar Science Laboratory
Environmental Research Institute of Michigan
Ann Arbor, Michigan

Remote sensing employs the logic of inference to determine how much of what is where from measurements of force fields at locations removed from the materials of interest. The force field then forms the communication link between the material of interest and the remotely located sensor.

I. Introduction

Remote sensing as defined in this chapter refers to the use of active and passive visible, infrared, and microwave techniques to obtain information about the polar oceans without direct *in situ* measurements. Remote sensing can be performed using instruments mounted on ground-based towers, sleds, ships, helicopters, aircraft, and satellites utilizing essentially all regions of the electromagnetic spectrum. From satellite platforms, it offers the potential to study the relatively inaccessible polar regions synoptically using timely sampling intervals.

Polar oceanography includes the study of sea ice as well as ice-free ocean areas. The emphasis in this chapter will be on remote sensing of sea ice rather

than the liquid ocean, for the remote sensing of the latter is well covered in two books (Stewart, 1985; Apel, 1987). Although visible, infrared, and microwave sensors will be discussed, microwave sensors, with their ability to penetrate clouds, rain, and snow and operate independently of solar illumination conditions, will be highlighted.

In this chapter, we first present some basic remote sensing concepts and introduce sea ice and ocean characteristics obtainable from analysis of data from various remote sensing instruments. The basic concepts are followed by a section dealing with the interaction of electromagnetic energy with various sea ice types, including the effects of snow cover. Following this is a section that illustrates through example that satellite, aircraft, and ground-based remote sensing instruments provide polar oceanographic information. The examples presented are primarily from the Arctic; however, the techniques discussed are equally applicable to the Antarctic region. Included with the examples are discussions of the algorithms utilized to extract the desired geophysical information from the satellite data.

II. Remote Sensing Basics

Active and passive remote sensors operating in the visible, infrared, and microwave regions of the electromagnetic spectrum have been used to provide information pertaining to the polar seas. Active remote sensors such as lasers and radars provide their own source of electromagnetic illumination. The instruments include altimeters, scatterometers, real aperture radars (RARs), and synthetic aperture radars (SARs). Their advantages include operation independent of solar illumination and the optimization of sensor geometry. A disadvantage of active sensors is the power required to operate them.

Passive remote sensors such as radiometers utilize either energy that is emitted from the ocean or sea ice or energy that originates in space and is reflected off the ocean or ice surface. Multispectral scanners (MSSs) such as those on Landsat and Spot satellites, infrared radiometers (PRT-5), and microwave radiometers are all passive instruments. These instruments, with the exception of the infrared and microwave radiometers, are dependent on solar illumination. However, they have lower power requirements than their active counterparts.

Figure 3.1 presents the electromagnetic spectrum from the visible through the microwave region, as well as the regions in which the various optical, infrared, millimeter, and microwave sensors operate. Most optical sensors
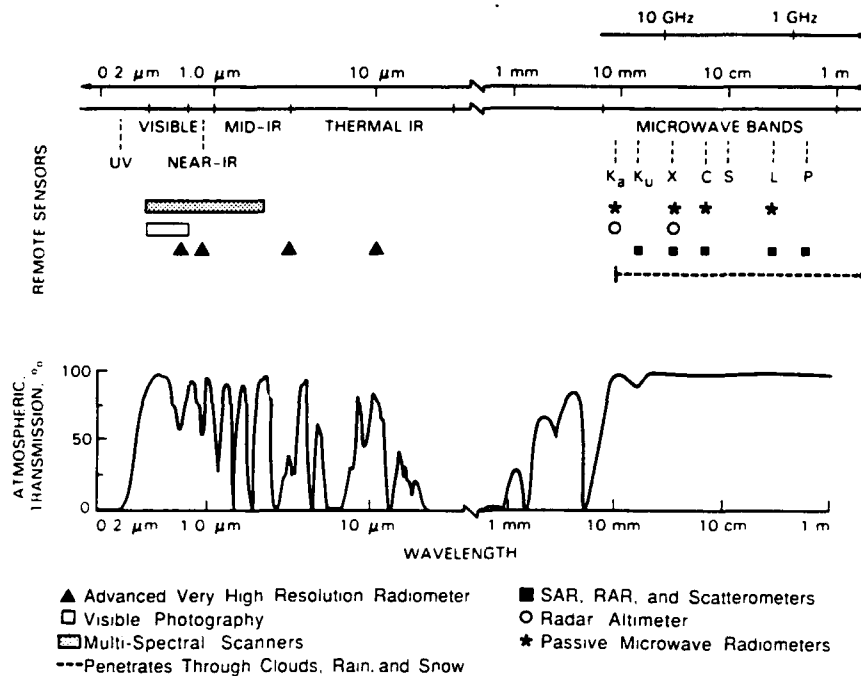
Figure 3.1 Electromagnetic spectrum from the visible through the microwave region. Wavelengths in which various optical and microwave sensors operate are indicated.

take advantage of atmospheric transmission windows, whereas at 10 mm and longer wavelengths the microwave remote sensors are generally unaffected by the atmosphere, rain, or snow.

The resolution (i.e., ability to resolve radiation from two distinct locations on the ground) of a remote sensor is a function of the wavelength utilized, the aperture of the antenna, and the distance to the objects being imaged. In the millimeter and microwave regions of the electromagnetic spectrum the resolution (ρ) of a real aperture system is

$$\rho = (\lambda/D)R \tag{3.1}$$

where D is the antenna dimension, λ the wavelength, and R the distance to the object. Equation (3.1) reveals that real aperture antennas in space produce very large footprints in resolution cells unless very high frequencies or

large antennas are employed. For example, for a typical satellite radiometer with a 3-m-long antenna operating at 1.25 GHz and a range of 850 km, the ground resolution would be approximately 68 km.

A special class of radars termed SAR utilize the motion of the sensor to synthesize a long "antenna," and the resolution obtainable is dramatically improved. SARs have the ability to produce resolutions equal to half the antenna length and thus are powerful tools for the range of polar problems where environmental changes on small scales must be monitored. A complete explanation of the calculation of resolution for RAR and SAR systems can be found in Ulaby et al. (1981, 1982).

The resolution of optical sensors, which is referred to as the instantaneous field of view (IFOV), is also a function of wavelength, aperture (in this case the size of the optical lens utilized), and distance to the object. Typical optical or infrared sensors (0.4–14 μm) such as Landsat, Spot, NOAA 9/10, and DMSP operating in a midaltitude orbit in space (850 km) achieve resolutions of 10 m to 1 km, depending on the size of the aperture.

A number of sea ice and ocean parameters and features are of interest to polar scientists. These include sea ice extent, ice concentration, ice type, ice thickness, ice kinematics, floe size distribution, detection of ocean swell and gravity wave propagation into the ice pack, locations of leads and polynyas, sea surface temperature, detection of fronts and eddies, determination of wind speed, indication of phytoplankton biomass, and mapping of internal waves. Table 3.1 is a summary of remote sensors that can be mounted in spaceborne systems to observe the geophysical parameters. For each parameter, a definition is presented along with comments. To bound the problem, the table is constrained to spaceborne systems. Table 3.2 provides specific details on existing and soon to be launched satellites that can provide the information identified in Table 3.1.

It is difficult to select optimum remote sensing instrumentation for polar oceanography. One must consider sensors on the basis of resolution (both spatial and spectral) and coverage (i.e., swath width) and at the same time not ignore the fact that the polar oceans are often cloud covered and, even if not cloud covered, are dark at least half the year. As a result, active and passive microwave sensors are potentially the most useful remote sensing instrumentation for most applications in polar oceanography, particularly if periodic temporal sampling is required.

A notable exception to the use of microwave remote sensing systems for polar oceanography is in the area of biological investigations. At present, visible and infrared passive sensors are used to provide information on chlorophyll distributions and location of upwellings, eddies, and fronts, due to their thermal characteristics.

Table 3.1 Spaceborne Remote Sensors Available for Observing Sea Ice and Ice-Free Ocean Parameters

Parameter	Comments
Ice extent. Sea ice–liquid ocean boundary	*Visual.* High-resolution (10–80 m, MSS) accurate; limited by clouds and darkness. Partial remedy: minimum brightness technique to eliminate clouds (but not darkness). In the case of Landsat or Spot, poor geographic coverage. *Infrared.* Good resolution and positional accuracy; limited by clouds and large atmospheric effects. Partial remedy: minimum brightness technique as above, but problems with atmospheric effects. DMSP and NOAA 9/10 provide IR data. *Passive microwave.* Lower resolution (instantaneous) but useful spatial and temporal resolution (50 km); no effect of darkness and only small effects of atmospheric conditions. Data presently come from SSM/I, which is part of DMSP. *Radar altimeter.* Provides accurate edge information at satellite nadir (i.e., profile mode). *Synthetic aperture radar.* Very high resolution (10–30 m); all weather and seasons; occasional problems with open water/new ice discrimination; high cost of data processing. Only limited data set available from Seasat.
Ice concentration. Amount of ice versus water per given area (total ice concentration). First-year ice/multiyear ice/open water (fraction ice concentration).	*Visual.* Same as ice extent. *Infrared.* Same as ice extent. *Passive microwave.* Similar to ice extent; some unresolved questions about accuracy, especially during freeze-up and melt. *Radar altimeter.* Provide concentration data in profile (10-km) mode. *Synthetic aperture radar.* Same as ice extent, except the small leads are not resolved.
Ice type. Limited to the distinction between first-year (including nilas) and multiyear ice.	*Visual.* No use. *Infrared.* Possible use in relating ice thickness to surface temperature, but rendered operationally uncertain because of overwhelming effect of unknown snow cover. *Passive microwave.* Very useful in principle, but existing algorithms give results at odds with other data. Severe problem with obtaining independent verification (ground truth). *Radar altimeter.* Algorithm to utilize altimeter data does not exist at present. *Synthetic aperture radar.* Research results to date indicate that a SAR system with a higher carrier frequency, C band or X band, would be effective.
Ice thickness and thickness distribution	No spaceborne system is available at present to sense ice thickness directly.

(continues)

Table 3.1 *(Continued)*

Parameter	Comments
Ice kinematics. Ice movement (i.e., displacement) as well as rotation.	*Visual.* Same as ice extent *Infrared.* Same as visual, except ice floes need to be on the order of 4 km to track with IR. *Passive microwave.* Present resolution of these systems is too coarse to provide any useful kinematic data. *Radar altimeter.* Profile mode not optimum to provide this information. *Synthetic aperture radar.* Same as ice extent; at present the most useful way to provide kinematic information from satellites.
Floe size distributions. Area dimensions of individual ice floes.	*Visual.* Same as ice extent. *Infrared.* Same as visual, except floes must be on the order of 1 km to be observed. *Passive microwave.* Insufficient resolution to be useful at present. *Radar altimeter.* Algorithm does not exist to provide this information. *Synthetic aperture radar.* Same as ice extent; limited to floes 30 m or greater, but at present the best way to obtain information.
Detection of sea and swell gravity waves. Both in ocean and within the pack (wavelengths of 100–600 m).	*Visual.* Landsat/Spot will detect waves if properly illuminated by the sun. *Infrared.* Insufficient resolution. *Passive microwave.* Insufficient resolution to be useful at present. *Radar altimeter.* Provides significant wave height under satellite (profile). *Synthetic aperture radar.* Particularly useful for observing wave propagation into the pack. Some imaging ambiguity of waves and swell in open water.
Location of leads. Open water areas within ice pack (orientation, width, and length).	*Visual.* Same as ice extent. *Infrared.* Same as ice extent. *Passive microwave.* Resolution at present is insufficient to provide useful lead information. *Radar altimeters.* Not optimum to map leads due to profiling mode of operation. *Synthetic aperture radar.* Same as ice extent.
Sea surface temperature. Upper first meter of the ocean.	*Visual.* Not capable of providing quantitative information. *Infrared.* Provides 0.5–1.0°C sea surface temperature data at 1-km resolution. *Passive microwave.* Provides 1°C information, unfortunately on a 50-km resolution grid at present.

Location of fronts and eddies.
The fronts and eddies can be either thermal or due to current shear.

Radar altimeter. Does not provide quantitative temperature information.
Synthetic aperture radar. Does not provide quantitative temperature information.

Visual. Will observe only fronts and eddies that have ocean color changes associated with them.
Infrared. Will detect thermal fronts.
Passive microwave. Present resolution prevents detection of fronts and eddies that are 50 km or smaller in diameter.
Radar altimeter. Not useful due to profiling mode.
Synthetic aperture radar. Fronts and eddies associated with either temperature or current shear have been visible on the radar images. Imaging mechanism has not been quantified.

Determination of wind speed and direction.
Determine wind speed over polynyas, leads, and the open ocean (techniques do not work over ice).

Visual. Not useful.
Infrared. Not useful.
Passive microwave. Useful for wind speeds greater than 5 m/s. On 50-km grid, and wind speed can be provided to 2-m/s accuracy. Not useful for wind speeds over leads due to resolution.
Radar altimeter. Can provide 2-m/s wind speed information directly under satellite.
Synthetic aperture radar. Potentially the best instrument to provide wind speed and direction, due to resolution. Algorithm is still under development.

Biological distribution.
Increased biological activity associated with eddies, upwelling, or seasonal changes.

Visual. Ratios of various visual bands, optimum technique at present to map pigment distribution.
Infrared. May provide some information on blooming if associated with thermal activity.
Passive microwave. Present resolution of system is too coarse to provide useful data.
Radar altimeter. Not useful.
Synthetic aperture radar. Useful only if bloom is associated with thermal or current shear.

Detection of internal waves.
Wavelengths on the order of 500 m to several kilometers

Visual. Same as ice extent.
Infrared. Limited to observing long internal waves (i.e., 2 km or greater).
Passive microwave. Resolutions of present systems are inadequate to map internal waves.
Radar altimeter. Not useful.
Synthetic aperture radar. At present the most useful system for detecting internal waves in the ice. The transfer function between the SAR signature and internal wave needs to be quantified.

ª When an algorithm for ice concentration and ice extent is assumed to be infinitely small.

129

130

Table 3.2 Satellite Sea Ice Data Sources

Satellite	Sensor	Type	Swath (km)	Resolution	Revisit time/day	Sea ice and ocean parameters measured	Advantage	Disadvantage	Status
Landsat	Multispectral Scanner (MSS)	Passive visible and infrared	186 × 186	30 m	0	Ice edge, ice concentration, floe size distribution, ice motion, chlorophyll concentration, suspended sediment, location of ocean fronts	High-resolution information is easily extracted	Clouds, coverage limited to 81°	Operational
Spot	Multispectral Scanner (MSS)	Passive visible and infrared	60 × 60	10 m	0–2	Ice edge, ice concentration, floe size distribution, ice motion, chlorophyll concentration, suspended sediment, location of ocean fronts	High-resolution information is easily extracted	Clouds, coverage limited to 81°	Operational
DMSP	Optical line Scanner (OLS)	Passive visible and infrared	2900	0.6–3 km	2–12	Meteorology, ice motion, ice edge location, eddy structure, sea surface temperature, ice kinematics	Large swath	Clouds	Operational
DMSP	Special Scanning Microwave Imager (SSM/I)	Passive microwave	750	50–60 km	0–2	Ice type, ice extent, ice concentration, eddy structure, water vapor, and ocean surface winds, sea surface temperature	Penetrates clouds	Resolution, melt and freeze period	Operational
NOAA 9/10	Advanced Very High Resolution Radiometer (AVHRR)	Passive visible and infrared	2500	1–4 km	2–12	See DMSP, OLS	Large swath	Clouds	Operational

Satellite	Instrument	Type		Resolution		Applications	Advantages	Disadvantages	Status
GEO-SAT	Radar Altimeter	Active microwave	Nadir profile 7-10	Height 10 cm, spot size 7-10 km	0	Ice edge, ice roughness, gravity wave detection, ice concentration, ocean height topography, geostrophic currents	All weather, minimum data processing	Limited polar coverage, profile only, large spot size	Operational
Japanese MOS-1	Multispectral Electronic Self-Scanning Radiometer (MESSR)	Passive visible and infrared	200	50 m	0	See Landsat, MSS	High-resolution information is easily extracted	Clouds	Operational
Japanese MOS-1	Visible and Thermal Infrared Radiometer (VTIR)	Passive visible and infrared	1500	1-3 km	2-12	See DMSP, OLS	Large swath	Clouds	Operational
Japanese MOS-1	Microwave scanning Radiometer (MSR)	Passive microwave	300	30-40 km	0-1	See DMSP, SSM/I	Penetrates clouds	Resolution, melt and freeze period	Operational
ESA ERS-1	Radar Altimeter	Active microwave	Nadir profile 7-10	Height 10 cm, spot size 7-10 km	0	Ice edge, ice roughness, gravity wave detection, ice concentration, ocean height topography, geostrophic currents	All weather, minimum data processing	Profile only, large spot size	Proposed launch 1990
ESA ERS-1	Synthetic-Aperture Radar (SAR)	Active microwave (C band)	80-100	30 m	0	Ice edge location, eddy and ocean front structure, ice type, floe size distribution, ice kinematics, gravity wave propagation, internal wave measurements, ice concentration, surface wind speed, detection of leads, mapping of icebergs	All weather, high resolution	Coverage, data processing	Proposed launch late 1990

III. Theory of Active and Passive Microwave Imaging of Sea Ice

Sea ice type or thickness and age are extremely important parameters to measure and study in the polar oceans. Ice strength is dependent on age and thickness, and the distribution of ice thickness is important in climatic studies. Figure 3.2 is a conceptual illustration of the active microwave return from multiyear and first-year sea ice and open water without wind. Multiyear ice (i.e., ice that has survived a summer melt) can be distinguished from first-year ice by its greater thickness (>2 m versus <2.5 m), its lower salinity ($<2.5‰$ versus $>7.7‰$), and thicker snow cover (>0.2 m versus <0.2 m). The return from multiyear ice is a function of surface and volume scattering, since the low salinity allows penetration into the ice sheets, whereas backscatter from snow-free first-year ice and ocean is dominated by scattering from the surface (i.e., both are high-loss materials).

In order to use satellite and aircraft data to estimate ice types and their respective concentrations, algorithms for use with microwave data have been developed and improved. Major advances have been made in establishing sea ice type and concentration because microwaves penetrate clouds and large areas can be covered repeatedly. Algorithms that differentiate first-year and multiyear ice are not always accurate because radiometric properties change when influenced by melting, wet snow, or water on the ice surface.

Seasonal investigations in the Arctic during the fall freeze-up, late winter, spring, and summer have been conducted to acquire empirical data to describe the microwave properties of sea ice. These data contribute to studies to determine the ability of remote sensing to classify ice types and to character-
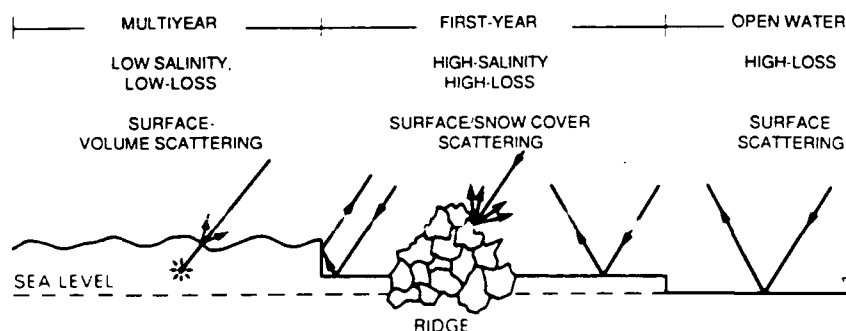
Figure 3.2 Backscatter interactions for multiyear ice, first-year ice, and smooth open water.

In interpreting active and passive microwave measurements, it is important to recognize that radars typically measure the monostatic scattering cross section. This is measured when the direction of incidence is exactly opposite to the direction of scattering. To calculate emissivity, the description of the bistatic scattering cross section must be complete so that the necessary integration can be performed over all angles.

The way in which sea ice forms, its history, and its age are important in determining its active and passive microwave properties. When ice is young, it may have a surface that is relatively smooth (i.e., formed during undisturbed growth in an open lead) or rough (with rims which are the remains of the pancake ice forms agitated into shapes by wave action). This ice may also exhibit a thin surface layer of brine which may reduce electromagnetic wave propagation to depths of a few millimeters. With a high concentration of brine within its structure, new ice near the freezing point is an extremely lossy material; penetration of electromagnetic energy is limited.

With age, the volume of brine decreases due to salt migration (see Chapter 2). However, first-year ice remains very lossy. During summer the surviving ice experiences melt processes which cause two significant modifications; development of additional surface relief and reduction in the density of the upper portion of the ice sheet. These two characteristics contribute to the difference in the microwave signatures of first-year and multiyear ice. The uppermost portion of the multiyear ice sheet closely governs its microwave signature. It is composed of ice which is almost pure and has very low loss (i.e., significant penetration of microwave energy). Different ice types are more easily distinguished at higher frequencies, and open water is easily distinguished from all sea ice types independent of frequency (Fig. 3.4).

Multiyear ice and first-year ice can be distinguished in the winter independent of frequency (C, X, K_u bands; Fig. 3.4b). However, in the spring and summer (Fig. 3.4c), discriminating first-year from multiyear ice becomes difficult because of the free water in the snow and within the surface of the ice. The free water prevents significant microwave penetration; thus, the volume scattering which distinguishes the multiyear ice return is not present. The only SAR satellite in space operated at L band. It proved to be poor at differentiating the desired ice types. The next scheduled SAR satellite will be launched in 1990 and will operate at C band (5.25 GHz, 6 cm).

The distance an electromagnetic wave travels through a medium before its intensity is reduced by $1/e$ is referred to as the penetration depth and is used to gauge where in a volume scattering may occur. To make this calculation the complex dielectric constant ϵ^* must be known. It is defined by $\epsilon^* = \epsilon_0(\epsilon_r' - j\epsilon_r'')$, where ϵ_0 is the free-space dielectric constant, ϵ_r' the relative dielectric constant, and ϵ_r'' the relative imaginary dielectric constant. The
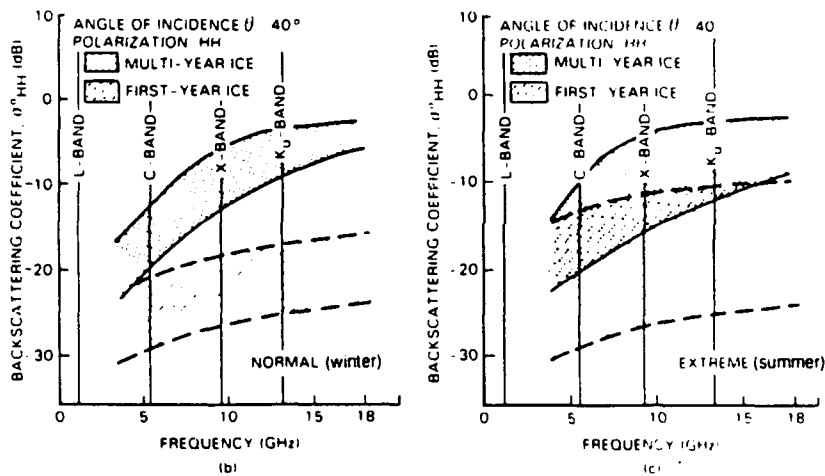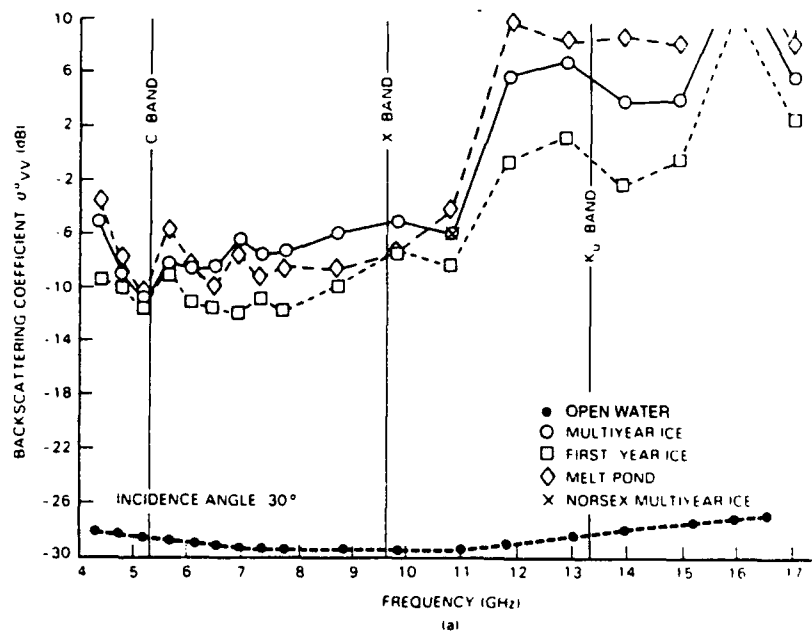
Figure 3.4 Frequency dependence of the backscatter coefficient for first-year and multiyear sea ice at two incidence angles: (a) 30°; (b and c) 40°. Theoretical σ° for multiyear and first-year ice under normal/winter (b) and extreme/summer (c) conditions is also shown. From Earth Observing Report, Volume IIf, SAR Synthetic Aperture Radar. Instrument Panel Report, NASA.

value of ϵ^* is dependent on the density of the ice, the volume of the brine, and the dielectric properties of the ice and brine. The penetration depth δ and loss L are determined by the following:

$$\delta = \frac{1}{2}\left(\frac{2\pi}{\lambda_0}\frac{\mu_r\epsilon'_r}{2}\left\{\left[1 + \left(\frac{\epsilon''_r}{\epsilon'_r}\right)^2\right]^{1/2} - 1\right\}^{1/2}\right)^{-1} \qquad (3.4)$$

and

$$L = 10 \log e^{1/\delta} \quad (\mathrm{dB/m}) \qquad (3.5)$$

where λ_0 is the wavelength for free space. At microwave frequencies the relative permeability μ_r is approximately equal to 1. Measurements by Vant *et al.* (1974, 1978) indicate that first-year ice with a salinity of 7 – 8 per mil at a temperature of $-5°C$ has a penetration depth of 2 – 4 cm and a loss of about 150 dB/m at X band (a wavelength of 3 cm). First-year ice also has few internal scatterers, and these are small compared to a wavelength. In contrast, the upper portion of multiyear ice provides a penetration depth of 60 cm and a significant number of air bubbles with diameters of 1 – 3 mm. The physical models of first-year and multiyear sea ice which have been useful in the development of theoretical penetration models are shown in Fig. 3.5.

During winter, the microwave signatures of desalinated multiyear ice are clearly different from those of the saline first-year ice. The situation in summer is more complex; this is the time of desalination, of melting snow and ice, and of melt pool formation. In addition, the microwave signatures respond quickly to meteorologically induced melt-and-freeze cycles of the upper surface.

In winter, as during most of the year, the dry snowpack and upper portion of the ice sheet are at temperatures much less than 0°C Under the dry snow on undulating multiyear ice are flat ice, ice mounds, and depressions filled with frozen meltwater, all with different emissivities (Fig. 3.6). Open water exhibits a large difference between emissivities at the two polarizations (Brewster angle effects) and has an emissivity which increases with increasing frequency. With the dielectric constant of sea ice (i.e., $3.7 - j0.3$ for first-year ice at 10 GHz, $S = 7.5$ per mil, and $T = -5°C$) much lower than that of seawater ($41 - j41$ for 10 GHz, $S = 30$ per mil, and $T = 0°C$), the sea ice has a lower reflectivity. The first-year ice signature is close to unity and is almost independent of polarization and frequency. The multiyear ice signature is not similar to that of either calm water or first-year ice, decreases with increasing frequency, and shows a moderate separation at the different polarizations throughout the entire range of frequencies.
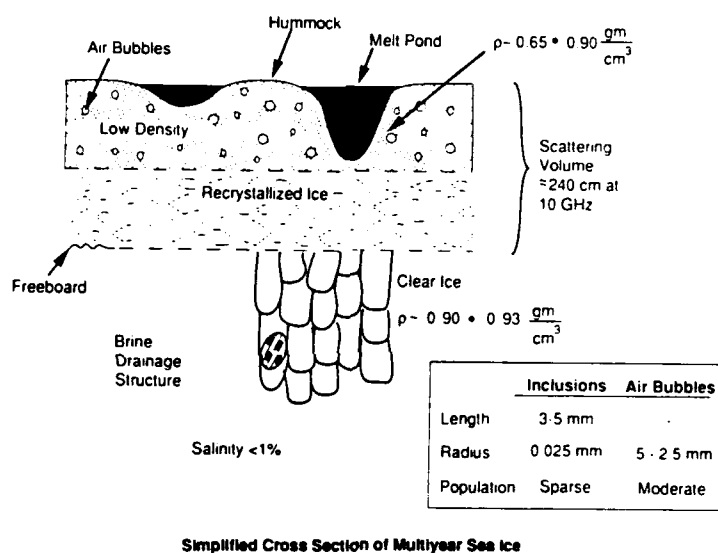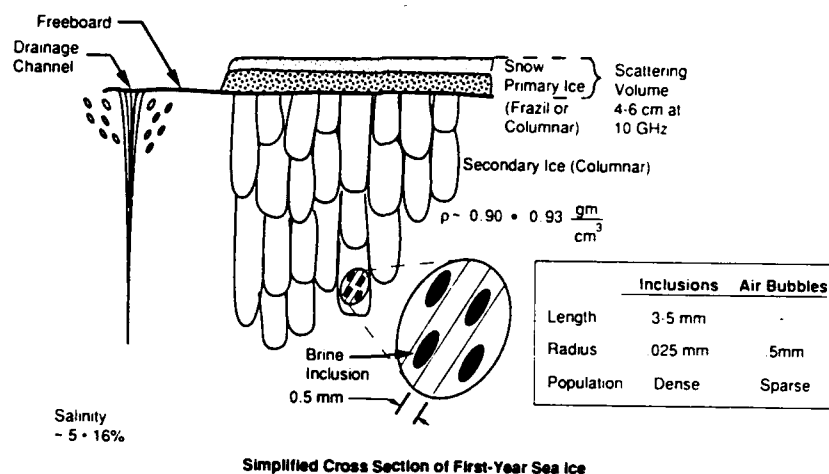
Simplified Cross Section of First-Year Sea Ice

	Inclusions	Air Bubbles
Length	3·5 mm	·
Radius	025 mm	.5mm
Population	Dense	Sparse

Simplified Cross Section of Multiyear Sea Ice

	Inclusions	Air Bubbles
Length	3·5 mm	·
Radius	0 025 mm	5 · 2 5 mm
Population	Sparse	Moderate

Figure 3.5 Simplified cross section of first-year and multiyear sea ice.

The active microwave backscatter of first-year and multiyear ice increases linearly with increasing frequency and the radar contrast between these two ice types also improves with increasing frequency. Especially important in the determination of ice concentration, the backscatter levels of water between floes in the ice pack is often considerably lower than those from the
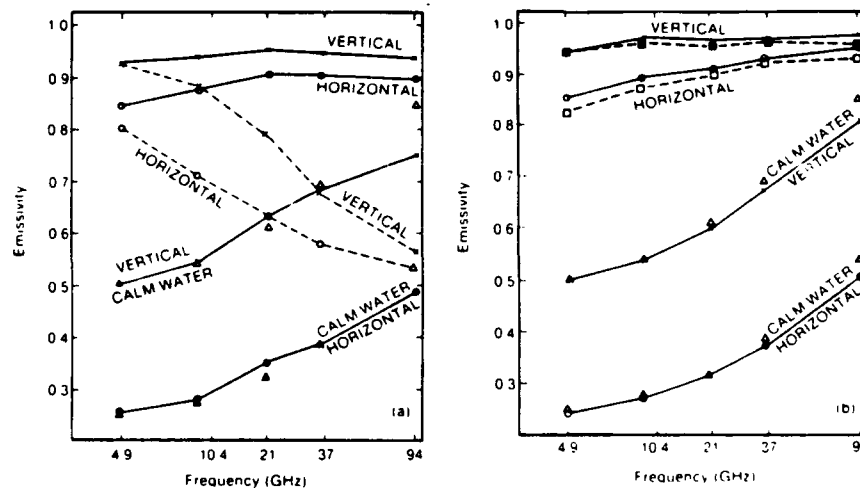
Figure 3.6 Microwave emissivity at 50° incidence angle versus frequency for first-year ice (solid line), multiyear ice (dashed line), and calm water. Triangles indicate theoretical emissivities of calm water. (a) Fall–winter conditions (NORSEX '79). (b) Summer conditions (MIZEX '83). From Matzler *et al.* (1984).

surrounding ice. This is equally true in winter and summer. Radar backscatter cross sections at *L*, *C*, *X*, and K_u bands (Figs. 3.7 and 3.8) illustrate the contrast in ice type and water signatures as a function of frequency and incidence angle.

When temperatures warm during late spring, the interior of the snowpack becomes moist, and moisture from the humid snow layer may collect on the cold ice surface and freeze. The superimposed ice which forms roughens the ice–snow interface. The roughness of this layer increases during the early melt process and eventually becomes the key contributor to the backscatter signatures of thin to medium first-year ice. By midsummer the snowpack has experienced considerable melt. Accumulations of meltwater on multiyear ice and thick first-year ice create slush layers, sometimes many centimeters thick, and drainage of water into depressions contributes to the formation of subsurface melt pools. After midsummer, open water melt pools become common on thick ice; about 50–60% of the snow has melted. A snow–ice crust is in place on elevated multiyear ice surfaces, on thick first-year ice, and on multiyear ice. On thin first-year ice and medium first-year ice the snowpack may have eroded into a 2-cm-thick granular snow–ice layer, and former melt pools may consist of collections of candled ice tips which rise about 1 cm above the freeboard of the thin, saturated ice sheet. Cross-sec-
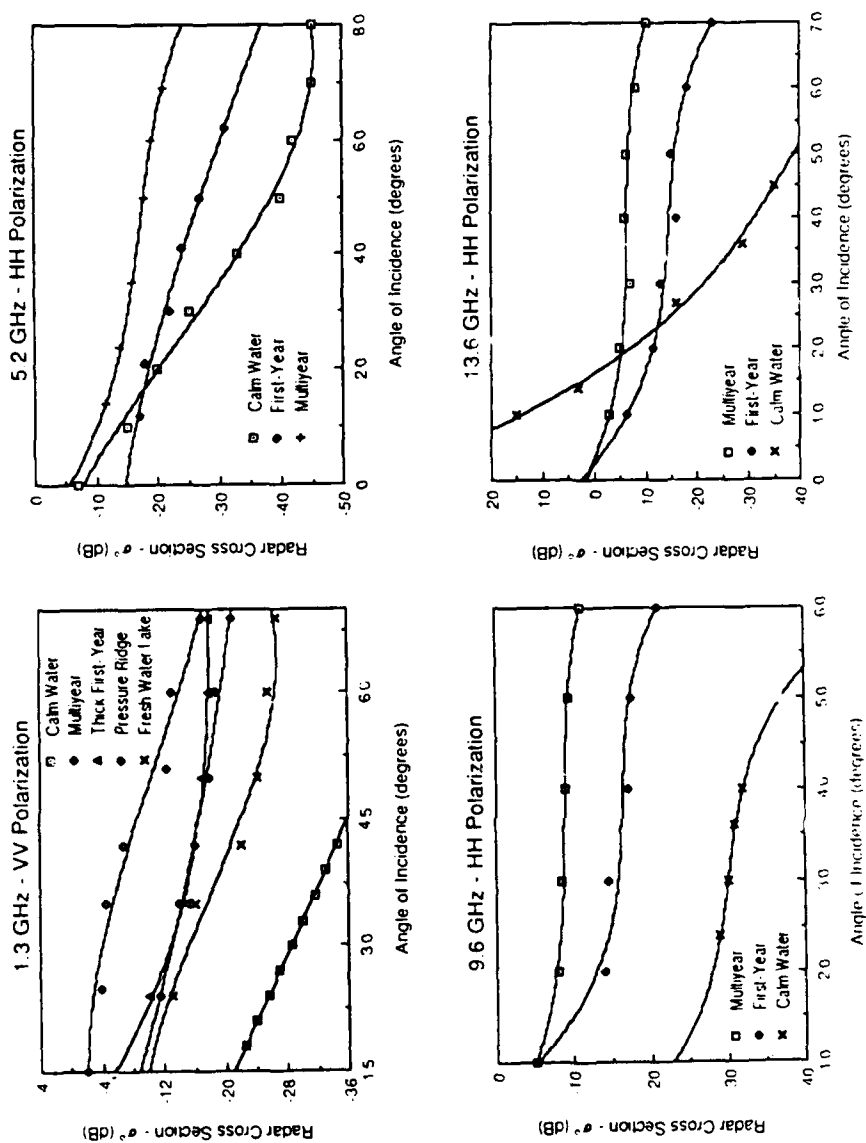
Figure 3.7 Radar backscatter cross sections at L, C, X, and K_u bands during winter, illustrating the contrast in ice type and water signatures as a function of frequency and incidence angle.

140
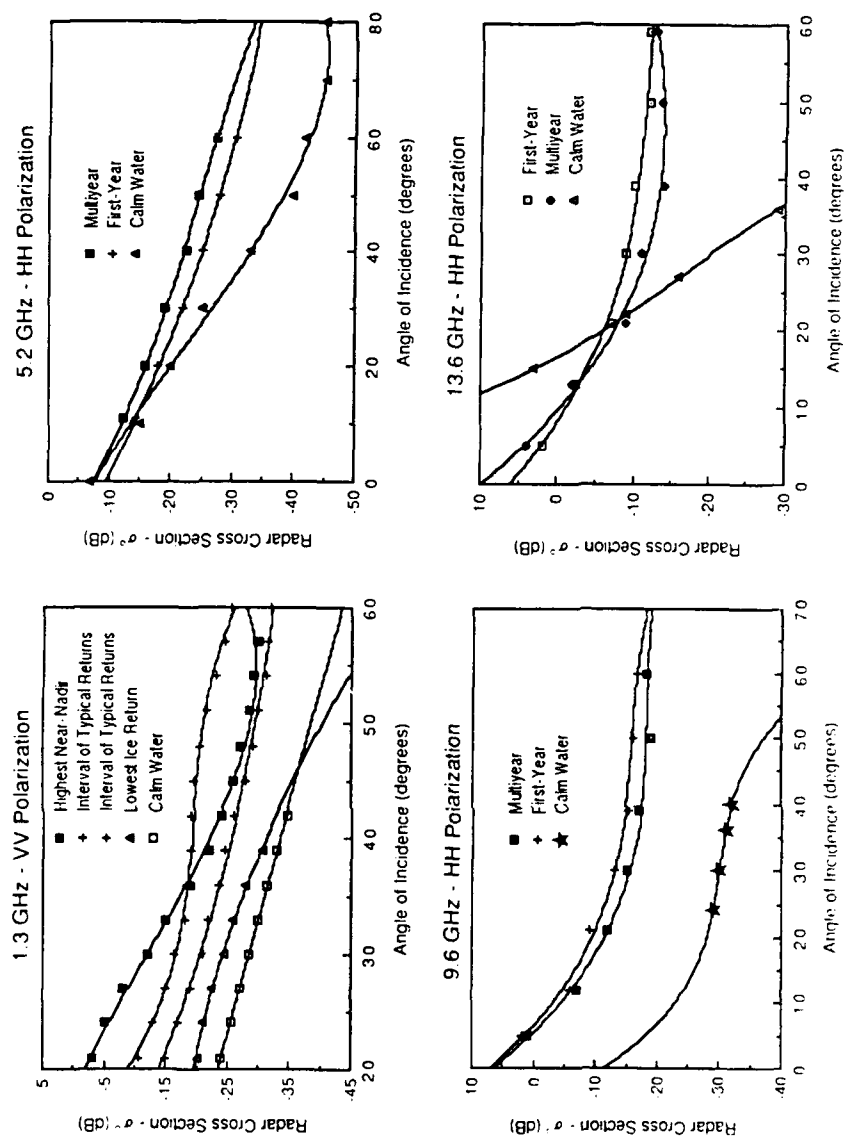
Figure 3.8 Radar backscatter cross sections at L, C, X, and K_u bands during summer, illustrating the contrast in ice type and water signatures as a function of frequency and incidence angle.

141
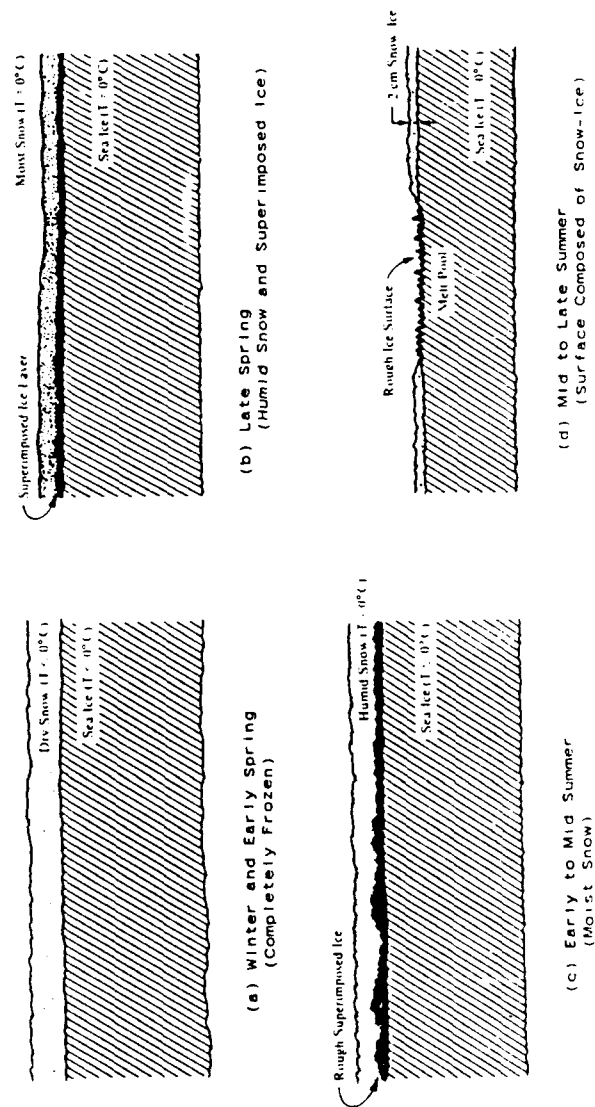
Figure 3.9 Cross-sectional views of first-year sea ice to illustrate the evolution of the ice sheet and snowpack during summer.
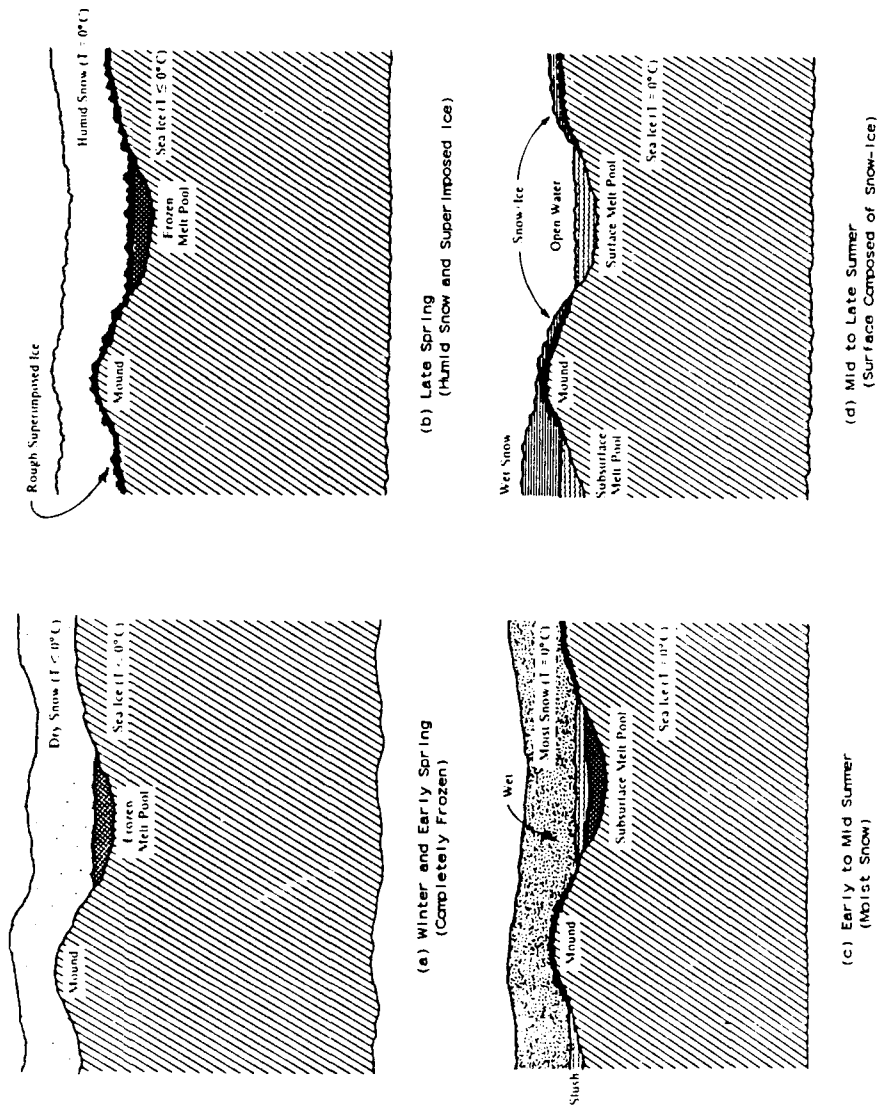
Figure 3.10 Cross-sectional views of multiyear sea ice to illustrate the evolution of the ice sheet and snowpack during summer.

Rough Superimposed Ice

Humid Snow (T = 0°C)

Sea Ice (T ≤ 0°C)

Frozen Melt Pool

Mound

(b) Late Spring
(Humid Snow and Superimposed Ice)

Snow-Ice

Open Water

Sea Ice (T = 0°C)

Surface Melt Pool

Mound

Wet Snow

Subsurface Melt Pool

(d) Mid to Late Summer
(Surface Composed of Snow-Ice)

Dry Snow (T < 0°C)

Sea Ice (T < 0°C)

Frozen Melt Pool

Mound

(a) Winter and Early Spring
(Completely Frozen)

Moist Snow (T = 0°C)

Sea Ice (T = 0°C)

Wet

Subsurface Melt Pool

Mound

Slush

(c) Early to Mid Summer
(Moist Snow)

143

tional views of first-year and multiyear sea ice are provided in Figs. 3.9 and 3.10 to help visualize the evolution of the ice sheet and snowpack during summer.

During the 2 months of summer the mean air temperature stabilizes near 0°C. During this period the microwave signatures of first-year and multiyear ice become very similar. The moist snowpack, warm ice sheet (surface temperatures at about 0°C), and liquid water accumulating at the snow–ice interface greatly limit the ability of microwave signatures to distinguish ice types. Snow-covered multiyear ice and first-year ice share a common emissivity and are represented by an infinitely thick wet snow layer. An emissivity of almost one is obtained at vertical polarization, showing the characteristics of an ideal blackbody.

Radar backscatter during summer is more complex, and discrimination between the major ice types appears possible. During the first part of summer, when the snowpack is moist and at its maximum annual thickness, backscatter signatures for thin and thick ice sheets are very similar if not identical. By midsummer the signature of thin first-year ice is enhanced because the snow layer has thinned to a point where scatter from the ice surface contributes to its backscatter. The distribution of meltwater signatures contributes to their character at this time and is of interest because contrast reversals have been shown to occur between first-year and multiyear ice, the two major summer ice types (Onstott *et al.*, 1987) (Fig. 3.11). By mid- to late summer, the backscatter from multiyear ice becomes greater than that from first-year ice and the contrast between thin and thick ice increases with decreasing frequency. This observation is explained by the fact that the multiyear ice is topographically rougher; has many tilted surfaces; and is complex mixture of ice, snow, and water features which, in total, provide strong surface scatter. The roughness elements on the new snow-free first-year ice are reduced in amplitude because of the continuation of melt, and as surfaces become smoother they produce a weaker backscatter.

Snow on ice plays a variety of roles. On cold multiyear ice, snow with depths greater than 2 m has been shown to be essentially transparent at frequencies below 10 GHz; and on very smooth first-year ice, snow may even dominate the microwave signature (Kim *et al.*, 1985b). In the marginal ice zone (MIZ) the snow thicknesses can become so great that the ice sheet is pushed below sea level, floods with seawater, and acquires a first-year ice signature. Arctic lows may also pass through a region during the spring, and the upper portion of the snowpack may experience melt and refreeze. The snow crystals may enlarge, and a multiyear-like signature may be provided at the highest millimeter-wave frequencies. During early summer the snow layer has a more dominant role. This is illustrated by the critical relationship between frequency and the volumetric liquid water content in the snow and
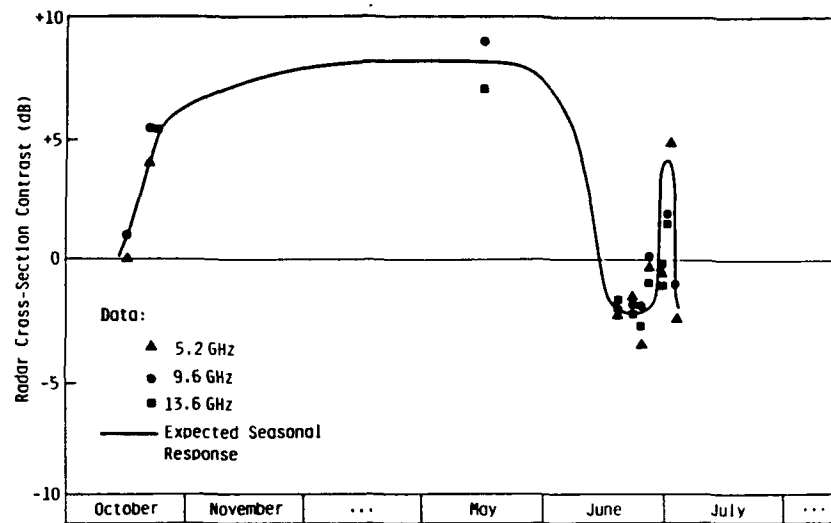
Figure 3.11 Contrast history illustrating contrast reversals which have been shown to occur between first-year and multiyear ice, the two major summer ice types. From Onstott and Gogineni (1985).

penetration depth (Fig. 3.12). The penetration depth is dramatically reduced with even part of a percent of liquid water (a quantity so small that present direct measurement methods provide this value with great difficulty). The penetration depth is further reduced with increasing wetness or increasing frequency. For example, in the Fram Strait region during the summers of 1983 and 1984, the bulk wetness of the snowpack was found to stay at about 5 or 6% (Onstott *et al.*, 1987). The penetration depth at a 30-cm wavelength (note that $\lambda = c/f$, where c is the speed of light and f is frequency) is about 1 m, but at a 6-cm wavelength it is only about 5 cm. Snow thickness prior to melt was about 45 cm on thick ice. As summer progresses, the major role of the snowpack is to provide free water, which accumulates in pools. Typically, there are alternating mounds and pools of ice and water. An important change in the summer microwave signature occurs when the snow becomes completely saturated with water, creating slush. At this point, the emissivity approaches that of open water, and the backscatter signature is increased beyond that of moist snow because of accompanying increases in surface roughness and dielectric constant.

The mean and standard deviation of the brightness temperature of sea ice for a 300 × 300 km region in Fram Strait are shown in Fig. 3.13. Measurements were made at 37 GHz with horizontal polarization using the Nimbus-7 Scanning Multichannel Microwave Radiometer (SMMR) for alter-
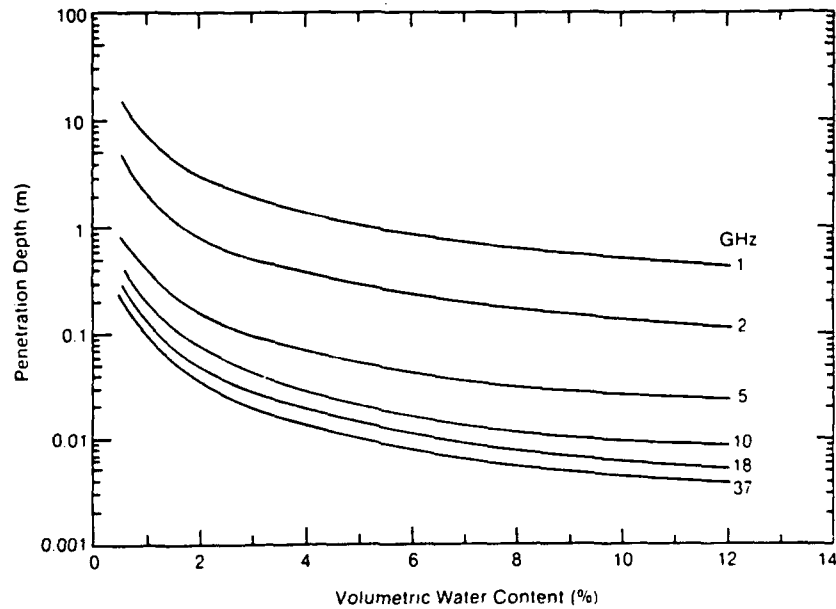
Figure 3.12 Penetration depth for snow with a density of 385 kg/cm³ for frequencies between 1 and 37 GHz. Calculations are based on experimental data acquired and results published by Matzler (1985), Hallikainen *et al.* (1984), and Tiuri *et al.* (1984).

nate days in a continuous time series record for 1984 (D. J. Cavalieri, unpublished results). During the cold of winter, brightness temperature fluctuations are small and variations are due to changes in ice concentration and in the temperature of the radiative portion of the ice sheets. During the spring warming, brightness temperatures respond accordingly. By late spring, Arctic lows may cause free water to form in the upper portion of the snowpack, inducing brightness temperatures which are almost summerlike. These then decrease below previous spring levels because of increased scattering losses due to enlarged ice crystals in the snowpack. Increases in scattering cause a reduction in the emission and an enhancement in backscatter. The onset of summer, with temperatures stabilizing at about 0°C, is accompanied by a rapid transition to an emissivity that is almost blackbody-like. By midsummer a significant portion of the snowpack has melted and open melt pools are more numerous. During periods of heavy melt followed by "drying" (where the areal extent of surface meltwater is reduced due to draining through cracks, thaw holes, and rotting ice), there may be rapid brightness temperature oscillations. By the beginning of fall, the ice is well drained, a
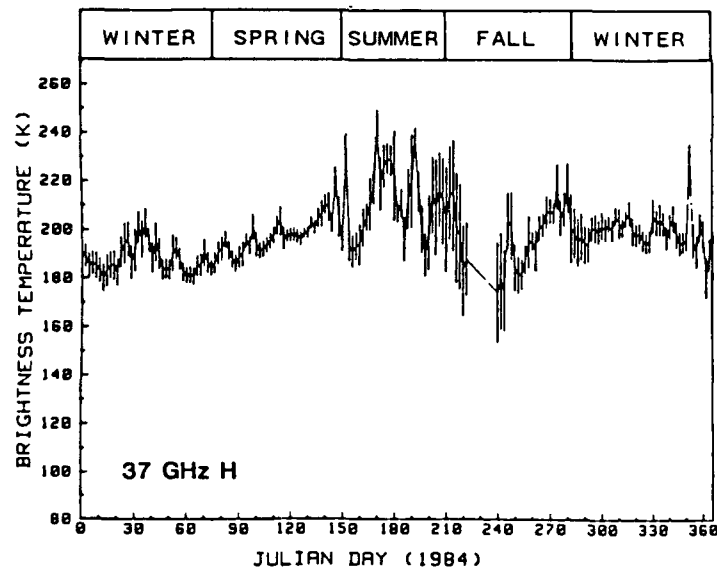
Figure 3.13 Time series of average Nimbus-7 horizontal polarization brightness temperatures at 18 and 37 GHz for a 300 × 300 km region in the Greenland Sea near the MIZEX study area during 1984. The short vertical lines represent 1 standard deviation (D. J. Cavalieri, unpublished).

rapid cooling proceeds, the ice concentration is at a yearly minimum, and the brightness temperature is at its yearly minimum. Within a few weeks brightness temperatures return to their winter levels.

Attempts have been made to explain theoretically the backscatter from sea ice. Models, when successful, prove useful in interpreting the microwave signatures of the many ice forms. Results have been used to refine and focus the measurement of physical and electrical properties in sea ice investigations. A parametric study by Kim *et al.* (1984) allowed an examination of the sensitivity of the microwave signature to changes in key ice sheet parameters, including salinity, temperature, brine volume, density, air bubble size, and surface roughness.

A first attempt to describe the radar backscatter for sea ice was made by Parashar *et al.* (1978). Results were mixed, prompting support for a program which included coincident backscatter measurements and physical property characterizations. A qualitative description of the critical scattering processes by Onstott *et al.* (1979, 1980, and 1982) was based on the results of a series of field investigations. This description provided a basis from which

theoretical formulations were selected for their application in describing backscatter from sea ice. The backscatter and characterization data acquired during these field investigations provided the necessary inputs for model verification.

Backscatter levels for multiyear ice are large and decrease gradually with increasing angle, which suggests that volume scattering is an important contributor. Surface scattering is also expected to be important because returns decrease too rapidly at large angles to be modeled by volume scattering alone. Calculations of the attenuation coefficient and penetration depths for multiyear ice further support this hypothesis. The penetration depth for multiyear ice at 10 GHz with a salinity of 0.5‰ and $T = -5°C$ is approximately 60 cm. Ice sheet characterization data show significant numbers of air bubbles (sizes of 1–3 mm) in the upper portion of the ice sheet of a diameter which is within an order of magnitude of the radar wavelength in ice. These bubbles provide the critical source of scatter within the volume. Another source of inhomogeneities is the brine pockets. They are very small compared to a wavelength (about 0.025 mm in radius and 3 mm long) and are not expected to enhance the backscatter.

It is also hypothesized that first-year ice is dominated by surface scatter, with only minor contributions arising from volume scatter. Backscatter data show a rapidly decaying angular response at angles near vertical. Sea ice surfaces are rough, with root-mean-square (rms) values ranging from 0.1 to 1.0 cm. Large attenuation coefficients further strengthen this argument. The scattering volume is small and, as ice characterization measurements show, air bubbles are infrequent and brine inclusions are extremely small. Therefore, surface scattering is the dominant backscatter mechanism.

These hypotheses provide the basis of theoretical and experimental studies of the radar backscatter from sea ice. Results of the application of a combined rough-surface and volume scattering theory to sea ice and snow backscatter were first presented by Fung and Eom (1982). A detailed discussion of the physical and electrical properties of sea ice, the extension of the model to include two ice layers, and a full discussion of the ability of a combined rough-surface and volume scattering theory to model sea ice were later presented by Kim *et al.* (1984).

The surface of homogeneous first-year ice is flat topographically but rough on the small scale. Formulations called the Kirchhoff approximations for rough-surface scattering were selected because of their apparent applicability. These formulations are summarized and derived in Ulaby *et al.* (1982). Predictions for slightly rough surfaces and very rough surfaces were compared to measured microwave signatures of first-year ice data for operation in the frequency range 1–18 GHz (Kim *et al.*, 1985a). The study showed that the physical optics model with an exponential correlation length

to describe the surface roughness statistics provided a reasonable prediction capability. The model includes a fast angular falloff in the small-incidence-angle region and the almost linearly increasing frequency behavior for angles off vertical. In addition, the frequency response was predicted using one set of surface parameters for the frequency range. The expression for the back-scatter cross section is

$$\sigma^\circ_{pp}(\theta) = 2|R_{pp}|^2 \cos^2 \theta \; e^{-k^2\sigma^2 \cos^2 \theta}$$

$$\times \sum_{n=1}^{\infty} \frac{(4k^2\sigma^2 \cos^2 \theta)^n}{n!} \frac{k^2(n/l)}{[4k^2 \sin^2 \theta + n^2/l^2]^{3/2}} \qquad (3.6)$$

where p is the polarization, θ the angle of incidence, R_{pp} the Fresnel reflection coefficient, k the wave number in air, σ the standard deviation of the surface height, and l the surface correlation length derived from the normalized autocorrelation function of the surface roughness profile. An average radius of curvature of the surface which is less than the wavelength and an rms slope which is less than 0.25 are required to satisfy the model assumptions. The role of the dielectric constant can be shown by assuming that the absolute backscatter level is proportional to the square of the Fresnel reflection coefficient.

The passive microwave return from first-year and multiyear sea ice can also be modeled. If a surface can be considered to be specular (i.e., the roughness elements are less than an eighth of the product of the wavelength and the sine of the incidence angle), the emissivity can be expressed as

$$\epsilon(\theta) = 1 - |R_p(\theta)|^2 \qquad (3.7)$$

where R_p is the Fresnel reflection coefficient. When the dielectric constant of sea ice ranges between 3 and 4 and surfaces are slightly rough, which is true for a wide range of first-year ice conditions, the expression above produces reasonable estimates. This is, in large part, due to a reasonable insensitivity to small roughness scales.

A key to the modeling of multiyear sea ice is determining how to account for the scattering by the inhomogeneities (i.e., the air bubbles) inside the upper portion of the ice sheet. This may be accomplished by a number of techniques. Radiative transfer theory (Chandrasekhar, 1960) has been attempted and predictions correlate well with measured data. This theory is based on describing the propagation of energy through the medium. By assuming that there is no correlation between the scattered fields, the problem is greatly simplified because intensities can be summed. Another advantage is that multiple scatterings between particles are easily included.

The general theoretical solution may be simplified by neglecting volume–surface interactions to a form that not only produces excellent

agreement with measured data but also improves the understanding of the importance of the surface scatter contribution, the dielectric constant, the density of the ice, and the bubble size. The backscattering cross sections may be described as

$$\sigma^{\circ}(\theta) = \sigma_s^{\circ}(\theta) + T^2(\theta)\sigma_v^{\circ}(\theta')$$
(3.8)

where $\sigma_s^{\circ}(\theta)$ is the contribution due to surface scattering, $T^2(\theta)$ a coefficient which describes the transmission of power into the ice sheet, $\sigma_v^{\circ}(\theta')$ the backscattering coefficient due to volume scattering within the ice sheet, and θ' the angle of propagation in the ice sheet which results from refraction. If it is further assumed that the air bubbles are spherical and of one size, the volume scattering component is given by

$$\sigma_v^{\circ}(\theta) = \frac{N\sigma_b \cos\theta'}{2k_e}\left[1 - \frac{1}{L^2(\theta')}\right]$$
(3.9)

where N is the number of bubbles, σ_b is the cross section of a single particle, k_e is the volume extinction coefficient, $L(\theta') = \exp[k_e d \sec(\theta')]$, and d is the depth of the low-density ice layer.
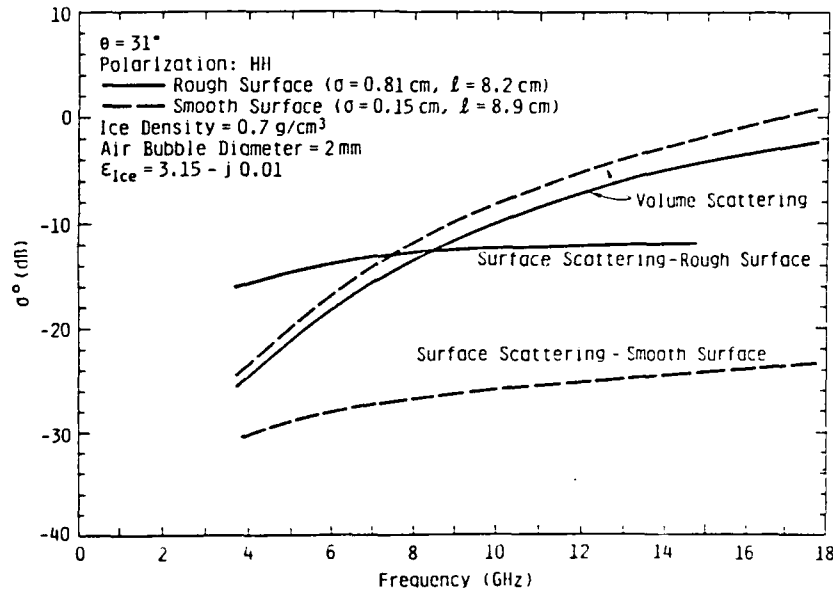
Figure 3.14 Theoretical backscatter response as a function of frequency. Surface and volume scattering contributions are shown separately for rough and smooth surfaces.

SEA ICE CONCENTRATION

100%

80%

60%

40%

20%

0%

>282 5
280K
270K
260K
250K
240K
230K
220K
210K
200K
190K
180K
170K
160K
150K
140K
<132 5

19.35 GHz HORIZONTAL POLARIZATION
BRIGHTNESS TEMPERATURE
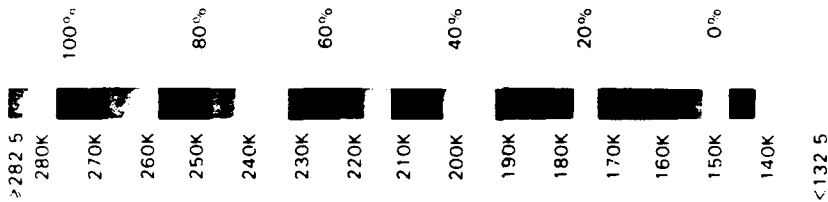
Plate 1 DMSP SSM/I brightness temperatures and resulting sea ice concentration map for the northern hemisphere for January 17, 1988. Data courtesy of Don Cavalieri, NASA Goddard Space Flight Center
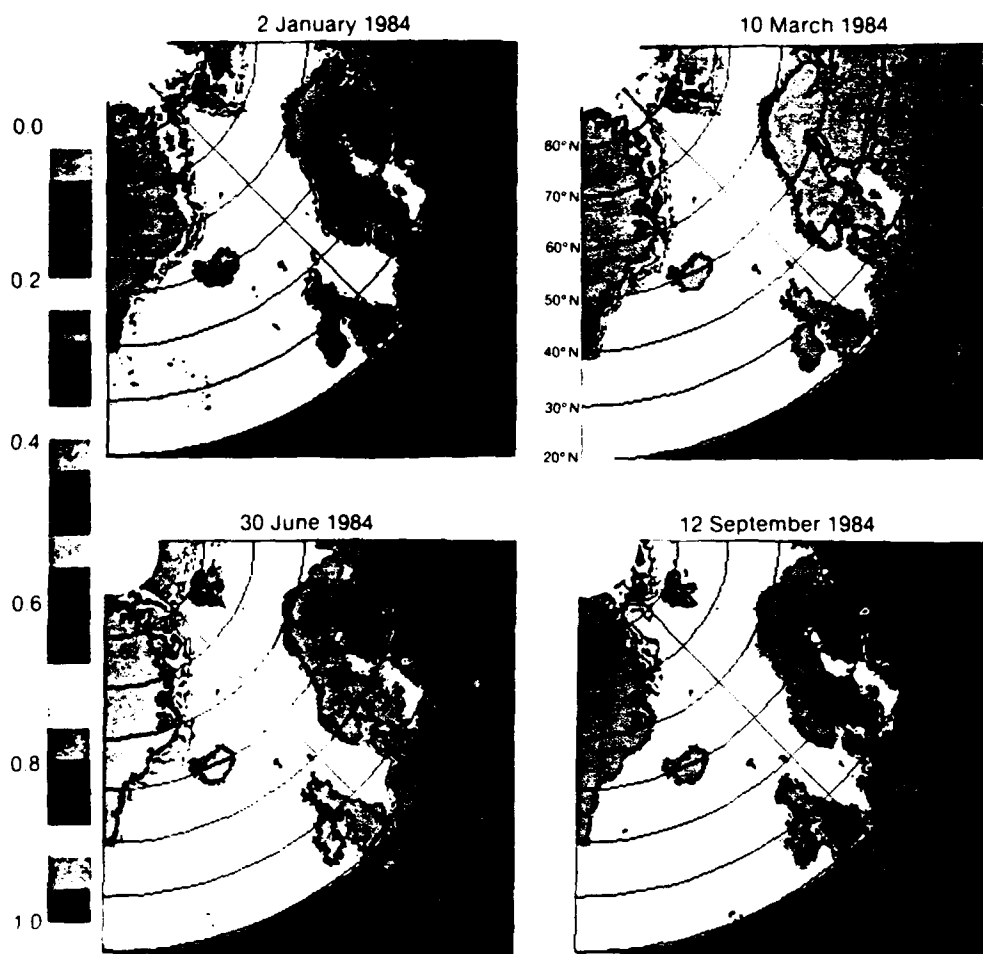
Plate 2 Total ice concentration obtained from Nimbus-7 SMMR for the four seasons over the Greenland Sea and the North Atlantic. Data courtesy of Per Gloersen. NASA Goddard Space Flight Center.

>108%
106%
102%
98%
94%
90%
86%
82%
78%
74%
70%
66%
62%
58%
54%
50%
46%
42%
38%
34%
30%
26%
22%
18%
14%
10%
< 8%
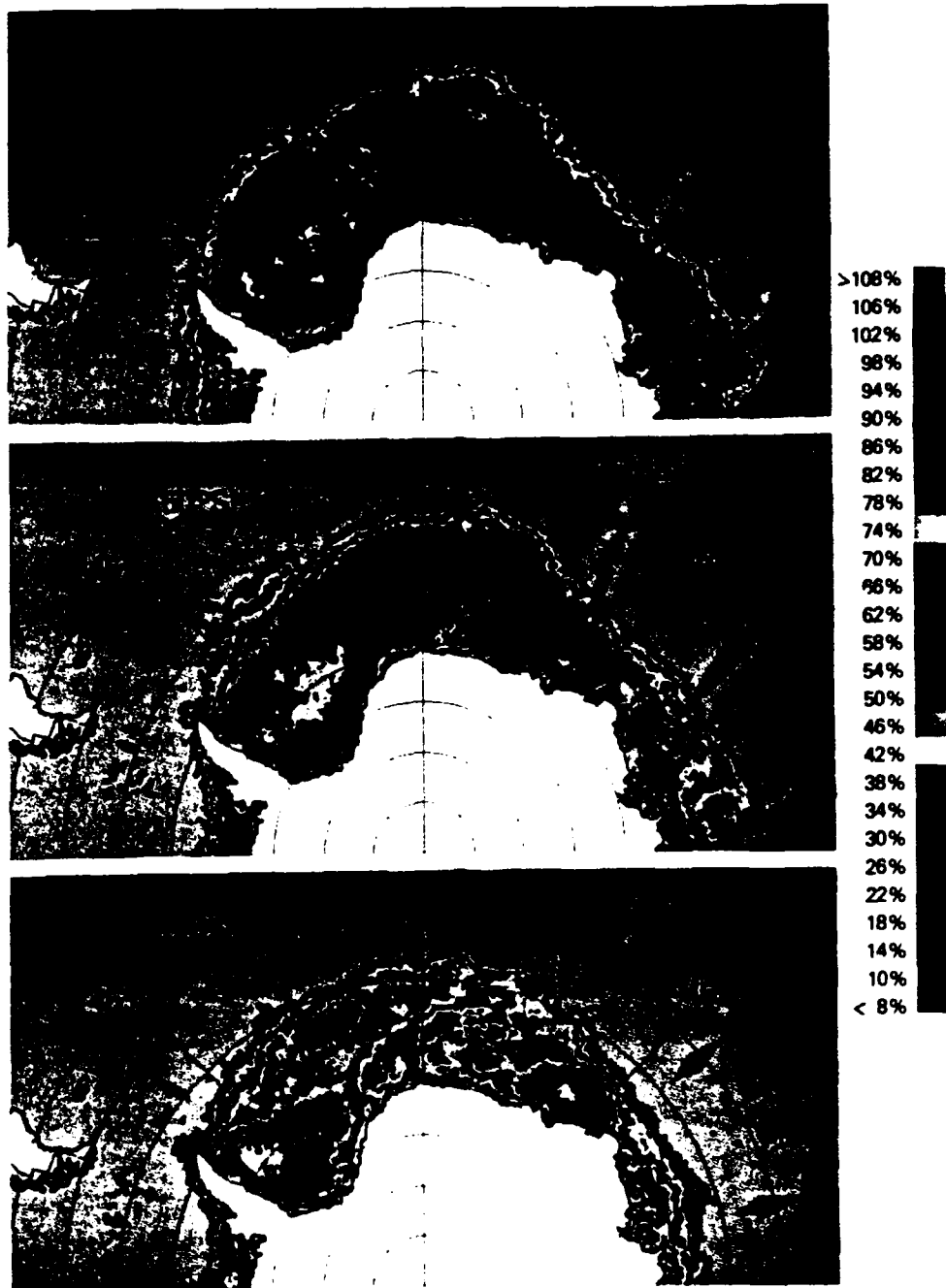
Plate 3 SMMR-derived sea ice concentration maps for the Weddell Sea. From Sullivan *et al.* (1988).

The modeled backscatter cross sections show that the range of returns produced by smooth and rough surfaces is quite large and independent of frequency (Fig. 3.14). A rough surface also acts to reduce the effect of volume scattering. At frequencies of about 5 GHz, volume and surface scattering may contribute equally to the backscatter of multiyear ice. Below 5 GHz, volume scattering decreases rapidly in importance as the frequency is reduced.

In modeling the emissivity of multiyear ice, two approaches have shown promise. A radiative transfer theory, which is an extensicn of the work described above, combines rough surface and volume scattering effects (Fung and Eom, 1982). Another approach assumes that the snow and ice sheet are a two-layer anisotropic random medium (Lee and Kong, 1985). In this formulation, the dyadic Green's function is obtained and then the first-order backscattering coefficients are calculated using the Born approximation. In both techniques, the emissivity is calculated by determining the difference between one and the total reflectivity, which consists of specular reflectivity and the integral of the bistatic scattering coefficients over the upper hemisphere. The emissivity of multiyear ice has yet to be reduced to a simple expression.

IV. Visible and Infrared Sensors

During the past 10 years, satellites have been used to sense ocean color remotely by measuring the spectral radiance backscattered from the ocean and converting the values into pigment (chlorophyll a) concentrations using previously validated algorithms (Gordon *et al.*, 1983). However. the application of the Coastal Zone Color Scanner (CZCS), Landsat and Spot to polar regions has been slow for a number of reasons. There are many validation problems with these sensors at high solar angles, principally the correction for Rayleigh (air) and aerosol scattering of the atmosphere. Polar regions also have more cloud cover than temperate or tropical regions. Because the sensors are passive and cannot penetrate through clouds, the data are less complete than those from other areas. Large solar zenith angles also reduce the penetration of radiant energy and the absolute amount backscattered. Finally. the presence of ice not only greatly complicates the direct observation of ocean color but also makes interpretation difficult due to the increased amount of reflectance by ice, which obscures the small color signal (Mueller, 1988). The CZCS sensor on board the Nimbus-7 satellite became inoperable in 1986. A more advanced color scanner (SeaWIFS), which will be part of the continuing Landsat series, is to be launched in 1991.

Despite the relatively short period of observation for the CZCS (1979–1986) and the difficulties in collecting, processing, and interpreting any images obtained from polar areas, a number of successful investigations of large-scale ocean color in polar regions have been completed. Maynard and Clark (1987) showed the large-scale distribution of pigments in the vicinity of the Yukon River plume in the Bering Sea and its relationship to a receding ice edge, and Sullivan *et al.* (1988) used CZCS images in conjunction with Advanced Very High Resolution Radiometer (AVHRR) data on ice concentrations to study the spatial extent and variations in phytoplankton blooms in the southern oceans, particularly those associated with the MIZ. A similar study using more advanced color algorithms was conducted by Comiso *et al.* (1990). These studies have provided large-scale coverage of ocean color in regions which are generally inaccessible and have thus extended our understanding of the magnitude of phytoplankton standing stocks in polar regions. Single CZCS images have been used to validate more synoptic trends found in ship-based sampling (Nelson *et al.*, 1987; El-Sayed, 1988).

Because the problem of clouds precludes study with satellite sensors in many polar regions, color sensors have been mounted on airplanes and helicopters which fly at variable altitudes. Although the area observed by aircraft-mounted sensors is much less than that observed by satellites, the aircraft-mounted sensors have the distinct advantage of being more reliable and hence are more applicable to mesoscale oceanographic studies such as those at the ice edge. Such systems can be either active (for example, laser-induced) or passive. Hoge *et al.* (1990) have shown the utility of the active lidar system in waters of the Greenland Sea, and Aiken *et al.* (1988) have investigated a region west of Svalbard using a passive system. However, the integration of aircraft-mounted color sensors into mesoscale oceanographic studies remains to be completed.

V. Satellite, Aircraft, and Ground-Based Remote Sensing Examples for Polar Oceanography

Sea ice is a vital, interactive component of the climate system, affecting and reflecting global changes of the atmosphere and oceans. The presence of sea ice restricts exchanges of heat, mass, momentum, and chemical constituents such as carbon dioxide and other gases between the ocean and the atmosphere, thereby reducing the amount of solar radiation absorbed at the earth's surface. This affects oceanic and atmospheric circulation. Because sea ice forms a layer of insulation between the ocean and the atmosphere, there is 5 to 20 times more heat flux from an open water area than from the same area of solid pack ice.

Since 1973, satellite passive-microwave data have provided excellent information on the large-scale oscillations of sea ice distribution in both the Arctic and the Antarctic. This information serves as useful background for both climate and mesoscale studies. The data obtained by the Electrically Scanning Microwave Radiometer (ESMR) on the NOAA Nimbus-5 satellite from 1973 to 1976 are presented in atlases of the Arctic and Antarctic by Parkinson *et al.* (1987) and Zwally *et al.* (1983), respectively. The data series was continued from 1978 to 1987 utilizing observations from the Nimbus-7 SMMR. Since 1987, the Special Sensor Microwave Imager (SSM/I) of the Defense Meteorological Satellite Program (DMSP) has provided passive microwave data as shown in Plate 1.

Plate 2 is plotted from data from the Nimbus-7 SMMR showing ice concentration (i.e., water versus ice) for the Greenland Sea and part of the North Atlantic as a function of season. The resolution of the SMMR data varies from 18 to 95 km as a function of frequency. The ice derived products which include total ice concentration and multiyear fraction are generally plotted on a 25–50-km grid. The algorithm for calculating the sea ice concentrations and type (multiyear fraction) from multispectral radiances obtained from the SMMR is discussed in detail by Cavalieri *et al.* (1984) and Gloersen and Cavalieri (1986). Briefly, the calculations utilize the vertically (V) polarized radiances obtained at a wavelength of 0.8 cm and the horizontally (H) and vertically polarized radiances at the 1.7 cm wavelength. Ratios of radiance are used to remove the physical temperature of the earth's surface to first order. To generate the concentration values shown in Plate 2, the H and V radiances at 1.7 cm were selected to calculate one of the ratios mentioned above, the polarization ratio (PR), which is used in the calculation of sea ice concentration (Cavalieri *et al.*, 1984). This combination was chosen because it resulted in the algorithm's being less sensitive to the combination of different instrument drifts in the selected channels over the 9-year period. The PR is used principally to distinguish between sea ice and open water because it is relatively insensitive to sea ice type. Another radiance ratio, the spectral gradient ratio (GR), is used to detect the ice type through the wavelength-dependent scattering due to empty brine cells present in the freeboard portion of multiyear ice and absent in first-year ice. The GR is calculated as the ratio of the difference to the sum of the vertical polarizations at the 0.8- and 1.7-cm wavelengths. Limiting the allowable range of GR is also important in reducing the weather effects, which previously led to ambiguous interpretation in the ice margins during storm passages (Gloersen and Cavalieri, 1986).

The accuracies of the calculations of sea ice area (i.e., ice concentration) with the 1.7-cm PR have been estimated (Cavalieri *et al.*, 1984) as about 5% in the central pack and about 9% in the MIZ, where as much as 30% of the ice

may be thin or new and without snow cover (two ice types not taken explicitly into account by the algorithm). The precision or repeatability of the ice coverage calculations is probably better than the accuracy, i.e., closer to the value expected on the basis of instrument noise and drift, 1-2% for a single footprint.

The annual and seasonal variations of the ice distribution of the northern and southern hemispheres have been studied for a number of years with these passive microwave sensors. For example, Gloersen and Campbell (1988), using SMMR data, estimated that the total sea ice extent in the northern hemisphere varies from a minimum of about 8 million km² in September to a maximum of about 15 million km² in March. Sutherland *et al.* (1989) used SMMR data to observe rapid ice formation and ablation (i.e., 200,000 km² in 48 h) in the "Odden" area of the Greenland Sea. The rapid oscillation of the Odden does not appear to be a result of wind-induced ice drift but rather of the rapid formation of thin ice off the main ice edge.

Ice concentration maps produced from SMMR for the Weddell Sea are shown in Plate 3. Color-coded images of ice concentrations derived from SMMR on October 1, November 2, and December 2, 1983, are shown from top to bottom in the figure. The set of images shows qualitatively and quantitatively the state of the ice cover from the time of near-maximum ice extent through the austral spring. The trend of ice decay and the areas most vulnerable to it during various time periods are also evident from the images. The concentration gradient at the MIZ is also observed to be variable, ranging from tens of kilometers to several hundred kilometers (Sullivan *et al.*, 1988).

Thus, one of the most important geophysical parameters that is measurable from space- and airborne sensors is ice concentration (Swift *et al.*, 1985). The determination of the mixture of ice and water (see Hollinger *et al.*, 1984: Svendsen *et al.*, 1983; Comiso, 1983; Carsey, 1985), accomplished by exploiting the large difference in emissivity and/or backscatter intensity between ice and water, was first demonstrated in the early 1970s, when *in situ* observations at manned drifting stations and airborne sensor data were correlated (Vant *et al.*, 1978; Campbell *et al.*, 1978; Gloersen *et al.*, 1973). The contrast in the emission for ice and water is unambiguous. In comparison, radar backscatter may have reduced contrast or even contrast reversals when there are large areas of water (e.g., near the ice edge) and moderate wind speeds, or with viewing angles from vertical to approximately 25°. Within the pack ice, contrasts between open water and sea ice for both active and passive microwave sensors have been generally quite high (Grenfell and Lohanick, 1985).

Algorithms using active- and passive-microwave data are very similar in their nature. At present, algorithms are based on knowing the signature for ice-free ocean and consolidated ice (both first-year and multiyear). Using the

expected signals S for either brightness, temperature, or backscatter intensities of ice and water, ice concentration C is calculated on the basis of linear interpolation as follows:

$$C = (S_o - S_w)/(S_i - S_w) \tag{3.10}$$

where S_o is the observed signal, S_w the mean signal for ice-free water, and S_i the mean signal for consolidated sea ice. At present, algorithms using this technique agree with aerial photography and passive microwave observations to within approximately 10% (Burns *et al.*, 1987).

Satellite radar altimeters have been designed to provide very accurate ocean height information. These data have a resolution on the order of 5 cm and a spot size of approximately 10 km and have been used to provide geoid, gravity wave height, currents, and ocean topography values (Cheney, 1982; Fedor and Brown, 1982). In addition to wave height information (i.e., the two-way time travel of the pulse), the amount of backscatter is analyzed to yield wind information. More recently, Hawkins and Lybannon (1989) have begun to use the U.S. Navy's radar altimeter on the Geosat satellite to provide sea ice information. Potentially, a radar altimeter can provide information about concentration, ice type, and roughness in addition to ice extent.

The return pulse from the radar altimeter has significantly different shapes for the sea ice and the open ocean. Ice, unlike water, tends to produce specular reflection, so a much larger portion of the radiated energy at any angle will reflect off the ice surface at an angle equal to the angle of incidence. In general, the signal strength is much larger than that of the ocean and the shape of the reflected pulse is also modified. Dwyer and Godin (1980), using Seasat altimeter data, developed a semiempirical algorithm for satellite radar altimeters that measures these differences. The algorithm is

$$\text{Ice index} = [(100 + \text{AGC})/(100 \times \text{AASG})] - 10 \tag{3.11}$$

where AGC is the automatic gain control signal and AASG the average altitude/specular gate.

The Geosat ice index is a number that ranges from 0.6 to 0.7 over water and is greater than 1 over ice. Therefore, water–sea ice transitions are evident in the time history of the ice index. Figure 3.15 is a plot of ice index for the Antarctic region with the Geosat satellite radar track as baselines (Hawkins and Lybannon, 1989). The orbital inclination of Geosat (72°) limits the coverage to 72° north and south.

In the past two decades, a series of large Arctic projects have yielded a considerable understanding of the growth, motion, and decay of sea ice in the interior of the Arctic Ocean (Pritchard, 1980). After the Arctic Ice Dynamics Joint Experiment (AIDJEX), attention shifted to the problem of
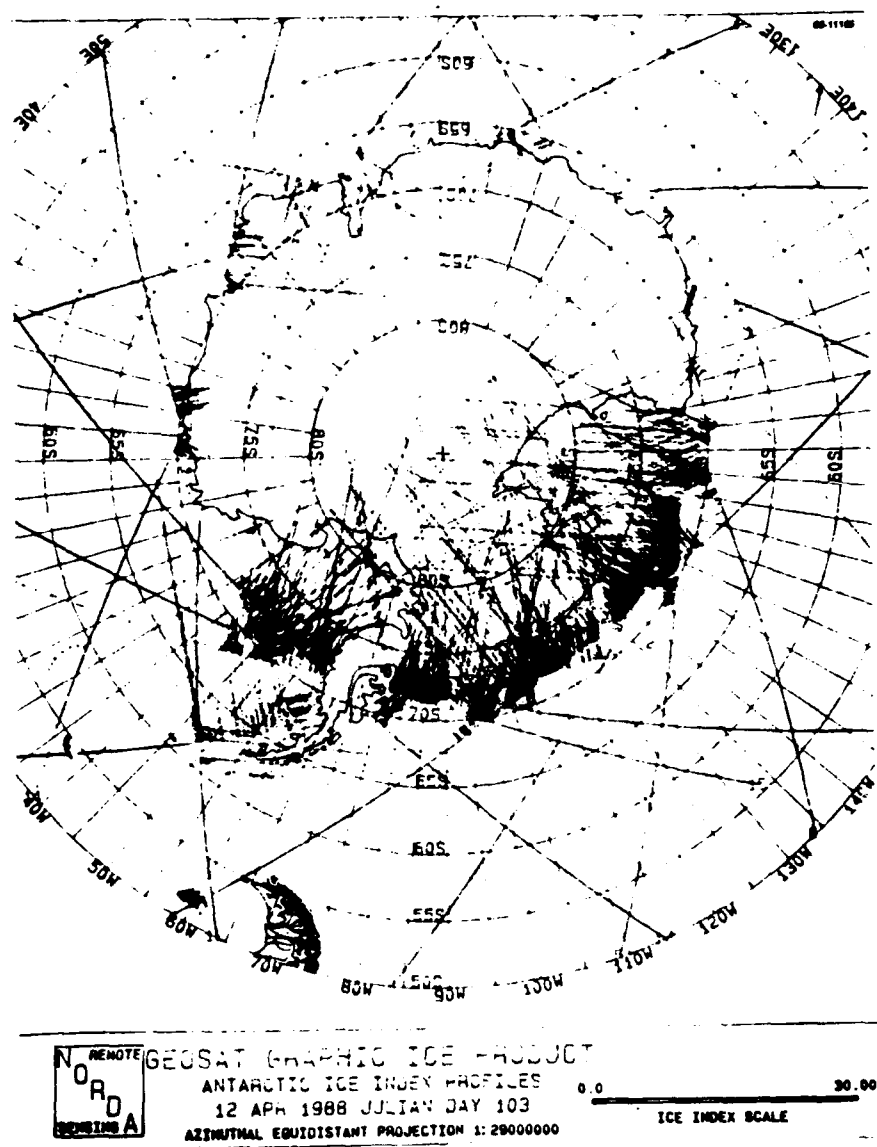
Figure 3.15 Plot of ice index for the Antarctic region with the Geosat satellite track as baselines. An index greater than 1 denotes ice. From Hawkins and Lybannon (1989), copyright © 1989 IEEE.

understanding the processes which occur at the MIZ, the area where the permanent ice pack meets the open ocean. By understanding the interaction between the atmosphere, ocean, and sea ice, the advance and retreat of the ice edge can be determined.

An important area for exchange of heat and mass between the Arctic Ocean and the North Atlantic is the Fram Strait area of the Greenland Sea (see Chapter 4). The Fram Strait area has been the site of three major Marginal Ice Zone Experiments (MIZEXs) conducted in 1983, 1984, and 1987. The warm northward-flowing North Atlantic current, the cold southward-flowing Arctic water, and the pack ice at the MIZ can be observed from AVHRR visible and infrared satellite data at 2-km resolution (Plate 4). Various eddies can also be observed along the ice edge.

Among the objectives of the MIZEX program were studies of the ice edge position, ice kinematics, ice concentration, ice types, locations of eddies, ice physics, ice thickness, ridges, ice floe distribution, leads, and polynyas. A SAR system housed in a CV-580 aircraft was used to provide information about the variables. In addition, the all-weather SAR was used in a real-time mode to guide the research vessels into the eddy regions. For example, a high-resolution SAR mosaic collected on July 5, 1984 (Fig. 3.16) clearly shows the detailed surface structure of an elliptically shaped eddy (E1) on the scale of $\approx$ 30 km. Because winds were light, the sea ice floe size distribution of 50–500 m reflected the upper-ocean circulation. The orbital motion of the eddy was cyclonic, while the spiral motion of ice toward the center indicated an inward frictionally driven radial motion. The ice concentration was more than 80% at the center of the eddy. This implied that there was convergence and that ageostrophic effects are important and must be included in realistic models of these eddies. A second eddy (E2) was seen south of E1. Slicks and bands of ice that indicated internal wave activity were also identified. The area marked "band of 'dead' water" off the ice edge was a distinct meltwater zone. A detailed interpretation of the SAR mosaic describes the location of large individual floes and polynyas, ice concentration estimates, and ice edge and floe size distributions (see Fig. 3.16). Fully automatic algorithms have been developed which can produce sea ice type classification and concentration maps from SAR data (Wackerman *et al.*, 1988). The sea ice type classification algorithm uses local statistics to determine ice type boundaries, and the ice concentration algorithm iteratively decomposes the histogram into ice and water statistical values.

SAR images collected 6 days apart over the same area provide information regarding the dynamic processes in the MIZ. Figure 3.17 shows the analysis of two SAR images collected 6 days apart (June 30 and July 6, 1984) and the transformation of a relatively north–south ice edge to a convoluted,
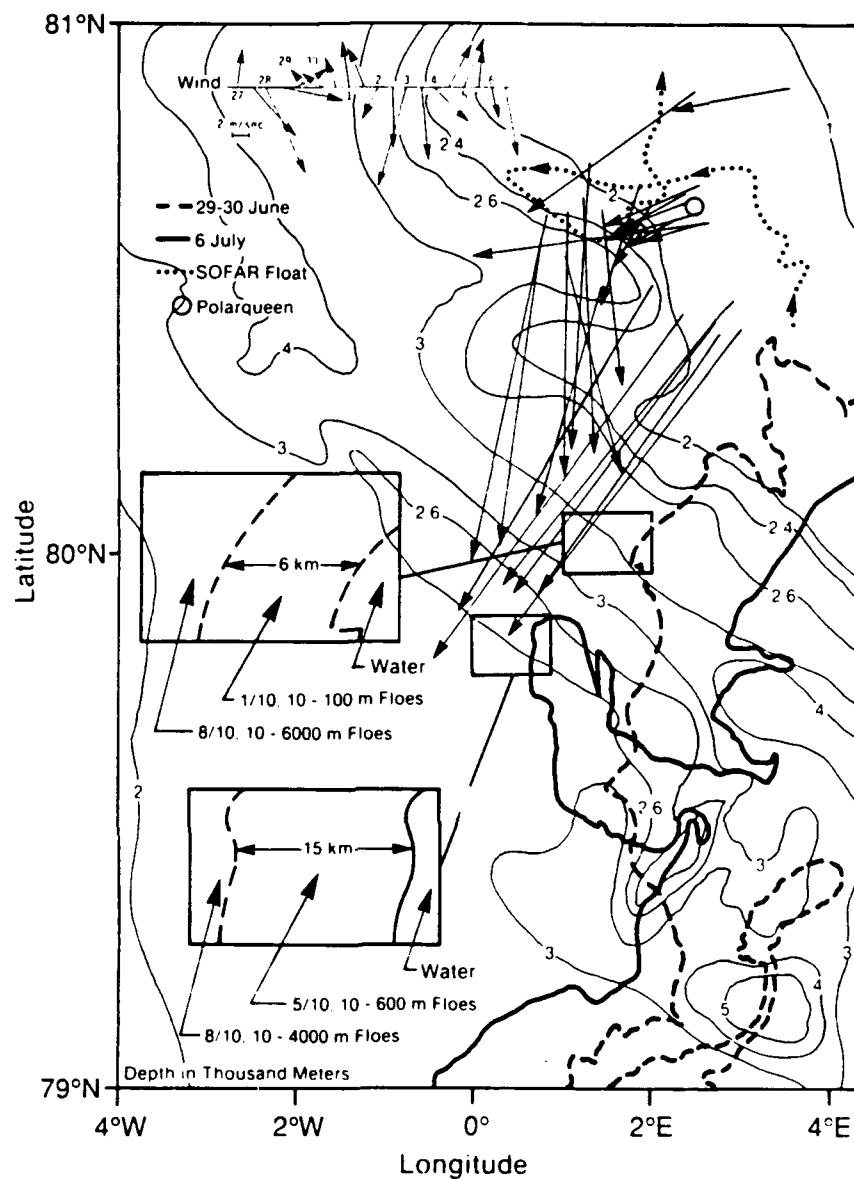
understanding the processes which occur at the MIZ, the area where the permanent ice pack meets the open ocean. By understanding the interaction between the atmosphere, ocean, and sea ice, the advance and retreat of the ice edge can be determined.

An important area for exchange of heat and mass between the Arctic Ocean and the North Atlantic is the Fram Strait area of the Greenland Sea (see Chapter 4). The Fram Strait area has been the site of three major Marginal Ice Zone Experiments (MIZEXs) conducted in 1983, 1984, and 1987. The warm northward-flowing North Atlantic current, the cold southward-flowing Arctic water, and the pack ice at the MIZ can be observed from AVHRR visible and infrared satellite data at 2-km resolution (Plate 4). Various eddies can also be observed along the ice edge.

Among the objectives of the MIZEX program were studies of the ice edge position, ice kinematics, ice concentration, ice types, locations of eddies, ice physics, ice thickness, ridges, ice floe distribution, leads, and polynyas. A SAR system housed in a CV-580 aircraft was used to provide information about the variables. In addition, the all-weather SAR was used in a real-time mode to guide the research vessels into the eddy regions. For example, a high-resolution SAR mosaic collected on July 5, 1984 (Fig. 3.16) clearly shows the detailed surface structure of an elliptically shaped eddy (E1) on the scale of ≈ 30 km. Because winds were light, the sea ice floe size distribution of 50–500 m reflected the upper-ocean circulation. The orbital motion of the eddy was cyclonic, while the spiral motion of ice toward the center indicated an inward frictionally driven radial motion. The ice concentration was more than 80% at the center of the eddy. This implied that there was convergence and that ageostrophic effects are important and must be included in realistic models of these eddies. A second eddy (E2) was seen south of E1. Slicks and bands of ice that indicated internal wave activity were also identified. The area marked "band of 'dead' water" off the ice edge was a distinct meltwater zone. A detailed interpretation of the SAR mosaic describes the location of large individual floes and polynyas, ice concentration estimates, and ice edge and floe size distributions (see Fig. 3.16). Fully automatic algorithms have been developed which can produce sea ice type classification and concentration maps from SAR data (Wackerman *et al.*, 1988). The sea ice type classification algorithm uses local statistics to determine ice type boundaries, and the ice concentration algorithm iteratively decomposes the histogram into ice and water statistical values.

SAR images collected 6 days apart over the same area provide information regarding the dynamic processes in the MIZ. Figure 3.17 shows the analysis of two SAR images collected 6 days apart (June 30 and July 6, 1984) and the transformation of a relatively north–south ice edge to a convoluted,

Figure 3.17 Composite sketch of ice edge, concentration, and floe size for 30 June and 6 July 1984 derived from the SAR. Also indicated are the track of a sofar buoy, bathymetry contours, and local surface wind. From Shuchman *et al.* (1987).

meandering ice edge. These meanders result from the complex interactions along the boundary between the rapid southward East Greenland Current, warm northward-flowing Atlantic waters, and highly variable winds. Ice edge meanders may play an important role in the generation of ice – ocean eddies because they provide the initial perturbation in the Ekman transport field that eventually results in eddies. These edge features are composed of ice floes ranging from 50 to 500 m in size, which are the result of gravity wave – ice interaction and eddy-induced floe collisions that break up large floes. Under moderate wind conditions, the ice in these meanders reflects the ocean circulation because the individual ice floes act as Lagrangian drifters moving with the current. This is particularly true in the summer season, when the winds are normally light (less than 4 m/s) and there is no formation of new ice that would freeze floes together.

The sequential images also give ice drift kinematic data. The ice drift vectors were derived by locating the same floe in images on June 29 and July 6. Three regimes of floe drift occurred during this 7-day period. First, the floes at the edge moved fastest, an average distance of 75 km (12.5 cm/s) in a southwesterly direction parallel to the ice edge. Second, floes west of 2°E, at distances greater than 40 km from the edge, moved approximately 45 km (7.5 cm/s) to the south (Shuchman *et al.*, 1987). Finally, in the region near the R/V *Polarqueen*, the ice drift was only 15 km (2.5 cm/s) to the southwest.

The decrease in speed and the change in direction of the ice floe drift across the MIZ result from different forces acting on the ice in the interior and at the edge. The interior, with greater ice concentration and larger floes, is more strongly influenced by internal ice stress than the ice edge, which normally has lower ice concentrations and smaller floe sizes. The wind force also varies across the MIZ because the edge region, with smaller floe size and lower ice concentration, has greater roughness than the interior. The third feature, the region of dramatically reduced ice drift, occurred at precisely the same time and location at which an ocean frontal meander was observed in the dynamic height topography (Manley *et al.*, 1987). Furthermore, the drift of a sound fixing and ranging (sofar) buoy at a depth of 100 m through this anomalous ice drift area showed that this meander was a cyclonic ocean eddy. The location and size of this eddy were such that its circulation was opposed to the general ice drift direction, which reduced the ice drift velocities. Hence, the eddy slowed the ice drift in one region, changed the drift direction in the other region, and possibly augmented the drift to the north.

Surface waves are a major factor determining the structure of the ice in the MIZ. As the waves propagate through the ice field from the open ocean, they are scattered and attenuated by the ice floes. Only the long-period swells propagate more than a few kilometers into the ice; therefore, the breakup by

short waves is most effective near the ice edge. The longest swells from storms can penetrate more than 100 km into the ice and can break up layer floes through flexure for tens of kilometers. The decay coefficient varies approximately as frequency squared, so the shorter waves are damped more quickly (Wadhams *et al.*, 1988). The result is a floe size distribution in which the maximum floe size increases within the pack. Airborne SAR can provide observations of wave penetration into the ice. Lyden *et al.* (1988) utilized SAR data and standard fast Fourier transform (FFT) techniques to observe 230-m-wavelength surface swell, generated by a passing meteorological low several hundred kilometers away, penetrating over 200 km into the pack before significant decay occurred.

In 1978 a free-flying NASA satellite called Seasat was flown in a near-polar orbit and carried a SAR. Although the satellite failed 100 days after launch, more than 150 passes of *L*-band (23.5-cm) SAR data were collected over the Arctic. The resolution of Seasat was 25 m and the swath width was 100 km. Figure 3.18 shows two Seasat 100 × 100 km images of the central ice pack in the Beaufort Sea taken 3 days apart. A kinematic vector image of ice floe motion over the 3-day period is also shown. The velocity vectors resulted from tracking over 750 floes common to both images (Curlander *et al.*, 1985). The vectors show the complexity of motion in an ice field that is the consequence of air stress, ocean surface tilt, water stress, and force transmitted through the ice. The first two stresses are perceived to be essentially constant over the 100-km dimension of the image, whereas the remaining two stresses are known to have spatial variability.

Both ground-based and helicopter-mounted instrumentation can be used to acquire backscatter information. Radars such as the sled-based scatterometer are being transported to the ice floes in the Arctic to couple the accurate measurement of backscatter with scene characterization measurements as well as surface-based passive-microwave measurements. This sled system (Onstott and Shuchman, 1988a) provides data on backscatter from various sea ice forms at frequencies from 0.5 to 10 GHz and relates the sources of scatter to locations within the snow and ice. These *in situ* observations may then be extended to the small scale with helicopter-borne instrumentation such as the *L-C-X*-band scatterometer (Onstott and Shuchman, 1988b) or to the mesoscale with aircraft and satellite sensors. These scatterometers make a powerful contribution to polar research because they provide backscatter values as a function of incidence angle. The measurements at various incidence angles can then be used for validation of backscatter models as well as interpretation of aircraft SAR data, which are typically collected at moderate angles (e.g., 45°), to predict responses of future SAR satellite systems that utilize steep angles of incidence (e.g., 25°) because of power limitations.

(a) SEASAT SAR BEAUFORT SEA

(b) SEASAT SAR BEAUFORT SEA ILLUMINATION

(c) RELATIVE VELOCITY VECTORS

N

20 km
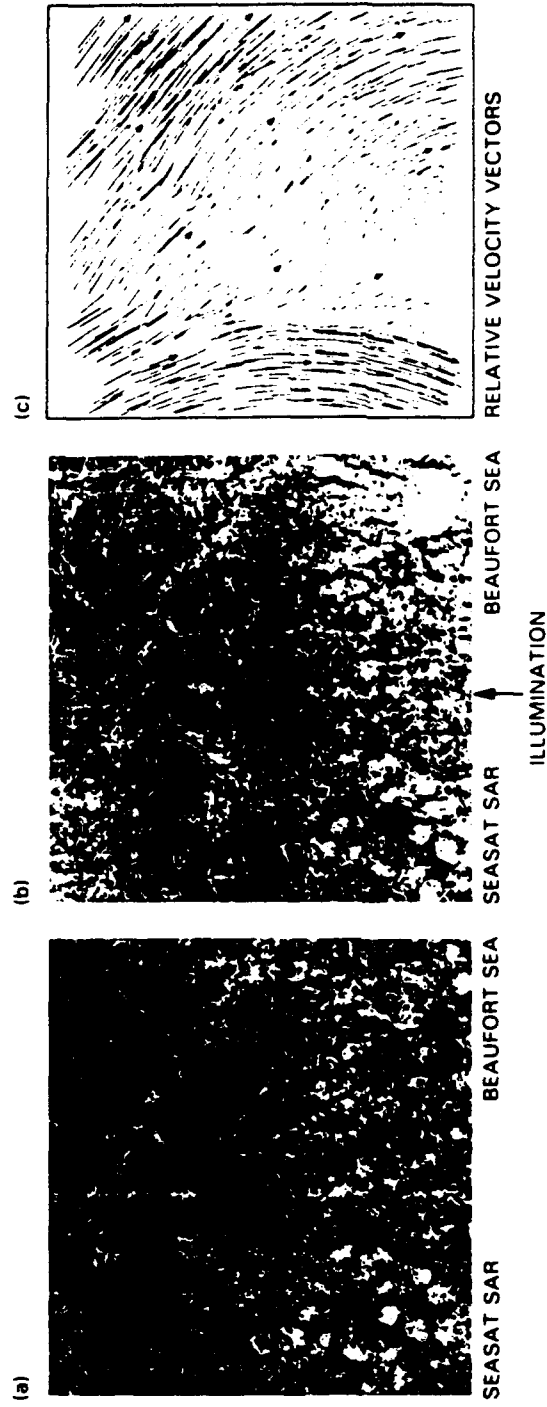
Figure 3.18 Two Seasat 100 × 100 km SAR images taken 3 days apart (while in a 3-day repeat orbit) of the central ice pack in the Beaufort Sea. A kinematic vector image of the ice motion over the 3-day period is also presented. From Curlander *et al.* (1985).

VI. Concluding Remarks

Satellite remote sensing offers the capability of synoptically mapping the Arctic and Antarctic oceans. If microwave sensors are employed, the mapping can be performed independently of weather and solar illumination. Passive-microwave radiometers provide sea ice concentrations with coarse resolution (25–50 km) for both the northern and southern hemispheres. These maps have been obtained on a near-daily basis since 1973. Designs in which the resolution of these passive-microwave systems is improved by an order of magnitude will be implemented within the next decade. Visible and infrared satellite sensors such as Landsat, NOAA AVHRR, and Spot are extremely useful in supplying water mass, biological, and ice information on cloud-free days.

SAR has the greatest potential for providing polar information from space. With its 10–30-m resolution, SAR has been demonstrated to provide observations on ice edge position, ice kinematics, ice concentration, ice types, ice physics, ridges, icebergs, ice flow distribution, leads, polynyas, wave propagation into the pack, locations of eddies and fronts, and determination of wind speed. A number of SARs in polar orbit are planned, beginning with the launch of Earth Resource Satellite-1 (ERS-1) by the European Space Agency (ESA) in 1990. It is thought that by the year 2000 continuous SAR data for both the Arctic and Antarctic will be routinely available.

Radar altimeters provide useful information (10-km resolution) on ice edge extent, ice roughness, gravity waves, significant wave height, wind speed and direction, ocean currents, and ocean surface topography. A series of radar altimeters, which are planned for the coming decades, will increase the availability of altimeter data for the polar regions.

The optical and thermal sensors (AVHRR, OLS, MSS), when weather conditions are favorable (i.e., cloud-free and proper solar illumination), provide excellent high-resolution (10–2000-m) information on sea ice extent, location of fronts and eddies, and mapping of individual water masses including chlorophyll concentration. Kinematics can also be performed if the area remains cloud-free during the required observation period.

Table 3.3 lists the currently planned free-flying satellite systems which can provide information about the Arctic and Antarctic. Not listed are the replacement satellites for the NOAA 9/10 and DMSP series. These replacements are presently scheduled, and thus continuous uninterrupted service should be provided by these satellites.

When selecting a remote sensor for polar oceanography, the trade-off between high resolution and swath width coverage must always be considered. In general, the coarse-resolution sensors (1 km, AVHRR; 50 km, passive microwave) can map a hemisphere over a 1–2-day period. The high-res-

164

Table 3.3 Earth Observation Missions That Will Provide Polar Information (Planned and Approved)

	Mission	Objectives	Main sensors	Orbit	Launch date	Status of approval
ESA	ERS-1	Ocean-ice monitoring	Synthetic-aperture radar Wind and wave scatterometer Radar altimeter Along-track scanning radiometer Precise range and range rate equipment	780 km alt. sun-synchr.	1990	Approved phase C/D started in 1985
Canada	Radarsat	Ice and land monitoring	Synthetic-aperture radar Wind scatterometer Optical sensor	1000 km alt. sun-synchr.	1994	Approved
Japan	MOS-1	Marine applications	MESSR VTIR MSR	909 km alt. sun-synchr.	1986	Launched
	J-ERS-1	Land applications	Synthetic-aperture radar Visible and near-infrared radiometer	570 km alt. sun-synchr.	1990	Approved

Country/Agency	Name	Application	Instruments	Orbit	Launch	Status
United States: NASA/France	TOPEX/ Poseidon	Ocean circulation	Two-frequency radar altimeter Microwave radiometer Precise positioning	1300 km alt., 63° inclination	1989	Phase B in progress
France	Spot	Land applications	High-resolution (10 m) Visible instruments (×2)	832 km alt. sun-synchr.	Spot-1 in 1986 Spot-2 in 1989	Launched Approved
United States: NOAA + private entity	Landsat 6 and 7	Land applications Ice and ocean	Thematic mapper Multilinear array SeaWifs	700 km alt. sun-synchr.	Landsat 6 in 1989 Landsat 7 in 1991	Under discussion in U.S. Congress
United States: DoD	DMSP	Meteorology Sea ice	High resolution Visible and IR (OLS) Special sensor microwave imager	883 km alt. polar sun-synchr.	May 1986	Launched
United States: NASA	EOS	Meteorology/ Ice and land monitoring	Radar altimeter Visible Passive micrometer Synthetic-aperture radar	850 km alt. polar sun-synchr.	2000	Under preliminary design

olution sensors (5–100 m; Spot, Landsat, and SAR) provide mesoscale regional coverage (i.e., 300 × 3000 km) daily, but a number of days are needed to assemble a hemispheric map. As satellite sensors become more sophisticated, Spot/Landsat and SAR data should be available with hemispheric coverage daily.

Acknowledgments

References

Aiken, J., J. W. Nolten, C. C. Trees & J. L. Mueller. 1988. Horizontal and vertical variability of bio-optical fields in the Greenland and Barents seas. *Eos* **69**: 1141 (abstr.).

Apel, J. R. (ed.). 1987. "Principles of Ocean Physics." Int. Geophys. Ser., Vol. 38. Academic Press, Orlando, Florida.

Burns, B. A., D. J. Cavalieri, M. R. Keller, W. J. Campbell, T. C. Grenfell, G. A. Maykut & P. Gloersen. 1987. Multisensor comparison of ice concentration estimates in the marginal ice zone. *J. Geophys. Res.* **92**: 6843–6856.

Campbell, W. J., J. Wayenberg, J. B. Ramseyer, R. O. Ramseier, M. R. Vant, R. Weaver, A. Redmond, L. Arsenault, P. Gloersen, H. J. Zwally, T. T. Wilheit, T. C. Chang, D. Hall, L. Gray, D. C. Meeks, M. L. Bryan, F. T. Barath, C. Elachi, F. Leberl & T. Farr. 1978. Microwave remote sensing of sea ice in the AIDJEX main experiment. *Boundary-Layer Meteorol.* **13**: 309–337.

Carsey, F. D. 1985. Summar Arctic sea ice character from satellite microwave data. *J. Geophys. Res.* **90**: 5015–5034.

Cavalieri, D. J., P. Gloersen & W. J. Campbell. 1984. Determination of sea ice parameters with the Nimbus-7 SMMR. *J. Geophys. Res.* **89**: 5255–5369.

Chandrasekhar, S. 1960. "Radioactive Transfer." Dover, New York.

Cheney, R. E. 1982. Comparison data for Seasat altimetry in the western North Atlantic. *J. Geophys. Res.* **87**: 3247–3253.

Comiso, J. C. 1983. Sea-ice effective microwave emissivities from satellite passive microwave and infrared observations. *J. Geophys. Res.* **88**: 7686–7704.

Comiso, J. C., N. G. Maynard, W. O. Smith, Jr. & C. W. Sullivan. (1990). Satellite ocean color studies of the Antarctic ice edge in summer/autumn. *J. Geophys. Res.* (in press).

Curlander, J. C., B. Holt & K. J. Hussen. 1985. Determination of sea ice motion using digital SAR imagery. *IEEE J. Oceanic Eng.* **OE-10**: 358–367.

Dwyer, R. W. & R. H. Godin. 1980. Determining sea ice boundaries and ice roughness using Geosat-3 altimeter data. *NASA [Contract. Rep.] CR* NASA-CR-156862.

Earth Observing Reports. "SAR Synthetic Aperture Radar Instrument Panel Report," Vol. 11F. NASA, Washington, D.C.

El-Sayed, S. Z. 1988. Productivity of the Southern Ocean: A closer look. *Comp. Biochem. Physiol.* **90**: 489–498.

Fedor, L. S. & G. S. Brown. 1982. Waveheight and wind speed measurements from the Seasat radar altimeter. *J. Geophys. Res.* **87**: 3254–3260.

Fung, A. K. & H. J. Eom. 1982. Application of a combined rough surface and volume scattering theory to sea ice and snow backscatter. *IEEE Trans. Geosci. Electron.* **GE-20**: 528–536.

Gloersen, P. & W. J. Campbell. 1988. Variations in the Arctic, Antarctic, and global sea ice cover during 1978–1987 as observed with the Nimbus-7 SMMR. *J. Geophys. Res.* **93**: 10666–10674.

Gloersen, P. & D. J. Cavalieri. 1986. Reduction of weather effects in the calculation of sea ice concentration from microwave radiances. *J. Geophys. Res.* **91**: 3913–3919.

Gloersen, P., W. Nordberg, T. J. Schmuigge, T. T. Wilheit & W. J. Campbell. 1973. Microwave signatures of first-year and multiyear sea ice. *J. Geophys. Res.* **78**: 3564–3572.

Gordon, H. R., D. K. Clark, J. W. Brown, O. B. Brown, R. W. Evans & W. W. Broenkow. 1983. Phytoplankton pigment concentrations in the middle Atlantic Bight: Comparison of ship determinations and CZCS estimates. *Appl. Opt.* **22**: 20–36.

Grenfell, T. C. & A. W. Lohanick. 1985. Temporal variations of the microwave signatures of sea ice during the late spring and early summer near Mould Bay NWT. *J. Geophys. Res.* **90**: 5063–5074.

Hallikainen, M., F. T. Ulaby & M. Abdelrazik. 1984. The dielectric behavior of snow in the 3 to 37 GHz range. *Eur. Space Agency [Spec. Publ.] ESA SP* **ESA SP-215**: 169–174.

Hawkins, J. D. & M. Lybannon. (1989). Geosat altimeter sea ice mapping. *IEEE J. Oceanic Eng.* **14**(2): 139–148.

Hoge, F. E., C. W. Wright, R. N. Swift & J. K. Yungel. (1990). Airborne discrimination between ice and water; application to the laser measurement of chlorophyll-in-water in a marginal ice zone. *J. Geophys. Res.* (submitted for publication).

Hollinger, J. P., B. E. Troy, R. O. Ramseier, K. W. Asmus, M. F. Hartman & C. A. Luther. 1984. Microwave emission from high Arctic sea ice during freeze up. *J. Geophys. Res.* **89**: 8104–8122.

Johannessen, O. M., J. A. Johannessen, E. Svendsen, R. A. Shuchman, W. J. Campbell & E. Josberger. 1987. Ice-edge eddies in the Fram Strait marginal ice zone. *Science* **236**: 427–429.

Kim, Y. S., R. K. Moore & R. G. Onstott. 1984. "Theoretical and Experimental Study of Radar Backscatter from Sea Ice." Rep. RSL TR 168, pp. 331–37. Univ. of Kansas, Lawrence.

Kim, Y. S., R. G. Onstott & R. K. Moore. 1985a. The effect of a snow cover on microwave backscatter from sea ice. *IEEE J. Oceanic Eng.* **OE-9**: 383–388.

Kim, Y. S., R. K. Moore, R. G. Onstott & S. Gogineni. 1985b. Towards identification of optimum radar parameters for sea ice monitoring. *J. Glaciol.* **31**: 214–219.

Lee, J. K. & J. A. Kong. 1985. Passive microwave remote sensing of an anisotropic random medium layer. *IEEE Trans. Geosci. Remote Sens.* **GE-23**: 924–932.

Lyden, J. R., R. A. Schuchman, C. Zago, R. Rottier, P. Wadhams & O. Johannessen. 1988. *Eur. Space Agency [Spec. Publ.] ESA SP* **ESA SP-284**: 1435–1437.

Manley, T. O., J. Z. Villanueva, J. C. Gascard, P. F. Jeannin, K. L. Hunkins & J. van Leer. 1987. Mesoscale oceanographic processes beneath the ice of Fram Strait. *Science* **236**: 432–434.

Matzler, C. 1985. "Interaction of Microwaves with Natural Snow Cover." Treatise No. 152. Inst. Appl. Phys., Univ. of Bern, Bern, Switzerland.

Matzler, C., T. Olaussen & E. Svendsen. 1984. "Microwave and Surface Observations of Water and Ice Carried out from R/V Polarstern in the Marginal Ice Zone North and West of Svalbard," 2nd ed., Geophys. Inst., Div. A., Univ. of Bergen, Bergen, Norway.

Maynard, N. G. & D. K. Clark. 1987. Satellite color observations of spring blooming in Bering Sea shelf waters during the ice edge retreat in 1980. *J. Geophys. Res.* **92**: 7127–7139.

Mueller, J. 1988. Nimbus-7 CZCS: Electronic overshoot due to cloud reflectance. *Appl. Opt.* **27**: 438.

Nelson, D. M., W. O. Smith, Jr., L. I. Gordon & B. H. Huber. 1987. Spring distribution of density, nutrients and phytoplankton biomass in the ice edge zone of the Weddell–Scotia Sea. *J. Geophys. Res.* **92**: 7181–7190.

Onstott, R. G. 1980. Radar backscatter study of sea ice. Ph.D. Diss., Univ. of Kansas, Lawrence.

Onstott, R. G. & S. Gogineni. 1985. Active microwave measurements of Arctic sea ice under summer conditions. *J. Geophys. Res.* **90**: 5035–5044.

Onstott, R. G. & R. A. Shuchman. 1988a. Multifrequency and multipolarization scatterometer for remote sensing. In "Proceedings of Instrumentation and Measurements in the Polar Regions Workshops," pp. 67–80. Monterey, California.

Onstott, R. G. & R. A. Shuchman. 1988b. Active microwave sensors for Arctic applications. *In* "Proceedings of Instrumentation and Measurements in the Polar Regions Workshop," pp. 81–92. Monterey, California.

Onstott, R. G., R. K. Moore & W. F. Weeks. 1979. Surface-based scatterometer results of Arctic sea ice. *IEEE Trans. Geosci. Electron.* **GE-17**, 78–85.

Onstott, R. G., R. K. Moore, S. Gogineni & C. Delker. 1982. Four years of low altitude sea ice broadband backscatter measurements. *IEEE J. Oceanic Eng.* **OE-7**: 44–50.

Onstott, R. G., T. C. Grenfell, C. Matzler, C. A. Luther & E. A. Svendsen. 1987. Evolution of microwave sea ice signatures during early and mid summer in the marginal ice zone. *J. Geophys. Res.* **92**: 6825–6835.

Parashar, S. K., A. K. Fung & R. K. Moore. 1978. A theory of wave scatter from an inhomogeneous medium with a slightly rough boundary and its application to sea ice. *Remote Sens. Environ.* **7**, 35–50.

Parkinson, C. L., J. C. Comiso, H. J. Zwally, D. J. Cavalieri & P. Gloersen. 1987. Arctic sea ice, 1973–1976: Satellite passive-microwave observations. *NASA [Spec. Publ.] SP* NASA SP-489: 1–296.

Pritchard, R. S. (ed.). 1980. "Sea Ice Processes and Models." Univ. of Washington Press, Seattle.

Shuchman, R. A., B. A. Burns, O. M. Johannessen, E. G. Josberger, W. J. Campbell, T. O. Manley & N. Lannelongue. 1987. Remote sensing of the Fram Strait marginal ice zone. *Science* **236**: 429–431.

Stewart, R. H. 1985. "Methods of Satellite Oceanography." Univ. of California Press, Berkeley.

Sullivan, C. W., C. R. McClain, J. C. Comiso & W. O. Smith, Jr. 1988. Phytoplankton standing crops within an Antarctic ice edge assessed by satellite remote sensing. *J. Geophys. Res.* **93**: 12487–12498.

Sutherland, L. L., R. A. Shuchman, P. Gloersen, J. A. Johannessen & O. M. Johannessen. 1989. SAR and passive microwave observations of the Odden during MIZEX '89. *Proc. IGARSS '89 Symp.* 1539–1544.

Svendsen, E., K. Kloster, B. Farelly, O. M. Jahannessen, J. A. Johannessen, W. J. Campbell, P. Gloersen, D. Cavalieri & C. Matzler. 1983. Norwegian remote sensing experiment: Evaluation of the Nimbus-7 scanning multi-channel microwave radiometer for sea ice research. *J. Geophys. Res.* **88**: 2781–2791.

Swift, C. T., L. S. Fedor & R. O. Ramseier. 1985. An algorithm to measure sea ice concentration with microwave radiometers. *J. Geophys. Res.* **90**: 1087–1099.

Tiuri, M., Shivola, E. Nyfors & M. Hallikainen. 1984. The complex dielectric constant of snow at microwave frequencies. *IEEE J. Oceanic Eng.* **OE-9**: 377–382.

Ulaby, F. T., R. K. Moore & A. K. Fung. 1981. "Microwave Remote Sensing," Vol. 1. Addison-Wesley, Reading, Massachusetts.

———. 1982. "Microwave Remote Sensing," Vol. 2. Addison-Wesley, Reading, Massachusetts.

Vant, M. R., R. B. Gray, R. O. Ramseier & V. Makios. 1974. Dielectric properties of fresh sea ice at 10 and 35 GHz. *J. Appl. Phys.* **45**: 4712–4717.

Vant, M. R., R. O. Ramseier & V. Makios. 1978. The complex dielectric constant of sea ice at frequencies in the range 0.1–40 GHz. *J. Appl. Phys.* **49**: 1264–1280.

Wackerman, C. C., R. R. Jentz & R. A. Shuchman. 1988. Sea ice type classification of SAR imagery. *Eur Space Agency [Spec. Publ.] ESA SP* ESA SP-284: 425–428.

Wadhams, P., V. A. Squire, D. J. Goodman, A. M. Cowan & S. C. Moore. 1988. The attenuation nodes of ocean waves in the marginal ice zone. *J. Geophys. Res.* **93**: 6799–6818.

Zwally, H. J., J. C. Comiso, C. L. Parkinson, W. J. Campbell, F. D. Carsey & P. Gloersen. 1983. Antarctic sea ice, 1973–1976: Satellite passive-microwave observations. *NASA [Spec. Publ.] SP* NASA SP-459: 1–206.

Investigation of the Effects of Summer Melt on the Calculation of Sea Ice Concentration Using Active and Passive Microwave Data

DONALD J. CAVALIERI

Laboratory for Oceans, NASA Goddard Space Flight Center, Greenbelt, Maryland

BARBARA A. BURNS AND ROBERT G. ONSTOTT

Radar Science Laboratory, Environmental Research Institute of Michigan, Ann Arbor

Active and passive microwave data sets acquired during the 1984 Marginal Ice Zone (MIZ) Experiment aircraft flights in the Fram Strait region are used to examine the effects of ice surface melt on microwave signatures and their resulting error in the calculation of sea ice concentration. Conditions examined with the active-passive data set include ice floes with moist and dry snow cover and both heavily ponded and ridged surfaces. Passive sensors on the NASA CV-990 aircraft included the aircraft electrically scanning microwave radiometer (ESMR) operating at 19.4 GHz and aircraft multichannel microwave radiometer (AMMR) operating at 10.7, 18.0, 21.0, and 37.0 GHz. Active microwave sensors flown on the Canadian Centre for Remote Sensing CV-580 aircraft included the Environmental Research Institute of Michigan synthetic aperture radar (SAR) operating at 1.2 and 9.4 GHz. Coincident AMMR and SAR measurements of individual floes identified in aerial photography are used to describe the effects of surface melt on the calculation of sea ice concentration, and in particular, the response of the passive microwave polarization and spectral gradient characteristics to different stages of surface melt. Although the onset and progression of summer melt are not uniform throughout the Arctic, the stages of summer melt observed in the MIZ are also observed on a large-scale in the central Arctic. This is demonstrated using Nimbus 7 SMMR data and Arctic Ocean buoy temperature data over one annual cycle. Finally, the potential of optimally combining both active and passive microwave data in an effort to ameliorate these surface melt effects during the summer months is also explored.

1. INTRODUCTION

The importance of having a long-term passive microwave data set of known accuracy for obtaining climatologically important ice parameters on both global and regional scales is well recognized. The Nimbus 7 scanning multichannel microwave radiometer (SMMR) has provided almost 9 years of global sea ice concentrations and numerous case studies have been carried out to determine the accuracy of these concentrations primarily under winter and premelt conditions [e.g., *Martin et al.*, 1987; *Steffen and Maslanik*, 1988]. Summer sea ice concentrations are more uncertain because of the presence of moist snow, wet ice surfaces, and the collection of free water in depressions (i.e., meltponds), and of temperature-dependent variations in ice emissivity near the melt point [*Cavalieri et al.*, 1984; *Onstott et al.*, 1987].

Problems associated with the interpretation of passive microwave data during summer months were recognized early on. Areas of low microwave radiance observed during summer in the central Arctic with the Nimbus 5 electrically scanning microwave radiometer (ESMR) were interpreted as low ice concentration areas [*Gloersen et al.*, 1978; *Campbell et al.*, 1980], whereas *Crane et al.* [1982] suggested an alternative explanation in terms of melt ponding effects. This problem was revisited by *Campbell et al.* [1984], who argued that the low radiance areas are primarily due to open leads and polynyas. A first attempt at actually mapping melt pond fractional coverage using microwave data was made by *Carsey* [1985]. From lead area estimates and from Nimbus 5

ESMR brightness temperature time series, Carsey argued that the time of minimum brightness (mid-July) corresponds to maximum pond coverage, but also noted that other surface phenomena cannot be unambiguously distinguished from the ponding maximum. Clearly, these areas of low radiances observed in passive microwave data will remain ambiguous in the absence of additional information. Recently, in a study of late summer Nimbus 7 SMMR brightness temperature variations in the Canadian Basin for the period 1979–1984, *Barry and Maslanik* [1989] used Defense Meteorological Satellite Program (DMSP) optical line scanner and NOAA advanced very high resolution radiometer (AVHRR) visible imagery as their additional source of information to establish that areas of low brightness temperature and increased polarization corresponded to areas of actual reduced ice concentration in 4 of the 6 years studied.

Since passive microwave satellite observations alone cannot distinguish between the collection of meltwater on an ice surface and the water between ice floes, a means is needed to estimate the areal extent of ponding within floe boundaries. This paper explores the potential of synthetic aperture radar (SAR) to provide the additional information needed to supplement the passive microwave data in order to unambiguously discriminate between open water areas and ponded floes. Previously, high-resolution aircraft SAR data have been used to discern individual floes and to provide information concerning the state of melt pool development and its areal extent [*Burns et al.*, 1984, 1985; *Onstott and Moore*, 1984; *Holt and Digby*, 1985].

A previous study of summer ice concentrations [*Burns et al.*, 1987] utilized active and passive microwave aircraft sensors flown during the 1984 Marginal Ice Zone Experiment

(MIZEX). The passive sensors on the NASA CV-990 aircraft included an ESMR operating at 19.4 GHz and an aircraft multichannel microwave radiometer (AMMR) operating at 10.7, 18.0, 21.0, and 37.0 GHz. The fixed-beam AMMR radiometers measured both horizontally and vertically polarized radiances at all frequencies except 21 GHz. The active microwave sensor included the Environmental Research Institute of Michigan (ERIM) SAR operating at 1.2 and 9.4 GHz on the Canadian Centre for Remote Sensing (CCRS) CV-580 aircraft. A detailed description of these sensors may be found in the Burns et al. paper.

A comparison of ice concentrations derived from the single-frequency (9.4 GHz) active and single-frequency (19.0 GHz) passive microwave aircraft imagery showed that they agreed to within 13%. It was determined that the primary cause of the discrepancy was ice signature variations of the X-band SAR. The SAR image statistics for an entire scene showed little bimodality; a broad ice intensity distribution resulted from variations in surface conditions including moist or saturated snow cover and wet ice surfaces, although local areas showed good ice/water discrimination. Speckle noise was also a contributing factor. This was in contrast to the 19 GHz passive microwave imagery which showed a distinct brightness distribution with two broad peaks.

Sea ice concentrations were also obtained from coincident aerial photography. Both the SAR and AMMR ice concentrations agreed to within 13–14% of the concentrations from the aerial photographs. Concentrations from the digitized photographic imagery, also subject to various uncertainties, were treated not as "ground truth," but simply as another remotely-sensed measurement of ice concentration.

In the same study, a comparison of SAR and AMMR ice concentration measurements, which spanned a range between 45% and 56%, showed a mean difference of 3.5%. In contrast to the single-channel ESMR concentrations, the AMMR algorithm results exhibited much less variability (5.6% versus 17.5% for ESMR) which was attributed in part to the sensor's lower spatial resolution (see Table 1 of *Burns et al.* [1987]) and in part to the ability of the algorithm to accommodate variations in ice surface emissivity. The rms difference between the concentrations from the AMMR and the photography was 10.4% for three of the four areas sampled, while the rms difference between the SAR and photography was 15.8%. The SAR and AMMR gave identical results (56%) for the fourth sample, in contrast to 83% derived from the digital photographic image. Interestingly, both the photograph and the SAR image showed evidence of surface melt.

In the present study we examine in much greater detail the effect of surface melt on microwave signatures and the resulting error in the calculation of sea ice concentration. We also explore the potential of optimally combining both active and passive microwave data in an effort to ameliorate the effects of melt ponding on the calculation of ice concentration during the summer months. As in the *Burns et al.* [1987] study, we use both the active and passive microwave data sets acquired during the 1984 MIZEX aircraft flights (see Figure 1). An overview of the large-scale sea ice conditions encountered during the experiment is provided by *Campbell et al.* [1987]. Conditions in the coincident active/passive microwave aircraft data set under consideration include ice floes with dry, moist and saturated snow covers and with both heavily ponded and ridged surfaces. A related study by
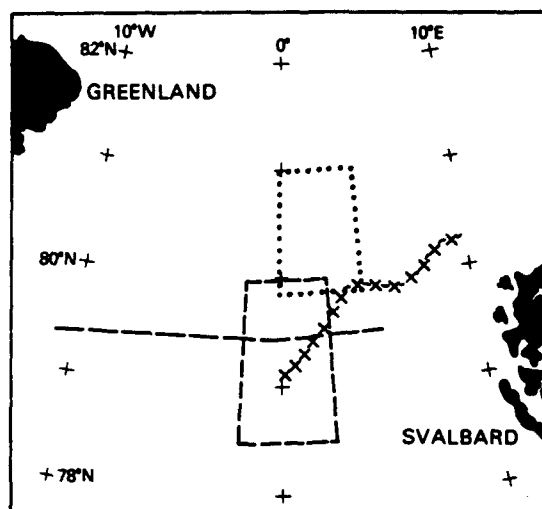
Fig. 1. Map of the Fram Strait region showing the location of the aircraft coverage used in this study. The two boxes indicate the SAR coverage on June 29 (dotted lines) and on June 30 (dashed lines). The E-W track (dashed line) gives the northern most leg of ESMR and AMMR coverage on June 30. The June 30 ice-edge position as determined from SMMR imagery is indicated by the cross-hatched line.

Gloersen and Campbell [1988] examined the influence of surface melt on the calculation of multiyear ice concentration. The emphasis in this study is on the dual-polarized, multifrequency passive microwave sensors and the single-channel SAR as these will be the types of satellite senso providing coincident or nearly coincident data in the near future.

2. MICROWAVE CALCULATION OF SEA ICE CONCENTRATION

2.1. Passive Microwave

In contrast to the simple linear ice concentration algorithm used with the 19 GHz ESMR, the AMMR sea ice algorithm uses the 18 and 37 GHz channels to calculate both total and multiyear sea ice concentration. Two ratios of radiances serve as the independent variables. These ratios are the polarization ratio PR and the spectral gradient ratio GR defined by

$$PR(f) = \frac{TBv(f) - TBh(f)}{TBv(f) + TBh(f)} \tag{1}$$

$$GR(18, 37) = \frac{TBv(37) - TBv(18)}{TBv(37) + TBv(18)} \tag{2}$$

where f is frequency (18 GHz is used in this study), and TBv and TBh are the observed microwave brightness temperatures at vertical and at horizontal polarization, respectively. The advantage of using these ratios is that they are almost orthogonal in the sense that variations in PR reflect mostly changes in ice concentration and are largely independent of ice type (first-year or multiyear), whereas variations in Gl reflect mostly changes in ice type. GR is also used to minimize weather-related effects including the microwave emission by atmospheric water vapor, cloud liquid water and wind-roughened seas which are known to result in false

indications of sea ice over open oceans [*Gloersen and Cavalieri*, 1986]. Under summer melt conditions, multiyear ice type discrimination becomes indeterminable; nevertheless, the orthogonal nature of these independent variables provides a mechanism for overcoming the effects of early melt on the calculation of total ice concentration as will be illustrated in section 4 below.

The expression for the total sea ice concentration (C) is actually a sum of the first-year (C_{FY}) and multiyear (C_{MY}) ice concentrations calculated as follows:

$$C_{FY} = \frac{F_0 + F_1 PR + F_2 GR + F_3 (PR)(GR)}{D_0 + D_1 PR + D_2 GR + D_3 (PR)(GR)} \quad (3)$$

$$C_{MY} = \frac{M_0 + M_1 PR + M_2 GR + M_3 (PR)(GR)}{D_0 + D_1 PR + D_2 GR + D_3 (PR)(GR)} \quad (4)$$

$$C = C_{FY} + C_{MY} \quad (5)$$

The algorithm is discussed in detail by *Cavalieri et al.* [1984] and further by *Gloersen and Cavalieri* [1986]. The values of the constants F_i, M_i and D_i ($i = 0$ to 3) are as follows:

$$F_0 = 2284.36 \quad F_1 = -21,403.00$$

$$F_2 = 16,003.92 \quad F_3 = 1424.94$$

$$M_0 = -561.20 \quad M_1 = 16,023.66$$

$$M_2 = -22,386.97 \quad M_3 = -38,971.83$$

$$D_0 = 1424.94 \quad D_1 = 8715.30$$

$$D_2 = -4125.98 \quad D_3 = -11,416.34$$

Note that the corresponding coefficients given in Gloersen and Cavalieri differ slightly from these due to a numerical error discovered after publication.

2.2. Active Microwave

The sea ice concentration algorithm used with the single-channel 9.4 GHz SAR data is the same as in the *Burns et al.* [1987] study, that is, a linear interpolation between the radar backscatter of open water and sea ice. As stated there this technique was adopted as an attempt to account for the ice signature variability and not because we are treating a mixed-pixel situation. In fact, because of the high resolution of the SAR, most pixels can be assumed to represent areas of 100% ice or 100% water, and mixed pixels covering both surface types are expected only at the ice/water boundaries. Here location at a boundary, the finite time-response of the sensor, and the smoothing effect of digital post-processing (geometric rectification and speckle reduction) all contribute to this situation which is clearly most frequent in the marginal ice zone. Even for SARs with ERS-1 resolution, this mixed-pixel situation would be minimal in pack ice areas.

The linear expression for sea ice concentration $C(I)$ is:

$$C(I) = (I - I_W)/I_I - I_W) \quad (6)$$

where I is the backscatter intensity for a given pixel, and I_I and I_W are the mean values of sea ice and of open water intensities, respectively, with $I_I > I_W$. Conditions other than those encountered during the summer MIZEX can result in
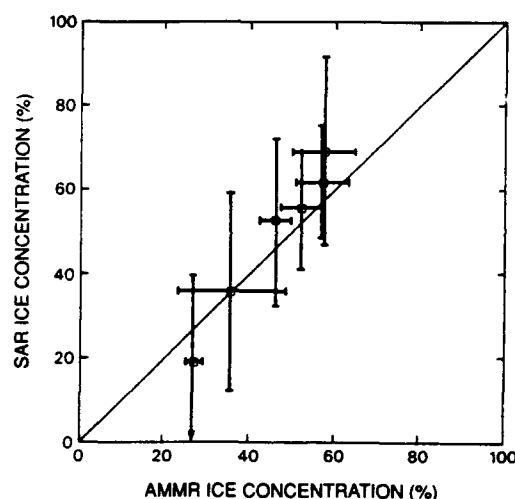
Fig. 2. Comparison of Greenland Sea MIZ ice concentrations derived using X-band SAR and AMMR measurements for six areas. The vertical and horizontal lines represent the standard deviation of the SAR and AMMR measurements respectively.

signature ambiguities that would lead to errors in ice concentration using this algorithm. One example is the presence of grease ice (soupy layer of coagulated ice crystals on the water surface) which has a signature similar to calm open water [*Gray et al.*, 1982]. Another is wind-roughened water which at low-incidence angles can appear brighter than the surrounding ice [*Askne and Ulander*, 1989]. In these cases, information in addition to image intensity must be used to obtain concentration estimates.

This algorithm was applied on a pixel-by-pixel basis to the 9.4 GHz SAR data which had been radiometrically rectified (although not calibrated) to remove intensity variations dependent on radar range. Only the 9.4 GHz data were used because of the more uniform ice signature at this frequency versus the 1.2 GHz data (see below). Further discussion of the algorithm is given by *Burns et al.* [1985, 1987].

2.3. Comparison

Six areas each of 6 km^2 in size were identified as having coincident SAR and AMMR coverage. The observations from these sensors were registered using both the NASA CV-990 and the Canadian CV-580 aerial photography. For each area, mean concentration values and their standard deviations were calculated from the SAR and AMMR data and are shown in Figure 2. The calculated ice concentrations for these six areas range from approximately 20% to approximately 70%. Examination of the figure shows that the SAR concentration estimates are on average 3.8% higher than the AMMR estimates and have an intrascene variability approximately three times greater. Similar results were obtained in the previous study by *Burns et al.* [1987, Table 6] which showed for four samples a mean difference of 3.5% between SAR and AMMR estimates. The lower AMMR measurements may be attributable in part to the lower resolution of the AMMR sensor through contamination by peripheral areas of open water seen by the wings of the relatively wide antenna pattern of the sensor itself. The large difference in the magnitude of the standard deviations results from the greater variability of the SAR ice signatures, from the ability

of the AMMR algorithm to accommodate some of the passive microwave signature variability, and to some degree from the higher spatial resolution of the SAR.

3. MICROWAVE SIGNATURES OF MELT EFFECTS

In this section we review briefly the characteristics of microwave sea ice signatures observed during the 1984 MIZEX and then show using Nimbus 7 SMMR data and Arctic Ocean buoy temperatures that the progression of summer melt observed in the MIZ is also observed in the central Arctic.

The snow and sea ice conditions and associated microwave signatures during the 1984 MIZEX have been discussed previously by *Onstott et al.* [1987]. They observed that during the experiment the sea ice and its snow cover underwent a transition from late spring to summer when air temperatures were within 2°C of the freezing point. As the air temperature increases, the snow cover becomes progressively moist, until in early summer it has become thoroughly moistened and free water percolates to the snow/ice interface where it collects to form subsurface pools. As the season progresses, surface melt ponds form and at about midsummer begin to drain.

Because of the considerable difference in the microwave emissivities of water and ice, the effect of this evolution of surface conditions on the microwave emission is a deviation from the winter signatures in proportion to the amount of free water present. As the liquid water content of the snow cover increases from 0 to 0.5%, the penetration depth will decrease by more than an order of magnitude [*Ulaby et al.*, 1982]. During winter when the snow cover is dry and the underlying sea ice is cold, the microwave emission for first-year ice is almost independent of frequency, while multiyear ice emission decreases with increasing frequency [e.g., *Cavalieri et al.*, 1984]. With the snow cover becoming moist in late spring, the multiyear ice signature becomes indistinguishable from that of first-year ice [e.g., *Comiso*, 1983]. In some instances during the early stages of summer melt, the radiometric brightness temperature of multiyear ice becomes greater than that of first-year ice [*Grenfell and Lohanick*, 1985]. Because this increase of free water is neither temporally or spatially uniform during this time of year, the overall distribution of multiyear pack ice may look quite different than during midwinter. As the snow cover becomes progressively wet, the microwave signatures become progressively less variable. This is because the average microwave emission is determined by conditions within the frequency dependent penetration depth, which in this period corresponds to a layer of moist snow with an emissivity close to unity. Thus the microwave emission is high at all frequencies and resembles that of winter first-year ice, making the differentiation of ice type indiscriminate [*Cavalieri et al.*, 1984; *Onstott et al.*, 1987]. Beginning about midsummer as surface melt ponds form and drain, the microwave emissivity becomes extremely variable reflecting the great spatial variability of surface conditions. In late summer and early fall the ice types once again become radiometrically distinguishable and their signatures approach their winter values.

Ice type discrimination is also lost during the first half of summer in the radar signature because the backscattering process is dominated by surface scattering and/or absorption
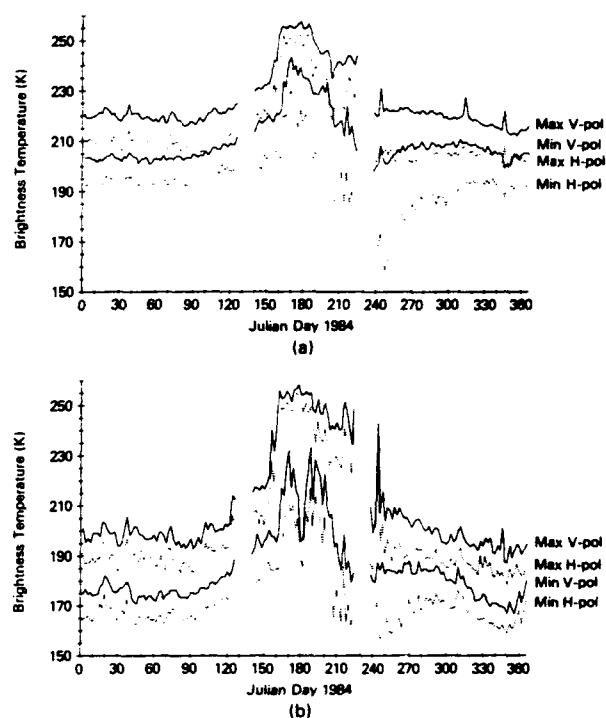
Fig. 3. Maximum and minimum (a) 18 GHz H and V and (b) 37 GHz H and V SMMR brightness temperatures for a 600×600 km^2 region north of the Canadian archipelago for 1984.

in the moist snow pack resulting in a loss of ice typ. classification [*Livingstone et al.*, 1987a, b]. Large intensity variability is still present, though, due to different degrees of surface wetness and amounts of snow cover. By early to midsummer the snowpack has experienced considerable melt and depressions in the ice or ice with a lower freeboard will have collected varying quantities of meltwater. Fully open water meltpools will appear as extremely low return areas at both 1.2 and 9.4 GHz. In areas where melt pools are still forming and the snow has been transformed into mixtures of snow, ice, and water, very strong returns are produced in the SAR imagery. For areas of thick snow, weak returns are produced at both frequencies, and the ice surface topography is well masked. As the frequency decreases, the contrast between areas with heavy and thin snow cover increases. In areas where melting has produced both a thin snow cover and small-scale surface roughness (of the order of 1–3 cm for first-year ice), enhanced returns are produced, especially at 1.2 GHz. Thus in late summer, as the ice surface is exposed and surface melt ponds drain, the radar backscatter, as well as the microwave emission, again reflects ice type differences.

This progression of surface melt conditions observed in the MIZ by *Onstott et al.* [1987] is also observed on a larger scale in the central Arctic. The change in the minimum and maximum sea ice brightness temperatures from the Nimbus 7 SMMR 18 and 37 GHz horizontal and vertical polarization channels over one annual cycle is illustrated in Figures 3 and 3b for a 600×600 km^2 area in the central Arctic north of the Canadian archipelago. From an examination of Figure 3 we observe that the discrimination between the 18 and 37 GHz radiances throughout winter and early spring is well defined. The actual difference between the two signatures is
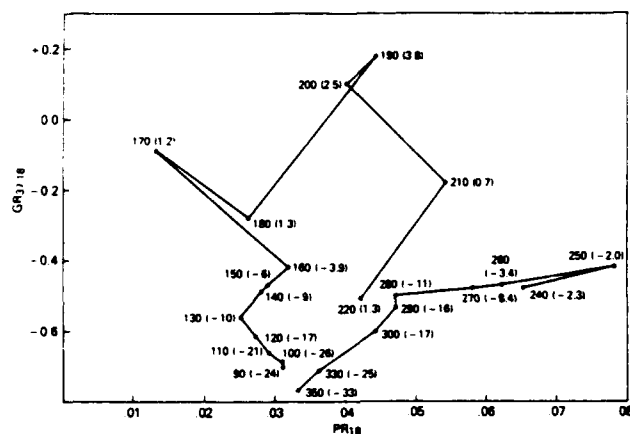
Fig. 4. Average values of GR and PR plotted every 10th day in 1984 from Julian day 90 through Julian day 350 together with corresponding Arctic Ocean buoy temperatures shown in parenthesis for the same Arctic region as for Figure 3.

a measure of the relative amounts of first-year and multiyear sea ice. This spectral difference, measured in terms of the spectral gradient ratio defined by (2), is used to obtain ice type concentrations. Beginning about Julian day (JD) 100 (April 9), all the brightness temperatures begin to increase as a result of the general seasonal warming. On or about JD 170 (June 18) there is a very sharp increase in the temperatures indicating the onset of summer melt. During summer the well-defined discrimination between the 18 and 37 GHz channels is lost as is the corresponding ice type information. Starting about JD 270 (September 26) the signatures begin to diverge and assume their characteristic winter values.

The average PR and GR values for this same central Arctic region are plotted every 10 days in 1984 from JD 90 through JD 350 and are shown in Figure 4. The gap between JD 220 and JD 240 is due to missing data. Each point also has associated with it a temperature shown in parentheses obtained from Arctic Ocean buoys 3835 and 3849 located within the 600 × 600 km² region. Although the reported temperatures [Colony and Munoz, 1986] are from a sensor within the buoy, they are believed to be within a few degrees of the ambient air temperature [Martin and Clarke, 1978]. From March (JD 90) through May (JD 150) the temperatures are well below freezing, but by mid-June the temperatures reach the freezing point and the PR and GR values approach zero (JD 170). This is consistent with the sequence of events described earlier whereby at some time in early to midsummer there is a period when the snow cover becomes very nearly a perfect blackbody emitter. Interestingly, in a related study of SMMR brightness temperature data and Arctic Ocean buoy temperature data for the summers of 1979 through 1982, Maslanik and Barry [1989] find that the rapid increase in brightness temperature typically occurs around June 20 (JD 171) which is within a day of what is shown in Figure 4. By June 28 (JD 180) the PR value has increased to wintertime values, but GR is appreciably greater indicating a loss of ice type information. Because polarization information remains largely intact, but with larger uncertainties, we can still derive useful total ice concentration information. From JD 180 until mid-September (JD 260) there is considerable variability in both PR and GR indicating a complicated mix of surface conditions including wet snow, surface

melt ponding, and open water. From September to mid-December the temperature decreases and the PRs and GRs return to their wintertime values.

4. EFFECTS OF SUMMER MELT ON CONCENTRATION CALCULATIONS

We now examine the microwave signatures of three ice floes which illustrate the progression of summer melt from early spring to late summer for the purpose of understanding the effect that these characteristics have on the calculated ice concentrations. These floes were identified with the aid of the NASA CV-990 aerial photograph record for the June 30 flight and are shown in Figure 5. The three images were taken with a KS87-B metric camera from an altitude of 33,000 feet and each frame has a field-of-view of approximately 10 km along the direction of flight (right to left). The across-track (up and down) distortion results from the camera looking off to the right of nadir at an angle of 45°.

The first floe, floe A, appears to the right of center in Figure 5a and is a composite floe made up of primarily multiyear ice. Cloud shadows are visible against the bright snow cover on the floe. The location of this floe was over 200 km west of the main ice edge (see Figure 1) where the local environmental conditions were closer to winter than summer. The CV-990 infrared radiometer (PRT-5) measurements gave surface water temperatures of −1.6°C to −2.1°C. There were also visual sightings of grease ice formation between floes [Gloersen et al., 1985], another indication of cold surface conditions. From an examination of an enlarged Figure 5a there appears to be a heavy snow cover and considerable ridging. From a survey of the physical properties of the ice in the experiment region during June and July, Tucker et al. [1987] found that of the 40 floes sampled, 27 were identified as multiyear, 9 as first-year, and 4 as composite floes of first-year and multiyear ice. Their measurements of snow depth revealed that multiyear floes had a significantly deeper snow cover averaging 28.5 cm as compared with first-year ice, which had an average cover of only 8 cm.

The second floe, floe B, is a large floe made up of smaller multiyear floes cemented together (Figure 5b). There are also some thin first-year ice areas, the areas that are grey in appearance. This floe was observed from the aircraft, and a few melt areas were reported to be visible [Gloersen et al., 1985]. An examination of the image shows that there is some evidence of melt ponds beginning to form in the right of center of the floe. The floe was located approximately 100 km west of the ice edge. Ships in the general vicinity reported surface air temperatures hovering around 0°C.

The third floe, floe C, is another large composite floe similar to floe B but shows a more advanced stage of melt as indicated by the small dark grey areas which are more or less evenly distributed across the floe (Figure 5c). This floe was located just inside the ice edge and an icebreaker located just west of the floe well within the pack ice reported surface air temperatures just above freezing.

Floe C was the only one of the three floes which was imaged coincidently by the active and passive sensors on June 30. In Figure 6 we show the 1.2 GHz and the 9.4 GHz SAR images which include a portion of this large floe. Observed differences result from the distortion produced by the side-looking camera on the CV-990 and the side-looking
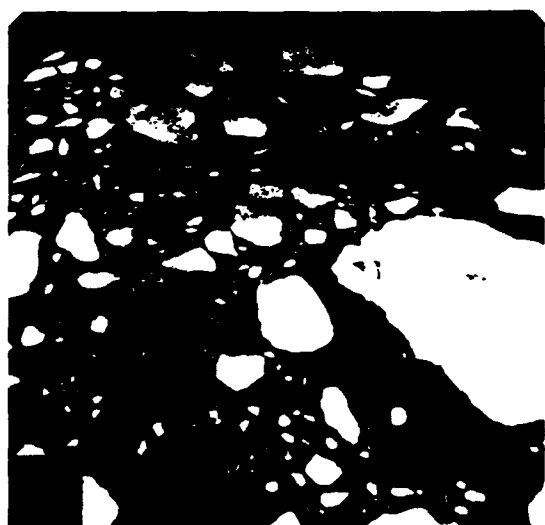
(a)
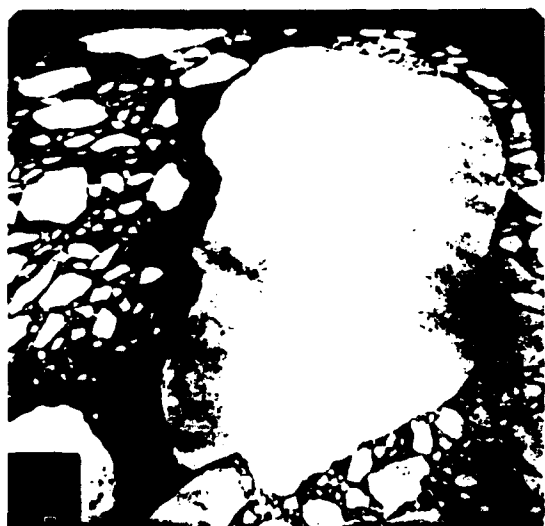
(b)

(c)

Fig. 5. NASA Convair-990 aerial photographs of floes (a) A, (b) B, and (c) C.

radar, and from actual ice motion during the time between the two aircraft overflights. Comparison with the aerial photography (Figure 5c) shows that the 1.2 GHz image most closely reflects the floe structure seen in the photograph. the areas of young ice or advanced melt areas appear brighter than the surrounding areas. which with a thick and moist snow cover produce a weaker backscatter. Some of these areas also produced strong returns in the 9.4 GHz data, but, in general, at this frequency the floe interior was more uniform in appearance than at 1.2 GHz due to the absorptivity of the moist snow cover. This image illustrates both the lower sensitivity of the 9.4 GHz data to variations in surface conditions as observed during early to midsummer throughout the MIZ, and the large intensity variability of floes in the ice field at this time.

PR and GR values calculated from the AMMR measured radiances on June 30 for the three floes shown in Figure 5 are plotted in Figure 7. The clusters of measurements corresponding to these floes are labeled "A," "B," and "C." The PR and GR values corresponding to the multichannel SMMR algorithm constants for open water (OW), first-year (FY), and multiyear (MY) sea ice are also plotted for reference and are indicated by open squares.

The cluster of points labeled A have PR and GR values typical of consolidated midwinter MY ice. The two observations of floe B have microwave signatures close to first-year ice and correspond to a concentration of about 90%. Factors which may have contributed to the less than 100% concentration include wet snow cover, ponding, and contamination from adjacent open water areas by the low resolution field of view of the aircraft radiometer. The degree to which we can attribute the relative position of the B cluster along the FY-MY line to actual ice type or surface wetness is uncertain, but the key point is that the wetness that is observed has not affected the computation of the concentration by more than 10%. The cluster of points labeled "C" corresponds to a calculated concentration of between 60% and 65%, which is considerably less than 100%. The low calculated concentration is attributed to the wet ice surfaces, the numerous open water melt ponds, and to areas of snow-ice-water mixtures.

Image statistics derived from the 9.4 GHz SAR image data for Figure 6 are shown in Figure 8. Here mean backscatter amplitude is plotted versus standard deviation for 60 × 60 m subimages of floe C and adjacent ice and water areas. This plot demonstrates the two main sources of error in the single channel SAR ice concentration algorithm. First, the ice exhibits a much greater signature variability than the water as seen from the greater scatter in the mean values in Figure 8. For these data the standard deviation of the ice means is approximately one third of the difference between the mean ice intensity (I_I) and the mean water intensity (I_W) used as tie points in the algorithm (section 2.2). By assuming that the distribution of ice signatures is Gaussian about the mean value, it can be shown that the error in the calculated concentration is directly proportional to the ratio of the standard deviation of the ice signatures to the difference between ice and water mean intensities. Using the values from Figure 8, this predicts underestimates of about 2% for 10% concentration and almost 20% for 100% concentration. This effect is seen in Figure 9a where estimates over floe C fall between 75% and 85%.

The second source of error, also illustrated in Figure 8, is
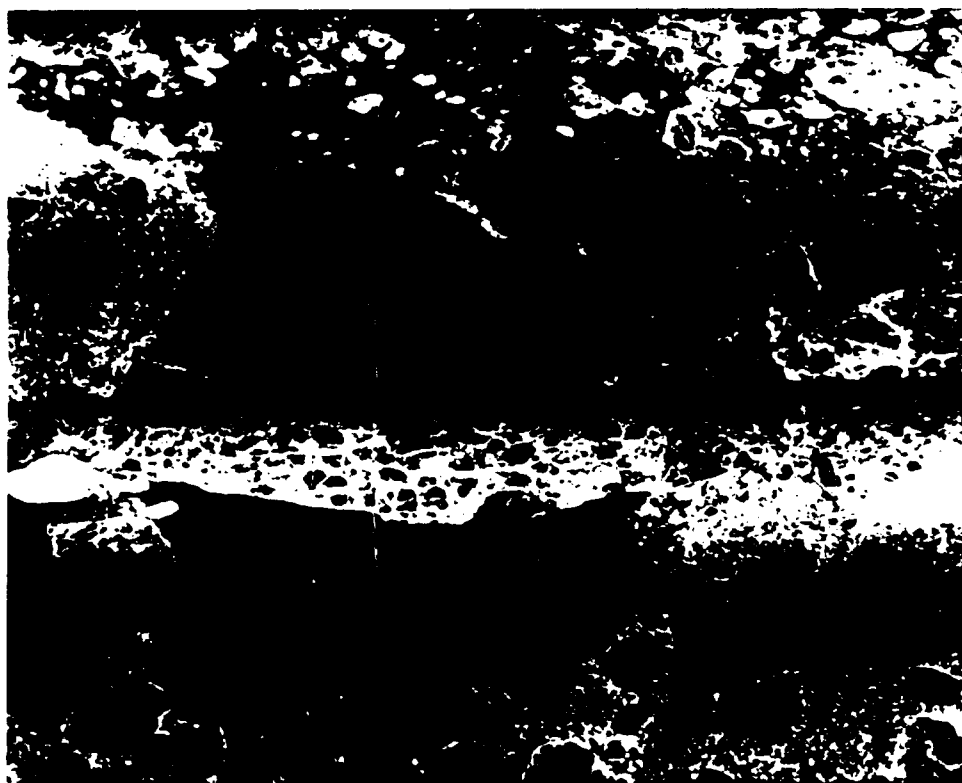
(A)
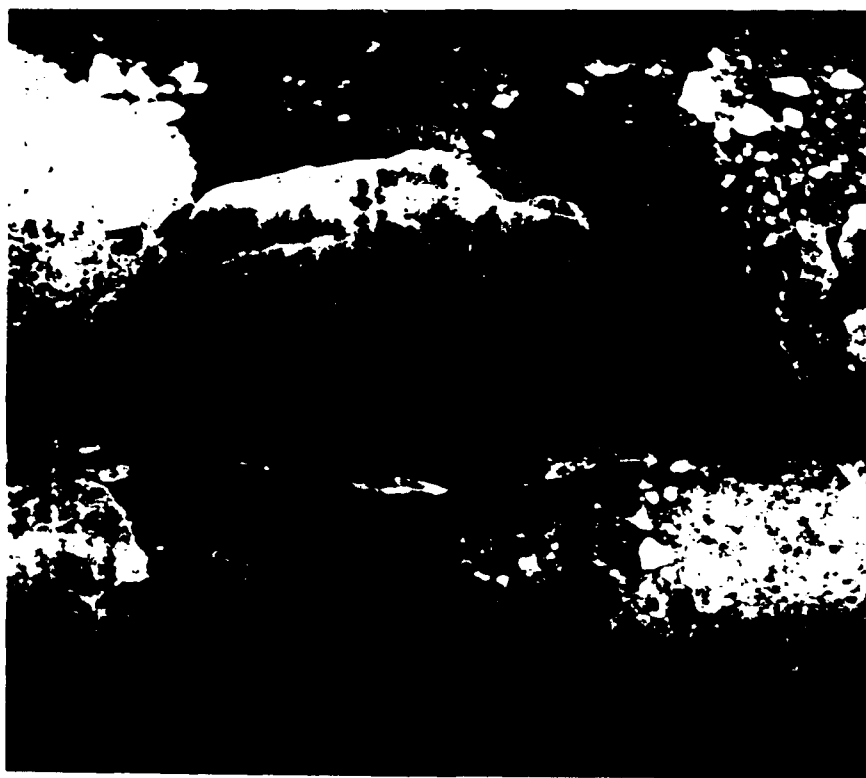
(B)

Fig. 6. SAR imagery of floe C obtained on 30 June for (a) 1.2 GHz (23 cm) and (b) 9.4 GHz (3.2 cm)
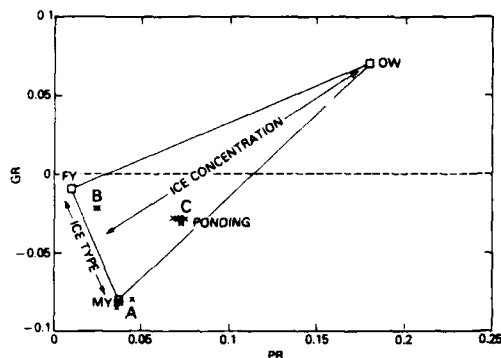
Fig. 7. GR versus PR plot for 30 June, 1984, showing clusters of measurements corresponding to floes A, B, and C shown in Figure 5.

(a)

(b)

Fig. 9. Mean concentration estimates for 900 × 300 m areas across floe C and open water calculated using two SAR techniques: (a) linear interpolation and (b) neighborhood classification.

that the standard deviation for the water signatures is much smaller than for the ice. This is due to the speckle noise inherent in the SAR imaging process which introduces a variance equal to the square of the mean divided by N, where N is the number of "looks" [Burns and Lyzenga, 1984]. In addition, the standard deviation of pixel values within ice subimages, induced mainly by speckle, is greater than that of the mean backscatter values for all the subimages. Because this algorithm calculates concentration on a pixel-by-pixel basis, it effectively resolves the speckle noise which thereby contributes directly to the large uncertainty in the concentration estimates (Figure 2).

There are two main implications of this analysis of the errors in the SAR algorithm: (1) pixel-by-pixel evaluation of concentration is not suitable for these high-resolution data and (2) specification of an ice tie point is not appropriate given the large signature variability. The linear interpolation algorithm, applied on a pixel-by-pixel basis, cannot therefore adequately account for this variability, as seen from the results. Simple thresholding on a pixel-by-pixel basis, al-

though more appropriate to the high-resolution case, also results in misclassification of ice as water again because of the large ice signature variability aggravated by speckle noise.   .ov

A better method that would avoid resolving the variability residual and still take advantage of the relatively high SAR resolution would be to evaluate concentration on a neighborhood basis using an intensity decision rule based on the water mean intensity value alone. Such a scheme has been used to calculate ice concentration over a portion of the floe C area. Using a 10 × 10 pixel (30 × 30 m) neighborhood and an intensity threshold equal to the water mean plus one standard deviation, each neighborhood is classified either as ice or as water on the basis of the majority of pixels having intensity values above or below the threshold, respectively. Once ice and water are detected in this way, concentration estimates at any spatial scale greater than the size of the neighborhood can be obtained. The results for the floe C area are shown in Figure 9b and indicate the significant improvement over the linear interpolation method. Although this algorithm needs to be tested on more data sets with a range of concentration and seasonal conditions, it clearly has potential for providing relatively accurate SAR estimates over consolidated ice areas under melt conditions where AMMR estimates are poorest.

5. POTENTIAL SOLUTION

A possible solution to the problem of reduced passive microwave concentrations due to surface melt effects may be obtained through the use of SAR imagery to estimate floe areas that are comprised of moist snow and areas of snow ue ice-water mixtures. In this section our working hypothesis for will be that the interior floc surface conditions may be acquired using 9.4 GHz SAR. If this hypothesis is valid, it may be possible to obtain, at least in a statistical sense, a measure of the ice surface area in a given region which is

Fig. 8. SAR X-band (3.2 cm) image statistics for floe C area based on 60 × 60 m sample area.

X-Band SAR

L-Band SAR

Aerial Photograph
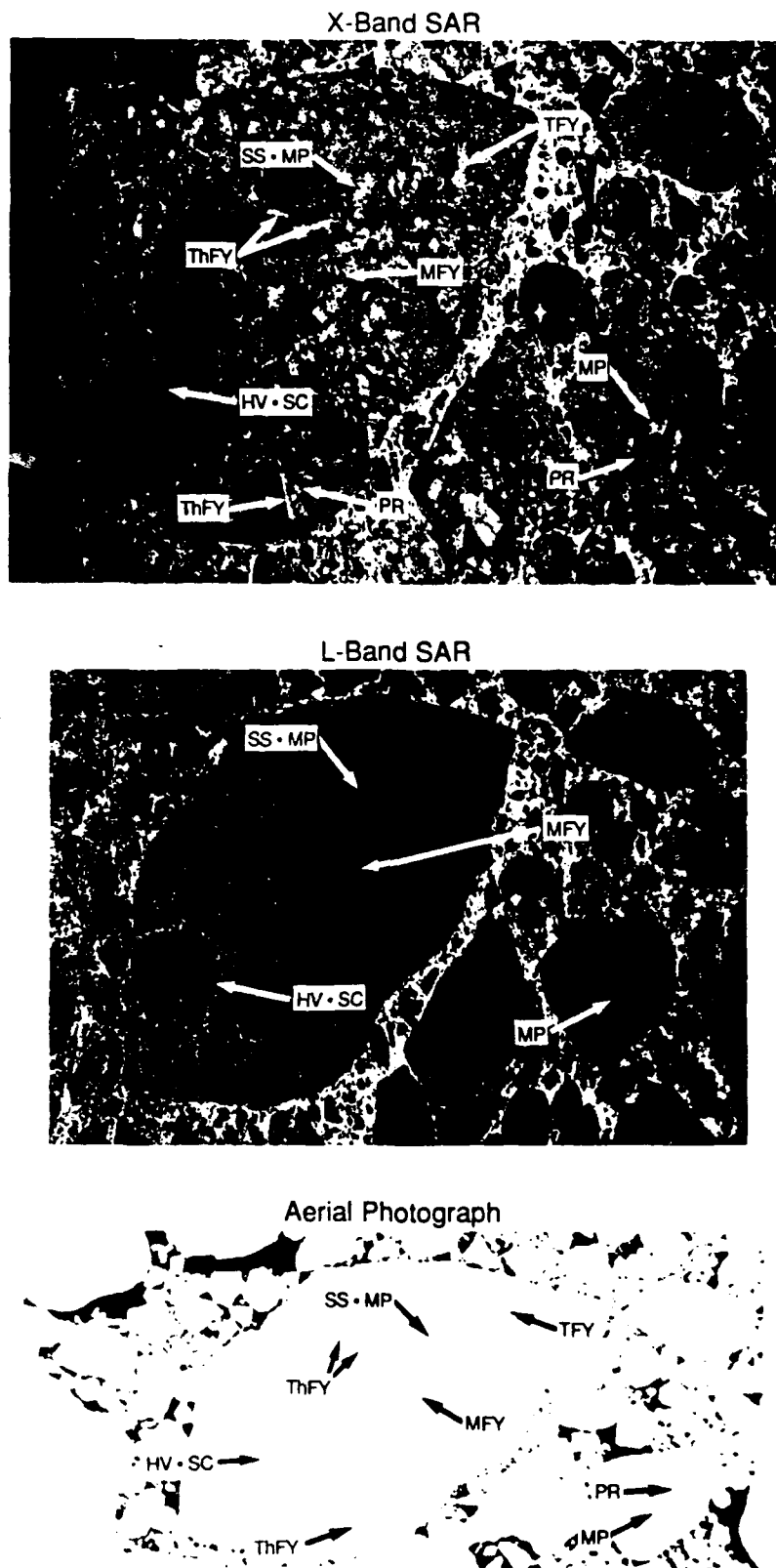
Fig. 10. Annotated ice floe imagery obtained on 29 June, 1984, with the ERIM X-band (9.4 GHz) and L-band (1.2 GHz) SAR and the CCRS aerial camera on the CV-580. Surface features include snow-covered ice (SCI); heavy-snow covered ice (HV.SC); thick (TFY), medium (MFY), and thin (ThFY) first-year ice; pressure ridges (PR); subsurface melt ponds (SS.MP); and melt ponds (MP).

ponded or sufficiently wetted to adversely affect the passive microwave ice concentrations.

To test this hypothesis, we examine a flow which was surveyed at the surface and imaged with the CV-580 SAR on June 29, 1984. Unfortunately, the poor image contrast and low signal-to-noise ratio of the floe C SAR image (Figure 6), prevented its use for testing this hypothesis. The 9.4 GHz (X-band) and 1.2 GHz (L-band) SAR images and an aerial photograph of the June 29 floe are shown in Figure 10 together with annotations of surface features. Areas identified include thick (TFY), medium (MFY), and thin (ThFY) first-year ice areas, heavy-snow covered ice (HV.SC), pressure ridges (PR), subsurface melt ponds (SS.MP) and melt ponds (MP). The snow-ice-water mixtures cover a considerable portion of the surface of this floe and also produce emission more similar to water than to ice. The procedure for testing this hypothesis is as follows. The surface areas of the floe were divided into two categories: mixed regions of snow-ice-water and areas of moist snow. SAR backscatter intensity thresholds were defined to separate the returns from these two types of areas. Their means are separated by 4 dB. With this technique it was determined that 70% of the floe area was snow-covered ice (SCI) and 30% was melt ponds (SS.MP and MP).

These results suggest that SAR can be used to estimate the fraction of developing meltpools which also cause the passive microwave sensor to measure a microwave signature more like water than like ice. An approach that may be developed would use the high-resolution capability of SAR first, to identify a statistically significant number of floes in a given region; second, to determine the state of melt pool development (i.e., to determine the period when the passive microwave sensor is sensing a water signature for the meltpools); and finally, to determine the areal extent of melt pools on the floes for that region. For example, if the results of the analysis for the floe imaged on June 29 were applicable to floe C, we could increment by 30% the ice concentration as determined by the passive microwave measurements (see Figure 7). This correction would bring the floe C concentration up to 90–95%, similar to the value obtained for floe B. Since this approach is believed to be independent of regional characteristics, developing a grid system across the Arctic Basin for which SAR melt-ponding statistics are obtained, areal ponding estimates for each grid may be used to adjust the synoptic passive microwave estimates of ice concentration.

6. SUMMARY

This paper describes the effects of summer melt on both active and passive microwave signatures of sea ice and on the calculation of sea ice concentrations. The progression of surface melt from late spring to midsummer in the central Arctic is observed to follow that in the MIZ and as such may contribute significantly to the uncertainty in the calculated sea ice concentrations from passive microwave satellite observations. We have demonstrated the advantage of utilizing both polarization and spectral gradient information from multichannel microwave sensors for calculating sea ice concentrations under conditions of surface melt. We have found that by using ratios of radiances, early changes in the free water content of the snow cover can be accommodated by the multichannel algorithm to the extent that variations in

the free water content alter the spectral gradient ratio and thus appear as variations in the relative proportion of "first year" and "multiyear" ice types. Under conditions of substantial surface ponding the polarization information will change significantly and the algorithm will underestimate the ice concentration.

With respect to the active sensors, we have shown that the large ice signature variability in the SAR data is responsible for the underestimates produced with the single-channel linear algorithm, and that the large estimate variances result from the algorithm being applied on a pixel-by-pixel basis. To avoid resolving the signature variability, a neighborhood segmentation algorithm was suggested and used on a ponded floe to demonstrate the potential for improved SAR concentration estimates during surface melt conditions. We have further demonstrated using high-resolution aircraft data that high-resolution SAR imagery can be used to obtain an areal measure of the degree to which individual floes have wetted surfaces and open melt ponds. This suggests that a combined active-passive microwave system of sensors may provide a means for improving the accuracy of the ice concentration determinations during the summer melt period through the development of a "microwave surface melt climatology" for different regions.

REFERENCES

Askne, J., and L. Ulander. Azimuth depend ce in SAR-imaging of open water leads in ice infested ar es. Proceedings of IGARSS'89. 12th Canadian Symposium on Remote Sensing. *IEEE 89CH2768-0*, Inst. of Elec. and Electron. Eng., New York, 1989.

Barry, R. G., and J. Maslanik, Arctic sea ice characteristics and associated atmosphere-ice interactions in summer inferred from SMMR data and drifting buoys: 1979–1984. *GeoJournal. 18*(1). 35–44, 1989.

Burns, B. A., and D. R. Lyzenga, Textural analysis as a SAR classification tool, *Electromagnetics. 4*, 309–322, 1984.

Burns, B. A., R. A. Shuchman, P. L. Jackson, J. D. Lyden, and C. E. Livingstone, SAR measurement of sea ice properties during MIZEX 1983. *Eur. Space Agency Spec. Publ., ESA SP 215*, 347–351, 1984.

Burns, B. A., R. R. Jentz, C. G. Caruthers, J. D. Lyden, and P. L. Jackson, Computer assisted techniques for geophysical analysis of SAR sea ice imagery, in *Proceedings of the Nineteenth International Symposium on Remote Sensing of the Environment*, pp. 947–959. Environmental Research Institute of Michigan, Ann Arbor, 1985.

Burns, B. A., D. J. Cavalieri, M. R. Keller, W. J. Campbell, T. C. Grenfell, G. A. Maykut, and P. Gloersen. Multisensor comparison of ice concentration estimates in the marginal ice zone. *J. Geophys. Res., 92*, 6843–6856, 1987.

Campbell, W. J., R. O. Ramseier, H. J. Zwally, and P. Gloersen. Arctic sea-ice variations from time-lapse passive microwave imagery, *Boundary Layer Meteorol., 13*, 99–106, 1980.

Campbell, W. J., P. Gloersen, and H. J. Zwally, Aspects of Arctic sea ice observable by sequential passive microwave observations from the Nimbus 5 satellite, in *Arctic Technology and Policy*,

Proceedings of the Second Annual MIT Sea Grant College Program Lecture and Seminar, edited by I. Dyer and C. Chrysostomidis, pp. 197–222, Hemisphere, New York, 1984.

Campbell, W. J., P. Gloersen, E. G. Josberger, O. M. Johannessen, P. S. Guest, N. Mognard, R. Shuchman, B. A. Burns, N. Lannelongue, and K. L. Davidson, Variations of mesoscale and large-scale sea ice morphology in the 1984 Marginal Ice Zone Experiment as observed by microwave remote sensing, *J. Geophys. Res.*, *92*, 6805–6824, 1987.

Carsey, F. D., Summer Arctic sea ice character from satellite microwave data, *J. Geophys. Res.*, *90*, 5015–5034, 1985.

Cavalieri, D. J., P. Gloersen, and W. J. Campbell, Determination of sea ice parameters with the Nimbus 7 SMMR, *J. Geophys. Res.*, *89*, 5355–5369, 1984.

Colony, R., and E. A. Munoz, Arctic Ocean Buoy Program, data report, Polar Sci. Center, Appl. Phys. Lab., Univ. of Wash., Seattle, 1986.

Comiso, J. C., Sea ice effective microwave emissivities from satellite passive microwave and infrared observations, *J. Geophys. Res.*, *88*, 7686–7704, 1983.

Crane, R. G., R. G. Barry, and H. J. Zwally, Analysis of atmosphere–sea ice interactions in the Arctic Basin using ESMR microwave data, *Int. J. Remote Sens.*, *3*, 259–276, 1982.

Gloersen, P., and W. J. Campbell, Satellite and aircraft passive microwave observations during the marginal ice zone experiment in 1984, *J. Geophys. Res.*, *93*, 6837–6846, 1988.

Gloersen, P., and D. J. Cavalieri, Reduction of weather effects in the calculation of sea ice concentration from microwave radiances, *J. Geophys. Res.*, *91*, 3913–3919, 1986.

Gloersen, P., Zwally, H. J., A. T. C. Chang, D. K. Hall, W. J. Campbell, and R. O. Ramseier, Time-dependence of sea ice concentration and multiyear ice fraction in the Arctic Basin, *Boundary Layer Meteorol.*, *13*, 339–360, 1978.

Gloersen, P., E. Mollo-Christensen, T. Wilheit, T. Dod, R. Kutz, and W. J. Campbell, MIZEX '84 NASA CV-990 flight report, *NASA Tech. Memo.*, *86216*, 149 pp., May 1985.

Gray, A. L., R. K. Hawkins, C. E. Livingstone, L. Drapier-Arsenault, and W. M. Johnstone, Simultaneous scatterometer and radiometer measurements of sea ice microwave signatures, *IEEE J. Oceanic Eng.*, *OE-7*(1), 20–33, 1982.

Grenfell, T. C., and A. W. Lohanick, Temporal variations of the microwave signatures of sea ice during the late spring and early summer near Mould Bay NWT, *J. Geophys. Res.*, *90*, 5063–5074, 1985.

Holt, B., and S. A. Digby, Processes and imagery of first-year fast sea ice during the melt season, *J. Geophys. Res.*, *90*, 5045–5062, 1985.

Livingstone, C. E., K. P. Singh, L. Drapier-Arsenault, and A. L. Gray, Seasonal and regional variations of active/passive microwave signatures of sea ice, *IEEE Trans. Geosci. Remote Sens.*, *GE-25*, 159–173, 1987a.

Livingstone, C. E., R. G. Onstott, L. Drapier-Arsenault, A. L. Gray, and K. P. Singh, Microwave sea-ice signatures near the onset of melt, *IEEE Trans. Geosci. Remote Sens.*, *GE-25*, 174–187, 1987b.

Martin, P. C., and M. Clarke, A test of barometric pressure and temperature measurements from ADRAMS buoys, *AIDJEX Bull.*, *40*, pp. 61–82, Univ. of Wash., Seattle, 1978.

Martin, S., B. Holt, D. J. Cavalieri, and V. Squire, Shuttle imaging radar B (SIR-B) Weddell Sea ice observations: A comparison of SIR-B and scanning multichannel microwave radiometer ice concentrations, *J. Geophys. Res.*, *92*, 7173–7179, 1987.

Maslanik, J., and R. G. Barry, Short-term interactions between atmospheric synoptic conditions and sea-ice behavior in the Arctic, *Ann. Glaciol.*, *12*, 113–117, 1989.

Onstott, R. G., and R. K. Moore, Active microwave measurements of sea ice in the marginal ice zone under summer conditions, *Eur. Space Agency Spec. Publ.*, *ESA SP 215*, 359–363, 1984.

Onstott, R. G., T. C. Grenfell, C. Matzler, C. A. Luther, and E. A. Svendsen, Evolution of microwave sea ice signatures during early summer and midsummer in the marginal ice zone, *J. Geophys. Res.*, *92*, 6825–6835, 1987.

Steffen, K., and J. A. Maslanik, Comparison of Nimbus 7 scanning multichannel microwave radiometer radiance and derived sea ice concentrations with Landsat imagery for the North Water area of Baffin Bay, *J. Geophys. Res.*, *93*, 10,769–10,781, 1988.

Tucker, W. B. III, A. J. Gow, and W. F. Weeks, Physical properties of summer sea ice in Fram Strait, *J. Geophys. Res.*, *92*, 6787–6803, 1987.

Ulaby, F. T., R. K. Moore, A. K. Fung, *Microwave Remote Sensing Active and Passive*, vol. 2, Addison-Wesley, Reading, Mass., 1982.

B. A. Burns and R. G. Onstott, Radar Science Laboratory, Environmental Research Institute of Michigan, Ann Arbor, MI 48107.

D. J. Cavalieri, Laboratory for Oceans, NASA Goddard Space Flight Center, Greenbelt, MD 20771.

Radar backscatter measurements over saline ice

S. GOGINENI, R. K. MOORE and Q. WANG

Radar Systems and Remote Sensing Laboratory,
University of Kansas Center for Research, Inc.,
2291 Irving Hill Road, Lawrence, Kansas 66045-2969, U.S.A.

A. GOW

U.S. Army Cold Regions Research and Engineering Laboratory,
72 Lyme Road, Hanover, New Hampshire 03755-1290, U.S.A.

and R. G. ONSTOTT

Environmental Institute of Michigan, Radar Division,
P.O. Box 8618, Ann Arbor, Michigan 48107, U.S.A.

Abstract. During the 1984 and 1985 winter seasons, radar backscatter measurements were performed on artificial sea ice at the U.S. Army Cold Regions Research and Engineering Laboratory (CRREL) at Hanover, New Hampshire. Radar data were collected at selected frequencies in the 4–17 GHz region for incidence angles from 0 to 60° with like and cross polarizations. These measurements were performed on smooth, rough, bare and snow-covered saline ice and open water. Backscattering from ice increased with its thickness until the ice was about 1 cm thick and then decreased gradually with further growth. Rough ice and snow-covered ice gave similar returns at 13·6 GHz, but the scattering coefficients of snow-covered ice were lower than that of rough ice at 9·6 GHz. Depolarized scattering from smooth, thin ice and water were much lower than from rough ice and snow-covered ice.

1. Introduction

Polar regions are covered with sea ice of variable extent and thickness. Information on the ice cover is important in the study of global climate and has operational applications in activities connected with off-shore resource exploitation and transportation in ice-covered waters. Sensors operating in the visible and infrared parts of the electromagnetic spectrum are of limited use in monitoring the polar regions. Since these areas are completely dark during mid-winter and are cloud covered in the summer season, sensors operating in the lower microwave region are required to provide all weather and day/night coverage. Several Earth observation satellites carrying microwave systems are scheduled to be launched during the 1990s. Monitoring of polar regions is among the stated objectives of these missions.

Radar was used to map sea ice as early as 1962 (Anderson 1966). Since then several experimental investigations have been carried out to determine the utility of radars in scientific and operational monitoring, and to determine optimum sensor parameters (Ketchum and Tooma 1973, Parashar 1974, Dunbar 1975, Gray et al. 1982, Onstott et al. 1982 a, Livingstone et al. 1987). However, very few of these measurement programmes included surface observations needed to develop theoretical models of radar backscattering from sea ice. In order to perform microwave

experiments in conjunction with detailed surface and structural measurements for obtaining data required for modelling purposes, an outdoor pond was constructed at U.S. Army Cold Regions Research and Engineering Laboratory (CRREL) at Hanover, New Hampshire, for growing saline ice.

In 1984 and 1985, the University of Kansas made radar backscatter measurements as a part of controlled experiments on artificial sea ice at the CRREL. The University of Massachusetts, University of Washington and Naval Oceans Research and Development Activity (NORDA) performed concurrent passive microwave measurement (Swift *et al.* 1986, Grenfell and Comiso 1986). CRREL personnel made detailed observations of ice sheets including measurements of salinity, internal structure and electrical properties (Arcone *et al.* 1986). The primary objective of these investigations was to measure electrical properties in a controlled environment for quantifying the influence of the structural parameters of ice on microwave scattering and emission.

We performed active measurements with a dual-antenna FM radar at selected frequencies between 4 and 17 GHz for like and cross polarizations over incidence angles from 0 to 60°. Ice categories studied during these experiments included open water, smooth and rough saline ice and snow-covered ice. The ice sheets we studied simulated, both physically and electrically, the thin ice encountered in the Arctic (Arcone *et al.* 1986).

The purpose of this paper is to report the results of active measurements. A method for reducing errors in estimating scattering coefficients from data collected with broad-beam antennas is discussed. The effects of ice growth, roughness and snow cover on backscattering from thin ice are investigated. Comparisons are made of backscattering characteristics of different ice categories studied in this investigation.

2. Experiment description

The radar experiments were conducted on saline ice grown in a $5\,\text{m} \times 15\,\text{m}$ outdoor pond at CRREL during the 1984 and 1985 winter seasons. Radars were mounted on a gantry provided by the University of Massachusetts. The gantry was capable of lateral movement for obtaining independent samples required to reduce fading. Radar data were acquired at 5° intervals to accurately determine the near-vertical angular response. Measurements were made at 12 closely-spaced frequencies between 4 and 17 GHz, but with emphasis on 5·0, 9·6, 13·6 and 16·6 GHz. CRREL investigators performed detailed structural and electrical characterizations including salinity, temperature, density and thickness. Surface roughness measurements were made by removing blocks and slicing the blocks into a number of thick sections. These sections were placed against a centimetre grid and photographed. These photographs were digitized and surface roughness statistics were estimated from the digitized data.

In 1985, we performed experiments on three saline ice sheets. The first measurements were on a saline ice sheet grown during 4–8 January. This sheet was divided into two sections: one seeded and the other unseeded. The measurements were started when the saline ice sheet was about 3 cm thick and were continued until it was 8 cm thick. Before this sheet was removed, the ice surface was artificially roughened and a natural snow cover of 4·5 cm was allowed to accumulate to permit the study of the effects of surface roughness and snow on backscattering from sea ice. The introduction of roughness by artificial means produced small-scale roughness similar, to a large extent, to that observed on natural ice.

The growth of a second sheet was started on 8 January. It was unseeded and allowed to grow until it was about 16 cm thick. Measurements were made at average thicknesses of about 0·3, 0·9, 2·1, 5, 6, 6·5, 7, 7·5, 11, 13, 14·5 and 16 cm. Ambient temperatures ranged from −8° to −15°C during the experiment period. This sheet was harvested on 14 January.

On 16 January a third and final sheet was initiated by spray seeding. The measurements on this sheet were made at thicknesses of 1·1, 3·5, 4·1, 12·5, 13·5, 15·8, 18·4, 19·1, 32 and 36 cm. This sheet was left in place until it rotted in March. The crystalline structure of this ice as sampled on 21 January, when 9·3 cm thick, is illustrated in figure 1 (*a*). Salinity profiles measured during the growth of this ice sheet are presented in figure 1 (*b*) and (*c*). During the first month of the growth, the ice sheet exhibited C-shaped profiles typical of Arctic sea ice. The C-shaped profile results from high salinity at the top and bottom and this has been observed on the Arctic ice (Gow 1986). This ice sheet underwent periodic flooding from rain and snow-melt during the latter part of February and early March. The downward percolation of the water caused desalination of the ice sheet. This is similar to meltwater flushing of brine on the Arctic sea ice.

3. Sensor

The radar system we used in both the 1984 and 1985 experiments was a low-power dual-antenna FM radar called SLEDSCAT. This system was capable of operation over the frequency range from 4 to 18 GHz and was suitable for like and cross polarized measurements over incidence angles from 0 to 60°. The antenna cluster consisted of four rectangular pyramidal horns and a quad-ridge horn-fed parabola. Two of the four horns were used for C band. The other two horns along with the reflector were utilized for receiving and transmitting X- and Ku-band signals.

We calibrated the system internally in these experiments by connecting a delay line of known loss between the transmitter and receiver and measuring the detector output. We did this before and after each data run. Also at the beginning and end of each experiment, we recorded returns from a Luneburg lens of known radar cross section for converting data over the ice sheets to scattering coefficients. A detailed description of the procedure used to convert measured returns to scattering coefficients is available in Onstott *et al.* (1982 b).

The important system specifications are given in the table.

4.1. *Beamshape correction*

Radar return from an area extensive target is given by

$$P_r = \frac{P_t G_{t\,max} G_{r\,max} \lambda^2}{4\pi^3} \int_0^{2\pi} \int_0^\pi \frac{g_t g_r \sigma^0(\theta, \phi)}{R^4} dA \tag{1}$$

where P_t is the transmitter power, P_r is the received power, $G_{t\,max}$ is the maximum gain of the transmit antenna, $G_{r\,max}$ is the maximum gain of the receive antenna, λ is the wavelength of the transmitted radiation, σ^0 is the scattering coefficient of the area target, R is the range to the target and g_t and g_r are the relative gain functions of the transmit and receive antenna, respectively.

Equation (1) is generally simplified assuming that the scattering coefficient is not a function of the azimuth angle ϕ and the received power is mainly from the illuminated

S. Gogineni et al.
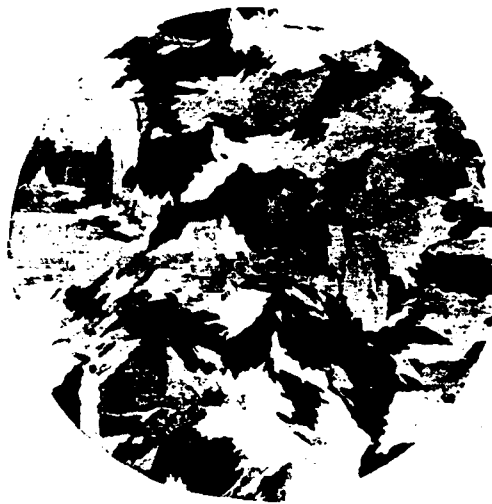
(a)

area defined by the antenna half-power beamwidths. The simplified equation is

$$P_r = \frac{P_t G_{t\max} G_{r\max} \lambda^2}{4\pi^3} \int_{-\beta_a/2}^{\beta_a/2} \int_{-\beta_e/2}^{\beta_e/2} \frac{g_t g_r \sigma^0(\theta)}{R^4} \, dA \qquad (2)$$

For estimating σ^0 from measured radar data, equation (2) is further simplified by assuming that the variables are constant over the illuminated area. This assumption is
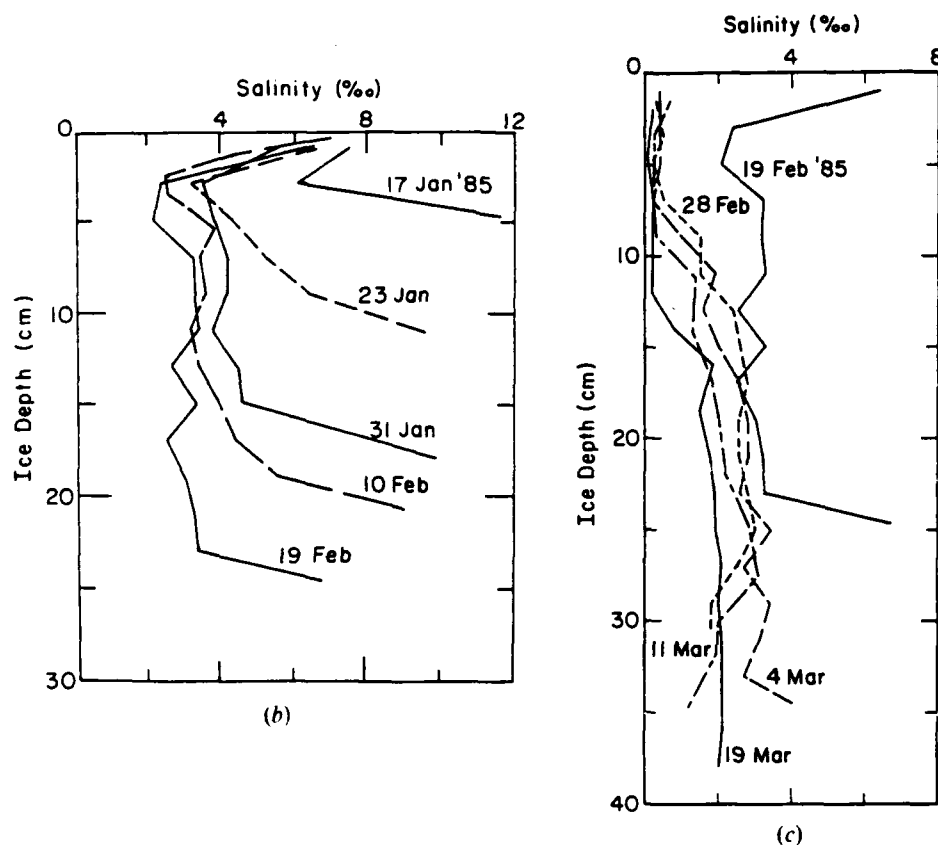
Figure 1. (a) Vertical and bottom horizontal thin sections of saline ice crystal structure photographed between crossed polarizers. Sample was taken from ice sheet 2 (seeded 16 January 1985) on 21 January 1985; ice thickness of 9·3 cm. (b) Salinity profiles during various stages of growth of ice sheet 2, January–March 1985, C-shaped profiles closely simulate those of Arctic first-year ice. (c) salinity profiles beginning with 28 February, closely resemble those found in second-year Arctic ice.

referred to as the narrow beam approximation. The simplified equation is

$$P_r = \frac{P_t G_{t\,max} G_{r\,max} \lambda^2 \sigma^0 A_1}{4\pi^3 R_0^4} \tag{3}$$

where A_1 is the illuminated area.

From equations (2) and (3), we can obtain an expression suitable for determining σ^0 accurately as

$$\sigma_t^0 = \frac{R_0^4 \int_{-\beta_e/2}^{\beta_e/2} \int_{-\beta_a/2}^{\beta_a/2} \frac{g_t g_r \sigma_m^0}{R^4} \, dA}{A_1} \tag{4}$$

where σ_m^0 is the measured scattering coefficient and σ_t^0 is the true scattering coefficient.

We measured the antenna patterns and fitted the measured mainlobe antenna patterns with a Gaussian function of the form $g(\theta) = \exp\left[-k(\theta/\theta_b)^2\right]$. We inverted

System specifications.

Types	FM-CW
Frequency range	4–17 GHz
RF bandwidth	400 MHz
Intermediate frequency (IF)	14·5 kHz
IF bandwidth	3·5 kHz
Polarization	VV, HH, VH, HV
Antenna beamwidths	
Azimuth	
HH	18°, 6·2°, 5·7° and 4·3° at 5·0, 9·6, 13·6 and 16·6 GHz, respectively
VV	18°, 7·6°, 6·7° and 5·3° at 5·0, 9·6, 13·6 and 16·6 GHz, respectively
Elevation	
HH	18°, 7·6°, 6·2° and 5·2° at 5·0, 9·6, 13·6 and 16·6 GHz, respectively
VV	18°, 6·2°, 5·7° and 4·3° at 5·0, 9·6, 13·6 and 16·6 GHz, respectively
Incidence angle range	0° to 60°
Calibration	
Internal	Signal injection
External	30 cm diameter Luneburg lens

measured data using the narrow beam approximation equation. We fitted this data set with an exponential model of the form $\sigma^0(\theta) = A \exp(-\theta/B)$. The constants A and B are selected to obtain a best fit to the measured data. The parameter B is first quantized into a finite set of $\{B_i\}$ and a σ^0 table is generated on the basis of quantized $\{B_i\}$. With A as a free parameter, we calculated the least-square error between the measured σ^0 and each element of the table. The constant B and corresponding A which gave minimum least-square error among $\{B_i\}$ are selected as model parameters. This model is then used to calculate the correction factor for the measured σ^0.

4.2. *Non-overlap correction*

Whenever dual-antenna radar systems are used for scattering measurements over a wide range of incidence angles at short ranges, the transmit and receive antenna beams may not fully overlap at all angles, as shown in figure 2. This introduces errors in the estimation of illuminated area. We corrected this type of error using formulas reported by Moore (1985) for antenna patterns approximated by Gaussian functions. For parallel Gaussian beams the correction factor is given by

$$C_p = \exp\left[\frac{-s_p^2 k^2}{\beta_p^2 R_0^2(1 + m_p^2)}\right] \tag{5}$$

where s_p is antenna separation, k is a constant, m is the ratio of transmit and receive antenna beamwidths and the subscript p refers either to the azimuth or the elevation plane.

Since this type of error occurs both in the elevation and azimuthal planes, the total correction factor is the sum of the individual correction terms in the elevation and the azimuthal plane.

$$C_T = C_a + C_e \tag{6}$$
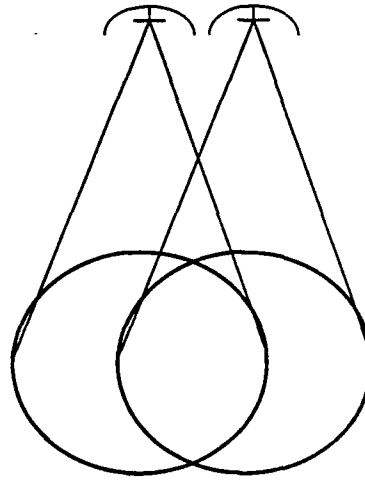
Figure 2. Geometry of non-overlapping antenna patterns of a short-range radar.

where C_T is the total correction factor, C_a is the correction factor in the azimuth direction and C_e is the correction factor in the elevation direction.

Figure 3 shows the uncorrected data as well as the data corrected both for beam shape error and non-overlapping beam error at 9·6 GHz. The combined error is as large as 5 dB near vertical and about 1 dB at angles greater than 35°. Some of the scatter in data around the regression lines is from fading effects. The average error over the entire angular region from fading is between −3·5 dB and 2·5 dB. Although we could have reduced the non-overlapping beam error by selecting one of the antennas so that its dimensions were half as small as those of the other, this would
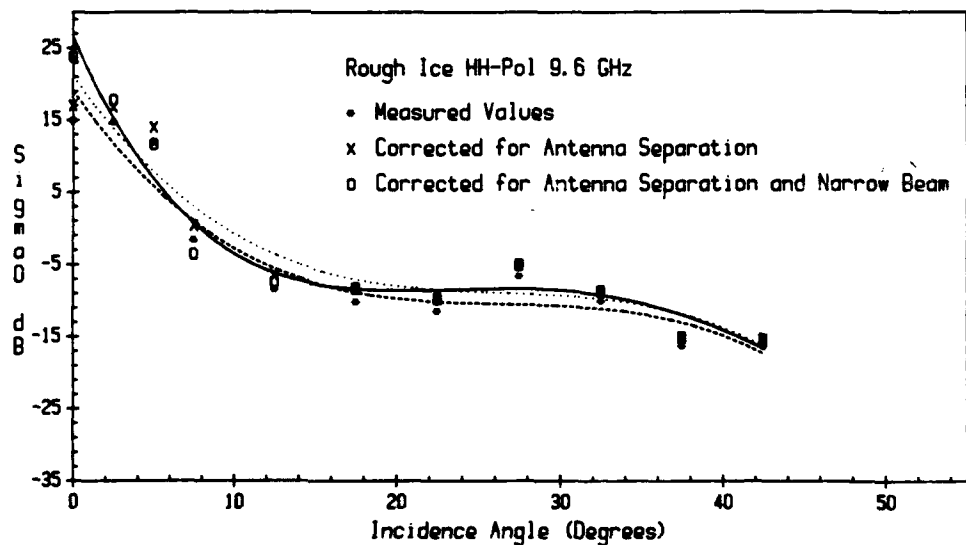
Figure 3. Effects of antenna separation and beam weighting on vertical polarization σ^c angle response from first-year ice.

have increased the effective beamwidths resulting in larger beam shape error as well as illuminating the walls of the tank. Also, the use of large focused antennas was ruled out by weight constraints imposed by the system. The combined error at 5 GHz is much larger than that at 9·6 GHz, but is smaller both at 13·6 and 16·6 GHz. We applied the same procedure to correct the data at 5 GHz. However, at 5 GHz the antenna beamwidth is very large and there is a large coherent component because of the smooth ice surface. This made it difficult to obtain the true scattering coefficient from the measured data at 5 GHz. A more accurate procedure that takes into account the presence of coherent component and can be applied to 5 GHz data is discussed by Ulaby *et al.* (1983).

5. Measurement results and discussion

5.1. *Effect of ice growth*

The effect of ice growth on backscattering at 5 GHz for vertical polarization is illustrated in figure 4. The scattering coefficient increased rapidly with thickness for ice thicknesses less than 1 cm and decreased with further growth for the next few centimetres. The initial increase was as large as 5 dB at 30°. This increase is associated with very high surface dielectric constant for very thin ice, which could be the result of surface flooding or high surface salinity. During the initial growth brine is expelled not only into the surrounding water, but also onto the ice surface. The ice surface is also flooded with salt water through the holes created by the surface tension. For very thin ice, surface salinities as large as 70 parts per thousand have been reported (A. Kovacs, personal communication, 1988). The high return is similar to that of moderately thick ice. This has implications on discriminating very thin ice from thicker types of ice. A similar effect was observed in field data analyzed by Parashar (1974) and Livingstone *et al.* (1987).
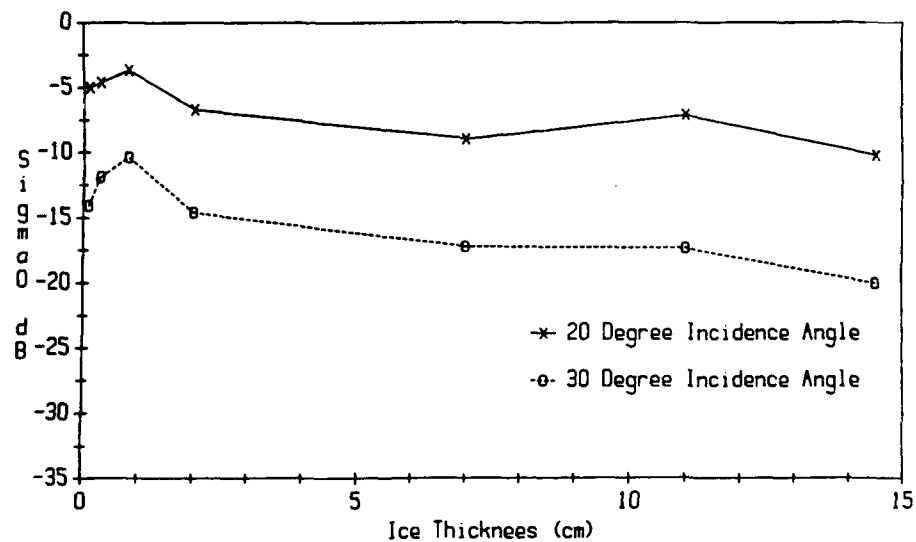
Figure 4. Effects of ice growth on vertical polarization σ° at 5·3 GHz.
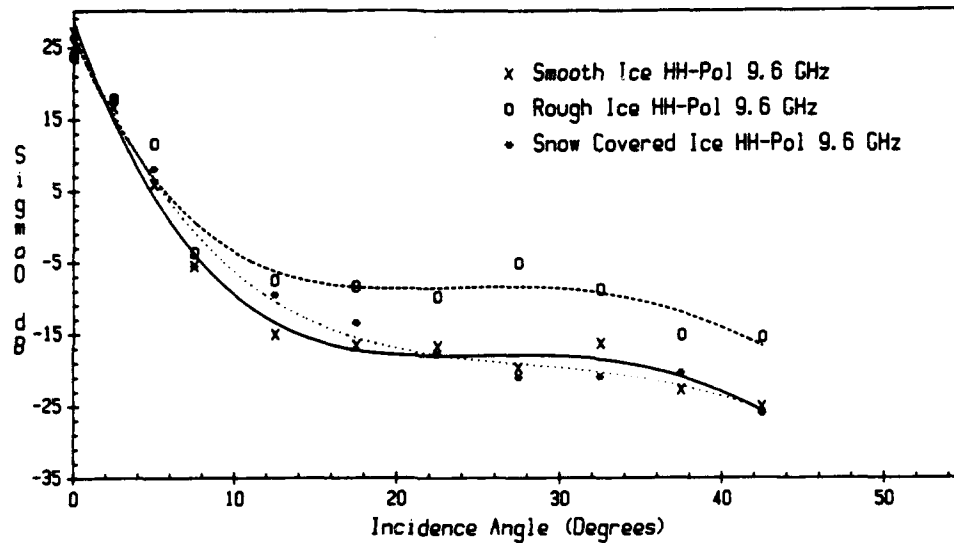
Figure 5. Effects of surface conditions on backscatter angle response at 9·6 GHz.

5.2. *Surface roughness and snow cover effects*

Angular responses of σ^0 for smooth ice, rough ice and snow-covered ice at 9·6 and 13·6 GHz are shown in figures 5 and 6 respectively. These results are from the second ice sheet investigated during the 1985 experiments. The snow on the ice sheet was dry and about 4·5 cm deep. The ice surface roughness was artificially induced using a rake. At both 9·6 and 13·6 GHz, rough ice returns were much higher than those from snow-covered ice and smooth ice. The returns from snow-covered ice and smooth ice
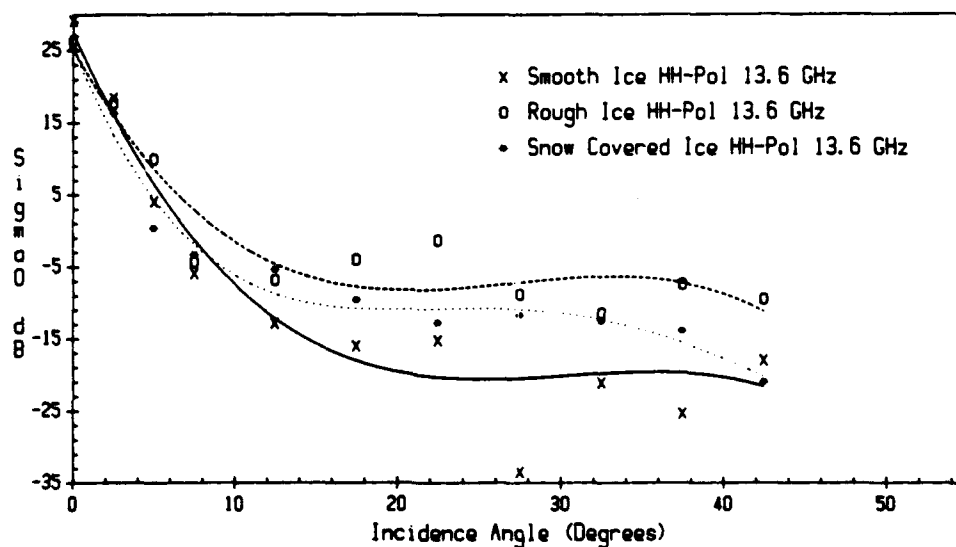
Figure 6. Effects of surface conditions on backscatter angle response at 13·6 GHz.

were similar at 9·6 GHz, indicating that dry snow of less than 5 cm thickness has a
negligible effect on backscattering from sea ice at this frequency. However, at
13·6 GHz, the presence of snow increased the backscattering from smooth ice by
about 3 dB for incidence angles greater than 20°. This is the result of increased volume
scattering from snow at higher frequencies.

5.3. *Polarization behaviour*

Figures 7, 8 and 9 show the angular response of σ^0 of smooth ice, rough ice and
snow-covered respectively. For smooth ice (figure 7), vertically-polarized returns are
higher than horizontally polarized returns at large incidence angles, with the
separation becoming larger with the incidence angle. The cross-polarized scattering
coefficients are about 22 dB lower than like-polarized values. These indicate that
backscattering is dominated by the surface. For smooth ice, the measured r.m.s.
height is 0·11 cm and the correlation length is about 23 cm. The validity conditions for
the small-perturbation model are $k\sigma < 0·3$ and $\sqrt{2}\sigma/l < 0·3$, where k is the wave
number, σ is the r.m.s. surface height and l is the correlation length. For smooth ice at
5·3 GHz these validity conditions are satisfield. This model correctly predicts mea-
sured angular response. However, this model does not predict depolarization charac-
teristics properly. The depolarized returns may be the result of a small amount of
volume scattering from brine inclusions in the ice.

For rough ice, as shown in figure 8, like-polarized returns were similar in
magnitude over the entire angular range from 0 to 45 and the cross-polarization
echoes are about 12 dB lower than the like-polarized ones. The measured surface
r.m.s. height is about 0·28 cm and the correlation length is 3·1 cm. At 9·6 GHz, these
satisfy the validity conditions ($kl > 6$ and $l^2 > 2·76\sigma\lambda$) of the Kirchhoff model. This
model correctly predicts the observed polarization behaviour. However, this model
predicts no depolarization. Thus, a combined volume and surface model similar to
that reported by Fung and Eom (1982) will have to be considered to explain the
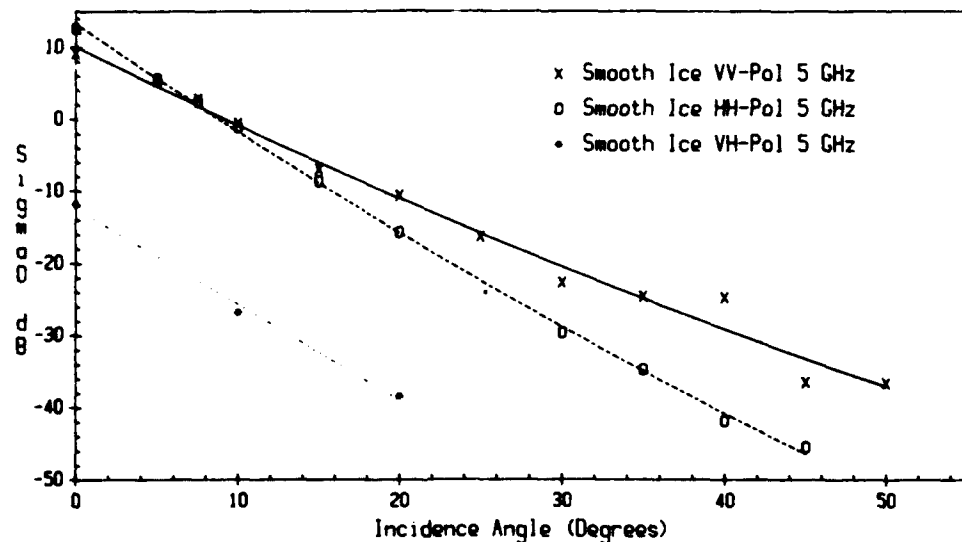
Figure 7. Smooth ice backscatter angle response for various polarizations.

may be possible to obtain, at least in a statistical sense, a
measure of the ice surface area in a given region which is

Radar backscatter measurements over saline ice 613
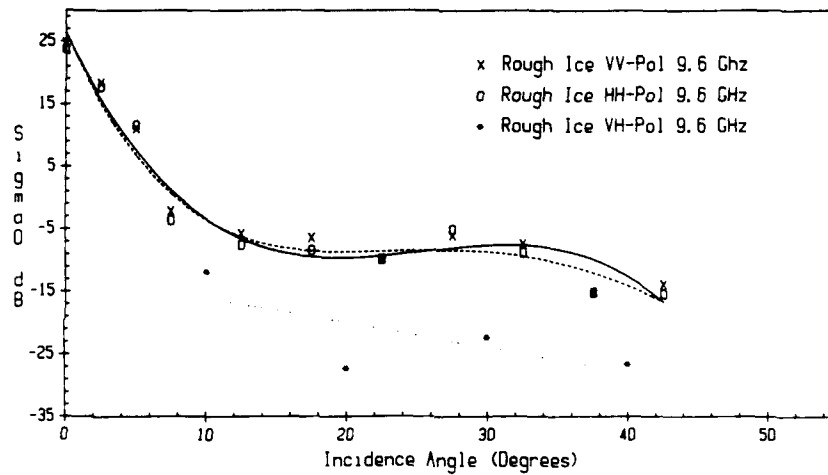
Figure 8. Rough ice backscatter angle response for various polarizations

depolarization characteristics instead of a purely surface model as posulated by Kim
et al. (1984).

At incidence angles larger than 20 , the vertical polarization returns from snow-
covered ice were about 2 dB higher than those for horizontal polarization. The cross-
polarization scattering coefficients are about 10 dB lower than scattering coefficients
for vertical polarization. The higher vertically polarized echoes and larger depolarized
returns suggest volume scattering from snow.
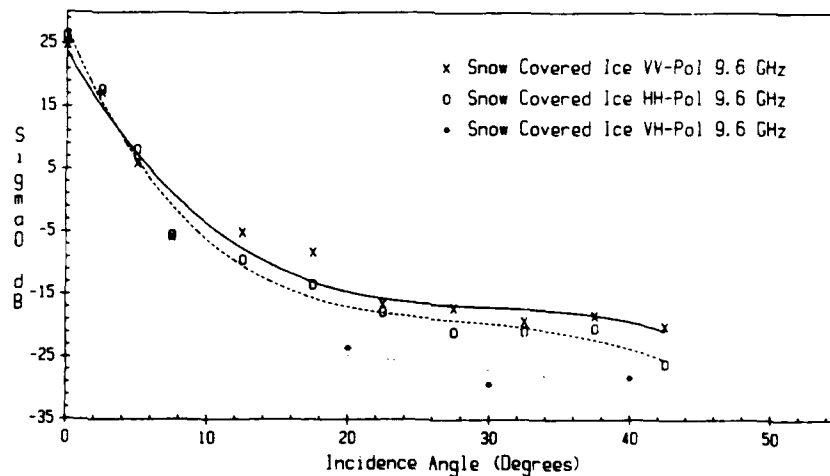
Figure 9. Snow-covered ice backscatter angle response for various polarizations.
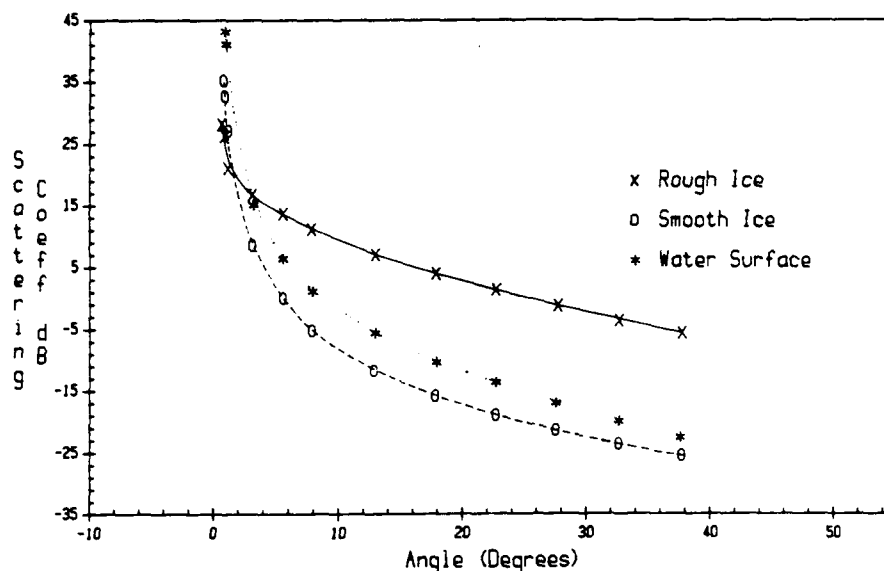
Figure 10.   True scattering coefficients at 13·6 GHz. VV polarization.

5.4. Comparisons with water

Scattering coefficients of smooth and rough ice are compared with those of open water in figure 10. At vertical incidence, backscattering from open water is much larger than that from smooth and rough ice surfaces. There is about 3 dB difference in scattering coefficients of smooth ice and calm water at large angles of incidence. This is somewhat smaller than what has been observed in the field (Livingstone et al. 1987). This could be the result of system sensitivity limitations. At incidence angles greater than about 30 , rough ice returns are much larger than both smooth ice and calm water echoes.

6.   Conclusions

This paper has shown the importance of careful use of measured antenna patterns in scatterometer measurements, particularly on smooth surfaces, and has discussed the backscattering properties of smooth, rough and snow-covered saline first-year ice. An iterative method for correcting errors associated with wide beam antennas and formulas for reducing errors introduced by non-overlapping beams are presented. The effects of ice growth, roughness and snow cover on radar backscattering from saline first-year ice and applicable models are discussed. The returns from saline ice sheets are similar to those from very thin ice observed in the Arctic. The results verified the field experiment findings that backscattering from saline ice is dominated by surface with a small contribution from the ice volume at large angles of incidence.

Acknowledgments

References

ANDERSON, V. H., 1966. High altitude side-looking radar images of sea ice in the Arctic. *Proceedings of the Fourth Symposium on Remote Sensing of Environment held at the University of Michigan. Ann Arbor, in April 1966* (Ann Arbor: Environmental Research Institute of Michigan), pp. 845–857.

ARCONE, S. A., GOW, A. J., and McGREW, S., 1986. Microwave dielectric, structural, and salinity properties of simulated sea ice. *I.E.E.E. Transactions on Geoscience and Remote Sensing*, **24**, 832–839.

DUNBAR, M., 1975. Interpretation of SLAR imagery of sea ice in Nares Strait and the Arctic Ocean. *Journal of Glaciology*, **15**, 193–213.

FUNG, A. K., and EOM, H. J., 1982. Application of rough surface and volume scattering theory to sea ice and snow backscatter. *I.E.E.E. Transactions on Geoscience and Remote Sensing*, **20**, 528–536.

GOW, J. A., 1986. Optical characterization of sea ice structure using polarized light techniques. *SPIE Ocean Optics VIII*, **637**, 264–270.

GRAY, A. L., HAWKINS, R. K., LIVINGSTONE, C. E., DRAPIER-ARSENAULT, L., and JOHNSTONE, W. M., 1982. Simultaneous scatterometer and radiometer measurements of Arctic sea-ice microwave signatures. *I.E.E.E. Journal of Ocean Engineering*, **7**, 44–50.

GRENFELL, T. C., and COMISO, J. C., 1986. Multifrequency passive microwave observations of first-year sea ice grown in a tank. *I.E.E.E. Transactions on Geoscience and Remote Sensing*, **24**, 826–831.

KETCHUM, R. D., JR. and TOOMA, S. G., JR. 1973. Analysis and interpretation of airborne multi-frequency side-looking radar sea ice imagery. *Journal of Geophysical Research*, **78**, 520–538.

KIM, Y. S., MOORE, R. K., and ONSTOTT, R. G., 1984. Theoretical and experimental study of radar backscatter from sea ice. Radar Systems and Remote Sensing Laboratory Technical Report 331-37. University of Kansas Center for Research, Inc., Lawrence, Kansas, U.S.A.

LIVINGSTONE, C. E., SINGH, K. P., and GRAY, A. L., 1987. Seasonal and regional variations of active passive microwave signatures of sea ice. *I.E.E.E. Transactions on Geoscience and Remote Sensing*, **25**, 159–173.

MOORE, R. K., 1985. Effect of pointing errors and range on performance of dual-pencil beam scatterometers. *I.E.E.E. Transactions on Geoscience and Remote Sensing*, **23**, 901–905.

ONSTOTT, R. G., MOORE, R. K., GOGINENI, S., and DELKER, C., 1982 a. Four years of low-altitude sea ice broadband backscatter measurements. *I.E.E.E. Journal of Ocean Engineering*, **7**, 44–50.

ONSTOTT, R. G., MOORE, R. K., GOGINENI, S. P., KIM, Y. S., and BUSHNELL, D. B., 1982 b. Helicopter-borne scatterometer. Technical Report RSL TR-331-24. Radar Systems and Remote Sensing Laboratory, University of Kansas Center for Research, Inc., Lawrence, Kansas, U.S.A.

PARASHAR, S. K., 1974. Investigation of radar discrimination of sea ice. Ph.D. thesis, University of Kansas, Lawrence, Kansas, U.S.A.

SWIFT, C. T., DEHORITY, D. C., and TANNER, A. B., 1986. Passive microwave spectral emission from saline ice at C-band during the growth phase. *I.E.E.E. Transactions on Geoscience and Remote Sensing*, **24**, 840–848.

ULABY, F. T., ALLEN, C. T., and FUNG, A. K., 1983. Method for retrieving the true backscattering coefficient from measurements with a real antenna. *I.E.E.E. Transactions on Geoscience and Remote Sensing*, **21**, 308–313.

196100-23-T

Technical Report

POLARIMETRIC RADAR MEASUREMENTS OF ARTIFICIAL SEA ICE DURING CRRELEX '88

R.G. ONSTOTT
Advanced Concepts Division

APRIL 1990

REPORT DOCUMENTATION PAGE		Form Approved OMB No. 0704-0188

1a REPORT SECURITY CLASSIFICATION N/A	1b RESTRICTIVE MARKINGS N/A	
2a SECURITY CLASSIFICATION AUTHORITY N/A	3 DISTRIBUTION AVAILABILITY OF REPORT Approved for public release: Distribution is unlimited.	
2b DECLASSIFICATION DOWNGRADING SCHEDULE N/A		

4 PERFORMING ORGANIZATION REPORT NUMBERS(S) 196100-23-T	5 MONITORING ORGANIZATION REPORT NUMBER(S) ----

6a NAME OF PERFORMING ORGANIZATION Environmental Research Institute of Michigan	6b OFFICE SYMBOL (if applicable)	7a NAME OF MONITORING ORGANIZATION Office of Naval Research

6c ADDRESS (City State and ZIP Code) P. O. Box 8618 Ann Arbor, MI 48107-8618	7b ADDRESS (City, State, and ZIP Code) SAR Division, Code 11201 NASA Headquarters 800 N. Quincy St. 600 Independence Ave., So. Arlington, VA 22217-5000 Washington, D.C. 20546

8a NAME OF FUNDING /SPONSORING ORGANIZATION Office of Naval Research	8b OFFICE SYMBOL (if applicable)	9 PROCUREMENT INSTRUMENT IDENTIFICATION NUMBER N00014-86-C-0469

8c ADDRESS (City State and ZIP Code) SAR Division, Code 11201 NASA Headquarters 800 N. Quincy St. 600 Independence Ave., So. Arlington, VA 22217-5000 Washington, D.C. 20546	10 SOURCE OF FUNDING NUMBERS			
	PROGRAM ELEMENT NO	PROJECT NO	TASK NO	WORK UNIT ACCESSION NO

11 TITLE (Include Security Classification)

POLARIMETRIC RADAR MEASUREMENTS OF ARTIFICIAL SEA ICE DURING CRRELEX '88

12 PERSONAL AUTHOR(S)   Robert G. Onstott

13a TYPE OF REPORT Technical	13b TIME COVERED FROM 09/88 TO 09/90	14 DATE OF REPORT (Year Month Day) 04-04-90	15 PAGE COUNT 72

16 SUPPLEMENTARY NOTATION

17 COSATI CODES			18 SUBJECT TERMS (Continue on reverse if necessary and identify by block number)
FIELD	GROUP	SUB-GROUP	Radar backscatter, sea ice

19 ABSTRACT (Continue on reverse if necessary and identify by block number)

During the winter of 1988, active microwave measurements were made of artificial sea ice. Radar backscatter data were collected at 1.8, 5, and 10 GHz for incidence angles 0° to 60°. Phase information was obtained for the complete determination of the scattering matrices of the various ice scenes. In addition, measurements were made for qualitatively characterizing the dominant scattering mechanisms by recording unprocessed backscatter returns. Polarimetric scattering data acquired at C- and X-band frequencies of two representative ice scenes, grey ice and rough grey ice, are provided here in the form of power scattering, covariance, and Mueller matrices.

20 DISTRIBUTION/AVAILABILITY OF ABSTRACT XX UNCLASSIFIED/UNLIMITED ☐ SAME AS RPT ☐ DTIC USERS	21 ABSTRACT SECURITY CLASSIFICATION UNCLASSIFIED
22a NAME OF RESPONSIBLE INDIVIDUAL Robert G. Onstott, Ph.D	22b TELEPHONE (Include Area Code) 313-994-1200 22c OFFICE SYMBOL

ERIM

TABLE OF CONTENTS

ERIM

LIST OF FIGURES

LIST OF FIGURES (continued)

ΣERIM

LIST OF TABLES

1. INTRODUCTION

There is an important need to acquire geophysically useful information concerning the polar regions, particularly of sea ice, through the interpretation of satellite data. Studies are ongoing to understand the relationships between the physical properties and the microwave signatures of first-year and old sea ice, and to produce a more complete understanding of the parameters and processes which effect the active and passive microwave signatures. In the pursuit of these goals, the ability to make microwave measurements of sea ice in a laboratory-like environment was developed at the U.S. Army Cold Regions Research and Engineering Laboratory (CRREL). A conclusion reached through discussion with both theoretical modelers and experimentalists is the need to coordinate very detailed laboratory type measurement investigations in which the physical properties needed to validate the developing models are measured, and that those persons developing models are fully aware of the constraints of what can be measured. Similar discussions are summarized in the "Workshop on Microwave Scattering and Emission from the Earth's Surface", Final Report [1].

The microwave properties of artificial sea ice grown at CRREL were investigated during the 1988 winter season. The sea ice facility is comprised of a 5 m x 15 m outdoor tank of a 1.2 m depth filled with sea water, a tent to protect the ice sheet from snow and rain, a gantry-style instrument mounting structure, and heated working environments in the immediate vicinity of the tank. The tank size, determined by instrument and experiment needs, allows for the acquisition of independent spatial samples and measurements at angles from vertical to 60°. These efforts, which are part of a new three-year, laboratory-based investigation, are focused on understanding the microwave signatures of sea ice; this will be accomplished by detailed studies of the various aspects of backscatter and emission and through

1

the intercomparison of measured data and theoretical predictions. Two strengths of the CRREL Ice Tank Facility are the ability to control the physical properties of the ice sheet and the time to rigorously measure the physical and microwave properties of ice which closely simulate that found in the Arctic.

Observations commenced with open water and continued until 15 cm of sea ice was formed. During this investigation, detailed scene characterizations were made. These included the standard array of measurements (i.e., fabric of the ice sheet, the salinity, the density, the temperature, location of layers, and location of internal inhomogeneities) and measurement of surface and interior ice sheet statistics. These active microwave measurements were coordinated with passive microwave observations, hence, a completely integrated comparison of backscatter and emission may be made with theoretical predictions. Physical properties which may influence backscatter and emission were measured; these data or their derivatives provide the critical inputs for the electromagnetic models. The roughness of the ice surface is important in determining the general backscatter level for first year ice. Experiments were performed to study the change in backscatter and polarization signatures with various roughness scales. Effects of freeze and thaw conditions were also examined.

For this investigation, a polarization diversified scatterometer has been enhanced by adding the sophistication necessary to measure phase. Previous measurements have been made to describe the noncoherent average scattering coefficients at VV, VH, HV, and HH polarizations (i.e., VH indicates vertical transmit and horizontal receive). This radar was used to measure the target scattering matrix (i.e., the matrix elements are the detected scattered fields at VV, VH, HV, and HH polarizations) which allows the examination of the functional dependence of intensity on polarization. During CRRELEX, polarimetric measurements were made at 1.8, 5, and 10 GHz in the configuration shown in Figure 1. The polarimetric radar is briefly

2

ERIM

described in the next section of this report. In addition, millimeter wave data were collected at 18, 35, and 94 GHz using a noncoherent radar. The microwave measurements and characterization measurements performed by ERIM during this investigation are summarized in Table 1.
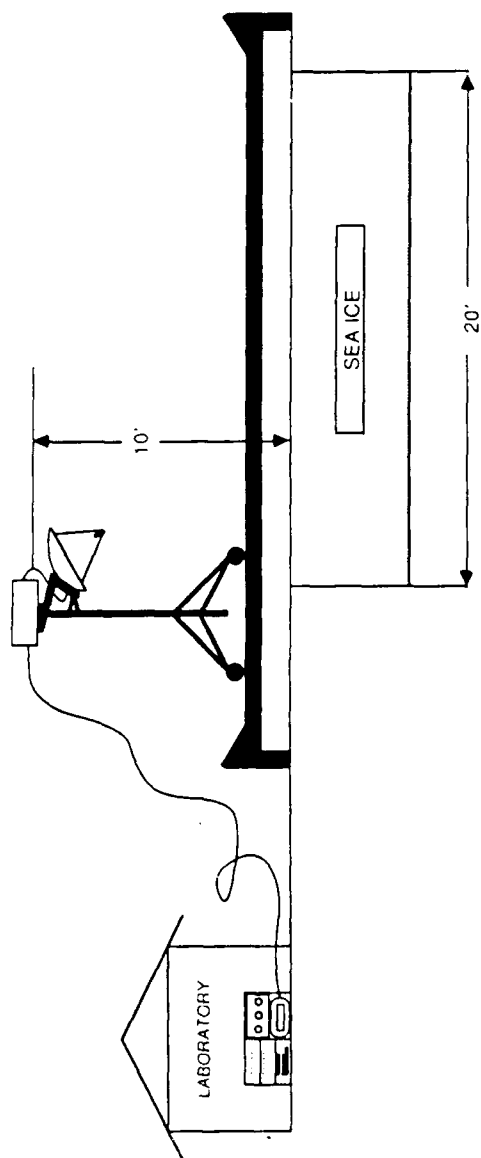
Figure 1. Configuration of Polarimetric Microwave Scatterometer at Sea Ice Tank

Table 1.

MICROWAVE AND ICE CHARACTERIZATION
MEASUREMENTS OF SEA ICE DURING CRRELEX '88

Scatterometer

Polarimetric:

Frequency	1.75, 5 and 10 GHz
Angles	Vertical to 60°
Height	3 m
Sampling	Point and Power Spectrums

Non-Coherent:

Frequency	10, 18, 35 and 94 GHz
Angles	15 to 60°
Height	3 m
Sampling	Point and Transect

Characterization

Surface Roughness
Photography

ΣERIM

6

2. POLARIMETRIC RADAR DESCRIPTION

This polarimetric radar has been developed to operate at 1.8, 5, and 10 GHz, and measures the amplitude and phase at four linear transmit-receive polarizations--the elements of the target scattering matrix. Designed for application in both the laboratory and the field, the capable HP8510B network analyzer and HP8341B synthesized frequency source serve as the heart of this system. This radar allows the target scattering matrix (TSM) to be acquired through measurement; hence, the description of the polarization properties of the scattered field is complete. Measurements support studies which address surface and volume scattering, repolarization, and depolarization.

The sensor is comprised of a synthesized frequency source, RF-antenna packages (at each frequency), a three-channel frequency converter, a network analyzer, system control circuitry, and a data acquisition computer (see Figure 2). Simultaneous measurements may be made at two frequencies. Each receiver is dual channel (See Figure 3); both vertical and horizontal polarizations are received coincidentally. The TSM elements are acquired by transmitting using a V-pol antenna and then an H-Pol antenna. The RF hardware is mounted in temperature controlled enclosures. Clusters of four antennas are mounted rigidly to these enclosures. Symmetry in the antenna cluster and RF hardware provides short, nearly identical electrical paths; further adjustment of channel balance was not required and the data acquisition software remained relatively uncomplicated and inherently quicker. The oscillator which is shared by each transmitter and receiver determines the RF frequency and also provides the phase reference. A swept IF signal (1-2 GHz) is provided for the up conversion at the transmitters. The RF and antennas are separated from IF processing by a distance of 13 meters. Losses and phase errors due to cable flexure were kept small by selecting the low IF frequency and using helix type cable.
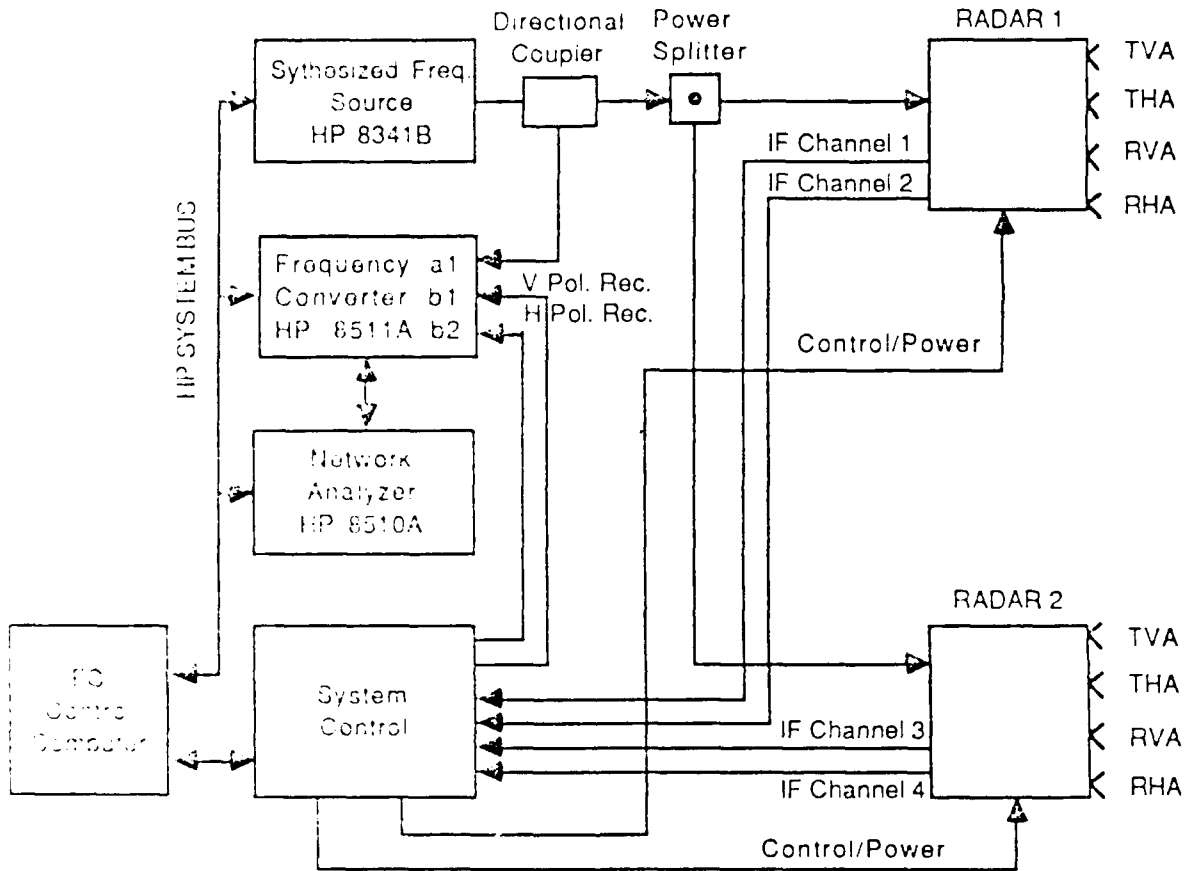
TVA = Trans. Vert. Antenna; THA = Trans. Horiz. Antenna;
RVA = Rec. Vert. Antenna; RHA = Rec. Horiz. Antenna

Figure 2.   Polarimetric Radar System Configuration

8
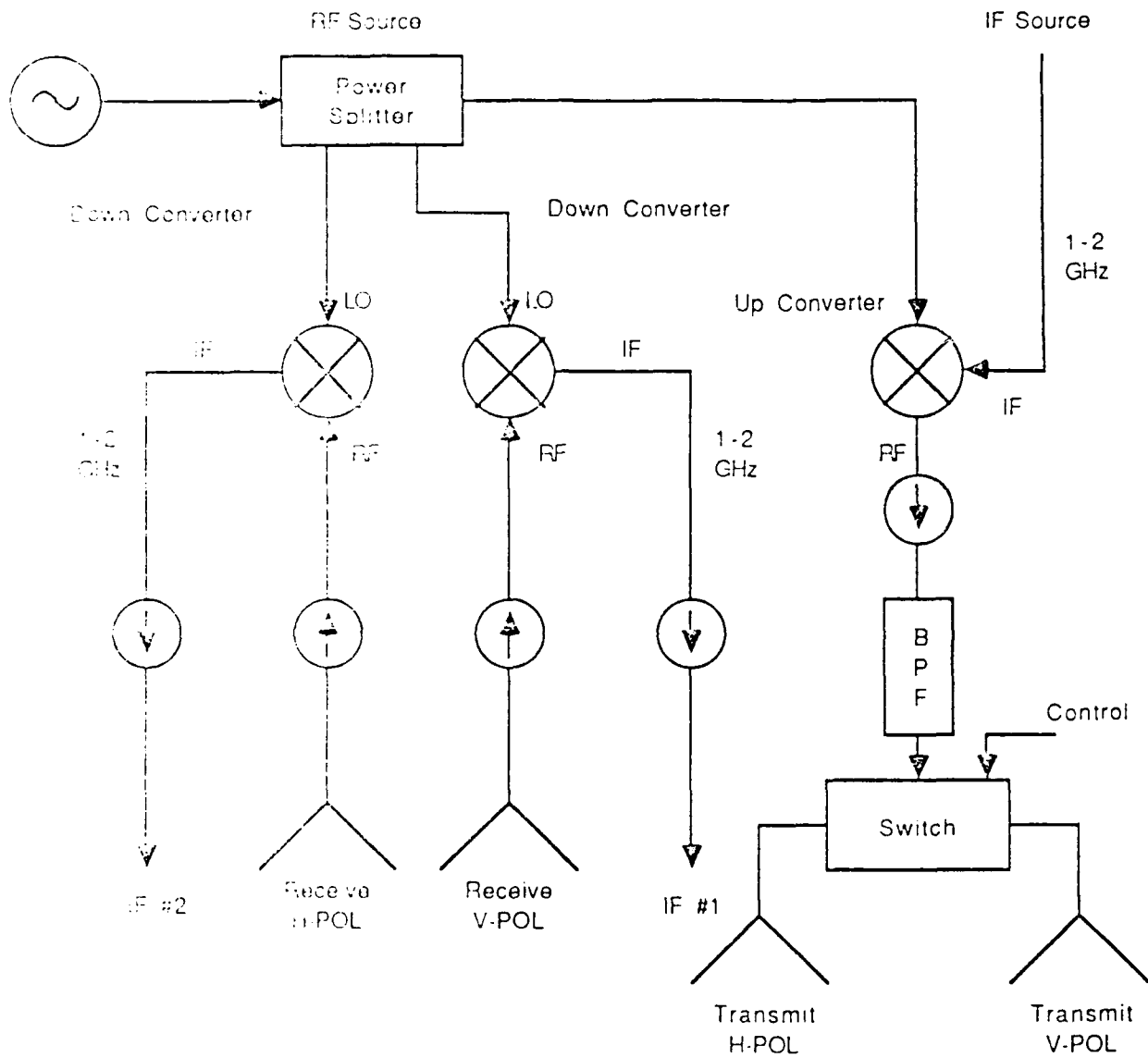
Figure 3.   Polarimetric Radar RF/IF Diagram

Data acquisition procedures greatly impact measurement accuracy. As backscatter levels become very small, locating the target returns in each of the four channels so that narrow range gates may be positioned precisely requires increased sophistication.

3. MEASUREMENT GOALS

There are two particularly interesting aspects to the acquisition
of polarimetric radar data. One, of course, is to examine the utility
of such a sensor to provide additional information. For example, by
examining the phase difference and correlation between the returns at
like polarization we hypothesize that information concerning the
preferred geometric orientations or internal anisotropic physical-
dielectric properties will be retrieved unambiguously. With a
complete description of polarization properties there should be an
increase in the number of ice forms that may be categorized and that
computer algorithms may be simplified because of the ability to better
select an optimum set of parameters from the scattering matrix.
Resolution requirements may be able to be relaxed because of
improvements in discrimination capability. A second aspect involves
the modeling of ice forms from new to young first-year ice. A major
question here is prompted by the apparent ability to adequately model
what appear to be a lossy dielectric half-space with using either
surface scattering and a volume scattering model approachs. In the
case of surface scattering, the key model parameters include the
complex permitivity of the ice sheet and the surface roughness
statistics (i.e. the spatial correlation length and the rms height).
The key parameters in the volume scattering model approach include
describing the ice sheet as an anisotropic medium due to the enclosed
brine pockets with a random permittivity with a tilt angle and a
three-dimensional correlation function with a variance, and horizontal
and vertical correlation lengths. These two approaches are modeled in
Figure 4. One of the goals of this investigation is to validate these
competing approaches.

a) Surface Scatter Model

b) Volume Scatter Model
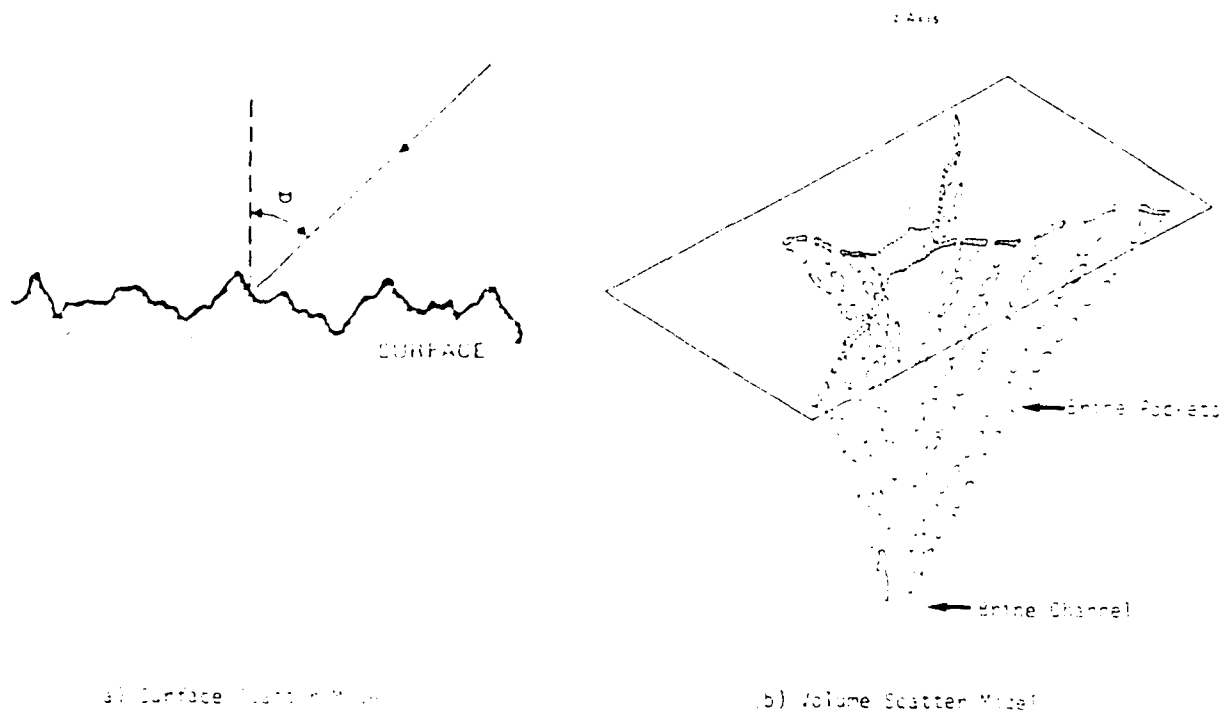
Figure 4. Surface and Volume Scattering Model Approximation Used
to Describe the Backscatter of New and Young First-Year
Ice.

12

4. OBSERVATIONS

An ice sheet was allowed to grow over a 2-month period. Observations were made of open water, 5-mm thick new ice, 8-cm thick grey ice, 12-cm thick grey ice which had a rough, air-ice interface (rms roughness of about 0.5 cm), and 12-cm thick grey ice with a liquid film water on its surface, and 20-cm thick ice which had undergone desalination and showed some of the characteristics associated with multiyear. These observations are summarized in Table 2.

During the period from 11 to 18 January, air temperatures ranged from -26°C to 2°C and ice surface temperatures from -16°C to -1.8°C (See Figure 5). The second ice sheet from which the data provided in this report were obtained, grew to about 15 cm. Its growth time plot is provided in Figure 6. Salinity profiles of the ice sheet were obtained in two locations by Tony Gow, (CRREL) for the period from 14 January to 8 February. These salinity versus depth data for the north and south ends of the tank are included in Figures 7 and 8, respectively. They are also provided in tabular form in Table 3. Temperature profile data (courtesy of Tony Gow, CRREL) for the period from 12 to 28 January is found in Figure 9. Surface roughness data were acquired for the calculation of roughness statistics. In Table 4, the statistical characterization of surface roughness are provided in terms of the surface height root-mean-square (rms) deviation and correlation length. The number of samples and length of samples prepared are also included.

Table 2.

OBSERVED SCENES DURING 1988

Open Water (θ = 45 to 55 Degrees)

New Ice ($\Delta z \cong 5$ mm)

Grey Ice ($\Delta z \cong 12$ cm)

Rough Grey Ice ($\Delta z \cong 12$ cm) With 1 cm Roughness Elements

Rough Grey Ice ($\Delta z \cong 12$ cm) With 2 cm Roughness Elements

Warrn Grey Ice ($\Delta z \cong 12$ cm)

Desalinated Grey Ice ($\Delta z \cong 20$ cm)

CRRELEX '88 ICE TEMP VS TIME (January)

CRRELEX '88 AIR TEMP VS TIME (January)
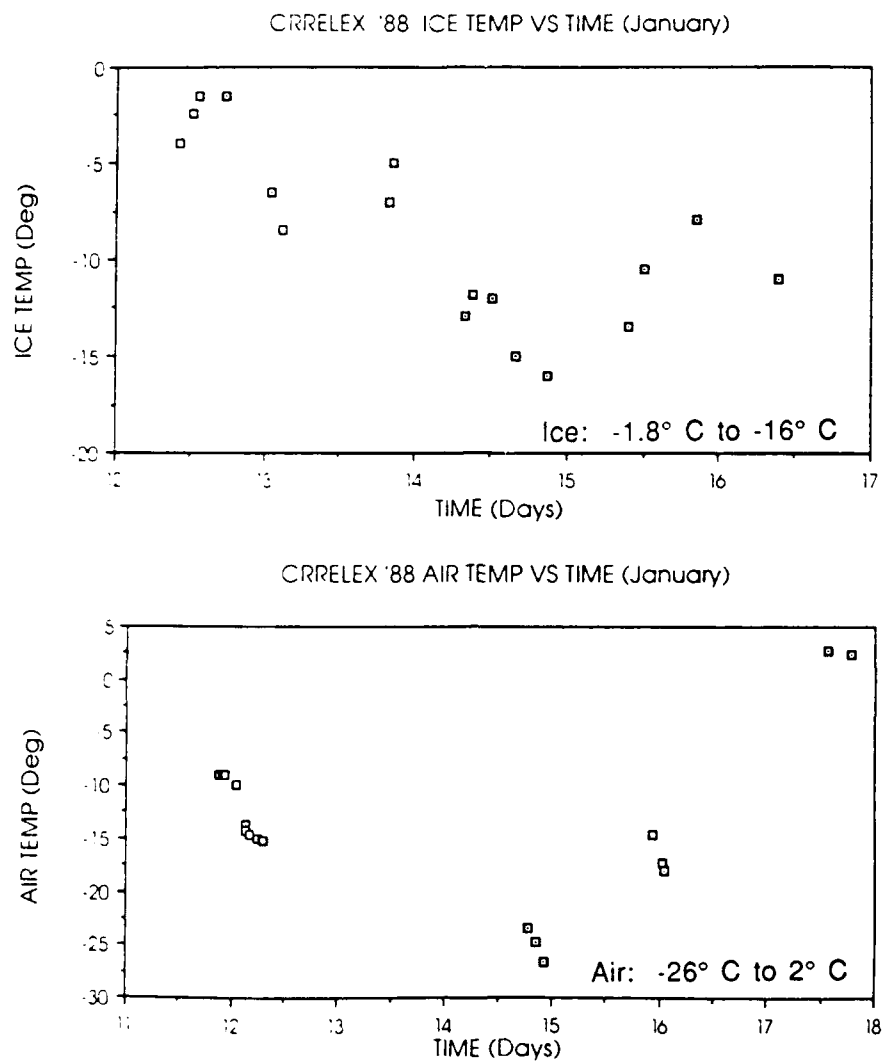
Figure 5.   CRRELEX '88 Ice and Air Temperature for the Period From 11
            to 18 January

15

CRRELEX '88 ICE THICKNESS VS TIME (January)
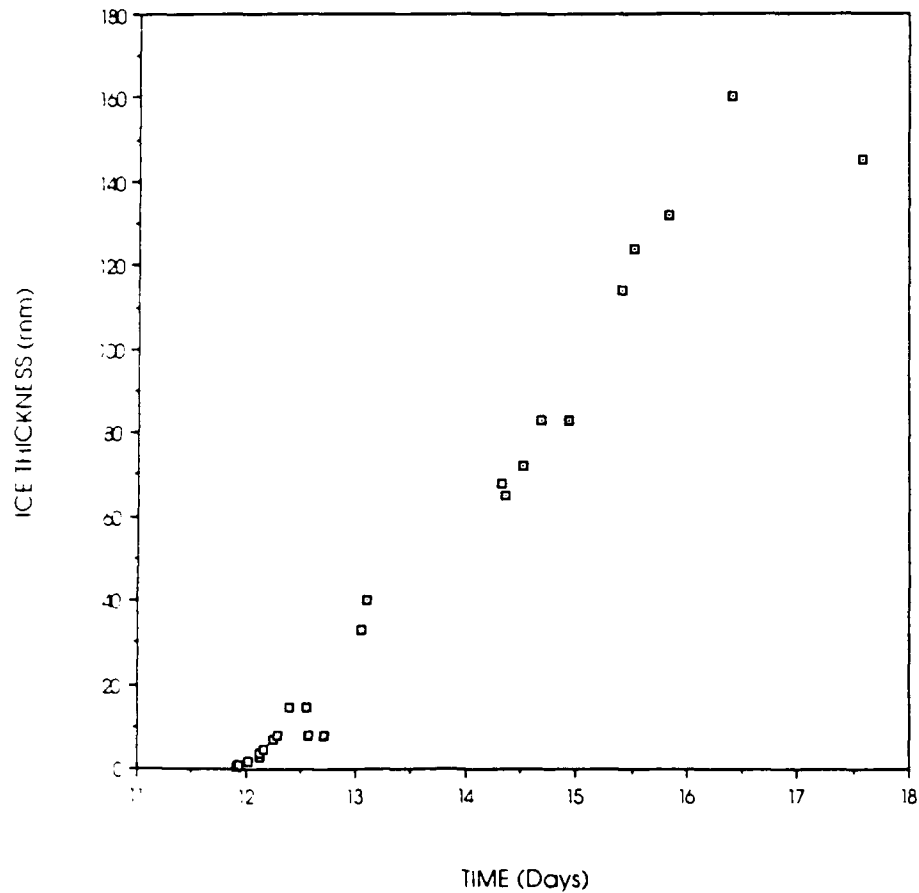
Figure 6.   CRRELEX '88 Ice Thickness Growth-Time Response for 12 to 18
            January

16
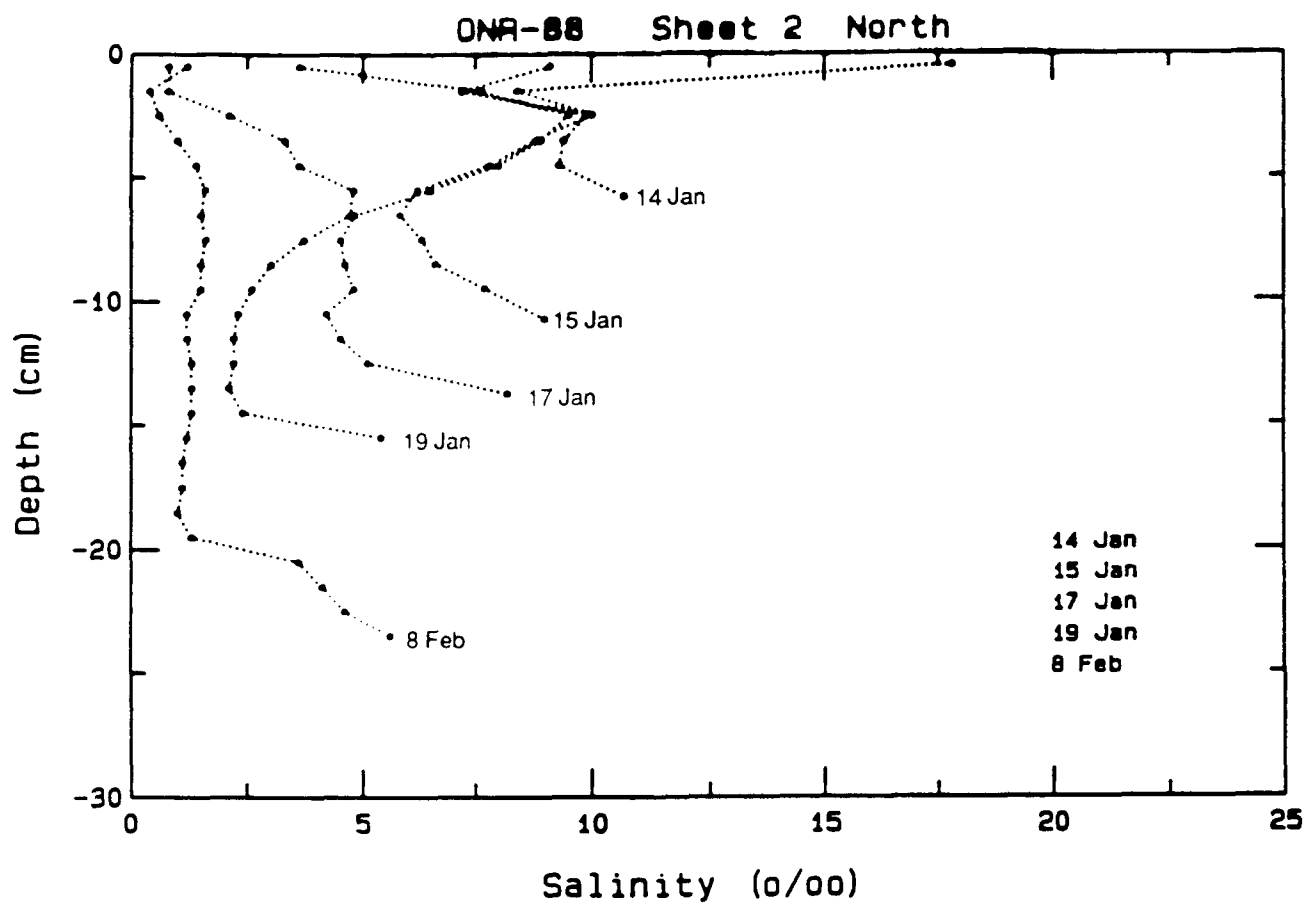
Figure 7. Salinity: ONR '88 Sheet #2 North End of Tank
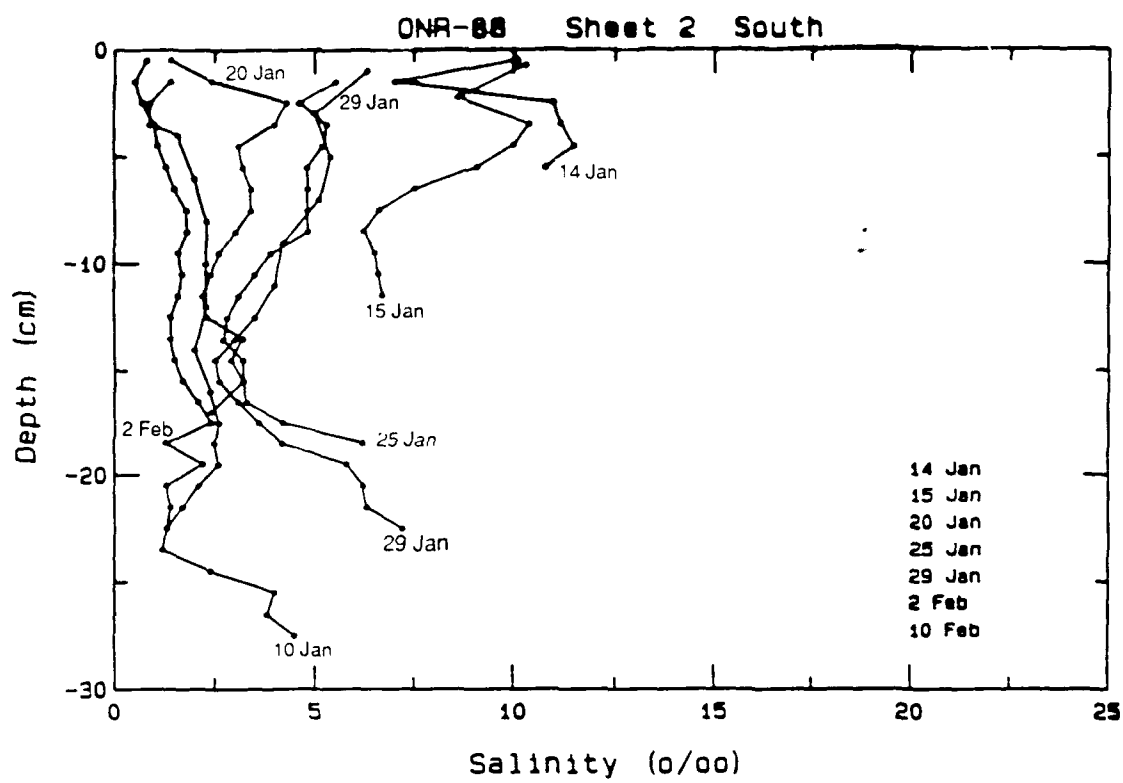
Figure 8. Salinity: ONR '88 Sheet #2 South End of Tank

18

Table 3.

SALINITY PROFILE DATA FROM 14 AND 15 JANUARY DURING CRRELEX '88

Sheet 2

Date	Depth Range	S0/00	Date	Depth Range	S0/00
14 January	0-1	9.1	14 January	0-1	10.1
(North)	1-2	7.2	(South)	1-2	7.0
	2-3	9.9		2-3	11.0
	3-4	9.4		3-4	11.2
	4-5	9.3		4-5	11.5
	5-6.5	10.7		5-6.5	10.8
15 January	0-1	17.8	15 January	0-1$\frac{1}{2}$	10.3
(North)	1-2	8.4	(South)	1$\frac{1}{2}$-3	8.6
	2-3	10.0		3-4	10.4
	3-4	8.8		4-5	10.0
	4-5	7.8		5-6	9.1
	5-6	6.2		6-7	7.5
	6-7	5.8		7-8	6.6
	7-8	6.3		8-9	6.2
	8-9	6.6		9-10	6.5
	9-10	7.7		10-11	6.6
	10-11.5	9.0		11-12	6.7

Ice Growth Began 11 January 1988 at 2030.

19
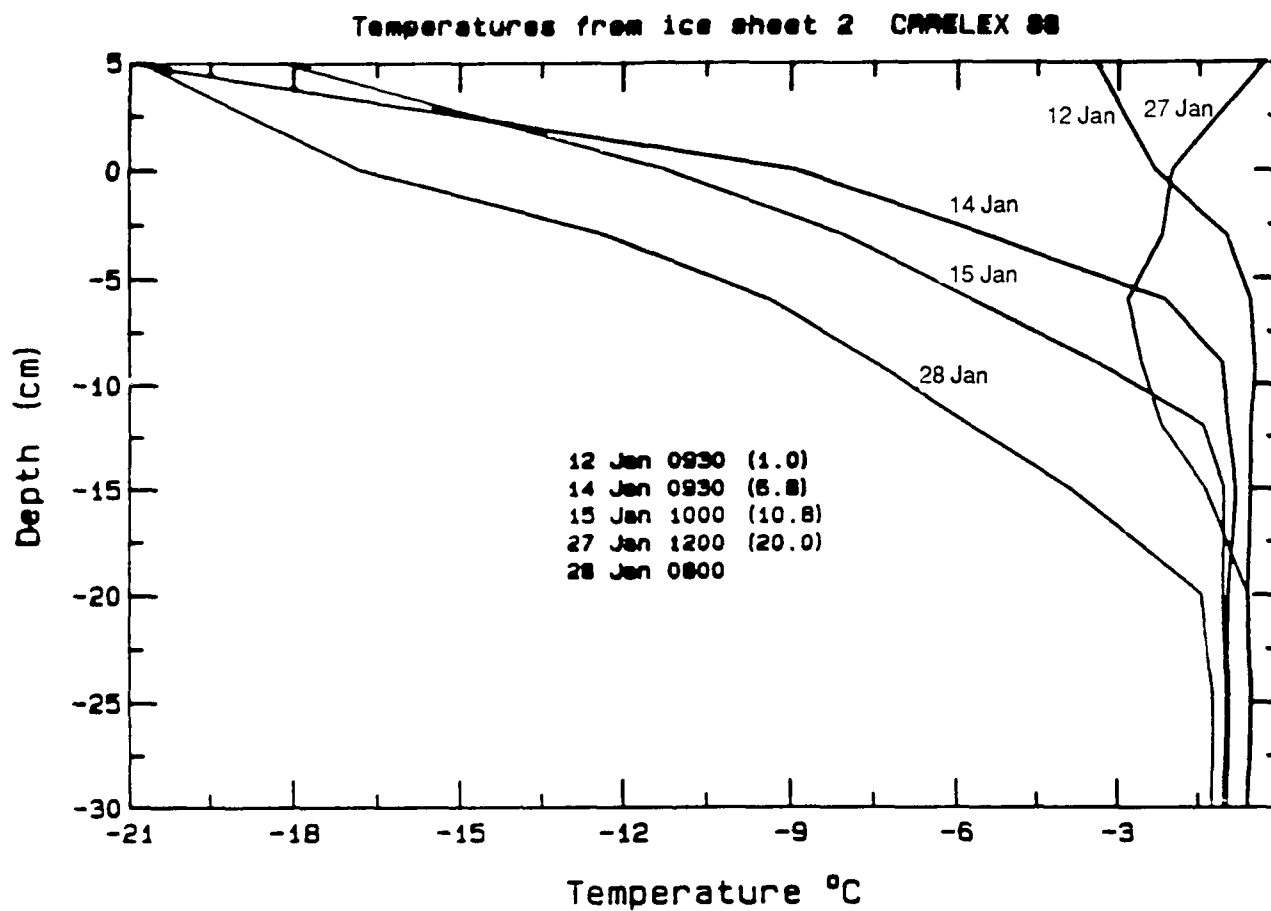
Figure 9.   CRRELEX '88:   Temperature Profiles for Ice Sheet 2 for the
Period from 12 to 28 January

Table 4.

CRRELEX '88
SURFACE ROUGHNESS RESULTS

Date	$T \Delta Z - T_0$ -hr-	ΔZ ice -cm-	σ -cm-	l -cm-	Samples	Sample Lengths -cm-	Comments
14 Jan	63.5	6.5	0.048	0.669	1	25	Top Surface
14 Jan	63.5	6.5	0.048	0.821	1	24	Bottom Surface
16 Jan	113	13	0.051 ± .003	1.635 ± .370	3	20	
15 Jan	99	8	0.544 ± .053	1.481 ± .334	4	23 to 55	Ice Roughened Using Cubed Ice (2 Layers)
15 Jan	95	8	0.611 ± .095	2.157 ± .862	2	25	Ice Roughened Using Cubed Ice (1 Layer)

21

5. DATA SET DESCRIPTION

Included in this data report are data acquired on the 14th and
15th of January. A two part experiment series was performed in which
an ice sheet, with its physical-electrical-chemical properties
changing slowly over time, was observed and then modified by adding a
layer of cold fresh water ice cubes, and then observed again to
determine the effect in the change in surface roughness. Photographs
of cross-section cuts made from ice slabs retrieved before and after
the cubes were placed on the surface are shown in Figures 10 and 11.
Radar measurements were made at 5.0 and 10.0 GHz and have been
included here. Data description parameters for these two scenes are
summarized in Tables 5 and 6. In the processing of these data the
target scattering matrices were calibrated based upon data collected
from trihedral corner reflectors, dihedrals oriented at 22.5°, and
dihedrals oriented at 45°. For the scenes, in this case the smooth
grey ice sheet, in which the ice sheet is very smooth and produced
specular backscatter responses, the near nadir response caused by the
convolution of the coherent scattering cross-section response and the
system radiation pattern response was determined and extracted to
obtain true scattering cross-sections. A paper is being written to
detail the operations performed here. Averages of the scattering
matrices generated from independent spatial samples are provided in
the form of covariance and Mueller matrices using the forms provided
in Figure 12. Angular response plots of the radar scattering
coefficients are provided in Appendix A. A comparison between the
very rough and slightly rough ice scenes at C- and X-band are shown in
Figure 13 to 22 for illustration. The covariance and Mueller matrix
data are provided in Appendix B.
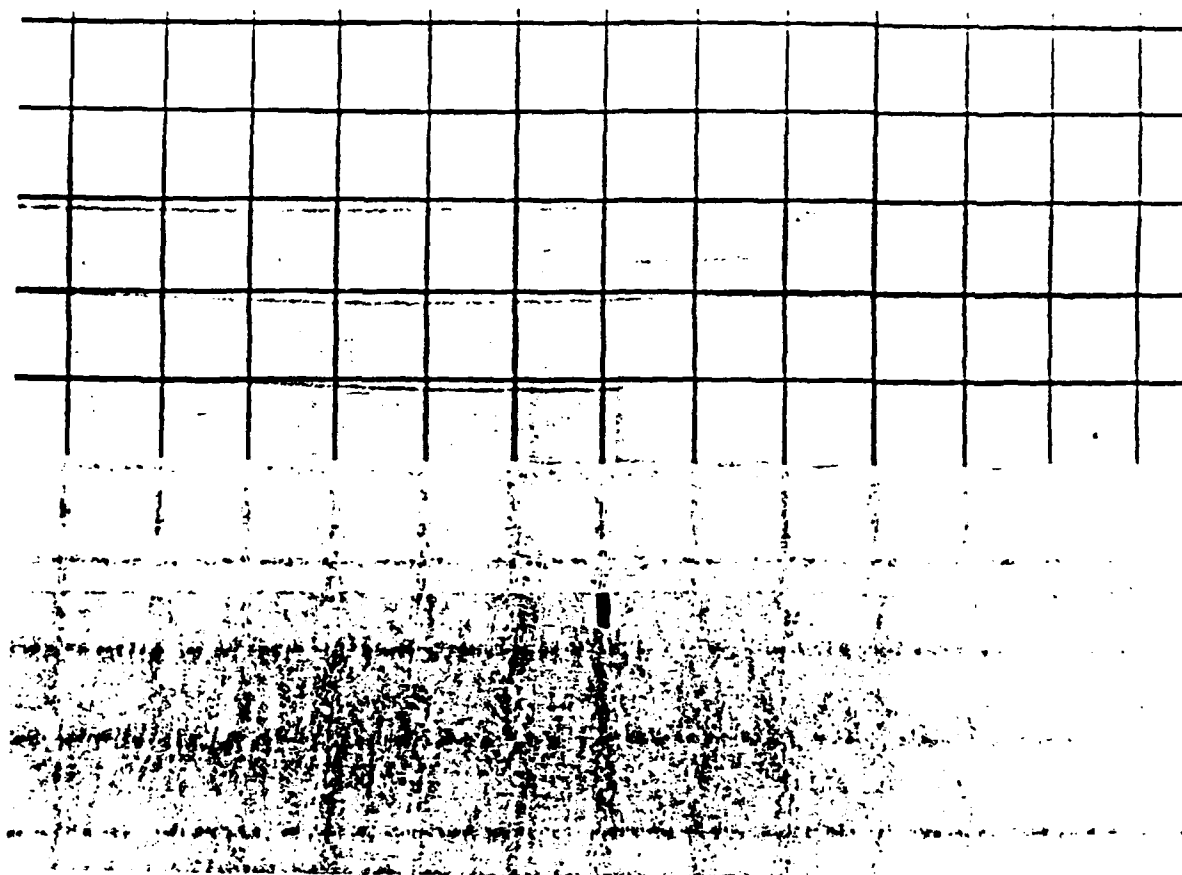
Figure 10.   Vertical Thick Section Showing the Air-Ice Interface for Slightly Rough Grey Ice on 14 January 88.
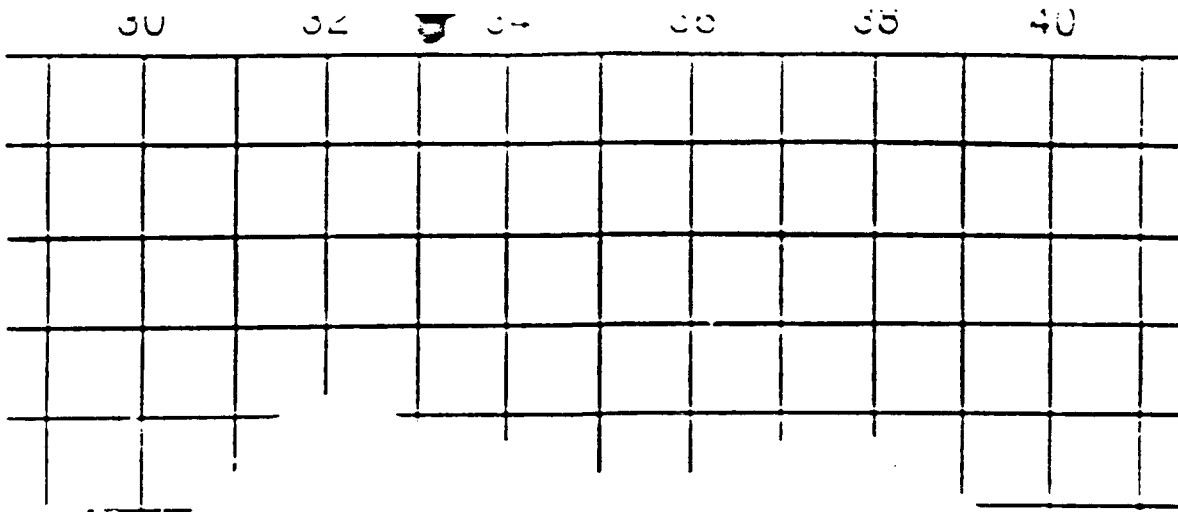
Figure 11. Vertical Thick Section Showing the Air-Ice Interface
for Very Rough Grey Ice on 15 January 88

Table 5. Grey Ice Sheet Observations on 14 January 1988

Date	14 January 88
Time Period	1910 to 2300
Scene	Bare Grey Ice (Sheet #2)
Age	70 hours
Thickness	75 mm
Roughness	
Height	0.048 cm rms
Correl. Length	0.669 cm
Tair	-23.5°C to -26.6°C
Tice	-16.0°C

Table 6. Rough Grey Ice Sheet Observations on 15 January 1988

Date	14 & 15 January 88
Time Period	2300 to 0130
Scene	Rough Grey Ice (Sheet #2)
Age	100 hours
Thickness	132 mm
Roughness	Cubes Formed 2.5 cm Thick Layer
Height	0.544 ± .053 cm rms
Correl. Length	1.481 ± .334 cm
Tair	-14.62°C to -18.1°C
Tice	-8.0°C (T=2016)

$\overline{\overline{M}}$ is defined by

$$\begin{pmatrix} |f_{hh}|^2 & |f_{hv}|^2 & \mathrm{Re}(f_{hv}f_{hh}^*) & -\mathrm{Im}(f_{hv}f_{hh}^*) \\ |f_{vh}|^2 & |f_{vv}|^2 & \mathrm{Re}(f_{vv}f_{vh}^*) & -\mathrm{Im}(f_{vv}f_{vh}^*) \\ 2\mathrm{Re}(f_{vh}f_{hh}^*) & 2\mathrm{Re}(f_{vv}f_{hv}^*) & \mathrm{Re}(f_{vv}f_{hh}^* + f_{hv}f_{vh}^*) & -\mathrm{Im}(f_{vv}f_{hh}^* - f_{vh}f_{hv}^*) \\ 2\mathrm{Im}(f_{vh}f_{hh}^*) & 2\mathrm{Im}(f_{vv}f_{hv}^*) & \mathrm{Im}(f_{vv}f_{hh}^* + f_{vh}f_{hv}^*) & \mathrm{Re}(f_{vv}f_{hh}^* - f_{vh}f_{hv}^*) \end{pmatrix}$$

$$\overline{\overline{C}} = \begin{pmatrix} |f_{hh}|^2 & f_{hh}f_{vh}^* & f_{hh}f_{vv}^* \\ f_{vh}f_{hh}^* & |f_{vh}|^2 & f_{vh}f_{vv}^* \\ f_{vv}f_{hh}^* & f_{vv}f_{vh}^* & |f_{vv}|^2 \end{pmatrix}$$

Figure 12. Forms of the modified Mueller $\bar{\bar{M}}$ and covariance $\bar{\bar{C}}$ matrices where fpq denotes the complex amplitude information which is a function of the polarizations p and q. The letters h and v denote horizontal and vertical, respectively.
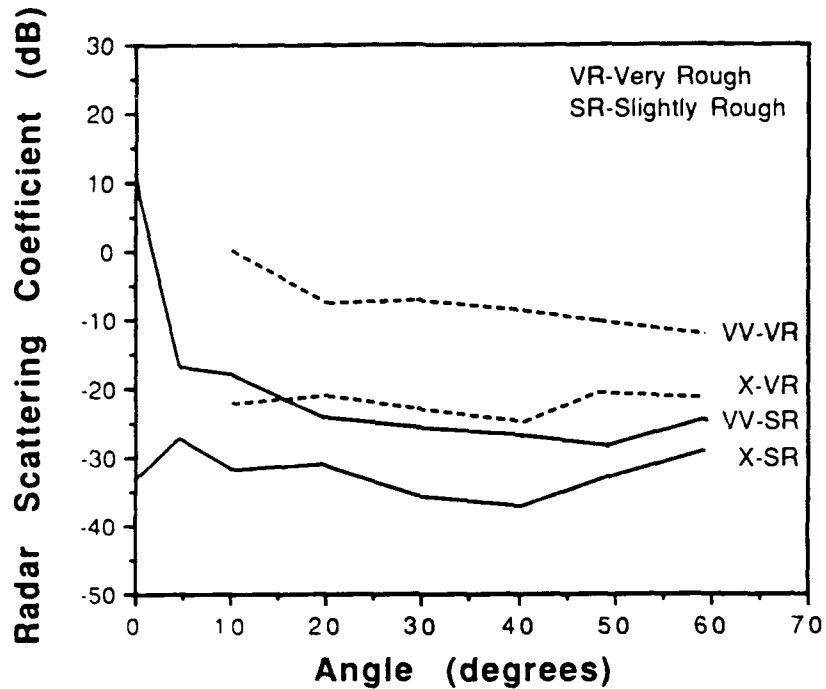
Figure 13: Radar scattering coefficient response for ice with a very
rough surface (VR) and slightly rough surface (SR) for like and cross
polarizations at 5.0 GHz.
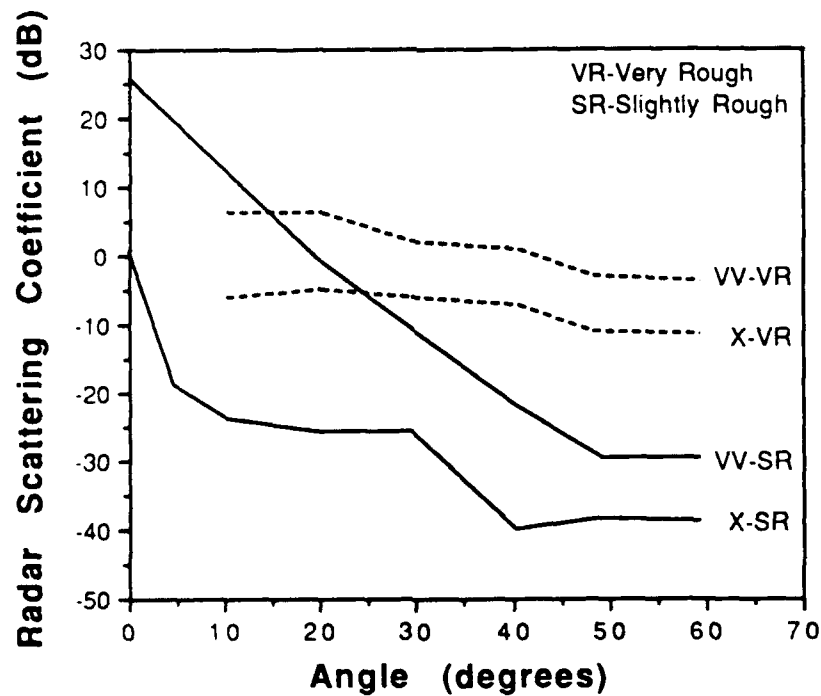
Figure 14: Radar scattering coefficient response for ice with a very
rough surface (VR) and slightly rough surface (SR) for like and cross
polarizations at 10.0 GHz.
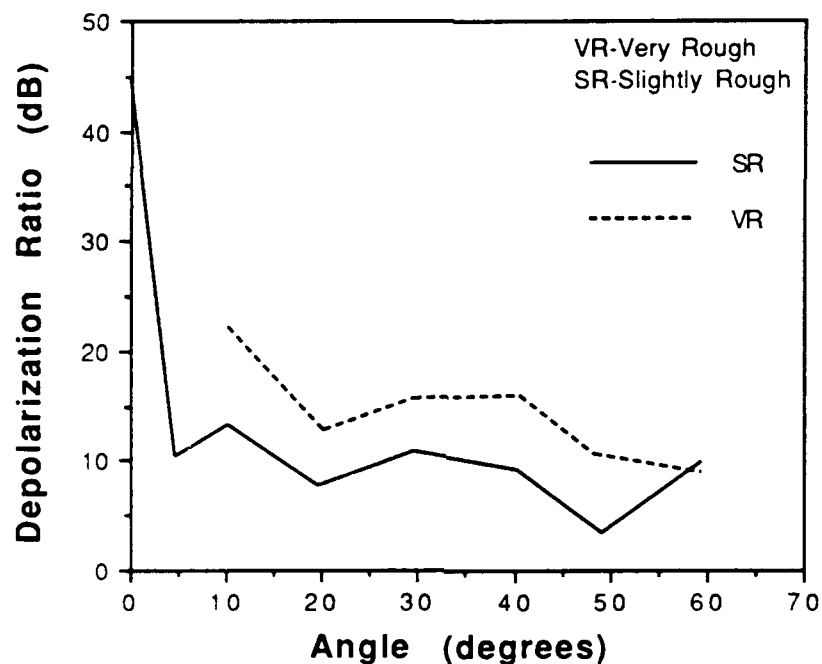
Figure 15: Depolarization response (VV + HH)/ (VH + HV) for ice with a very rough surface (VR) and slightly rough surface (SR) for like and cross polarizations at 5.0 GHz.
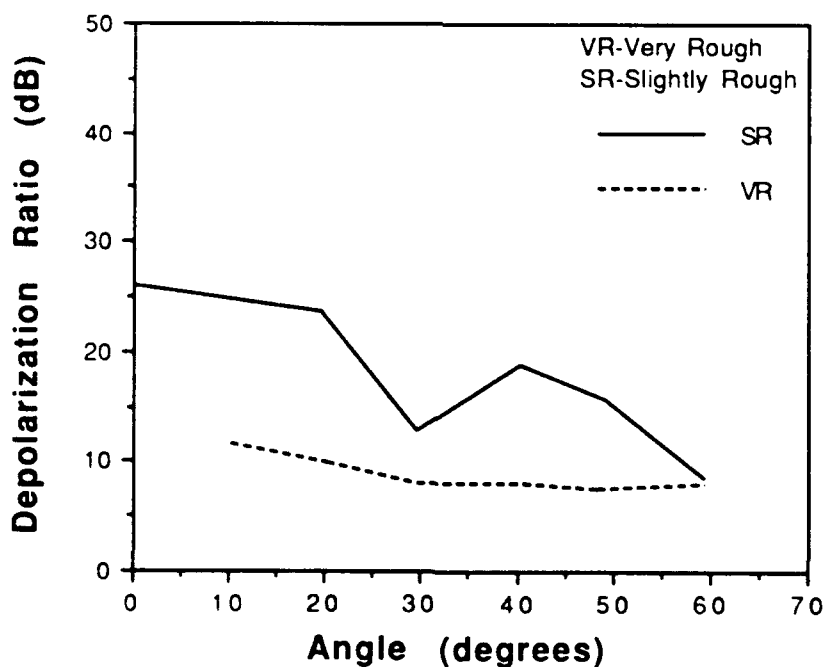
Figure 16: Depolarization response (VV + HH)/ (VH + HV) for ice with a very rough surface (VR) and slightly rough surface (SR) for like and cross polarizations at 10.0 GHz.

29
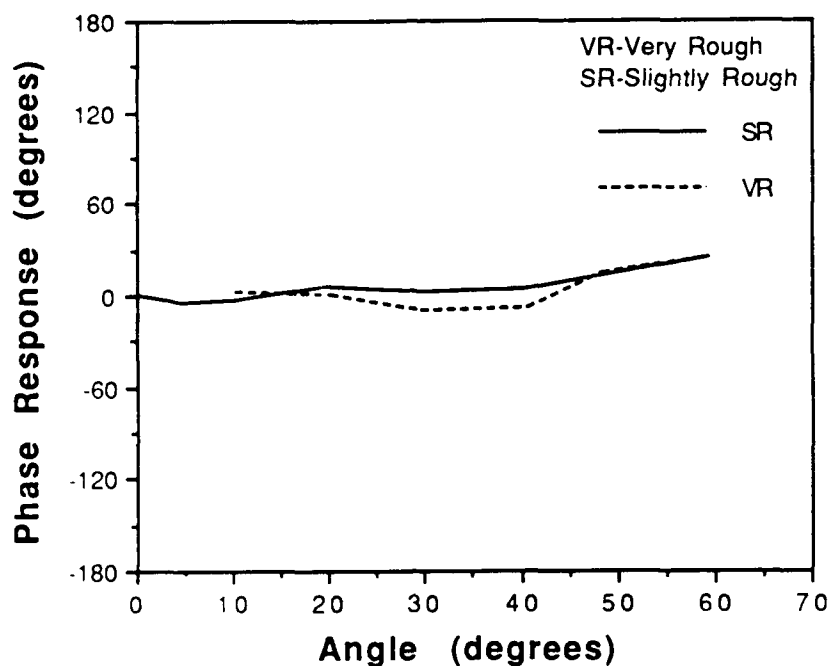
Figure 17: Phase difference (HH - VV) response for ice with a very rough surface (VR) and slightly rough surface (SR) for like and cross polarizations at 5.0 GHz.
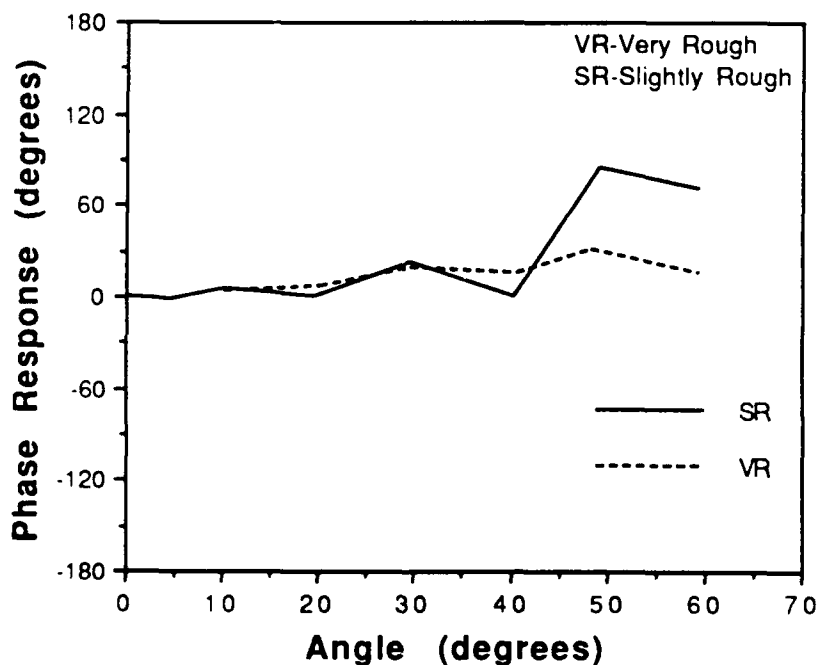
Figure 18: Phase difference (HH - VV) response for ice with a very rough surface (VR) and slightly rough surface (SR) for like and cross polarizations at 10.0 GHz.
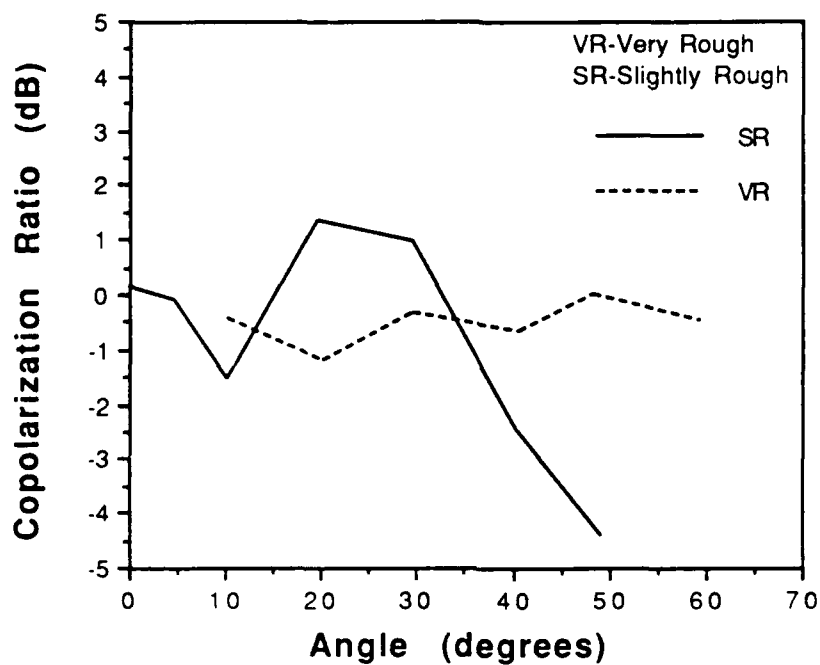
Figure 19: Copolarization response (VV / HH) for ice with a very rough surface (VR) and slightly rough surface (SR) for like and cross polarizations at 5.0 GHz.
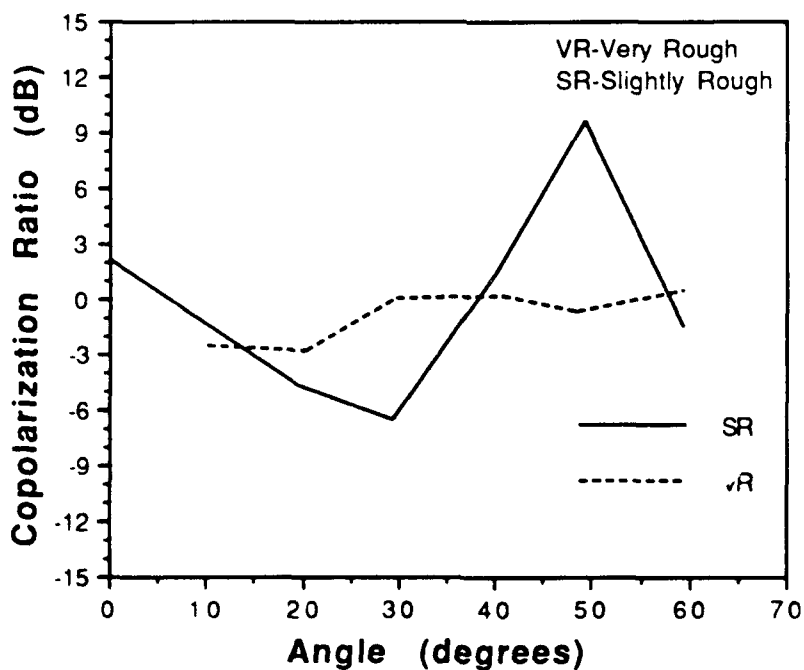
Figure 20: Copolarization response (VV / HH) for ice with a very rough surface (VR) and slightly rough surface (SR) for like and cross polarizations at 10.0 GHz.

31
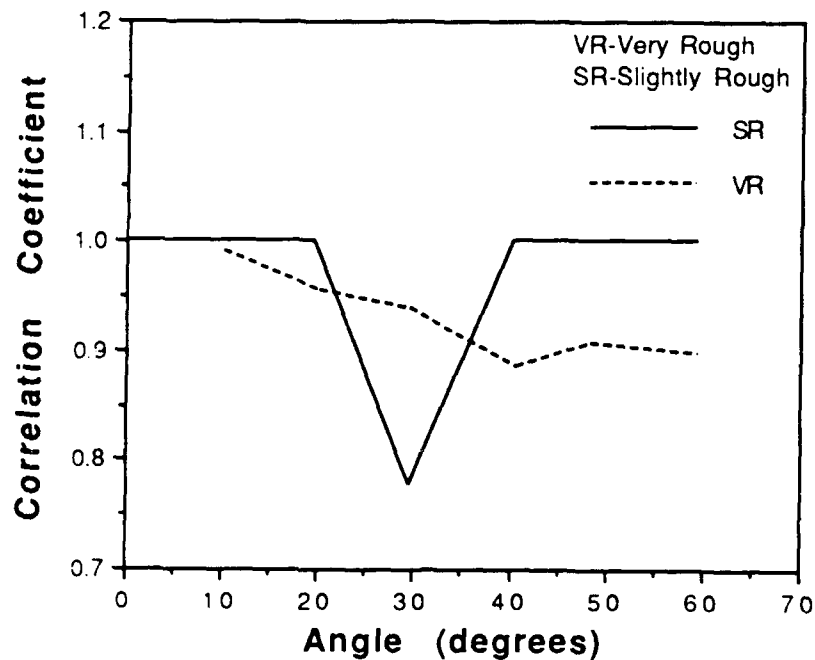
Figure 21: Correlation coefficient response for ice with a very rough surface (VR) and slightly rough surface (SR) for like and cross polarizations at 5.0 GHz.
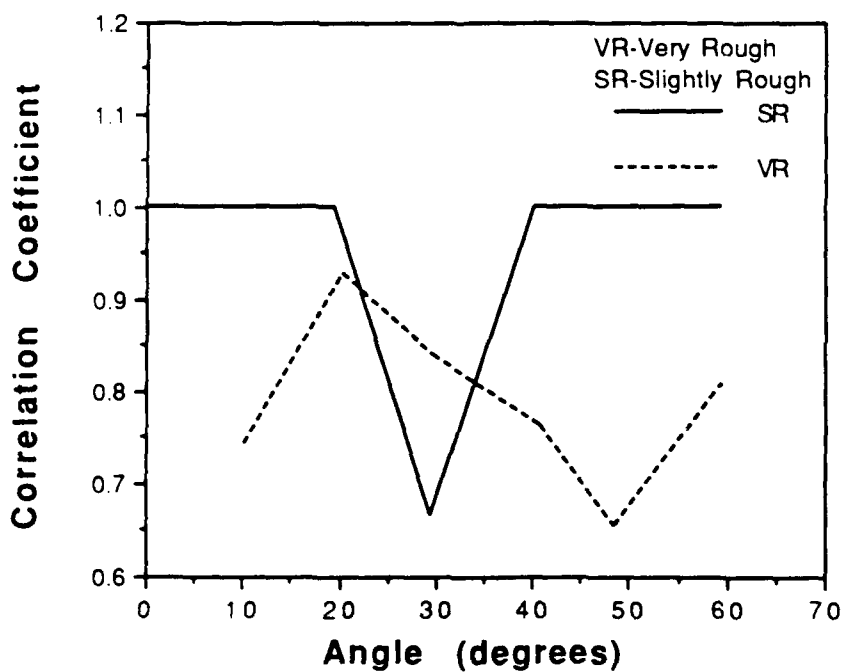
Figure 22: Correlation coefficient response for ice with a very rough surface (VR) and slightly rough surface (SR) for like and cross polarizations at 10.0 GHz.

6. CONCLUSIONS

Absolute backscatter levels for new to grey ice are small, except for the large, coherent returns at vertical. The backscatter responses of new, grey, rough grey, and desalinated first-year ice at linear polarization were found to be dissimilar. This was further demonstrated by examining their polarization signatures.

Results show that, in general, the backscatter response at VV and HH polarizations are similar at angles from vertical to 40 degrees, with the possibility of a few dB of spreading at the larger angles. Examination of the change in the Fresnel reflection coefficients at large angles explain the degree of separation. The nearly identical returns at VH and HV suggest reciprocity, i.e., that VH = HV. The rapidly decaying angular response and the large separation between like and cross polarized returns, especially between vertical to 20 degrees, are characteristic of scatter from a dielectric with a smooth surface in which there is sufficient penetration to produce a small volume scatter. This is necessary to generate the cross-polarized return. Study of the measurement system response to cross-polarization isolation will also be required to validate these conclusions.

ERIM

REFERENCES

1. Carver, K.R. and R.H. Lang, Workshop on Microwave Scattering and Emission from the Earth's surface, held at George Washington University, Washington, DC, April 1985.

APPENDIX A

Average Radar Scattering Cross-Section σ^o and Phase Difference
(HH/VV) Angular Response Data for 14 and 15 January 1988.

1988 CRREL Experiment
14 January C-Band Set A
Average RCS Magnitude
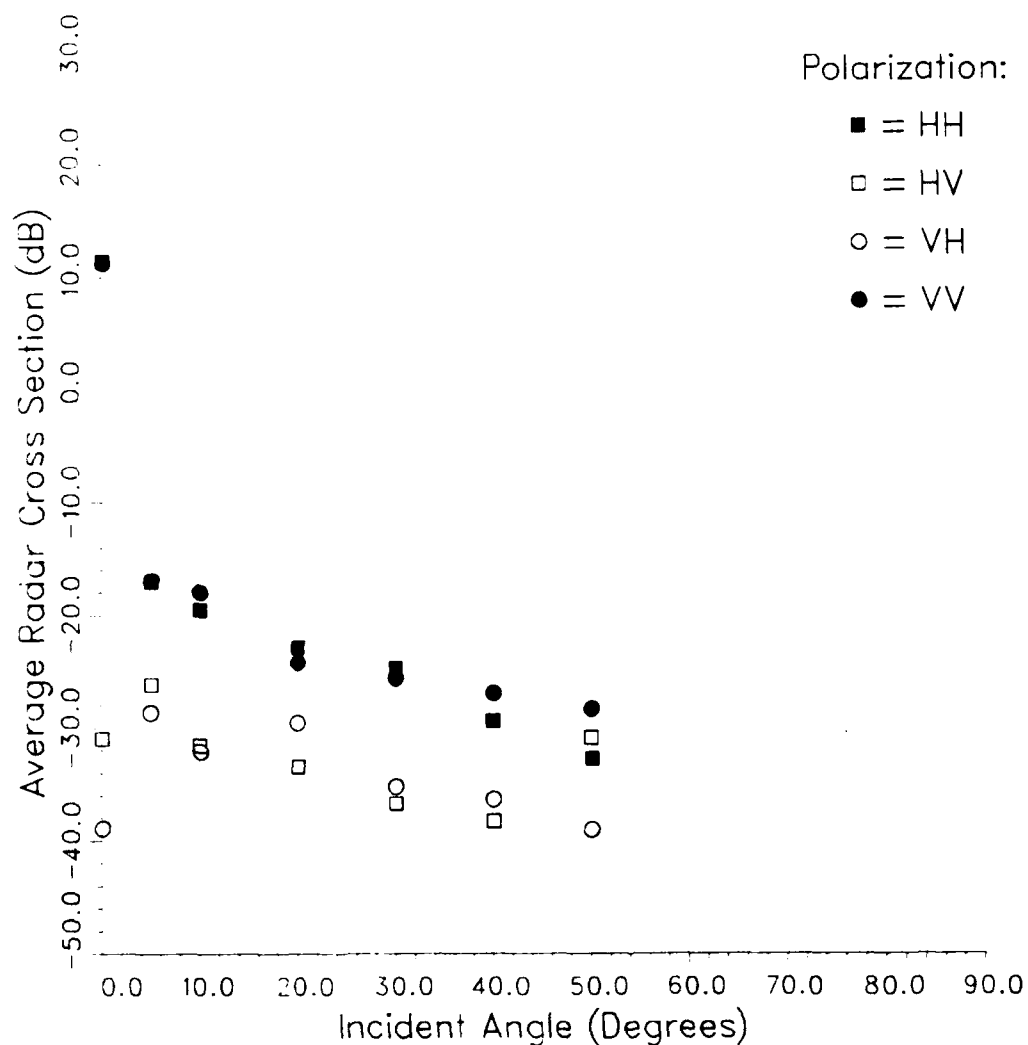
Polarization:
■ = HH
□ = HV
○ = VH
● = VV

1988 CRREL Experiment
14 January C-Band Set A
Average HH-VV Phase

1988 CRREL Experiment
14 January X-Band Set A
Average RCS Magnitude

Polarization:

■ = HH

□ = HV

○ = VH

● = VV

Average Radar Cross Section (dB)

Incident Angle (Degrees)

1988 CRREL Experiment
14 January X-Band Set A
Average HH-VV Phase

Average RCS Phase Difference (Degrees)

180.0
120.0
60.0
0.0
-60.0
-120.0
-180.0

0.0 10.0 20.0 30.0 40.0 50.0 60.0 70.0 80.0 90.0

Incident Angle (Degrees)

A-5

1988 CRREL Experiment
15 January C-Band Set A
Average RCS Magnitude

1988 CRREL Experiment
15 January C-Band Set A
Average HH-VV Phase

1988 CRREL Experiment
15 January X-Band Set A
Average RCS Magnitude

Polarization:

- ■ = HH
- □ = HV
- ○ = VH
- ● = VV

1988 CRREL Experiment
15 January X-Band Set A
Average HH-VV Phase

A-9
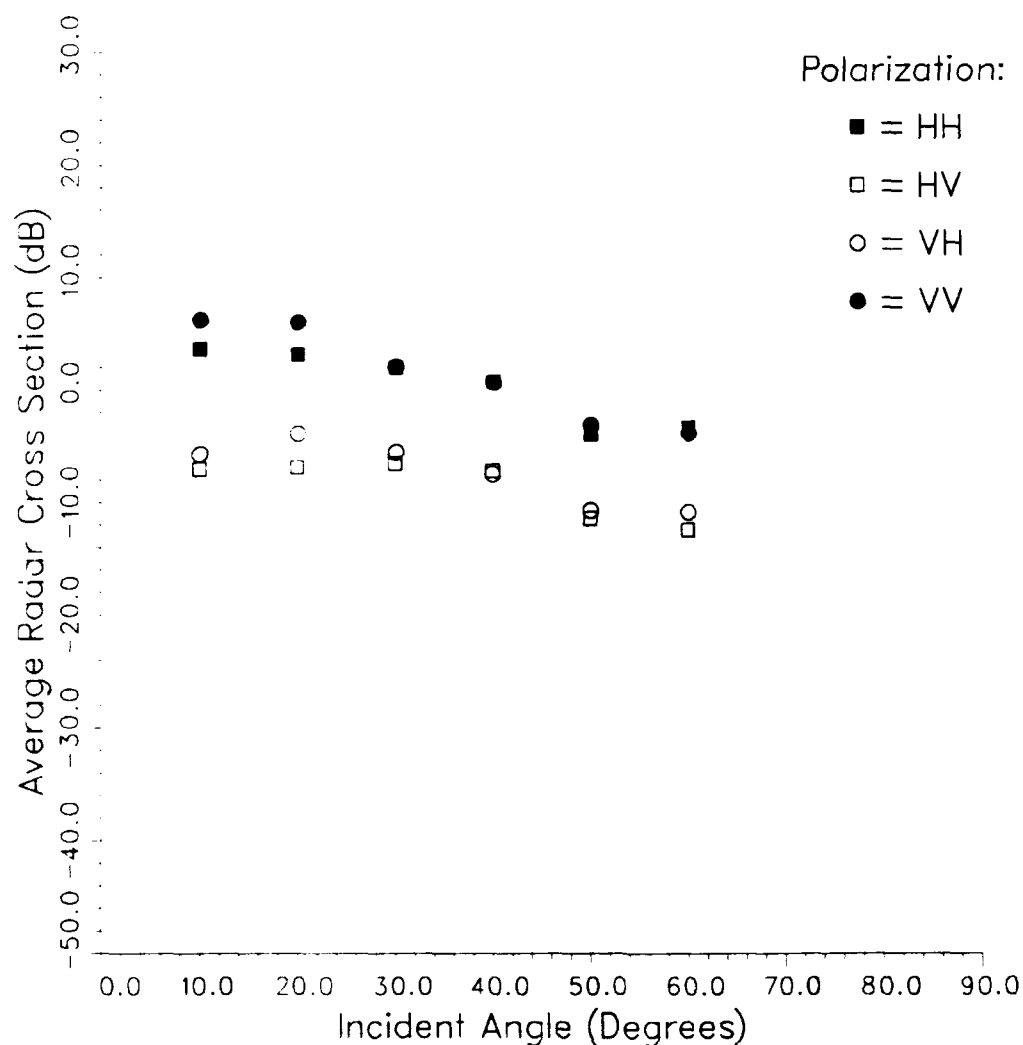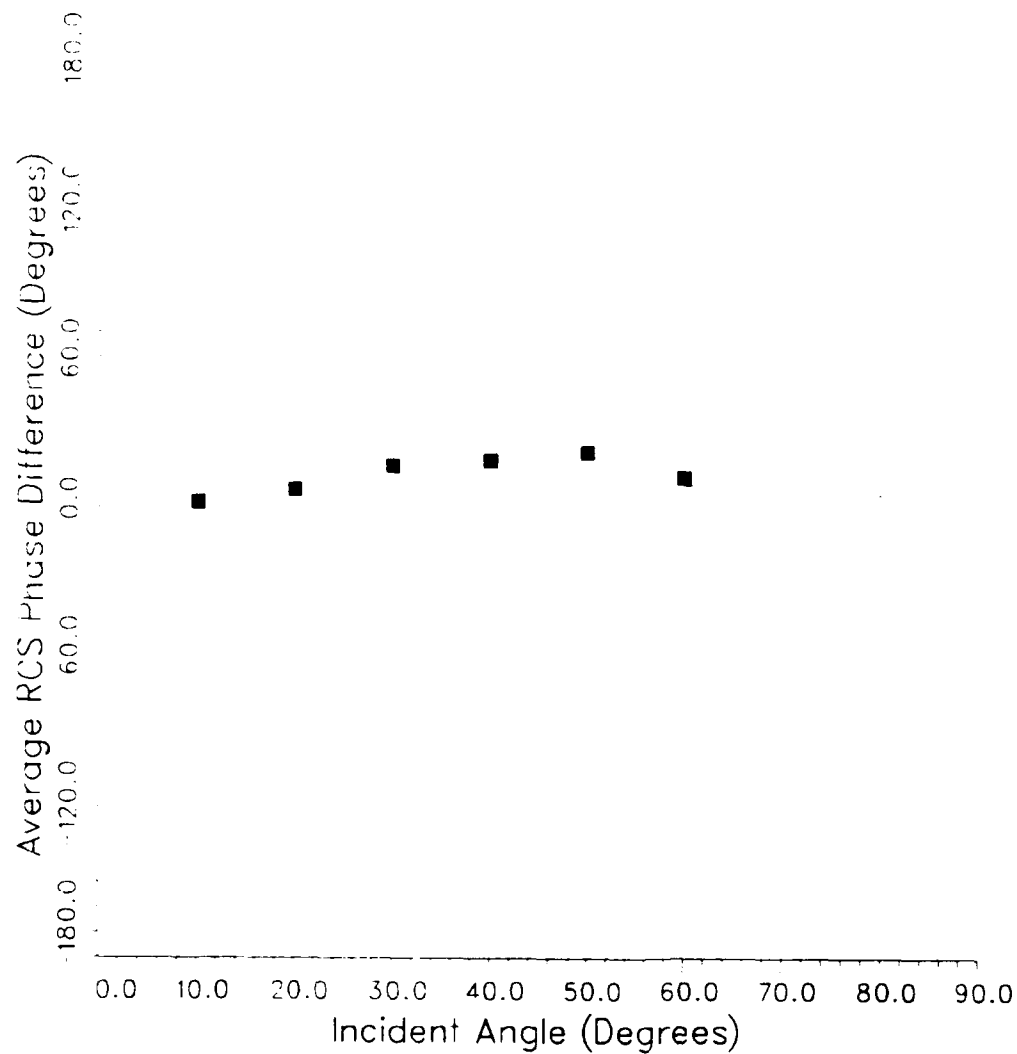
APPENDIX B

Average Mueller and Covariance Matrix Data for 14 and 15 January
1988.

Average Mueller matrix file
Number of samples = 1

Average Mueller matrix:

0.1364583E+02	0.7998347E-03	-0.3888219E-01	-0.9696692E-01
0.1285287E-03	0.1324342E+02	0.2364647E-01	0.3380832E-01
0.4800609E-01	-0.7660916E-01	0.1344329E+02	-0.2683505E-03
0.6863627E-01	-0.1910529E+00	-0.2683505E-03	0.1344329E+02

Standard Deviation of Mueller matrices:

0.0000000E+00	0.0000000E+00	0.0000000E+00	0.0000000E+00
0.0000000E+00	0.0000000E+00	0.0000000E+00	0.0000000E+00
0.0000000E+00	0.0000000E+00	0.0000000E+00	0.0000000E+00
0.0000000E+00	0.0000000E+00	0.0000000E+00	0.0000000E+00

Average Covariance Matrix (dB,Phase)

11.351	0.00	-13.780	-55.03	11.284	0.00
-13.780	55.03	-38.911	0.00	-13.845	55.03
11.284	0.00	-13.845	-55.03	11.219	0.00

Average Covariance Matrix (Mag,Phase)

13.650	0.00	0.042	-55.03	13.440	0.00
0.042	55.03	0.000	0.00	0.041	55.03
13.440	0.00	0.041	-55.03	13.240	0.00

Standard Deviation of Covariance matrices:

0.000	0.00	0.000	0.00	0.000	0.00
0.000	0.00	0.000	0.00	0.000	0.00
0.000	0.00	0.000	0.00	0.000	0.00

Polarimetric Discriminants:

1. RCS VV	11.22	dB
2. RCS HH	11.35	dB
3. RCS X	-33.33	dB
4. Copolarization Ratio	0.13	dB
5. Depolarization Ratio	44.62	dB
6. Total Power	14.30	dB
7. Phase Relative to VV	0.00	degrees
8. Correlation Coeff.	1.000	

```
  01_14_A  RUN: 0010  C BAND   DATE: JAN 14 TIME: 21:20:00 INANG:  4.7
Average Mueller matrix file
Number of samples =  1
```

Average Mueller matrix:

0.1976969E-01	0.2415461E-02	-0.5134582E-02	-0.4624822E-02
0.1358313E-02	0.2013725E-01	-0.1369482E-02	0.5047495E-02
-0.3531116E-02	-0.9557330E-02	0.2148266E-01	-0.2501096E-02
0.9743971E-02	-0.1015974E-01	0.7964446E-03	0.2148266E-01

Standard Deviation of Mueller matrices:

0.0000000E+00	0.0000000E+00	0.0000000E+00	0.0000000E+00
0.0000000E+00	0.0000000E+00	0.0000000E+00	0.0000000E+00
0.0000000E+00	0.0000000E+00	0.0000000E+00	0.0000000E+00
0.0000000E+00	0.0000000E+00	0.0000000E+00	0.0000000E+00

Average Covariance Matrix (dB,Phase)

-17.040	0.00	-22.855	-109.92	-17.001	-4.74
-22.855	109.92	-28.671	0.00	-22.816	105.18
-17.001	4.74	-22.816	-105.18	-16.959	0.00

Average Covariance Matrix (Mag,Phase)

0.020	0.00	0.005	-109.92	0.020	-4.74
0.005	109.92	0.001	0.00	0.005	105.18
0.020	4.74	0.005	-105.18	0.020	0.00

Standard Deviation of Covariance matrices:

0.000	0.00	0.000	0.00	0.000	0.00
0.000	0.00	0.000	0.00	0.000	0.00
0.000	0.00	0.000	0.00	0.000	0.00

Polarimetric Discriminants:

1. RCS VV   -16.96 dB
2. RCS HH   -17.04 dB
3. RCS X   -27.24 dB
4. Copolarization Ratio -0.08 dB
5. Depolarization Ratio 10.24 dB
6. Total Power   -13.60 dB
7. Phase Relative to VV -4.74 degrees
8. Correlation Coeff.   1.000

01_14_A   RUN: 0009   C BAND   DATE: JAN 14 TIME: 21:12:00 INANG: 10.2
Average Mueller matrix file
Number of samples = 1

Average Mueller matrix:

0.1116863E-01	0.6966266E-03	-0.5307955E-03	0.2738361E-02
0.6180162E-03	0.1584893E-01	0.9061458E-03	0.2995630E-02
0.1215931E-02	-0.1654924E-02	0.1262487E-01	-0.7730430E-03
0.5111858E-02	0.6436177E-02	0.8282249E-03	0.1262487E-01

Standard Deviation of Mueller matrices:

0.0000000E+00	0.0000000E+00	0.0000000E+00	0.0000000E+00
0.0000000E+00	0.0000000E+00	0.0000000E+00	0.0000000E+00
0.0000000E+00	0.0000000E+00	0.0000000E+00	0.0000000E+00
0.0000000E+00	0.0000000E+00	0.0000000E+00	0.0000000E+00

Average Covariance Matrix (dB,Phase)

-19.519	0.00	-25.805	-76.62	-18.760	-3.45
-25.805	76.62	-32.090	0.00	-25.045	73.17
-18.760	3.45	-25.045	-73.17	-18.000	0.00

Average Covariance Matrix (Mag,Phase)

0.011	0.00	0.003	-76.62	0.013	-3.45
0.003	76.62	0.001	0.00	0.003	73.17
0.013	3.45	0.003	-73.17	0.016	0.00

Standard Deviation of Covariance matrices:

0.000	0.00	0.000	0.00	0.000	0.00
0.000	0.00	0.000	0.00	0.000	0.00
0.000	0.00	0.000	0.00	0.000	0.00

Polarimetric Discriminants:

1. RCS VV   -18.00 dB
2. RCS HH   -19.52 dB
3. RCS X   -31.82 dB
4. Copolarization Ratio   -1.52 dB
5. Depolarization Ratio   13.13 dB
6. Total Power   -15.48 dB
7. Phase Relative to VV   -3.45 degrees
8. Correlation Coeff.   1.000

Average Mueller matrix file
Number of samples = 1

Average Mueller matrix:

```
 0.5176069E-02      0.4528977E-03    -0.4061349E-04     0.1530549E-02
 0.1109175E-02      0.3775723E-02    -0.2007123E-02     0.3992416E-03
-0.4603730E-02      0.1528286E-03     0.4226176E-02    -0.3105708E-03
 0.1330539E-02      0.2610883E-02    -0.1061179E-02     0.4226176E-02
```

Standard Deviation of Mueller matrices:

```
0.0000000E+00      0.0000000E+00     0.0000000E+00     0.0000000E+00
0.0000000E+00      0.0000000E+00     0.0000000E+00     0.0000000E+00
0.0000000E+00      0.0000000E+00     0.0000000E+00     0.0000000E+00
0.0000000E+00      0.0000000E+00     0.0000000E+00     0.0000000E+00
```

Average Covariance Matrix (dB,Phase)

```
-22.860    0.00    -26.205 -163.88    -23.545    4.87
-26.205  163.88    -29.551    0.00    -26.890  168.75
-23.545   -4.87    -26.890 -168.75    -24.230    0.00
```

Average Covariance Matrix (Mag,Phase)

```
0.005    0.00    0.002 -163.88    0.004    4.87
0.002  163.88    0.001    0.00    0.002  168.75
0.004   -4.87    0.002 -168.75    0.004    0.00
```

Standard Deviation of Covariance matrices:

```
0.000    0.00    0.000    0.00    0.000    0.00
0.000    0.00    0.000    0.00    0.000    0.00
0.000    0.00    0.000    0.00    0.000    0.00
```

Polarimetric Discriminants:

1. RCS VV   -24.23 dB
2. RCS HH   -22.86 dB
3. RCS X   -31.07 dB
4. Copolarization Ratio   1.37 dB
5. Depolarization Ratio   7.58 dB
6. Total Power   -19.78 dB
7. Phase Relative to VV   4.87 degrees
8. Correlation Coeff.   1.000

Average Mueller matrix file
Number of samples = 9

Average Mueller matrix:

0.3392237E-02	0.2123712E-03	0.3244430E-03	-0.1544954E-04
0.2997580E-03	0.2732587E-02	-0.9584693E-04	0.4071987E-03
0.1865634E-03	0.2733726E-03	0.2402951E-02	0.5288879E-04
0.7880249E-03	-0.9766961E-05	-0.3555640E-04	0.2402951E-02

Standard Deviation of Mueller matrices:

0.5705443E-03	0.9523863E-04	0.3664935E-04	0.1027911E-02
0.5997397E-03	0.2164184E-04	0.1663427E-02	0.2653654E-03
0.3341917E-02	0.7767264E-03	0.1115412E-02	0.1349563E-02
0.5565481E-03	0.1502253E-02	0.5257352E-03	0.1115412E-02

Average Covariance Matrix (dB,Phase)

-24.695	0.00	-33.926	-76.68	-26.255	1.07
-33.926	76.68	-35.232	0.00	-33.785	103.24
-26.255	-1.07	-33.785	-103.24	-25.634	0.00

Average Covariance Matrix (Mag,Phase)

0.003	0.00	0.000	-76.68	0.002	1.07
0.000	76.68	0.000	0.00	0.000	103.24
0.002	-1.07	0.000	-103.24	0.003	0.00

Standard Deviation of Covariance matrices:

0.001	0.00	0.002	-9.46	0.001	-49.07
0.002	9.46	0.001	0.00	0.002	-9.06
0.001	49.07	0.002	9.06	0.000	0.00

Polarimetric Discriminants:

1. RCS VV	-25.63	dB
2. RCS HH	-24.70	dB
3. RCS X	-35.92	dB
4. Copolarization Ratio	0.94	dB
5. Depolarization Ratio	10.78	dB
6. Total Power	-21.78	dB
7. Phase Relative to VV	1.07	degrees
8. Correlation Coeff.	0.778	

```
      01_14_A  RUN: 0005  C BAND   DATE: JAN 14 TIME: 20:20:00 INANG: 40.3
Average Mueller matrix file
Number of samples =  1

Average Mueller matrix:

   0.1145513E-02      0.1479109E-03     -0.3314410E-03      0.2440916E-03
   0.2312064E-03      0.2009093E-02     -0.4504516E-03     -0.5114767E-03
  -0.7341283E-03     -0.8290401E-03      0.1696179E-02      0.1354098E-03
  -0.7214260E-03      0.7080670E-03     -0.8310520E-04      0.1696179E-02

Standard Deviation of Mueller matrices:

   0.0000000E+00      0.0000000E+00      0.0000000E+00      0.0000000E+00
   0.0000000E+00      0.0000000E+00      0.0000000E+00      0.0000000E+00
   0.0000000E+00      0.0000000E+00      0.0000000E+00      0.0000000E+00
   0.0000000E+00      0.0000000E+00      0.0000000E+00      0.0000000E+00

Average Covariance Matrix (dB,Phase)

    -29.408    0.00    -32.885  135.50    -28.190    4.13
    -32.885 -135.50    -36.360    0.00    -31.665 -131.37
    -28.190   -4.13    -31.665  131.37    -26.970    0.00

Average Covariance Matrix (Mag,Phase)

     0.001    0.00     0.001  135.50     0.002    4.13
     0.001 -135.50     0.000    0.00     0.001 -131.37
     0.002   -4.13     0.001  131.37     0.002    0.00

Standard Deviation of Covariance matrices:

     0.000    0.00     0.000    0.00     0.000    0.00
     0.000    0.00     0.000    0.00     0.000    0.00
     0.000    0.00     0.000    0.00     0.000    0.00


Polarimetric Discriminants:

1. RCS VV              -26.97 dB
2. RCS HH              -29.41 dB
3. RCS X               -37.22 dB
4. Copolarization Ratio  -2.44 dB
5. Depolarization Ratio   9.20 dB
6. Total Power         -24.52 dB
7. Phase Relative to VV   4.13 degrees
8. Correlation Coeff.     1.000
```

Average Mueller matrix file
Number of samples = 1

Average Mueller matrix:

0.5308844E-03	0.8184647E-03	-0.3015116E-03	0.5861747E-03
0.1250259E-03	0.1465547E-02	0.3534895E-03	0.2414055E-03
-0.5135536E-03	-0.4471863E-03	-0.5628178E-03	-0.8505330E-03
0.4195106E-04	-0.2144299E-02	0.2596681E-03	-0.5628178E-03

Standard Deviation of Mueller matrices:

0.0000000E+00	0.0000000E+00	0.0000000E+00	0.0000000E+00
0.0000000E+00	0.0000000E+00	0.0000000E+00	0.0000000E+00
0.0000000E+00	0.0000000E+00	0.0000000E+00	0.0000000E+00
0.0000000E+00	0.0000000E+00	0.0000000E+00	0.0000000E+00

Average Covariance Matrix (dB,Phase)

-32.750	0.00	-35.890	-175.33	-30.545	-141.00
-35.890	175.33	-39.031	0.00	-33.685	34.33
-30.545	141.00	-33.685	-34.33	-28.339	0.00

Average Covariance Matrix (Mag,Phase)

0.001	0.00	0.000	-175.33	0.001	-141.00
0.000	175.33	0.000	0.00	0.000	34.33
0.001	141.00	0.000	-34.33	0.001	0.00

Standard Deviation of Covariance matrices:

0.000	0.00	0.000	0.00	0.000	0.00
0.000	0.00	0.000	0.00	0.000	0.00
0.000	0.00	0.000	0.00	0.000	0.00

Polarimetric Discriminants:

1. RCS VV   -28.34 dB
2. RCS HH   -32.75 dB
3. RCS X   -33.26 dB
4. Copolarization Ratio   -4.41 dB
5. Depolarization Ratio   3.26 dB
6. Total Power   -25.32 dB
7. Phase Relative to VV -141.00 degrees
8. Correlation Coeff.   1.000

Average Mueller matrix file
Number of samples = 1

Average Mueller matrix:

0.2009093E-01	0.8147043E-03	0.2617867E-03	-0.4037281E-02
0.1682675E-02	0.3589218E-02	-0.2162176E-02	-0.1168109E-02
-0.1158789E-01	-0.1162424E-02	0.7609494E-02	0.4554925E-02
-0.9730631E-03	-0.3216423E-02	-0.2239013E-02	0.7609494E-02

Standard Deviation of Mueller matrices:

0.0000000E+00	0.0000000E+00	0.0000000E+00	0.0000000E+00
0.0000000E+00	0.0000000E-00	0.0000000E+00	0.0000000E+00
0.0000000E+00	0.0000000E+00	0.0000000E+00	0.0000000E+00
0.0000000E+00	0.0000000E-00	0.0000000E+00	0.0000000E+00

Average Covariance Matrix (dB,Phase)

-16.970	0.00	-22.355	175.20	-20.710	23.58
-22.355	-175.20	-27.739	0.00	-26.095	-151.62
-20.710	-23.58	-26.095	151.62	-24.450	0.00

Average Covariance Matrix (Mag,Phase)

0.020	0.00	0.006	175.20	0.008	23.58
0.006	-175.20	0.002	0.00	0.002	-151.62
0.008	-23.58	0.002	151.62	0.004	0.00

Standard Deviation of Covariance matrices:

0.000	0.00	0.000	0.00	0.000	0.00
0.000	0.00	0.000	0.00	0.000	0.00
0.000	0.00	0.000	0.00	0.000	0.00

Polarimetric Discriminants:

1. RCS VV	-24.45	dB
2. RCS HH	-16.97	dB
3. RCS X	-29.04	dB
4. Copolarization Ratio	7.48	dB
5. Depolarization Ratio	9.77	dB
6. Total Power	-15.82	dB
7. Phase Relative to VV	23.58	degrees
8. Correlation Coeff.	1.000	

Average Mueller matrix file
Number of samples = 1

Average Mueller matrix:

0.6039485E+03	0.2113489E-01	-0.3439773E+01	0.9655808E+00
0.2421029E+01	0.3664375E+03	0.2707741E+02	-0.1240844E+02
0.6952439E+02	-0.5358704E+01	0.4702628E+03	0.1463063E+00
-0.3186011E+02	0.1504245E+01	0.1463063E+00	0.4702628E+03

Standard Deviation of Mueller matrices:

0.0000000E+00	0.0000000E+00	0.0000000E+00	0.0000000E+00
0.0000000E+00	0.0000000E+00	0.0000000E+00	0.0000000E+00
0.0000000E+00	0.0000000E+00	0.0000000E+00	0.0000000E+00
0.0000000E+00	0.0000000E+00	0.0000000E+00	0.0000000E+00

Average Covariance Matrix (dB,Phase)

27.810	0.00	15.825	24.62	26.725	0.00
15.825	-24.62	3.840	0.00	14.740	-24.62
26.725	0.00	14.740	24.62	25.640	0.00

/ erage Covariance Matrix (Mag,Phase)

603.900	0.00	38.236	24.62	470.400	0.00
38.236	-24.62	2.421	0.00	29.788	-24.62
470.400	0.00	29.788	24.62	366.400	0.00

Standard Deviation of Covariance matrices:

0.000	0.00	0.000	0.00	0.000	0.00
0.000	0.00	0.000	0.00	0.000	0.00
0.000	0.00	0.000	0.00	0.000	0.00

Polarimetric Discriminants:

1. RCS VV   25.64 dB
2. RCS HH   27.81 dB
3. RCS X   0.87 dB
4. Copolarization Ratio   2.17 dB
5. Depolarization Ratio   25.99 dB
6. Total Power   29.88 dB
7. Phase Relative to VV   0.00 degrees
8. Correlation Coeff.   1.000

Average Mueller matrix file
Number of samples = 1

Average Mueller matrix:

0.1002306E-09	0.1140250E-01	-0.1062599E-05	-0.1173122E-06
0.1538155E-01	0.1002306E-09	0.2774105E-06	0.1210267E-05
0.4950917E-06	-0.2118782E-05	-0.1200284E-02	-0.1318891E-01
0.2433453E-05	-0.2868474E-06	-0.1318891E-01	-0.1200284E-02

Standard Deviation of Mueller matrices:

0.0000000E+00	0.0000000E+00	0.0000000E+00	0.0000000E+00
0.0000000E+00	0.0000000E-00	0.0000000E+00	0.0000000E+00
0.0000000E+00	0.0000000E+00	0.0000000E+00	0.0000000E+00
0.0000000E+00	0.0000000E-00	0.0000000E+00	0.0000000E+00

Average Covariance Matrix (dB,Phase)

-99.991	0.00	-59.059	-78.50	-99.990	-1.41
-59.059	78.50	-18.130	0.00	-59.061	77.09
-99.990	1.41	-59.061	-77.09	-99.991	0.00

Average Covariance Matrix (Mag,Phase)

0.000	0.00	0.000	-78.50	0.000	-1.41
0.000	78.50	0.015	0.00	0.000	77.09
0.000	1.41	0.000	-77.09	0.000	0.00

Standard Deviation of Covariance matrices:

0.000	0.00	0.000	0.00	0.000	0.00
0.000	0.00	0.000	0.00	0.000	0.00
0.000	0.00	0.000	0.00	0.000	0.00

Polarimetric Discriminants:

1. RCS VV   -99.99 dB
2. RCS HH   -99.99 dB
3. RCS X   -18.73 dB
4. Copola-ization Ratio   0.00 dB
5. Depolarization Ratio -81.26 dB
6. Total Power   -15.72 dB
7. Phase Relative to VV   -1.41 degrees
8. Correlation Coeff.   1.000

```
   01_14_A   RUN: 0009   X BAND    DATE: JAN 14 TIME: 21:12:00 INANG: 10.2
Average Mueller matrix file
Number of samples =  1


Average Mueller matrix:

  0.1002306E-09      0.9225712E-03     -0.3039816E-06      0.8066253E-08
  0.7277799E-02      0.1002306E-09     -0.8033883E-06     -0.2898713E-06
 -0.1652858E-05     -0.6039741E-06      0.2523761E-02      0.5872971E-03
 -0.4311533E-06      0.7137822E-07      0.5872971E-03      0.2523761E-02


Standard Deviation of Mueller matrices:

  0.0000000E+00      0.0000000E+00      0.0000000E+00      0.0000000E+00
  0.0000000E+00      0.0000000E+00      0.0000000E+00      0.0000000E+00
  0.0000000E+00      0.0000000E+00      0.0000000E+00      0.0000000E+00
  0.0000000E+00      0.0000000E+00      0.0000000E+00      0.0000000E+00


Average Covariance Matrix (dB,Phase)

    -99.991     0.00    -60.685   165.38    -99.990     5.22
    -60.685  -165.38    -21.380     0.00    -60.685  -160.16
    -99.990    -5.22    -60.685   160.16    -99.991     0.00


Average Covariance Matrix (Mag,Phase)

     0.000     0.00     0.000   165.38     0.000     5.22
     0.000  -165.38     0.007     0.00     0.000  -160.16
     0.000    -5.22     0.000   160.16     0.000     0.00


Standard Deviation of Covariance matrices:

     0.000     0.00     0.000     0.00     0.000     0.00
     0.000     0.00     0.000     0.00     0.000     0.00
     0.000     0.00     0.000     0.00     0.000     0.00



Polarimetric Discriminants:

1. RCS VV               -99.99 dB
2. RCS HH               -99.99 dB
3. RCS X                -23.87 dB
4. Copolarization Ratio   0.00 dB
5. Depolarization Ratio -76.12 dB
6. Total Power          -20.86 dB
7. Phase Relative to VV   5.22 degrees
8. Correlation Coeff.    1.000
```

01_14_A   RUN: 0008   X BAND   DATE: JAN 14 TIME: 21:00:00 INANG: 19.6
Average Mueller matrix file
Number of samples = 1

Average Mueller matrix:

0.3111716E+00	0.5584705E-03	-0.1292612E-01	0.2587588E-02
0.4897790E-02	0.9225715E+00	-0.1173044E-01	0.6618880E-01
-0.1343735E-01	-0.4449225E-01	0.5357543E+00	-0.3441678E-03
0.7691326E-01	0.9019715E-02	-0.2962562E-02	0.5357543E+00

Standard Deviation of Mueller matrices:

0.0000000E+00	0.0000000E+00	0.0000000E+00	0.0000000E+00
0.0000000E+00	0.0000000E+00	0.0000000E+00	0.0000000E+00
0.0000000E+00	0.0000000E+00	0.0000000E+00	0.0000000E+00
0.0000000E+00	0.0000000E+00	0.0000000E+00	0.0000000E+00

Average Covariance Matrix (dB,Phase)

-5.070	0.00	-14.085	-99.91	-2.710	0.14
-14.085	99.91	-23.100	0.00	-11.725	100.05
-2.710	-0.14	-11.725	-100.05	-0.350	0.00

Average Covariance Matrix (Mag,Phase)

0.311	0.00	0.039	-99.91	0.536	0.14
0.039	99.91	0.005	0.00	0.067	100.05
0.536	-0.14	0.067	-100.05	0.923	0.00

Standard Deviation of Covariance matrices:

0.000	0.00	0.000	0.00	0.000	0.00
0.000	0.00	0.000	0.00	0.000	0.00
0.000	0.00	0.000	0.00	0.000	0.00

Polarimetric Discriminants:

1. RCS VV   -0.35 dB
2. RCS HH   -5.07 dB
3. PCS X   -25.64 dB
4. Copolarization Ratio   -4.72 dB
5. Depolarization Ratio   23.54 dB
6. Total Power   0.93 dB
7. Phase Relative to VV   0.14 degrees
8. Correlation Coeff.   1.000

B-13

01_14_A RUN: 0007 X BAND   DATE: JAN 14 TIME: 20:45:00 INANG: 29.5
Average Mueller matrix file
Number of samples = 9

Average Mueller matrix:

0.1814275E-01	0.3675611E-03	-0.6884908E-04	-0.6605790E-03
0.5100552E-02	0.8195166E-01	-0.7281893E-02	-0.6085666E-02
0.4351518E-03	-0.1683905E-02	0.2332316E-01	0.1021065E-01
0.3708761E-02	-0.1356754E-02	-0.9866958E-02	0.2332316E-01

Standard Deviation of Mueller matrices:

0.1290285E-01	0.2476112E-03	0.3514185E-03	0.2569524E-02
0.4564755E-02	0.4249974E-01	0.1022299E-03	0.2195536E-02
0.8588553E-02	0.6134886E-02	0.3215335E-01	0.1751499E-01
0.3950748E-02	0.7673441E-02	0.1836222E-01	0.3215335E-01

Average Covariance Matrix (dB,Phase)

-17.413	0.00	-27.289	-83.32	-15.912	23.05
-27.289	83.32	-22.923	0.00	-20.227	-140.12
-15.912	-23.05	-20.227	140.12	-10.864	0.00

Average Covariance Matrix (Mag,Phase)

0.018	0.00	0.002	-83.32	0.026	23.05
0.002	83.32	0.005	0.00	0.009	-140.12
0.026	-23.05	0.009	140.12	0.082	0.00

Standard Deviation of Covariance matrices:

0.013	0.00	0.005	-24.70	0.037	29.34
0.005	24.70	0.005	0.00	0.002	87.33
0.037	-29.34	0.002	-87.33	0.043	0.00

Polarimetric Discriminants:

1. RCS VV   -10.86 dB
2. RCS HH   -17.41 dB
3. RCS X   -25.63 dB
4. Copolarization Ratio   -6.55 dB
5. Depolarization Ratio   12.63 dB
6. Total Power   -9.76 dB
7. Phase Relative to VV   23.05 degrees
8. Correlation Coeff.   0.665

01_14_A   RUN: 0005   X BAND   DATE: JAN 14 TIME: 20:20:00 INANG: 40.3
Average Mueller matrix file
Number of samples = 1

Average Mueller matrix:

0.8770010E-02	0.3698280E-04	-0.4567394E-04	0.5676737E-03
0.1678804E-03	0.6280581E-02	0.1026097E-02	-0.3888062E-04
0.2423942E-02	-0.6723792E-04	0.7418718E-02	0.1564729E-03
-0.1172784E-03	0.9615473E-03	0.1037210E-05	0.7418718E-02

Standard Deviation of Mueller matrices:

0.0000000E+00	0.0000000E+00	0.0000000E+00	0.0000000E+00
0.0000000E+00	0.0000000E+00	0.0000000E+00	0.0000000E+00
0.0000000E+00	0.0000000E+00	0.0000000E+00	0.0000000E+00
0.0000000E+00	0.0000000E+00	0.0000000E+00	0.0000000E+00

Average Covariance Matrix (dB,Phase)

-20.570	0.00	-29.160	2.77	-21.295	0.60
-29.160	-2.77	-37.749	0.00	-29.885	-2.17
-21.295	-0.60	-29.885	2.17	-22.020	0.00

Average Covariance Matrix (Mag,Phase)

0.009	0.00	0.001	2.77	0.007	0.60
0.001	-2.77	0.000	0.00	0.001	-2.17
0.007	-0.60	0.001	2.17	0.006	0.00

Standard Deviation of Covariance matrices:

0.000	0.00	0.000	0.00	0.000	0.00
0.000	0.00	0.000	0.00	0.000	0.00
0.000	0.00	0.000	0.00	0.000	0.00

Polarimetric Discriminants:

1. RCS VV   -22.02 dB
2. RCS HH   -20.57 dB
3. RCS X   -39.90 dB
4. Copolarization Ratio   1.45 dB
5. Depolarization Ratio   18.66 dB
6. Total Power   -18.17 dB
7. Phase Relative to VV   0.60 degrees
8. Correlation Coeff.   1.000

Average Mueller matrix file
Number of samples = 1

Average Mueller matrix:

0.9638291E-02	0.1355189E-03	0.3290802E-04	-0.1142404E-02
0.1573983E-03	0.1064143E-02	0.3832931E-03	0.1434599E-03
0.1051964E-02	-0.7547557E-03	0.1355451E-03	0.3125389E-02
-0.2227459E-02	-0.8479286E-04	-0.3257681E-02	0.1355451E-03

Standard Deviation of Mueller matrices:

0.0000000E+00	0.0000000E+00	0.0000000E+00	0.0000000E+00
0.0000000E+00	0.0000000E+00	0.0000000E+00	0.0000000E+00
0.0000000E+00	0.0000000E+00	0.0000000E+00	0.0000000E+00
0.0000000E+00	0.0000000E+00	0.0000000E+00	0.0000000E+00

Average Covariance Matrix (dB,Phase)

-20.160	0.00	-29.094	64.72	-24.944	85.24
-29.094	-64.72	-38.030	0.00	-33.880	20.52
-24.944	-85.24	-33.880	-20.52	-29.731	0.00

Average Covariance Matrix (Mag,Phase)

0.010	0.00	0.001	64.72	0.003	85.24
0.001	-64.72	0.000	0.00	0.000	20.52
0.003	-85.24	0.000	-20.52	0.001	0.00

Standard Deviation of Covariance matrices:

0.000	0.00	0.000	0.00	0.000	0.00
0.000	0.00	0.000	0.00	0.000	0.00
0.000	0.00	0.000	0.00	0.000	0.00

Polarimetric Discriminants:

1. RCS VV   -29.73 dB
2. RCS HH   -20.16 dB
3. RCS X   -38.34 dB
4. Copolarization Ratio   9.57 dB
5. Depolarization Ratio   15.63 dB
6. Total Power   -19.59 dB
7. Phase Relative to VV   85.24 degrees
8. Correlation Coeff.   1.000

```
    01_15_A  RUN: 0032  C BAND   DATE: JAN 16 TIME: 11:08:29 INANG: 10.2
Average Mueller matrix file
Number of samples = 10


Average Mueller matrix:

   0.9398540E+00       0.6090157E-02      0.6322323E-02       0.3869399E-02
   0.5821473E-02       0.1039014E+01      0.6327598E-02      -0.9631803E-02
   0.1383620E-01       0.9903564E-02      0.9791873E+00       0.2953304E-01
  -0.1459526E-01       0.1994299E-01     -0.2544824E-01       0.9791873E+00

Standard Deviation of Mueller matrices:

   0.6707005E+00       0.1498175E-02      0.2358056E-01       0.2675904E-01
   0.3404237E-02       0.7109191E+00      0.4632493E-01       0.2558872E-01
   0.8281478E-01       0.4473582E-01      0.6868425E+00       0.1060761E-01
   0.3890819E-01       0.4943384E-01      0.1596229E-01       0.6868425E+00

Average Covariance Matrix (dB,Phase)

      -0.269    0.00    -19.976   46.53     -0.090    1.61
     -19.976  -46.53    -22.350    0.00    -19.385  -56.69
      -0.090   -1.61    -19.385   56.69      0.166    0.00

Average Covariance Matrix (Mag,Phase)

       0.940    0.00      0.010   46.53      0.979    1.61
       0.010  -46.53      0.006    0.00      0.012  -56.69
       0.979   -1.61      0.012   56.69      1.039    0.00

Standard Deviation of Covariance matrices:

       0.671    0.00      0.046  -25.17      0.682    1.12
       0.046   25.17      0.003    0.00      0.053   28.92
       0.682   -1.12      0.053  -28.92      0.711    0.00


Polarimetric Discriminants:

1. RCS VV                0.17 dB
2. RCS HH               -0.27 dB
3. RCS X               -22.25 dB
4. Copolarization Ratio  -0.44 dB
5. Depolarization Ratio  22.20 dB
6. Total Power            2.99 dB
7. Phase Relative to VV   1.61 degrees
8. Correlation Coeff.     0.991
```

01_15_A   RUN: 0022   C BAND   DATE: JAN 16 TIME: 09:58:05 INANG: 20.3
Average Mueller matrix file
Number of samples = 10

Average Mueller matrix:

0.1269704E+00	0.6360862E-02	-0.6074651E-02	0.3919881E-02
0.9068301E-02	0.1673510E+00	-0.2496575E-02	-0.9112185E-02
-0.7866858E-02	-0.1902704E-01	0.1405997E+00	0.7306580E-03
-0.1790308E-01	0.1754902E-01	0.2095750E-02	0.1405997E+00

Standard Deviation of Mueller matrices:

0.6902757E-01	0.4451009E-02	0.4442619E-02	0.3697739E-02
0.3623273E-02	0.4145854E-01	0.5880348E-02	0.3391775E-01
0.4417202E-02	0.1198436E-01	0.5417249E-01	0.6119418E-02
0.5123632E-01	0.1774387E-01	0.2804436E-02	0.5417249E-01

Average Covariance Matrix (dB,Phase)

-8.963	0.00	-20.098	113.73	-8.558	-0.28
-20.098	-113.73	-20.425	0.00·	-20.247	-105.32
-8.558	0.28	-20.247	105.32	-7.764	0.00

Average Covariance Matrix (Mag,Phase)

0.127	0.00	0.010	113.73	0.139	-0.28
0.010	-113.73	0.009	0.00	0.009	-105.32
0.139	0.28	0.009	105.32	0.167	0.00

Standard Deviation of Covariance matrices:

0.069	0.00	0.026	85.07	0.054	1.76
0.026	-85.07	0.004	0.00	0.034	-80.16
0.054	-1.76	0.034	80.16	0.041	0.00

Polarimetric Discriminants:

1. RCS VV   -7.76 dB
2. RCS HH   -8.96 dB
3. RCS X   -21.13 dB
4. Copolarization Ratio -1.20 dB
5. Depolarization Ratio 12.80 dB
6. Total Power   -5.09 dB
7. Phase Relative to VV   -0.28 degrees
8. Correlation Coeff.   0.956

O1_15_A RUN: OO13   C BAND   DATE: JAN 16 TIME: O8:57:57 INANG: 29.7
Average Mueller matrix file
Number of samples = 9

Average Mueller matrix:

```
 0.1719787E+00      0.3342652E-02      0.1616784E-02      0.1522670E-02
 0.6433079E-02      0.1867187E+00      0.4911976E-02     -0.6365882E-02
 0.1908273E-01     -0.2681602E-02      0.1671723E+00     -0.2858806E-01
-0.9308816E-02      0.5473140E-02      0.2943294E-01      0.1671723E+00
```

Standard Deviation of Mueller matrices:

```
 0.1252052E+00      0.9160410E-03      0.1675385E-02      0.8609590E-02
 0.5331845E-03      0.1164114E+00      0.1119432E-01      0.2154369E-01
 0.6342480E-02      0.9912864E-02      0.1117405E+00      0.3031259E-01
 0.3493898E-01      0.1962949E-01      0.2384578E-01      0.1117405E+00
```

Average Covariance Matrix (dB,Phase)

```
    -7.646     0.00    -19.741   25.99     -7.748    -9.95
   -19.741   -25.99    -21.916    0.00    -20.947   -52.35
    -7.748     9.95    -20.947   52.35     -7.288     0.00
```

Average Covariance Matrix (Mag,Phase)

```
     0.172     0.00      0.011   25.99      0.168    -9.95
     0.011   -25.99      0.006    0.00      0.008   -52.35
     0.168     9.95      0.008   52.35      0.187     0.00
```

Standard Deviation of Covariance matrices:

```
     0.125     0.00      0.018  -79.72      0.111   -14.06
     0.018    79.72      0.001    0.00      0.024    62.54
     0.111    14.06      0.024  -62.54      0.116     0.00
```


Polarimetric Discriminants:

1. RCS VV   -7.29 dB
2. RCS HH   -7.65 dB
3. RCS X   -23.11 dB
4. Copolarization Ratio -0.36 dB
5. Depolarization Ratio 15.65 dB
6. Total Power   -4.34 dB
7. Phase Relative to VV   -9.95 degrees
8. Correlation Coeff.   0.937

Average Mueller matrix file
Number of samples = 9

Average Mueller matrix:

0.1081651E+00	0.2709920E-02	-0.2177921E-02	-0.1502540E-02
0.3511765E-02	0.1267241E+00	0.7349306E-02	0.2953803E-03
0.9108718E-02	-0.7463287E-02	0.1021633E+00	-0.1467612E-01
0.5162742E-02	0.5121990E-02	0.1443734E-01	0.1021633E+00

Standard Deviation of Mueller matrices:

0.1397612E-01	0.3591019E-03	0.1690208E-01	0.1000354E-01
0.3519061E-03	0.1715581E-01	0.2881597E-01	0.9455880E-02
0.4365052E-01	0.4411388E-01	0.1080952E-01	0.1580600E-01
0.1103987E-01	0.1544536E-01	0.1615189E-01	0.1080952E-01

Average Covariance Matrix (dB,Phase)

-9.659	0.00	-22.811	-29.55	-9.844	-8.07
-22.811	29.55	-24.545	0.00	-21.334	2.30
-9.844	8.07	-21.334	-2.30	-8.971	0.00

Average Covariance Matrix (Mag,Phase)

0.108	0.00	0.005	-29.55	0.104	-8.07
0.005	29.55	0.004	0.00	0.007	2.30
0.104	8.07	0.007	-2.30	0.127	0.00

Standard Deviation of Covariance matrices:

0.014	0.00	0.023	14.19	0.021	49.24
0.023	-14.19	0.000	0.00	0.030	-18.17
0.021	-49.24	0.030	18.17	0.017	0.00

Polarimetric Discriminants:

1. RCS VV   -8.97 dB
2. RCS HH   -9.66 dB
3. RCS X   -25.07 dB
4. Copolarization Ratio   -0.69 dB
5. Depolarization Ratio   15.77 dB
6. Total Power   -6.18 dB
7. Phase Relative to VV   -8.07 degrees
8. Correlation Coeff.   0.885

Average Mueller matrix file
Number of samples = 5

Average Mueller matrix:

0.9369382E-01	0.4137609E-02	-0.5250036E-03	-0.2170575E-02
0.1189678E-01	0.9334470E-01	-0.1676074E-01	0.1221437E-01
-0.2198932E-01	-0.8111399E-02	0.8538236E-01	0.2131577E-01
0.3614878E-01	-0.9823559E-02	-0.1735384E-01	0.8538236E-01

Standard Deviation of Mueller matrices:

0.1480781E-01	0.5003523E-02	0.7077865E-03	0.2468224E-01
0.8089664E-03	0.1280686E-01	0.5401239E-02	0.1768973E-01
0.1211688E-01	0.2651861E-02	0.3265873E-02	0.3222272E-02
0.2639526E-01	0.4336460E-01	0.2765836E-02	0.3265873E-02

Average Covariance Matrix (dB,Phase)

-10.283	0.00	-16.746	-121.31	-10.715	13.17
-16.746	121.31	-19.245	0.00	-16.832	143.92
-10.715	-13.17	-16.832	-143.92	-10.299	0.00

Average Covariance Matrix (Mag,Phase)

0.094	0.00	0.021	-121.31	0.085	13.17
0.021	121.31	0.012	0.00	0.021	143.92
0.085	-13.17	0.021	-143.92	0.093	0.00

Standard Deviation of Covariance matrices:

0.015	0.00	0.015	-65.34	0.005	33.14
0.015	65.34	0.001	0.00	0.018	73.02
0.005	-33.14	0.018	-73.02	0.013	0.00

Polarimetric Discriminants:

1. RCS VV   -10.30 dB
2. RCS HH   -10.28 dB
3. RCS X   -20.96 dB
4. Copolarization Ratio   0.02 dB
5. Depolarization Ratio   10.67 dB
6. Total Power   -6.92 dB
7. Phase Relative to VV   13.17 degrees
8. Correlation Coeff.   0.907

Average Mueller matrix file
Number of samples = 5

Average Mueller matrix:

0.5363394E-01	0.4468897E-02	0.6601255E-02	0.5164735E-02
0.9761373E-02	0.5972799E-01	-0.6973383E-02	0.6653366E-02
-0.5997235E-02	0.1715822E-01	0.4453234E-01	0.2192730E-01
0.2174884E-01	-0.4041471E-02	-0.2063802E-01	0.4453234E-01

Standard Deviation of Mueller matrices:

0.1454986E-01	0.9082993E-02	0.5245155E-02	0.1456661E-01
0.1726112E-02	0.2448384E-02	0.6851107E-02	0.2305886E-01
0.2692482E-01	0.3722223E-01	0.3791615E-01	0.1665341E-01
0.8620939E-02	0.8114000E-02	0.3058408E-01	0.3791615E-01

Average Covariance Matrix (dB,Phase)

-12.706	0.00	-19.477	-105.42	-12.941	24.77
-19.477	105.42	-20.105	0.00	-20.161	136.35
-12.941	-24.77	-20.161	-136.35	-12.238	0.00

Average Covariance Matrix (Mag,Phase)

0.054	0.00	0.011	-105.42	0.051	24.77
0.011	105.42	0.010	0.00	0.010	136.35
0.051	-24.77	0.010	-136.35	0.060	0.00

Standard Deviation of Covariance matrices:

0.015	0.00	0.014	-17.75	0.039	-37.11
0.014	17.75	0.002	0.00	0.024	73.46
0.039	37.11	0.024	-73.46	0.002	0.00

Polarimetric Discriminants:

1. RCS VV   -12.24 dB
2. RCS HH   -12.71 dB
3. RCS X   -21.48 dB
4. Copolarization Ratio   -0.47 dB
5. Depolarization Ratio   9.01 dB
6. Total Power   -8.94 dB
7. Phase Relative to VV   24.77 degrees
8. Correlation Coeff.   0.898

Average Mueller matrix file
Number of samples = 10

Average Mueller matrix:

```
 0.2305057E+01      0.1967947E+00      0.2250885E+00      0.2503940E+00
 0.2677150E+00      0.4187535E+01     -0.6152098E+00     -0.1690820E+00
-0.5318984E+00      0.3974928E+00      0.2252922E+01      0.1245258E+00
-0.1010559E+00     -0.3293315E-01     -0.1220732E+00      0.2252922E+01
```

Standard Deviation of Mueller matrices:

```
 0.1851115E+01      0.3441177E-01      0.2996719E+00      0.6487030E-01
 0.3928870E-02      0.2694741E+01      0.1228545E+00      0.5729320E+00
 0.1700192E+00      0.1307388E+01      0.1549825E+01      0.8706433E+00
 0.1245862E+00      0.7763484E+00      0.3768399E+00      0.1549825E+01
```

Average Covariance Matrix (dB,Phase)

```
  3.627    0.00     -5.674  169.25      3.633    3.06
 -5.674 -169.25     -5.723    0.00     -1.952 -164.63
  3.633   -3.06     -1.952  164.63      6.220    0.00
```

Average Covariance Matrix (Mag,Phase)

```
  2.305    0.00      0.271  169.25      2.308    3.06
  0.271 -169.25      0.268    0.00      0.638 -164.63
  2.308   -3.06      0.638  164.63      4.188    0.00
```

Standard Deviation of Covariance matrices:

```
  1.851    0.00      0.105   36.22      1.765   20.69
  0.105  -36.22      0.004    0.00      0.586   77.91
  1.765  -20.69      0.586  -77.91      2.695    0.00
```

Polarimetric Discriminants:

1. RCS VV   6.22 dB
2. RCS HH   3.63 dB
3. RCS X   -6.34 dB
4. Copolarization Ratio -2.59 dB
5. Depolarization Ratio 11.45 dB
6. Total Power   8.42 dB
7. Phase Relative to VV   3.06 degrees
8. Correlation Coeff.   0.743

01_15_A   RUN: 0022   X BAND   DATE: JAN 16 TIME: 09:55:02 INANG: 20.3
Average Mueller matrix file
Number of samples = 10

Average Mueller matrix:

0.2055983E+01	0.2037657E+00	-0.1544038E+00	0.1248436E+00
0.4050978E+00	0.3961591E+01	0.3757907E+00	-0.2049435E+00
0.5428420E+00	-0.2270354E+00	0.2708747E+01	0.4411764E+00
-0.3072005E+00	0.3069519E+00	-0.2608405E+00	0.2708747E+01

Standard Deviation of Mueller matrices:

0.1621473E+01	0.1205740E+00	0.1827779E+00	0.2898813E+00
0.1754829E+00	0.1379331E+01	0.1137566E+01	0.9259010E-01
0.1086990E+01	0.9924646E+00	0.1577411E+01	0.6125240E+00
0.1371050E-01	0.1671847E+01	0.8878970E+00	0.1577411E+01

Average Covariance Matrix (dB,Phase)

3.130	0.00	-5.060	29.51	4.230	7.62
-5.060	-29.51	-3.924	0.00	-3.685	-28.61
4.230	-7.62	-3.685	28.61	5.979	0.00

Average Covariance Matrix (Mag,Phase)

2.056	0.00	0.312	29.51	2.649	7.62
0.312	-29.51	0.405	0.00	0.428	-28.61
2.649	-7.62	0.428	28.61	3.962	0.00

Standard Deviation of Covariance matrices:

1.622	0.00	0.544	-0.73	1.807	24.53
0.544	0.73	0.176	0.00	1.141	-4.65
1.807	-24.53	1.141	4.65	1.380	0.00

Polarimetric Discriminants:

1. RCS VV   5.98 dB
2. RCS HH   3.13 dB
3. RCS X   -5.17 dB
4. Copolarization Ratio   -2.85 dB
5. Depolarization Ratio   9.95 dB
6. Total Power   8.21 dB
7. Phase Relative to VV   7.62 degrees
8. Correlation Coeff.   0.928

Average Mueller matrix file
Number of samples = 9

Average Mueller matrix:

0.1566614E+01	0.2219684E+00	0.3096237E-01	-0.5448891E-01
0.2781518E+00	0.1584334E+01	-0.3105961E+00	-0.3029896E+00
-0.8238786E+00	0.2712003E+00	0.1281607E+01	0.4526463E+00
-0.5276459E+00	-0.3225166E-01	-0.3999676E+00	0.1281607E+01

Standard Deviation of Mueller matrices:

0.1432549E+01	0.7061230E-01	0.4068727E+00	0.4576068E+00
0.2195380E+00	0.1911772E+00	0.3716350E-01	0.2199666E+00
0.1232518E+00	0.4987694E+00	0.5884373E+00	0.1004963E+01
0.6689486E-01	0.4683458E+00	0.1004651E+01	0.5884373E+00

Average Covariance Matrix (dB,Phase)

1.949	0.00	-3.105	147.36	1.213	18.81
-3.105	-147.36	-5.557	0.00	-3.626	-135.71
1.213	-18.81	-3.626	135.71	1.998	0.00

Average Covariance Matrix (Mag,Phase)

1.567	0.00	0.489	147.36	1.322	18.81
0.489	-147.36	0.278	0.00	0.434	-135.71
1.322	-18.81	0.434	135.71	1.584	0.00

Standard Deviation of Covariance matrices:

1.432	0.00	0.070	-28.47	1.230	-54.78
0.070	28.47	0.220	0.00	0.223	80.40
1.230	54.78	0.223	-80.40	0.191	0.00

Polarimetric Discriminants:

1. RCS VV   2.00 dB
2. RCS HH   1.95 dB
3. RCS X   -6.02 dB
4. Copolarization Ratio   -0.05 dB
5. Depolarization Ratio   7.99 dB
6. Total Power   5.62 dB
7. Phase Relative to VV   18.81 degrees
8. Correlation Coeff.   0.839

01_15_A RUN: 0002 X BAND   DATE: JAN 15 TIME: 06:49:10 INANG: 40.7
Average Mueller matrix file
Number of samples = 10

Average Mueller matrix:

0.1163452E+01	0.1889042E+00	0.1488350E+00	-0.1894218E+00
0.1770590E+00	0.1142075E+01	0.8234985E-01	0.5441031E-01
0.1549878E+00	0.2296646E+00	0.8674929E+00	0.2188571E+00
0.7561356E-01	-0.6344675E+00	-0.2395085E+00	0.8674929E+00

Standard Deviation of Mueller matrices:

0.7368722E+00	0.5097910E-01	0.1582905E+00	0.9996105E-01
0.6448713E-01	0.1936563E+00	0.4792923E+00	0.3218490E+00
0.6720559E+00	0.1724239E+00	0.7995250E+00	0.5712527E+00
0.3049058E+00	0.3177732E+00	0.1682001E+00	0.7995250E+00

Average Covariance Matrix (dB,Phase)

0.657	0.00	-10.644	-26.01	-0.552	15.08
-10.644	26.01	-7.519	0.00	-10.056	33.45
-0.552	-15.08	-10.056	-33.45	0.577	0.00

Average Covariance Matrix (Mag,Phase)

1.163	0.00	0.086	-26.01	0.881	15.08
0.086	26.01	0.177	0.00	0.099	33.45
0.881	-15.08	0.099	-33.45	1.142	0.00

Standard Deviation of Covariance matrices:

0.737	0.00	0.369	24.41	0.736	-30.17
0.369	-24.41	0.064	0.00	0.577	33.88
0.736	30.17	0.577	-33.88	0.194	0.00

Polarimetric Discriminants:

1. RCS VV	0.58 dB
2. RCS HH	0.66 dB
3. RCS X	-7.38 dB
4. Copolarization Ratio	0.08 dB
5. Depolarization Ratio	7.99 dB
6. Total Power	4.27 dB
7. Phase Relative to VV	15.08 degrees
8. Correlation Coeff.	0.764

01_15_A RUN: 0052 X BAND   DATE: JAN 16 TIME: 09:41:46 INANG: 48.5
Average Mueller matrix file
Number of samples = 5

Average Mueller matrix:

0.4038437E+00	0.7148244E-01	0.5252818E-01	-0.1358217E-01
0.8404490E-01	0.4796913E+00	0.6097469E-01	-0.4440476E-01
0.6313759E-01	-0.6985443E-01	0.2550314E+00	0.1517850E+00
-0.2793700E-02	-0.2145900E+00	-0.1483729E+00	0.2550314E+00

Standard Deviation of Mueller matrices:

0.1785281E-01	0.3083812E-01	0.1834231E+00	0.1604976E-01
0.1852030E-01	0.1321552E+00	0.2344677E+00	0.3006196E-01
0.4492504E+00	0.1676234E+00	0.1880564E+00	0.1195568E+00
0.1518749E+00	0.2248754E+00	0.1618946E+00	0.1880564E+00

Average Covariance Matrix (dB,Phase)

-3.938	0.00	-15.002	2.53	-5.418	31.50
-15.002	-2.53	-10.754	0.00	-11.224	-36.06
-5.418	-31.50	-11.224	36.06	-3.190	0.00

Average Covariance Matrix (Mag,Phase)

0.404	0.00	0.032	2.53	0.287	31.50
0.032	-2.53	0.084	0.00	0.075	-36.06
0.287	-31.50	0.075	36.06	0.480	0.00

Standard Deviation of Covariance matrices:

0.018	0.00	0.237	-18.67	0.197	-45.60
0.237	18.67	0.019	0.00	0.236	7.31
0.197	45.60	0.236	-7.31	0.132	0.00

Polarimetric Discriminants:

1. RCS VV	-3.19	dB
2. RCS HH	-3.94	dB
3. RCS X	-11.09	dB
4. Copolarization Ratio	-0.75	dB
5. Depolarization Ratio	7.54	dB
6. Total Power	0.17	dB
7. Phase Relative to VV	31.50	degrees
8. Correlation Coeff.	0.653	

B-27

Average Mueller matrix file
Number of samples = 5

Average Mueller matrix:

```
 0.4562880E+00      0.5658693E-01     -0.5815751E-01     -0.1592315E-01
 0.8081822E-01      0.4078551E+00     -0.1192471E+00     -0.1487186E-01
-0.1427525E+00     -0.1047566E+00      0.3352596E+00      0.6655870E-01
-0.3948974E-02      0.6073492E-01     -0.1149890E+00      0.3352596E+00
```

Standard Deviation of Mueller matrices:

```
 0.2377424E-01      0.3567018E-01      0.8546229E-01      0.1547606E+00
 0.1293796E-01      0.3882846E-01      0.6867963E-01      0.9588367E-01
 0.2124272E-01      0.1270666E+00      0.8904418E-01      0.1825169E+00
 0.3879265E+00      0.3446553E+00      0.3005943E+00      0.8904418E-01
```

Average Covariance Matrix (dB,Phase)

```
  -3.408    0.00    -11.462  178.42    -4.575   15.09
 -11.462 -178.42    -10.925    0.00    -9.202 -172.88
  -4.575  -15.09     -9.202  172.88    -3.895    0.00
```

Average Covariance Matrix (Mag,Phase)

```
   0.456    0.00     0.071  178.42     0.349   15.09
   0.071 -178.42     0.081    0.00     0.120 -172.88
   0.349  -15.09     0.120  172.88     0.408    0.00
```

Standard Deviation of Covariance matrices:

```
   0.024    0.00     0.194  -86.86     0.246  -78.54
   0.194   86.86     0.013    0.00     0.118  -54.40
   0.246   78.54     0.118   54.40     0.039    0.00
```

Polarimetric Discriminants:

1. RCS VV   -3.89 dB
2. RCS HH   -3.41 dB
3. RCS X   -11.63 dB
4. Copolarization Ratio   0.49 dB
5. Depolarization Ratio   7.99 dB
6. Total Power   0.01 dB
7. Phase Relative to VV   15.09 degrees
8. Correlation Coeff.   0.808

NEAR SURFACE MEASUREMENTS OF ARCTIC SEA ICE
DURING THE FALL FREEZE-UP

Robert G. Onstott

Radar Science Laboratory
Advanced Concepts Division
Environmental Research Institute of Michigan
Ann Arbor, MI 48107 USA

ABSTRACT

Near-surface millimeter and microwave measurements were made during the September-October 1989 segment of the Coordinated Eastern Arctic Experiment (CEAREX) in regions located to the North and East of Svalbard. Microwave signatures and physical properties were acquired at a large number of stations and included floes composed of first-year, multiyear, pancake, and new sea ice. One of the unanticipated success stories of CEAREX was the finding of systematic variations in the thickness and density of the ice located in the uppermost portion of multiyear ice sheets. Understanding the formation of this layer and its microwave signature is important to interests in both global climate change (potentially) and remote sensing science.

DISCUSSION

Backscattering data were collected from the wheelhouse of the ice-strengthened ship "R/V Polarbjorn" and from a sled-based tower using polarization diversified radars operating at 0.5, 1.5, 5.25, 9.38, 18, 35, and 94 GHz over the incidence angle range from 15° to 80°. Data were acquired during transit (.e., for spatial statistics) and when at station (i.e., very detailed coordinated measurements). Measured ice thicknesses ranged from 0^+ to over 5 meters. Scene characterizations (general description, layer thickness, density, salinity, gas bubble size statistics, bubble geometries, and surface roughness statistics) and passive microwave observations were also an integral part of this program.

Understanding physical property and microwave signature variations, a goal of this effort, is important in the study of ice physics and to the process of retrieving geophysical information. Observations by the author on previous investigations clearly indicate that the physical properties in the upper few centimeters of cold multiyear ice dominate the backscatter response at frequencies greater than about 5 GHz. The conditions found during CEAREX could not have been better -- they were laboratory-like in all aspects. A critical feature of these data is the diversity of the measurements with observations at sites where the upper ice sheet layer thickness ranged between 0 and 20 cm, density from 0.75 to 0.9 qm cm^{-3}, and gas bubble size from 0.5 to 3 mm (illustrated in Table 1). An example sled transect is shown in Figure 1 to illustrate signal variation along the Drift Station track. This detail adds considerably to the ability to

theoretically model multiyear backscatter to the study of how the properties of this layer, particularly, density and gas-bubble size statistics, vary with layer thickness, ice thickness, and ice age. Results relating the microwave response to ice properties and how this information impacts geophysical satellite algorithms was presented.

Table 1.
UPPER ICE SHEET CHARACTERIZATIONS

Figure 1.   Backscatter Response Along Drift Station Study Track

MIZEX '84 MULTIFREQUENCY HELICOPTER-BORNE
ALTIMETER OBSERVATIONS OF SUMMER MARGINAL SEA ICE

Robert G. Onstott

Radar Science Laboratory
Advanced Concepts Division
Environmental Research Institute of Michigan
Ann Arbor, MI 48107 USA

ABSTRACT

Airborne radar measurements were acquired in
ine and July 1984 with a frequency-modulated,
ntinuous-wave radar scatterometer operating at
25, 9.6, 13.6, and 16.6 GHz from helicopter over
ie Fram Strait marginal ice zone. Altimeter
iservations were coordinated with surface
iaracterizations so that reflectivities are
:latable with particular ice types and forms and
ie quantification of responsible physical
operties. Results show that variations in
:flectivity are directly attributable to liquid
:ean conditions, ice type, and deformation
iaracteristics. Results also illustrate that
itentially both ice extent and concentration are
:ophysical information that may be retrieved
;ing altimeters and that selection of sensor
irameters impact the accuracy of the estimates.
:termination of ice type based on reflectivity
lone appears to be tenuous during summer.

INTRODUCTION

Monitoring of polar ice is important in the
nderstanding of the cryosphere. Determination of
ce sheet mass balance and sea ice extent and
hickness is very important in this study, since
t is known that these properties have a
easurable effect upon, and are impacted by,
lobal climate and high latitude weather. With
icrowave sensor-equipped, polar-orbiting
atellites these and other processes may be
)served temporally and our understanding
nproved. Remote sensing instruments such as the
adar altimeter (the subject here), provides the
eans in which this may be done; in an environment
iat allows very limited access and is immense in
real extent.

During the summer of 1984, an experiment was
)nducted from land and from surface ship in the
arginal ice zone in the Fram Strait region of the
reenland Sea. Data were acquired to evaluate the
)ility of radars operating at normal incidence to
rovide information which may be used to
:curately determine ice edge location, ice
)ncentration, ice type or thickness, and large-
:ale surface roughness. Measurements were made
rom an aircraft equipped with a 13.8 GHz
ltimeter called the RAL altimeter and from a
elicopter equipped with a nadir-looking
:atterometer which operated at 5.25, 9.6, 13.6,
nd 16.6 GHz. The emphasis with the helicopter-

borne instrument was to provide accurate
scattering coefficients (σ°) or reflectivities of
ice with well documented physical properties and
to provided data which very accurately allows the
correlation between measured reflectivites with
specific ice and water features.

HELICOPTER-BORNE RADAR SCATTEROMETER

Signatures of a variety of summer sea ice
forms were acquired at incidence angles from
vertical to about 70°. Multiple antenna transmit-
receive polarizations were also used, of
significance at angles off vertical. Antenna
beamwidths, ranging from 2° to 5° over this
frequency range, produced ground cells of from 1m
to 2m diameters at a nominal operation altitude of
20m. The radar used was a wideband frequency-
modulated continuous-wave radar. It was operated
from the side of a Bell Model 206 small helicopter
and with a geometry shown in Figure 1. Nominal
system parameters are provided in Table 1.
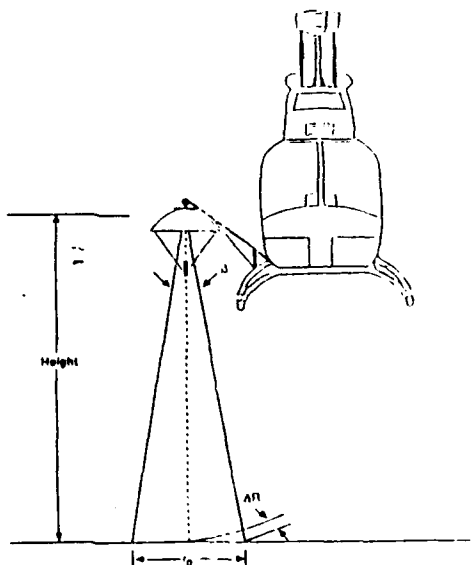
Figure 1. Geometry of Radar Scatterometer Operating in Altimeter Mode

RESULTS

Data were acquired by flying scans from several nautical miles into the open ocean, across the ocean-ice edge, and deep into the marginal ice zone until large floes were encountered. Two such examples are shown in Figures 2 and 3. To illustrate the inverse correlation in the magnitude between returns obtained when operating at vertical versus off-axis (i.e., 25°), transects are shown at (a) 9.6 GHz, HH polarization, and 25° and (b) 13.6 GHz and 0°. Five distinct liquid ocean signatures were detected. At vertical, reflectivities became progressively stronger with propagation into the MIZ. Ocean features were identified as follows:

> open ocean signature,
> ocean at ice edge signature,
> ocean at ice edge no-return band signature,
> MIZ interior-ice ocean signature, and
> MIZ interior-ice floe shadow signature.

In the off axis radar geometry case these ocean signatures varied over a range of about 20 dB, with very weak returns possible in the ice interior. In the vertical geometry as illustrated in Figure 3 very strong specular returns may be produced, up to 17 dB greater than those produced in the open ocean. Hence, water shadowed by ice floes is very smooth and specular in nature. A second observation is that returns produced from sea ice in the MIZ with a moist snowpack are as much as 30 dB weaker than the returns produced by the liquid ocean. Ice reflectivities at vertical for ice with a thick snow cover are about 8.5 dB lower than that of the open ocean. With identical surface roughnesses a difference of 8.7 dB is anticipated due to an almost order of magnitude difference in their dielectric constants.

A summary of radar scattering coefficients and their standard deviations for seven general scene classes is provided in Table 2. Detection of the ice edge is not difficult in either the 0° and 25° viewing angle cases given knowledge of the expected edge ocean-ice microwave signature responses. It is also apparent that positioning errors may be possible and are dependent on altimeter algorithm properties. A potential example is the dead water zone (2km width) at the ice-ocean interface which may be confused with grease ice.

Relationships between regional scattering coefficients and ice concentrations were determined at 9.6 GHz and 25°, at 13.6 GHz and 0°, and 9.6 GHz and 0°, and are shown in Figure 4 to 6 respectively. Regional averages were performed in the log domain and linear relationships between cross-sections and ice concentration resulted for both the on-axis and off-axis cases. This relationship result is expected for our case where resolution is of at least a scale finer than the size of individual ice floes or the spacing between ice floes and where there is ample contrast between ice and water.

The difference in the reflectivities between ice types is small, typically on the order of 5 dB, and attributable to minor variations in surface roughness scales. However, floes, such as heavily meltpooled multiyear ice (a case shown in

Table 2), are also capable of producing large reflectivities. In a case at 5.25 GHz, reflectivities similar to those of the interior ocean were produced. An additional feature of significance in describing ice and ocean reflectivities at vertical is the, oftentimes, very large standard deviation in signal returns. This and the similarity between ice type mean reflectivities suggests that ice type discrimination based on reflectivity during summer will be difficult.

ACKNOWLEDGEMENTS

Table 1. **NOMINAL SYSTEM SPECIFICATIONS**

Description	C-Band	X-Band	Ku-Band	Ku-Band
Type	FM CW	FM CW	FM CW	FM CW
Frequency GHz	5 2	9 6	13 6	16 6
Modulation	Triangular	Triangular	Triangular	Triangular
Sweep Bandwidth MHz	75*	75*	75	75*
Transmit Power dBm	10	10	10	10
IF Bandwidth KHz	13 5	13 5	13 5	13 5
IF Frequency-KHz	50	50	50	50
Antennas	Parabolic	Parabolic	Parabolic	Parabolic
Feed Type	Log Periodic	Log Periodic	Log Periodic	Log Periodic
Polarization	HH	HH	HH	HH
Size cm	61	61	61	61
Beamwidth Degrees	5 4	3 4	2 6	1 9
Incidence Angles Deg	0 to 70	0 to 70	0 to 70	0 to 70
Altitude-m	20	20	20	20
Illuminated Area at 0° m2	2 4	0 60	0 35	0 35
Aircraft Speed m/s	250*	250*	250*	250*
Sampling Rate Hz	10	10	10	10
Calibration Relative	Signal Inj	Signal Inj	Signal Inj	Signal Inj
Calibration-Absolute	Luneberg Lens	Luneberg Lens	Luneberg Lens	Luneberg Lens

Table 2. Radar Scattering Coefficients (dB) at Vertical in the Marginal Ice Zone on 5 July 1984

Scene	Frequency			
	5 25 GHz	9 6 GHz	13 6 GHz	16 6 GHz
Ocean-Open		14 5 ± 1 6	15 9 ± 0 7	
Ocean-Edge		17 4 ± 2 4	21 5 ± 6 9	
Ocean-Interior	13 3 ± 10 1	22 8 ± 22 6	24 5 ± 2 4	
Thin FY	2 0 ± 1 2	6 4 ± 9 4	9 2 ± 6 8	8 9 ± 5 9
Med FY	-0 8 ± 2 4	2 9 ± 3 0	4 7 ± 2 9	
Multiyear-SC	-1 3 ± 3 0		7 9 ± 3 9	6 1 ± 5 0
Multiyear-MP	10 4 ± 8 3	8 3 ± 9 8		

H5001
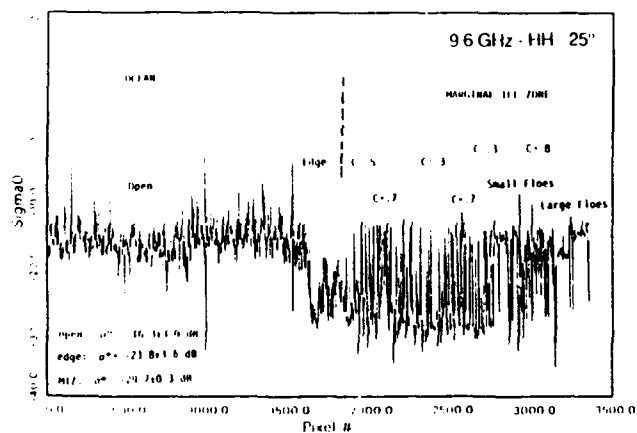
Figure 2. Transect Across the Ice Edge on 5 July 1984 at 9.6 GHz-HH-25°

H5101
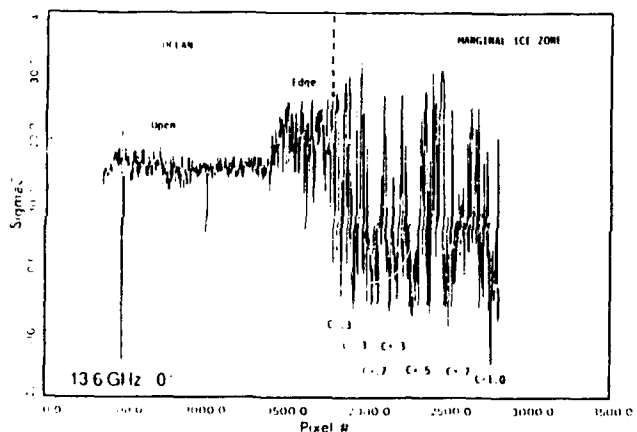
Figure 1. Transect Across the Ice Edge on 5 July 1984 at 13.6 GHz-0°
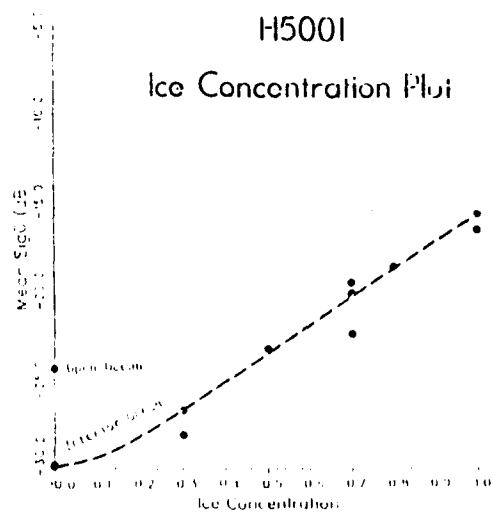
H5001

Ice Concentration Plot

Figure 3. Relationship Between Regional Scattering Coefficient dB Averages and Ice Concentration at 9.6 GHz-HH-25° (5 July 1984)

H5101

Ice Concentration Plot
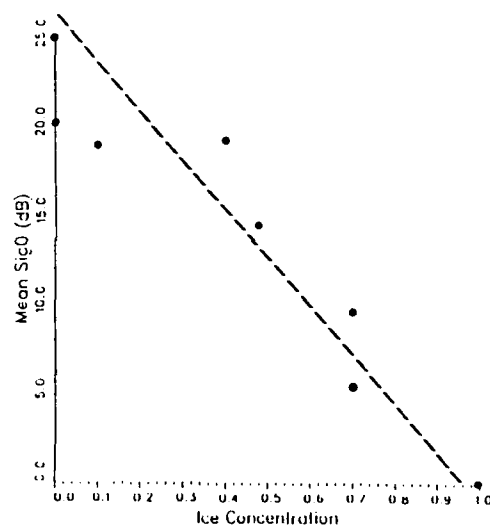
Figure 5. Relationship Between Regional Scattering Coefficient dB Averages and Ice Concentration at 13.6 GHz -0° (5 July 1984)

H5133

Ice Concentration Plot
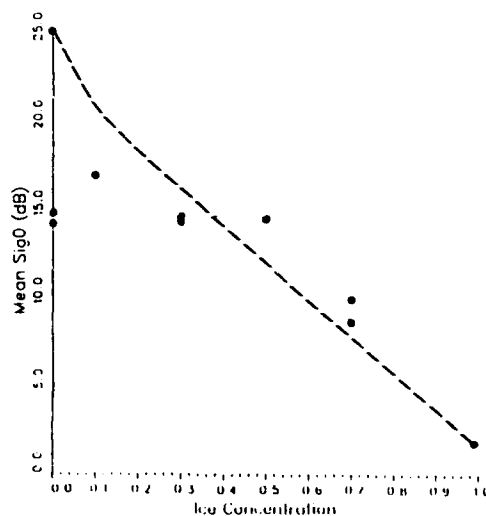
Figure 6. Relationship Between Regional Scattering Coefficient dB Averages and Ice Concentration at 9.6 GHz -0° (5 July 1984)

POLARIMETRIC RADAR MEASUREMENTS OF ARCTIC SEA ICE
DURING THE COORDINATED EASTERN ARCTIC EXPERIMENT

Robert G. Onstott

Radar Science Laboratory
Advanced Concepts Division
Environmental Research Institute of Michigan
Ann Arbor, MI   48107   USA

ABSTRACT

During March 1989, the first fully polarimetric radar data of Arctic sea ice coordinated with detailed surface characterizations were obtained in the Greenland Sea and at frequencies of 1.8, 5, 10, and 35 GHz from the rail of an ice-strengthened ship as part of the Coordinated Eastern Arctic Experiment (CEAREX). Observations were made of numerous ice forms and included multiyear ice, first-year ice, and many stages of new ice, with the addition of the thinnest forms, very fine spicules of ice in suspension. Transits were made from open water through the ice edge and, after a significant opportunity when off-ice winds created a diffuse marginal ice zone (MIZ), to nearly 35 nm through the MIZ into the pack ice.

INTRODUCTION

During the eight-month CEAREX investigation, the ice strengthened ship "R/V Polarbjorn" was utilized as a platform from which to measure active and passive microwave signatures of snow and sea ice. Observations began with fall freeze-up, continued through the winter ice growth period, and were completed during early spring. A study approach was developed so that microwave measurements were closely coupled to surface observations with the purpose to allow ice feature signatures and physical properties to be documented for later use in detailed examinations and in theoretical model validation. Microwave signature studies extended from 500 MHz to 100 GHz, included complete polarization diversification (i.e. VV, VH, HV, HH), and complex data (magnitude and phase) collected at selected frequencies from both ship and aircraft sensors. The active microwave measurements and scene characterization measurements conducted during CEAREX have been briefly summarized in Table 1 and 2, respectively.

During March, scientific operations were carried out in the Fram Strait area as indicated in Figure 1. The first polarimetric measurements of sea ice with documented physical properties were made from ship and aircraft. These measurements were conducted to complement the other ongoing shipboard passive and active (non-coherent) microwave collections. The coordination between the airborne synthetic aperture radar (SAR) and surface-ship measurement program is discussed in a companion paper titled, "Comparison of SAR and Scatterometer Data Collected during CEAREX." Ice types encountered during the early spring conditions (March) included nilas, new ice with frost flower growths, pancake, first-year ridged ice, second year, and multiyear. Measured ice thicknesses varied from less than a millimeter to greater than 5 meters. First-year ice thicknesses grouped into 0.3, 0.5, 0.8, and 1.6 m bins. In addition to measurements at sites of representative major ice types, a in situ measurement program similar in scope to that performed at the U.S. Army Cold Regions Research and Engineering Laboratory in an outdoor tank and similar to that proposed in the future LEADS investigation where the microwave signature of ice as it forms from open water and until it attains a several centimeter thickness, in this case 3 cm, is continuously observed. Additional liquid ocean measurements were made at several positions near the ice edge and under varying wind speed conditions. Transits through the Odden, a feature of new ice, many 10s of kilometers in extent, which juts out from the mean ice edge in the shape of a tongue, was made on two occasions. These polarimetric scatterometer observations were performed at angles from 20° to 70° and have been summarized in Table 3.

Scene characterization measurements were conducted to provide documentation of the general makeup of the sites chosen for study and to provide detailed descriptions as to the characteristics the of snowlayer, the low density ice layer on multiyear ice, the high density ice layer for both first year and multiyear ice in terms of layer thickness, density, salinity, gas bubble size statistics, bubble geometries. Small scale roughness measurements of the ice-snow interface were also performed to obtain information for their statistical description.

In making these scattering measurements, the amplitude and phase of the scattered field at V and H polarizations for each of the like transmit polarizations (i.e. V and H) were measured. These data will be used to produce covariance matrices which are composed of complex scattering coefficients and are of the form

$$CM = \begin{vmatrix} <S_{vv}S_{vv}^*> & <S_{vv}S_{vh}^*> & <S_{vv}S_{hh}^*> \\ <S_{vh}S_{vv}^*> & <S_{vh}S_{vh}^*> & <S_{vh}S_{hh}^*> \\ <S_{hh}S_{vv}^*> & <S_{hh}S_{vh}^*> & <S_{hh}S_{hh}^*> \end{vmatrix}$$

where Spj is complex and represents the scattered field produced when the transmit polarization is p and the receive polarization is j. In the analysis of these polarimetric radar data, the absolute and relative magnitudes of the real scattering coefficients (i.e. $\sigma^\circ vv$, $\sigma^\circ hh$, and $\sigma^\circ vh$), the correlation between the returns at vv and hh, and the difference in phase between the two co-polarized elements of the scattering matrix (i.e. $\theta hh - \theta vv$) will be of particular interest.

SUMMARY

Preliminary results from this investigation are summarized in Table 4. During the oral presentation, the interpretation and implication of these results were described as well as to how this information may impact geophysical satellite algorithms.

ACKNOWLEDGEMENTS

Figure 1. Operation Area

Table 2. Ice Characterization Measurements During CEAREX - 88/89

- Snow Characterization (General)
- Surface Roughness
- Low Density Ice Layer
- High Density Ice Layer
- Density
- Salinity
- Temperature
- Inhomogenieties in Ice (Thick Section)

Table 3. Ship-Based Polarimetric Scatterometer Site

Date	Time	Description
18 Mar	1935	Multiyear Ice Floe
19 Mar	0000	Open Water-Ice Growth Evolution Experiment (T = 0 to 5 cm)
19 Mar	1000	Young First-Year Ice Floe (T = 50 cm)
19 Mar	1730	New Ice (T = 5.5 cm) with 80% Frost Flower Coverage
19 Mar	2230	Grey White First-Year Ice (T = 35 cm)
20 Mar	0830	Large Thick Multiyear Ice
20 Mar	1950	Open Water
21 Mar	1150	Multiyear Ice
21 Mar	1850	Open Water
22 Mar	1330	Open Water
23 Mar	1400	Multiyear Ice
24 Mar	1030	Open Water
24 Mar	2200	First-Year Ice (T = 1.6 m)
26 Mar	1200	Multiyear Ice
27 Mar	1230	Open Water
28 Mar	1150	Multiyear Ice

Table 1.
COORDINATED EASTERN ARCTIC EXPERIMENT
ACTIVE MICROWAVE MEASUREMENT PROGRAM

Sensors			Sept-Oct '88 Fall Freeze Up Eastern Arctic	Oct-Dec '88 Fall-Winter Eastern Arctic	Feb '89 Winter Barents Sea	March '89 Late Winter Fram Strait
Name	Based	Description				
HELOSCAT	Ship	L-C-X/Quad-Pol	..	..	..	..
DRaaR	Ship	Ku-Ka-W/Quad-Pol	..		..	..
DRaaR	Ship	X-Ku-Ka-W/Quad-Pol	..	..		
PSCAT	Ship	0-6 GHz/HH	..		..	..
VHFSCAT	Ship	0-15 GHz/Like				..
Color Video	Ship	Timer/Remote	..	..		..
POLRAD	Ship	L-C-X-Ka/Radiometric				..
Radiometer	Ship	C/Quad-Pol			..	..

Table 4. Preliminary Polarimetric Scatterometer Results

	Dielectric Constant	Surface Roughness	$\sigma^\circ VV/\sigma^\circ HH$	$\sigma^\circ VV + \sigma^\circ HH$	Correlation Coefficient
Open Water	Large (≈ 40)	σ = .2 cm l = 7 cm	≈ 4 dB	≈ 20 dB	≈ .99
New Ice (2 cm)	Large (≈ 20 to 80)	σ = .05 cm l = 1 cm	≈ 2 dB	≈ 20 dB	≈ .98
Grey Ice (20 cm)	Low (≈ 4)	σ = .05 cm l = 1 cm	≈ 0 dB	≈ 16 dB	≈ .95
First Year Ice (≈ 160 cm)	Low (≈ 4)	σ = .2 cm l = 7 cm	≈ 1 dB	≈ 12 dB	≈ .80
Multiyear Ice (300 + cm)	Low (≈ 3)	σ = 2 cm l = 7 cm	≈ 0 dB	≈ 9 dB	≈ .70

COMPARISON OF SAR AND SCATTEROMETER DATA COLLECTED DURING CEAREX

Robert G. Onstott
Robert A. Shuchman
Laura L. Sutherland

Radar Science Laboratory
Advanced Concepts Division
Environmental Research Institute of Michigan
Ann Arbor, MI 48107 USA

ABSTRACT

A comprehensive data set consisting of L-, C-, and X-band polarimetric synthetic aperture radar (SAR) and P-, L-, C-, Ku-, Ka-, and W-band scatterometer measurements were collected during the Seasonal Ice Zone Experiment (SIZEX) portion of the Coordinated Eastern Arctic Experiment (CEAREX). The scatterometer data was obtained from rail-mounted instruments on the ice strengthened research vessel POLARBJORN. Coincident with the aircraft SAR and ship-based scatterometer measurements were in situ samplings of sea ice and snow cover construction and physical properties. Ice types encountered during the March 1989 exercise included nilas, pancake, first-year ridged ice, second year, and multi-year. The ice thickness varied from less than a millimeter to greater than 5 meters. Areas of open water with varying wind speeds and open water with grease ice were also coincidentally imaged by the SAR and scatterometers. For the first time, polarimetric SAR and scatterometer data of documented sea ice types were obtained.

INTRODUCTION

The use of remote sensing during CEAREX was considered from both a tool and science discipline. As a tool, remote sensing techniques and products will be utilized to provide geophysical information on ice and ice-free ocean processes within the MIZ. Such observations [1-5] have been shown to provided data on a wide variety of phenomena such as the detection of eddies, fronts, upwelling areas, internal wave, gravity waves, surface winds, ice thickness, ice concentration, ice kinematics, floe size distributions, and ice surface roughness. Remote sensing is the only means to obtain mesoscale synoptic coverage of these phenomena at sufficiently high spatial resolution. Remote sensing science issues include sensor validation, algorithm development and utilization of products obtained through remote sensing to solve arctic problems.

An ice strengthened ship was utilized during the eight month CEAREX period as a platform to measure active and passive microwave signatures of snow and various sea ice types from fall freeze-up through winter ice growth until early spring. Microwave signatures studies were developed to closely coupled to surface observations so that ice features and physical properties to be correlated and studied in detail. Microwave signature studies extended from 500 MHz to 100 GHz, include complete polarization diversification (i.e. VV, VH, HV, HH), with complex data (magnitude and phase) collected at selected frequencies (i.e. fully polarimetric data at 1, 2, 5, 9, 10, and 35 GHz). System parameters for the polarimetric SAR and scatterometer systems are provided in Tables 1 and 2, respectively. It should also be noted that synoptic satellite data products from NOAA 9/10, DMSP(SSM/I) and MOS-1 have been obtained for intercomparison and study.

During March, scientific operations were carried out in the Fram Strait area, shown in Figure 1. Two experiment types were conducted. A region composed of ice, the ice edge, and ocean and as large as 200 km x 200 km was imaged using SAR and so that the operation area of the POLARBJORN was included. Eight missions which covered areas contained in the region from 76° N to 79° N and 7° W to 1° E were flown during this month using the ERIM/NADC P-3 SAR to simulate ERS-1 (C-VV) every third day coverage. Supplemental mosaics were created at L-, and X-band for support of frequency sensitivity studies. Observations were made from ship to document in detail ice sheet microwave and physical properties throughout this region. At the completion of a each SAR mosaic mission a narrow swath transect was imaged in the polarimetric mode with the purpose to complement the SAR mosaic and to provide additional polarimetric coverage of the most recent ice study sites. This event sequence is illustrated in Figure 2. In addition, a dedicated polarimetric mission was conducted in which star patterns consisting of three passes at each of the three SAR frequencies were flown with the ship as the intersection point. Specifics concerning the polarimetric flights as well as the mosaic missions are provided in Table 3. Polarimetric scatterometer measurement sites were observed at angles from 20° to 70° and are summarized in Table 4. A summary of the major ice characterization measurements performed during this investigation are provided in Table 5.

RESULTS

Very preliminary results from the polarimetric scatterometer measurements are described in a companion paper. At the time of the writing of this paper, no digital processing

had been done with the SAR data collected during the March phase of the CEAREX investigation. Real-time imagery have been assembled into mosaics and are being used in the planning of future analysis efforts and the extraction of geophysical information about the MIZ.

REFERENCES

1. O.M. Johannessen et al., "Ice-Edge Eddies in the Fram Strait Marginal Ice Zone", SCIENCE, Vol 236, pp. 427-429, April 1987.

2. R.A. Shuchman, et al., "Remote Sensing of the Fram Strait Marginal Ice Zone", SCIENCE, Vol 236, pp. 429-431, April 1987.

3. T.O. Manley, R.A. Shuchman, B.A. Burns, "Use of Synthetic Aperture Radar-Derived Kinematics in Mapping Mesoscale Ocean Structure Within the Interior Marginal Ice Zone", Journal of Geophysical Research, Vol 92, No. C7, pp. 6837-6842, June 1987.

4. T.O. Manley, et al., "Mesocale Oceanographic Process Beneath the Ice of Fram Strait, SCIENCE, Vol 236, pp.432-434, April 1987.

5. W.J. Campbell et al., "Variations of Mesoscale and Larch-Scale Ice Morphology in the 1984 Marginal Ice Zone Experiment as Observed by Microwave Remote Sensing", Journal of Geophysical Research, Vol 92, No. C7, pp. 6805-6824, June 1987.
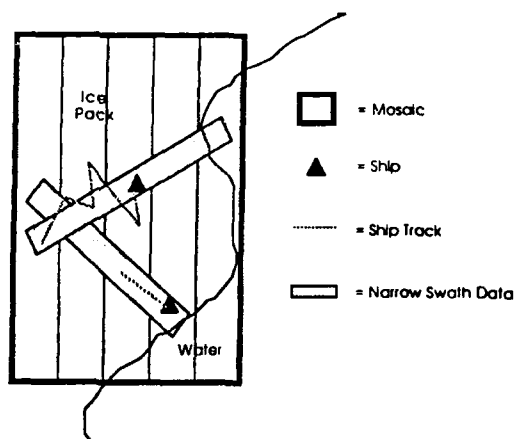
Figure 2. CEAREX SAR Data Collection Diagram

Table 1. P-3 SAR System Specifications

Parameter	X	L	C
Wavelength	3.2 cm	24 cm	5.7 cm
Frequency	9.375 GHz	1.25 GHz	5.26 GHz
Pack Transmitter Power	1.5 kW	50 kW	1.4 kW
Receiver Noise Figure	5.0 dB	4.0 dB	5.0 dB
System Losses	6.1 dB	5.0 dB	7.1
dBTransmitted Pulse Width	4.0 μsec	4.0 μsec	4.0 μsec
Maximum Ground Speed	350 Knots	350 Knots	350 Knots
Antenna Azimuth Beamwidth	1.25°	10° (V) 9.5° (H)	2.2°
Antenna Azimuth Beamwidth	CSC1.5	45°	CSC1.5
Polarization Isolation	23 dB	23 dB	23 dB

Figure 1. Operation Area

Table 2.

COORDINATED EASTERN ARCTIC EXPERIMENT

ACTIVE MICROWAVE MEASUREMENT PROGRAM

Sensors			Sept-Oct '88 Fall Freeze Up Eastern Arctic	Oct-Dec '88 Fall Winter Eastern Arctic	Feb '89 Winter Barents Sea	March '89 Late Winter Fram Strait
Name	Based	Description				
HELOSCAT	Ship	L C X/Dual Pol	·	··	··	··
ERIM	Ship	Ku Ka X/Dual Pol	··		··	··
ERIM	Sled	X Ku Ka X/Dual Pol	··	··		
PSCAT	Ship	8 8 GHz HH	··		··	··
VHFSCAT	Ship	0.15 GHz Lin			··	··
Color Video	Ship	Time/Remote		·	·	··
POLRAD	Ship	L C X Ka Polarimetric	··		··	··
Radiometer	Ship	C/Dual Pol			··	··

Table 3. SAR Flights in Support of SIZEX/CEAREX

Date	SAR System	Band	Pass	Mode	Location	Objective	Polarization
17 February	CCRS CV 580	C, X	1 24	Nadir (Full) Wide Swath	Barents Sea	ERS-1 Simulation	VV
20 February	CCRS CV 580	C, X	1 24	Nadir (Full) Wide Swath	Barents Sea	ERS-1 Simulation	VV
23 February	CCRS CV 580	C, X	1-4	Wide Swath	Barents Sea	ERS-1 Simulation	VV
26 February	CCRS CV 580	C, X	1-4	Wide Swath	Barents Sea	ERS-1 Simulation	VV
27 February	CCRS CV 580	C, X	1-2	Wide Swath	Barents Sea	ERS-1 Simulation	VV
17 March	ERIM/NADC P-3	C, X X	1-7 8	Double Swath Narrow Swath	Greenland Sea	ERS-1 Simulation EOS Simulation	VV Full
18 March	ERIM/NADC P-3	C, L C, L	1-4 5-7	Double Swath	Central Arctic	"O" Camp Locations "A" Camp Locations	VV VV
20 March	ERIM/NADC P-3	C, X, L X	1-8 9	Double Swath Narrow Swath	Greenland Sea	ERS-1 Simulation EOS Simulation	VV Full
21 March	ERIM/NADC P-3	C, X, L X	1-12 13	Narrow Swath Double Swath	Greenland Sea	Polarimetric Flights	Full Full
23 March	ERIM/NADC P-3	C, X, L C	1-7 8	Double Swath Narrow Swath	Greenland Sea	ERS-1 Simulation EOS Simulation	VV Full
24 March	ERIM/NADC P-3	C, X, L L	1-7 8	Double Swath Narrow Swath	Greenland Sea	Polarization Comparison EOS Simulation	HH Full
26 March	ERIM/NADC P-3	C, X C	1-8 9	Double Swath Narrow Swath	Greenland Sea	ERS-1 Simulation EOS Simulation	VV HH Full
27 March	ERIM/NADC P-3	C, X, L X, L	1-8 8-14	Double Swath Narrow Swath	Greenland Sea	ERS-1 Simulation Waves in Ice	VV HH
14 April	ERIM/NADC P-3	C, X, L	1-8	Double Swath	Central Arctic/ Greenland Sea	"A" and "O" Camp and Acoustic Tomography Support	VV
15 April	ERIM/NADC P-3	C, X, L	1-8	Double Swath	Central Arctic/ Greenland Sea	"A" and "O" Camp and Acoustic Tomography Support	VV
16 April	ERIM/NADC P-3	C, X, L	1-8	Double Swath	Central Arctic/ Greenland Sea	"A" and "O" Camp and Acoustic Tomography Support	VV

Table 5. Ice Characterization Measurements During CEAREX - 88/89

- Snow Characterization (General)
- Surface Roughness
- Low Density Ice Layer
- High Density Ice Layer
- Density
- Salinity
- Temperature
- Inhomogenieties in Ice (Thick Section)

Table 4. Ship-Based Polarimetric Scatterometer Site

Date	Time	Description
18 Mar	1935	Multiyear Ice Floe
19 Mar	0000	Open Water-Ice Growth Evolution Experiment (T = 0 to 5 cm)
19 Mar	1000	Young First-Year Ice Floe (T = 50 cm)
19 Mar	1730	New Ice (T = 5.5 cm) with 80% Frost Flower Coverage
19 Mar	2230	Grey White First-Year Ice (T = 35 cm)
20 Mar	0830	Large Thick Multiyear Ice
20 Mar	1950	Open Water
21 Mar	1150	Multiyear Ice
21 Mar	1850	Open Water
22 Mar	1330	Open Water
23 Mar	1400	Multiyear Ice
24 Mar	1030	Open Water
24 Mar	2200	First-Year Ice (T = 1.6 m)
26 Mar	1200	Multiyear Ice
27 Mar	1230	Open Water
28 Mar	1150	Multiyear Ice

POLARIMETRIC RADAR MEASUREMENTS OF ARTIFICIAL SEA ICE

Robert G. Onstott and Scott H. Gaboury

Environmental Research Institute of Michigan
Radar Science Laboratory
Advanced Concepts Division
P.O. Box 8618
Ann Arbor, MI 48107 USA

ABSTRACT

During the winters of 1988 and 1989, fully polarimetric microwave measurements were made of artificial sea ice at frequencies of 1.8, 5, 10, and 35 GHz and incidence angles ranging from 0° to 60°. A 5 m x 15 m outdoor tank was filled with sea water and the time evolution of the growth cycle of sea ice was observed over two 2-month periods. During this investigation, continuous detailed scene characterizations and passive microwave observations were made so that an integrated comparison of backscatter and emission could be supported with theoretical predictions. Details of this investigation and preliminary results are presented herein.

INTRODUCTION

The microwave properties of sea ice grown at the U.S. Army Cold Regions Research and Engineering Laboratory (CRREL) were investigated during the 1988 and 1989 winter seasons. The sea ice facility is comprised of a 5 x 15 meter outdoor tank of a 1.2 meter depth filled with sea water, a tent to protect the ice sheet from snow and rain, a gantry style instrument mounting structure, and heated working environments in the immediate vicinity of the tank (See Figure 1). The tank size, determined by instrument and experiment needs, allows for the acquisition of independent spatial samples and measurements at angles from vertical to 60 degrees. These efforts, part of a new three year laboratory-based investigation which began in 1988, are focused on understanding the microwave signatures of sea ice. This is being accomplished by detailed studies of the various aspects of the backscatter and emission and through the intercomparison of measured data and theoretical predictions. Strengths of the CRREL Ice Tank Facility are the ability to control the chemistry of the ice sheet, to control to a reasonable degree the ice crystal structure of the ice, and to provide an environment which allows the time required to rigorously measure the physical and microwave properties of ice which closely simulates that found in the Arctic. The time factor is particulary important because of the scientific interest in fully characterizing the microwave properties and scene. The number of frequencies, incidence angles, polarizations, spatial samples, and temporal samples are extensive. In addition, active and passive observations are not made simultaneously to prevent any potential corruption of the complete accuracy of the data.

Observations were made of the growth cycle of sea ice over two 2-month periods during the winters of 1988 and 1989. Maximum ice thickness was 20 cm. The standard array of physical property observations (i.e. fabric analysis, salinity, density, and temperature) were assembled and supplemented by location, description, and statistical analysis of internal inhomogeneities and surface roughness statistics. These observations are being performed to document and study their influence on backscatter and emission. These data or derivatives provide the critical inputs for the validation and further development of electromagnetic scattering and emission models. The roughness of the ice surface is known to be important in determining the general backscatter level for first-year ice. Experiments were performed to study the change in backscatter and polarization signatures with various roughness scales. Effects of freeze and thaw conditions were also examined.

During this investigation, fully polarimetric measurements were made to acquire the complex scattering coefficients at VV, VH, HV, and HH polarizations (i.e. VH indicates vertical transmit and horizontal receive). The data are recorded such that the scattered field is completely described. This radar has been briefly described in a paper by Onstott [1]. Measurements were also made to qualitatively determine the dominant scattering mechanisms by recording unprocessed backscatter returns. In addition, millimeter wave data were collected during the 1988 investigation at 18, 35, and 94 GHz using a noncoherent radar. Scatterometer parameters used during Cold Regions Research and Engineering Lab Experiment (CRRELEX) are included in Table 1.

Active and passive microwave measurements were temporally multiplexed so that an integrated study of backscatter, emission, physical properties, and electromagnetic modeling of sea ice could be pursued rigorously. An overall goal of this program is to advance the state of understanding of the microwave properties of sea ice so that future satellite data may be fully utilized by the scientific community. Fundamental questions which are of particular interest in sea ice science are; how do the contributions of surface and volume scattering change as ice ages, what information is contained in the co-pol phase difference, what is the correlation between HH and VV scattering coefficients, do important geometric orientations exist in the ice sheet, and is scattering sensitive to them, and what are the

internal anisotropic physical-electrical properties?

OBSERVATIONS

During 1988, multiple ice sheets were grown which were observed over a 2 month period. Observations were made of open water, 5 mm thick new ice, 8 cm thick grey ice, 12 cm thick grey ice which had a rough, air-ice interface (rms roughness of about 1 cm), 12 cm thick grey ice with a liquid film water on its surface, and 20 cm thick ice which had undergone desalination and showed some of the characteristics associated with multiyear (See Table 2). Description of the rms roughness and spatial correlation length statistics are provided in Table 3. Microwave observations of the angular responses of the new and grey ice at C-band, provided in Figure 2, indicate that the fundamental property change during the growth period of new to grey ice is in the reduction of the complex dielectric constant. The surface roughness statistics for both of these scenes were identical to those of a very smooth surface (i.e., an rms height variation of 0.05 cm and a correlation length of 0.7 cm). It was observed by Onstott [2] in 1985 that effects due to blowing snow and the erosion of the upper ice surface, attributed to evaporation, did roughen the ice surface of grey ice as it aged. When air temperatures are cold (T < -20°C), typical of the major sea ice growth periods in the Arctic, the formation of frost flowers rapidly changes the very-smooth, low-dielectric slabs of grey ice to highly scattering slabs who have an overlay composed of high-dielectric needles. Observations made during 1988 show that during the transition from new to grey ice the dielectric constant changes by an order of magnitude (ie. from an $\epsilon_{r'}$ of 38 to 4) resulting in a 6.7 dB offset between the signatures shown in Figure 2. These results also show that for these two ice types the backscatter response at VV and HH polarizations are similar at angles from vertical to 40 degrees, with the possibility of a few dB of spreading at the larger angles. Nearly identical returns at VH and HV suggests reciprocity, i.e., that VH = HV. Angular response decays rapidly (i.e., at 5 GHz it is a minimum of 5 dB per 10°) and the large separation between like and cross polarized returns, from nadir to 20 degrees (i.e., at 5 GHz it is a minimum of 20 dB for the range of angles between 0° and 20°), is characteristic of scatter from a dielectric with a smooth surface but with sufficient penetration and size and number of inhomogeneities to produce the small volume return necessary to generate the very weak cross-polarized value. Study of the measurement system response, the inhomogeneities in the upper most portion of the ice sheet, and theoretical model predictions will be used to validate this hypothesis.

The change in backscatter levels for arbitrary co-polarizations may be derived from the target scattering matrix [3]. The illustrations provided in Figure 3 of new, grey, rough grey, and desalinated first-year ice at 5.0 GHz and 40 degrees are shown for visualizing the polarization properties of ice as it evolves. It was anticipated that based on the backscatter responses at the linear polarizations that the polarization signatures would further illustrate the differences in the processes which are responsible for scattering at each of these ice scenes. It is expected that the differences in the size of the pedestal on which the signatures rise, the width of the peaks and nulls, and the difference in the magnitudes between peaks and nulls are a few of the properties which may be exploited through polarimetric measurement.

During 1989, two ice sheets were observed with one observed continuously over a 6-week period. Thickness ranged from 0 to 20 cm. Measurements were multiplexed (i.e. half-hour sampling periods) during the rapid growth phase to allow both active and passive microwave signatures to be characterized. To simulate multiyear ice, an ice sheet was grown to 20 cm, harvested, and then placed on pallets prior to the beginning of the previously iterated measurement series. Over a period of several weeks the brine trapped within the ice sheet drained and the porosity of the ice increased because of the many freeze-thaw periods. Desalination and a reduced density are two important characteristics which determine the microwave signatures of multiyear ice. Observations of an ice sheet composed of one and two layers of this desalinated ice were made. These data were undergoing signal processing at the time of writing this paper. Scenes observed during 1989 are partially listed in Table 4.

CONCLUSIONS

Absolute backscatter levels for new to grey ice are small, except for the (large) coherent returns at vertical. The backscatter responses of new, grey, rough grey, and desalinated first-year ice at linear polarization were found to be dissimilar. This was further demonstrated by examining their polarization signatures. At C-band the critical difference between new and grey ice signatures lies in the order of magnitude difference in their dielectric constants. Surface roughness observations and microwave signature angular variation suggest identical roughness statistics for these two ice types. This will be confirmed by examining the 1989 data.

REFERENCES

1) Onstott, R.G. and S.H. Gaboury, "A Polarimetric Microwave Scatterometer," IGARSS '88 Proc., Vol 1, p. 571, Edinburgh, Scotland, Sept. 1988.

2) Xue, D., R. K. Moore, T. H. Lee and R. G. Onstott, "Microwave Backscatter Coefficients of Artificially Grown First-Year Sea Ice," IGARSS '86 Proc., Vol 1, pp. 139-146, Sept. 1986.

3) Deschamps, G.A., "Part II - Geometrical representation of the polarization of a plane wave," Proc. IRE, vol. 39, pp. 540-544, May 1951.

ACKNOWLEDGEMENTS

TABLE 1. SCATTEROMETER PARAMETERS USED DURING CRRELEX

Polarimetric:

Freq	=	1.75, 10 and 35 GHz
Polarization	=	Quad
Angles	=	Vertical to 60 Degrees
Height	=	3 m
Sampling	=	Point & Power spectrums

Non-Coherent:

Freq.	=	10, 18, 35, and 94 GHz
Polarization	=	Quad (10 GHz) and Dual (18, 35 and 94 GHz)
Angles	=	15 to 60 Degrees
Height	=	3 m
Sampling	=	Point and Transect

TABLE 3. CRRELEX '88 SURFACE ROUGHNESS RESULTS

Date	TΛZ To - hr -	Λ Z Ice - cm -	σ - cm -	l - cm -	Samples	Sample Lengths - cm -	Comments
14 Jan	63.5	6.5	0.046	0.669	1	25	Top Surface
14 Jan	63.5	6.5	0.046	0.821	1	24	Bottom Surface
16 Jan	113	13	0.051 ± .003	1.635 ± .370	3	20	
15 Jan	99	8	0.544± .053	1.481± .334	4	23 to 55	Ice Roughened Using Cubed Ice (2 Layers)
15 Jan	95	8	0.611± .096	2.157± .862	2	25	Ice Roughened Using Cubed Ice (1 Layer)

TABLE 2. OBSERVED SCENES DURING 1988

Open Water (θ = 45 to 55 Degrees)

New Ice ($\Delta z \cong$ 5 mm)

Grey Ice ($\Delta z \cong$ 12 cm)

Rough Grey Ice ($\Delta z \cong$ 12 cm) With 1 cm Roughness Elements

Rough Grey Ice ($\Delta z \cong$ 12 cm) With 2 cm Roughness Elements

Warm Grey Ice ($\Delta z \cong$ 12 cm)

Desalinated Grey Ice ($\Delta z \cong$ 20 cm)

TABLE 4. OBSERVED SCENES DURING 1989

Open Water

New Ice (Δz = 0 to 5 cm)

Grey Ice (Δz = 5 to 20 cm)

Grey Ice With a Thin Slush Layer

Grey Ice With 1 cm Wet Snow

Grey Ice With a Melt Roughened Surface

Grey Ice With 4 cm Moist Snow

Desalinated Ice (Δz = 20 cm)

Desalinated Ice (Δz = 40 cm)

Figure 1. Photograph Showing CRRELEX Ice Tank Facility and Microwave Scatterometers

Figure 2. Radar Scattering Coefficients at 5 25 GHz for 5 mm Thick
New Ice and 12 cm Thick Grey Ice

(A)

(B)

(C)

(D)

Figure 3. Co-Polarization Signatures of (a) New. (b) Grey,
(c) Rough Grey. and (d) Desalinated Grey Sea Ice

THEORETICAL AND EXPERIMENTAL STUDY OF THE
RADAR BACKSCATTER OF ARCTIC SEA ICE

Robert G. Onstott

Radar Science Laboratory
Advanced Concepts Division
Environmental Research Institute of Michigan
P.O. Box 8618, Ann Arbor, MI 48107

A theory has been developed to model the backscatter from sea ice. This model has proven useful in interpreting the microwave signatures of the many ice forms. Results have also been used in providing direction in the measurement of physical and electrical properties in recent sea ice investigations. The parametric studies which have followed have allowed the examination of the sensitivity of the microwave signature to changes in key ice sheet parameters. These include salinity, temperature, brine volume, density, air bubble size, and surface roughness.

The first attempt to describe theoretically the radar backscatter for sea ice was by Parashar et al [1974]. Results were mixed prompting support for a program which included coincident near-surface backscatter measurements and physical property characterizations. A qualitative description of the critical scattering processes at work was made by Onstott [1980] and was were based upon the results of these field investigations [Onstott et al, 1979, Onstott et al, 1982]. An empirical model was also developed to describe the angular and frequency variations of thick first-year sea ice, multiyear sea ice, and lake ice.

This qualitative discussion provided a basis from which theoretical formulations were selected for their application in describing backscatter from sea ice. The data acquired during the field investigations also provided model inputs and the radar data for model verification.

Let's first consider the model for multiyear ice. Backscatter levels are large and reduce gradually with increasing angle. This suggests that volume scattering contributes to multiyear ice backscatter. Surface scattering is also expected to be important because returns fall off too rapidly at large angles to be able to be modeled by volume scattering alone. Calculation of the attenuation coefficient and skin depth for multiyear ice further support this hypothesis. The scattering volume at 10 GHz with a salinity of $1^o/oo$ and T = -5 C is approximately 2.4 m. Ice sheet characterization data show significant numbers of air bubbles (sizes of 1 to 3 mm) in the upper portion of the ice sheet of a size which is within an order of magnitude of the size of the radar wavelength in ice. These bubbles provide the critical source of scatter within the volume. Another ice sheet inhomogeneity is the brine pocket. They are very small in size compared to a wavelength (radius of about 0.025 mm and lengths of about 3 to 5 mm) and are shown to have a negligible contribution.

It is also hypothesized that first-year ice is dominated by surface scatter with at most a minor contribution arising from volume scatter. Backscatter data show a rapidly decaying angular response at angles near vertical which supports this hypothesis. The surface is rough, and roughness elements are typically on an order less than a wavelength. A dramatically large attenuation coefficient (i.e., ice with a salinity of $8^o/oo$ and a T = -5 C has an attenuation coefficient of 300 - 500 dB/m and a skin depth of 2-3 cm at 10 GHz) further strengthens this argument. The scattering volume is obviously small and, as ice characterization measurements show, air bubbles are infrequent and brine inclusions are extremely small. It is argued that surface scattering provides the dominate backscatter mechanism.

Lake ice and frozen melt pools (fresh water ice) of sea ice are found to produce weak radar returns. Ice surfaces are smoother than typical sea ice, and the upper ice sheet layer does not contain large numbers of air bubbles. The absolute level of surface scattering is expected to be lower. However, in fresh water ice penetration depths are very large. It is suggested that the volume scatter which may arise from the small air bubbles found throughout the ice sheet and the long drainage tubes (diameters are on the order of .5 mm and lengths are on the order of a wavelength)

which are found near the bottom of the ice sheet be considered.

These hypotheses provided the basis of the theoretical and experimental studies which follow. The results of the application of a combined rough surface and volume scattering theory to sea ice and snow backscatter was first presented by Fung and Eom [1982]. A detailed discussion of the physical and electrical properties of sea ice, the extension of the model to include two ice layers, and a full discussion of the ability of a combined rough surface and volume scattering theory to model sea ice was later presented by Kim, Moore and Onstott [1984]. The applicability of these models and modeling results are presented in the remainder of this paper.

The surface of homogeneous first-year ice it flat topographically but rough in the small scale. The Kirchoff formulations for rough surface scattering were selected because of their apparent applicability. These formulations are derived in Ulaby, Moore and Fung [1982]. The predictions of the physical-optics formulation for slightly rough surfaces and the geometrical-optics formulation for very rough surfaces were compared to measured microwave signatures of first-year ice. For operation in the frequency range from 1 to 18 GHz there is an expectation that there will be some overlap in describing the surfaces as slightly rough or very rough. Results show that the physical-optics model with an exponential correlation length provides a good ability to predict the scattering characteristics of measured data. This includes the fast angular fall-off in the small incidence angle region and the almost linearly increasing frequency behavior at angles off vertical. The latter is a fatal flaw in using the physical-optics model with a gaussian correlation function. An important note is that the successful prediction of the frequency response shown in the empirical data was accomplished with the same surface parameters throughout the frequency range. However, recent measurements of multiyear ice during summer [Onstott et al 1987] when the backscatter response is dominated by surface scatter suggests that in this situation different correlation lengths and possibly different correlation functions may be required to predict the backscatter response for operation at frequencies from 1 to 18 GHz.

Backscatter data acquired during summer show that radar contrast between first-year and multiyear ice is greatly reduced. The theoretical models also predict a significant reduction in contrast. Volume scatter from multiyear ice will be less because penetration depths reduce when the ice sheet warms, collects moisture and the imaginary part

of its dielectric constant increases. Recent backscatter investigations [Onstott et al, 1987] show that differences in surface roughness, the thickness of snowpack, the distribution of meltwater, and the differences in deformation characteristics are the primary contributors to differences in the microwave signatures of the various ice types during summer. As an example, signatures of thin and medium first-year ice differ from those of thicker ice when the snow-ice interface is roughened by a superimposed ice layer.

Radiative transfer theory was used in the modeling the volume scattering. Sea ice is modeled as a continuous random medium with a cylindrically symmetric correlation function for its permittivity function. It is assumed that the Born approximation is applicable for computing the scattering phase function of the inhomogeneous medium. A description of this formulation is provided in Fung and Eom [1982].

In the Kim, Moore and Onstott model the physical and electrical properties of multiyear sea ice were generalized and described using two layers. These included a layer of low density ice and an ice layer representative of the mid portion of the ice sheet. The upper most ice layer may have densities as low as 700 kg/cm^3 and a thickness of many centimeters. It is also almost salt-free. Air bubbles with diameters of 1 to 3 mm are the key inhomogeneities in this layer. The second layer is composed of clear ice with occasional, small air bubbles. Densities are much greater and may range from 850 to 926 kg/cm^3 (pure ice has a density of 926 kg/cm^3). It is useful to note the corresponding reduction in the air bubble volume. In addition, the bubbles are smaller in size (typically with diameters less than 1 mm). Salinity often ranges from 1°/oo to 2°/oo. This layer is modeled as a half-space because microwave energy is not expected to be either reach or be reflected from the ice-water interface. As the ice water interface is approached, temperatures gradually increase until the sea water temperature is reached (typically about -1.8 C). Salinity also increases to about the salinity of sea water (typically about 32°/oo). Complete absorption is expected prior to reaching this interface.

The two ice layers are described using the five physical and electrical parameters: (a) the average permittivity of the ice layer, (b) the permittivity of the inhomogeneities (air bubbles), (c) the depth of the upper ice layer, (d) the average density of each ice layer, and (e) the diameters of the inhomogeneities (the air bubbles were shown to be adequately described as Rayleigh scatterers). These parameters allow the calculation of the absorption

coefficient, the volume fraction of air bubbles, the number of scatterers per unit of volume, and the volume scattering coefficient for each layer.

Comparison with measurements have produced the following conclusions for snow free multiyear ice. Absolute scattering cross-section levels are most sensitive to the imaginary part of the dielectric constant, to the size of the air bubbles, and to the number of air bubbles; hence it is very sensitive, if not dominated by, the low density portion of the ice sheet. Model predictions show that backscatter levels increase rapidly when the thickness of this upper layer increases from zero thickness, but backscatter levels increase very slowly once a thickness of about 20 cm is reached. Results also indicate that below about 8 GHz the importance of surface roughness and topography increases as frequency decreases.

The magnitude of the volume scattering component for snow free first-year ice has been examined and the contribution of both air bubbles and brine inclusions considered. First-year ice is more saline. The density is high (about 900 kg/cm^3 or higher), the air bubbles are small in size compared to those in multiyear ice, and the brine inclusions are extremely small in size. Model results indicate that volume scattering levels only reach those provided by surface scattering when the ice surface is very smooth, the upper portion of the ice sheet has an unusually low density, and the radar is operating at frequencies greater than 10 GHz and at large angles. Brine pocket (modeled as spheres having diameters of 0.1 mm) contributions are found to be negligible. Only when diameters reach an extreme (diameters of 0.5 mm) is there any contribution and then only at the highest frequencies and for very smooth ice.

The parametric study suggests that first-year and multiyear ice may be confused when first-year ice is very rough, has an exceptionally high salinity, and is a few degrees from the melting point, and when multiyear ice is slightly more saline, the temperature is a few degrees from the melting point, the surface is moderately rough, and the air bubbles are small but still typical of multiyear ice. This confusion reduces as frequencies increase.

REFERENCES

1. Parashar, S.K., "Investigation of Radar Discrimination of Sea Ice," Ph.D. Thesis, University of Kansas, Lawrence, Kansas, 1974.

2. Onstott, R.G., R.K. Moore and W.F. Weeks, "Surface-Based Scatterometer Results of Arctic Sea Ice," IEEE Trans., vol. GE-17(3), 1979, pp.78-85.

3. Onstott, R.G., R.K. Moore, S. Gogineni and C. Delker, "Four Years of Low Altitude Sea Ice Broadband Backscatter Measurements," IEEE J. Oceanic Engrg., vol OE-7, January 1982, pp. 44-50.

4. Onstott, R.G., "Radar Backscatter Study of Sea Ice," Ph.D. Thesis, University of Kansas, Lawrence, Kansas, 1980.

5. Fung, A.K. and H.J. Eom, "Application of a Combined Rough Surface and Volume Scattering Theory to Sea Ice and Snow Backscatter," IEEE Trans., vol GE-20, no. 4, October 1982, pp. 528-536.

6. Kim, Y.S., R.K. Moore, and R.G. Onstott, "Theoretical and Experimental Study of Radar Backscatter From Sea Ice," University of Kansas, Lawrence, Kansas, Report #RSL TR 331-37, January 1984.

7. Ulaby, F.T., R.K. Moore and A.K. Fung, Microwave Remote Sensing, Vol. i: Fundamentals and Radiometry; Vol. II: Radar Remote Sensing and Surface Scattering and Emission Theory; Reading, Massachusetts; Addison-Wesley Publishing Company, 1981, 1982.

8. Onstott, R.G., T.C. Grenfell, C. Matzler, C.A. Luther, and E.A. Svendsen, "Evolution of Microwave Sea Ice Signatures During Early and Mid Summer in the Marginal Ice Zone", JGR Oceans (in press).

EFFECTS OF CHANNEL IMBALANCE, COUPLING, AND NOISE IN POLARIMETRIC RADAR MEASUREMENTS

D.R. Sheen and R.G. Onstott

Environmental Research Institute of Michigan
Ann Arbor, MI 48107, USA

ABSTRACT

Polarimetric radar measurements are corrupted by numerous sources which may contribute errors when attempting to derive true scattering coefficient information. The coupling between the transmit channels, the coupling between receive channels, gain imbalance between channels, and the influence of the system noise floor may all have detrimental impacts on the ability to accurately retrieve required information. The information provided by various radars varies with the unique differences in these error sources. In this paper, the importance of each of the error sources will be examined by a perturbation study. The impact of the error sources on the discriminability among various clutter types will be discussed along with the practical limits for removing the various sources of error.

1 INTRODUCTION

In the following derivation we will assume linear distortion and bound the errors one would observe in polarimetric measurements. Simplifying assumptions concerning the form of the covariance matrix and the distortion matrix are made to get analytic results. The same approach could be used for any non-singular covariance matrix and numerical results could be obtained.

The goal of this research was to determine how channel imbalance, channel coupling, and system noise could be specified so that no single source of error would predominate. Since the errors due to each source vary with the measured covariance matrix, one must know what covariance matrices will be measured with a system as well as the needed precision of these measurements in order to specify needed system performance.

2 DERIVATION

A received radar signal P_s at a specific receive polarization $\underline{R}$ can be expressed in terms of a transmit polarization $\underline{T}$ and the scattering matrix S as follows:

$$P_s = \underline{R}^T S \underline{T} \tag{1}$$

where superscript T indicates transpose. Expanding the above equation,

$$P_s = \left(\begin{array}{cc} R_1 & R_2 \end{array} \right) \left(\begin{array}{cc} S_{11} & S_{12} \\ S_{21} & S_{22} \end{array} \right) \left(\begin{array}{c} T_1 \\ T_2 \end{array} \right) \tag{2}$$

$$P_s = S_{11}R_1T_1 + S_{12}R_1T_2 + S_{21}R_2T_1 + S_{22}R_2T_2 \tag{3}$$

The above equation can be rewritten as an inner product between two vectors $\underline{S}$ and $\underline{V}$,

$$\underline{S} = \left(\begin{array}{cccc} S_{11} & S_{12} & S_{21} & S_{22} \end{array} \right)^T \tag{4}$$

$$\underline{V} = \left(\begin{array}{cccc} R_1T_1 & R_1T_2 & R_2T_1 & R_2T_2 \end{array} \right)^H \tag{5}$$

$$P_s = \underline{V}^H \underline{S} \tag{6}$$

where superscript H indicates the complex conjugate of the transpose. The received intensity is then given by,

$$|P_s|^2 = \underline{V}^H \underline{S} \underline{S}^H \underline{V} \tag{7}$$

The expected value (denoted with $\langle\rangle$'s) of the received intensity we refer to as the average power and is given by,

$$\left\langle |P_s|^2 \right\rangle = \underline{V}^H \mathbf{C} \underline{V} \tag{8}$$

where C is the covariance matrix defined by,

$$\mathbf{C} = \left\langle \underline{S}\underline{S}^H \right\rangle \tag{9}$$

The scattering matrix measured by a polarimetric radar will be distorted and corrupted by noise. Assuming a linear model for distortion D and noise given by $\underline{N}$, the measured scattering matrix M written in a vector form $\underline{M}$ is,

$$\underline{M} = \mathbf{D}\underline{S} + \underline{N} \tag{10}$$

where,

$$\underline{M} = \left(\begin{array}{cccc} M_{11} & M_{12} & M_{21} & M_{22} \end{array} \right)^T \tag{11}$$

$$\underline{N} = \left(\begin{array}{cccc} N_{11} & N_{12} & N_{21} & N_{22} \end{array} \right)^T \tag{12}$$

The measured signal P_m at a given polarization is then

$$P_m = \underline{V}^H \underline{M} \tag{13}$$

The intensity is then,

$$|P_m|^2 = \underline{V}^H \underline{M}\underline{M}^H \underline{V} \tag{14}$$

Assuming noise $\underline{N}$ and scatter $\underline{S}$ are uncorrelated, the average power is given by,

$$\left\langle |P_m|^2 \right\rangle = \underline{V}^{H} \mathbf{D} \mathbf{C} \mathbf{D}^{H} \underline{V} + \underline{V}^{H} \mathbf{N} \underline{V} \qquad (15)$$

where,

$$\mathbf{N} = \left\langle \underline{N} \underline{N}^{H} \right\rangle \qquad (16)$$

The distortion matrix $\mathbf{D}$ can be written as the sum of the identity matrix $\mathbf{I}$ plus two small perturbations due to channel imbalance $\mathbf{B}$ and channel coupling or leakage $\mathbf{L}$

$$\mathbf{D} = \mathbf{I} + \mathbf{B} + \mathbf{L} \qquad (17)$$

Equation 17 can be can be substituted into 15 and after neglecting second order terms,

$$\langle |P_m|^2 \rangle = V^H C V + V^H [CB^H + BC]V + V^H[CL^H + LC]V + V^H N V$$

$$(18)$$

The above equation shows that the measured power $\langle |P_m|^2 \rangle$ at a specific transmit-receive polarization $\underline{V}$ is given by the sum of four terms: (1) the uncorrupted signal $\underline{V}^H \mathbf{C}\underline{V}$; (2) the channel imbalance power $\underline{V}^H[\mathbf{CB}^H + \mathbf{BC}]\underline{V}$; (3) the channel coupling power $\underline{V}^H[\mathbf{CL}^H + \mathbf{LC}]\underline{V}$; and (4) the noise power $\underline{V}^H \mathbf{N}\underline{V}$.

We want to measure the total scattering properties of targets at arbitrary polarizations with minimum error. Thus, we will examine the value of each of the error terms relative to the uncorrupted signal. We define the following error ratios:

$$E_B = \frac{\underline{V}^H[\mathbf{CB}^H + \mathbf{BC}]\underline{V}}{\underline{V}^H \mathbf{C}\underline{V}} \qquad (19)$$

$$E_L = \frac{\underline{V}^H[\mathbf{CL}^H + \mathbf{LC}]\underline{V}}{\underline{V}^H \mathbf{C}\underline{V}} \qquad (20)$$

$$E_N = \frac{\underline{V}^H \mathbf{N}\underline{V}}{\underline{V}^H \mathbf{C}\underline{V}} \qquad (21)$$

These ratios are all highly dependent on the covariance matrix $\mathbf{C}$. Thus, to make logical conclusions about the effect of various distortions one must assume or have knowledge of the covariance matrices one is likely to measure.

We will assume a realistic yet simple form of the covariance matrix and bound the errors due to imbalance, coupling, and noise. To simplify the mathematics we know that most scattering is reciprical and $S_{12} = S_{21}$. The four dimensional vectors and matrices can then all be reduced to three dimensions as follows:

$$\underline{S} = \begin{pmatrix} S_{11} & S_{12} & S_{22} \end{pmatrix}^T \qquad (22)$$

$$\underline{V} = \begin{pmatrix} R_1 T_1 & R_1 T_2 + R_2 T_1 & R_2 T_2 \end{pmatrix}^H \qquad (23)$$

$$\mathbf{C} = \begin{pmatrix} \langle S_{11}S_{11}^* \rangle & \langle S_{11}S_{12}^* \rangle & \langle S_{11}S_{22}^* \rangle \\ \langle S_{12}S_{11}^* \rangle & \langle S_{12}S_{12}^* \rangle & \langle S_{12}S_{22}^* \rangle \\ \langle S_{22}S_{11}^* \rangle & \langle S_{22}S_{12}^* \rangle & \langle S_{22}S_{22}^* \rangle \end{pmatrix} \qquad (24)$$

The above equation will be further simplified by assuming the cross-correlations $\langle S_{11}S_{12}^* \rangle$ and $\langle S_{12}S_{22}^* \rangle$ are zero. This

is a reasonable approximation for scatter from most distributed targets. A further approximation will be made by assuming the co-polarized channels have equal intensity or $\langle S_{11}S_{11}^* \rangle = \langle S_{22}S_{22}^* \rangle$. This approximation is crude but makes the mathematics much easier. The resulting covariance matrix is normalized so that the 11 element has value one and the matrix has the following form:

$$\mathbf{C} = \begin{pmatrix} 1 & 0 & c \\ 0 & a & 0 \\ c & 0 & 1 \end{pmatrix} \qquad (25)$$

In the above covariance matrix it is assumed both a and c are real and $-1 \leq c \leq 1$. The channel imbalance matrix is assumed to have the following form:

$$\mathbf{B} = \begin{pmatrix} b_1 & 0 & 0 \\ 0 & b_2 & 0 \\ 0 & 0 & b_3 \end{pmatrix} \qquad (26)$$

The channel coupling matrix is assumed to have the following form:

$$\mathbf{L} = \begin{pmatrix} 0 & l_2 & 0 \\ l_1 & 0 & l_4 \\ 0 & l_3 & 0 \end{pmatrix} \qquad (27)$$

The noise covariance matrix is assumed to have the following form:

$$\mathbf{N} = \begin{pmatrix} n & 0 & 0 \\ 0 & n & 0 \\ 0 & 0 & n \end{pmatrix} \qquad (28)$$

The error ratios E_B, E_L, E_N defined in equations (19) through (21) cannot be evaluated exactly without knowing the exact values for the polarization $\underline{V}$, the signal covariance $\mathbf{C}$, the channel imbalance $\mathbf{B}$, the coupling $\mathbf{L}$, and the noise covariance $\mathbf{N}$. However, these errors can be bounded by first assuming the functional forms for $\mathbf{C}$, $\mathbf{B}$, $\mathbf{L}$, and $\mathbf{N}$ given respectively in equation (25) through (28). Then the polarization vector $\underline{V}$ will be varied to maximize the amplitude of the error ratios. To evaluate the maximum of the error ratios for various polarizations let

$$\underline{U} = \mathbf{C}^{\frac{1}{2}}\underline{V} \qquad (29)$$
$$\underline{V} = \mathbf{C}^{-\frac{1}{2}}\underline{U}$$

The error ratios the become:

$$E_B = \frac{\underline{U}^H \mathbf{C}^{-\frac{1}{2}}[\mathbf{CB}^H + \mathbf{BC}]\mathbf{C}^{-\frac{1}{2}}\underline{U}}{\underline{U}^H \underline{U}} \qquad (30)$$

$$E_L = \frac{\underline{U}^H \mathbf{C}^{-\frac{1}{2}}[\mathbf{CL}^H + \mathbf{LC}]\mathbf{C}^{-\frac{1}{2}}\underline{U}}{\underline{U}^H \underline{U}} \qquad (31)$$

$$E_N = \frac{\underline{U}^H \mathbf{C}^{-\frac{1}{2}}\mathbf{N}\mathbf{C}^{-\frac{1}{2}}\underline{U}}{\underline{U}^H \underline{U}} \qquad (32)$$

The maximum amplitude of the above ratios are given by the maximum amplitude eigenvalues of $\mathbf{C}^{-\frac{1}{2}}[\mathbf{CB}^H + \mathbf{BC}]\mathbf{C}^{-\frac{1}{2}}$, $\mathbf{C}^{-\frac{1}{2}}[\mathbf{CL}^H + \mathbf{LC}]\mathbf{C}^{-\frac{1}{2}}$ and $\mathbf{C}^{-\frac{1}{2}}\mathbf{N}\mathbf{C}^{-\frac{1}{2}}$. The three eigenvalues

for each matrix were calculated and the maximum eigenvalues were determined.

The eigenvalues for the channel imbalance error are dependent on the phases and amplitudes of b_1, b_2, and b_3. However, the maximum error can be bounded if we assume the imbalances are the same amplitude as follows:

$$|b_1| = |b_2| = |b_3| = b \qquad (33)$$

The phases of b_1, b_2, and b_3 are then chosen to yield the maximum eigenvalue amplitude. This is the maximum relative error and is

$$|E_B|_{max} = \frac{2b}{\sqrt{1-c^2}} \qquad (34)$$

Note that this error can be infinite when $c \to \pm 1$. This is because for $c = \pm 1$ there is a polarization combination where the uncorrupted received power is zero and so the error is infinite relative to the signal.

The eigenvalues for the channel coupling error are dependent on the phases and amplitudes of l_1, l_2, l_3, and l_4. However, the maximum error can be bounded if we assume the couplings are the same amplitude as follows:

$$|l_1| = |l_2| = |l_3| = |l_4| = l \qquad (35)$$

The phases of l_1, l_2, l_3, and l_4 are then chosen to yield the maximum eigenvalue amplitude. This is the maximum relative error and is

$$
\begin{aligned}
|E_L|_{max} &= l\sqrt{4 + \frac{2a}{1+c} + \frac{2}{a}(1+c)} \\
&\quad \text{or} \\
&= l\sqrt{4 + \frac{2a}{1-c} + \frac{2}{a}(1-c)} \\
&\quad \text{or} \qquad (36) \\
&= l\sqrt{\frac{2a}{1+c} + \frac{2}{a}(1-c)} \\
&\quad \text{or} \\
&= l\sqrt{\frac{2a}{1-c} + \frac{2}{a}(1+c)}
\end{aligned}
$$

The values of a and c will determine which of the above expressions has the maximum value. Note that this error can be infinite when $c \to \pm 1$. This is because for $c = \pm 1$ there is a polarization combination where the uncorrupted received power is zero and so the error is infinite relative to the signal. Similarly, the error can be infinite when $a \to \pm\infty$ or $a \to 0$. The $a \to \pm\infty$ is of concern since we normalize the covariance matrix by dividing by the 11 element. Thus, a zero 11 element in the covariance matrix would cause a to be undefined.

The maximum eigenvalue for the system noise error

has amplitude:

$$|E_N|_{max} = \frac{n}{a} \text{ or } \frac{n}{1-c} \text{ or } \frac{n}{1+c} \qquad (37)$$

Again, the values of a and c determine which of these expressions is the largest.

3 RESULTS

To quantify the results we will assume various reasonable values for a and c. Then we will calculate the magnitudes of the imbalance b, the leakage l, and the noise n which all give rise to the same relative error. For ease of comparison, results will be presented in dB with the following definitions:

cross-polarized relative intensity This is the intensity of the cross-polarized channels relative to the co-polarized channels. In dB it is defined as $10\log a$.

co-polarized correlation This is the value of the cross-correlation between the two co-polarized channels. In dB it is defined as $10\log c$.

minimum signal-to-error ratio This is the inverse of the error ratios defined in the previous section. Here we have assumed all the error ratios are equal $E_B = E_L = E_N = E$ and in dB the minimum signal to error ratio is $-10\log E$.

channel balance This is a measure of how well balanced the channels of the radar are. In dB it is defined as $20\log(1+b)$.

channel coupling this is a measure of how much leakage between channels there is in the radar. In dB it is defined as $20\log l$.

co-polarized SNR This is the signal-to-noise ratio in the co-polarized channels. In dB it is defined as $-10\log n$.

Results for some assumed scatter characteristics are presented in Table 1.

4 CONCLUSIONS

Table 1 shows some of the needed system parameters to accurately measure (minimum signal-to-error of 3 dB) some example covariance matrices. Based roughly on this table we can simply state needed system parameters. First, the channel balance needed is dependent on the correlation between the co-polarized channels. If this correlation coefficient is -3.0 dB the channel gains must be balanced to within 1.6 dB. Second the channel coupling is most strongly dependent on the ratio of the powers in the co- and cross-polarized channels. The coupling must be approximately 10 dB less than the ratio of the lower-powered channel to the higher-powered channel. Again, more exact specifications

could be calculated for a specific covariance matrix.

It should be pointed out that linear distortions (if known) could always be removed. The problem is measuring the distortion exactly. For example, an imaging radar with a broad swath might have spatially varying distortions and to characterize this distortion would require deploying many calibration targets over the whole swath. These targets must all be measured with enough signal-to-noise (or clutter) that the distortions can be accurately measured. Also, to remove distortions would require an extra step in processing data. For these reasons it is important to strive for minimal distortions from the start.

5 ACKNOWLEDGEMENTS

Table 1: Some example relationships between covariance matrix parameters and various sources of error.

covariance matix parameters		system parameters			minimum signal-to-error
cross-polarized intensity	co-polarized correlation	channel balance	channel coupling	co-polarized SNR	
-30.0 dB	-3.0 dB	1.6 dB	-40.8 dB	33.0 dB	3.0 dB
-30.0 dB	-1.0 dB	1.2 dB	-41.6 dB	33.0 dB	
-30.0 dB	-0.2 dB	0.6 dB	-41.9 dB	33.0 dB	
-20.0 dB	-3.0 dB	1.6 dB	-30.8 dB	23.0 dB	
-20.0 dB	-1.0 dB	1.2 dB	-31.6 dB	23.0 dB	
-20.0 dB	-0.2 dB	0.6 dB	-32.0 dB	23.0 dB	
-10.0 dB	-3.0 dB	1.6 dB	-21.3 dB	13.0 dB	
-10.0 dB	-1.0 dB	1.2 dB	-22.0 dB	13.0 dB	
-10.0 dB	-0.2 dB	0.6 dB	-22.4 dB	16.5 dB	
0.0 dB	-3.0 dB	1.6 dB	-15.5 dB	6.0 dB	
0.0 dB	-1.0 dB	1.2 dB	-17.5 dB	9.9 dB	
0.0 dB	-0.2 dB	0.6 dB	-22.9 dB	16.5 dB	
10.0 dB	-3.0 dB	1.6 dB	-22.5 dB	6.0 dB	
10.0 dB	-1.0 dB	1.2 dB	-26.1 dB	9.9 dB	
10.0 dB	-0.2 dB	0.6 dB	-32.5 dB	16.5 dB	
-30.0 dB	-3.0 dB	0.9 dB	-46.8 dB	36.0 dB	6.0 dB
-30.0 dB	-1.0 dB	0.6 dB	-47.6 dB	36.0 dB	
-30.0 dB	-0.2 dB	0.3 dB	-47.9 dB	36.0 dB	
-20.0 dB	-3.0 dB	0.9 dB	-36.8 dB	26.0 dB	
-20.0 dB	-1.0 dB	0.6 dB	-37.6 dB	26.0 dB	
-20.0 dB	-0.2 dB	0.3 dB	-38.0 dB	26.0 dB	
-10.0 dB	-3.0 dB	0.9 dB	-27.3 dB	16.0 dB	
-10.0 dB	-1.0 dB	0.6 dB	-28.0 dB	16.0 dB	
-10.0 dB	-0.2 dB	0.3 dB	-28.4 dB	19.5 dB	
0.0 dB	-3.0 dB	0.9 dB	-21.5 dB	9.0 dB	
0.0 dB	-1.0 dB	0.6 dB	-23.5 dB	12.9 dB	
0.0 dB	-0.2 dB	0.3 dB	-28.9 dB	19.5 dB	
10.0 dB	-3.0 dB	0.9 dB	-28.5 dB	9.0 dB	
10.0 dB	-1.0 dB	0.6 dB	-32.1 dB	12.9 dB	
10.0 dB	-0.2 dB	0.3 dB	-38.5 dB	19.5 dB	

THE DISCRIMINATION OF SEA ICE TYPES USING SAR BACKSCATTER STATISTICS

Robert A. Shuchman, Christopher C. Wackerman, Andrew L. Maffett*,
Robert G. Onstott and Laura L. Sutherland,

Radar Science Laboratory
Environmental Research Institute of Michigan
Ann Arbor, MI 48107 USA

*ERIM Consultant

ABSTRACT

X-band (HH) synthetic aperture radar (SAR) data of sea ice collected in March and April 1987 during the Marginal Ice Zone Experiment (MIZEX) was statistically analyzed with respect to discriminating open water, first-year ice, multiyear ice and Odden. Odden is large expanses of nilas ice that rapidly form in the Greenland Sea and transforms into pancake ice. A first order statistical analysis indicated that mean versus variance can segment out open water and first-year ice, and skewness versus modified skewness can segment the Odden and multiyear catagories. In addition to first order statistics a model has been generated for the distribution function of the SAR ice data. Segmentation of ice types was also attempted using textural measurements. In this case, the general co-occurrency matrix was evaluated. The textural method did not generate better results than the first order statistical approach.

1. INTRODUCTION

Active microwave measurements were made of various sea ice forms in March and April 1987 during the Marginal Ice Zone Experiment (MIZEX). The microwave measurements were made at 1, 5, 10, 18, and 35 GHz using a ship-based scatterometer and aircraft mounted synthetic aperture radar (SAR). The SAR measurements were made at 9.8 GHz, horizontal transmit and receive polarization.

The sea ice forms present in the Greenland Sea MIZEX operations area included: open water; open water with grease ice streamers; new ice (5-8 cm thick); first-year ice (20-40 cm thick); first-year ice with rubble (.60-1.5 m thick); and multiyear ice (2-4 m thick). Large expanses (200,000 km²) of new nilias sea ice (5 cm thick) forms in the Greenland Sea as a result of oceanographic upwelling of cold water interacting with cold (< -10°c) northerly polar winds. This rapid ice formation is referred to as the Odden and is discussed in Ref. [1]. The nilas transitions into pancake floes (10-15 cm thick) due to continued growth and wave action.

The scatterometer data were used to validate the SAR backscatter values obtained at 10 GHz. Additionally, the scatterometer data extended the SAR sea ice type classification to C- and L-band frequencies in order to predict the performance of the SAR instruments to be flown on the European, Canadian, and Japanese SAR satellites.

NASA is presently building a satellite receiving station in Fairbanks, Alaska that will collect and process in near real-time SAR data from these satellites that will be launched in the next 5-7 years. The SAR facility will contain a geophysical processor, a dedicated computer that will utilize the processed SAR data to provide sea ice concentration, ice type, and kinematics information. The MIZEX '87 data although it was collected at X-band (HH) offers a unique opportunity to develop and evaluate algorithms that can be implemented on the geophysical processor. As reported in ref. [2], the radar backscatter response between X-band (HH) and C-band (VV) is very similar.

This SAR analysis included the generation of standard statistics (i.e., mean, standard deviation, variance, skewness, and kurtosis), within areas that were intensively "sea truthed" by scientists operating from the M/V POLAR CIRCLE. In addition to the standard statistics generated from the SAR data several probability distributions were evaluated to describe the various ice types present within the SAR scene. These distributions include: uniform, gamma, Gaussian, inverse Guassian, lognormal, and modified Beta. It is postulated that such distributions can be used to further differentiate ice types (particularly first-year ice with rubble). The distributional analysis has suggested that the SAR sea ice data are best fitted by gamma and lognormal (and sometimes inverse Gaussian) distributions and that these distributions may prove useful in differentiating all ice types present within the MIZEX SAR scenes.

The use of textural methods (i.e., higher order statistics) were also evaluated with respect to differentiating the ice sea forms present in the MIZEX SAR data set. The general co-occurrence matrix was used and found to generate very similar results to the mean and standard deviation analysis.

In this paper, we will first describe the MIZEX '87 SAR data set and then discuss four cases of sea ice forms that were selected for the statistical analysis. The statistics results will then be presented.

2. DATA SETS

MIZEX '87 in the Greenland and Barents Seas combined observations from both remote sensing and in situ data collections to provide an integrated approach to the study of winter marginal ice zone (MIZ) conditions. Favorable weather permitted 18 consecutive days of SAR coverage and field operations. The SAR system, with its high resolution (15 x 15 m), clarity of image and real-time availability, proved to be a powerful and efficient tool to aid in the planning and carrying out of field experiments.

MIZEX was the first international experiment having daily SAR coverage with real-time imagery down-linked

to the ships in the field. This imagery was used on-board POLAR CIRCLE to identify areas of interest such as the location of the ice edge, eddies, and ocean fronts. The ship would then proceed to the SAR identified areas to collect sea truth. The data was also used to select sites for detailed active and passive microwave measurements and characterization of physical and electrical properties of the ice and snow. In addition to being down-linked, the SAR data was recorded on-board the aircraft on high density digital tapes.

During MIZEX '87, two Intera SAR equipped aircrafts; STAR-1 and STAR-2 were deployed to collect ice edge imagery. These missions are described in refs. [3-4]. The Intera STAR-1 and STAR-2 systems are X-band (9.8 GHz) radars that transmit and receive with horizontal polarization. Table 1 summarizes the parameters of both systems while Figure 1 indicates the imaging geometries. Figure 2 is a representative mosaic covering a 445 x 195 km area of the MIZ. On the X-band SAR data, bright tones on the image represent multiyear ice while the darker tones are various stages on young ice. The blackest signatures on the image are open water. The SAR mosaic was interpreted using a hybrid manually assisted digital technique to provide the interpretation key shown in Figure 3. Note that the ice type and concentration information is obtainable from this data based on tonal signatures.

TABLE 1. STAR SPECIFICATIONS AS USED IN MIZEX

PROPERTY	STAR-2	STAR-1
Operating Altitude	29,000 ft.	
Wave length	X-band	
Polarization	HH	
Viewing Direction	Left or Right	
Processing	Real time	
Recording	8 bit data, full bandwidth data recording on parallel HDDR	4 bit data, either 12 x 12m or 24 x 24m pixels on serial HDDR
Swath width		
Narrow (Hi-Res)	17 km	23 km
Wide (Lo-Res)	63 km	45 km
Pixel size	Along track/ cross track	Along track/ cross track
Hi-Res	4 x 4 m	Not used
Lo-Res	5.2 x 16m	12 x 12m or 24 x 24m
Downlink	4 bits	4 bits
Azimuth Looks	7	7
Lo-Res	16 x 16m or 32 x 32m	12 x 12m or 24 x 24m

For this study, the generic ice types present within the test site were divided into four categories. These included: open water; first-year ice; multiyear ice; and the areas termed Odden (i.e., nilas and pancake). These four ice types represent ice thickness intervals that are accepted product outputs of the Alaska geophysical processor.
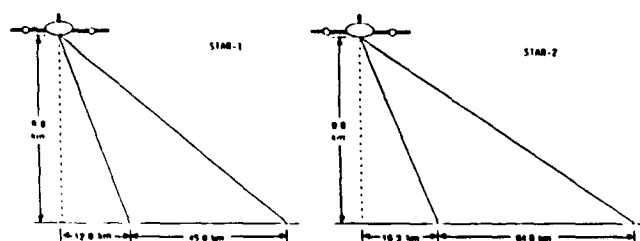
Figure 1.   Viewing Geometry for STAR-1 and -2 in Wide Swath Mode

Fifty-four areas from twelve SAR flights during the 31 March to 8 April 1987 time period were used in the statistical analysis. Each area was approximately 100 x 100 pixels which corresponds to a ground area of approximately 700 x 700 meters. The areas selected included incident angles of 30° to 70°. Typical open water (w), first-year ice (f), multiyear ice (m), and Odden (0) areas used in the study are shown on Figure 2.

SAR Imagery
4 April 1987
1800-2145 UT
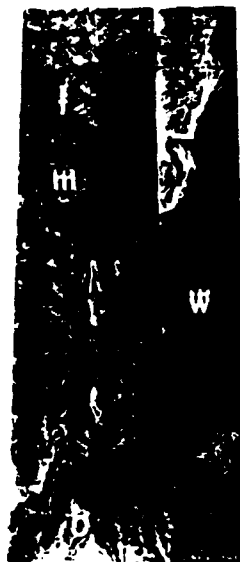
Ice Concentration
and Floe Size Interpretation

Figure 2.   Figure 3.

50% Multi-Year Fragments. (1 5 - 3 5 m Thick), 50-250 m in Diameter in a First Year Ice Framework. (< 1 m Thick) 20-45% Total Ice Concentration

50-60% Multi-Year Floes. (1 5 - 4 m Thick) 50-250 m in Diameter Surrounded by First Year Ice. (< 1 m Thick) 70-90% Total Ice Concentration. Some Open Water Leads Exist

40-50% Multi-Year Floes. 1-30 km in Diameter Surrounded by First-Year Floes. (< 1 m Thick) 95% Total Ice Concentration, Some Open Water Leads Exist

Ice Free Ocean and Polynyas

New Nilas Ice. 3-15 cm Thick Transitioning to Pancake Floes. 10-100 cm in Diameter 75-90% Total Ice Concentration

Large Individual Floes

3. DISCRIMINATION USING FIRST-ORDER STATISTICS
The ability of first-order statistics (i.e., statistics based on individual pixel values, not spatial correlations) to segment the SAR images into their appropriate four classes; open water, first-year ice, multiyear ice and Odden was analyzed. Since the results of an initial distributional fitting analysis [Ref. 2] indicated that two parameter functions did a good job of fitting the data, segmenting the data with

pairs of statistics was tried. The two best pairs are shown in Figures 4 and 5. Figure 4 shows mean versus standard deviation (all of these statistics are intensity values). Note that although Odden ice and multiyear ice are very mixed, the other two classes segment out rather nicely; almost linearly along the curve we have open water, then first-year ice, then the combination of multiyear ice and Odden ice.
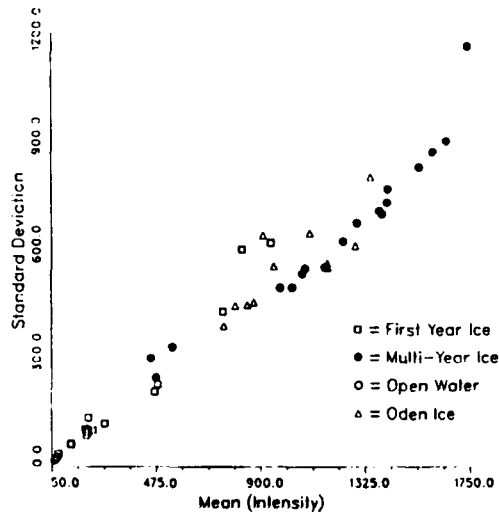
Figure 4.   Segmentation Using Modified Skewness and Skewness
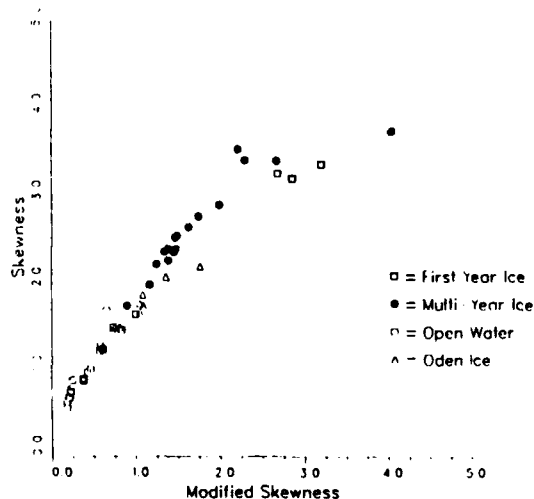
Figure 5.   Standard Deviation vs Mean Segmentation of Intensity Ice Data

The Odden is representative of new first-year ice that has undergone extensive deformation due to wave action. The nilas ice that transitions into pancake floes have very rough edges (see Figures 2 and 4 in ref [1]). These rough edges reflect radar energy and as such the scattering coefficient for pancake ice is large [Ref. 2]. Thus, it is not surprising that multiyear and Odden ice types overlap on the mean versus standard deviation curve.

Figure 5 shows skewness versus modified skewness. Note that this also does a nice job of segmenting, although the distinction of first-year ice from Odden ice is somewhat less sharp then on Figure 4. However, multiyear ice and Odden ice are much better separated

then on Figure 4. Again, almost linearly along the curve, we have open water, first-year ice, Odden ice and multiyear ice.

In conclusion, it appears that mean versus variance can segment out open water and first-year ice, then skewness versus modified skewness can segment out Odden ice and multiyear ice. In general, first-order statistics appear to do a good job.

Currently under progress is an attempt to optimize the combination of first order statistics for segmentation. Eigenvector analysis is being performed on the covariance matrices for each ice class to determine which linear combination of parameters generates the most variation within the class and the least variation within the class. In addition, the same analysis is being performed on the entire set of SAR images. Optimal open water (for example) classification can then be performed by finding the linear combination that minimizes the variation within the class but maximizes the variation between classes.

4. DISTRIBUTION FUNCTION ANALYSIS

An attempt has been made to generate a model for the distribution function of the SAR ice data that would fit all of the MIZEX '87 images. If this is possible, then the parameters of the distribution function would suffice to characterize the image, and we could segment the images based on their parameters alone. Unfortunately, we have found no model that passes the statistical tests for all of the images; this search is still in progress. We have tested a number of simple analytical forms but the results indicate that the actual distribution function is more complicated than this. Currently, work is being performed on a model that deals more with the physical scattering phenomena [Ref. 5] and the results look encouraging. Unfortunately, with complexity comes computational cost so no definite results for the ice data are available yet.

For the analytical forms, we tested uniform, gamma, inverse gaussian, gaussian, lognormal and modified beta. Figure 6 shows the Kolmogorov statistic (a statistical measure of how different the analytical distribution function is from the actual SAR image distribution function) for the ice data set for all the types. Lognormal, inverse gaussian and modified beta all produce similar results with a preference to the modified beta. It should be noted that the modified beta is the only model that allows the distribution function to be fit to higher order moments (i.e., width and skewness) while the other models fit only the mean and variance. This appears to support the results in section 3 where these higher order moments are necessary to separate Odden ice from multiyear ice, and in addition did a fair job of segmenting the other types.

Although these three models do a good job of fitting to the data, they do not pass the statistical tests (i.e. it can not be said with statistical certainty that they are a good fit, we can only say that the fit looks good to the eye). Figure 7 shows the same Kolmogorov statistic but subtracted by the threshold that it has to be less than in order to pass the test. Thus values less than zero on Figure 7 mean it passed and values greater than zero indicate failure. Note the very large amount of failures; although there are a few passes. In addition, it appears that the modified beta advantage goes away for this plot; a result that is not explainable at the present time.

It is interesting to note how the amount of passes and failures change with ice type. Figure 8-11 shows the same numbers as Figure 7, but separated according to ice type. Note that open water fails miserably; an

interesting result which indicates that the scattering going on is not simple. First-year ice and multiyear ice do about the same; much more successful (for the three candidate models) then open water. This seems to indicate that scattering from these types is more "traditional". Finally, Odden does the best of all; the points are very clustered at zero. Perhaps this is the most "traditional"? Also note that the most successes appears to be for multiyear ice with first-year ice next.
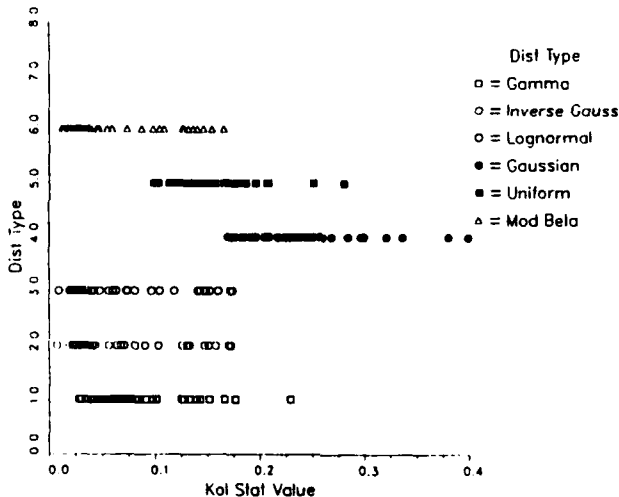
Figure 6.   Ice Measurements Kolmogorov Statistics
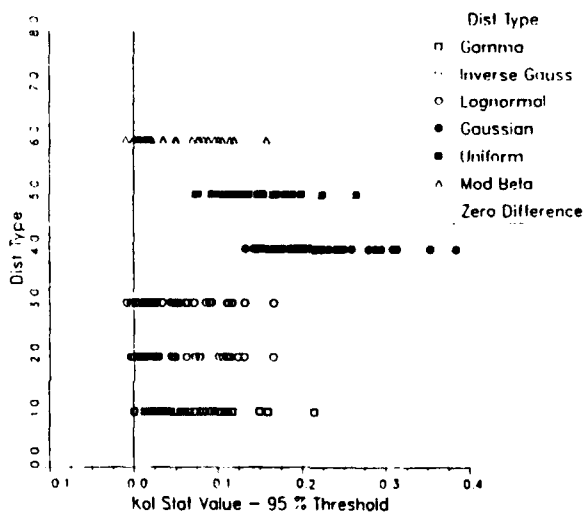
Figure 7. Ice Measurements Kolomgorov Statistics
Subtracted by the Threshold Value

All of the above distribution models had their parameters generated from the data statistics. We also investigated generating optimal parameters by iteratively finding the ones that minimized a mean square error metric between the model and the data. Figure 12 shows the result for optimizing the parameters of a gamma model, then generating a cluster plot of the equivalent mean and standard deviations from these optimal parameters. Comparing to Figure 4, we get much better segmentation this way then simply taking the data statistics; although Odden and multiyear are still mixed. We are currently trying this for other models, specifically the modified beta and the more complicated model mentioned above.
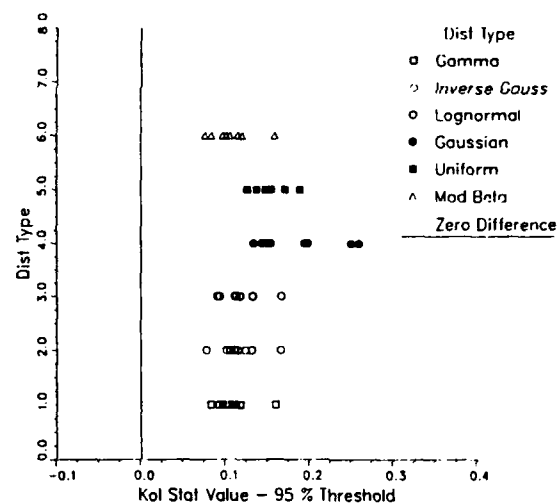
Figure 8.   Ice Measurements Kolmogorov Statistics
(Open Water)
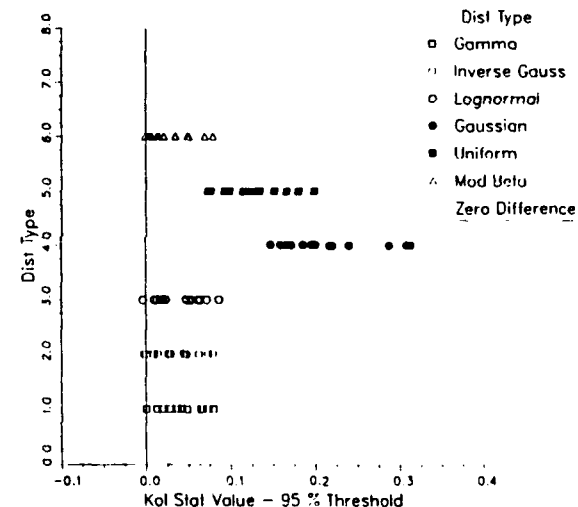
Figure 9.   Ice Measurements Kolmogorov Statistics
(First-Year Ice)
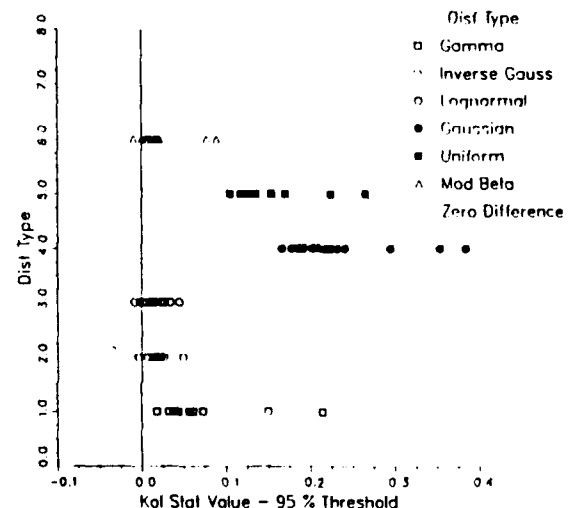
Figure 10. Ice Measurements Kolmogorov Statistics
(Multiyear Ice)
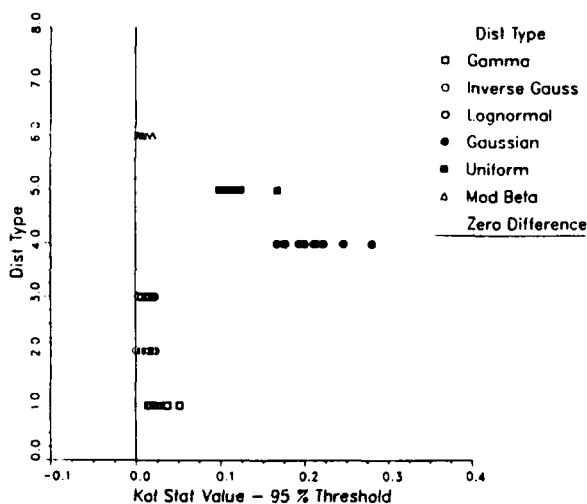
Figure 11. Ice Measurements Kolmogorov Statistics
(Odden Ice)
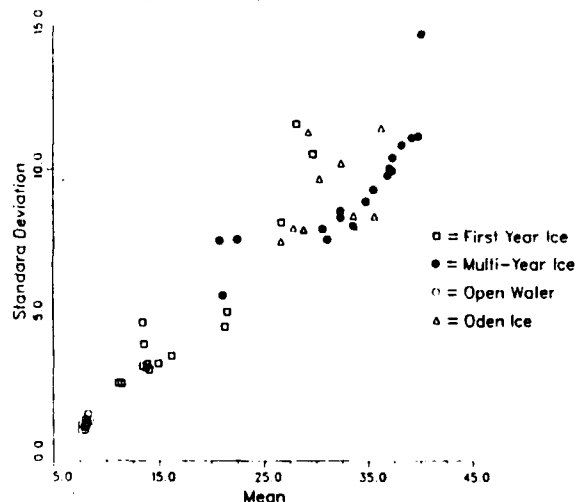
Figure 12. Standard Deviation vs Mean Segmentation
From Simple Gamma Model
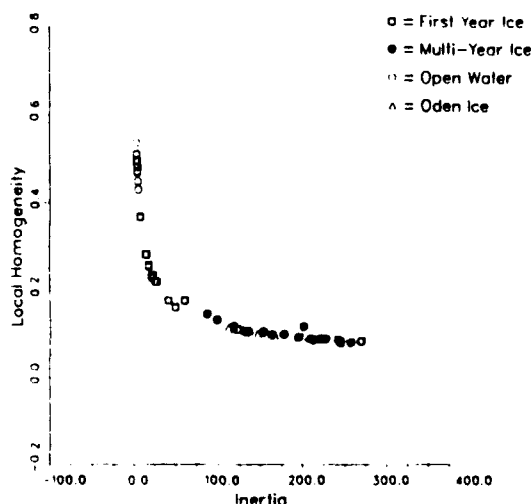
Figure 13. Segmentation Using Texture Measures

5. SEGMENTATION USING TEXTURE MEASURES

Segmentation of the four ice types was also evaluated using textural methods. We used the most favorite texture measure among image processors; the general co-occurency matrix (GCM). In general, the GCM measure the spatial correlation structure of the data and generates estimates of the direction of correlation, the strength of correlation, etc. We again generated cluster plots of pairs of various measures; the best pair is shown in Figure 13. The results appear very similar to the mean and standard deviation plots; open water and first-year are well segmented from the rest, but Odden and multiyear are mixed. We are currently applying the eigenvector analysis to this data also to generate optimal combinations; however we do not anticipate any better results than the first order statistics have given.

6. SUMMARY

The MIZEX '87 X-band SAR data was divided into four sea ice classes (open water, first-year, multiyear, and Odden) to evaluate first-order statistics, higher order statistics (texture), and distribution analysis to segment the SAR image into the required classes. The first order statistical analysis (i.e., statistics based on individual pixel values, not statistical correlations) indicated that mean versus variance can segment out open water and first-year ice, and skewness versus modified skewness can segment out Odden and multiyear ice. The use of texture techniques, in this case the use of the general co-occurency matrix, did not yield results superior to the first older statistical analysis. In general, the first older statistics appear to do a good job and considering computation efficiency is the recommended algorithm approach for the Alaska geophysical processor.

The search for a distribution function of the SAR ice data that will fit the majority of MIZEX '87 imagery is continuing. The distribution analysis suggests the data are best fitted by gamma and lognormal (and sometimes inverse Gaussian) distributions.

7. ACKNOWLEDGEMENTS

8. REFERENCES

1. Sutherland, L.L. and R.A. Shuchman, "SAR and Passive Microwave Observations of the Odden During MIZEX '87", these proceedings.

2. Shuchman, R.A., R.G. Onstott, L.L. Sutherland, and C.C. Wackerman, "Intercomparison of Synthetic and Real-Aperture Radar Observations of Arctic Sea Ice During Winter MIZEX '87, IGARSS '88, Edinburgh, Scotland, September 1988.

3. Shuchman, R.A., L.L. Sutherland, O.M. Johannessen, and E.D. Leavitt, "Geophysical Information on the Winter Marginal Ice Zone Obtained From SAR", IGARSS '88, Edinburgh, Scotland, September 1988.

4. Shuchman, R.A., L.L. Sutherland, B.A. Burns and E.D. Leavitt, "MIZEX 1987 SAR Data Summary" ERIM Report #154600-34-T, 1988.

5. Wackerman, C.C., "Calculation of the Spatial Distribution of Scatterers in a Diffuse Scene from SAR Data", these proceedings.

ACTIVE MICROWAVE CLASSIFICATION OF SEA ICE

Robert G. Onstott
Environmental Research Institute of Michigan
Advanced Concepts Division
Radar Science Laboratory
P.O. Box 8618
Ann Arbor, MI 48107

ABSTRACT

Radar backscatter studies of Arctic sea ice have been carried out over a number of years now with the intent to acquire physical property information through by the examination of microwave signatures. The breadth of these studies continues to expand. As an example, measurements are now conducted at frequencies from 500 MHz to about 100 GHz. One of the scientific goals of this work has been to develop an improved understanding of the scattering processes at play. A second, equally important, goal has been to apply the knowledge gained in examining the backscatter response of ice and snow made in conjunction with detailed scene characterizations, the insight gained through theoretical modeling and parametric study, and the data entered into the radar signature library to develop procedures to convert microwave signal information, available in the very near future, into valuable data products, ultimately providing the opportunity for us to better understand our environment. The purpose of this paper is to provide a discussion of what has been learned through the many efforts associated with the near-surface scatterometer measurement programs and how the knowledge gained is assisting in the development of future sea ice type satellite algorithms.

INTRODUCTION

One of the most important pieces of geophysical information that must be obtained from satellite observation of the frozen ocean is ice type. A wide array of categories have been defined by the World Meteorological Organization and are related to thickness, age or formation characteristic. Basic categories include new (0 to 10 cm thick), young (10 to 30 cm thick), first year (> 30 cm thick), second year (survived one melt season) and multiyear (survived multiple melt seasons). The ability of determining ice type using space-based sensors is dependent on spatial resolution and the region under observation. In the marginal ice zone (MIZ) the mixture of floes of various ice types have diameters which are small, ranging from 10 to 200 m, and at some point have experienced moderate deformation. Ice tends to be thick either because ice must be thick to survive in this dynamic region, because thin ice is rapidly crushed during the constant collisions with other floes, or because of the rafting of thin ice

floes. Small ice pieces between floes, and the ridges or blocks strewn around floe rims, and the moderately deformed floe interiors produce significant backscatter. In regions of constant shear, such as between shorefast and pack ice, processes are very dynamic and result in topographically rough, spatially variable, and very thick formations. Backscatter is strong and variable regardless of original ice type. The region which is spatially the most significant is the pack ice portion of the Arctic Ocean. Here floes are frozen into fields which float as sheets with sizes often many ten's of kilometers. Ridge building due to pressure is the major deformation event.

IN-SITU SCATTEROMETER PROGRAMS

By 1976 the need to coordinate detailed microwave and surface measurements was well recognized. In addition, because existing sensor parameters varied and future sensors were still undefined it was important to acquire data over a wide range of frequencies, polarizations, and incidence angles. It is interesting to note that the first measurements were made at 1.5 GHz and multiple frequencies between 8 and 18 GHz [1]. Today they are made from 0.5 to 100 GHz (i.e. CEAREX). The sea ice measurement program began at the University of Kansas by Richard K. Moore and the author with a tripod-type structure (1976) whose characteristic was to provide a constant range. It has been extended to operation from helicopter, surface ship, sled, and gantry (laboratory facility). Microwave scene characterization experiments began in 1977 at Point Barrow in conjunction with W.F. Weeks (CRREL and Univ. of Alaska) who served as mentor for sea ice property measurements. Numerous measurement programs were then conducted with R. Ramsieier (AES Canada) with whom measurement of physical-chemical properties would be finely honed with the goal of relating specific microwave responses and processes to ice properties. Measurements were made of the surface for the calculation of roughness statistics (rms height and correlation length), of the salinity and density profiles with fine depth resolution (1 cm spacings in the top 20 cm of the ice sheet) to describe a rapidly changing permittivity, and of the brine or brine-slush layer which resides on all new and first-year ice forms. Coordinated active (near-surface scatterometer and SLAR) and passive microwave (aircraft imager and profilers) measurements began with those made at Mould Bay in 1981 as did the use of radar (SLAR) imagery in-situ experiment planning. Coordination of surface active and passive microwave

measurements which began at Mould Bay in 1982 have continued with CEAREX and CRRELEX being examples of the most recent investigations. Basic information about these measurements programs is provided in Table 1. It is important to note that as of this year significant studies have been conducted during all seasons, except perhaps the very end of summer when the ice drains, remains drained, and then begins to freeze. All major ice types have now been observed. Possibly the greatest weakness in the existing observations is that of region. Studies have been made in the Chuckchi, Beaufort, Greenland, and Barents Seas, with almost no study of the Central Arctic.

OBSERVATIONS

In examining under what conditions ice types may be discriminated using radar it was determined that it was important to (a) have data acquired over a wide range of conditions where both the microwave and physical-electrical properties are well-characterized, (b) be able to interpret the empirical observations with supporting electromagnetic scattering theory and model predictions, and (c) to study the variation in sea ice physical-electrical properties. Early on it was hypothesized that first year ice backscatter is dominated by surface scattering and multiyear ice by volume scatter. The critical issues have been in documenting under what conditions this is true, at what frequencies and polarizations, can this difference be exploited, what are the optimum radar parameters for ice type discrimination, and given a radar parameter set what is the anticipated performance.

The parameters and conditions which have a critical influence on backscatter intensity and are typical are listed in Table 2 as a function of major ice type. The attempt here is to list these parameters in their relative order of importance. When optimizing for ice type discrimination, the keys to information exploitation are (a) multiyear ice produces a strong volume scatter due to the presence of a low density ice layer in the upper portion of the ice sheet (a minimum thickness of about 2 cm is required), (b) first year ice returns are dominated by surface scatter and variations in surface roughness scales produce large changes in backscatter levels, and (c) new ice returns are weak (off-vertical) because surfaces are very smooth.

For multiyear ice during winter, volume scatter dominates at frequencies beyond 10 GHz where as at some frequency below about 5 GHz surface scattering begins to dominate. For first year ice surface scattering dominates below 15 GHz. Snow has little impact on multiyear ice backscatter but enhances first year and new ice backscatter [2].

The evolution of the microwave signatures during summer is quite complex. The reader is referred to the discussion provided in the paper by Onstott et al [3]. During the first part of summer the wet snowpack and warm ice sheet produces no significant volume scatter. First-year and multiyear ice backscatter becomes difficult to distinguish. By midsummer, thin first year ice backscatter is enhanced due to an increased small scale surface roughness from a superimposed ice layer which forms at the snow-ice interface and a snow thickness reduced by melt. After midsummer, the backscatter contrast between first year and multiyear is improved because first year ice roughness elements are smoothed by melt and multiyear ice continues to have a complex topography.

Data have been acquired to verify empirically the importance of volume scattering and the low density ice layer to multiyear ice backscattering and of surface scattering as the dominant process for first

year ice. Spatial scanning a surface-based scatterometer operating at 5 GHz produced the radar maps provided in Figure 1 and 2. Range is inversely proportional to the (intermediate) frequency shown. The key features are that (a) the returns for first year ice backscatter are confined to its surface and few emanate from within the ice sheet, (b) returns are strong in the region where the low density ice layer is present and are produced below the snow-ice interface, and (c) the returns in the meltpool region of the multiyear ice sheet where the 3-m thick ice sheet is topped by 40 cm of fresh ice the returns are weak even though the ice contained larger gas bubbles (3 to 4 mm diameters) but in numbers not large enough to create a significant backscatter. In Figure 2 is a 24m x 20 m ground map of backscatter intensities acquired for these same multiyear ice features. These data show that the returns are 20 dB lower in the region of the meltpool. What is demonstrated here is the important of the low density ice layer in producing the enhanced return observed from multiyear ice. In addition, it not enough that discontinuities are present, they have to be present in sufficient numbers, hence, upper ice sheet density is a critical factor.

Based upon measured data, physical properties, and a theoretical foundation, predictions based on electromagnetic modeling were made. The role of volume and surface scattering were examined in the context of multiyear and first year ice. Characterizations were made in terms of the low density ice layer (i.e. thickness, air bubble size, density, and complex dielectric constant) of the multiyear ice and the surface of the first year ice (rms height, correlation length, and dielectric constant). In addition, the importance of the surface roughness of multiyear ice was examined as illustrated in Figure 3. Multiyear ice with a rough surface produces an enhanced backscatter at the low frequencies, but a slightly reduced volume scatter at high frequencies. This figure shows the range of surface scatter which may be occur for reasonable surface roughness values.

One of the key studies made during CEAREX by Onstott was of the variation in the thickness, density and air bubble composition of the multiyear low density ice layer. Based upon these in-situ observations predictions of backscatter levels as a function of density and layer thickness have been made for intercomparison with measured data. As is supported by the model predictions shown in Figure 4, backscatter intensity should be very sensitive to layer thickness for surfaces that are not rough. This response is observed in the CEAREX data. Layer thicknesses range from 0 to 15 cm and air bubble sizes of about 1.5 mm is typical.

Significant variations in the backscatter of both multiyear and first year ice can occur due to variations in surface roughness and properties of the low density ice layer of multiyear. The range of variations illustrated in Figure 5 are predicted values based on measured physical properties values. Observations shown in Figure 6 were made during CRRELEX-89 [4] and serve to illustrate the extreme range of possible signatures, in this case, those of thin first-year ice. Data have been acquired to address the important issue as to what is typical and what is the variation in the physical properties?

For this discussion it is assumed that the number of spatial samples included in an observation is large enough that sampling is not the dominant issue and we can examine floe-to-floe variability and differences in mean cross-sections. In discriminating multiyear ice from thinner ice the enhancement gained through volume scattering is exploited. Air bubbles are

typically about 1mm to 2mm in diameter. Operation at frequencies greater than about 4 GHz is necessary and contrast is known to improve with frequency up to at least 18 GHz, with optimum frequencies probably from 8 to 18 GHz. Operation at L-band (i.e. 1.25 GHz) has been demonstrated to be too low and at Ka-band (i.e. 35 GHz) all surfaces may appear rough. The enhancement in volume scatter by choosing a smaller wavelength may be offset by an enhanced surface scatter. Operation at C-band is a reasonable compromise because during the period after midsummer it is important to penetrate the thin snow pack and produce scatter from the rough snow-ice interface which allows the discrimination of thin and thick ice.

Discrimination of second year from multiyear ice depends on differences in backscatter intensity which arises due to differences in the thickness of the low density ice layer. Observations at Mould Bay in 1983 and CEAREX-88 suggest that the second-year low-density ice layer is less well developed in both thickness and size on air bubbles. Returns fall between multiyear ice and moderately-rough first-year.

To discriminate between first year and thin ice types it is necessary to exploit the differences between surface roughness and dielectric constant. There are two major dielectric constant regimes; one when the ice is very new and the other contains all remaining cases. The case in which a slush layer is present on thin-to-thick ice probably falls into the second category due to the presence of snow and its expected effect. Observations during CEAREX suggest that a slush and snow layer composite tends to reduce backscatter intensities. New ice can be discriminated older first year ice because of its very smooth surface. As first year ice ages the key consideration is a canopy composed potentially of frost flower remnants, snow, and metamorphosed snow. As the canopy becomes thicker, ice crystals enlarge, and the ice surface roughens backscatter will be enhanced. Analysis of CEAREX data will provide the additional information needed to determine if medium and thick first-year ice are discriminable.

SUMMARY

This paper presents the logic and mechanisms used in discriminating sea ice types. The quantitative analysis was reserved for the presentation at the symposium. The ability to discriminate ice types have been summarized in Figures 7 for winter conditions and figure 8 for summer conditions. These curves are based on measured data and model predictions.

ACKNOWLEDGEMENTS

REFERENCES

1) Onstott, R. G., R. K. Moore, and W. F. Weeks, "Surface-Band Scatterometer Results of Arctic Sea Ice," IEEE Trans. Geosci. Electron., GE-17 (3), 78-85, 1979.

2) Kim, Y. S., R. G. Onstott, and R. K. Moore, "The Effect of a Snow Cover on Microwave Backscatter from Sea Ice," IEEE Journal of Oceanic Eng., Vol. OE-9, No. 5, December, 1984.

3) Onstott, R. G., T. C. Grenfell, C. Matzler, C. A. Luther, and E. A. Svendsen, "Evolution of Microwave Sea Ice Signatures During Early Summer and Midsummer in the Marginal Ice Zone," Journal of Geophysical, Vol. 92, No. C7, pp. 6825-6835, June, 1987

4) Onstott, R. G. and S. H. Gaboury, "Polarimetric Radar Measurements of Artificial Sea Ice," IGARSS '89 Proceedings, July 1989.

5) Kim, Y. S., R. K. Moore, R. G. Onstott, and S. Gogineni, "Towards Identification of Optimum Radar Parameters for Sea Ice Monitoring," Journal of Glaciology, Vol. 31, No. 109, 1985.

TABLE 1. NEAR-SURFACE SCATTEROMETER INVESTIGATIONS

Year	Investigation	Location	Months	Ice Types	Frequencies	Comment
1989	CEAREX	From Sr	Mar	OW TLPC FY MY		
1990	CEAREX	Barents	Feb	OW TLPC FY MY		
1989	CRRELEX	Ice Tank	Jan Feb	OW TFY		
1988	CEAREX	Ice Tank		FY MY		
1988	CEAREX	Ice Tank		OW FY MY		
1988	CRRELEX	Ice Tank	Jan Feb	OW TFY		
1988						
1987						
1985	CRRELEX	Ice Tank		OW TFY	5 to 19	Evolution Study
1984		From Sr	Jun Jul			Summer
1984						
1983	FIREX	Mould Bay	Apr	FY SY	5 to 19	Thick Study
1982	FIREX	Mould Bay	Jun Jul	OW FY MY	5 to 18	Summer
1982	LAB SEA	Labrador	Feb	OW MW FY	5 to 18	
1981	SURSAT	Mould Bay	Sep Oct	FY MY	5 to 18	
1980	YMER	FGS		OW FY MY	5 to 18	
1979	SURSAT	T.K	Mar	FY MY	1 5 to 18	Winter
1978	UKANSAS	Pt Barrow	Apr	FY MY	5 to 18	Winter
1977	UKANSAS	Pt Barrow	Mar	FY MY	5 8 to 18	Spring

Legend

Locations are From Sr (From Strait), FGS (Fram Strait), Greenland Sea and TUK is (Tuktoyuktuk, N.W.T.)

Ice Types are OW (Open Water), TFY (Thin First Year), FY (First Year), MY (Multiyear), SY (Second Year)

TABLE 2. SCENE PARAMETER WHICH INFLUENCE BACKSCATTER INTENSITY

MULTIYEAR ICE

- Presence of LDI Layer in Upper Portion of Ice Sheet
  - LDI Thickness
  - LDI Density
  - LDI Air Bubble Distribution
- Surface Roughness
- Topography
  - First Ice
  - Pressure Ridges
  - Meltpools
- ϵ' and Flooding of Ice Sheet

FIRST YEAR ICE

- Surface Roughness
- Brine Slush Layer (Significant Influences on Magnitude of ϵ')
- Snow Cover
- Topography
  - Undisturbed Ice
  - Pressure Ridges and Rubble

NEW ICE

- Brine Layer (significant Influence on Magnitude of ϵ')
- Surface Roughness and Presence of Frost Flowers
- Topography
  - Homogeneous Ice
  - Rafting
  - Pancakes

Legend
LDI - Low Density Ice Layer
ϵ' - Real Part of Complex Dielectric Constant
ϵ'' - Imaginary Part of Complex Dielectric Constant

DIMENSIONS OF ICE REGIONS
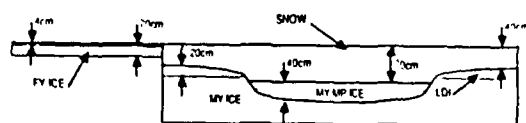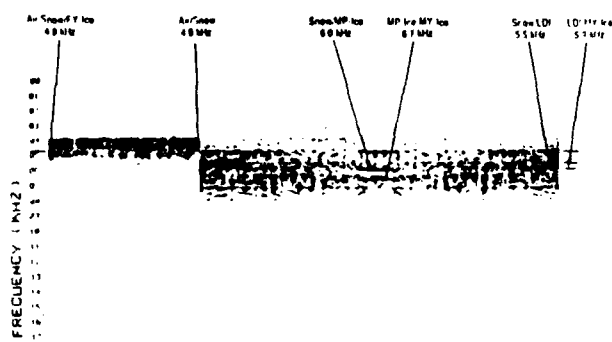
FREQUENCIES WHERE INTERFACES OCCUR

Figure 1. Examination of the Return Power Spectra Have Provided Empirical Validation of the Important Scattering Mechanisms of First-Year (i.e., Surface Scattering) and Multiyear (i.e., Volume Scattering) Ice. These Data were Collected at 5.0 GHz, VV-Polarization.

Figure 2. Data Acquired Using the Sled-Based Scatterometer to Create a Radar Backscatter Map of a 24 m x 20 m area. These Data Were Acquired at 5.0 GHz, VH-Polarization, and an Incidence Angle of 40 Degrees. The Scene is Composed of a Frozen Fresh Water Meltpool in a Multiyear Sea Ice Background.

Figure 3. Theoretical Frequency Behavior of Radar Scattering Coefficient for Smooth and Rough Surfaces.

Figure 4. Predicted Scattering Coefficients at 5 GHz
for Various Low Density Ice Layer
Conditions.

Figure 6. Radar Scattering Coefficients at 5.25 GHz
for Very-Rough ($\sigma \approx 0.5$ cm and $\ell \approx 1.5$ cm)
and Slightly-Rough ($\sigma \approx 0.05$ cm and $\ell \approx 1.6$
cm) Observed During CRRELEX '89 [Ref. 4].

Figure 5. Theoretical Angular Variations of σ° of
Multiyear Ice and First-Year Ice Using
Measured Physical Property Parameters.
[Kim et al, 1985].

Ice Thickness Discrimination
− Winter −

Water

New

Nilas

Young
ThFY

MFY
TFY

SY

MY

| | 0.0 | 100.0 | 200.0 | 300.0 | 400.0 | 500.0 |

Ice Thickness (cm)

Figure 7. Major Ice Types Which May be Discriminated
During Winter.

Ice Thickness Discrimination
− Summer −

Water

New

ThFY
MFY

TFY
SY
MY

| | 0.0 | 100.0 | 200.0 | 300.0 | 400.0 | 500.0 |

Ice Thickness (cm)

Figure 8. Major Ice Types Which May be Discriminated
During Summer.

POLARIMETRIC RADAR MEASUREMENTS OF ARTIFICIAL SEA ICE

Robert G. Onstott and Scott H. Gaboury

Environmental Research Institute of Michigan
Radar Science Laboratory
Advanced Concepts Division
P.O. Box 8618
Ann Arbor, MI 48107 USA

ABSTRACT
During the winters of 1988 and 1989, fully polarimetric microwave measurements were made of artificial sea ice at frequencies of 1.8, 5, 10, and 35 GHz and incidence angles ranging from 0° to 60°. A 5 m x 15 m outdoor tank was filled with sea water and the time evolution of the growth cycle of sea ice was observed over two 2-month periods. During this investigation, continuous detailed scene characterizations and passive microwave observations were made so that an integrated comparison of backscatter and emission could be supported with theoretical predictions. Details of this investigation and preliminary results are presented herein.

INTRODUCTION
The microwave properties of sea ice grown at the U.S. Army Cold Regions Research and Engineering Laboratory (CRREL) were investigated during the 1988 and 1989 winter seasons. The sea ice facility is comprised of a 5 x 15 meter outdoor tank of a 1.2 meter depth filled with sea water, a tent to protect the ice sheet from snow and rain, a gantry style instrument mounting structure, and heated working environments in the immediate vicinity of the tank (See Figure 1). The tank size, determined by instrument and experiment needs, allows for the acquisition of independent spatial samples and measurements at angles from vertical to 60 degrees. These efforts, part of a new three year laboratory-based investigation which began in 1988, are focused on understanding the microwave signatures of sea ice. This is being accomplished by detailed studies of the various aspects of the backscatter and emission and through the intercomparison of measured data and theoretical predictions. Strengths of the CRREL Ice Tank Facility are the ability to control the chemistry of the ice sheet, to control to a reasonable degree the ice crystal structure of the ice, and to provide an environment which allows the time required to rigorously measure the physical and microwave properties of ice which closely simulates that found in the Arctic. The time factor is particulary important because of the scientific interest in fully characterizing the microwave properties and scene. The number of frequencies, incidence angles, polarizations, spatial samples, and temporal samples are extensive. In addition, active and passive observations are not made simultaneously to prevent any potential corruption of the complete accuracy of the data.

Observations were made of the growth cycle of sea ice over two 2-month periods during the winters of 1988 and 1989. Maximum ice thickness was 20 cm. The standard array of physical property observations (i.e. fabric analysis, salinity, density, and temperature) were assembled and supplemented by location, description, and statistical analysis of internal inhomogeneities and surface roughness statistics. These observations are being performed to document and study their influence on backscatter and emission. These data or derivatives provide the critical inputs for the validation and further development of electromagnetic scattering and emission models. The roughness of the ice surface is known to be important in determining the general backscatter level for first-year ice. Experiments were performed to study the change in backscatter and polarization signatures with various roughness scales. Effects of freeze and thaw conditions were also examined.

During this investigation, fully polarimetric measurements were made to acquire the complex scattering coefficients at VV, VH, HV, and HH polarizations (i.e. VH indicates vertical transmit and horizontal receive). The data are recorded such that the scattered field is completely described. This radar has been briefly described in a paper by Onstott [1]. Measurements were also made to qualitatively determine the dominant scattering mechanisms by recording unprocessed backscatter returns. In addition, millimeter wave data were collected during the 1988 investigation at 18, 35, and 94 GHz using a noncoherent radar. Scatterometer parameters used during Cold Regions Research and Engineering Lab Experiment (CRRELEX) are included in Table 1.

Active and passive microwave measurements were temporally multiplexed so that an integrated study of backscatter, emission, physical properties, and electromagnetic modeling of sea ice could be pursued rigorously. An overall goal of this program is to advance the state of understanding of the microwave properties of sea ice so that future satellite data may be fully utilized by the scientific community. Fundamental questions which are of particular interest in sea ice science are; how do the contributions of surface and volume scattering change as ice ages, what information is contained in the co-pol phase difference, what is the correlation between HH and VV scattering coefficients, do important geometric orientations exist in the ice sheet, and is scattering sensitive to them, and what are the

internal anisotropic physical-electrical properties?

OBSERVATIONS

During 1988, multiple ice sheets were grown which were observed over a 2 month period. Observations were made of open water, 5 mm thick new ice, 8 cm thick grey ice, 12 cm thick grey ice which had a rough, air-ice interface (rms roughness of about 1 cm), 12 cm thick grey ice with a liquid film water on its surface, and 20 cm thick ice which had undergone desalination and showed some of the characteristics associated with multiyear (See Table 2). Description of the rms roughness and spatial correlation length statistics are provided in Table 3. Microwave observations of the angular responses of the new and grey ice at C-band, provided in Figure 2, indicate that the fundamental property change during the growth period of new to grey ice is in the reduction of the complex dielectric constant. The surface roughness statistics for both of these scenes were identical to those of a very smooth surface (i.e., an rms height variation of 0.05 cm and a correlation length of 0.7 cm). It was observed by Onstott [2] in 1985 that effects due to blowing snow and the erosion of the upper ice surface, attributed to evaporation, did roughen the ice surface of grey ice as it aged. When air temperatures are cold ($T < -20°C$), typical of the major sea ice growth periods in the Arctic, the formation of frost flowers rapidly changes the very-smooth, low-dielectric slabs of grey ice to highly scattering slabs who have an overlay composed of high-dielectric needles. Observations made during 1988 show that during the transition from new to grey ice the dielectric constant changes by an order of magnitude (ie. from an ϵ_r, of 38 to 4) resulting in a 6.7 dB offset between the signatures shown in Figure 2. These results also show that for these two ice types the backscatter response at VV and HH polarizations are similar at angles from vertical to 40 degrees, with the possibility of a few dB of spreading at the larger angles. Nearly identical returns at VH and HV suggests reciprocity, i.e., that VH = HV. Angular response decays rapidly (i.e., at 5 GHz it is a minimum of 5 dB per 10°) and the large separation between like and cross polarized returns, from nadir to 20 degrees (i.e., at 5 GHz it is a minimum of 20 dB for the range of angles between 0° and 20°), is characteristic of scatter from a dielectric with a smooth surface but with sufficient penetration and size and number of inhomogeneities to produce the small volume return necessary to generate the very weak cross-polarized value. Study of the measurement system response, the inhomogeneities in the upper most portion of the ice sheet, and theoretical model predictions will be used to validate this hypothesis.

The change in backscatter levels for arbitrary co-polarizations may be derived from the target scattering matrix [3]. The illustrations provided in Figure 3 of new, grey, rough grey, and desalinated first-year ice at 5.0 GHz and 40 degrees are shown for visualizing the polarization properties of ice as it evolves. It was anticipated that based on the backscatter responses at the linear polarizations that the polarization signatures would further illustrate the differences in the processes which are responsible for scattering at each of these ice scenes. It is expected that the differences in the size of the pedestal on which the signatures rise, the width of the peaks and nulls, and the difference in the magnitudes between peaks and nulls are a few of the properties which may be exploited through polarimetric measurement.

During 1989, two ice sheets were observed with one observed continuously over a 6-week period. Thickness ranged from 0 to 20 cm. Measurements were multiplexed (i.e. half-hour sampling periods) during the rapid growth phase to allow both active and passive microwave signatures to be characterized. To simulate multiyear ice, an ice sheet was grown to 20 cm, harvested, and then placed on pallets prior to the beginning of the previously iterated measurement series. Over a period of several weeks the brine trapped within the ice sheet drained and the porosity of the ice increased because of the many freeze-thaw periods. Desalination and a reduced density are two important characteristics which determine the microwave signatures of multiyear ice. Observations of an ice sheet composed of one and two layers of this desalinated ice were made. These data were undergoing signal processing at the time of writing this paper. Scenes observed during 1989 are partially listed in Table 4.

CONCLUSIONS

Absolute backscatter levels for new to grey ice are small, except for the (large) coherent returns at vertical. The backscatter responses of new, grey, rough grey, and desalinated first-year ice at linear polarization were found to be dissimilar. This was further demonstrated by examining their polarization signatures. At C-band the critical difference between new and grey ice signatures lies in the order of magnitude difference in their dielectric constants. Surface roughness observations and microwave signature angular variation suggest identical roughness statistics for these two ice types. This will be confirmed by examining the 1989 data.

REFERENCES

1) Onstott, R.G. and S.H. Gaboury, "A Polarimetric Microwave Scatterometer," IGARSS '88 Proc., Vol 1, p. 571, Edinburgh, Scotland, Sept. 1988.

2) Xue, D., R. K. Moore, T. H. Lee and R. G. Onstott, "Microwave Backscatter Coefficients of Artificially Grown First-Year Sea Ice," IGARSS '86 Proc., Vol 1, pp. 139-146, Sept. 1986.

3) Deschamps, G.A., "Part II - Geometrical representation of the polarization of a plane wave," Proc. IRE, vol. 39, pp. 540-544, May 1951.

TABLE 1. SCATTEROMETER PARAMETERS USED DURING CRRELEX

Polarimetric:

Freq	=	1.75, 10 and 35 GHz
Polarization	=	Quad
Angles	=	Vertical to 60 Degrees
Height	=	3 m
Sampling	=	Point & Power spectrums

Non-Coherent:

Freq.	=	10, 18, 35, and 94 GHz
Polarization	=	Quad (10 GHz) and Dual (18, 35 and 94 GHz)
Angles	=	15 to 60 Degrees
Height	=	3 m
Sampling	=	Point and Transect

TABLE 3. CRRELEX '88 SURFACE ROUGHNESS RESULTS

Date	$T_AZ - T_0$ - hr -	ΔZ_{ice} - cm -	σ - cm -	l - cm -	Samples	Sample Lengths - cm -	Comments
14 Jan	63.5	6.5	0.048	0.669	1	25	Top Surface
14 Jan	63.5	6.5	0.048	0.821	1	24	Bottom Surface
16 Jan	113	13	0.051 ± .000	1.635 ± .370	3	20	
15 Jan	99	8	0.544 ± .053	1.481 ± .334	4	20 to 55	Ice Roughened Using Cubed Ice (2 Layers)
15 Jan	96	8	0.611 ± .095	2.157 ± .662	2	25	Ice Roughened Using Cubed Ice (1 Layer)

TABLE 2. OBSERVED SCENES DURING 1988

Open Water (θ = 45 to 55 Degrees)

New Ice ($\Delta z \cong 5$ mm)

Grey Ice ($\Delta z \cong 12$ cm)

Rough Grey Ice ($\Delta z \cong 12$ cm) With 1 cm Roughness Elements

Rough Grey Ice ($\Delta z \cong 12$ cm) With 2 cm Roughness Elements

Warm Grey Ice ($\Delta z \cong 12$ cm)

Desalinated Grey Ice ($\Delta z \cong 20$ cm)

TABLE 4. OBSERVED SCENES DURING 1989

Open Water

New Ice (Δz = 0 to 5 cm)

Grey Ice (Δz = 5 to 20 cm)

Grey Ice With a Thin Slush Layer

Grey Ice With 1 cm Wet Snow

Grey Ice With a Melt Roughened Surface

Grey Ice With 4 cm Moist Snow

Desalinated Ice (Δz = 20 cm)

Desalinated Ice (Δz = 40 cm)

Figure 1. Photograph Showing CRRELEX Ice Tank Facility and Microwave Scatterometers

Figure 2. Radar Scattering Coefficients at 5.25 GHz for 5 mm Thick
New Ice and 12 cm Thick Grey Ice

(A)

(B)

(C)

(D)

Figure 3. Co-Polarization Signatures of (a) New, (b) Grey,
(c) Rough Grey, and (d) Desalinated Grey Sea Ice

SCATTEROMETER MEASUREMENTS OF WIND, WAVES, AND OCEAN FRONTS DURING NORCSEX

Robert G. Onstott and Robert A. Shuchman
Radar Science Laboratory
Advanced Concepts Division
Environmental Research Institute of Michigan
Ann Arbor, MI 48107 USA

J.A. Johannessen and O. Skagseth
Nansen Remote Sensing Center
Bergen, Norway

K. Davidson
Department of Meteorology
Naval Postgraduate School
Monterey, CA 93940 USA

ABSTRACT

During March 1988, active microwave radar coefficient measurements were made from a ocean going research platform during a wind-wave-current field experiment on the Norwegian Continental Shelf (NORCSEX). Radar backscatter data were collected at 1.5, 5.25, and 9.38 GHz for incidence angles 20° to 80° and with both like and cross polarizations. One of the primary objectives of this study was to investigate the ability of SAR to image ocean surface features caused by current fronts and eddies in the moderate circulation regime off the Norwegian coast. In addition to supporting the SAR imaging aspects of the study, data were acquired for use in the study of the backscatter response of a wind driven sea. Detailed sea truth and meteorological characterizations acquired spatially and temporally coincident with the scattering measurements, and SAR imagery allows the examination of the influence of wind speed, wind direction, and sea state on radar cross section.

1. INTRODUCTION

In preparation for the 1990 launch of the first European Space Agency (ESA) Earth Resource Satellite (ERS-1) which will include a C-band synthetic aperture radar (SAR), a two week wind-wave-current oceanographic field investigation was conducted during March 1988 along the Norwegian Continental Shelf known as the Haltenbanken. A primary objective of this Norwegian Continental Shelf Experiment (NORCSEX) was to investigate the capability of SAR to image ocean surface features associated with current fronts and eddies in the moderate current regime off the Norwegian coast. Secondary objectives of the study were to assess the potential of a C-band SAR to measure ocean surface wind and waves.

In support of the SAR imaging aspects of the study, data were acquired to study the microwave backscatter response of a wind driven sea. A three-frequency four-channel scatterometer operated from the research vessel HAKON MOSBY collected microwave data at frequencies centered at 1.5, 5.25, and 9.38 GHz (L-, C-, and X-band, respectively), with incidence angles from 20° to 80°, and at like and cross linear polarizations. The scatterometer collects microwave data in a real-aperture mode, and thus is not dependent on platform motion (i.e., Doppler effects) as in the case of the SAR.

In this paper the L-, C-, and X-band scatterometer data collected during NORCSEX is first described. Data collected over a meteorological and oceanographic front that was imaged coincidentally with the C-band

SAR is then presented. Exponents relating the scattering coefficients (σ_0) to wind speed are then calculated for the L-, C-, and X-band coincidentally collected radar data.

2. DATA SETS

The location of the March '88 NORCSEX investigation is shown in Figure 1. The remote sensing, meteorological and oceanographic data collected during NORCSEX is summarized in Table 1. The remote sensing data included the ship scatterometer, the C- and X-band SAR, the NOAA satellite Advance Very High Resolution Radiometer (AVHRR) imagery, the GEOSAT satellite altimeter, and DMSP satellite Special Scanning Microwave Imager (SSM/I).
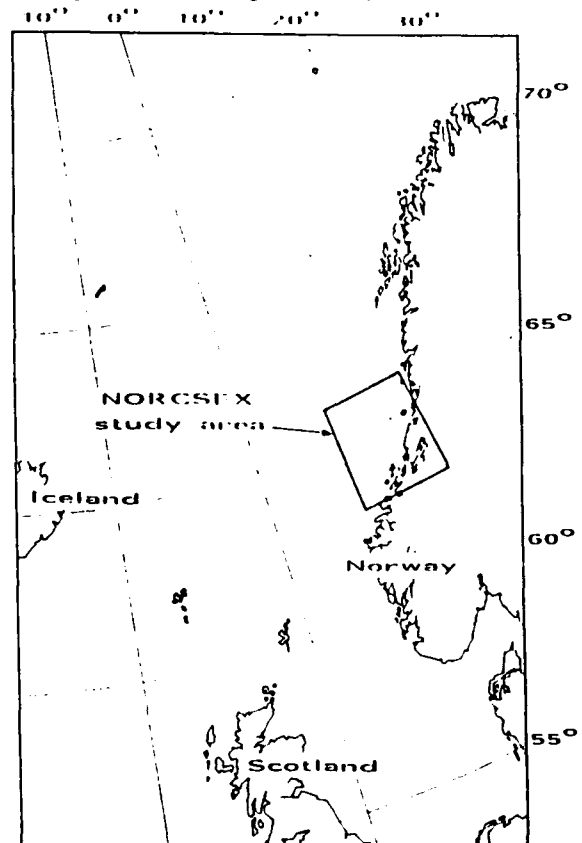
Figure 1. Location of the Norwegian Continental Shelf Experiment Study Area

Table 1. OVERVIEW HALTENBANKEN EXPERIMENT 1988

PLATFORM / INSTRUMENT	OCEAN CURRENT	TEMPERATURE SALINITY DENSITY	SURFACE WAVES WIND/SWELL	INTERNAL WAVES	FRONTS EDDIES	NEAR SURFACE WIND	AIR-SEA STABILITY
HAKON MOSBY							
SHIP RADAR						X	
WEATHER STATION						X	X
ADCP	X					X	
SEASOAR		X				X	
SCATTEROMETER	X (R)					X	
FRONSJON							
CODE	X						
R.D./APN							
WEATHER STATION	X					X	X
MIR #2							
MOORINGS							
CURRENT	X				X	X	
THERMISTOR		X				X	
WAVES			X	X		F	
METEOROLOGY							X
NOAA 9,10							
AVHRR		T			X		
GEOSAT							
ALTIMETER	X		X	X		X (R)	X
DMSP							
SSM/I						X (L)	
SFT							
SLAR				X	X (R)		
AIRCRAFT							
SAR	X (R)		WAVELENGTH	X	X	X (R)	

R: Research Evaluation.   L: Limitation due to land effect.

The meteorological measurements and data assimilation were conducted during the entire NORCSEX field investigation period. Time series of surface layer meteorological data from ship mounted sensors and profilers of temperature, humidity and vector wind from rawinsondes were obtained. Surface layer wind fluxes (i.e, dragg coefficients) were obtained from ship mounted hot-film and the use of miniature cups.

The oceanographic sea truth was obtained by the use of a ship mounted thermistor (sea surface temperature), a towed undulating SeaSoar (salinity and temperature from the surface to 250 m), and the ship mounted 150 KHz Acoustic Doppler Current Profiler (ADCP). The ADCP provides a measure of absolute current every 5 m from the surface to near the ocean bottom.

3. SCATTEROMETER OBSERVATIONS

During this investigation the L-, C-, and X-band radar scatterometer was mounted on the starboard side of the wheelhouse of the R/V HAKON MOSBY (Figure 2). Detailed scatterometer system specifications have been included in Table 2. It was positioned as far forward on the ship as possible and pointed slightly forward of where the ship generated bow waves are produced. Thus, the effects of the bow generated waves were minimized. Bow waves which interacted with the ambient ocean wave field did however, break near the ship creating minimum observation angles of incidence which were sea state dependent. Calm conditions allowed observations at incident angles as small as 20 degrees, where as, in the extreme wave cases minimum angles were between 40 and 50 degrees. Ship roll and pitch motions were recorded as part of the data stream and when they were great enough to cause the backscatter returns to fall outside of the radar intermediate frequency processing filter, these data were noted and not included in the averaging process. To date, 2 and 10 minute averages have been processed. As the ship transited through the oceanographic features and wind fields, four channels of backscatter data and a visual time-encoded video record were acquired.

Radar observations at L-VV, C-HH, X-VV and X-VH or L-HH, C-VV, X-VV and X-VH were made as the ship transited through ocean fronts and internal waves. The first letter refers to the radar frequency used while the VV, HH, and VH denotes the transmit and receive polarizations. For example, VH indicates a cross polarization measurements where vertical polarization was transmitted and horizontal received. The range of meteorological and oceanographic conditions that occurred during the period of scatterometer observations 5 to 18 March are summarized in Table 3.

Figure 2. Three - Frequency, Four - Channel Scatterometer Operated at 1.5, 5.25, and 9.38 GHz, at Angle From 20° to 80°, and Like and Cross Linear Polarization

Table 2. SCATTEROMETER SYSTEM PARAMETERS

Parameter	L-Band	C-Band	X-Band
Frequency (GHz)	1.50	5.25	9.38
Wavelength (cm)	20.0	5.7	3.2
Polarization		- VV, VH, HV, HH -	
Incidence Angle		20° to 80°	
Height (m)		10	
Spot Size (m) at 40°	2.1	0.7	0.7
Bandwidth (MHz)	350	525	575
Independent Samples* Per Meter at 40°	12	6	8
Precision* (dB) at 40°	±1.1	±3.0	±2.8
Absolute Accuracy	±1.0	±1.0	±1.0
Ship Speed (m/s)		4	
Look Direction		Starboard	

* Assumes the Surface is Stationary

An example of an ocean front observed on 13 March is shown in the photograph provided in Figure 3. The temperature gradient for this front was +2°C and was created at the boundary between warm Atlantic Ocean water (T~7°C) and the colder Norwegian coastal water (T~5°C). The photograph illustrates the importance of sea surface temperature on the small scale surface roughness. Backscatter angular and polarization response measurements were made on each side of this ocean frontal feature. Quad-polarization measurements (VV, VH, HV, AND HH) were made at L- and C-band and dual-polarization measurements (VV and VH) at X-band. Seven leg star patterns were made to address wave and wind aspect angle dependencies.

An interesting data collection took place on 17 March in which fluctuations in wind speed of 2 to 13 m/s were experienced during a ten hour period as the ship transited an oceanographic/meteorological front. Sea temperatures ranged from 5° to 8°C while the air temperature was 3°C. The air-sea temperature difference ($T = T_{air} - T_{sea}$) ranged from -2°C to -5°C producing unstable conditions since $T < -2°$ C. A gravity wave swell traveling in the same direction as the wind with 2-4 m significant wave height was present during the scatterometer observation. The wind and wave direction with respect to the radar was approximately 90° (i.e., upwind/downwind look direction). In Figure 4a, the L-, C-, and X-band radar scattering coefficients measured during this ten hour period are shown as a function of time. The wind speed and direction measured coincidentally with the scatterometer at a height of 15 m is shown in Figure 4b. These figures visually shows the correlation between wind speed and radar scattering cross section. Features that are instructive include the general increase in cross section as wind speed increases, the hysteresis associated with wave decay after a reduction in wind speed, and the change in the scattering coefficients of 10-13 dB for an increase in wind speed of 3 m/s to 13 m/s.
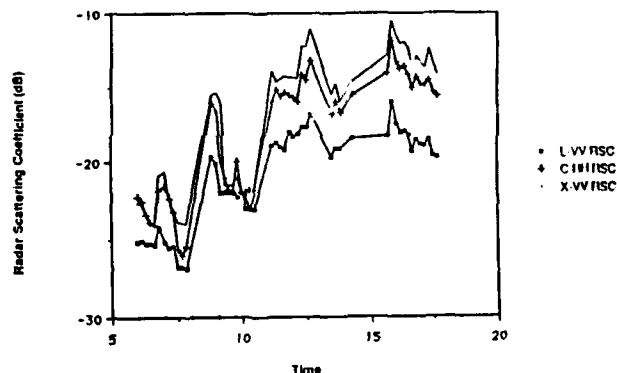
Figure 4a. Radar Scattering Coefficient at L-, C-, and X-band Measured While Crossing an Ocean-Meteorological Front on 17 March

Figure 3. Example of an Ocean Front which was Transited on 13 March. The Temperature Gradient was 2 °C. The Front was Created at the Boundary of Warm Atlantic Water (7 °C) and Colder Coastal Water (5 °C).
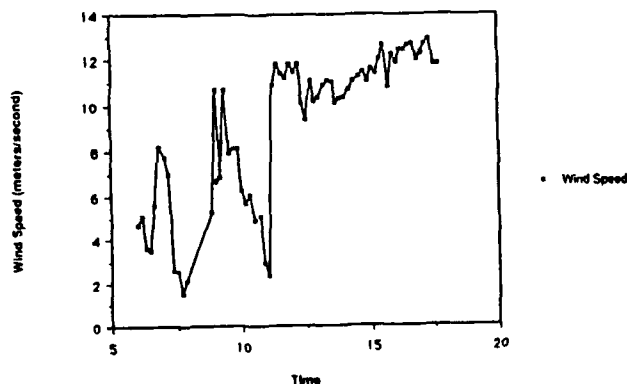
Figure 4b. Wind Speed Measured From Ship While Crossing an Ocean-Meterorological Front on 17 March.

It is also interesting to report that a response identical to that of the C-band scatterometer was observed by the SAR 5.6 GHz data. During this period a rapid transition from a spatially large region of weak returns where winds were calm (<3m/s) to strong radar returns where the winds greatly increased (>10 m/s) produced a 10 dB difference in backscatter intensity for these two regions [reported by Shuchman et al, 1989, these proceedings]. The ship transited across this front about 30 minutes after the SAR and noted this change in wind speed immediately prior to crossing the ocean front at 11 GMT. The wind friction velocity (U*) can be related to dragg coefficient (C$_d$) and true wind speed (U) by the following expression

$$U^* = C_d^{1/2} U \qquad (1)$$

In this case U* changed from 0.1 to 0.5 m/s across this front illustrating the important difference in sea surface roughness.

The radar scattering coefficient σ* has historically been related to wind speed through a transfer function of the form

$$\sigma^*(U) = CU^\gamma \qquad (2)$$

where U is related to the surface wind vector, C the scaling coefficient, and γ the wind vector exponent. In addition to the local wind vector, the radar scattering coefficient can be additionally influenced by a array of other environmental parameters which include wave slope, sea surface temperature, air-sea temperature difference, and surfactants [Donelan and Pierson, 1987; Plant, 1986]. In Figure 5, the radar scattering coefficients at L-, C-, and X-bands are shown as a function of equivalent 10 m (height above the ocean surface) winds. Forty ten-minute intervals were used in producing these plots. All three frequencies produce approximately the same scaling coefficient, but yield different wind vector exponents and correlation coefficients (i.e., they range from 0.6 to 0.8). Exponents increased with increasing frequency and ranged from 1.30 to 1.76.

Keller et al [1989] reported data collected from a tower situated in the North Sea for C-VV and an incident angle of 45° which showed a response very similar to the NORCSEX observations. The radar cross-sections ranged in value from about -24 to -15 dB for a change in wind speed of 2 to 10 m/s. For this same change in wind speed, our scattering coefficients ranged from about -26 to -17 dB. Recall the NORCSEX C-band measurements utilized HH polarization. This change in polarization from vertical to horizontal is sufficient to account for the observed difference. The agreement in absolute level is reasonable and each set of measurements produced a 9 dB change in cross-section for this wind speed difference. The computed wind vector exponent for the results reported by Keller was 1.50. In our case, the exponent is 1.64.

4. SUMMARY

A wide range in meteorological and oceanographic conditions with respect to winds, waves, temperatures occurred during NORCSEX. Several distinct moderate to high winds (greater than 10 m/s) events were encountered as well as low wind conditions (2-4 m/s). Preliminary analysis indicates excellent correlation between variation of observed wind conditions and drag coefficients and variations of shipboard and aircraft remote sensing data. Future efforts will be directed at examining the relationships between wind stress, sea surface temperature, stability, sea and swell on remote wind vector determination.
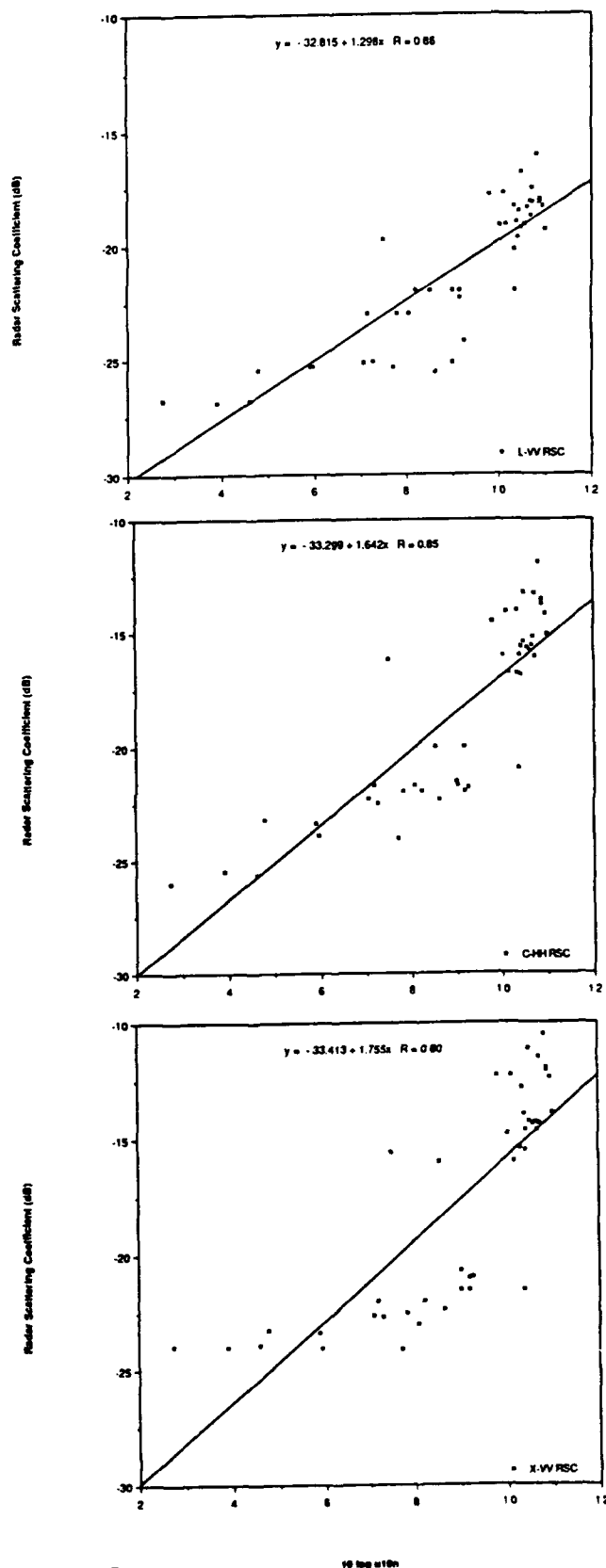
Figure 5

Radar Scattering Coefficients Measured on 17 March at L-VV, C-HH, and X-VV are Shown as a Function of Equivalent 10-m Winds.

REFERENCES

[1] Shuchman, R.A., D.L. Lyzenga, J.A. Johannessen, and C. Livingstone, "SAR Detection of Mesoscale Ocean Circulation Features During NORCSEX '88", these proceedings.

[2] Donelan, M.A. and W.J. Pierson, Jr., "Radar Scattering and Equilibrium Ranges in Wind-Generated Waves With Application to Scatterometry, JGR., 92, pp 4971-5029, 1987.

[3] Plant, W.J., "A Two-Scale Model of the Short Wind-Generated Waves and Scatterometry, JGR., 91, pp 10,735-10,749 1986.

[4] Keller, W.C., V. Wismann, and W. Alpers, "Tower-Based Measurements of the Ocean C-Band Radar Backscattering Cross Section, JGR., 94, pp 924-930, 1989.

ACTIVE MICROWAVE CLASSIFICATION OF SEA ICE

Robert G. Onstott
Environmental Research Institute of Michigan
Advanced Concepts Division
Radar Science Laboratory
P.O. Box 8618
Ann Arbor, MI 48107

ABSTRACT

Radar backscatter studies of Arctic sea ice have been carried out over a number of years now with the intent to acquire physical property information through by the examination of microwave signatures. The breadth of these studies continues to expand. As an example, measurements are now conducted at frequencies from 500 MHz to about 100 GHz. One of the scientific goals of this work has been to develop an improved understanding of the scattering processes at play. A second, equally important, goal has been to apply the knowledge gained in examining the backscatter response of ice and snow made in conjunction with detailed scene characterizations, the insight gained through theoretical modeling and parametric study, and the data entered into the radar signature library to develop procedures to convert microwave signal information, available in the very near future, into valuable data products, ultimately providing the opportunity for us to better understand our environment. The purpose of this paper is to provide a discussion of what has been learned through the many efforts associated with the near-surface scatterometer measurement programs and how the knowledge gained is assisting in the development of future sea ice type satellite algorithms.

INTRODUCTION

One of the most important pieces of geophysical information that must be obtained from satellite observation of the frozen ocean is ice type. A wide array of categories have been defined by the World Meteorological Organization and are related to thickness, age or formation characteristic. Basic categories include new (0 to 10 cm thick), young (10 to 30 cm thick), first year (> 30 cm thick), second year (survived one melt season) and multiyear (survived multiple melt seasons). The ability of determining ice type using space-based sensors is dependent on spatial resolution and the region under observation. In the marginal ice zone (MIZ) the mixture of floes of various ice types have diameters which are small, ranging from 10 to 200 m, and at some point have experienced moderate deformation. Ice tends to be thick either because ice must be thick to survive in this dynamic region, because thin ice is rapidly crushed during the constant collisions with other floes, or because of the rafting of thin ice

floes. Small ice pieces between floes, and the ridges or blocks strewn around floe rims, and the moderately deformed floe interiors produce significant backscatter. In regions of constant shear, such as between shorefast and pack ice, processes are very dynamic and result in topographically rough, spatially variable, and very thick formations. Backscatter is strong and variable regardless of original ice type. The region which is spatially the most significant is the pack ice portion of the Arctic Ocean. Here floes are frozen into fields which float as sheets with sizes often many ten's of kilometers. Ridge building due to pressure is the major deformation event.

IN-SITU SCATTEROMETER PROGRAMS

By 1976 the need to coordinate detailed microwave and surface measurements was well recognized. In addition, because existing sensor parameters varied and future sensors were still undefined it was important to acquire data over a wide range of frequencies, polarizations, and incidence angles. It is interesting to note that the first measurements were made at 1.5 GHz and multiple frequencies between 8 and 18 GHz [1]. Today they are made from 0.5 to 100 GHz (i.e. CEAREX). The sea ice measurement program began at the University of Kansas by Richard K. Moore and the author with a tripod-type structure (1976) whose characteristic was to provide a constant range. It has been extended to operation from helicopter, surface ship, sled, and gantry (laboratory facility). Microwave scene characterization experiments began in 1977 at Point Barrow in conjunction with W.F. Weeks (CRREL and Univ. of Alaska) who served as mentor for sea ice property measurements. Numerous measurement programs were then conducted with R. Ramseier (AES Canada) with whom measurement of physical-chemical properties would be finely honed with the goal of relating specific microwave responses and processes to ice properties. Measurements were made of the surface for the calculation of roughness statistics (rms height and correlation length), of the salinity and density profiles with fine depth resolution (1 cm spacings in the top 20 cm of the ice sheet) to describe a rapidly changing permittivity, and of the brine or brine-slush layer which resides on all new and first-year ice forms. Coordinated active (near-surface scatterometer and SLAR) and passive microwave (aircraft imager and profilers) measurements began with those made at Mould Bay in 1981 as did the use of radar (SLAR) imagery in-situ experiment planning. Coordination of surface active and passive microwave

measurements which began at Mould Bay in 1982 have continued with CEAREX and CRRELEX being examples of the most recent investigations. Basic information about these measurements programs is provided in Table 1. It is important to note that as of this year significant studies have been conducted during all seasons, except perhaps the very end of summer when the ice drains, remains drained, and then begins to freeze. All major ice types have now been observed. Possibly the greatest weakness in the existing observations is that of region. Studies have been made in the Chuckchi, Beaufort, Greenland, and Barents Seas, with almost no study of the Central Arctic.

OBSERVATIONS

In examining under what conditions ice types may be discriminated using radar it was determined that it was important to (a) have data acquired over a wide range of conditions where both the microwave and physical-electrical properties are well-characterized, (b) be able to interpret the empirical observations with supporting electromagnetic scattering theory and model predictions, and (c) to study the variation in sea ice physical-electrical properties. Early on it was hypothesized that first year ice backscatter is dominated by surface scattering and multiyear ice by volume scatter. The critical issues have been in documenting under what conditions this is true, at what frequencies and polarizations, can this difference be exploited, what are the optimum radar parameters for ice type discrimination, and given a radar parameter set what is the anticipated performance.

The parameters and conditions which have a critical influence on backscatter intensity and are typical are listed in Table 2 as a function of major ice type. The attempt here is to list these parameters in their relative order of importance. When optimizing for ice type discrimination, the keys to information exploitation are (a) multiyear ice produces a strong volume scatter due to the presence of a low density ice layer in the upper portion of the ice sheet (a minimum thickness of about 2 cm is required), (b) first year ice returns are dominated by surface scatter and variations in surface roughness scales produce large changes in backscatter levels, and (c) new ice returns are weak (off-vertical) because surfaces are very smooth.

For multiyear ice during winter, volume scatter dominates at frequencies beyond 10 GHz where as at some frequency below about 5 GHz surface scattering begins to dominate. For first year ice surface scattering dominates below 15 GHz. Snow has little impact on multiyear ice backscatter but enhances first year and new ice backscatter [2].

The evolution of the microwave signatures during summer is quite complex. The reader is referred to the discussion provided in the paper by Onstott et al [3]. During the first part of summer the wet snowpack and warm ice sheet produces no significant volume scatter. First-year and multiyear ice backscatter becomes difficult to distinguish. By midsummer, thin first year ice backscatter is enhanced due to an increased small scale surface roughness from a superimposed ice layer which forms at the snow-ice interface and a snow thickness reduced by melt. After midsummer, the backscatter contrast between first year and multiyear is improved because first year ice roughness elements are smoothed by melt and multiyear ice continues to have a complex topography.

Data have been acquired to verify empirically the importance of volume scattering and the low density ice layer to multiyear ice backscattering and of surface scattering as the dominant process for first year ice. Spatial scanning a surface-based scatterometer operating at 5 GHz produced the radar maps provided in Figure 1 and 2. Range is inversely proportional to the (intermediate) frequency shown. The key features are that (a) the returns for first year ice backscatter are confined to its surface and few emanate from within the ice sheet, (b) returns are strong in the region where the low density ice layer is present and are produced below the snow-ice interface, and (c) the returns in the meltpool region of the multiyear ice sheet where the 3-m thick ice sheet is topped by 40 cm of fresh ice the returns are weak even though the ice contained larger gas bubbles (3 to 4 mm diameters) but in numbers not large enough to create a significant backscatter. In Figure 2 is a 24m x 20 m ground map of backscatter intensities acquired for these same multiyear ice features. These data show that the returns are 20 dB lower in the region of the meltpool. What is demonstrated here is the important of the low density ice layer in producing the enhanced return observed from multiyear ice. In addition, it not enough that discontinuities are present, they have to be present in sufficient numbers, hence, upper ice sheet density is a critical factor.

Based upon measured data, physical properties, and a theoretical foundation, predictions based on electromagnetic modeling were made. The role of volume and surface scattering were examined in the context of multiyear and first year ice. Characterizations were made in terms of the low density ice layer (i.e. thickness, air bubble size, density, and complex dielectric constant) of the multiyear ice and the surface of the first year ice (rms height, correlation length, and dielectric constant). In addition, the importance of the surface roughness of multiyear ice was examined as illustrated in Figure 3. Multiyear ice with a rough surface produces an enhanced backscatter at the low frequencies, but a slightly reduced volume scatter at high frequencies. This figure shows the range of surface scatter which may be occur for reasonable surface roughness values.

One of the key studies made during CEAREX by Onstott was of the variation in the thickness, density and air bubble composition of the multiyear low density ice layer. Based upon these in-situ observations predictions of backscatter levels as a function of density and layer thickness have been made for intercomparison with measured data. As is supported by the model predictions shown in Figure 4, backscatter intensity should be very sensitive to layer thickness for surfaces that are not rough. This response is observed in the CEAREX data. Layer thicknesses range from 0 to 15 cm and air bubble sizes of about 1.5 mm is typical.

Significant variations in the backscatter of both multiyear and first year ice can occur due to variations in surface roughness and properties of the low density ice layer of multiyear. The range of variations illustrated in Figure 5 are predicted values based on measured physical properties values. Observations shown in Figure 6 were made during CRRELEX-89 [4] and serve to illustrate the extreme range of possible signatures, in this case, those of thin first-year ice. Data have been acquired to address the important issue as to what is typical and what is the variation in the physical properties?

For this discussion it is assumed that the number of spatial samples included in an observation is large enough that sampling is not the dominant issue and we can examine floe-to-floe variability and differences in mean cross-sections. In discriminating multiyear ice from thinner ice the enhancement gained through volume scattering is exploited. Air bubbles are

typically about 1mm to 2mm in diameter. Operation at frequencies greater than about 4 GHz is necessary and contrast is known to improve with frequency up to at least 18 GHz, with optimum frequencies probably f-- 3 to 18 GHz. Operation at L-band (i.e. 1.25 GHz) been demonstrated to be too low and at Ka-band (i.e. 35 GHz) all surfaces may appear rough. The enhancement in volume scatter by choosing a smaller wavelength may be offset by an enhanced surface scatter. Operation at C-band is a reasonable compromise because during the period after midsummer it is important to penetrate the thin snow pack and produce scatter from the rough snow-ice interface which allows the discrimination of thin and thick ice.

Discrimination of second year from multiyear ice depends on differences in backscatter intensity which arises due to differences in the thickness of the low density ice layer. Observations at Mould Bay in 1983 and CEAREX-88 suggest that the second-year low-density ice layer is less well developed in both thickness and size on air bubbles. Returns fall between multiyear ice and moderately-rough first-year.

To discriminate between first year and thin ice types it is necessary to exploit the differences between surface roughness and dielectric constant. There are two major dielectric constant regimes; one when the ice is very new and the other contains all remaining cases. The case in which a slush layer is present on thin-to-thick ice probably falls into the second category due to the presence of snow and its expected effect. Observations during CEAREX suggest that a slush and snow layer composite tends to reduce backscatter intensities. New ice can be discriminated older first year ice because of its very smooth surface. As first year ice ages the key consideration is a canopy composed potentially of frost flower remnants, snow, and metamorphosed snow. As the canopy becomes thicker, ice crystals enlarge, and the ice surface roughens backscatter will be enhanced. Analysis of CEAREX data will provide the additional information needed to determine if medium and thick first-year ice are discriminable.

SUMMARY

This paper presents the logic and mechanisms used in discriminating sea ice types. The quantitative analysis was reserved for the presentation at the symposium. The ability to discriminate ice types have been summarized in Figures 7 for winter conditions and Figure 8 for summer conditions. These curves are based on measured data and model predictions.

ACKNOWLEDGEMENTS

REFERENCES

1) Onstott, R. G., R. K. Moore, and W. F. Weeks, "Surface-Band Scatterometer Results of Arctic Sea Ice," IEEE Trans. Geosci. Electron., GE-17 (3), 78-85, 1979.

2) Kim, Y. S., R. G. Onstott, and R. K. Moore, "The Effect of a Snow Cover on Microwave Backscatter from Sea Ice," IEEE Journal of Oceanic Eng., Vol. OE-9, No. 5, December, 1984.

3) Onstott, R. G., T. C. Grenfell, C. Matzler, C. A. Luther, and E. A. Svendsen, "Evolution of Microwave Sea Ice Signatures During Early Summer and Midsummer in the Marginal Ice Zone," Journal of Geophysical, Vol. 92, No. C7, pp. 6825-6835, June, 1987

4) Onstott, R. G. and S. H. Gaboury, "Polarimetric Radar Measurements of Artificial Sea Ice," IGARSS '89 Proceedings, July 1989.

5) Kim, Y. S., R. K. Moore, R. G. Onstott, and S. Gogineni, "Towards Identification of Optimum Radar Parameters for Sea Ice Monitoring," Journal of Glaciology, Vol. 31, No. 109, 1985.

TABLE 1. NEAR-SURFACE SCATTEROMETER INVESTIGATIONS

Year	Investigation	Location	Month	Ice Types	Frequencies	Comment
1983	CEAREX	Fram Str	Mar	OW, FY, FYY, MY	C to 18	
1983	CEAREX	Barents	Feb	OW, FY, FYY, MY	9.5 to 100	
1989	CORELEX	Ice Tank	Jan-Feb	OW, FY	1 to 35	
1988	CEAREX	Ice Tank	Dec	FY, MY		
1988	CEAREX	Ice Tank	Dec	FY, FYY, MY		
1988	CORELEX	Ice Tank	Jan-Feb	OW, FY	1 to 100	
1988	ICEPEG		Mar		10	
1987	MIZEX	Fram Str	Mar	FY, MY		
1985	CORELEX	Ice Tank	Jan-Mar	OW, FY	5 to 18	
1984	MIZEX	Fram Str	Jun-Jul	OW, FY, FYY	1.5 to 18	
1984	MIZEX	Fram Str	Jun-Jul	OW, FY, FYY		
1983	FIREX	Mould Bay	Apr	FY, SY	5 to 18	
1982	FIREX	Mould Bay	Jun-Jul	OW, FY, MY	1.5 to 18	
1982	LARSEA	Labrador	Feb	OW, FYY, FY	1.5 to 18	
1981	SURSAT	Mould Bay	Sep-Oct	G, MY	1 to 18	
1980	YMER	FGS	Sep	OW, FY, FYY	1.5 to 18	
1979	SURSAT	TUK	Mar	FY, MY	1.5 to 18	Winter
1978	UKANSAS	Pt Barrow	Apr	FY, L MY	1.5 to 18	Winter
1977	UKANSAS	Pt Barrow	Mar	FY, MY, L MY	1.5, 9 to 18	Spring

Legend

Locations are from Str (Fram Strait), FGS (Fram Greenland Sea) and TUK (Tuktoyaktuk, NW T)

Ice types are OW (Open Water), FYY (First Year ...), FY (Thin First Year), SY (Second Year) and MY (Multiyear)

TABLE 2. SCENE PARAMETER WHICH INFLUENCE BACKSCATTER INTENSITY

MULTIYEAR ICE

- Presence of LDI Layer in Upper Portion of Ice Sheet
    - LDI Thickness
    - LDI Density
    - LDI Air Bubble Distribution
- Surface Roughness
- Topography
    - Flat Ice
    - Pressure Ridges
    - Meltpools
- rr' and Flooding of Ice Sheet

FIRST YEAR ICE

- Surface Roughness
- Brine Slush Layer (Significant Influences on Magnitude of rr')
- Snow Cover
- Topography
    - Undisturbed Ice
    - Pressure Ridges and Rubble

NEW ICE

- Brine Layer (significant influence on Magnitude of rr')
- Surface Roughness and Presence of Frost Flowers
- Topography
    - Homogeneous Ice
    - Rafting
    - Pancakes

Legend
LDI - Low Density Ice Layer
rr' - Real Part of Complex Dielectric Constant
rr'' - Imaginary Part of Complex Dielectric Constant

Figure 2. Data Acquired Using the Sled-Based Scatterometer to Create a Radar Backscatter Map of a 24 m x 20 m area. These Data Were Acquired at 5.0 GHz, VH-Polarization, and an Incidence Angle of 40 Degrees. The Scene is Composed of a Frozen Fresh Water Meltpool in a Multiyear Sea Ice Background.

DIMENSIONS OF ICE REGIONS

FREQUENCIES WHERE INTERFACES OCCUR

Figure 1. Examination of the Return Power Spectra Have Provided Empirical Validation of the Important Scattering Mechanisms of First-Year (i.e., Surface Scattering) and Multiyear (i.e., Volume Scattering) Ice. These Data were Collected at 5.0 GHz, VV-Polarization.

Figure 3. Theoretical Frequency Behavior of Radar Scattering Coefficient for Smooth and Rough Surfaces.

Figure 4. Predicted Scattering Coefficients at 5 GHz
for Various Low Density Ice Layer
Conditions.

Figure 5. Theoretical Angular Variations of $\sigma°$ of
Multiyear Ice and First-Year Ice Using
Measured Physical Property Parameters.
[Kim et al, 1985].

Figure 6. Radar Scattering Coefficients at 5.25 GHz
for Very-Rough ($\sigma \approx 0.5$ cm and $\ell \approx 1.5$ cm)
and Slightly-Rough ($\sigma \approx 0.05$ cm and $\ell \approx 1.6$
cm) Observed During CRRELEX '89 [Ref. 4].

Ice Thickness Discrimination
- Winter -
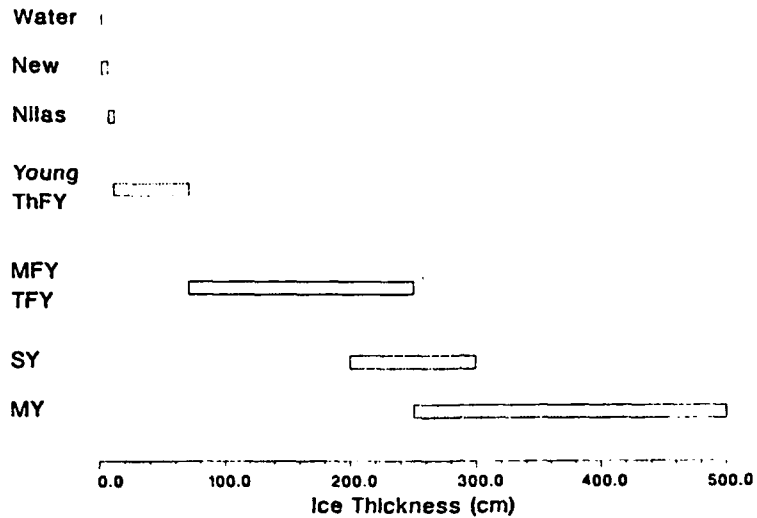
Water

New

Nilas

Young
ThFY

MFY
TFY

SY

MY

0.0   100.0   200.0   300.0   400.0   500.0
Ice Thickness (cm)

Figure 7. Major Ice Types Which May be Discriminated
During Winter.

Ice Thickness Discrimination
- Summer -

Water

New

ThFY
MFY

TFY
SY
MY

0.0   100.0   200.0   300.0   400.0   500.0
Ice Thickness (cm)
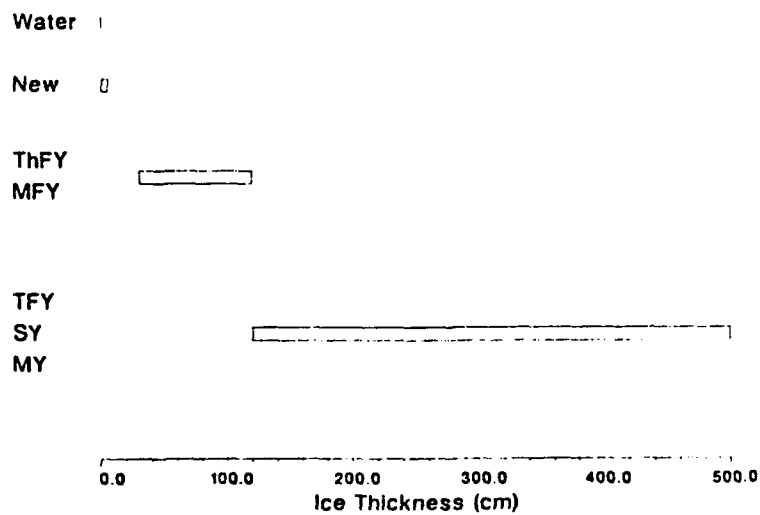
Figure 8. Major Ice Types Which May be Discriminated
During Summer.

MULTIFREQUENCY AND MULTIPOLARIZATION SCATTEROMETER

FOR REMOTE SENSING

Robert G. Onstott
Robert A. Shuchman
Radar Science Laboratory
Advanced Concepts Division
Environmental Research Institute of Michigan

ABSTRACT

A multifrequency, multipolarization helicopter-borne scatterometer has been developed for the measurement of backscatter coefficients of Arctic sea ice. The radar, designed to operate at low altitudes, allows high-quality scattering measurements from a mobile platform. The advantages of the helicopter-borne scatterometer is that it provides the ability to make the detailed measurements characteristic of those made from ground-based system, the ability to rapidly move from one experiment location to another, the ability to make large area surveys, and overcomes many of the problems associated with aircraft-based systems which include simultaneously measuring at all frequencies and polarizations and obtaining a large number of independent observations at a scene. The radar operates at 1.25, 5.25, and 9.38 GHz simultaneously, at angles of incidence from vertical to 80°, and with VV, VH, HV, and HH polarization. A description of this instrument is provided in this paper.

Introduction

There is a demonstrated need for accurate measurement of the radar backscattering cross sections of a variety of Earth scenes. These data are used in developing radar data bases and in the study of the ability to convert electromagnetic signal data into information about the Earth, i.e., geophysical and environmental information. Measurement programs are at their best when there is coordination among airborne sensors, surface-based sensors, and scene characterization measurements. Accurate in-situ data have proven to be invaluable in assisting in the interpretation of both aircraft and satellite data products. In addition, coordination of microwave measurements with detailed scene characterizations is critical in the study of fundamental scattering processes.

An instrument has been developed which plays an important role in measuring scatter from distributed scenes. Commonly referred to as the "scatterometer" it is designed so that backscatter from the region under observation is described accurately. This region is often an incoherent collection of a very large number of scatterers and the term differential radar scattering coefficient σ° is applied. This coefficient is the scattering cross section σ on a per unit area A basis (i.e., $\sigma^{\circ} = \sigma/A$). Typically the scatterometer is used to measure radar scattering coefficients over an extensive array of radar geometries and parameters which may include the following:

(a) Frequencies in the microwave to millimeter wave range;

(b) Polarizations such as linear, circular, or even synthesized;

(c) Angles of incidence which range from vertical to beyond 70°;

(d) Aspect angle;

(e) Space scales from the local to the regional; and

(f) Time scales such as daily, seasonal, or instantaneous.

The role of a scatterometer flown from a helicopter becomes apparent upon examining the characteristics of the variety of sensors which existed prior to the development of this system and upon examining the Earth scenes for which additional information is needed. Aircraft and satellite synthetic aperture radar (SAR) provide images (and digital products) of large expanses. Some systems allow the use of multiple frequencies and are polarization diversified, but practically all observe at only one incidence and aspect angle. Aircraft and satellite scatterometers typically operate at one frequency, may be dual-polarized, and acquire continuous data profiles over large areas at many incidence angles and with moderate to coarse resolution. Coordinating scene characterizations with sensors that provide mesoscale coverage has been difficult. Ground-based scatterometers have their own set of peculiarities. They may operate over a wide range of frequencies, polarizations, incidence angles, and aspects angles, and the coordination of microwave measurements and scene characterizations is very doable. Difficulties may occur as to how measurements which inherently tend to be made on the field level (a field may be defined as a scene which

exhibits the same scattering properties throughout) relate to the larger scales; such as, a scene composed of a collection of fields, as well as the local and regional levels.

Surface-based or airborne sensors may have difficulty with a variety of special situations. In the case of forest canopies, the sensor needs to be positioned above the tree tops. Trees may be very tall, limiting the utility of towers and booms. In addition, individual tree canopies may be large; hence, there is the need to acquire large spatial samples. In the case of vegetation and soil studies, the positioning within a field needs to be flexible and the ability to do regional surveys is important. Surface-based snow studies have been limited to reasonably flat terrain (i.e., in the valleys, but not on the critical and very hazardous mountain slopes). Scatterometer measurements of the ocean are being made from towers. Special problems include the effects of the platform, the ability to easily measure the critical aspect angle dependence, to quickly transit across hydrodynamic features, and to provide regional coverage. In Arctic sea ice and snow studies (the original purpose the helicopter-borne scatterometer was developed) there is a need to be able to shuttle the instrument and in-situ party to remote locations. In addition, the sensor has the task of providing local and regional coverage in support of aircraft-based sensors, such as the SAR and passive microwave imagers (PMI).

In summary, the helicopter-borne scatterometer was born out of the desire to satisfy the needs expressed above. This sensor complements well the satellite, the aircraft and surface-based measurements. It characteristics may be summarized as follows:

(a) Rapid transportation to remote locations of the sensor and surface party,

(b) Detailed local measurements,

(c) Regional survey capability,

(d) Ability to adapt to special measurement situations, and

(e) Ability to quickly gather (i.e., before the scene has time to change) very large numbers of spatial measurements.

HELOSCAT System Description

The multifrequency, multipolarization helicopter-borne scatterometer described herein and shown in Figure 1 has been developed for the measurement of backscatter coefficients for use in remote sensing applications. The radar, designed to operate at low altitudes, allows high-quality scattering measurements from a mobile platform. The frequencies at which the radar operates are based upon complementing existing and future microwave remote sensors (See Table 1.). From an active microwave viewpoint, the frequencies of 1.25, 5.25, and 9.38 GHz are critical and were selected for initial operation. Additionally, the understanding of the frequency response characteristic is of such importance that the radar was designed so that backscatter could be recorded at these three frequencies simultaneously; thus allowing accurate frequency response correlation studies of specific features and their microwave signature to be made. Incidence angles may range from vertical to greater than 70 degrees, and antenna transmit-receive polarizations include VV, VH, HV, and HH (the first letter represents the transmit polarization, the second letter the receive polarization, V indicates vertical polarization, and H indicates horizontal polarization). Sensor specifications are summarized in Table 2 and sensor geometry in Figure 2. Note that the antenna mounting structure is designed so that the vertical may be viewed. This was done to more completely describe the scattering processes, to relate Fresnel reflection coefficients with a scene's bulk dielectric constant, and to provide added information for inverting surface roughness parameters. Operation at vertical also allows calibrated measurements to be made in support of altimeter scattering studies.

This first generation of HELOSCAT was developed at the University of Kansas in 1979 by R.G. Onstott and R.K. Moore [1,2]. To illustrate the evolution of the HELOSCAT a brief description is provided. This system is a single channel frequency-modulated continuous-wave (FM-CW) radar which operates at frequency selected between 4 GHz to 18 GHz; at antenna polarizations of VV, VH, and HH; and at a data rate of 5 samples/sec. During the period from 1980 to 1984, this radar was used in numerous Arctic sea ice, tower-based liquid ocean, and land-based studies [3,4].

The HELOSCAT-II system is also based on the proven application of FM-CW radar for use in obtaining accurate scattering measurements. This system, shown in the block diagram provided in Figure 3, includes three radar front ends, with each containing a two channel homodyne receiver (See Figure 4), two parabolic dish center-fed antennas, a radar altimeter, a remote controlled solid state color video system, an electronically controlled antenna positioning system, radar control and processing circuitry, a 24-channel data acquisition system, and a DC-to-DC converter-based power supply system. Instrumentation also exists to precisely measure pitch and roll. Note that there is complete electrical control of all radar parameters.

The radars were designed to operate in discrete narrow frequencies bands because (1) the testing of an earlier hypothesis that there may be important backscatter resonances for sea ice (and terrain) was not demonstrated to be of great importance, and (2) radar performance is enhanced through use of narrow-band components which have higher performance. All four linear polarizations are possible. High-gain and narrow-beamwidth antennas are used for improved performance. Important gains have been made in the performance of the data acquisition system. Data may be continuously sampled at rates up to 150 samples/sec. Sampling can be done such that spatial samples are uncorrelated and contiguous with aircraft speeds beyond 80 knots. All available independent spatial samples are retrieved for the purpose of achieving the highest measurement precision possible and to provide continuous and detailed coverage of spatially small features, such as an ocean wave train or a sea-ice pressure-ridge. A time coded color video system (bore sighted with the radar) with voice channel has also been integrated into the sensor. Radar parameters which may be specified in an experiment plan include altitude, viewing angle, frequency, polarization, spot size (dependent on altitude, viewing angle, and frequency), required measurement precision (or number of independent samples), and data sampling rate (or aircraft speed).

In this radar the radio frequency (RF) signal is frequency modulated with a triangular sweep. This allows the target response to be associated with range. The free-space range resolution r_r is equal to $c/2B$ where c is the speed of light and B is the RF bandwidth. The effective range

resolution is determined by either the filter action of the antenna or the bandwidth of the intermediate frequency (IF) filter. This filter is selected to have a band narrow enough such that only target returns are detected. Multiple independent samples arise when there is excess RF bandwidth and the returns within the IF processing filter are true root-mean-square detected (See Figure 5). Target returns may also be recorded directly for future processing and for use in determining where within a scattering volume the dominant sources of scatter are located. Recording of the IF signal is easily implemented because the transmitted RF signal mixes with the received RF signal to produce an audio-frequency IF.

YIG oscillators are chosen to provide the RF signal because of their linear tuning characteristics. Sweeping these oscillators with a DC offset triangular waveform selects a carrier frequency and an RF bandwidth B (typically between 0.5 to 1.0 GHz). A wide bandwidth is chosen to reduce signal scintillations due to constructive and destructive interference often referred to as fading. The transmit signal is sampled prior to being routed to the transmit antenna port to provide the local oscillator for the receiver mixer. Switches allow the L-band and C-band radars to share a common antenna and the ability to choose between either the V and H antenna ports. The RF block diagram of the X-band radar is essentially identical to the above.

This radar in its present configuration uses two antennas, each having two-port linearly-polarized feeds. The L-band and C-band radars share the 1 meter diameter dish antenna, while a 66 cm diameter dish is used solely at X-band. With two antennas it is possible to use four of the six available IF channels at a time. The 1 meter antenna may be operated at L-band and C-band concurrently obtaining measurements at like polarization, or at one of the frequencies allowing the recording of both like and cross polarized returns. Note that operation at each of the four linear polarizations is possible. Selectable polarization states are provided in Table 3.

The data acquisition and display system, illustrated in Figure 6, was almost entirely assembled from off the shelf components. These include a 8088-based single board microcomputer with extended memory, a hardened 20 megabyte (MB) hard disk, a high speed magnetic tape unit for storage up to

60 MB, an EPROM card for internal storage of software, a real time clock, and a 24-channel 12-bit data acquisition module. A 160 character liquid crystal display and a standard keyboard are used to interface to the computer. Data recording functions are prompted by one or two key stroke commands. Many of the parameters which are entered into the data stream are displayed during data acquisition. All recorded parameters are provided in Table 4.

In the normal operation of the radar in the helicopter, the range to the target may change due to altitude variations. In the case of a distributed target, the return signal is the distribution of amplitude-modulated difference frequencies. Circuitry has been developed which locates the mean or centroid of this distribution, which creates an error signal which is proportional to the offset of the frequency associated with the centroid from the center frequency of the IF processing filter, and which corrects the modulation frequency so that the return signal is precisely positioned at the center of the IF filter.

Calibration of the radar is done both externally and internally. Absolute calibration is performed by measuring the return power from a precision calibration reference, such as a Luneberg lens retrograde reflector. Absolute calibration is dependent upon the care taken to minimize background clutter and multipath effects. This is accomplished best when the calibration reference is supported with the sky as the background. Internal calibration is performed periodically by direct injection of a sample of the transmitted signal into the receiver at a point immediately preceding the antenna ports. Instantaneous calibration is assisted by continuously monitoring the transmitted power.

A ground support facility has been developed which allows data to be processed and examined on site. In processing, operations of unpacking, reformatting, and conversion of power returns to scattering coefficients are performed. The resulting time series data may be displayed graphically on a CRT or in hardcopy.

The HELOSCAT system interfaces to the Bell Model 206B helicopter. This helicopter was chosen because it is widely available and operation costs are modest. The interior instrumentation (See Figure 7) requires 15 amperes of aircraft 28 VDC power and takes the place of one person in the

passenger compartment. The radar is operated by one person. There are no special modifications to the airframe of the helicopter. The exterior equipment mounts directly to the tubular landing structure. Cables are ran from the exterior to the interior through a window.

This radar is very flexible. Data may be acquired in either one of two modes: profiles made along well defined flight tracks or scans made from a hover across features of interest. In addition, this radar has the potential to be operated from a variety of other platforms, i.e., towers, small aircraft, and ships.

This sensor, which has just been developed, has participated in a winter sea ice investigation [5] into the marginal ice zone (MIZEX-87) and in an ERIM sponsored terrain and ocean water study (November 1987).

SUMMARY

The purpose of this paper is to briefly describe the HELOSCAT-II calibrated radar and outline its measurement capabilities. This instrument has the ability to make detailed scattering measurements of a variety of important Earth scenes and acquire the many spatial samples necessary for a comprehensive statistical description. The importance of this tool is derived from the ability to make scientific measurements when scene characterizations and scattering measurements must be localized and timely. This is of particular importance in studies directed toward understanding the radar-scene interaction processes. This instrument becomes especially powerful when coordinated with SAR or PMI data collections.

REFERENCES

Onstott, R.G., et al., Helicopter-Borne Scatterometer, Remote Sensing Laboratory Technical Report, TR 331-24, University of Kansas Center for Research, Inc., Lawrence, KS, Oct. 1981.

Ulaby, F.T., R.K. Moore, and A.K. Fung, Microwave Remote Sensing, Active and Passive, Vol. II: Radar Remote Sensing and Surface Scattering and Emission Theory, Addison-Wesley Publishing Co., Reading, MA, 1982.

Onstott, R.G., et al., "Four Years of Low-Altitude, Sea-Ice, Broadband Backscatter Measurements," IEEE J. Oceanic Engineering, Vol OE-7, pp. 44-50, Jan. 1981.

Chaudry, A.H. and R.K. Moore, "Tower-Based Backscatter Measurements of the Sea," IEEE J. Oceanic Engineering, OE-5, pp. 309-317, 1985.

MIZEX 87 Bulletin, VIII: A Science Plan for a Winter Marginal Ice Zone Experiment in the Fram Strait/Greenland Sea: 1987/89, CRREL Special Report 86-9, Hanover, NH, April, 1986.

Figure 1. The helicopter-borne scatterometer named HELOSCAT-II.
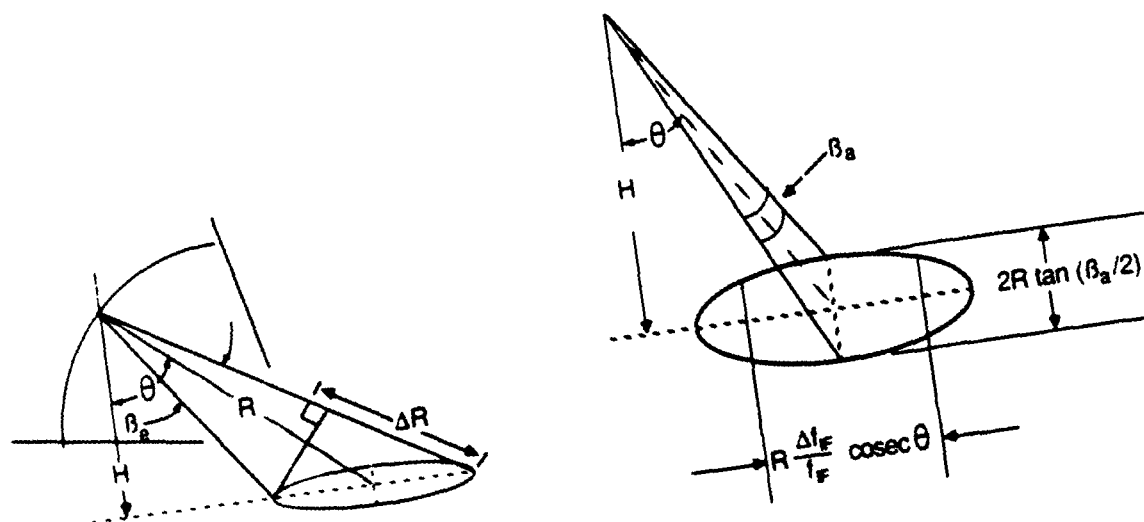
Figure 2. The radar's illuminated area is determined by either the antenna's beamwidth (a) or by the bandwidth of the IF filter (b).
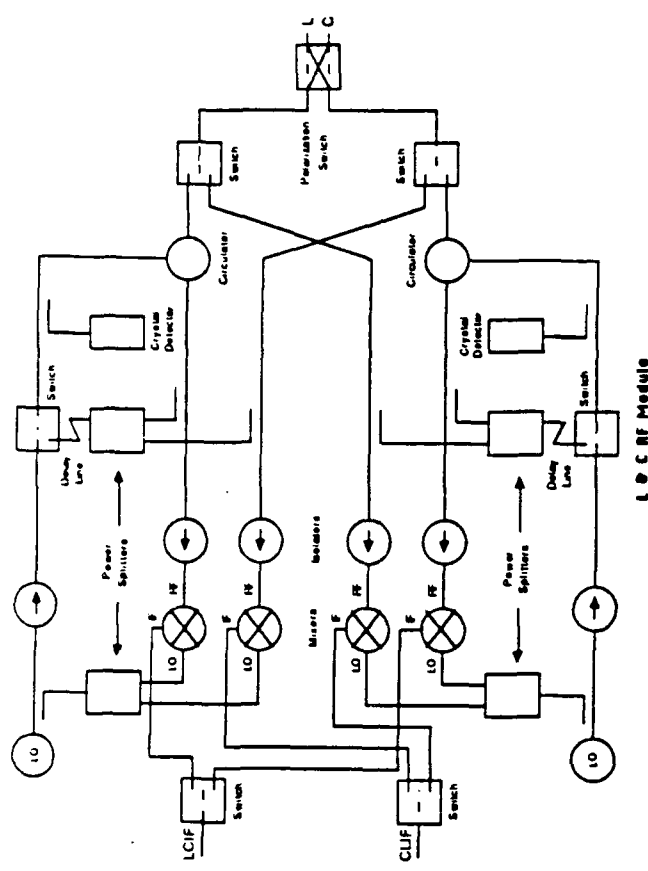
Figure 4. RF block diagram.
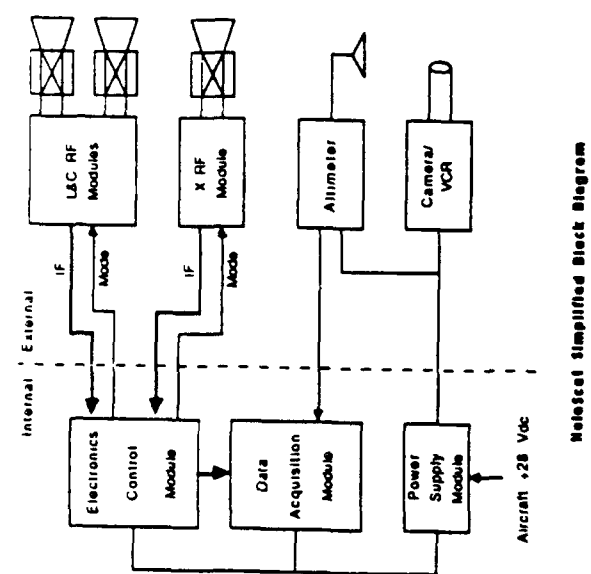
Figure 3. The HELOSCAT system block diagram.
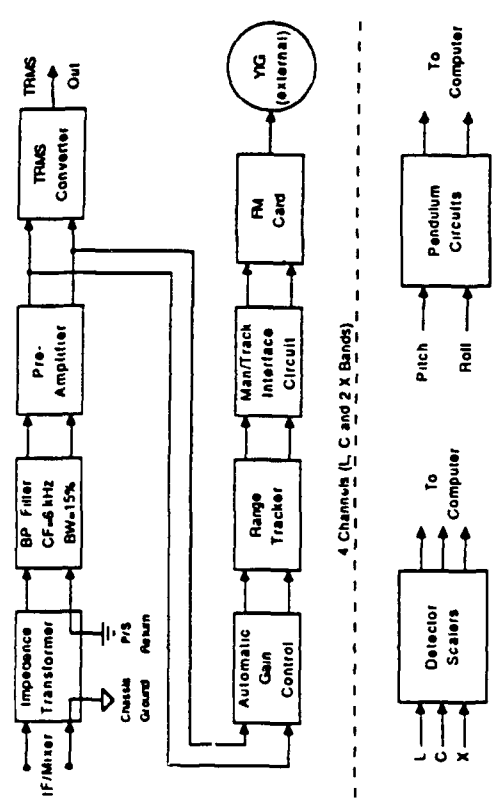
Figure 5. IF block diagram.

Analog inputs

— 13 lines

Digital inputs

8 lines

Data Acquisition
Controller
-12 bit analog resolution-

Keyboard

8088 Microprocessor
Based Single
Board Computer
640 K DRAM

Liquid Crystal
4x40 Character
Display

20 MB Hardened
Fixed Hard Disk

60 MB High
Speed Tape Drive

EPROM Card
-program storage

Realtime Clock
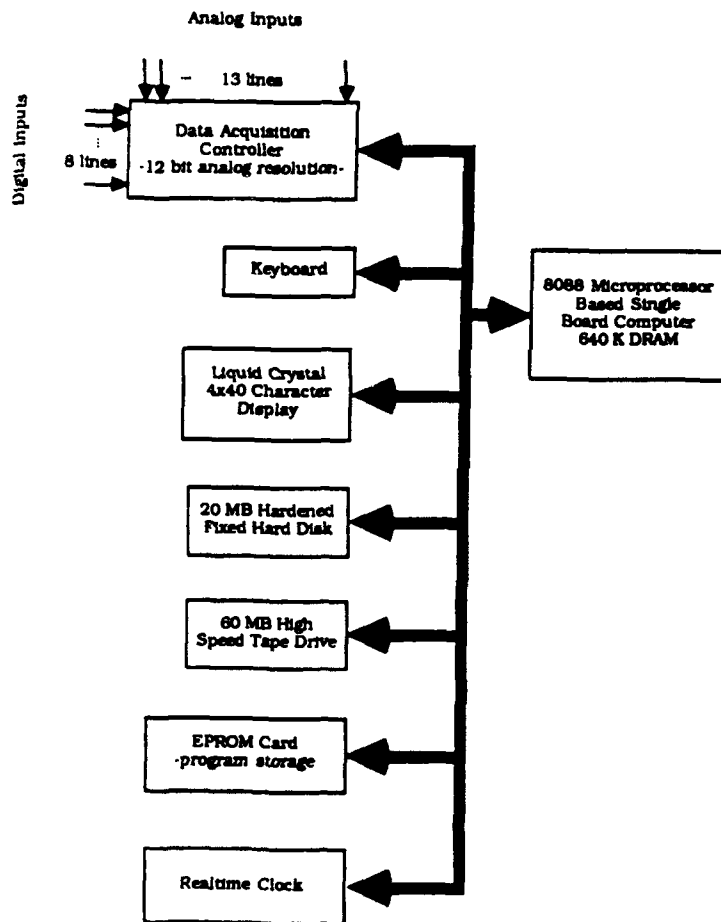
Computer Module Block Diagram

Figure 6. Data acquisition system block
diagram.

7. HELOSCAT-II interior
equipment.

TABLE 1
MICROWAVE REMOTE SENSING INSTRUMENTS

Instrument	Operating Frequency (GHz)
Aircraft	
NADC ERIM P3 SAR, active	1.25, 5.3, 9.35
USN-NRL P3, passive	19, 22, 31, 37, 90
NASA-CV 990, passive	18, 21, 37, 90
CCRS-IRIS SAR, active	5.3
INTERA STAR-1 SAR, active	9.4
INTERA STAR-2 SAR, active	9.4
Spaceborne Spacecraft	
SMMR, passive	6.6, 10.7, 18, 21, 37
SSM/I, passive	19.3, 22.2, 37, 85.5
Proposed Instruments	
SIR-C (SAR)	1.25, 5.3, 9.6
ERS-1(SAR)	5.3
NROSS-2 (SAR & SCATT)	TBD
RADARSAT (SAR & SCATT)	5.3, 14
J-ERS-1(SAR)	5.3
EOS (SAR & SCATT)	TBD

TABLE 2
HELOSCAT SPECIFICATIONS

Type	EM-CW	EM-CW	EM-CW
Frequency (GHz)	1.25	5.25	9.38
Polarization		– VV, VH, HV, HH –	
Incidence Angle		0° to 70°	
Height, Typical		23m	
Spot Size (m) at 40°	4.5	1.6	1.3
Independent Samples Per Meter at 40°	24.0	12.0	15.0
Precision (dB) at 40°	±1.4	±2.1	±1.9
Absolute Accuracy	±1.0	±1.0	±1.0

TABLE 3
HELOSCAT POLARIZATION STATE TABLE

MODE	L BAND VV, VH, HH, HV	C BAND VV, VH, HH, HV	X BAND VV, VH, HH, HV
1			
2			
3			
4			
5			
6			
7	CAL 1		
8		CAL 2	

TABLE 4
HELOSCAT PARAMETERS RECORDED

- Power Return (4 Channels)
- Power Transmitted
- Modulation Rate
- Altitude
- Incidence Angle
- Pitch Angle
- Polarization/Frequency Mode
- Time (Real)
- Event Strobe or Code
- Color Video
- Time Encoded
- Bore Sighted
- Remote Controlled
- Voice

A POLARIMETRIC MICROWAVE SCATTEROMETER

Robert G. Onstott & Scott H. Gaboury

Radar Science Laboratory
Advanced Concepts Division
Environmental Research Institute of Michigan
Ann Arbor, MI 48107 USA

ABSTRACT

A polarimetric radar has been developed that operates at 1.8, 5, 10, and 35 GHz, and measures the amplitude and phase at *four* linear transmit-receive polarizations -- the elements of the target scattering matrix. Designed for application in both the laboratory and the field, the capable HP8510B network analyzer and HP8341B synthesized frequency source serve as *the heart of this system.* Presentation included the system concept, hardware, and measured backscatter responses of calibration reference targets and distributed rough surfaces.

Keywords: Polarimetric, Scatterometer, Microwave

1. DESCRIPTION

This radar allows the target scattering matrix (TSM) to be acquired through measurement; hence, the description of the polarization properties of the scattered field is complete. Measurements support studies which address surface and volume scattering, repolarization, and depolarization.

The sensor is comprised of a synthesized frequency source, RF-antenna packages (at each frequency), a three-channel frequency converter, a network analyzer, system control circuitry, and a data acquisition computer (see Figure 1). *Simultaneous measurements may be made at two frequencies.*

Each receiver is dual channel (see Figure 2); *both vertical and horizontal polarizations are received coincidently.* The TSM elements are acquired by transmitting using a V-pol antenna and then an H-Pol antenna. The RF hardware is mounted in temperature controlled enclosures. Clusters of four antennas are mounted rigidly to these enclosures. Symmetry in the antenna cluster and RF hardware provides short, *nearly identical electrical paths;* further adjustment of channel balance was not required and the data acquisition software remained relatively uncomplicated and inherently quicker. The oscillator which is shared by each transmitter and receiver determines the RF frequency and also provides the phase reference. A swept IF signal (1-2 GHz) is provided for the up conversion at the transmitters. The RF and antennas are separated from IF processing by a distance of 13 meters. Losses and phase errors due to cable flexure were kept small by selecting the low IF frequency and using heliax type cable.

Data acquisition procedures greatly impact measurement accuracy. As backscatter levels become *very small, locating the target returns in each of the four channels so that narrow range gates may be positioned precisely requires increased sophistication.*

TVA = Trans. Vert. Antenna; THA = Trans. Horiz. Antenna; RVA = Rec. Vert. Antenna; RHA = Rec. Horiz. Antenna

Figure 1. Polarimetric Radar System Configuration
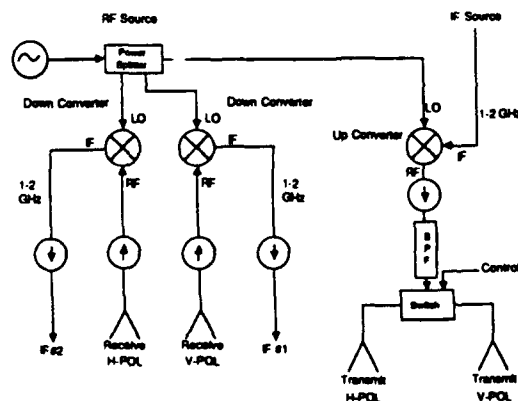
Figure 2. Polarimetric Radar RF/IF Diagram

1

INTERCOMPARISON OF SYNTHETIC- AND REAL-APERTURE RADAR OBSERVATIONS OF ARCTIC SEA ICE DURING WINTER MIZEX '87

R.A. Shuchman, R.G. Onstott, L.L. Sutherland & C.C. Wackerman

Radar Science Laboratory
Advanced Concepts Division
Environmental Research Institute of Michigan
Ann Arbor, MI   48107   USA

ABSTRACT

Active microwave measurements were made of various sea ice forms in March and April 1987 during the Marginal Ice Zone Experiment (MIZEX). These measurements were made at 1, 5, 10, 18 and 35 GHz using a synthetic aperture radar (SAR) and helicopter- and ship-based scatterometers. The X-band (9.8 GHz) SAR data were compared to the scatterometer data and it was determined that for 5 GHz and higher frequencies both the SAR and scatterometers can differentiate open water, new ice (5 - 30 cm), first-year ice with rubble (.60 -1.5 m), and multiyear ice. The analysis further confirmed that the C-band (5 GHz) SAR's flying on ESA ERS-1 and RADARSAT will differentiate the above mentioned ice types.

Keywords: SAR, Microwaves, Scatterometer, Radar Backscatter, Sea Ice, MIZEX.

Figure 1.   MIZEX '87 Operations Overview Showing Ice-Edge Variation, Research Foci, and Key Ship Positions

1. INTRODUCTION

Active microwave measurements were made of various sea ice forms in March and April 1987 during MIZEX. The study area was located between 76°N and 80°N and 10°W to 10°E, in an area of the Fram Strait in the Greenland Sea (see Figure 1). The ice conditions within the Greenland Sea during the three week experiment included: 1) grease ice actively forming at the open ocean boundary; 2) a combination of young frazil, nilas, and small pancake first-year ice forms in the Odden; 3) multiyear ice (3 to 5 meters thick) with floe sizes ranging from 30 m to 50 km from the edge to the interior; and 4) older first-year ice (3 to 150 cm thick) of varying floe size dimensions interspersed among the multiyear.

The active microwave observations included: 1) a rail mounted ship-borne scatterometer system which made measurements at 1, 5, 10, 18, and 35 GHz; 2) a helicopter-based scatterometer which collected parallel and cross polarized (HH; VV; VH) data at 1.75, 5 and 10 GHz; and 3) an aircraft equipped with a SAR that operated at 9.8 GHz with horizontally transmitted and received polarizations.

In this paper we first present the X-band (9.8 GHz) values for the various ice types within the marginal ice zone and then compare these SAR values to the 1, 5, 10, 18, and 35 GHz measurements obtained by the real aperture radar operated from the ship and helicopter. The real aperture data has undergone the typical temporal and spatial averaging and thus the effects of image speckle or radar fading are minimal (Ref. 1). The multi-frequency scatterometer data in conjunction with the X-band SAR data is then used to evaluate the use of the European Space Agency's Earth Resources Satellite-1 (ESA ERS-1) and Canada's RADARSAT SAR's (Refs. 2, 3) for ice type classification.

2. DATA SETS

Twenty-two SAR data collection missions were flown daily throughout the experiment using the Intera STAR systems. Each mission covered approximately a 200 by 200 km area surrounding the ice-strengthened research vessel POLAR CIRCLE. During flights, SAR data which were transmitted via radio link to the POLAR CIRCLE, were used to select sites to perform detailed microwave measurements as a function of incidence angle using the helicopter and ship mounted scatterometers. At each of the detailed sites,

1

"sea ice truth parties" from POLAR CIRCLE would characterize the physical and electrical properties of snow and ice. In addition to the specific sites, the ship borne scatterometers collected data in transit. Thus, for the first time, SAR sea ice imagery can be correlated with coincidence scatterometer and sea truth data.

The parameters of the STAR system are presented in Table 1. Figure 2 is an image of a high resolution (4 x 4 m) 17 x 36 km area that was extensively "sea truthed" both from the ship and the helicopter. Indicated on Figure 2 are letters A through G which correspond to the seven open water and sea ice types found within this test area.

The ship-based scatterometers operated at 1, 5, 10, 18, and 35 GHz and are described in these proceedings by Onstott and Shuchman (Ref. 4). The 1, 5, and 10 GHz ship-based scatterometer was also operated on a Bell 206 helicopter and is described in this issue, Onstott and Gaboury (Ref. 5).

3. BACKSCATTER RESULTS

Thirty-three areas within the SAR ice image shown in Figure 2 were selected for statistical analysis. Standard statistics (i.e., mean, standard deviation, variance, skewness, and kurtosis) were generated on these areas and combined into the seven water and sea ice catagories identified on Figure 2 and presented in Table 2. The SAR data is seven-look and using an equation of Lyzenga et. al., (Ref. 6) the variance due to speckle can be removed, leaving just the spatial variation of the scatterers. To illustrate this, Figure 3 shows the data from Table 2 plotted in dB. The boxes in Figure 3 represent the means of the classes and the extent of the error bars are determined by adding and subtracting the standard deviation of the spatial variations (i.e., with the speckle component removed) to the mean values. Note that categories A through E have a significant amount of spatial variation, while categories F through G have none. The relativity higher spatial variation of catagories B and C are thought to be due to the effects of rubble on the surface. This suggests that automated techniques (Ref. 7) utilizing SAR texture information (i.e., the spatial variations) may prove useful in sea ice classification.

Examination of Figure 3 reveals that in general categories A and C through G are separable indicating that multiyear ice can be differentiated from first-year ice with rubble, thick and thin young ice, and open water on the X-band (9.8 GHz) SAR data. Category B which included a mixture of multiyear, first-year and open water was not separable due to the mixed nature of the category. The grease ice area had a lower return than the ice free open water suggesting the grease ice dampened the capillary waves which made the surface appear smooth to the radar.

The SAR values for multiyear, first-year with rubble, first-year without rubble and thin new ice were then compared to the scatterometer measurements made at 1, 5, 10, 18 and 35 GHz (see Table 3). The standard deviation of the scatterometer data is approximately +.5 dB.

Examination of Table 3 indicates that the SAR and scatterometer measurements made at 10 GHz were similar. In general, as the frequency increases the ability to separate multiyear from first-year ice also increases. The opposite trend occurs with decreasing frequency. L-band (1 GHz) which is dominated by volume scattering and the effect of topography has similar signatures for multiyear and first-year. C-band (5 GHz) appears to produce signatures that are very similar to X-band (i.e., volume scattering from bubbles dominates the return from multiyear ice).

4. SUMMARY

The X-band SAR data successfully separated the sea ice types within the image. The SAR derived backscatter values compared favorably to the measurements made by the temporally and spatially averaged scatterometer data. The performance with respect to sea ice classification of the ESA ERS-1 and RADARSAT which will operate at C-band (5 GHz) should be comparable to the X-band SAR system used in MIZEX. The performance of the Japanese ERS-1 operating at L-band (1.2 GHz) will be degraded with respect to discriminating first-year from multiyear ice. All three of the above mentioned satellites should distinguish open water from sea ice, thus producing useful ice concentration information.

6. REFERENCES

1. Ulaby F et al 1982, Microwave Remote Sensing, Addison-Wesley Publ. Co., vol II.

2. Louet J 1986, The ESA approach for ERS-1 sensor calibration and performance verification, Proc IGARSS '86 Symp, Zurich 8-11 September 1986, ESA SP-254, 167-174.

3. Oceans Working Group 1985, Ocean satellite data opportunities for Canada: a long-term view, Canadian Advisory Committee on Remote Sensing, Ottawa.

4. Shuchman R & Onstott R 1988, Radar backscatter of sea ice during winter, Proc IGARSS '88 Symp, Edinburgh, Scotland 13-16 September 1988.

5. Onstott R & Gaboury S 1988, Active microwave measurements of artificial sea ice, Proc IGARSS '88 Symp, Edinburgh, Scotland 13-16 September 1988.

6. Burns B & Lyzenga D 1984, Textural analysis as a SAR classification, Electromagnetics 4, 309-322.

7. Shuchman R et al 1984, Textural analysis and real-time classification of sea-ice types using digital SAR data, IEEE Transactions on Geoscience and Remote Sensing, vol GE-22(2).

Table 1. STAR System Parameters As Used in MIZEX

PROPERTY	STAR-2	STAR-1
Operating Altitude	29,000 ft.	
Wave length	X-band	
Polarization	HH	
Viewing Direction	Left or Right	
Processing	Real time	
Recording	8 bit data, full bandwidth data recording on parallel HDDR	4 bit data, either 12 x 12m or 24 x 24m pixels on serial HDDR
Swath width		
Narrow (Hi-Res)	17 km	23 km
Wide (Lo-Res)	63 km	45 km
Pixel size	Along track/ cross track	Along track/ cross track
Hi-Res	4 x 4 m	Not used
Lo-Res	5.2 x 16m	12 x 12m or 24 x 24m
Downlink	4 bits	4 bits
Azimuth Looks	7	7
Lo-Res	16 x 16m or 32 x 32m	12 x 12m or 24 x 24m

Figure 2. STAR-2 Extensively "Sea-Truthed" High-Resolution Imagery. Letters A Through G Correspond to the Seven Open Water and Sea Ice Types Found Within This Test Area.

3

Key	# of Areas	Min Value	Max Value	Mean	Variance	Standard Deviation
A	6	41	14178	1471	806527	885
B	1	9	9604	488	146850	383
C	4	19	10969	804	443262	608
D	1	4	1024	190	11840	109
E	1	4	729	124	3717	61
F	10	14	266	67	543	23
G	2	7	196	62	337	18

Legend

A · 50-60% Multiyear Ice in Consolidated First-Year Ice Framework (1-3 cm snow)

B · 30-40% Multiyear Ice with Rubble in Loose First Year Ice Framework (some open water)

C · First-Year Ice with Rubble (.60-1.5 m thick)

D · First-Year Ice (20-40 cm thick)

E · New Ice (5-8 cm thick)

F · Open Water

G · Open Water with Grease Ice Streamers

Table 2. MIZEX '87 SAR Clutter Statistics -- Averaged Values for Similar Areas
6 April - Mission 15
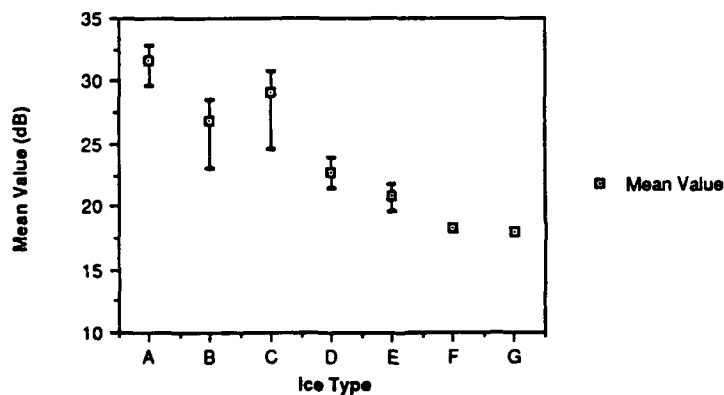
Figure 3. SAR Mean Backscatter at 40° Incident Angle for Sea Ice and Open Water

Frequency GHz \ Ice Type	Scatterometer					SAR
	1	5	10	18	35	10
MY	13	17	20	25	25	20
FY	16	9	11	15	12	11
FYR	NA	6	7	15	10	4.7
New	NA	3	3	3	3	3

Legend

MY = 50 - 60% Multi-Year Ice in Consolidated First-Year Ice Framework (1-3 cm snow)
FYR = First-Year Ice with Rubble (.60-1.5 m thick)
FY = First-Year Ice (20-40 cm thick)
New = New Ice (5-8 cm thick)
NA = Not Available

Table 3. Scatterometer and SAR Values at 40° Incident Angle for Four Categories of Sea Ice
Referenced to Open Water

RADAR BACKSCATTER OF SEA ICE DURING WINTER

Robert G. Onstott and Robert A. Shuchman

Radar Science Laboratory
Advanced Concepts Division
Environmental Research Institute of Michigan
Ann Arbor, MI 48107   USA

ABSTRACT

Active microwave measurements were made during the 1987 Marginal Ice Zone Experiment (MIZEX). Backscatter data were acquired at frequencies from 1.25 to 35 GHz, at incidence angles from 0 to 80 degrees, and with linear antenna polarizations. The objective was to make descriptions of the scattering coefficients of the major ice types in the region and to study the winter conditions and their influence on the microwave response. Results show that multiyear and pancake ice produce strong backscatter, while returns from open water between floes and new ice are weak. First-year ice has a wide range of returns; when the surface is smooth *returns are weak, and if roughened, i.e., like* pancake ice, the returns increase substantially.

Keywords: Backscatter, Sea Ice, Radar, Scatterometer

1. INTRODUCTION

Radar backscatter data were acquired from the ice-strengthened ship M/V POLAR CIRCLE which was positioned in the Fram Strait marginal ice zone (MIZ) during March and April 1987. These measurements were coordinated with those of an aircraft equipped with synthetic aperture radar (SAR), satellite sensors, surface-based passive microwave radiometers, and detailed ice characterizations. Synoptic coverage by satellites, higher resolution 100 km x 100 km coverage by aircraft SAR, local area coverage by the helicopter scatterometer, and very detailed local coverage from the ship were integrated with success.

The MIZEX '87 winter campaign was of great interest because well-coordinated measurement programs have been directed at other seasons but never in the winter in the Fram Strait. A winter experiment allowed us to examine the seasonal variation in the microwave and physical properties for the various ice types and features. These microwave and physical property data are needed to better evaluate and produce geophysical quantities from SAR.

2. SENSOR AND EXPERIMENT DESCRIPTION

Two radar scatterometers were operated during this investigation: one from the Norwegian ice strengthened ship, and a second from a small helicopter. Ice and ocean data were collected from the ship during transects through the MIZ. During the times the ship was held against ice floes, detailed surface measurements were made. These included radar backscatter cross sections (ERIM), brightness temperatures (University of Washington), ice and snow characterization (CRREL, ERIM, and University of Washington) and dielectric properties (ERIM). Measurements were made to study the temporal changes in the properties of the various ice types and to examine the variety of ice conditions in the MIZ. Floes were selected using the SAR downlink data. The floes selected from the SAR data were representative of both typical and anomalous conditions in the immediate region about the ship. The helicopter scatterometer made measurements at these floes and extended the detailed local measurements to the regional measurements made by the SAR. The helicopter-borne scatterometer was used to link the mesoscale programs and provide the high mobility needed to study ice conditions throughout the experimental region.

Surface measurements were made of the physical-electrical properties of various ice and snow types present at the remote sensing test sites. Physical property information acquired includes temperature profile, small-scale roughness of surfaces and layers, salinity distributions, thickness, density, snow grain size, snowpack construction, snow-ice interface descriptions, ice sheet construction, ice sheet discontinuity profile (scatterers in the ice sheet such as air bubbles), and ice sheet freeboard. Dielectric constant measurements were made using coaxial resonators and cavities at approximately 1, 5, and 10 GHz.

The ship-based sensor shown in Figure 1 is a millimeter wave radar and was mounted on the wheel house deck, approximately 15 m above the ice. Backscatter data were acquired at 18 and 35 GHz. Looking to the side of the ship, scenes could be viewed from 15 to 80 degrees from vertical. Angular response measurements were made when the ship was stationed next to ice floes. Additional data were acquired as the ship traversed through

extensive regions of new ice. Sensor specifications are summarized in Table 1.

The helicopter-borne scatterometer shown in Figure 2 was flown at an altitude of 15 to 30 m. The radar operated at 1.25, 5.25, and 9.38 GHz simultaneously. This is an important aspect of both this radar and the millimeter radar. Collecting data simultaneously improves the ability to study frequency and polarization signature behavior and to correlate specific features with their microwave signatures. Incidence angles ranged from vertical to 70 degrees, and antenna transmit-receive polarizations included VV, VH, HV, and HH (i.e., VH indicates vertical transmit and horizontal receive). This sensor allows the data to be acquired so that it is uncorrelated but spatially contiguous, with reasonable aircraft speeds (i.e., up to 60 knots) making full use of available independent spatial samples. A color video record of the scenes observed was produced. Sensor specifications are summarized in Table 2.

Internal calibration for both radars necessary for short-term variations in the radar was accomplished by passing the radar signal through a delay line of known loss. Overall system calibration was performed by measuring the backscatter from targets of known cross section, a Luneberg lens or a trihedral.

3. PRELIMINARY RESULTS

The MIZ was comprised of numerous floes which were typically less than 200 m in diameter. These floes also showed various degrees of deformation. There were also extensive areas of new ice. These included homogeneous and reasonably undisturbed areas to those composed of pancakes with rough edges which form because of wave action. The thickness of the young first-year (FY) sea ice ranged from about 20 to 80 cm, multiyear (MY) ice from 165 to 410 cm, and new and pancake ice (PC) from 1 to 10 cm.

Preliminary results at the L-band frequency (see Figure 3) show that FY ice at VV- and HH-polarizations were within about one dB of being identical at angles from 35 to 65 degrees. Signatures of FY and MY ice were also similar, with FY about one dB higher. These measurements are consistent with observations made in 1976 (Ref. 1). Cross-polarization returns were not similar. The returns of FY ice were higher and decayed more rapidly with increasing angle than those of MY ice. This result was not anticipated and further investigation of the data is underway.

Results at the C-band frequency (see Figure 4) show that PC ice returns were greater than those of MY ice at angles less than 40 degrees. Like- and cross-polarized MY ice returns were well separated, between 6 and 14 dB.

At the X-band (see Figure 5), PC ice again provided the strongest returns at angles less than 30 degrees. However, beyond 30 degrees MY ice produced the greatest backscatter. At 45 degrees FY and PC ice signatures merged at a level of about 7 dB lower than that of MY ice. As was the case at the L-band, FY cross-polarized returns were higher than those of MY ice.

MY ice returns were the highest from 20 to 70 degrees at the Ku-band frequency (see Figure 6).

PC ice backscatter fell between those of MY and FY ice. FY ice returns were about 10 dB lower than those of MY ice. This is similar to the cases at the lower frequencies. Open water (OW) produced weak backscatter in the angular region between 10 and 50 degrees. The contrast between MY ice and OW was greater than 20 dB in the region from 30 to 50 degrees. Smooth, undisturbed new ice returns were an additional 5 dB lower than OW at 40 degrees. MY ice continued to produce strong backscatter at 35 GHz (see Figure 7). FY ice and OW returns were similar and decayed rapidly beyond 10 degrees. PC ice produced strong scatter, about 5 dB lower than that of MY ice from 35 to 70 degrees. These cross sections were considerably larger than those for the smooth-surfaced FY ice.

4. CONCLUSIONS

Based upon the preliminary results described here, the contrast between MY ice and FY ice with a relatively smooth surface improves with frequency in the region between 1 and 35 GHz. When the ice is young and rough, i.e., PC ice, returns are significantly greater and occur at levels similar to those of MY ice. This is seen to be especially true at angles from 20 and 30 degrees. OW between floes was found to produce weak returns suggesting that radar should perform well in separating ice from water.

5. ACKNOWLEDGEMENTS

6. REFERENCE

1. Onstott R G, R K Moore, S Gogineni & C V Delker 1982, Four years of low altitude sea ice broadband measurements, IEEE J. Oceanic Eng. vol OE-7(1), 44-50.

Figure 1. Ship-Based Scatterometer

2

Photograph

Figure 2. The Helicopter-Borne Scatterometer Named
HELOSCAT-II

Figure 5. Radar Backscatter Responses at 9.38 GHz
for Pancake Ice, 19-cm Thick First-Year
Ice, and 392-cm Thick Multiyear Ice

Figure 3. Radar Backscatter Responses at 1.25 GHz
for 19-cm Thick First-Year Ice and
392-cm Thick Multiyear Ice
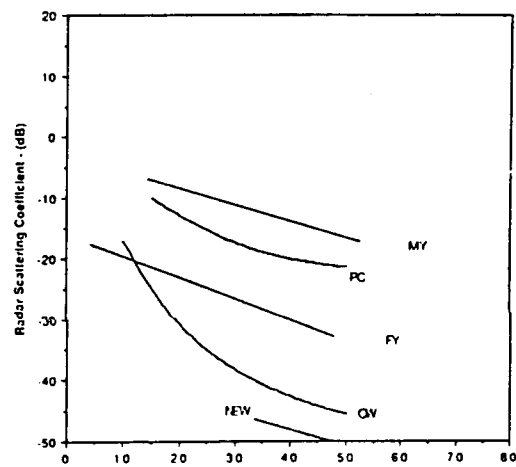
Figure 6. Radar Backscatter Responses at 18 GHz
and VV Polarization for 19-cm Thick
First-Year Ice, 392-cm Thick Multiyear
Ice, Pancake Ice, and Open Water

Figure 4. Radar Backscatter Responses at 5.25 GHz
for 19-cm Thick First-Year Ice and
392-cm Thick Multiyear Ice
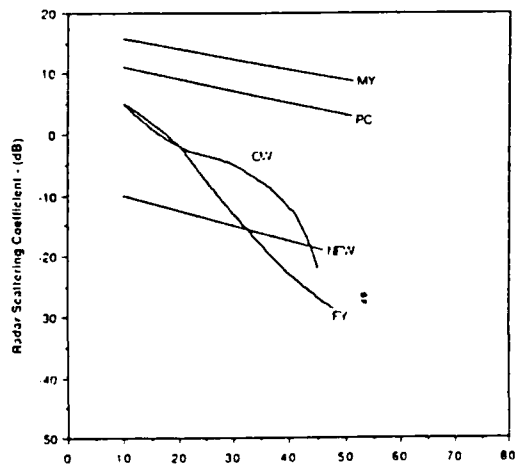
Figure 7. Radar Backscatter Responses at 35 GHz
and VV Polarizatio or 19-cm Thick
First-Year Ice, 39 m Thick Multiyear
Ice, Pancake Ice, New Ice, and Open
Water

3

Type	FM-CW		
Frequency (GHz)	18	35	94
FM Sweep (MHz)	1000	1100	400
Antenna Beamwidth (°)	5	3.5	3
Polarizations[1]	V or H	V or H	V or H
Height (m)	16	16	16
Footprint[2] (m)	2.0	1.4	1.2
N-Freq[3]	9	6	6
N-Spatial[4]	13	9	30
N-Total[5]	117	54	180
σ ° Precision (dB)	± 0.6	± 1.0	± 0.5

[1] V = VV, H = HH, X = VH or HV
[2] Footprint at 40 ° (Except for 0.5 GHz)
[3] Number of Independent Samples Via Excess Bandwidth
[4] Independent Samples per Spatial Footprint
[5] Total Number of Independent Samples per Footprint

Table 1. Shipscat Specifications

Type	FM-CW		
Frequency (GHz)	1.25	5.25	9.38
Polarization	— VV, VH, HV, HH —		
Incidence Angle	0° to 70°		
Height, Typical	23 m		
Spot Size (m) at 40 °	4.5	1.6	1.3
Independent Samples Per Meter at 40 °	24.0	12.0	15.0
Precision (dB) at 40 °	±1.4	±2.1	±1.9
Absolute Accuracy	±1.0	±1.0	±1.0

Table 2. Heloscat Specifications

4

ACTIVE MICROWAVE MEASUREMENTS OF ARTIFICIAL SEA ICE

R.G. Onstott and S.H. Gaboury

Radar Science Laboratory
Advanced Concepts Division
Environmental Research Institute of Michigan
Ann Arbor, MI 48107 USA

Jon Bredow and Prasad Gogineni

University of Kansas
Lawrence, KS 66045 USA

ABSTRACT

During the winter of 1988, active microwave measurements were made of artificial sea ice. A 5 m x 15 m outdoor tank of a 1.2 m depth was filled with sea water. Polarimetric radar backscatter data were collected at 1.8, 5, and 10 GHz for incidence angles 0 degrees to 60 degrees. Observations commenced with open water and continued until 30 cm of sea ice were formed. The roughness of the ice surface is important in determining the general backscatter level for first-year ice. Experiments were performed to study the change in backscatter with various roughness scales. Effects of freeze and thaw conditions were also examined.

Keywords: Scatterometer, Polarimetric, Sea Ice

1. INTRODUCTION

The microwave properties of sea ice grown at the U.S. Army Cold Regions and Engineering Laboratory (CRREL) were investigated during the 1988 winter season. The sea ice facility is comprised of a 5 m x 15 m outdoor tank, a tent to protect the ice sheet from snow and rain, a gantry style instrument mounting structure, and heated working environments in the immediate vicinity of the tank. The tank size, determined by instrument and experiment needs, allows for the acquisition of independent spatial samples and measurements at angles from vertical to 60 degrees. These efforts, which are part of a new three-year, laboratory-based investigation, are focused on understanding the microwave signatures of sea ice; this will be accomplished by detailed studies of the various aspects of backscatter and emission and through the intercomparison of measured data and theoretical predictions. Two strengths of the CRREL Ice Tank Facility are the ability to control the physical properties of the ice sheet and the time to rigorously measure the physical and microwave properties of ice which closely simulate that found in the Arctic.

Observations were made of ice as it grew to 20 cm. Physical properties (i.e., fabric of the ice sheet, the salinity, the density, the temperature, location of layers, location of internal inhomogeneities, and surface roughness) which may influence backscatter and emission were measured; these data or their derivatives provide the critical inputs for the electromagnetic models.

For this investigation, the polarization diversified ERIM and KU scatterometers have been enhanced by adding the sophistication necessary to measure phase. Note that previous measurements were made to describe the noncoherent average scattering coefficients at VV, VH, HV, and HH polarizations (i.e., VH indicates vertical transmit and horizontal receive). These radars were used to measure the target scattering matrix (i.e., the matrix elements are the detected scattered fields at VV, VH, HV, and HH polarizations) which allows the examination of the functional dependence of intensity on polarization. During CRRELEX, polarimetric measurements were made at 1.8, 5, and 10 GHz in the configuration shown in Figure 1. The ERIM polarimetric radar (Ref. 1) is briefly described in a paper found in these proceedings entitled, "A Polarimetric Microwave Radar". In addition, millimeter wave data were collected at 18, 35, and 94 GHz using a noncoherent (ERIM) radar.

2. OBSERVATIONS

An ice sheet was allowed to grow over a 2-month period. Observations were made of open water, 5-mm thick new ice, 8-cm thick grey ice, 12-cm thick grey ice which had a rough, air-ice interface (rms roughness of about 1 cm), and 12-cm thick grey ice with a liquid film water on its surface, and 20-cm thick ice which had undergone desalination and showed some of the characteristics associated with multiyear.

Preliminary results show that, in general, the backscatter response at VV and HH polarizations are similar at angles from vertical to 40 degrees, with the possibility of a few dB of spreading at the larger angles. Examination of the change in the Fresnel reflection coefficients at large angles should explain the degree of separation. The backscatter response of 12-cm thick grey ice as shown in Figure 2 illustrates this. Antenna gain pattern effects have been removed to obtain true scattering coefficients (Ref. 2). The nearly identical

1.

returns at VH and HV suggest reciprocity, i.e., that VH = HV. The rapidly decaying angular response and the large separation between like and cross polarized returns, especially between vertical to 20 degrees, are characteristic of scatter from a dielectric with a smooth surface in which there is sufficient penetration to produce a small volume scatter. This is necessary to generate the cross-polarized return. Study of the measurement system response to cross-polarization isolation will also be required to validate these conclusions.

The polarization difference (note that these are preliminary results, and, in this case, the antenna gain pattern response has not been removed) data show three angular trends: (a) new and desalinated first-year ice; (b) wet new ice; and (c) rough grey ice. The phenomenology may be described as scattering by a dielectric with a smooth surface in which there is some subsurface penetration, scattering by a smooth surface which is more rough and has a higher dielectric constant, and scattering from a rough surface.

The change in backscatter levels for arbitrary co-polarizations may be derived from the target scattering matrix (Ref. 3). The illustrations provided in Figure 3 of new, grey, rough grey, and desalinated first-year ice at 5.0 GHz and 40 degrees are shown for visualizing the polarization properties of ice as it evolves. It was anticipated that, based on the backscatter responses at the linear polarizations, the polarization signatures would further illustrate the differences in the processes which are responsible for scattering at each of these ice scenes. It is interesting to note the differences in the size of the pedestal on which the signatures rise, the width of the peaks and nulls, and the difference in the magnitudes between peaks and nulls.

3. CONCLUSIONS

Absolute backscatter levels for new to grey ice are small, except for the large, coherent returns at vertical. The backscatter responses of new, grey, rough grey, and desalinated first-year ice at linear polarization were found to be dissimilar. This was further demonstrated by examining their polarization signatures.

4. ACKNOWLEDGEMENTS

5. REFERENCES

1. Onstott R G & S H Gaboury 1988, A polarimetric microwave scatterometer, Proc IGARSS '88 Symp, Edinburgh, Scotland 13-16 September 1988.

2. Xue D et al 1986, Microwave backscatter coefficients of artificially grown first-year sea ice, Proc IGARSS '86 Symp, Zurich 8-11 September 1986, ESA SP-254.

3. Deschamps G A 1951, Part II -- Geometrical representation of the polarization of a plane wave, Proc IRE vol 39, 540-544.
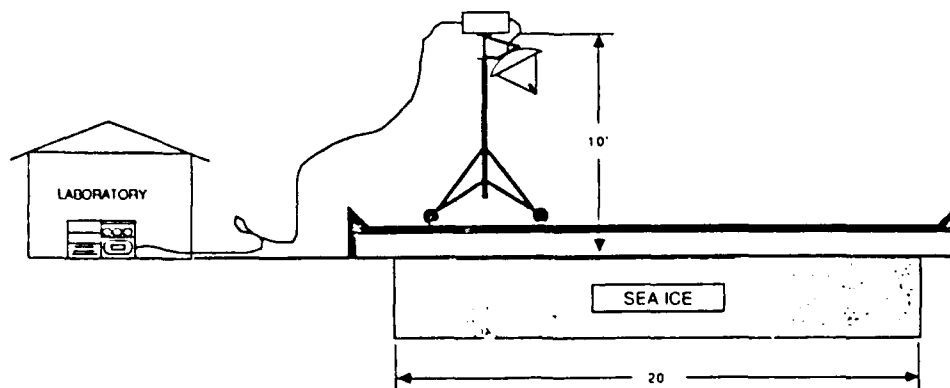
Figure 1. Configuration of Polarimetric Microwave Scatterometer at Sea Ice Tank
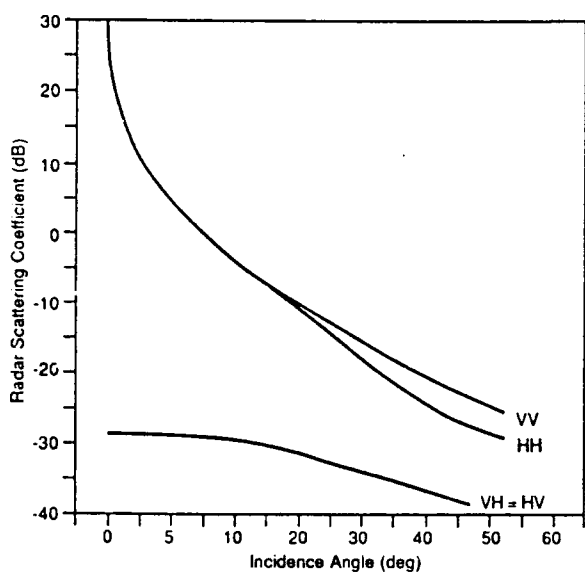
Figure 2. Radar Scattering Coefficient Angular Response of 12 cm thick grey ice at 5.0 GHz (ERIM/CRRELEX '88)
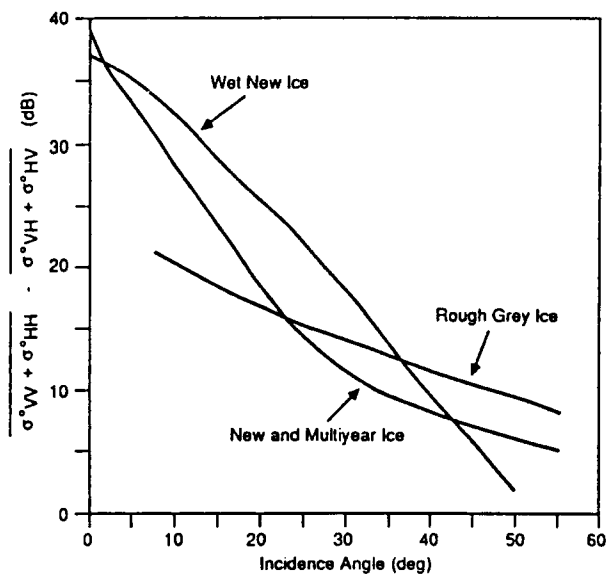
Figure 3. Ratio Between Like and Cross Linear Polarizations as a Function of Incidence Angle at 5 GHz for (a) Wet New Ice, (b) Rough Grey Ice, and (c) New and Multiyear Ice.

(a)

(b)

(c)

(d)
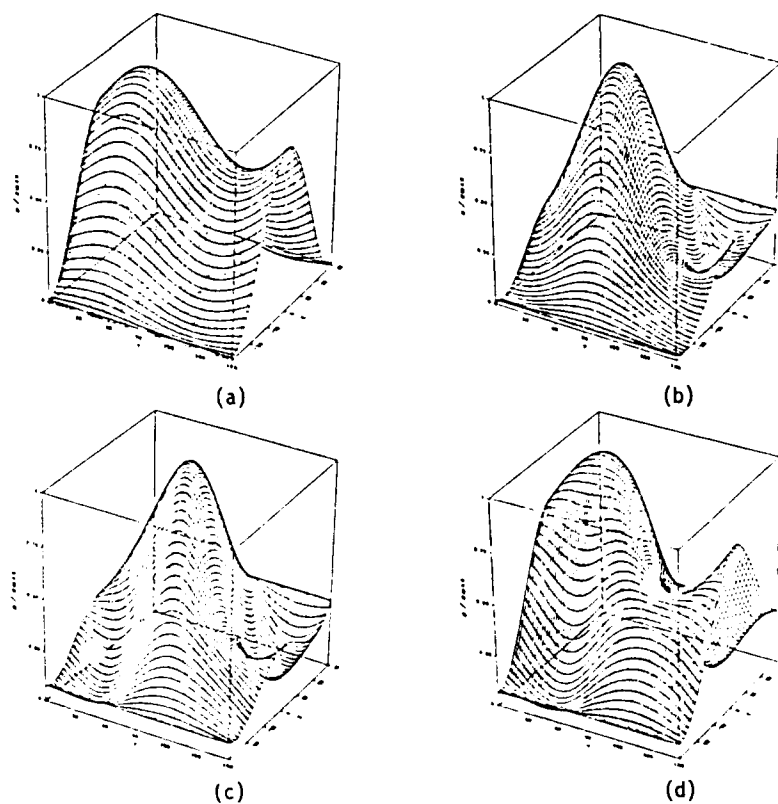
Figure 4. Co-Polarization Signatures of (a) New, (b) Grey, (c) Rough Grey, and (d) Multiyear Sea Ice

3.

Microwave Sea-Ice Signatures Near the Onset of Melt

CHARLES E. LIVINGSTONE, R. G. ONSTOTT, MEMBER, IEEE, L. D. ARSENAULT,
A. LAURENCE GRAY, MEMBER, IEEE, AND KESHAVA P. SINGH, SENIOR MEMBER, IEEE

Abstract—On June 22, 1982, the Canada Centre for Remote Sensing's Convair 580 aircraft (CCRS CV-580) made X-band SAR, Ku-band scatterometer, and K-band Radiometer measurements of the sea ice in Crozier Channel. Measurements of the physical properties of the ice and snow cover were in progress at a site in the southern portion of the CV-580 measurement area at the time of overflight.

The CV-580 X-band SAR and Ku-band scatterometer were cross calibrated with the University of Kansas Heloscat to examine the frequency dependence of surface signatures.

Analysis of the combined airborne and surface characterization data set shows that the microwave signatures of the surface, under the conditions present, were dominated by the snow cover and, in bare ice areas, by surface moisture. At frequencies above 9.35 GHz no scattering cross section/brightness temperature signatures could be uniquely related to ice type over the entire experiment area.

I. INTRODUCTION

BOTH ACTIVE and passive microwave remote-sensing techniques have proven to be valuable for investigating and monitoring ice-infested oceans at both global and local scales.

The strong emissivity contrast between sea ice and water permits satellite-borne radiometers to provide global sea-ice concentration measurements to reasonable levels of accuracy over most of the year [29], [3]. Under cold conditions, the emissivities of various sea-ice types are known over a wide range of microwave frequencies [11], [28], [21], [5], and are sufficiently stable to permit the use of satellite radiometer frequency and polarization diversity for global-ice-type concentration measurements [2], [3]. During the winter-to-summer transition period *and the summer melt period, the presence of free water on the ice and in the snow cover changes ice-type emissivities and degrades the sensitivity of space-borne radiometers for ice classification. Recent work by Carsey [31] has shown that the summer period microwave signature variations observed from space can be interpreted in terms of the ice surface transitions that occur at this time.

In the L- to K-band portion of the electromagnetic spectrum the strong scattering cross-section contrast between sea ice and water, and between ice floes of different ice types with varied topographies (various radar textures), permits airborne imaging radar systems to provide accurate sea-ice edge position, ice concentration, and ice dynamics measurements year round in local areas ($\leq 10^5$ km^2 per flight [18], [12], [30], [1]). Under cold conditions, differences in microwave scattering cross sections characteristic of different ice types, when augmented by radar texture, permit the determination of the spatial distribution of ice types from radar imagery [7], [10], [22], [24]. During the summer melt period, accumulation of free water in the snow and on the ice surfaces modifies the scattering cross sections sufficiently to make ice-type identification from radar imagery difficult and at times impossible [15], [10], [16], [7], [24].

Quantitative studies of the microwave scatterometric and radiometric properties of various sea-ice types, have resulted in a good understanding of characteristic arctic sea-ice type and surface deformation signatures under cold conditions [11], [20], [24], [7], [19]. During the cold season, simultaneous spatially coherent 19.4-GHz radiometer measurements and 13.3-GHz scatterometer measurements can be combined to create a three-dimensional feature space in which major ice types can be classified to accuracies in excess of 90 percent [11], [19], [20]. During the summer melt season this feature space fails to provide adequate ice-type signature separation for accurate classification [11], [7]. Distinct summer signatures are found, however, that appear to be related to snow-free water content as suggested by [4], [23], but these signatures are not temporally stable. The observed temporal variations in summer sea-ice signatures are believed to be a result of competition between those surface processes that create scattering centers within the snow cover and in the ice surface layers and those that mask or annihilate them.

In June and July of 1982, a joint U.S./Canadian experiment was conducted in the vicinity of Prince Patrick Island (Fig. 1) as part of the Radarsat/Firex[1] ice experiment series. During this experiment an extensive ice surface

[1] Radarsat—An ongoing Canadian program to develop and launch a Canadian radar-equipped satellite. Firex—A U.S. program to define a future free-flying SAR satellite.
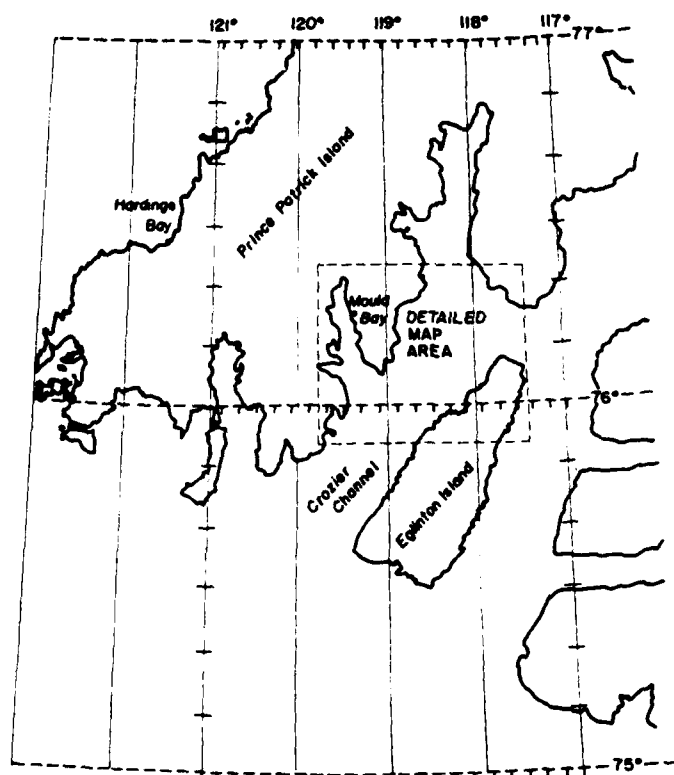
Fig. 1. Summer 1982 Radarsat/Firex experiment area.

characterization program was combined with surface and airborne microwave remote-sensing programs and was conducted by several U.S. and Canadian agencies [26].

The remote sensing components of the experiment included both site-specific temporal studies of microwave brightness temperature and scattering cross-section signatures of the ice cover and time-specific large-area studies. The temporal studies were based on surface radiometer measurements along local experiment lines [9] and on helicopter-borne scatterometer (Heloscat) measurements along these same lines over the period of June 18 to July 7, 1982 [24]. Time-specific area coverage was provided by

1) the Canadian Atmospheric Environment Service (AES) Electra with an *X*-band SLAR on May 20, and July 3, 1982;

2) the Canada Centre for Remote Sensing (CCRS) CV-580 with *K*-band Radiometer, *Ku*-band Scatterometer, and *X/L*-band SAR on June 22 and July 7, 1982; and

3) The NORDA P3 with a *Ku*-band imaging radiometer on May 14, 1982.

This paper is based on the CCRS data set of June 22, combined with the surface characterization and near-surface microwave remote-sensing data sets of June 22 and June 26. *Ku*-band Heloscat and CV-580 Scatterometer data are compared to establish the relative calibrations of these two instruments for the June 22 measurement period. *X*-band Heloscat data is used to provide a calibration

reference for the CV-580 *X*-band SAR. CV-580 SAR, scatterometer, and radiometer data are used to examine the sea-ice signatures along the CV-580 profiling sensor track.

II. THE EXPERIMENT SITES AND DATA ACQUISITION

A. The Experiment Site and Surface Conditions

On June 22, 1982 the Crozier Channel was covered by a fast ice sheet consisting primarily of first-year ice (Fig. 2). North and east of Manson Point a large grouping of old ice floes were frozen into the first-year ice matrix. The old ice was generally snow covered, however the first-year ice surface was frequently bare between snow drifts.

Two floes within the old ice group are identified in Fig. 2. Floe 1 (also known as Peach Pit Floe) was occupied by surface characterization teams engaged in temporal studies of ice signatures on June 22; Floe 2 (Intrepid Floe) was first visited by surface teams on June 26.

In the vicinity of Floe 1, the snow cover on the multiyear ice varied in depth from 2 to 6 cm on the hummock tops to 60 cm along the sides of ridges. On the adjacent first-year ice, the snow depth varied from 0 (bare ice) to a maximum depth of 1 m in drifts, but was generally 2 to 5 cm in depth. The snow cover had a thin (1 mm) ice crust, showed evidence of recrystallization, and occasionally contained ice nodules.

Although no quantitative measurements were made of the free water content of the snow, from qualitative descriptions on elevated surfaces the snow as moist [9] and in depressions was fully saturated (Radarsat/Firex 1982). The snow–ice interface was described as "wet." Grenfell and Lohanick [9] reported "moist" snow extinction coefficients in the range of 3.4 to 4.2 m^{-1} at 10 GHz. Extinction coefficients for wet corn snow and a wet surface crust were 20 and 30 m^{-1}, respectively. Onstott and Gogenini [25] reported the presence of a rough (at centimeter scales) superimposed ice layer on exposed first-year ice.

Detailed surface data is not available elsewhere in the area covered by the CV-580 sensors (Fig. 2); however, good-quality low-altitude (1500-ft) photography was obtained and was used to infer some of the general properties of the ice and snow surface. While no open melt ponds are found in the photographic record, some regions of water-saturated snow are seen at the southwest end of the CV-580 flight line up to and including the floe 1 area. Bare ice in this portion of the Crozier Channel is generally wet. At the northeast end of the experiment area, in the vicinity of floe 2, there is no evidence of free water on exposed surfaces.

B. Data Acquisition

On June 22 near-surface (Heloscat) HH-polarized scatterometer measurements of the floe 1 ice were made at 5.2, 9.6, and 13.3 GHz along the Heloscat experiment line shown in Figs. 2 and 3. Data were acquired at seven incidence angles ranging from 5° to 60° over the course of the day's operations.

In parallel with the Heloscat measurements, sled-borne
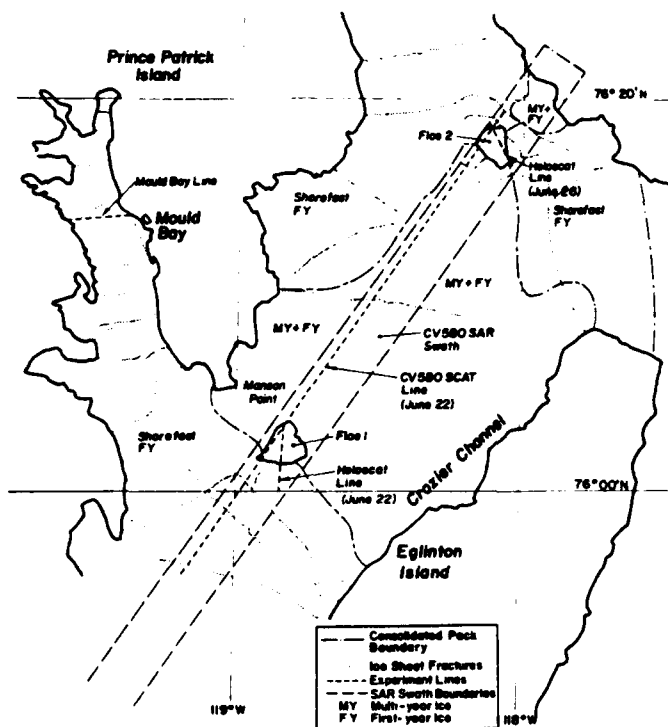
Fig. 2. The Crozier Channel experiment site, summer 1982.
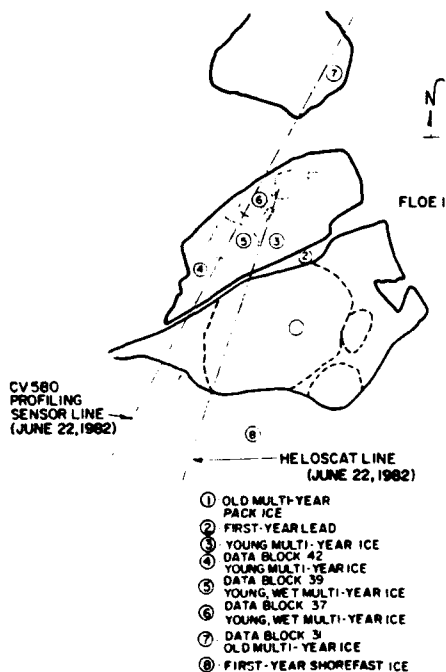
Fig. 3. Floe 1 experiment site map based on SAR and photographic data.

microwave radiometer measurements of adjacent ice were made at 10, 18.7, 33, and 37.6 GHz along the same data acquisition line. Snow and ice surface characterization measurements were made along the radiometer track.

The CV-580 overflew the Crozier Channel experiment site in the middle of the day's surface measurement activity at floe 1. The first data acquisition pass was made at 10 000-ft altitude and provided X-band (9.35-GHz) SAR imagery of the central region of the channel (Fig. 2) that included both floe 1 and floe 2. The second data acquisi-

tion pass at 1370-ft altitude provided Ku-band (13.3-GHz) HH- and HV-polarized fan beam scatterometer, K-band (19.4-GHz) H-polarized radiometer, infrared radiometer (8.5- to 14-μm) data, and 1:2750 scale black and white photography along a line that crossed both floe 1 and floe 2 as shown in Fig. 2.

The results discussed in this paper are based on Heloscat measurements at 9.6 and 13.6 GHz, surface radiometer measurements at 10 and 18.7 GHz, CV-580 Scatterometer measurements at 13.3 GHz, SAR measurements at 9.35 GHz, and radiometer measurements at 19.4 GHz. The relevant sensor parameters are outlined in Table I.

III. INTERCALIBRATION OF HELOSCAT AND CV-580 Ku-BAND SCATTEROMETERS

For the June 22 CV-580 overflight, the CV-580 Ku-band scatterometer and the Heloscat Ku-band scatterometer operated simultaneously only during the CV-580 profiling sensor transit of floe 1 and vicinity. Because of its pencil beam radar geometry and incremented incidence angle implementation the Heloscat system required most of the day's operation to accumulate data over the incidence angle range covered by the CV-580 scatterometer. Surface measurements indicated that surface conditions were sufficiently stable to allow the Heloscat Ku-band data set to be used without first-order temporal corrections. From the floe 1 experiment site map, Fig. 3, it is evident that the CV-580 profiling sensor line and the Heloscat line did not intersect. The CV-580 scatterometer and Heloscat comparison was based on spatially proximate ice samples whose X-band synthetic aperture radar signatures and surface conditions (as judged from the photographic records) were similar. The selected data sets for the CV-580 sensor consisted of first-year fast ice with visual evidence of wet patches (scatterometer data block 44) and an old rough multiyear floe north of floe 1 (scatterometer data block 31, feature 7 in Fig. 3).

The Heloscat data set consisted of fast first-year ice south of floe 1 (near number 8 in Fig. 3) and the old rough multiyear floe contained within floe 1 (feature 1 in Fig. 3).

The data from each sensor were processed to yield sample average backscattering cross sections ($\sigma°HH$) at incidence angles (θ) spanning the range of 5° to 60° using the best available estimates of the sensor calibrations. Fig. 4 shows the 13.6-GHz Heloscat and 13.3-GHz CV-580 scatterometer $\sigma°HH(\theta)$ signatures for these data samples.

For the first-year ice samples selected, both the Heloscat and CV-580 scatterometer yield $\sigma°HH$ values whose incidence angle dependences are the same to within the relative calibration accuracies of the sensors (± 1.5 dB) from 8° to 45° incidence angles. The Heloscat $\sigma°HH(\theta)$ values are 4 dB larger. At 55° the CV-580 scatterometer $\sigma°HH$ values drop 3 dB from the 45° value while the Heloscat $\sigma°HH$ at 55° is the same as at 45°. Part of this discrepancy may be attributed to antenna pattern structure in the CV-580 scatterometer.

The Heloscat and CV-580 scatterometer $\sigma°HH(\theta)$ re-

TABLE I
SELECTED SENSOR PARAMETERS FOR JUNE 22, 1982

Heloscat

Radar Description: FM/CW   Pencil Beam Scatterometer
Data Acquisition:

Altitude	Ground Speed	Sample Interval	Incidence Angles/Pass
30 m	18 m/s	0.25	1

Channel Characteristics:

Polarization	HH , HV	
Beamwidth	$1.9°$	$2.6°$
Calibration	± 2 dB	
Frequency	X-band (9.6 GHz)	Ku-band (13.6 GHz)
Incidence Angles	5, 12, 21, 30, 39, 50°	5, 12, 21, 30 39, 60°

Ground Radiometers

Resolution Cell	1 m X 1.4 m (at 45° incidence)	
Incidence Angle	45° on traverses 0° to 70° at selected points	
Radiometric calibration	± 1.5 K	
Frequency	X-band (10 GHz)	K-band (18.7 GHz)
Polarization	H and V	H

CV-580 Sensors

Ku-band Scatterometer
Radar Description: CW/Doppler Fan Beam Scatterometer

Data Acquisition:	Altitude	Ground Speed	Sample Interval	Incidence Angles/Pass
	418 m	85 m/s	0.33 s	8° to 60° (simultaneous)

Channel Characteristics

Frequency	13.3 GHz
Polarization	HH , HV
Receiver Bandwidth	8 KHz
Noise Equivalent $\sigma°$	-40 dB
Calibration $\sigma°$ (?)	±1.5 dB (relative)
Resolution Cell	26 m across track X 30 m along track (at 45°)

K-band Radiometer

Frequency	19.4 GHz
Polarization	H
Incidence Angle	45°
Resolution Cell	47 m across track X 80 m along track
Radiometric Calibration	±1.5 K

X-band SAR

Radar Description: Fully focussed Synthetic Aperture Radar

Data Acquisition

Altitude	Ground Speed	Swath Width	Incidence Angle Range
3048 m	270 nm/h	OPT 5.2 km slant range	$10°-68°$
		DIG 6.0 km slant range	$10°-70°$

Channel Characteristics

Frequency	9.35 GHz
Polarization	HH , HV
Resolution	3 m slant range X 3 m azimuth
Noise Equivalent $\sigma°$	-21 dB
Radiometric Resolution	Dependent on area averaged in 1 look image
Recording	Optical and Digital

sults for multiyear ice are not as well matched as the first-year ice signatures. The differences in multiyear incidence angle dependence shown in Fig. 4 lie within the floe-to-floe multiyear ice variability range observed by the CV-580 scatterometer along the data acquisition line and are believed to be real differences in floe signatures.

The Heloscat system, being a pencil beam scatterometer, is readily calibrated by means of a standard radar re-flector viewed against a sky background. During the June 22 measurement period such a calibration was performed. Since the absolute calibration of the CV-580 fan beam scatterometer is a more difficult task and has been partly based on indirect measurements, the 4-dB offset shown in Fig. 4 is accepted as an absolute calibration error until more evidence is available. In the remainder of this paper, the addition of 4 dB to the CV-580 results should yield
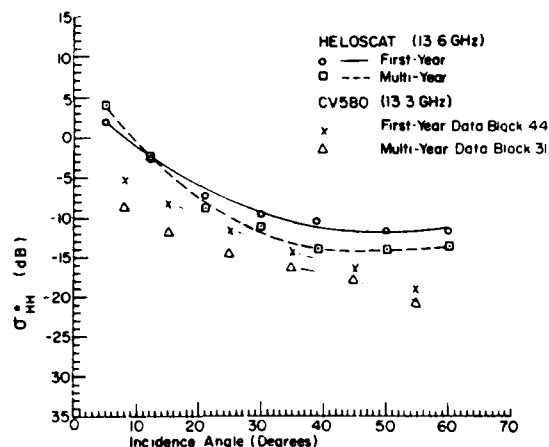
Fig. 4. 13.6-GHz Heloscat and 13.3-GHz CV-580 scatterometer HH-polarized scattering cross sections for similar ice based on June 22, 1982 data acquired in the floe 1 experiment site.

Fig. 5. Digitally processed. slant-range corrected. 9.35-GHz HH-polarized SAR image of the floe 1 experiment site and surrounding area, June 22, 1982. The SAR incidence angle scale is marked in degrees at the right-hand side of the image. The floe 1 complex is enclosed in the dashed white line and the CV-580 scatterometer track is marked by the solid white line.

the equivalent Heloscat *Ku*-band results to within the confidence of the foregoing test (± 1.5 dB).

IV. OBSERVATIONS AND DATA ANALYSIS

A. Microwave Signatures of the Floe 1 Experiment Site

On June 22, the ice in the floe 1 experiment site was covered with snow whose surface was dry over most of the experiment site. Notable exceptions to this were

1) Melt features on the northern half of floe 1 that were visible as saturated snow surface (features 5 and 6) and the other dotted boundaries in Fig. 3.
2) Small areas of saturated snow in some melt pond bottoms on the southern portion of floe 1.
3) Some areas of wet, windswept, first-year fast ice along the profiling sensor line south of floe 1.

Fig. 5 is a digitally processed ground-range-corrected 9.35-GHz HH-polarized SAR image of the floe 1 experiment area and contains the features identified in Fig. 3. The scale at the right-hand side of the image is the SAR incidence angle.

Although the CCRS SAR is not a calibrated radar, relative scattering cross sections within a single digitally processed scene can be measured at constant incidence angle to within ± 2 dB.

In Fig. 5, the CV-580 profiling sensor line lies along the 43° incidence angle contour in the SAR image thus permitting surface feature contrast measurements at both 9.35 and 13.3 GHz at that incidence angle. Following this line and using the floe 1 young multiyear ice as a reference (Fig. 3, feature 3), the highest 9.35-GHz radar returns correspond to

1) The first-year ice at the southern edge of floe 1: 3 ± 2 dB above the reference.
2) The melt feature corresponding to Fig. 3, feature 6: 7 ± 2 dB above the reference.
3) The interstitial first-year ice along the northern boundary of floe 1 and the southern boundary of data block 31 (Fig. 3. feature 7): 8 ± 2 dB above the reference.
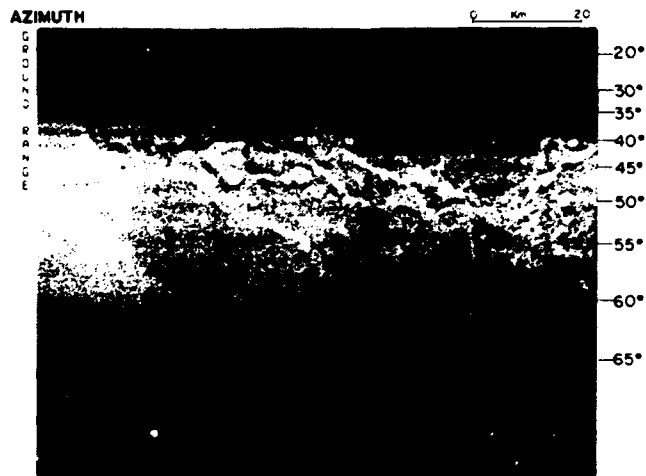
All high-return surfaces were either saturated snow or wet bare ice. The lowest 9.35-GHz radar returns along the profiling sensor line correspond to

1) The southern boundary of the high-return melt feature corresponding to Fig. 3, feature 6: 6 ± 2 dB lower than the reference.
2) The old multiyear floe near floe 1 corresponding to Fig. 3. feature 7: 7 ± 2 dB lower than the reference.

All the low-return SAR image areas, as well as the reference surface along the profiling sensor line in Fig. 5, are snow covered and have a visibly dry surface. The lowest radar returns in this part of Fig. 4 are generated by ridge boundary snow drifts on the old multiyear floe designated as feature 7 in Fig. 3.

The dynamic range of $\sigma°$ at 9.35 GHz and 43° incidence angle (as inferred from Fig. 5) is 15 ± 2 dB.

Where the Heloscat line crosses the southern boundary of floe 1 (51° incidence angle in Fig. 5) the old multiyear floe in floe 1 yields radar returns that are 4 ± 2 dB smaller than those from the adjacent first-year fast ice. The higher return areas within this old floe have been identified as melt pond bottoms with wet snow surfaces and occasional hummock tops.

Table II summarizes the CV-580 13.3-GHz scatterometer and radiometer results for the floe 1 experiment area. Data blocks 31 to 42 are identified in Fig. 3 and in the preceding discussion. Data blocks 44 and 45 represent different surface conditions found in the first-year fast ice south of floe 1.

As expected. the presence of surface water has a strong influence on the 19.4-GHz brightness temperature and thus in Table II visibly wet ice or snow surfaces yield brightness temperatures below 240 K and visibly dry surfaces have brightness temperatures greater than 255 K. Simultaneous 18.7-GHz surface radiometer scans of the Heloscat line gave "dry-surface" brightness tempera-

TABLE II
FLOE 1 ICE-TYPE SIGNATURES FROM CV-580 PROFILING SENSOR DATA

Data Block	Type	T_B at 19.4 GHz (K)	$\sigma°HH$ in dB at 13.3 GHz for Incidence Angle					
			8°	15°	25°	35°	45°	55°
31	M Dry	260.2±0.6	-8.5±.7	-12.2±.4	-14.7±.7	-16.2±.8	-18.2±1	-21.3±.8
37	M Wet	220±2	-8.0±2	-10±1	-13.5±1.2	-15.3±1.2	-17.3±.8	-20.7±1.2
39	M Wet	234±2	-7.3±1.1	-10±1	-13.0±1.2	-14.7±1.1	-16.8±0.8	-19.7±1.2
42	M Dry	259±1	-8.8±0.8	-12±0.7	-14.2±0.7	-15.8±0.8	-17.8±0.8	-20.5±0.8
44	F Wet	203±4	-5.1±0.4	-8±0.4	-11.9±0.4	-14.4±0.5	-16.8±0.5	-19.7±0.6
45	F 2 Dry	258±1	-8.0±0.4	-10±0.5	-11.8±0.6	-13.6±0.6	-15.7±0.6	-18.8±0.8

The standard deviations in this table are measures of the radiometric and scatterometric
textures of the data samples and do not include the instrument calibration uncertainties.
The absolute calibration of the radiometer used may be in error by as much as 6K.

tures in the 250- to 260-K range and "wet-surface" brightness temperatures as low as 220 K (Grenfell and Lohanick in [26]).

One of the most notable features of Table II is the small range of $\sigma°HH$ (45) observed at 13.3 GHz (2.5 ± 1.6 dB) when compared to the 9.35-GHz SAR image contrast range 15 ± 2 dB for the same ice.

Fig. 6 presents data acquired along the Heloscat line on June 22. The Heloscat data in interval 1 corresponds to the fast first-year ice south of floe 1 and thus $\sigma°HH$ (50°) at 9.6 GHz for this interval, -16 ± 2 dB, provides a SAR image intensity calibration point near the floe 1 boundary. The Heloscat contrast between the fast first-year ice and the old multiyear ice of floe 1 (3 ± 1 dB) is comparable to the observed 9.35-GHz SAR contrast (4 ± 2 dB) at the same point.

Assuming that the first-year fast ice in interval 1 is similar to that seen by the SAR and the CV-580 scatterometer near the floe 1 boundary; the 9.6-GHz $\sigma°$ (39°) data, -15 ± 2 dB, provide a $\sigma°$ calibration for the SAR contrast sequence presented previously. This calibration was applied to SAR data along the CV-580 profiling sensor line, and the CV-580 scatterometer data was offset to match the 13.6-GHz Heloscat calibration and produce the entries in Table III. Because of uncertainties in the gain stability of the SAR, analysis was restricted to data collected within 12 km of the reference point.

Table III examines two hypotheses, 1) returns from bare ice are the result of scattering from rough surfaces and 2) returns from snow-covered areas are the result of Rayleigh scattering within the snow cover. In the first instance, the scattering cross sections are independent of radar frequency over the 9.35 to 13.3 GHz bands given the cm scale roughness elements reported on the bare ice surface on and near floe 1 at the time of the CV-580

overflights [25], [9]. Surface roughness distributions are unfortunately not available. In the second case, the ratio $\sigma°$ 13.3 GHz/$\sigma°$ 9.35 GHz is proportional to $(9.35/13.3)^4$ if the majority of the scattering originates in millimeter-scale water-coated ice crystals in the snow cover.

The 10-GHz extinction coefficients reported by Grenfell and Lohanick [9] for the floe 1 area were 4 m^{-1} for "damp" snow and 20 m^{-1} for "wet" coarsely crystallized snow on June 22, 1982. Qualitative descriptions of snow wetness variations with depth [26] state that the snow was damp at the upper surface and water-saturated (slush) at the snow base. No quantitative snow-wetness profiles are available; however, simple model calculations based on a linear increase in the extinction coefficient with snow depth and a water-saturated snow base give X-band radar return losses greater than 30 dB for 20-cm snow depths (also commonly reported by surface parties). The observed radar returns at 9.35 and 13.3 GHz from snow-covered areas, thus, contain negligible contributions from the underlying ice and originate within the upper layers of the snow cover.

B. General Characteristics of the Crozier Channel Pack Ice from the June 22 CV-580 Data Set

The X-band SAR imagery covered an 8-km swath near the center of the channel (Fig. 2) and the low-altitude large-format photography yielded a 0.68-km-wide strip mosaic along the SAR image 43° incidence angle contour. Both the SAR image and the photography contain representative samples of the radar-identifiable ice types in the channel. North and east of Manson Point (Fig. 1) the composition of the ice pack is very similar to that reported by Hollinger *et al.* [13] for the previous fall.

From the photography it was seen that the snow drifts
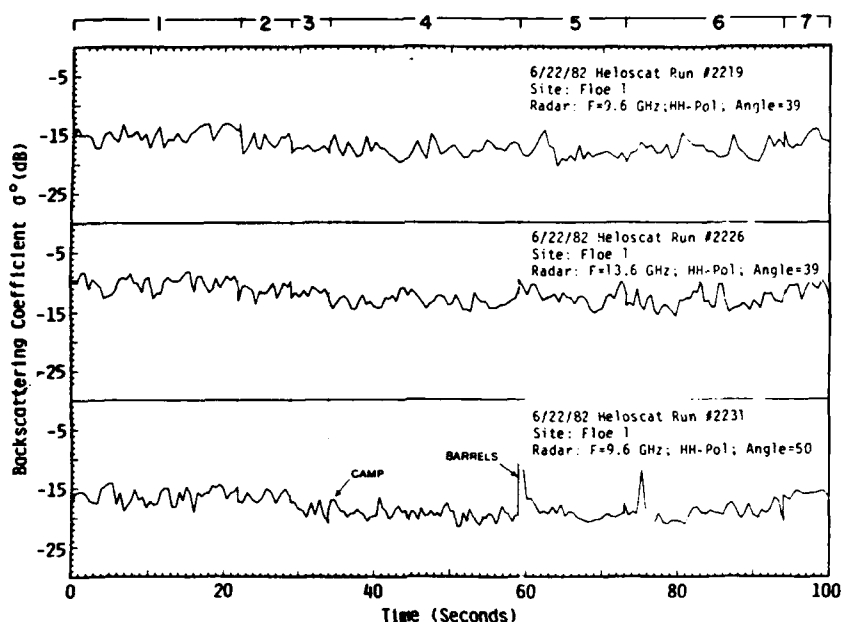
Fig. 6. 13.6- and 9.6-GHz Heloscat data at 39° and 50° incidence angles from the June 22 floe 1 Heloscat line data set. With reference to Fig. 3 Region 1 is the first-year fast ice south of flow 1. Regions 3 to 6 correspond to the old multiyear floe in floe 1. Region 7 is the first-year lead between the two parts of floe 1.

TABLE III
CV-580 SAR/Scatterometer Signature Along the Profiling Sensor Line

Feature Designation	Instrument and Frequency GHz	Raw Data σ°_{HH} dB	Scatt Cal. Correction dB	Relative σ°_{HH} dB	Rayleigh Adjustment dB	Corrected σ°_{HH} dB
First year fast ice	9.35 SAR	-16 ± 2		-16 ± 3.5		-16 ± 3.5
(Data block 45)	13.3 Scat	-15.7 ± 3.1	$+4\pm1.5$	-11.7 ± 4.6	-6	-17.7 ± 4.6
Young MY ice Figure 3,	9.35 SAR	-18 ± 4		-18 ± 5.5		-18 ± 5.5
feature 4	13.3 Scat	-17.8 ± 3.3	$+4\pm1.5$	-13.8 ± 4.8	-6	-19.8 ± 4.8
MY ice melt feature Figure 3	9.35 SAR	-11 ± 4		-11 ± 5.5	N/A	-11 ± 5.5
feature 6	13.3 Scat	-16.8 ± 3.3	$+4\pm1.5$	-12.8 ± 4.8		-12 ± 4.8
Low return near Figure 3	9.35 SAR	-24 ± 4		-24 ± 5.5		-24 ± 4
feature 6	13.3 Scat	-21.8 ± 3.3	$+4\pm1.5$	-17.8 ± 4.8	-6	-23.8 ± 5.5
Bare FY ice At northern Floe 1	9.35 SAR	-10 ± 4		-10 ± 5.5	N/A	-10 ± 5.5
Boundary	13.3 Scat	-14 ± 3.5	$+4\pm1.5$	-10 ± 5.0		-10 ± 5.0
Figure 3 feature 7	9.35 SAR	-25 ± 4		-25 ± 5.5		-25 ± 5.5
Data block 31	13.3 Scat	-18.2 ± 3.5	$+4\pm1.5$	-14.2 ± 5.5	-6	-20.2 ± 5.5

on the fast ice at the southern end of the line were generally smaller and more uniformly distributed than those in the interstitial first-year ice contained within the pack or those on the fast ice at the northern end of the line. The bare ice was frequently visibly wet, especially at the southern end of the line. Some melt features (saturated snow surfaces) were visible on smooth multiyear floes near the southern end of the line and a few of the rough multiyear floes had damp patches in melt pond areas. No open water ponds were detected. Photographic data shows the southern area to be at a more advanced stage of melt than the northern area.

Fig. 7 shows typical samples of optically processed 9.35-GHz HH-polarized SAR imagery progressing from

(a) Southern consolidated pack limit showing Floe I   experiment area
Features A Shorefast first year ice E Old, snow-covered multi-year ice F Bare, young multi-year ice
          G Typical multi-year ice

(b) Central consolidated pack area of the CV580 data acquisition line
Features B Interstitial first-year ice D Snow-covered first-year ice with multi-year bits H First-year/multi-year
          boundary - very wet snow

(c) Northern consolidated pack limit near Intrepid Channel, showing Floe 2
experiment area
Features C Interstitial first-year ice I Intrepid floe J First-year fast ice

Fig. 7. Segments of the optically processed slant range 9.35-GHz HH-polarized SAR image of the Crozier Channel acquired on June 22, 1982. (a) is the floe 1 experiment site and surrounding area, (b) is the central region of the SAR line, (c) is the floe 2 experiment site and surrounding area.

the southwesterly to the northeasterly ends of the study area. The pronounced radar antenna pattern effects visible in the imagery were a result of the relatively low scattering cross sections of the ice (at 9.6 GHz the multiyear ice $\sigma°HH$ was 8 dB lower than winter values [25] coupled with the radar operating parameters selected to maximize the SAR linearity.

A general overview of Fig. 7 shows that the scattering cross-section inversion reported by Hawkins *et al.* [10] had already occurred in this area in that the high-return (large $\sigma°HH$) regions are predominantly on first-year ice and the low-return regions (small $\sigma°HH$) are often found on multiyear ice.

Four distinct first-year ice image intensity and texture signatures are found in Fig. 7. Southern fast ice, feature A, at the left of Fig. 7(a), produces a large average radar return and a very fine-grained image texture. The inter-

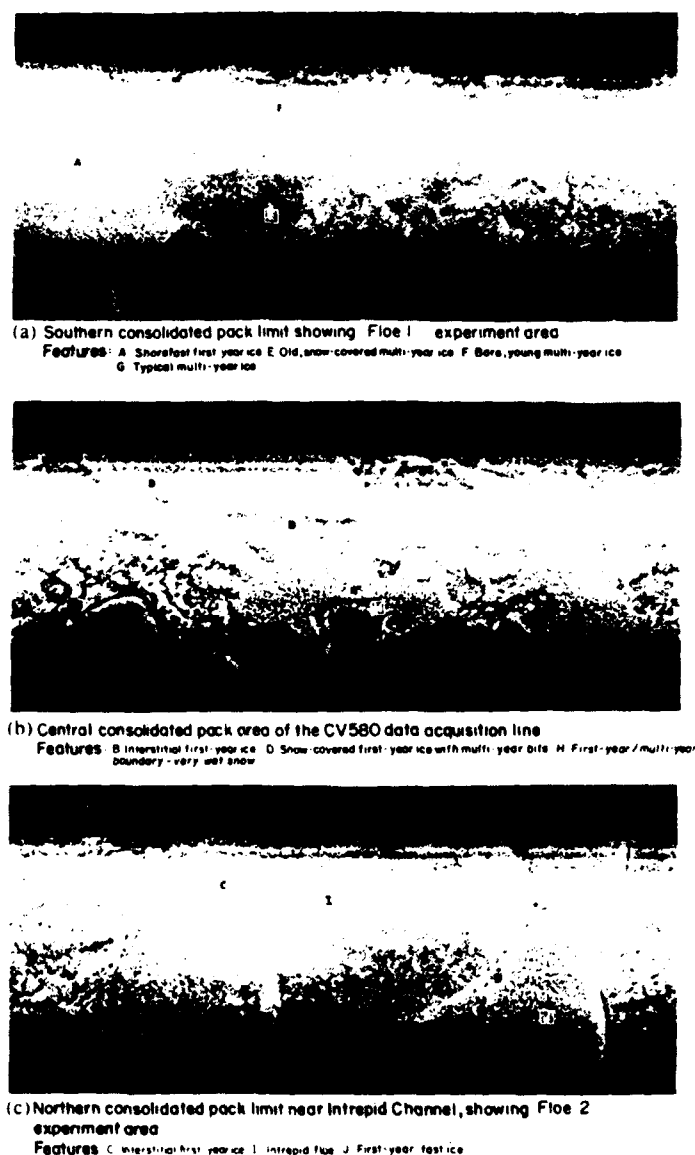stitial first-year ice, feature B, in Fig. 7(b), yields a slightly smaller average radar return and a coarser, more pronounced image texture. The interstitial first-year ice, feature C in Fig. 7(c), produces approximately the same average radar return as feature B, but has a coarser, less pronounced image texture. The interstitial first-year ice, feature D in Fig. 7, is characterized by the lowest average radar returns of the four groups.

In the first-year ice regions, the high radar returns are produced by regions of bare ice and regions with saturated snow cover. The low return elements are snow drifts whose surfaces are visibly dry. The dynamic range of the radar returns associated with first-year ice texture elements frequently exceeded 10 dB locally (within a 200-m radius).

The multiyear ice radar returns vary widely with the extremes being represented by an old multiyear floe, Feature G in Fig. 7(a) and the high return patches in the younger multiyear portion of the same floe (feature F)[2] Many multiyear floe image texture elements varied over a moderate (6-dB) local intensity (radar return) range and were related to large-scale topographic features such as ridges, hummocks, and melt ponds. The boundary snow drifts skirting the large (6-m-high) ridge on the right-hand side of floe 2 (Fig. 7(c), feature I) and the ridge boundary drifts on the old multiyear floe identified as feature G in Fig. 7(a) produce radar returns that are 3 to 6 dB lower than the surrounding materials. The saturated snow surfaces in the melt pond bottoms on floe 1 (Fig. 7(a), feature E) produce radar returns that are 6 dB higher than the surrounding area.

Some multiyear floes, for example the floe above and to the right of feature D in Fig. 7(b), were characterized by gradual variations in radar reflectivity near the floe boundaries and by low return zones exterior to the floe boundaries. These radar signatures are not obviously correlated with the floe topography or with surface melt features and are believed to be the results of spatial variations of free water content and/or scatterer distribution within the snow volume.

Under the conditions found in the experiment area on June 22, there is no simple consistent 9.35-GHz HH-polarized radar signature that can be used to unambiguously assign ice type from radar imagery spanning the incidence angle range of 0° to 67°. As was the case in the floe 1 experiment area, the 9.35-GHz radar signatures over the entire Crozier channel are determined by the state of the exposed surfaces and by conditions within the snow cover. There is evidence in the SAR images for the presence of warmer wetter conditions at the southwesterly end of the experiment area and for the presence of colder dryer conditions at the northeasterly end as was noted previously from the photographic record.

The profiling sensor data for the entire flight line was analyzed to determine the scattering cross section and brightness temperature statistics. Five ensembles (data

[2]See Section IV-A for detailed discussion.
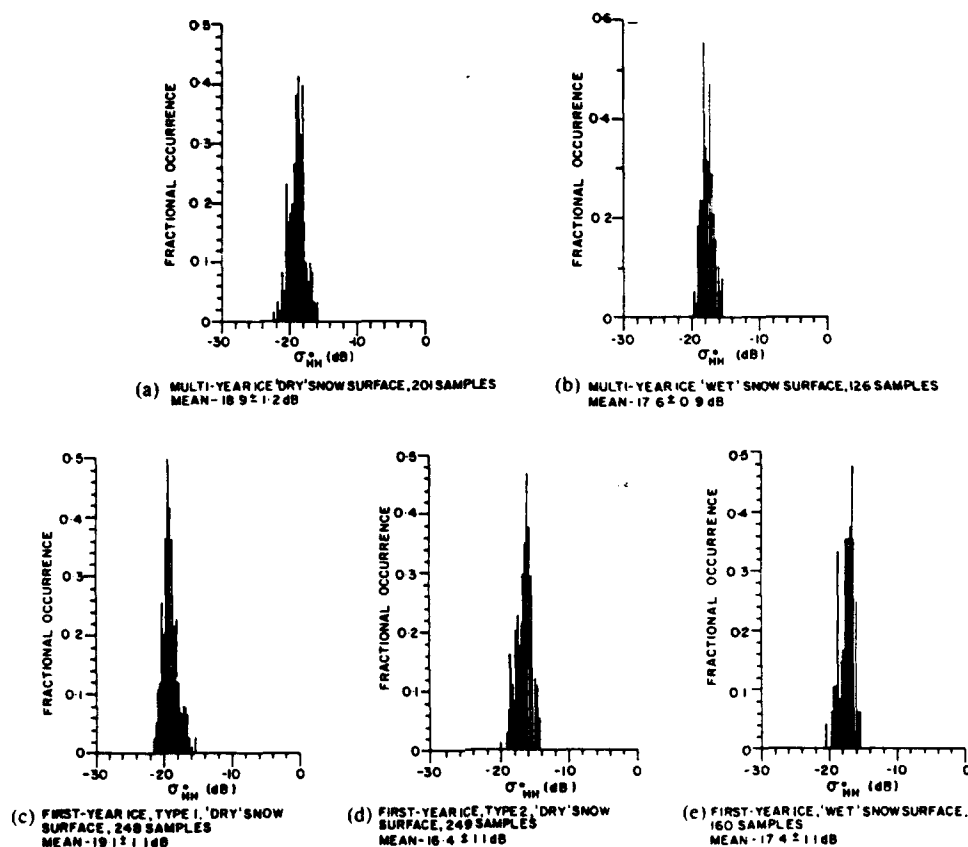
Fig. 8. CV-580 13.3-GHz $\sigma°$HH distributions at 45° incidence angle for the Crozier Channel profiling sensor line.

clusters) were identified in terms of ice type and surface conditions. The relative frequency distributions of $\sigma°$HH (45°) for these are presented in Fig. 8. The distributions do overlap on the $\sigma°$HH axis, do not appear to be Gaussian and, in some cases, are slightly skewed.

The corresponding feature space is shown in Fig. 9 as cluster unit standard deviation elipsoid projections onto the $\sigma°$HH (45°), ϵ_H (45°) plane (Fig. 9(a)) and onto the $\sigma°$HH (45°), $\sigma°$HV (45°) plane (Fig. 9(b)) as well as $\sigma°$HH(θ) curves (Fig. 9(c)). Tables IV and V summarize the data of Fig. 9(a) and (b) in terms of feature space cluster centroid coordinates, cluster centroid separations, and separation uncertainties.

Of the five clusters displayed in Fig. 9 and Tables III and IV, four are identifiable from the photography. The high-emissivity clusters (brightness temperatures from 240 to 270 K) correspond to first-year and multiyear ice that was predominantly snow covered and had a visibly dry surface. The low-emissivity clusters (brightness temperatures from 200 to 240 K) correspond to first-year ice and multiyear ice that was either snow-covered or bare and had a visibly wet (saturated) surface.

Neither of the two distinct first-year ice clusters, FY1 and FY2, found in the high-emissivity group is unambiguously identified as a subclass from the photographic record; however, FY1 data blocks are primarily found at

the colder dryer end of the experiment line and FY2 data blocks are primarily found at the warmer wetter end of the experiment line. The CV-580 profiling sensor feature space results, Tables III and IV, show that the FY1 signatures are statistically indistinguishable from the multiyear dry surface cluster. The FY2 cluster is a statistically independent entity.

Combining the profiling sensor feature space data with the SAR image data in Fig. 7 and the results from the floe 1 experiment site analysis in Section IV-B we find

1) The first-year and multiyear wet surface clusters of Fig. 9 are statistically indistinguishable in both 13.3-GHz HH and 9.35-GHz radar reflectivity at 43° incidence angles, and their scattering cross sections are independent of frequency to within experimental error. The results are compatible with surface scattering from rough reflective surfaces.

2) The FY2 and multiyear ice dry surface ice clusters are separable in both the feature space and the 9.35-GHz SAR image. In both instances the calculated values of σHH at 9.35 and 13.3 GHz differ by 6 dB to within experimental error and are compatible with Rayleigh scattering from a thick lossy medium.

3) When 9.35- and 13.3-GHz σHH measurements are compared for the FY1 cluster, it is seen that this group also is compatible with Rayleigh scattering.

MULTI-YEAR ICE,
'DRY' SURFACE
— — MULTI-YEAR ICE,
'WET' SURFACE
----- FIRST-YEAR ICE,
TYPE I 'DRY' SURFACE
········· FIRST-YEAR ICE,
TYPE 2, 'DRY' SURFACE
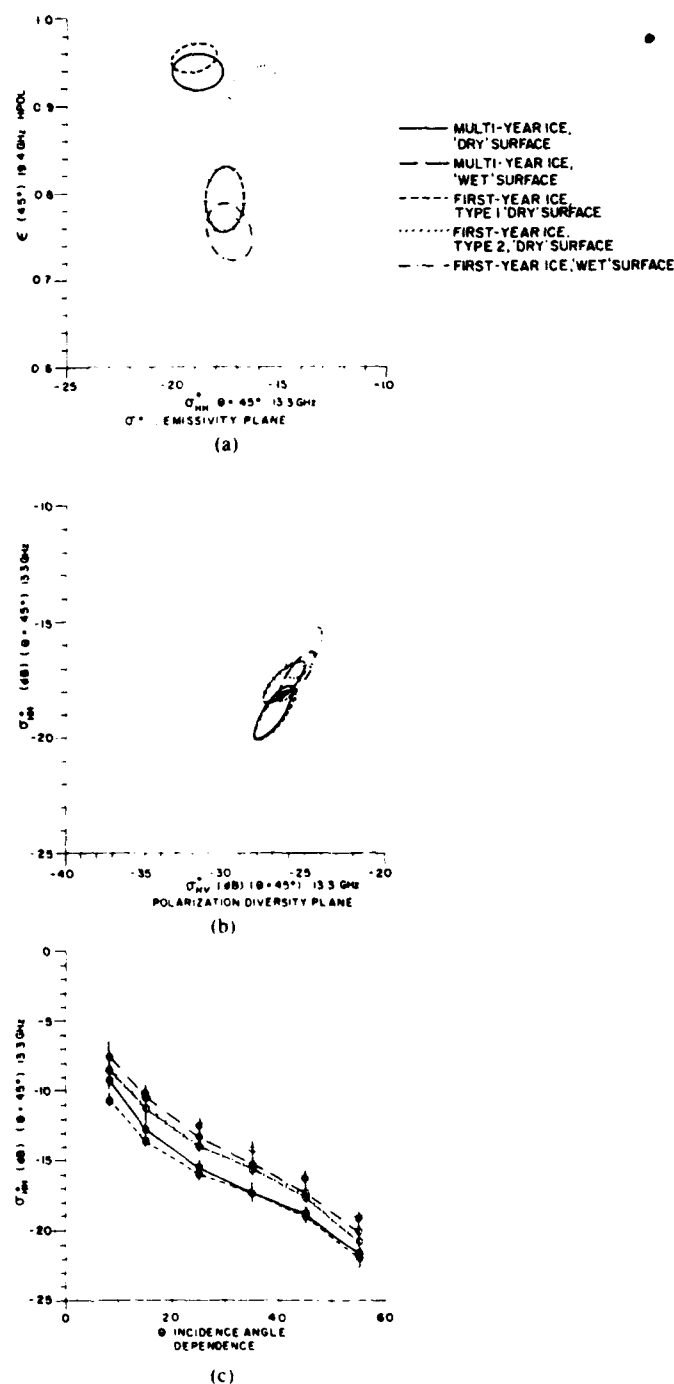— · — FIRST-YEAR ICE, 'WET' SURFACE

(a)

(b)

(c)

Fig. 9. Ice signature feature space derived from the June 22 CV-580 profiling sensor data set. (a) Cluster unit standard deviation contour projections onto the 19.4-GHZ ϵ_H (45°), 13.3-GHz $\sigma°HH$ (45°) plane. (b) Cluster unit standard deviation contour projections onto the 13.3-GHz $\sigma°HV$ (45°), 13.3-GHz $\sigma°HH$ (45°) plane. (c) The dependence of 13.3-GHz $\sigma°HH$ on incidence angle.

The difference in feature space position of the FY1 and FY2 classes is believed to indicate differences in scatterer size distribution and snow-cover moisture distribution for the two classes.

C. The Melt Transition at the Floe 2 Experiment Site

The floe 2 experiment site was imaged by the CV-580 SAR and measured by the CV-580 profiling sensors on June 22, 1982. Surface characterization studies of this area

TABLE IV
FEATURE SPACE CLUSTERING OF ICE CLASSES AT 45° INCIDENCE ANGLE

Ice Type (cluster)	Emissivity	$\sigma°HH$ (dB)	$\sigma°HV$ (dB)
MY Wet	0.79 ± 0.04	-17.6 ± 0.9	-26.3 ± 1.3
FY Wet	0.79 ± 0.03	-17.3 ± 1.7	-25.6 ± 1.2
MY Dry	0.94 ± 0.02	-18.9 ± 1.2	-27. ± 1.3
FY1 Dry	0.95 ± 0.02	-19.1 ± 1.1	-27.0 ± 1.3
FY2 Dry	0.93 ± 0.02	-16.4 ± 1.1	-25.1 ± 1.1

TABLE V
FEATURE SPACE CLUSTER SEPARATION OF ICE CLASSES AT 45° INCIDENCE ANGLE

Class Comparison	Cluster Centroid Separation	Separation Uncertainty
Wet MY-FY	0.71	±1.31
Dry MY-FY1	0.15	±1.32
Dry MY-FY2	3.24	±1.98
FY1 Dry-FY Wet	3.28	±0.74
FY2 Dry-FY Wet	2.15	±0.36
MY Dry-Wet	2.40	±0.44

did not start until June 26. In the intervening period, the Crozier Channel ice surface was subjected to an extensive melt cycle that removed much of the snow, flooded the ice surface, and transformed the microwave signatures of the surface to those reported previously [11] for decaying summer ice.

To illustrate the dramatic sea-ice signature changes associated with the melting process June 22 CV-580 data are compared with June 26 Heloscat and surface characterization data.

Fig. 10 is a map of the floe 2 experiment site derived from CV-580 June 22 SAR images, July 7 high-altitude photography and from surface characterization team low-altitude photography. Floe 2 is composed of multiyear ice of various ages and is similar in structure and surface topography to many multiyear floes seen in the Beaufort Sea pack ice. The two most prominent surface features are a large (6-m-high) multiyear ridge (Fig. 10, feature 4) and a large hummock (Fig. 10, feature 6). Both of these lay on the Heloscat line and were investigated by surface characterization teams.

On June 22 the ice surface in the vicinity of the profiling sensor line was snow covered and had a visibly dry surface with no melt features. The CV-580 profiling sensor microwave signatures, Table VI, show no significant difference in $\sigma°HH(\theta)$ between floe 2 and the surrounding first-year ice. Both adjacent first-year-ice data blocks belong to the FY1 class discussed in the previous section.

The June 22 9.35-GHz SAR image corresponding to Fig. 10 may be found in slant range form in Fig. 6(c). In this image, floe 2 is feature *I*. Note that the internal composition of the floe is not visible in this image. The profiling sensor line follows the 42° incidence angle contour

TABLE VI
FLOE 2 ICE-TYPE SIGNATURES FROM CV-580 DATA

Data Block	Type	T_S (°C)	T_B (K)	σ°HH at 13.3 GHz for Incidence Angle, in dB					
				8°	15°	25°	35°	45°	55°
49	F Dry 1	0.8±0.2	250 ±0.7	-9.0 ±0.7	-13.4±0.8	-16.5±0.9	-18.9±1.0	-20.1±0.8	-24.2±1.2
50	M Dry	1.0±0.1	256.5±4.3	-9.2 ±0.9	-13.2±0.9	-16.2±1.0	-18.3±0.7	-19.5±0.9	-22.6±0.7
51	F Dry 1	1.1±0.1	260.6±1.5	-10.1±0.6	-13.7±0.5	-16.0±0.6	-17.1±0.6	-19.0±0.6	-21.8±0.7

① CV580 BLOCK 51FIRST-YEAR ICE
② CV580 BLOCK 50 OLD MULTI-YEAR ICE
③ CV580 BLOCK 49 FIRST-YEAR ICE
④ LARGE (6m) PRESSURE RIDGE
⑤ SURFACE TRUTH BASE CAMP
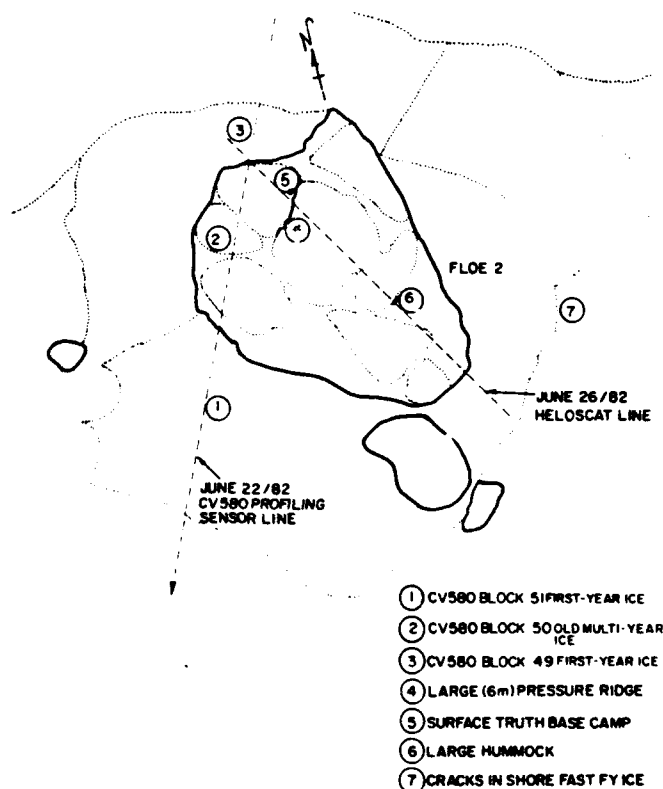⑥ LARGE HUMMOCK
⑦ CRACKS IN SHORE FAST FY ICE

Fig. 10. Floe 2 experiment site map derived from X-band SAR data and photographic images.

through the SAR image and along this line the first-year ice to multiyear ice contrast at 9.35 GHz is 3 ± 2 dB.

When the SAR image intensity is translated into an approximate σ°HH value for 9.35 GHz at the 43° incidence angle using the floe 1 Heloscat/SAR cross correlation, the resulting values are −20 ± 3 dB, −21 ± 3 dB, −23 ± 3 dB for Fig. 10, features 1, 2, and 3, respectively. When these results are compared to σ°HH (45°) for the corresponding scatterometer data blocks; (51, 50, and 49, respectively) from Table VI, and when the CV-580 13.3-GHz scatterometer data are corrected for the relative Heloscat/CV-580 scatterometer calibration, the signatures of all samples are consistent with Rayleigh scattering from a layer whose thickness exceeds its penetration depth [17]. Combining this result with the undetectability of the constituent floes within floe 2 in the SAR image suggests that the scattering processes in the floe 2 experiment site on

June 22 are totally dominated by the snow cover at both 13.3 and 9.35 GHz.

In the four-day interval between the CV-580 overflight and the June 26 surface characterization studies at floe 2 most of the snow cover melted. Surface study teams found 0 to 5 cm of saturated snow remaining on the higher drained areas of floe 2, up to 1 m of saturated snow along ridge skirts and open melt ponds up to 17 cm deep. In many areas cm scale size ice crystals were found on or near the snow surface. Scattering cross sections from the June 26/82 Heloscat line are summarized in Fig. 11, 33° incidence angle σ°HH variation with frequency, and Fig. 12, incidence angle dependence of σ°HH at 9.6 GHz.

As was expected from the saturated surface condition reported, only surface scattering phenomena are present and first-year ice surfaces are scatterometrically indistinguishable from multiyear ice surfaces. In Fig. 11 it is seen that the scattering cross sections of all ice vary by no more than 3 dB from 4.5 to 13.6 GHz. This result is compatible with scattering from a moderately rough reflective surface. Fig. 12 shows that the 9.6-GHz scattering cross section varies rapidly with incidence angle (18 dB change from 5° to 33°).

Although no X-band incidence angle dependence data is available for wet bare ice in the June 22 data set 1, it is instructive to note that the minimum reported 9.6-GHz σ°HH for the June 26 data set, −15 dB, at 33° is smaller than the −14-dB σ°HH at 43° incidence angle estimated from the June 22 9.35-GHz SAR image for a patch of wet bare ice near floe 1.

A comparison between the June 26 13.6-GHz Heloscat results at 33° incidence angle, Fig. 11 and the June 22 13.3-GHz CV-580 scatterometer measurements at 35° incidence angle, for scattering regions with wet surfaces shows the June 26 results to be approximately 4 dB lower than their June 22 equivalents when the relative calibrations of the two scatterometers are taken into account.

V. SUMMARY AND CONCLUSION

On June 22, 1982, the ice and snow in the Crozier Channel was near the onset of melt. The snow cover was saturated at the snow–ice interface, was extensively recrystallized throughout the snow volume, and was opaque to radars operating at and above 9.35 GHz. Investigations
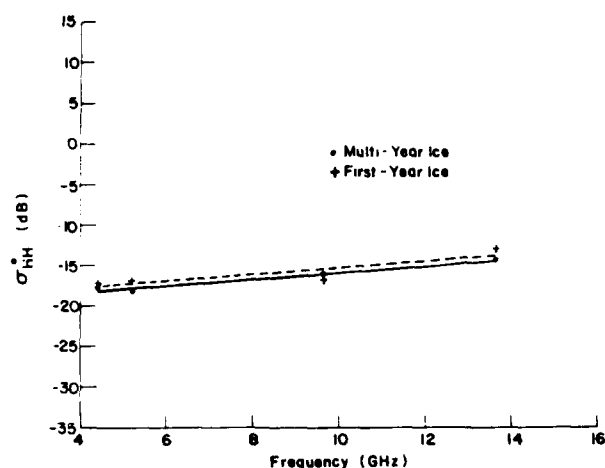
Fig. 11. Variation of Heloscat backscattering cross section at 33° incidence angle with frequency, near floe 2, June 26, 1982.
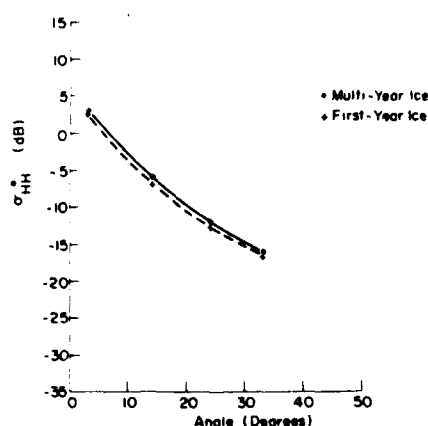

Fig. 12. Variation of Heloscat 9.6-GHz backscattering cross section with incidence angle, near floe 2, June 26, 1982.

of the HH-polarized scattering cross sections at 9.35-, 9.6-, 13.3-, and 13.6-GHz combined radar and surface characterization data to show that the differential scattering cross sections measured in the X- and Ku-bands could be adequately explained (to within experimental error) in terms of two simple models:

1) For saturated snow and wet bare ice surfaces $\sigma°HH$ measurements at X- and Ku-bands are compatible with each other under the assumption of surface scattering from a rough surface.

2) For snow-covered areas with dry surfaces $\sigma°HH$ measurements at X- and Ku-bands become compatible with each other under the assumption of Rayleigh scattering from a thick opaque layer.

The 19.4-GHz radiometric signatures of the Crozier Channel ice sheet were very sensitive to the presence of surface water and the visibly wet areas where surface scattering was dominant at X- and Ku-bands were radiometrically colder (by more than 20 K) than the surrounding ice.

For snow-covered first-year ice without surface saturation two separate radiometric and scatterometric classes arbitrarily designated FY1 and FY2 were observed. Cluster analysis showed that the FY1 class had 13.3-GHz

$\sigma°HH(\theta)$ values approximately 3 dB less than; and 19.4-GHz brightness temperatures approximately 7 K greater than the FY2 class. Differences in snow-grain transformation stages and snow-cover moisture profiles are believed to be responsible for these microwave signatures.

No measured combination of scatterometric and radiometric signatures could be used to uniquely classify ice type over the entire experiment area although in some regions many multi-year floes had distinctive depressed $\sigma°HH$ signatures at 9.35 GHz due to secondary (snow thickness/snow recrystallization/snow moisture distribution) effects.

The period of extensive surface melting between June 22 and June 26, 1982 resulted in a marked transformation in the microwave scattering signatures of the ice surface. By June 26 only surface scattering phenomena were observed over the frequency range of 4.4 to 13.6 GHz. The frequency dependence of $\sigma°HH$ on June 26 suggests that the surface roughness at this time was somewhat reduced from that characteristic of bare ice-surface scattering regions measured on June 22. Further smoothing of exposed surfaces due to continuing ablation was reported in an analysis of July 7 SAR data [14].

In the June 26 data set first-year ice scattering cross sections were indistinguishable from multiyear ice scattering cross sections.

Although the area measured in this experiment is small when compared with a satellite radiometer footprint, the complex dependence of 19.4-GHz emissivity on the snow properties and moisture distribution observed here should be accounted for in any modeling effort aimed at understanding radiometric summer ice signatures as was suggested by [5]. Some of the specific observations made in this experiment indicate that snow depth may be less important than free water distribution in determining the optical thickness, and thus the impact, of the snow cover on microwave signatures.

During the melt onset period characterized by the June 22 data set, the use of X-band SAR imagery to classify ice types is becoming problematical. The familiar ice-type/image-intensity signatures characteristic of cold-season sea-ice imagery have been replaced by surface roughness and snow-cover-dominated signatures that are not consistently related to ice type. During this part of the melt cycle large multiyear floes can often be identified by floe shape signatures, but the probability of misclassification is becoming large and floe-like shape patterns that are simply surface wetness patterns are sometimes found. As melt progresses, ice classification from SAR signatures becomes progressively more difficult until, during periods of extreme surface wetness [14], [11] SAR data at any radar frequency above and including L-band cannot be used to obtain reliable ice-type classifications.

REFERENCES

[1] B. A. Burns, R. A. Shuchman, P. L. Jackson, J. D. Lyden, and C. E. Livingstone, "SAR measurements of sea ice properties during MIZEX '83," in *Proc. IGARSS* (Strasbourg, France) pp. 347–352, Aug. 1984.

[2] W. J. Campbell, R. O. Ramseier, H. J. Zwally, and P. Gloersen, "Arctic sea ice variations from time-lapse passive microwave imagery," *Boundary Layer Meteorol.*, vol. 18, no. 6, pp. 99-106, 1980.

[3] D. J. Cavalieri, P. Gloersen, and W. J. Campbell, "Determination of sea ice parameters with the Nimbus 7 SMMR," *J. Geophys. Res.*, vol. 89, no. D4, pp. 5355-5369, 1984.

[4] J. C. Comiso, S. F. Ackley, and A. L. Gordon, "Antarctic sea ice microwave signatures and their correlation with *in situ* ice observations," *J. Geophys. Res.*, vol. 89, no. C1, pp. 662-672, 1984.

[5] J. C. Comiso, "Sea-ice effective microwave emissivities from satellite passive microwave and infrared observations," *J. Geophys. Res.*, vol. 88, no. C12, pp. 7686-7704, Sept. 1983.

[6] S. A. Digby, "Mould bay experiment II, June-July, 1982: Experiment summary and surface characteristics," Radarsat Rep. 82-13, 1982.

[7] A. L. Gray, R. K. Hawkins, C. E. Livingstone, L. Drapier-Arsenault, and W. M. Johnstone, "Simultaneous scatterometer and radiometer measurements of sea ice microwave signatures," *IEEE J. Oceanic Eng.*, vol. OE-7, pp. 20-32, 1982.

[°] A. L. Gray, "Microwave remote sensing of sea ice," in *Proc. COSPAR/SCOR/IVRCM Symp. Oceanography from Space*. New York: Plenum, 1981, pp. 785-800.

[9] T. C. Grenfell, and A. W. Lohanick, "Temporal variations of the microwave signatures of sea ice during the late spring and early summer near mould bay, N. W. T.," *J. Geophys Res*, vol. 90, no. C3, pp. 5063-5074, May 20, 1985.

[10] R. K. Hawkins, A. L. Gray, C. E. Livingstone, and L. D. Arsenault, "Seasonal effects on the microwave signatures of beaufort sea ice," in *Proc. 15th Int. Symp. Remote Sensing Environment* (Ann Arbor, MI), pp. 239-257, 1981.

[11] R. K. Hawkins, C. E. Livingstone, A. L. Gray, K. Okamoto, L. D. Arsenault, and D. E. Pearson, "Single and multiple parameter microwave signatures of sea ice," in *Proc. 6th Canadian Symp. Remote Sensing* (Halifax, Canada), pp. 217-230, 1980.

[12] H. E. Hengeveld, "The utilization and benefits of SLAR in operational ice data acquisition," in *Proc. 6th Canadian Symp. Remote Sensing* (Halifax, Canada), pp. 81-88, 1980.

[13] J. P. Hollinger, B. E. Troy, R. O. Ramseier, K. W. Asmus, M. F. Hartman and C. A. Luther, "Microwave emission from high arctic sea ice during freeze up," *J. Geophys. Res.*, vol. 89, no. C5, pp. 8104-8122, Sept. 20, 1984.

[14] B. Holt and S. A. Digby, "Processes and imagery of fast first-year sea ice during the melt season," *J. Geophys Res.*, vol. 90, no. C3, pp. 5045-5062, May 20, 1985.

[15] R. D. Ketchum, Jr. and L. D. Farmer, "Eastern arctic Sursat SAR ice experiment: radar signatures of sea ice features," NORDA Tech. Note 68, 1980.

[16] R. D. Ketchum, Jr., "Dual frequency radar ice and snow signatures," NORDA Tech. Note 135, 1981.

[17] Y. S. Kim, R. K. Moore, and R. G. Onstott, "Theoretical and experimental study of radar backscatter from ice," Univ. of Kansas Remote Sensing Lab. Rep. RSL TR, pp. 331-337, Jan. 1984.

[18] F. Leberl, M. L. Bryan, C. Elachi, T. Far, and W. Campbell, "Mapping of sea ice and measurement of its drift using aircraft synthetic aperture radar," *J. Geophys. Res.*, vol. 84, no. C4, pp. 1827-1835, 1979.

[19] C. E. Livingstone, R. K. Hawkins, A. L. Gray, L. D. Arsenault, K. Okamoto, T. L. Wilkinson, and D. Pearson, "The CCRS/Sursat active-passive experiment 1978-1980: The microwave signatures of sea ice," Canada Centre for Remote Sensing. Data Acquisition Division Rep., 1983.

[20] C. E. Livingstone, R. K. Hawkins, A. L. Gray, K. Okamoto, T. L. Wilkinson, S. Young, L. D. Arsenault, and D. Pearson, "Classification of Beaufort sea ice using active and passive microwave sensors," in *Proc. COSPAR/SCOR/IUCRM Symp. Oceanography from Space* (Venice), pp. 813-821, 1981.

[21] A. W. Lohanick, "Snow thickness and vertically polarized brightness temperature on multi-year ice," NORDA Tech. Note 171, Nov. 1982.

[22] C. A. Luther, J. D. Lyden, R. A. Shuchman, R. W. Larse, Q. A. Holmes, D. R. Meusch, R. T. Lowry, and C. E. Livingstone, "Synthetic aperture radar studies of sea ice," in *Proc. IGARSS*, vol. 2, sec. TA 8, pp. 1.1-1.9, 1982.

[23] C. Matzler and E. Schanda, "Snow mapping with active microwave sensors," *Int. J. Remote Sensing*, vol. 5, no. 2, pp. 409-422, 1984.

[24] R. G. Onstott, R. K. Moore, S. Gogineni, and C. Delker, "Four years of low altitude sea ice broadband backscatter measurements," *IEEE J. Oceanic Eng.*, vol. OE-7, no. 1, pp. 44-50, 1982.

[25] R. G. Onstott and S. P. Gogineni, "Active microwave measurements of arctic sea ice under summer conditions," *J. Geophys Res.*, vol. 90, no. C3, pp. 5035-5044, May 20, 1985.

[26] Radarsat/Firex Group, "Summer ice study data report. Mould Bay, Prince Patrick Island, N. W. T., Canada." Radarsat/Firex Program Rep., Jet Propulsion Lab., Pasadena, CA, 1982.

[27] E. Svendsen, K. Kloster, B. Farelly, O. M. Johannessen, J. A. Johannessen, W. J. Campbell, P. Gloersen, D. Cavalieri, and C. Matzler, "Norwegian remote sensing experiment: evaluation of the Nimbus 7 scanning multi-channel microwave radiometer for sea ice research," *J. Geophys. Res.*, vol. 88, no. C5, pp. 2781-2791, 1983.

[28] B. E. Troy, J. P. Hollinger, R. M. Lerner, and M. M. Wisler, "Measurements of the microwave properties of sea ice at 90 GHz and lower frequency," *J. Geophys. Res.*, vol. 86, pp. 4283-4289, 1981.

[29] H. J. Zwally and P. Gloersen, "Passive microwave images of the polar regions and research applications," *Polar Rec.*, vol. 18, no. 116, pp. 431-450, 1977.

[30] D. M. Johannessen, J. A. Johanessen, J. Morison, B. A. Farrelly, and E. A. S. Svendsen, "Oceanic conditions in the marginal ice zone north of Svalbard in early fall 1979 with an emphasis on mesoscale processes," *J. Geophys. Res.*, vol. 88, no. C5, pp. 2755-2769, 1983.

[31] F. D. Carsey "Summer Arctic sea ice character from satellite microwave data," *J. Geophys. Res.*, vol. 90, no. C3, pp. 5015-5034, 1985.

*

Charles E. Livingstone received the B.Sc. degree in physics in 1965 and the M.Sc. degree in geophysics in 1967 from the University of British Columbia; he received the Ph.D. degree in physics in 1969 from the University of Western Ontario.

From 1969 to 1976, he was an Assistant Professor of Electrical Engineering at the University of Western Ontario. Since 1976, he has worked at the Canada Centre for Remote Sensing. During this time he has been involved in the specification and development of hardware for radar remote sensing and has led a number of research projects on the microwave signatures of sea ice. His present activities are focused on the commissioning of an advanced remote sensing SAR, the IRIS system.

*

R. G. Onstott (S'73-M'79), photograph and biography not available at the time of publication.

*

L. D. Arsenault is with Cold Regions Remote Sensing, Stittsville, Ontario Canada.

*

A. Laurence Gray (M'85) graduated in physics and applied mathematics from Queens University, Belfast, in 1964. He received the M.Sc. degree in biophysics in 1966 and the Ph.D. degree in experimental physics in 1971, both from the University of Calgary.

Between 1971 and 1974, he worked on laser light scattering in the Physics Department of the University of Guelph, Ontario, Canada. In 1974, he joined the Canada Centre for Remote Sensing and has worked since then principally on ice and

cold ocean reconnaissance. On a leave of absence from CCRS during 1979–1980, he was a Guest Professor at the Technical University of Denmark, and from 1980 to 1983, was Chairman of the CACRS Ice Working Group. He was one of the principal investigators in the Shuttle Imaging Radar (SIR-B) experiment. Currently, he is a member of the AMI team advising the European Space Agency on the design and use of the SAR-Scatterometer sensor system known as the Active Microwave Instrument, which will be flown on the ESA remote sensing satellite ERS-I.

*

Keshava P. Singh (M'74–SM'84) was born in Jaunpur, Uttar Pradesh, India, in January 1947. He received the B.Sc. degree in electrical engineering and the Ph.D. degree in electronics engineering from the Banaras Hindu University, Varanasi, India, in 1969 and 1973, respectively.

In January 1970, he was awarded a Banaras Hindu University Research Fellowship. From November 1970 to November 1971, he was a Junior Research Fellow of the Council of Scientific and Industrial Research, India, and from November 1971 to March 1973, he was a Research Associate in a U.S. Air Force sponsored research project at the Institute of Technology, Banaras Hindu University. From March 1973 to December 1974, he was with the Department of Electrical Engineering, Nagoya University, Japan, as a Post Doctoral Fellow where he worked on high-power microwave interaction with plasmas. From April 1975 to July 1975, he was a Scientific Pool Officer at the Department of Electronics Engineering, Institute of Technology, Barnaras Hindu University, where he became a faulty member in July 1975 and an Associate Professor in February 1979. He visited the University of Kansas, Lawrence, and the University of California at Los Angeles between December 1980 and February 1981. From February 1982 to November 1982, he was an Associate Professor with the University of Aden, P.D.R. Yemen, on foreign assignment form the Government of India. He was a visiting scientist with the Canda Centre for Remote Sensing, Ottawa, from December 1982 to March 1985, where he also worked as an Airborne Systems Scientist from April 1985 to July 1985. He was involved with the research analysis of airborne microwave scatterometers, radiometers, and synthetic aperture radar data from various targets, and the calibration of airborne microwave remote sensors. He has published approximately 50 papers. His areas of research interest include microwave remote sensing, plasma physics, E.M. wave interactions with various media, and communications.

Evolution of Microwave Sea Ice Signatures During Early Summer and Midsummer in the Marginal Ice Zone

R. G. Onstott,[1] T. C. Grenfell,[2] C. Matzler,[3] C. A. Luther,[4] and E. A. Svendsen[5]

Emissivities at frequencies from 5 to 94 GHz and backscatter at frequencies from 1 to 17 GHz were measured from sea ice in Fram Strait during the Marginal Ice Zone Experiment in June and July of 1983 and 1984. The ice observed was primarily multiyear; the remainder, first-year ice, was often deformed. Results from this active and passive microwave study include the description of the evolution of the sea ice during early summer and midsummer; the absorption properties of summer snow; the interrelationship between ice thickness and the state and thickness of snow; and the modulation of the microwave signature, especially at the highest frequencies, by the freezing of the upper few centimeters of the ice.

Introduction

Active and passive microwave remote sensing of sea ice offer the potential of obtaining synoptic data of large expanses of remote, ice-covered oceans under all weather conditions irrespective of the amount of solar illumination. This is of particular importance for Arctic applications where much of the polar ice canopy is under clouds or in darkness.

Numerous late winter and spring experiments have concentrated on the ability to classify ice types, to detect scientifically interesting features, and to describe ice field kinematics and dynamics. Efforts also focused on a determination of optimum frequencies, polarizations, and incidence angles and on the development of algorithms for extracting geophysical parameters from sea ice imagery. *Campbell et al.* [1975], *Ramseier and Lapp* [1980], and *Livingstone et al.* [1981] conclude their studies by stating that many features, including ice types, ridges and roughness features, lead and polynya formations, and icebergs, have distinct signatures which are observed using active and passive microwave sensors. They also present the hypothesis that a combination of multifrequency, active and passive (microwave and millimeter wave) sensors is especially valuable for extracting information about the state of the ice. They present the hypothesis that emissivity and backscatter are influenced by different aspects of the sea ice structure and that the relationship between microwave frequency and penetration depth may be exploited robustly.

The more limited experimentation by *Gray et al.* [1982], *Onstott et al.* [1982], *Onstott and Gogineni* [1985], *Grenfell and Lohanick* [1985], and *Lohanick and Grenfell* [1986] during the summer melt period illustrate the extreme difficulty in detecting and classifying sea ice features when surface conditions change rapidly. They concluded that use of microwave sensors to classify sea ice type and features unambiguously requires

understanding of the emissivity and reflectivity characteristics of the various ice types and that to understand the electromagnetic characteristics requires the understanding of sea ice physical properties.

Intensive measurement of summer sea ice signatures were made in Fram Strait during June and July of 1983 and 1984. These data were acquired during participation in the Marginal Ice Zone Experiment (MIZEX) [*Johannessen and Horn*, 1984], a multinational interdisciplinary effort to study the air-sea-ice interaction processes in the transition region where the pack ice meets the open ocean. An objective of MIZEX is to define the geophysical processes which govern these interactions and to understand how these interactions influence ice edge location, ice morphology, ice sheet deformation, and ice band formation.

This paper presents a comprehensive discussion of the summer microwave signatures of the major classes of Arctic sea ice in the marginal ice zone (MIZ) and their relationship to snow and ice physical properties. The discussion begins by examining winter and spring signatures using data from previous experiments. Electromagnetic interaction arguments are developed to describe the effect of summer metamorphosis on sea ice signatures. The discussions provided may also be extended to include sea ice scenes found in other regions.

Electrical Properties of Sea Ice and Snow

Frozen sea water, sea ice, is a lossy dielectric. It consists of pure ice, liquid brine, and air. Snow blankets the top of this low-density solid. During winter, the microwave signatures of the desalinated multiyear ice are clearly different from those of the saline first-year ice. The situation in summer is more complex; this is the time of desalination, of melting snow and ice, of melt pool formation, and of the melt-and-freeze cycling of the upper surface. Microwave signatures track these meteorologically induced melt-and-freeze cycles.

Important in remote sensing science is how the electrical and physical properties of snow and ice are modified as they experience summer melt. The physial parameters which influence the microwave observables are snow wetness, snow grain size, snow density, and snow and ice roughness. Sensor parameters, such as wavelength, polarization, and incidence angle, also influence the intensity of backscatter and emission. In the microwave and millimeter wave region the electrical properties of dry snow (a mixture of ice crystals and air) are approximately frequency independent. Following *Matzler* [1985], who summarizes the results of many investigations,

TABLE 1. Brief Summary of Ice Descriptions During MIZEX 1983 and 1984

Ice Type*	Ice Thickness Range, cm	Snow Thickness Range, cm	Snow Thickness Average, cm	Ice Salinity in Top 10 cm, ‰	Ice Salinity in Top 40 cm, ‰
MY	174–536	3–65	29	0–1	0–1
TFY	175–236	2–20	10	1–4	4–5
MFY	90–120	2–14	6	1	2–3
ThFY	38–70	2–6	4	3–4	4–5

*See text for explanation of abbreviations.

the real part of the dielectric constant expressed as a function of snow density is

$$\varepsilon_{dry}' = 1 + \frac{1.6\rho}{(1 - 0.35\rho)} \qquad (1)$$

In (1), ρ is the density of dry snow in kilograms per cubic meter. Three important notes are as follows: (1) freshly deposited snow quickly attains a density of at least 330 kg m^{-3}, (2) during MIZEX, densities in the dry surface layer were about 400–500 kg m^{-3} for old snow and less than 100 kg m^{-3} for new snow, and (3) the density of pure solid ice is 916 kg m^{-3}.

The imaginary part of the complex dielectric constant is important in that it is one of the parameters which describe the absorption properties of a dielectric medium. The complex dielectric constant of wet snow is strongly dependent on frequency, density, and wetness [Matzler, 1985]. It may be expressed using the simple Debye relaxation spectra by neglecting the low dielectric losses of dry snow as

$$\varepsilon = \varepsilon_{dry}' + \frac{0.23w}{1 + if/f_0} \qquad (2)$$

where w is the percent volumetric liquid water content, f_0 is 10 GHz (relaxation frequency of wet snow), and f is frequency in gigahertz.

The propagation distance through a medium over which the intensity is reduced by e^{-1} is often referred to as the penetration depth (PD). The penetration depth is given by

$$PD = 0.5\alpha^{-1} \qquad (3)$$

where

$$\alpha = \frac{2\pi}{\lambda} |Im [\sqrt{\varepsilon}]| \qquad (4)$$

In (4), λ is the free space wavelength. Ignoring scattering losses, a 9-dB round-trip loss is experienced in propagating over this distance. It is also important to note that up to two or three penetration depths may need to be considered when examining potential contributions to the microwave signature.

ICE CONDITIONS AND EXPERIMENT DESCRIPTION

The Fram Strait is the key outflow region of the Arctic Basin. Ice may originate from any region of the basin. This is not a typical MIZ and is unique both oceanographically and in its sea ice characteristics. Hence both ice physical and microwave properties may be quite diverse, since the area of origin strongly influences the environment in which an ice sheet grows.

As ice from the very close pack approaches the margins, it breaks up into smaller floes. Still nearer the ice edge, higher-frequency components of swell are greater in amplitude, and floes are further reduced in size, often into patches of small, similarly sized floes. During MIZEX, sea ice was investigated throughout the region from the edge of the central pack to the extreme ice margin. It is worth noting that our observations show that ice and snow conditions at sites close to the edge of the pack and ice in the interior of the MIZ are similar.

Most of the ice in the MIZ has experienced dynamic forcing, which increases surface and subsurface topography as well as floe thickness prior to entering Fram Strait. Deformed ice is found in the form of pressure ridges and rubble, each of which has its own roughness scale. Ice may also have regions of surface and subsurface meltwater pools and areas of flat ice and mounds. The microwave properties of these diverse scenes may be equally varied.

The major summer sea ice forms found during June and July included (1) multiyear (MY) ice which has survived at least one summer's melt and typically has a thickness greater than 2.5, (2) thick first-year (TFY) ice which began growing early in the season and attains a thickness greater than 120 cm, (3) medium first-year (MFY) ice which began growing later in the growing season, reaching a thickness of 70–120 cm, and (4) thin first-year (ThFY) ice which began growing late in the season and has a thickness of 30–70 cm.

Floe size ranged from small, a horizontal extent of 20–100 m, to giant, a horizontal extent greater than 10 km. Most of the ice was multiyear. The proportion of first-year (FY) ice was difficult to estimate but was probably less than one third of the total ice cover. Because of the melting conditions, new ice formation in leads was not significant and would not affect lead signatures. Snowpack was typically heavy and wet, with depths up to 65 cm on many MY ice floes. This is very thick by Arctic standards. A more detailed description of the range of conditions found during MIZEX is assembled in Table 1. During the experiment period the snowpack and ice sheets underwent a transition from late spring to summer melt conditions. Air temperatures were typically within 2° of 0°C. Extremes ranged from −10°C to +4°C. Measured using alcohol calorimetry, volumetric snow wetness in both the interior and the upper few centimeters ranged from 0% to 10%, except for variations in a thin surface layer. The bulk snow wetness stayed at about 5–6% over much of the experiment duration. Figure 1 shows the microwave penetration depths for the con-
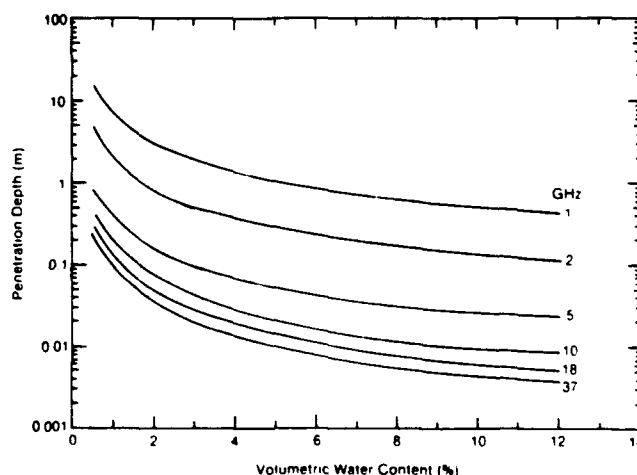

Fig. 1. Penetration depth for snow with a density of 385 kg m^{-3} for frequencies between 1 and 37 GHz. Calculations are based on experimental data acquired and results published by Matzler [1985], Hallikanen et al. [1984] and Tiuri et al. [1984].

TABLE 2. In Situ Microwave Sensor Description and Specification

	University of Washington	University of Kansas	University of Bern
Sensor	radiometer*	scatterometer†	radiometer‡
Sensor type	Dicke and total power	FM-CW	Dicke
Icebreaker/year	PB and PS in 1983, PQ in 1984	PB and PS in 1983, PS in 1984	PS in 1983
Platform	sled	helicopter and ship	ship
Frequencies, GHz	6, 10, 18, 37, and 90	1.5, 5.2, 9.6, 13.6, and 16.6	4.9, 19.4, 21, 35, and 94
Polarization	V and H	VV, HH, and HV	V and H
Nadir viewing angle	20°–60°	0°–75°	20°–60°
Precision	1–5 K	1 dB	0.1–1.2 K
Accuracy	3–7 K	2 dB	1 K
Beamwidth	15°	2°–11°	9°–10°
Height	1½ m	15–45 m	17 m
Calibration	sky and internal	Luneberg lens reflector	sky and internal

PB, Polarbjorn; PS, Polarstern; PQ, Polarqueen.
*Radiometer named UW/RAD.
†Scatterometer named HELOSCAT.
‡Radiometer named PAMIR.

ditions described here, shown as a function of snow wetness and frequency. Flooding of the ice-snow interface with fresh water was occurring due to continual snowpack ablation during much of the investigation.

Our observations show that snow cover thickness of ThFY (2–6 cm), MFY (6–15 cm), TFY (6–20 cm), and MY (15–65 cm) ice was variable. New snow also fell during these investigations (0.5–1 cm). Snow on pressure ridges and other elevated features was shallow and consisted of very coarse grains up to 2 cm in size. We feel that grains of this size must have formed under the temperature gradient metamorphism during the previous winter. A hexagonal shape indicated a slight rounding by melt metamorphism. Old snow was similar to firn, with grain diameters of 1 mm. Snow crystal sizes of 0.5–2 mm diameter were typical. First-year ice and advanced areas of melt on MY ice showed 3–5 mm diameter with occasional ice crystal globes exceeding a diameter of 1 cm.

Salinities in the upper layer of the ice sheet were much less than 1‰ for MY and around 2‰ in the case of FY ice, typically. In 1984 the FY upper ice sheet salinity decreased over the experiment duration, and the MY ice salinity increased to about 0.3‰ [Tucker et al., this issue].

Measurement Approach

The integration of microwave measurements by a comprehensive set of satellite, aircraft, ship, and surface-based sensors with sea ice scene characterization measurements is a fundamental accomplishment of the MIZEX Remote Sensing Program [MIZEX Group, 1986]. All sensor parameters overlap well by design. Imagery was collected of specifically chosen representative ice floes on which coincident in situ surface, shipboard, and helicopter-borne measurements of scattering and emission characteristics and ice physical properties were made. For detailed discussion of the near-surface sensor parameters and experimental procedure, refer to Grenfell and Lohanick [1985], Matzler et al. [1984], Gogineni et al. [1984], and Table 2.

The surface-based measurements include (1) snow thickness, wetness, density, physical construction, dielectric constant, and temperature, (2) ice thickness, wetness, density, physical con-

struction, salinity profile, temperature profile, surface roughness, state of deformation, and dielectric constant, (3) general floe topography, and (4) the spatial distribution of meltwater on the ice sheet.
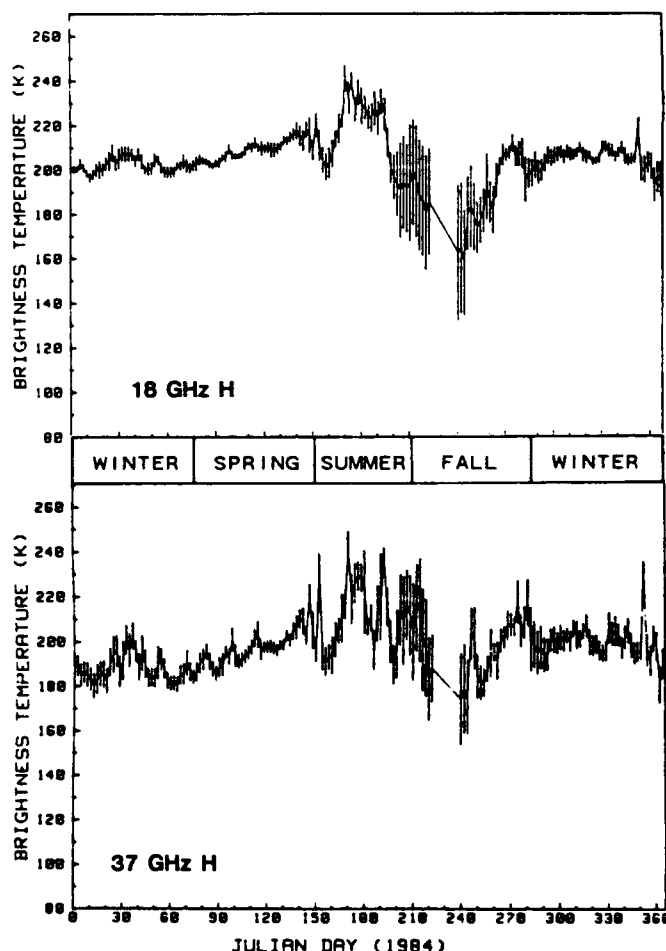

Fig. 2. Time series of average Nimbus 7 H polarization brightness temperatures at 18 GHz and 37 GHz for a 300 km by 300 km region in the Greenland Sea near the MIZEX study area during 1984. The short vertical lines represent one standard deviation (D. J. Cavalieri, NASA, Goddard, unpublished data, 1986).
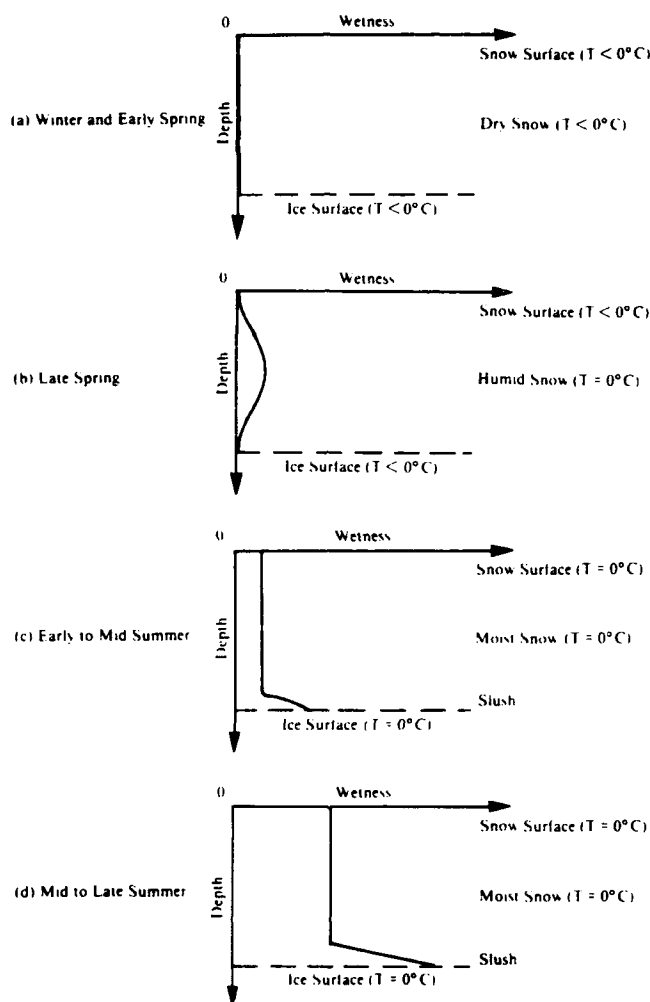
Fig. 3. Free water fraction versus depth for snow on sea ice, illustrating conditions encountered during (a) winter and early spring, (b) late spring, (c) early summer, and (d) midsummer.

Satellite-Acquired Sea Ice Temporal Signatures

The mean and standard deviation of the brightness temperatures at 18 GHz and 37 GHz with horizontal polarization of sea ice as derived from the Nimbus 7 scanning multichannel microwave radiometer (SMMR) in a 300 km by 300 km region in Fram Strait in the vicinity of the MIZ are shown for alternate days in Figure 2 (D. J. Cavalieri, NASA, unpublished data, 1986). These brightness temperature data show the big picture, the continuous time series record for the 1984 Arctic year. They illustrate the transition from winter to summer signatures and provide the forum from which the in situ "snapshots" are discussed.

During the cold winter months, between December and March (Julian days 335–90), the sea ice brightness temperature variations are small and are primarily due to changes in ice concentration or to variations in the physical temperatures of the radiative portion of the ice or both. Starting in April (Julian day 91) the steadily increasing spring warming trend translates into a similarly increasing scene brightness temperature. By May (Julian days 121–151) this trend was disturbed. As we observed during MIZEX, the emission at 36 GHz is very sensitive to the presence of free water and the recrystallization of the upper few centimeters of the snowpack. Weather records indicate that a series of atmospheric lows of warm air passed through this region during this critical period. Our hypothesis is that the upper layer of the snowpack experiences a metamorphism causing an enlargement of ice crystals. Once temperatures return to normal and the snowpack refreezes, the brightness temperature will be lower due to an additional scattering loss which arises from the increase in ice crystal size.

The sudden jump in brightness temperature from June 8 to 18 (Julian days 160 to 170) marks the onset of summer melt, when temperatures stabilize at about 0°C. It will be demonstrated that the new brightness temperature threshold during the first half of this period indicates a moist snowpack. In addition, the melt-freeze cycles which occur throughout the Arctic summer contribute to the wide range of brightness temperatures. By the second half of summer (beginning about Julian day 180), melt has advanced to a stage where a significant proportion of the snowpack has melted and open pools of meltwater are more numerous. The brightness temperature shows a decrease of at least 10 K (see 18-GHz data) and larger standard deviations. Standard deviations at 37 GHz are even larger, due in part to the larger number of footprints at 37 GHz than at 18 GHz in the 300 km by 300 km region. The dip in brightness temperature is then followed by an increase (about Julian day 195). This represents a very interesting and important event. Sea ice may experience periods of drying during which the areal extent of surface meltwater is reduced due to draining through cracks, thaw holes, and rotting ice. Such cycles of draining and melting were observed during MIZEX. At about the middle of July (Julian day 195) the brightness temperature shows a significant increase. We attribute this to the reduction in the areal extent of open water in melt pools and to wet air-snow and air-ice interfaces.

By the beginning of September (Julian day 244) the ice is well drained, the rapid cooling of the Arctic proceeds, the ice concentration is at its minimum, and the minimum brightness temperature for the year is reached. By the end of September, brightness temperatures have returned to wintertime conditions.

MICROWAVE SIGNATURE AND SCENE INTERCOMPARISONS

The microwave signature of the evolving summer sea ice as measured in situ is discussed for the periods of winter, late spring, early summer, and midsummer. Two additional influences, very heavy melt and rain and frozen surface crust, and included because of their ability to alter the seasonal microwave signature. Figures 3 and 4 illustrate the general distribution of wetness (liquid water content) in the snow on ice as observed during MIZEX. Cross-sectional representations of gross changes in the physical construction of the snowpack, the snow-ice interface, and the ice sheet are provided in Figures 5 and 6.

In what follows, emissivities are shown at frequencies from 5 to 94 GHz for a 50° nadir angle and horizontal (H) and vertical (V) polarizations. Radar backscatter cross sections are at frequencies from 1 to 17 GHz, at angles from 0° to 60°, and at HH polarization. Since backscatter effects at VV and HH polarizations were very similar for both FY and MY ice, we follow tradition and discuss HH polarization. Radar angular response data are shown to elucidate the strong dependence of backscatter on incidence angle. The rate of falloff of backscatter beyond vertical provides information about scene roughness and the effective dielectric constant.
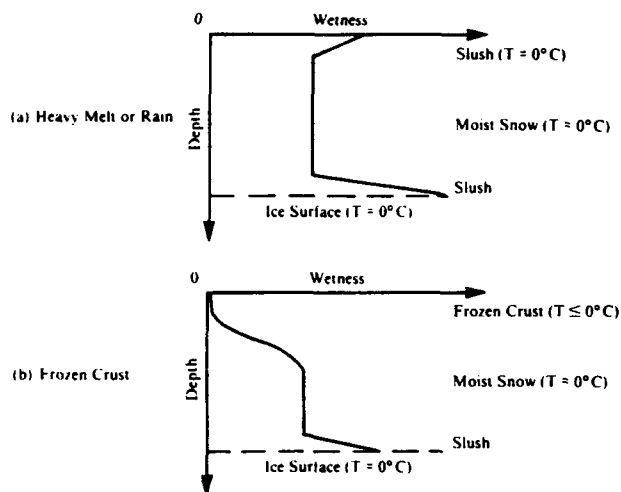
Fig. 4. Free water fraction versus depth for snow on sea ice, illustrating conditions encountered during (a) heavy melt or rain and (b) freezing of the upper snow layer.

Winter

In winter, as during most of the year, the dry snowpack and upper portion of the ice sheet are at temperatures much less than 0°C. As Figure 3a shows, there is no liquid water in the snow or on the ice sheet. Cross-sectional views of FY and MY ice sheets are shown in Figures 5a and 6a. Under the dry snow on undulating MY ice are flat ice, ice mounds, and depressions filled with last summer's frozen meltwater. This set of conditions serves as an excellent reference from which to examine the evolution of sea ice properties during summer.

The emissivities of FY and MY ice and calm water during winter as reported by NORSEX Group [1983] are shown in Figure 7a. Open water exhibits a large difference between emissivities at the two polarizations (Brewster angle effects) and has an emissivity which increases with increasing frequency. In contrast, the FY ice signature is close to unity and is almost independent of polarization and frequency. The multiyear ice signature is not similar to either the calm water or the FY ice. Its emissivity decreases with increasing frequency and shows a moderate separation at the different polarizations throughout the entire range of frequencies.

The radar backscatter of FY and MY ice is shown as a function of frequency at a 40° incidence angle in Figure 8a. These data show radar cross sections which increase linearly with increasing frequency. The radar contast between these two ice types also improves with increasing frequency. Returns from open water in the MIZ are found to be considerably lower than those from ice.

Scattering within the snow and ice reduces emission and enhances backscatter. First-year ice is very lossy because of its high salinity; hence penetration depths are small. In addition, it has few internal scatterers, such as air bubbles, whose diameters are within an order of magnitude of a wavelength. In contast, the upper portion of a MY ice sheet is composed of low-loss, almost pure ice and has significant numbers of air bubbles with diameters of 1–3 mm. The microwave signatures of sea ice at low frequencies (1–4GHz) are, for the most part, controlled by its dielectric constant and surface roughness. As wavelengths grow shorter, volume scattering from the inhomogeneities within the snow and ice becomes increasingly important. At frequencies of about 10 GHz, volume scattering begins to dominate the electromagnetic interaction process. The interested reader is referred to Kim et al. [1984b] for a detailed discussion of surface and volume scattering of sea ice.

Late Spring

By late spring, temperatures have warmed from winter lows of about −35°C; there may be periods with temperatures near

(a) Winter and Early Spring
(Completely Frozen)

(b) Late Spring
(Humid Snow and Superimposed Ice)

(c) Early to Mid Summer
(Moist Snow)

(d) Mid to Late Summer
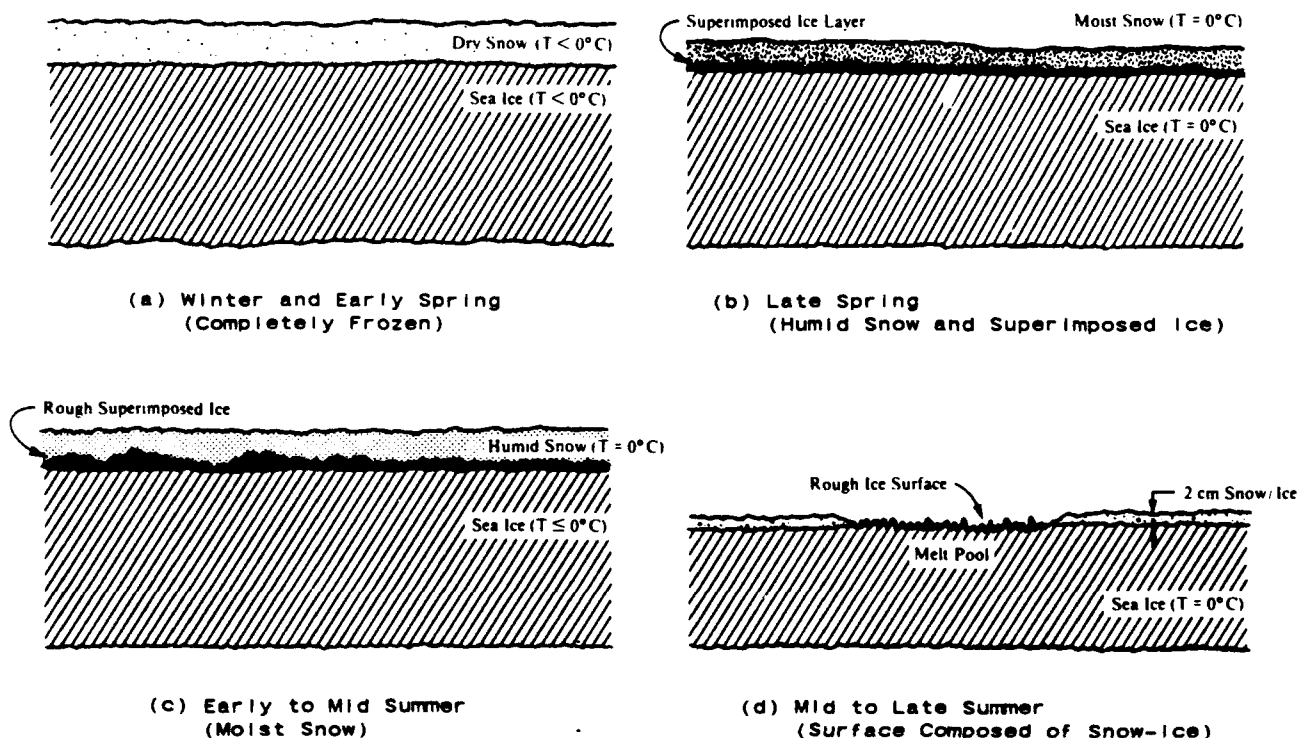(Surface Composed of Snow-Ice)

Fig. 5. Snow and ice conditions encountered on first-year ice during (a) winter and early spring, (b) late spring, (c) early summer to midsummer, and (d) midsummer to late summer.

(a) Winter and Early Spring
(Completely Frozen)

(b) Late Spring
(Humid Snow and Superimposed Ice)

(c) Early to Mid Summer
(Moist Snow)

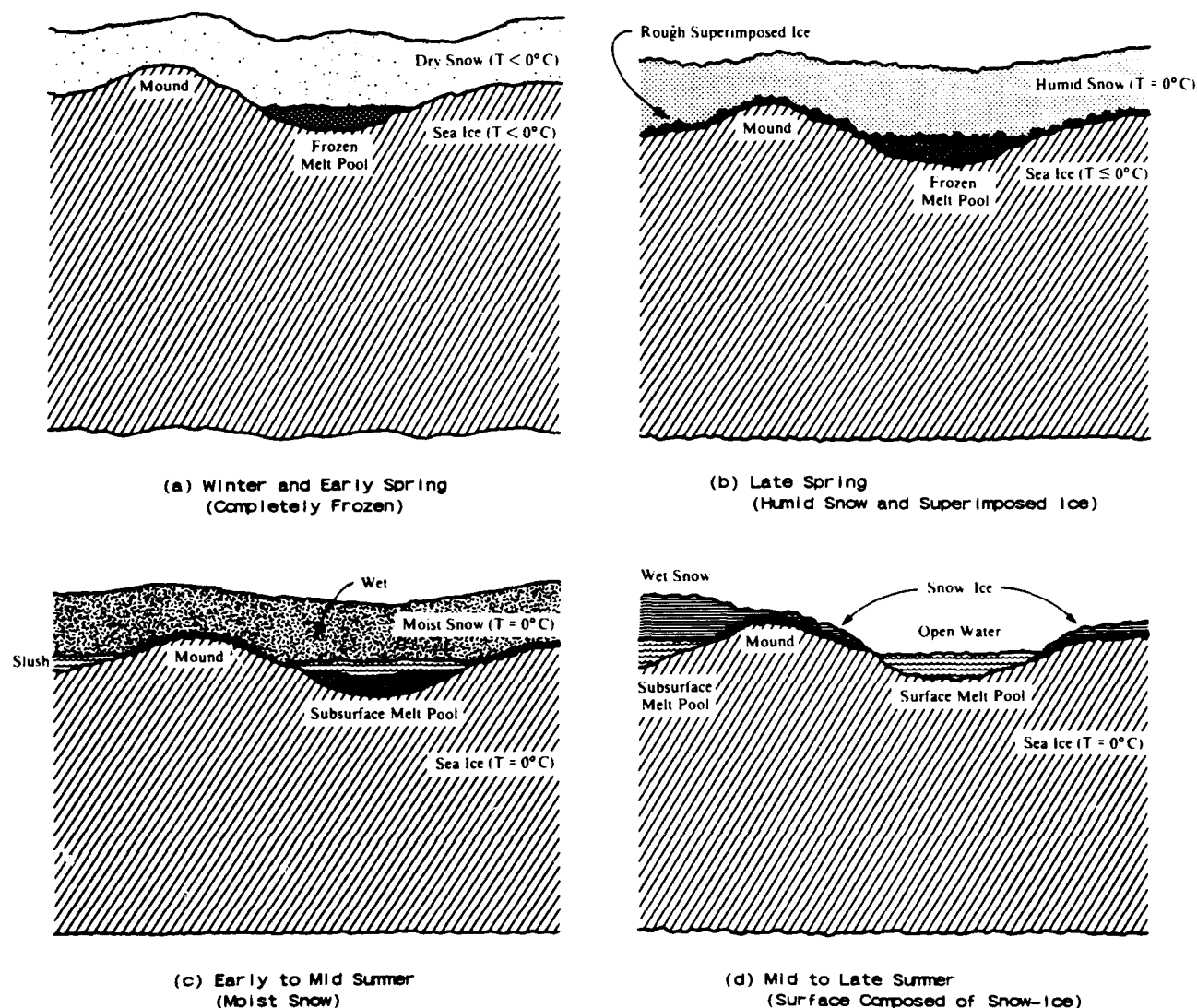(d) Mid to Late Summer
(Surface Composed of Snow-Ice)

Fig. 6. Snow and ice conditions encountered on multiyear ice during (a) winter and early spring, (b) late spring, (c) early summer to midsummer, and (d) midsummer to late summer.

0°C. This rise in physical temperature is accompanied by an increase in the imaginary part of the complex dielectric constant; this increase is rapid once temperatures are within a few degrees of 0°C. During this period the interior of the snowpack becomes humid. Figure 3b illustrates the common occurrence of cool air above the snow, a dry snow surface layer, a humid snow interior, and a cold ice sheet surface. Moisture from the humid snow layer may collect on the cold ice surface and freeze. The superimposed ice roughens the ice-snow interface, illustrated in Figures 5b and 6b. This roughness will increase in time and influence the microwave signatures of ThFY and MFY ice during midsummer.

Signatures representative of late spring conditions are shown in Figures 7b and 9a. In contrast with winter conditions, FY and MY ice emissions are almost identical. The snow has attained a wetness sufficiently large (about 2%) that scene emissivity is determined by the snowpack and not by the cold ice sheet below.

Radar contrast at 9.6 GHz and 5.2 GHz is also reduced (see Figure 9a). Volume scattering, which dominated the microwave signature of MY ice during winter and early spring at

9.6 GHz, has been reduced effectively by the humid snowpack. Backscatter at 5.2 GHz is affected less because volume scattering has a reduced role at this frequency, scattering from the ice surface contributes strongly, and a penetration depth of 20 cm (3 times that at 9.6 GHz) is sufficient to continue sensing the surface and upper portion of the ice sheet.

Early Summer

Early summer may be described as the start of the 2-month period during which the mean air temperature remains close to 0°C. Summer FY and MY ice microwave signatures will be shown to be very similar. Early summer signature differences between ice types are at best subtle. The thoroughly moistened snow is at its maximum annual thickness. Free meltwater percolates through the snow and collects at the snow-ice interface, forming a thin layer of slush as shown in Figures 3c and 6c or additional superimposed ice as shown in Figure 5c.

During this period the emissivities of MY and FY ice share a common signature, shown in Figure 7c, that of an infinitely thick wet snow layer. In addition, an emissivity of almost unity was obtained at V polarization; hence the wet snow
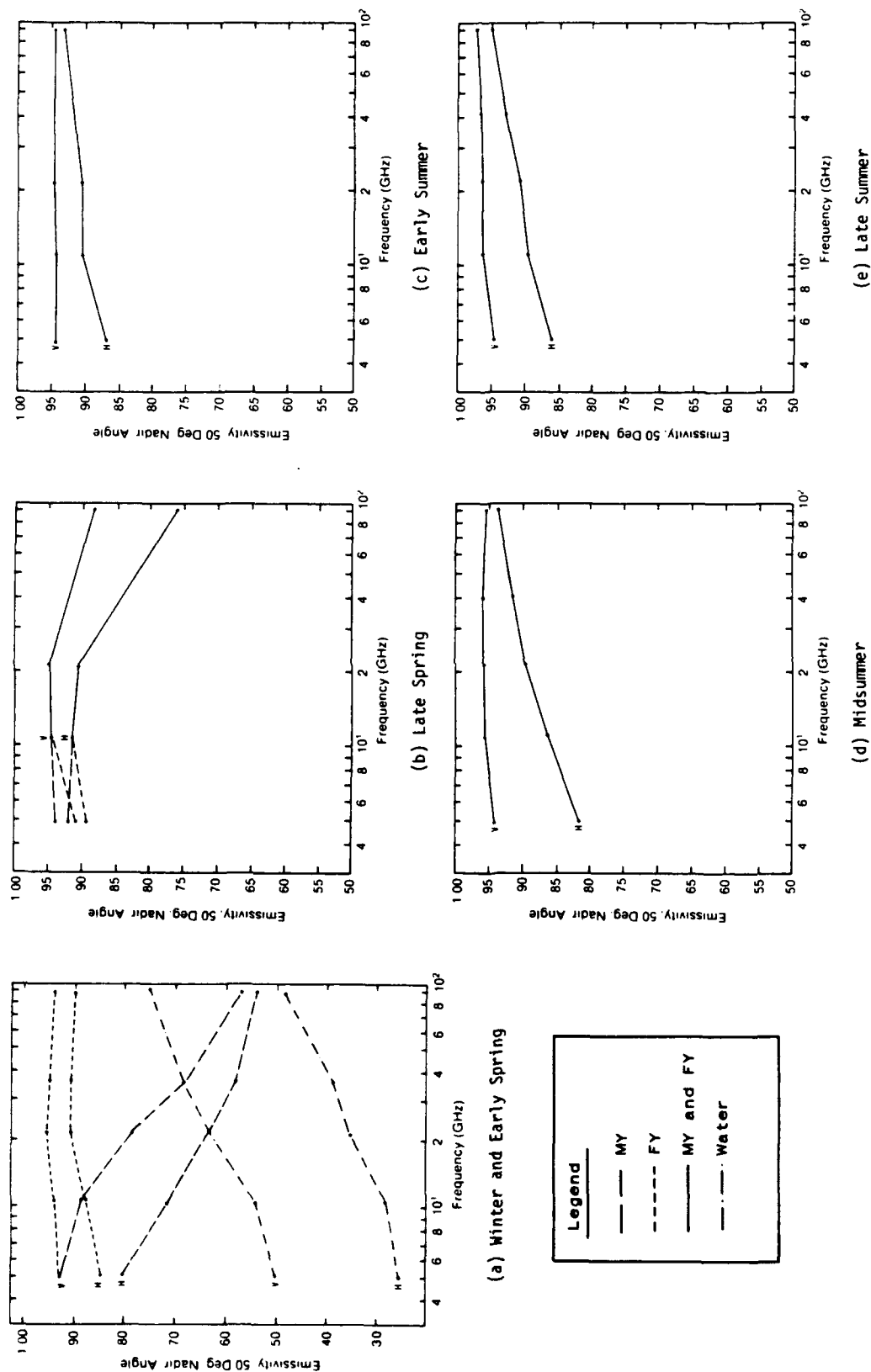
Fig. 7. Emissivity at 50° off nadir in both vertical (V) and horizontal (H) polarization versus frequency of multiyear and first-year ice (and calm water) measured during (a) winter with passive and active microwave and infrared radiometer (PAMIR) (NORSEX, 1979), (b) late spring with University of Washington radiometer (UW/RAD) when the surface snow is dry and the bulk wetness is 2% by volume (June 20, MIZEX '84), (c) early summer with UW/RAD when the associated surface free water content is about 4% by volume (June 26, MIZEX '84), (d) midsummer with PAMIR when the associated free water content is about 5% by volume (July 7-9, MIZEX '83) and (e) late summer with PAMIR when the associated free water content is about 5% by volume (July 11, MIZEX '83).

Fig. 8. Radar scattering cross section frequency response of (a) water and first-year (FY) and multiyear (MY) sea ice at frequencies from 4 to 17 GHz at HH polarization acquired during winter by Onstott et al. [1982] and (b) water and thin first-year (ThFY), medium first-year (MFY), and multiyear (MY) sea ice at 1.5, 5.2, 9.6, 13.6, and 16.6 GHz at HH polarization during midsummer when the bulk wetness is 5% by volume (July 5, MIZEX '84).

(about 4%) shows the characteristics of an ideal blackbody, which absorbs all incident radiation, reflecting none, and is a perfect emitter.

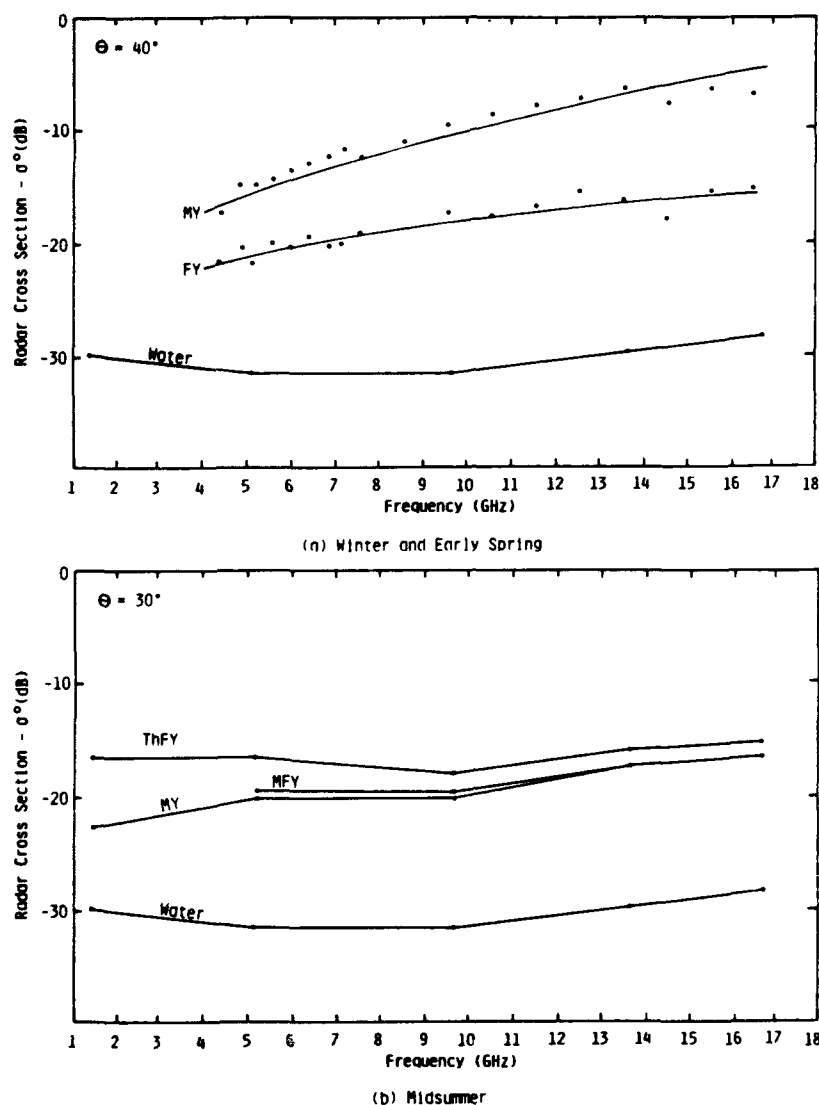Data acquired in conjunction with the above show that backscatter is relatively weak (Figure 9b), and data demonstrate further the effective absorption of the incident energy by the thorough y wet snow layer. Roughness measurements indicate that its surface was smooth at these radar wavelengths (an rms roughness of about 0.3 cm); smooth surfaces produce weak backscatter at angles off vertical.

In review, when the snow scattering volume is reduced to a few centimeters and the snow thickness is at its annual maximum, the wet snow is extremely effective in masking surface ice features at frequencies as low as 5 GHz.

Midsummer

By midsummer the snowpack has experienced considerable melt. Drained snow attains a wetness of about 6% throughout its interior. As is illustrated in the snow wetness diagram in Figure 3c, meltwater continues to accumulate on the MY and

TFY ice sheets, creating a slush layer several centimeters thick. Draining of water into depressions on TFY and MY ice contributes to the formation of subsurface melt pools as illustrated in Figure 6c. The slight increase in liquid water in the snow now limits the penetration of microwaves to distances less than one wavelength. The microwave observables continue to be dominated by the properties of the top layer. Emissivity increases within increasing frequency and remains "blackbodylike" at V polarization (see Figure 7d). With the Brewster effect enhancing the V-polarized radiation, surface reflection is the dominant reflection mechanism. Since the internal scattering in the lossy snow is very small, the Fresnel reflectivity provides a good description of the microwave emission at H polarization at frequencies up to at least 35 GHz.

In Figure 8b, radar backscatter data are shown for MY, MFY, ThFY, and open water at a 30° incidence angle. Snow wetness of 5% results in microwave penetration depths of about 50 cm at 1.5 GHz, 6 cm at 5.2 GHz, and 2 cm at 9.6 GHz, 13.6 GHz, and 16.6 GHz. Contrast between MY and ThFY ice improves with decreasing frequency (6 dB at 1.5
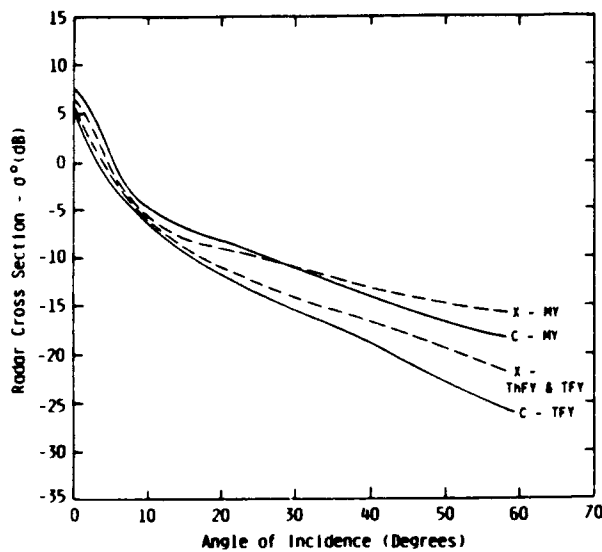
(a) Late Spring
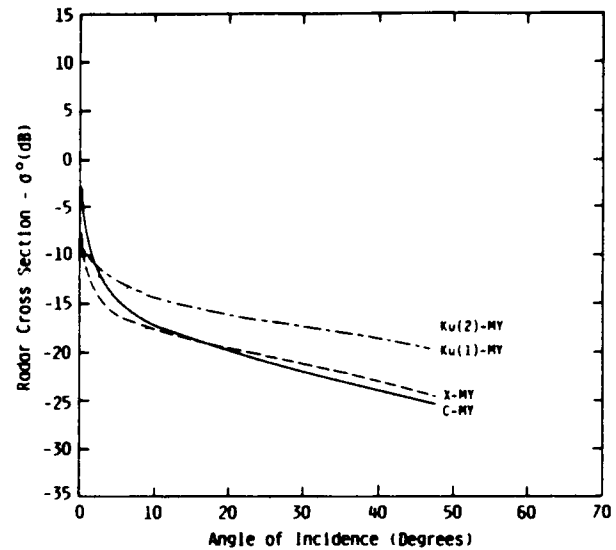
(b) Early Summer

(c) Mid to Late Summer

(d) Rain on Moist Snow

Fig. 9. Radar scattering cross sections acquired during (a) late spring of thin first-year (ThFY), medium first-year (MFY), thick first-year (TFY) and multiyear (MY) sea ice at 5.2 (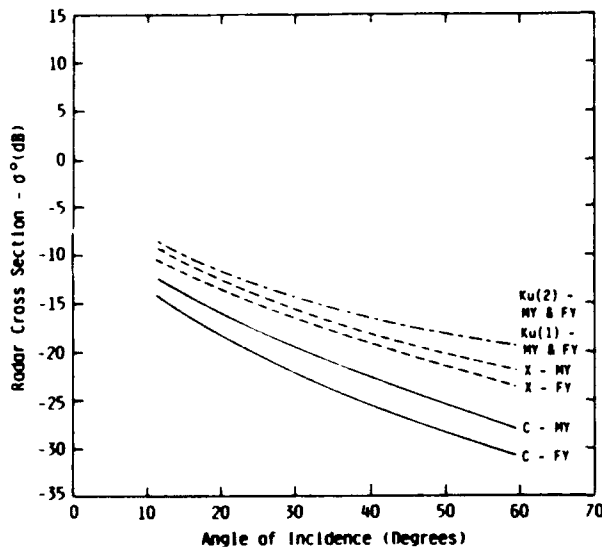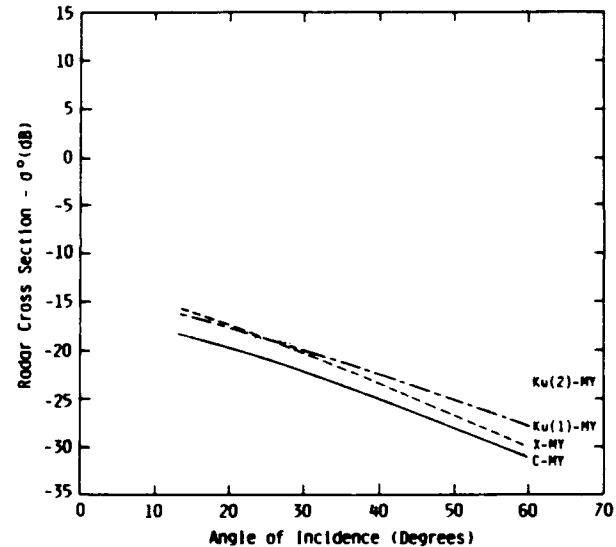C) and 9.6 (X) GHz at HH polarization when the surface snow is dry and the bulk wetness is 2% by volume (June 20, MIZEX '84), (b) early summer of first-year (FY) and multiyear (MY) sea ice at 5.2, 9.6, 13.6 (Ku(1)), and 16.6 (Ku(2)) GHz at HH polarization when the bulk snow wetness is 4% by volume (June 26, MIZEX '84), (c) midsummer to late summer of first-year (FY) and multiyear (MY) sea ice at 5.2, 9.6, 13.6, and 16.6 GHz at HH polarization (July 25, MIZEX '83), and (d) rainy conditions in summer of first-year (FY) and multiyear (MY) sea ice at 5.2, 9.6, 13.6, and 16.6 GHz at HH polarization (June 25, MIZEX '83).

GHz, 4 dB at 5.2 GHz, and about 2 dB at frequencies from 10 to 17 GHz). Physical property measurements suggest that cross-section differences are attributable to the 2- to 3-cm roughness elements of superimposed ice coupled with the thin snow cover on ThFY and MFY ice (snow thickness is 2–6 cm on ThFY and 2–14 cm on MFY). These data show that uniformly distributed wet snowpack on MY ice with a surface relief greater than 1 m is effective at masking ice features.

Midsummer to Late Summer

Some time after midsummer, open water melt pools become common on thick ice. About 50–60% of the snow has melted

(about 1 cm per day). A snow-ice crust is in place on elevated MY ice surfaces, on ThFY ice, and on MY ice. The residual snowpack and snow-ice crust are wet (about 6%). On ThFY and MFY ice the snowpack has eroded into a 2-cm-thick, granular snow-ice layer, and former melt pools consist of collections of candled ice tips which rise about 1 cm above the freeboard of the thin, saturated ice sheet (see Figure 5d).

Natural scene intervariability makes it difficult to determine if emission varies with ice type during this period. The data show a keen sensitivity to small physical-property variations in the snow-ice layer, such as density, depth of all the layers, grain size, and wetness. A larger variability in the dielectric
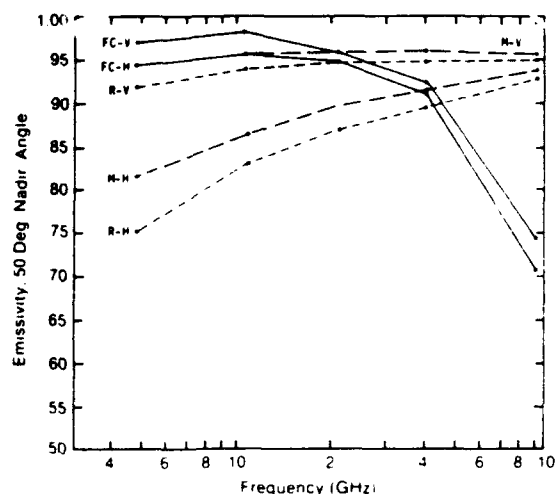
Fig. 10. Emissivity at 50 off nadir in both vertical (V) and horizontal (H) polarization versus frequency representing both multiyear and first-year ice measured during rainy (R) weather with UW RAD when the snow wetness is about 8% by volume (June 24, MIZEX '84), midsummer with PAMIR when the moist (M) snow wetness is about 5% by volume (July 7 9, MIZEX '83), and midsummer with PAMIR and UW RAD when the upper layer of the snowpack is a frozen crust (FC) (July 11, MIZEX '83; June 26, MIZEX '84).

constant of FY ice was noted during this period. It is believed that the thinner snow depth observed on FY ice allows sensing of the liquid water which has collected at certain locations on the ice surface. On average it is felt that the emissions of FY and MY ice are still very similar. Emissivities shown in Figure 7e are slightly higher than those shown for midsummer.

Backscatter from MY ice is greater than or equal to that from FY ice; a contrast reversal has taken place. Contrast between ice types increases with decreasing frequency, shown in Figure 9c. After midsummer, FY ice roughness elements have been eroded by melt to a point where they are small in relation to the radar wavelength; surfaces appear smooth and produce weak backscatter (see Figure 5d). Multiyear ice remains topographically more rough and has many tilted surfaces and a complex mixture of ice, snow, and water features which provide a strong surface scatter (see Figure 6d).

Very Heavy Melt or Rain

Heavy melt or rain causes a saturation in the upper portion of the snowpack, illustrated in the free water versus depth diagram shown in Figure 4a, and reduces the H-polarized emission as shown in Figure 10. In this example the emissivity at 5 GHz for early summer conditions is reduced from 0.86 to 0.75 when rain increased the surface wetness from 4% to 8%. The input of additional free water increases the dielectric constant. The V-polarized emission is less sensitive to this change due to Brewster angle effects. The reflectivity at V polarization is small, and changes in dielectric constant have a correspondingly minor effect. At H polarization a change in dielectric constant translates into a significant change in reflectivity and emission. In addition, as the wavelength increases, the surface now composed of wet snow grains and water looks physically and electrically smoother. This combination works together to reduce emission at this polarization and at low frequencies dramatically. Backscatter intensity was also reduced, reaching

its summer low (see Figure 9d). Much of this reduction is attributed to the creation of a more specular surface.

Frozen Surface Crust

During periods when long-wave heat loss dominates, such as under cloud free conditions, or when weather systems reduce air temperatures, the upper portion of the snowpack or snow-ice layer freezes, forming a crust. The wetness-depth diagram is provided in Figure 4b. An additional circumstance of interest is the mixture of cloud free and cloudy skies. Cloud free skies may produce regions with frozen surfaces; cloud-covered regions a few kilometers away may be under melt because of atmospheric radiation.

Freezing of a snow layer was limited to the upper 5 cm typically. The crust that forms has an important characteristic of snow crystal grain sizes which have enlarged to about 1.5-2 mm in diameter. The increase in size is attributed to the refreezing process. Emissivity at 37 and 94 GHz is reduced significantly because of scattering within this layer. The level of decrease in emission correlates with crust thickness. It is important to note the similarity in emission at 94 GHz between a frozen snow layer with enlarged ice crystals and snow-covered winter MY ice. At the lower frequencies the wavelengths are large compared to the size of the ice crystals in the thin crust, so scattering losses are small and the emission is not reduced. This scattering behavior can be understood by examining Rayleigh scattering of densely packed ice particles [Matzler, 1985].

The formation and disappearance of a frozen crust contributes to the large variability seen in the 37-GHz SMMR data during summer (Figure 2). In contrast, note that the 18-GHz signature is less dynamic. This is expected if the upper snow layer is undergoing melt-freeze cycling and not changes in ice concentration. The effect of frozen crust on backscatter is interesting. An increase in backscatter is expected for all ice types at frequencies above 5 GHz due to an enhanced volume scatter. Such an enhancement is not noted in these data. However, the relative contrast between ice types is expected to be preserved and is. The freezing of a thin layer of ice on open melt pools produces a significant increase in backscatter (observed in scatterometer data) for this feature and changes the floe's appearance in the radar imagery.

Summary

Emissions at 5-94 GHz and backscatter at 1-17 GHz were measured for a variety of sea ice scenes present in the summer at the marginal ice zone. Data were obtained with ship-, sled-, and helicopter-mounted instruments. Meltwater, snow thickness, the freezing of the upper few centimeters of a snow layer, and snowpack and ice surface morphology control the microwave signature of sea ice. During the first half of summer the high absorptivity of a thick, wet snow greatly reduces variability in sea ice microwave signatures.

Results during the peak of summer melt indicate that physical processes within one penetration depth in snow (less than a wavelength) are adequate to dominate the microwave response and mask surface ice features. This does not mean that all ice sheet information is lost during summer. Snow and meltwater are not distributed uniformly about a floe. The distribution of free water is often related to snow thickness and construction and to ice sheet type and deformation characteristics. These ice-type-related surface nonuniformities are not

well understood and are being examined to see if they produce identifiable two-dimensional microwave signature characteristics. The importance of surface features is illustrated by examining the cause of the large variance observed in the SMMR brightness temperature data shortly after midsummer. Our observations show a correlation with a peak in the areal extent of open water within floe boundaries on thick ice; the more open water, the lower the average brightness temperature. Note that prior to this, meltwater collected in subsurface pools did not affect the average scene microwave response. Future rises and falls in brightness temperature may coincide with melt-drain cycling. However, as the end of summer is approached, the contribution to the signature by a melt-induced reduction in ice concentration is expected to be much greater.

The emissions of FY and MY ice during summer were nearly identical. The passive microwave data show an ability to map the spatial distribution of wetness in the upper layers in the snowpack within floe boundaries. The emission at 95 GHz was dramatic in its response to the freezing and melting of the upper few centimeters of the snow layer.

Multiyear and FY ice backscatter underwent multiple contrast reversals. During winter and late spring, MY ice cross sections are larger than those of FY ice due to strong volume scatter from the upper p.rtion of the ice sheet. Wet snowpack, with a maximum seasonal thickness during early summer, causes similar signatures for each of these ice types. By midsummer, ThFY ice backscatter is stronger due to an increased small-scale roughness from a superimposed ice layer which forms at the snow-ice interface and a snow thickness reduced by melt. After midsummer the backscatter contrast again reverses (at the lower frequencies). The ThFY roughness elements are smoothed by melt, and MY ice continues to have a complex surface topography. Based upon the results to date, operation at frequencies of about 5 GHz may be optimal for the summer MIZ.

Results suggest that the ability to discriminate between the various ice types during summer is closely linked to our ability to continuously monitor the distribution of wetness features within floe boundaries. There is synergism in using both active and passive microwave sensors when wetness features are fully developed; the radiometer senses the scene wetness and volume scattering properties, and the radar senses scene wetness, volume scattering properties, and roughness.

REFERENCES

Campbell, W. J., R. O. Ramseier, W. F. Weeks, and P. Gloerson. An integrated approach to the remote sensing of floating ice, in *Proceedings Third Canadian Symposium on Remote Sensing*, pp. 36–72. Canadian Aeronautics and Space Institute, Ottawa, Ont., 1975.

Gogineni, S. P., R. G. Onstott, R. K. Moore, Y. S. Kim, and D. B. Bushnell, Mobile microwave spectrometer for backscatter measurements, *Microwaves Radio Frequency*, 23, 156–166, 1984.

Gray, A. L., R. K. Hawkins, C. E. Livingstone, L. Drapier Arsenault,

and W. M. Johnstone, Simultaneous scatterometer and radiometer measurements of sea-ice microwave signatures, *IEEE J. Oceanic Eng.*, OE-7(1), 20–32, 1982.

Grenfell, T. C., and A. W. Lohanick, Temporal variations of the microwave signatures of sea ice during the late spring and early summer near Mould Bay NWT, *J. Geophys. Res.*, 90(C3), 5063–5074, 1985.

Hallikanen, M., F. T. Ulaby, and M. Abdelrazik, The dielectric behavior of snow in the 3 to 37 GHz range, in *Proceedings IGARSS'84, Spec. Publ. ESA SP-215*, pp. 169–174, European Space Agency, Paris, 1984.

Johannessen, O. M., and D. Horn (Eds.), MIZEX 84 summer experiment PI preliminary reports, *MIZEX Bulletin V, Spec. Rep. 84-29*, 176 pp., U.S. Army Cold Reg. Res. and Eng. Lab., Hanover, N. H., 1984.

Kim, Y. S., R. G. Onstott, and R. K. Moore, Effect of snow cover on microwave backscatter from sea ice, *IEEE J. Oceanic Eng.*, OE-9(5), 383–388, 1984a.

Kim, Y. S., R. K. Moore, and R. G. Onstott, Theoretical and experimental study of radar backscatter from sea ice, *Rep. 331-31*, 168 pp., Remote Sensing Lab., Univ. of Kans., Lawrence, 1984b.

Livingstone, E. C., R. K. Hawkins, A. L. Gray, K. Okamoto, T. L. Wilkinson, S. Young, L. Drapier Arsenault, and D. Person, Classification of Beaufort Sea ice using active and passive microwave sensors, in *Oceanography From Space*, edied by J. F. R. Gower, pp. 813–826, Plenum, New York, 1981.

Lohanick, A. W., and T. C. Grenfell, Variations in brightness temperature over cold first-year sea ice near Tuktoyaktuk, Northwest Territories, *J. Geophys. Res.*, 91(C4), 5133–5144, 1986.

Matzler, C., Interaction of microwaves with natural snow cover, Habilitationsschrift, 152 pp., Inst. of Appl. Phys., Univ. of Bern, Bern, Switzerland, 1985.

Matzler, C., R. O. Ramseier, and E. Svendsen Polarization effects in sea-ice signatures, *IEEE J. Oceanic Eng.*, OE-9, 333–338, 1984.

MIZEX Group, MIZEX East 83 84: The summer marginal ice zone program in the Fram Strait/Greenland Sea, *Eos Trans. AGU, 67*, 513–517, 1986.

NORSEX Group, The Norwegian remote sensing experiment in a marginal ice zone, *Science, 220*(4599), 781–787, 1983.

Onstott, R. G., and S. P. Gogineni, Active microwave measurements of Arctic Sea ice under summer conditions, *J. Geophys. Res.*, 90(C3), 5035–5044, 1985.

Onstott, R. G., R. K. Moore, S. Gogineni, and C. V. Delker, Four years of low altitude sea ice broadband backscatter measurements, *IEEE J. Oceanic Eng.*, OE-7(1), 44–50, 1982.

Ramseier, R. O., and D. J. Lapp (Eds.), Proceedings Final, SURSAT Ice Workshop, 563 pp., SURSAT Project Office Report, Atmos. Environ. Ser., Ottawa, Ont., Canada, 1980.

Tiuri, M., A. Sihvola, E. Nyfors, and M. Hallikainen, The complex dielectric constant of snow at microwave frequencies, *IEEE J. Oceanic Eng.*, OE-9(5), 377–382, 1984.

Tucker, W. B., III, A. J. Gow, and W. F. Weeks, Physical properties of summer sea ice in the Fram Strait, *J. Geophys. Res.*, this issue.

T. C. Grenfell, Department of Atmospheric Sciences, University of Washington, Mail Stop AK-40, Seattle, WA 98195.

C. A. Luther, Office of Naval Research, Arctic Sciences, Code 1125AR, 800 N. Quincy Street, Washington, DC 22217.

C. Matzler, Institute of Applied Physics, University of Bern, Sidlerstrasse 5, CH-3012, Bern Switzerland.

R. G. Onstott, Environmental Research Institute of Michigan, Advance Concepts Division, Radar Science Laboratory, P. O. Box 8618, Ann Arbor, MI 48107.

E. A. Svendsen, Geophysical Institute and Nansen Ocean and Remote Sensing Center, University of Bergen, N-5037 Solheimsvik, Norway.

MICROWAVE PROPERTIES OF SEA ICE IN THE MARGINAL ICE ZONE

Robert G. Onstott and Richard W. Larson

Radar Science Laboratory
Environmental Research Institute of Michigan
Ann Arbor, Michigan USA

ABSTRACT

Measurements were made during the 1984 Marginal Ice Zone Experiment to document the active microwave properties of summer sea ice. Backscatter data were acquired at frequencies from 1 to 17 GHz, at angles from 0 to 70 degrees from vertical, and with like and cross antenna polarizations. Results show that melt-water, snow thickness, snowpack morphology, snow surface roughness, ice surface roughness and deformation characteristics are the fundamental scene parameters which govern the summer sea ice backscatter response. For example, a thick, wet snow cover will dominate the backscatter response and mask any ice sheet features below. However, snow and melt-water are not distributed uniformly and the stage of melt may also be quite variable. These non-uniformities which are related to ice type are not necessarily well understood and produce unique microwave signature characteristics.

I. INTRODUCTION

Near-surface calibrated radar backscatter data were obtained of Arctic sea ice during June and July of 1984 as part of the Marginal Ice Zone Experiment (MIZEX-84)[1] in Fram Strait, a region located between Spitzbergen and Greenland. These measurements were made as part of a remote sensing effort whose purpose was the simultaneous collection of near-surface and airborne, active and passive microwave signature data in conjunction with the study of the key physical and electrical properties of the major summer sea-ice scenes in the study area. The role of the near-surface data collection effort was to catalog the summer MIZ scattering coefficients, to relate specific sea ice features with their microwave response, to support the interpretation of aircraft and satellite data products and to provide electromagnetic scene-modeling inputs to further advance the understanding of the interaction processes which govern the sea ice backscatter response. Overall, remote sensing efforts were directed to the development of the ability to unambiguously convert microwave signal information into critical geophysical parameters. Solid ocean descriptions of key

interest include: (a) ice type, (b) ice thickness, (c) ice concentration, (d) ice floe size, (e) snow and ice-sheet physical and electrical properties, (f) deformation characteristics, and (g) kinematics.

II. EXPERIMENT DESCRIPTION

Radar scattering cross-section data were acquired using a multi-frequency, multi-polarization and multi-angle-of-incidence calibrated radar (scatterometer)[2]. This system was operated from both helicopter and ship. Key radar parameters included frequencies of 1.5, 5.2, 9.6, 13.6 and 16.6 GHz; viewing angles from 0 to 70 degrees from vertical; and antenna polarization capabilities of HH, VV and HV (H = horizontal, V = vertical; the first letter identifies the transmit polarization and the second the receive polarization). Scenes investigated included small-to-vast multiyear (MY), thick first-year(TFY), medium first-year(MFY) and thin first-year(ThFY) ice. Floes chosen for microwave observations were visually representative of ice types in the MIZ and the adjacent pack ice region. General ice condition descriptions, oblique photography, and detailed descriptions of snowpack and ice sheet were made. Sea ice characterizations included the description of the construction of the snowpack, snow thickness, snow density, snow wetness, the measurement of snow-ice complex dielectric constants, ice sheet physical-chemical properties, ice thickness, and surface and sub-surface roughness. Ice thicknesses ranged from 30 to well over 300 cm. Snowpack was typically heavy and wet with depths up to 60 cm on many of the multiyear ice floes. Melt-water collected creating a slush at the snow-ice interface on flat ice and in sub-surface pools in depressed areas. Ice, snow and air temperatures were typically within a couple ⚡ degrees of 0 C. The snow cover on thin first-year, medium first-year, thick first-year and multiyear ice was typically 2-6 cm, 6-15 cm, 6-20 cm, and 15 - 65 cm, respectively. Snow crystal sizes of 1-2 mm diameter were typical. First-year ice and advanced areas of melt on MY ice showed 3-5 mm diameter crystals with occassional ice crystal globes exceeding a diameter of 1 cm. Salinities in the upper layer of the ice sheet were typically much less than

one part per thousand for MY and around two parts per thousand in the case of FY. During the experiment period the snowpack and ice sheets underwent a transition from early-summer to mid-summer melt conditions. For example, the salinity in the upper ice sheet decreased in the case of FY, but increased to about .3 parts per thousand for MY [3].

III. PRELIMINARY RADAR BACKSCATTER RESULTS

Two questions were central to the microwave investigation during MIZEX: a) what is the influence of the MIZ and summer-melt on sea ice properties and, b) how do these changes affect the ability to discriminate ice from water and among ice types. Results show that the MIZ microwave signatures are greatly influenced by summer-melt. In addition, there is excellent correlation between the evolving sea ice summer scene and its microwave signatures. Scene parameters which have been found to have the greatest impact on active microwave signatures are: thickness of wet snowpack, distribution of melt-water about the ice sheet, floe topography, presence and magnitude of rough surface scatterers, and the increased dielectric constant composed of regions of mixtures of ice, snow, and water, such as strings of hummocks and surface and subsurface melt pools. It has yet to be determined if the MIZ contibutes to changes in the summer microwave signature, other than to promote melt, and by moderating the population of melt-pools because of regional dynamic forces which work to reduce floe size.

In the MIZ it is important to determine ice extent and percent ice coverage. These data are inputs into a variety of geophysical models. Results show that there is significant contrast from 10 to 15 dB between ice and water when operating at 1.5, 5.2, 9.6, 13.6 and 16.6 GHz, HH-polarization and with angles about 25 degrees. The 5.2 GHz backscatter response (See Figure 1) shows that this contrast exists over the range of angles which will be used by spaceborne synthetic aperture radar. It is expected that the angular trends at other frequencies will be similar. These data are available and will be assembled in the future.

Radar backscatter cross-sections of three major ice scenes acquired during mid-summer peak melt are shown in Figures 1, 2 and 3. These angular responses are of MY, MFY, and ThFY which have thicknesses of 275, 105 and 75 cm, respectively. Snow depth ranges are 2-10, 5-14, and 20-43 cm, respectively. Snow wetness of 5% by volume results in microwave penetration depths of about 1-2 m at 1.2 GHz, 5-10 cm at 5.2 GHz, 3-5 cm at 9.6 GHz, 2-3 cm at 13.6 GHz, and 1-2 cm at 16.6 GHz.

Transects across a large 3 km floe composed of MY and ThFY are shown in Figure 4 for frequencies from 5 to 17 GHz. Contrast between the ice types is 6 dB at 1.5 GHz, 3.6 dB at 5.2 GHz, and about 1.7 dB at frequencies from 10 to 17 GHz. The physical properties most responsible for the cross-section difference are the surface and subsurface roughness of the ThFY. Roughness elements of 3 cm have superimposed ice and firnification process origin.

It is interesting to note that a balance exists between snow absorptivity and the scales of roughness at frequencies above 10 GHz; while at the lower frequencies reduced absorptivity results in increased backscatter. Examination of the variance of the backscatter return with frequency is also instructive (See Figure 4 and Table 1). The effect of a uniformly distributed wet snowpack on MY ice which does have meter or greater surface relief is to mask these features. This ability increases with increasing frequency as expected. In this example, most features were well masked when operating above 10 GHz and there is almost no hint of any surface features at 16.6 GHz. In addition, as frequency is reduced there is an exponential-like increase in scene variance.

The angular response at 5.2 GHz of MY, MFY, ThFY and water is shown in Figure 1. MFY has a slightly thicker ice sheet and snow layer than ThFY, but similar surface roughness. The angular responses of MY and MFY are shown as a function of frequency in Figures 2 and 3. There is a modest increase in cross-section with increasing frequency, but not as quickly as the square of the wavelength which means that there are similar roughness scales at all wavelengths. Comparing the responses of MY and MFY suggests that 6 or more centimeters of snowpack is all that is required when operating at frequencies above 5 GHz to effectively mask surface ice features. Note that the angular responses of these ice types at these frequencies are nearly identical. The importance here is the determination of the number of penetration depths of snow necessary before there is an effective mask. Note that penetration depth is a calculation of when a distance is traveled over which transmitted power is reduce by 1/e. The scene beyond this depth still contributes to the backscatter response. In the case of the sea ice scene described here, the contribution below one penetration depth appears minor. During this period, frequencies of 1 to 6 GHz are most applicable for use in discriminating these ice types.

Figure 5 was created to demonstrate the effect increasing snow wetness has on the contribution of surface roughness to the backscatter response. A wetness of 5% by volume increases the dielectric constant from 1.9 to 2.5 for snow with a density of about .5 gm/cubic-cm. Using an rms roughness of .3 cm and a correlation length of 1.8 cm, represents roughness of a typical smooth snow scene, surface scattering responses were calculated for 1.2 and 10 GHz and dielectric constants of 1.8 and 2.5. A Kirchoff surface scatter model with an exponential correlation length, which has been validated as especially applicable to FY ice, was used for demonstration purposes. Results suggest that surface scatter will increase about 2-3 dB for all frequencies. This is basically due to an increased Fresnel reflection coefficient. Additionally, snow of this roughness accounts well for the general backscatter level measured at 10 GHz. The signatures at 1-2 GHz are very weak at this surface roughness scale. This agrees with observations of weak returns when the ice sheet is flat and the snow is smooth. Returns are strongest in areas with significant ice features with tilted surfaces.
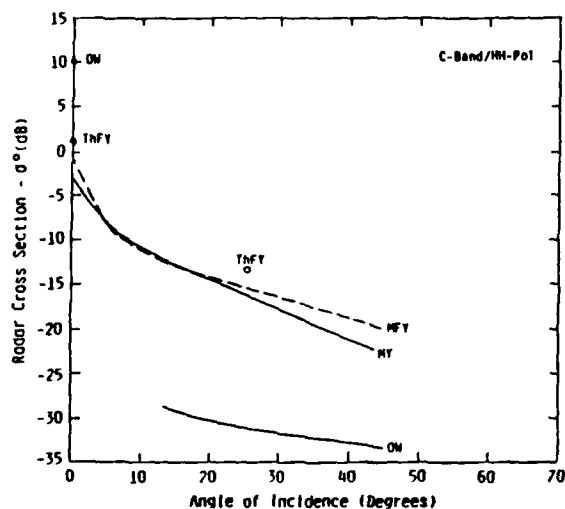
2

Figure 1. Radar scattering cross-section angular response of thin first-year (ThFY), medium first-year (MFY) and multiyear (MY) sea ice and open water (OW) between floes in the MIZ at 5.2 GHz and HH-polarization (5 July, MIZEX-84).

Figure 2. Radar scattering cross-section angular response of multiyear sea ice at 1.5 (L), 5.2 (C), 9.6 (X), 13.6 (K1), and 16.6 (K2) GHz and HH-polarization (5 July, MIZEX-84).
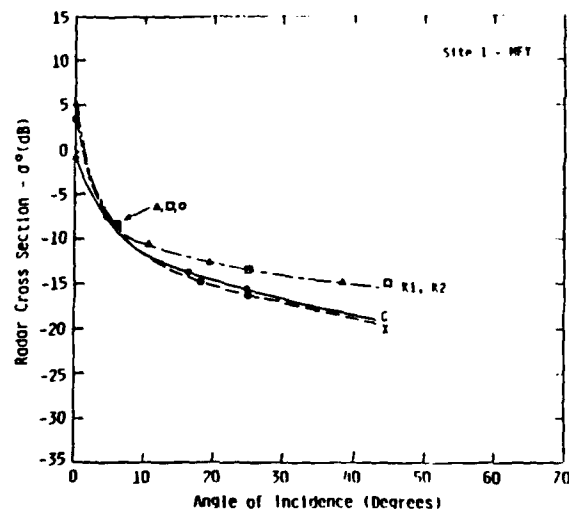
Figure 3. Radar scattering cross-section angular response of medium first-year sea ice at 5.2 (C), 9.6 (X), 13.6 (K1) and 16.6 (K2) GHz and HH-polarization (5 July, MIZEX-84).
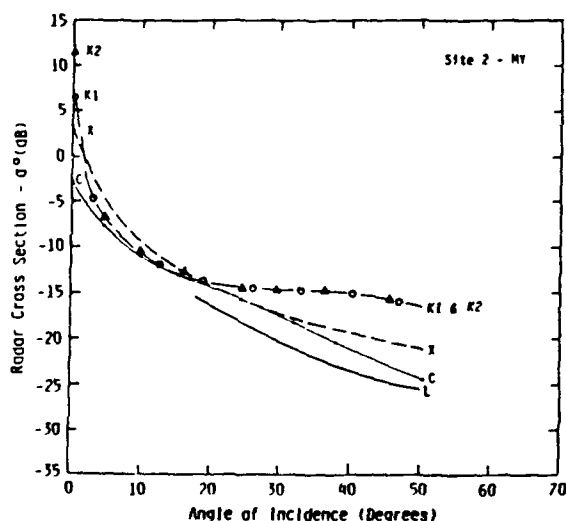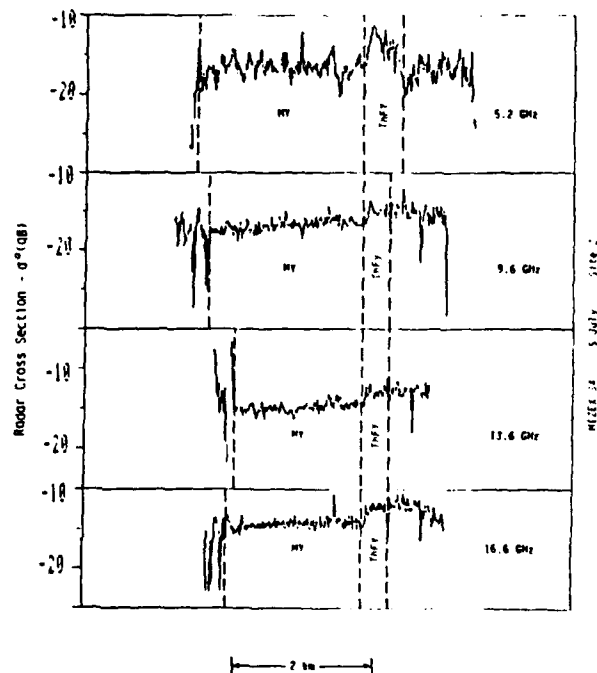

Figure 4. Radar scattering cross-section transects across a large multiyear (MY) and thin first-year (ThFY) sea ice flow at 5.2, 9.6, 13.6 and 16.6 GHz, an incidence angle of 25 degrees and HH-polarization (5 July, MIZEX-84).

3

TABLE 1.

Backscatter cross-sections of multiyear
and thin first-year sea ice at HH-
polarization and 25 degree incidence angle
for 5 July (MIZEX-84)

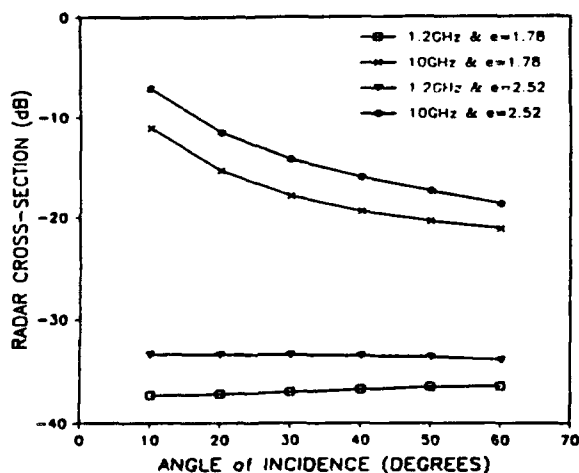| FREQ	MEAN		VARIANCE	
-GHz-	MY	ThFY	MY	ThFY
5.2	-16.7	-13.1	1.5	2.1
9.6	-16.5	-14.8	1.1	.67
13.6	-14.6	-12.9	.77	.64
16.6	-14.1	-12.3	.75	.86

Figure 5. Radar cross-sections of surface
scatter from wet (e = 2.52) and dry
(e = 1.78) snowpack at 1.2 and 10 GHz
at HH-polarization as derived from a
Kirchoff surface scatter model with
an exponential correlation length.

IV. SUMMARY

Radar backscatter measurements were made at
frequencies from 1 to 17 GHz of a variety of sea
ice scenes present in the summer at the marginal
ice zone. Data were obtained with a ship and
helicopter based scatterometer. Results indicate
that melt-water, snow thickness, snowpack and
ice surface morphology control the microwave
signatures of sea ice. Results during the peak
of the summer melt indicate that one penetration
depth of snow effectively dominates the
microwave response and masks surface ice
features. This may represent as little as 6 cm
of snow when operating at 10 GHz when the snow
has a wetness of 5% by volume. This does not
necessarily mean that all ice sheet information
is lost during summer. Snow and melt water are
not distributed uniformly about a floe. During
MIZEX 83 and 84, depth of snow cover and stages
of melt correlated well with ice type. Medium
and thin first-year ice have snow covers
typically less than 15 cm and enhanced surface
roughness. Hence, the knowledge of the spatial
distribution of microwave returns is critical.

It also follows that operation at frequencies
about 5 GHz will be optimal for the summer MIZ.
Based upon these results it is expected that the
ERS-1 ESA C-band satellite SAR has the potential
to discriminate ice types during both winter
and summer. In addition, use of multiple
frequencies will allow information from
different depths and ice features to be
retrieved.

REFERENCES

1. Johannessen O M and D Horn (Ed.) 1984,
   MIZEX 84 Summer Experiment PI Preliminary
   Reports (MIZEX Bulletin V), U.S. Army Cold
   Regions Research and Engineering Laboratory,
   CRREL Special Report, 84-29.

2. Onstott R G, R K Moore, S Gogineni Y S Kim
   and D B Bushnell, "Helicopter-Borne
   Scatterometer", Remote Sensing Laboratory
   Technical Report 331-24, University of Kansas
   Centre for Research, Inc., Lawrence Kansas,
   October 1982.

3. Tucker W B III, A J Gow and W F Weeks, 1985,
   Physical Properties of Sea Ice in the
   Greenland Sea, U.S. Army Cold Regions
   Research and Engineering Lab, POAC 6-13
   Sept. 1985.

A SAR/SCAT INTERCOMPARISON OF MICROWAVE SIGNATURES OF ARCTIC SEA ICE

Robert G. Onstott and Robert A. Shuchman

Radar Science Laboratory
Environmental Research Institute of Michigan (ERIM)

ABSTRACT

Active microwave and physical property measurements were made of Arctic sea ice in the marginal ice zone during the summer of 1984. Results of an intercomparison of data acquired by aircraft synthetic aperture radar and helicopter-based scatterometer indicate that early-to-mid summer sea ice microwave signatures are dominated by snowpack characteristics. Measurements made at 1-17 GHz show the greatest contrast between thin first-year and multiyear sea ice occurs when operating between 5 and 10 GHz.

I. INTRODUCTION

Measurements of the microwave signatures of Arctic sea ice were made during June and July of 1984 in the Fram Strait of the Greenland Sea in an area to the north and west of Spitzbergen as part of the Marginal Ice Zone Experiment (MIZEX) [1]. In this investigation, microwave signatures were acquired from the start of summer until a time immediately after peak melt. An important aspect of MIZEX was the emphasis placed on the comparison of coincident active and passive aircraft, satellite, and surface-based in-situ microwave observations with intensive ice characterization measurements.

II. BACKGROUND

The goals of the MIZEX remote sensing program are (1) to better understand sea ice scattering and emission processes, (2) to better interpret present and future remote sensing observations, (3) to define operating parameters as well as predict performance of future air- and space-borne sensors, and (4) to develop algorithms to convert microwave signal data into geophysical processes information. In the MIZ as well in the central Arctic the geophysical information of greatest interest include: (a) ice age, type, and thickness; (b) ice concentration; (c) floe size; (d) ice sheet and snowpack physical properties; and (e) deformation characteristics.

III. ICE SCENE DESCRIPTION

During MIZEX-84 the major summer sea ice scenes were multiyear (MY), thick first-year (TFY), medium first-year (MFY), and thin first-year (ThFY). Multiyear is sea ice which has survived at least one summer's melt. It has an ice thickness greater than 2.5 meters and during MIZEX-84 a snowpack thickness which ranged from 35 to 60 cm. Thick first-year is ice which began growing during the fall and has a thickness greater than 120 cm and a snowpack thickness of 25-35 cm. Medium first-year represents a class of ice which began growing late in the season. It has a thickness of 70 to 120 cm with a 10-15 cm snowpack. Thin first-year ice began growing very late in the season and therefore has only an ice thickness of 30 to 70 cm and a snowpack thickness of 2-6 cm. Note that snow thickness and the various ice types observed in MIZEX-84 have a high degree of correlation.

Ice found in the MIZEX study area exhibits considerable deformation due to dynamic forces experienced prior to entering the Fram Strait. Deformation characterisitics include a significant number of ridges, rubble, increased surface and sub-surface topography, and increased floe thickness. Other features of significance on multiyear and thick first-year ice are regions of surface and sub-surface meltwater pools, and areas of flat ice and mounds.

IV. EXPERIMENT DESCRIPTION

During this investigation the SAR, operating at both 1.2 and 9.4 GHz, provided synoptic MIZ coverage by producing 80 km x 80 km mosaics at 3 meter pixel resolution. The SAR data was collected at incident angles from 30 to 70 degrees. The microwave measurements made by the scatterometer are at a similar resolution, an extended range of viewing angles (0 to 70 degree incident angles) and at frequencies of 1.5, 5.2, 9.6, 13.6 and 16.6 GHz. Physical property information acquired included the physical description of the snowpack and ice sheet, snow wetness, surface roughness, salinity profiles, and dielectric

constants.

IV. DISCUSSION OF RESULTS

During summer, the state of the snowpack becomes especially important. Percolation of snow melt-water onto the ice sheet creates either a rough superimposed ice- or a slush-layer depending on environmental conditions. Furthermore, during the first half of the summer, the high absorptivity of a wet snowpack greatly reduces the overall variability in sea ice microwave signatures.

The ability of a wet snow layer to temporarily mask ice sheet features during summer has been reported previously in other regions [2,3]. The thickness of the layer of wet snow required to mask sub-surface topography may be estimated by taking two or three microwave penetration depths, found as a function of snow wetness and frequency (see Figure 1). It is important to note that the distance traveled into wet snow before complete absorption is easily two orders of magnitude less than in dry snow.
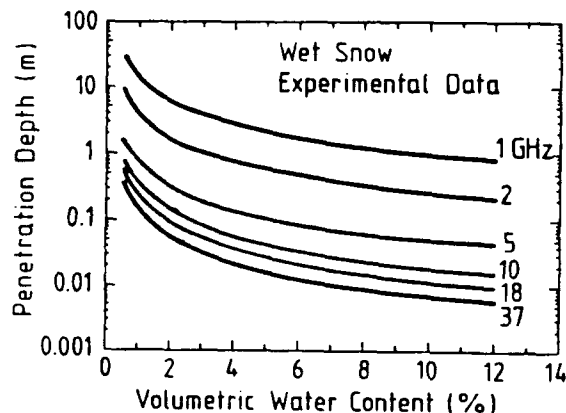

Figure 1. Penetration depth for wet snow between 1 GHz and 37 GHz, calculated from experimental data [4,5]

Additionally, there is a significant reduction in the ability to penetrate either wet or dry snow as frequency increases and as snow acquires a very modest wetness (for example, 2-4% wetness by volume). Hence during early to mid summer and at frequencies above 10 GHz much of the information about homogeneous ice scenes is derived from the physical and electrical properties in the snowpack's top several centimeters. The freezing of the upper few centimeters of the snowlayer, and the way melt water accumulates on the ice sheet which is controlled by the large scale topography, also contribute to an ice sheet's microwave signature.

In the case of thinner ice, the increased small scale-surface roughness due to a superimposed ice layer at the snow-ice interface is a key contributor to the backscatter cross section.

An inventory of sea ice signatures in the MIZ has been made and includes: (a) the mixture of brash ice and small floes; (b) refrozen ThFY leads; (c) MFY ice, often found as one of the ice types in large floes; (d) regions of very heavy snow cover found in severely deformed areas on MY or TFY ice; (e) pressure ridges; (f) sub-surface melt pools; and (g) open water either in surface melt pools or between floes.

Relative radar backscatter cross section ratios have been calculated using both SAR and scatterometer data and are presented in Table 1. This table utilized data collected in late June and thus represents the start of the peak melt period. The cross section ratios are presented in dB and referenced to open water. Examination of Table 1 shows significant contrast between all the MIZ ice types and open water. The SAR images further illustrate the Table 1 results. Individual ice floes are clearly delineated on both the X- and L-band data.

The L-band (1.2 GHz) ratios indicate brash ice can be distinguished from the other ice and snow catagories. Thick snow cover also has a unique cross section signature.

The C-band (5.3 GHz) ratios confirm that operation at the higher microwave frequencies is better for differentiating first year from multiyear ice. Thin first-year ice can also be differentiated from medium first-year ice. The European Space Agency (ESA) will launch a free-flyer (ERS-1) SAR satellite that will operate at C-band.

The X-band (9.4 GHz) data yields results similar to those at C-band. Brash ice can be differentiated from multiyear, but not from first-year. However, examination of SAR X-band images shows that brash ice is separable from first-year based on its shape and location (i.e., context).

The contrast between first-year and multiyear ice decreases at 13.6 and 16.6 GHz. This appears to be due to an increased absorptivity of the snow which results in the snow/ice roughness at the snow/sea ice interface to be less of a contributor.

V. SUMMARY

Microwave measurements were made at 1.2, 5.3, 9.4, 13.6 and 16.6 GHz of a variety of snow and ice types present in the summer at the marginal ice zone. The measurements which were obtained by a SAR and helicopter-based scatterometer during the peak of the summer melts indicated that the snow cover dominates the radar backscatter return. At frequencies below 9.4 GHz (X-band) the slush or

superimposed fresh water ice layer that forms at the snow/ice interface is important in determining the received backscatter. Since in MIZEX-84 the amount of snow cover and type of snow correlated to individual ice type, it was not surprising that the 5-10 GHz data discriminated the thinner first-year from multiyear ice. The C-band (5.3 GHz) frequency which will be utilized on the ERS-1 ESA satellite SAR should do a respectable job differentiating first-year from multiyear ice types within the MIZ.

The backscatter ratios further suggest that a multi-frequency approach would provide additional information on ice and snow types. This is due to increased penetration at the lower frequencies and the roughness match of the multiple wavelengths with constituents within the snow and ice media.

Table 1. Radar Backscatter Cross-Section Ratios at 35° Incident Angles for Summer Sea Ice

Scene	-GHz-				
	1.2	5.3	9.4	13.6	16.6
Brash	11.0	12.0	13.5	---	---
ThFY	7.5	11.5	15.0	15.0	15.0
MFY	7.5	9.0	13.5	14.0	14.0
HV·SC	5.0	7.0	11.0	13.5	13.5
PR	7.0	---	10.0	---	---
OW	.0	.0	.0	.0	.0
MY·SC	6.5	8.0	11.0	13.5	12.5
MY·HV·MF	10.0	11.0	14.5	15.5	14.5

Ratios are in dB and have been referenced to open water.

ThFY - Thin First-Year Ice
MFY - Medium First-Year
HV·SC - Heavy Snow Cover
PR - Pressure Ridge
OW - Open Water
MY SC - Multiyear with Snow Cover
MY·HV·MP - Multiyear with Numerous Melt Pools

REFERENCES

1. Johannessen, O.M. and D. Horn (Ed.) 1984, MIZEX 84 Summer Experiment PI Preliminary Reports (MIZEX Bulletin V), U.S. Army Cold Regions Research and Engineering Laboratory, CRREL Special Report, 84-29.

2. Gray, A.L., R.K. Hawleing, C.E. Livingstone, L. Drapier Arsenault, and W.M. Johnstone, "Simultaneous Scatterometer and Radiometer Measurements of Sea-Ice Microwave Signatures", J. Oceanic Engr., OE-7, No. 1, pp. 20-32, 1982.

3. Onstott, R.G. and S.P. Gogineni, "Active Microwave Measurements of Arctic Sea Ice Under Summer Conditions", J. Oceanic Engr. OE-9, pp. 383-388, 1984.

4. Hallikanen, M., F.T. Ulaby and M. Abdelrazik, "The Dielectric Behavior of Snow in the 3 to 37 GHz Range, Proc. IGARS'84, ESA SP-215, pp. 169-174, Strasbourg, August 27-30, 1984.

5. Tiuri, M., A. Sihvola, E. Nyfors, and M. Hallikainen, "The Complex Dielectric Constant of Snow at Microwave Frequencies", J. Oceanic Engr., OE-9, No. 5, pp. 377-382, 1984.

AN INTER-SENSOR COMPARISON OF THE MICROWAVE SIGNATURES OF ARCTIC SEA ICE

MIZEX-84 Remote Sensing Special Topic Working Group*

Robert G. Onstott, Chairman
Radar Science Laboratory
Environmental Research Institute of Michigan
Ann Arbor, Michigan

ABSTRACT

Active and passive microwave and physical property measurements were made of Arctic sea ice in the marginal ice zone during the summer of 1984. Preliminary results of an intercomparison of data acquired by an aircraft synthetic aperture radar, a passive microwave image and a helicopter-mounted scatterometer indicate that early-to-mid summer sea ice microwave signatures are dominated by snowpack characteristics. Measurements show that the greatest contrast between thin first-year and multiyear sea ice occurs when operating actively between 5 and 10 GHz. Significant information about the state of melt of snow and ice is contained in both the active and passive microwave signatures.

I. INTRODUCTION

Measurements of the microwave signatures of Arctic sea ice were made during June and July of 1984 in the Fram Strait of the Greenland Sea in an area north and west of Spitzbergen as part of the Marginal Ice Zone Experiment (MIZEX) [1]. In this investigation, microwave signatures were acquired from the start of summer until a time immediately after peak melt. An important aspect of MIZEX was the emphasis placed on the comparison of coincident active and passive aircraft, satellite, and surface-based in-situ microwave observations in conjunction with intensive ice characterization measurements.

The goals of the MIZEX remote sensing program are (1) to better understand sea ice scattering and emission processes, (2) to better interpret present and future remote sensing observations, (3) to define operating parameters as well as predict performance of future air- and space-borne sensors, and (4) to develop algorithms to convert microwave signal data into geophysical processes information. In the MIZ, as well as in the central Arctic, the geophysical information of greatest interest includes: (a) ice age, type, and thickness; (b) ice concentration; (c) floe size; (d) ice sheet and snowpack physical properties; and (e) deformation characteristics.

II. ICE SCENE AND EXPERIMENT DESCRIPTION

During MIZEX-84 the major summer sea ice scenes were multiyear (MY), thick first-year (TFY), medium first-year (MFY), and thin first-year (ThFY). Multiyear is sea ice which has survived at least one summer's melt. It has an ice thickness greater than 2.5 meters and during MIZEX-84 a snowpack thickness which ranged from 35 to 60 cm. Thick first-year is ice which began growing during the fall and has a thickness greater than 120 cm and a snowpack thickness of 25-35 cm. Medium first-year represents a class of ice which began growing late in the season. It has a thickness of 70 to 120 cm with a 10-15 cm snowpack. Thin first-year ice began growing very late in the season and therefore has only an ice thickness of 30 to 70 cm and a snowpack thickness of 2-6 cm. Note that snow thickness and the various ice types observed in MIZEX-84 have a high degree of correlation.

Ice found in the MIZEX study area exhibits considerable deformation due to dynamic forces experienced prior to entering the Fram Strait. Deformation characterisitics include a significant number of ridges, rubble, increased surface and sub-surface topography, and increased floe thickness. Other features of significance on multiyear and thick first-year ice are regions of surface and sub-surface meltwater pools, and areas of flat ice and mounds.

During this investigation a synthetic aperture radar (SAR) operating at 1.2 and 9.4 GHz with 3 meter resolution and passive microwave imager (PMI) operating at 19, 37, 90 and 94 GHz with up to 16 meter resolution, if flown at low levels, provided synoptic MIZ coverage by producing 80 km x 80 km mosaics. The SAR data were collected at incident angles from 30 to 70 degrees. The microwave measurements made by the scatterometer are at a similar resolution, an extended range of viewing angles (0 to 70 degree incident angles) and at frequencies of 1.5, 5.2, 9.6, 13.6 and 16.6 GHz. Passive microwave images were assembled by scanning about nadir. Satellite imagery consisted of NIMBUS-7 SMMR (passive

1

microwave) and NOAA-7 AVHRR (visual and infrared). Nimbus-7 operates at 6.6, 10.7, 18, 21, and 37 GHz with coverage of the entire Fram Strait. Aircraft passive microwave profiles were also acquired at these frequencies. Surface-based radiometer measurements were made at angles from 20 to 60 degrees and at 6, 10, 18, 37, and 90 GHz. Physical property information includes the physical description of the snowpack and ice sheet, snow wetness, surface roughness, salinity profiles, and dielectric constant values.

III. DISCUSSION OF RESULTS

During summer, the state of the snowpack becomes especially important. Percolation of snow melt-water onto the ice sheet creates either a rough superimposed ice- or slush-layer depending on environmental conditions. Furthermore, during the first half of the summer, the high absorptivity of a wet snowpack greatly reduces the overall variability in sea ice microwave signatures.

The ability of a wet snow layer to temporarily mask ice sheet features during summer has been reported previously in other regions [2,3]. The thickness of the layer of wet snow required to mask sub-surface topography may be estimated by taking two or three microwave penetration depths, found as a function of snow wetness and frequency (see Figure 1). It is important to note that the distance traveled into wet snow before complete absorption is easily two orders of magnitude less than in dry snow.
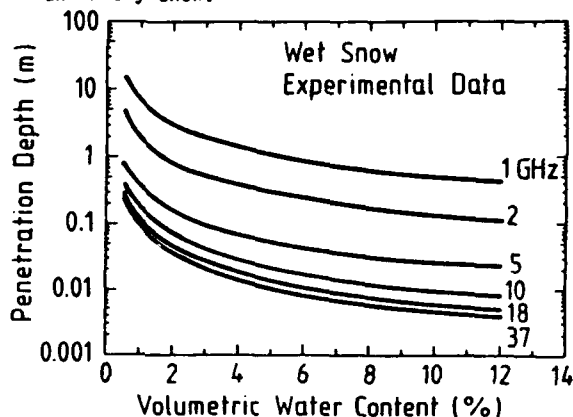

Figure 1. Penetration depth for wet snow between 1 GHz and 37 GHz, calculated from experimental data.

Additionally, there is a significant reduction in the ability to penetrate either wet or dry snow as frequency increases and as snow acquires a very modest wetness (for example, 2-4% wetness by volume). Hence during early to mid summer and at frequencies above 10 GHz much of the information about homogeneous ice scenes is derived from the physical and electrical properties in the snowpack's top several centimeters. The freezing of the upper few centimeters of the snowlayer, and the way melt water accumulates on the ice sheet which is controlled by the large scale topography, also contribute to an ice sheet's microwave signature.

In the case of thinner ice, the increased small scale-surface roughness due to a

superimposed ice layer at the snow-ice interface is a key contributor to the backscatter cross section.

On June 29 SAR (ERIM CV-580) "daytime" and PMI (NRL P-3) "nighttime" data were collected over an area about the MIZEX drift ship. In Figure 2 a subset of these data is shown with an aerial photograph for the visual intercomparison of specific ice features.

An inventory of sea ice signatures in the MIZ has been made and includes: (a) the mixture of brash ice and small floes; (b) refrozen ThFY leads; (c) MFY ice, often found as one of the ice types in large floes; (d) regions of very heavy snow cover found in severely deformed areas on MY or TFY ice; (e) pressure ridges; (f) sub-surface melt pools; and (g) open water either in surface melt pools or between floes.

Relative radar backscatter cross section ratios and brightness temperatures from measurements made at the start of the peak melt period have been calculated using SAR, scatterometer and PMI data and are presented in Table 1. The cross section ratios are presented in dB and referenced to open water. The brightness temperatures are referenced to nadir.

Table 1.
Radar Backscatter Cross-Section Ratios at 35°
Incident Angle and Brightness Temperatures
at 0° Incidence Angle for Summer Sea Ice

Scene \ GHz	Backscatter Cross-Section Ratios (dB)					T_B (K)
	1.2	5.3	9.4	13.6	16.6	90.0
Brash	11.0	12.0	13.5	----	----	205
ThFY	7.5	11.5	15.0	15.0	15.0	200
MFY	7.5	9.0	13.5	14.0	14.0	184
HV SC	5.0	7.0	11.0	13.5	13.5	186
PR	7.0	----	10.0	----	----	----
OW	.0	.0	.0	.0	.0	205
MY SC	6.5	8.0	11.0	13.5	12.5	190
MY HV MP	10.0	11.0	14.5	15.5	14.5	----

Backscatter Ratios Have Been Referenced to Open Water

ThFY - Thin First-Year Ice
MFY - Medium First-Year Ice
HV SC - Heavy Snow Cover
PR - Pressure Ridge
OW - Open Water
MY SC - Multiyear with Snow Cover
MY HV MP - Multiyear with Numerous Melt Pools

Significant contrast exists between all the MIZ ice types and open water, except for an ambiguity between the passive microwave signatures of brash ice and open water at 90 GHz. The contrast between ice and water is illustrated in Figure 2 by the clear delineation between floe boundaries.

The L-band (1.2 GHz) ratios indicate brash ice can be distinguished from the other ice and snow categories. Thick snow cover also has a unique cross section signature. The C-band (5.3 GHz) ratios confirm that operation at the higher microwave frequencies is better for differentiating first year from multiyear ice. Thin first-year ice can also be differentiated from medium first-year ice. Note, that the European Space Agency (ESA) will launch a

2

W-Band PMI

X-Band SAR

L-Band SAR

Aerial Photograph

86-823

Figure 2. Synthetic aperture radar images (ERIM CV-580) at 1.3 and
9.8 GHz a passive microwave image (NRL-P3) at 90 GHz, and
an aerial photograph (ERIM CV-580) acquired during
MIZEX-84 serve to illustrate the inter-relationships
between microwave signatures and sea ice features for mid-
summer conditions.

free-flyer (ERS-1) SAR satellite that will operate at C-band. The X-band (9.4 GHz) data yield results similar to those at C-band. Brash ice can be differentiated from multiyear, but not from first-year. However, examination of SAR X-band images shows that brash ice is separable from first-year based on its shape and location (i.e., context). The radar contrast between first-year and multiyear ice decreases at 13.6 and 16.6 GHz. This appears to be due to an increased absorptivity of the snow which results in the snow/ice roughness at the snow/sea ice interface to be less of a contributor.

The W-band data (90 GHz) show significant sensitivity to the distribution of moisture within the boundary of an ice floe. In examining Figure 2, the dark areas within a floe indicate a high snowpack wetness; whereas, the lighter grey-tone indicates better-drained snow in combination with more extensive freezing in its upper layers. Open water meltpools are easily identifiable. MFY has a cooler brightness temperature due to the volume scattering which arises from frozen snow. This, however, is not a unique signature and may be seen in areas of MY ice.

IV. SUMMARY

Microwave measurements were made at frequencies from 1 to 94 GHz of a variety of snow and ice types present in the summer at the marginal ice zone. The measurements which were obtained by a SAR, PMI and helicopter-based scatterometer during the peak of the summer melt, indicated that the snow cover dominates the microwave response. At frequencies below 9.4 GHz (X-band) the slush or superimposed fresh water ice layer that forms at the snow/ice interface is important in determining the observed backscatter. Since in MIZEX-84 the amount of snow cover was well correlated to the individual ice types as as the scale of roughness at the snow-ice interface, it follows that operation at 5 to 10 GHz may be optimal for the discrimination of the thinner first-year ice from the heavily snow covered multiyear ice. Therefore the C-band (5.3 GHz) frequency which will be utilized on the ERS-1 ESA satellite SAR should do a respectable job differentiating first-year from multiyear ice types within the MIZ.

The backscatter ratios further suggest that a multi-frequency approach would provide additional information on ice and snow types. This is due to increased penetration at the lower frequencies and the roughness match of the multiple wavelengths with constituents within the snow and ice media. The passive microwave data show the ability to map the spatial distibution of wetness in the upper layers in the snowpack within floe boundaries. This wetness is often related to snowpack thickness and construction, as well as ice sheet deformation characteristics.

*MIZEX-84 Remote Sensing Special Topic Working Group:

Barbara A. Burns, ERIM, Ann Arbor, Michigan
Donald Cavelieri, NASA Goddard, Greenbelt, Maryland
Per Gloerson, NASA Goddard, Greenbelt, Maryland
Anthony J. Gow, USACRREL, Hanover, New Hampshire
Thomas C. Grenfell, Univ. of Washington, Seattle, Washington
Jim Hollinger, NRL, Washington, D.C.
Mary R. Keller, NRL, Washington, D.C.
Richard K. Moore, Univ. of Kansas, Lawrence, Kansas
Robert G. Onstott, ERIM, Ann Arbor, Michigan
Duncan Ross, Univ. of Miami, Miami, Florida
Robert A. Shuchman, ERIM, Ann Arbor, Michigan
Terry Tucker, USACRREL, Hanover, New Hampshire

REFERENCES

1. Johannessen, O.M. and D. Horn (Ed.) 1984, MIZEX 84 Summer Experiment PI Preliminary Reports (MIZEX Bulletin V), U.S. Army Cold Regions Research and Engineering Laboratory, CRREL Special Report, 84-29.

2. Gray, A.L., R.K. Hawkins, C.E. Livingstone, L. Drapier Arsenault, and W.M. Johnstone, "Simultaneous Scatterometer and Radiometer Measurements of Sea-Ice Microwave Signatures", J. Oceanic Engr., OE-7, No. 1, pp. 20-32, 1982.

3. Onstott, R.G. and S.P. Gogineni, "Active Microwave Measurements of Arctic Sea Ice Under Summer Conditions", J. Oceanic Engr. OE-9, pp. 383-388, 1984.

4. Hallikanen, M., F.T. Ulaby and M. Abdelrazik, "The Dielectric Behavior of Snow in the 3 to 37 GHz Range, Proc. IGARS'84, ESA SP-425, pp. 169-174, Strasbourg, August 27-30, 1984.

5. Tiuri, M., A. Sihvola, E. Nyfors, and M. Hallikainen, "The Complex Dielectric Constant of Snow at Microwave Frequencies", J. Oceanic Engr., OE-9, No. 5, pp. 377-382, 1984.